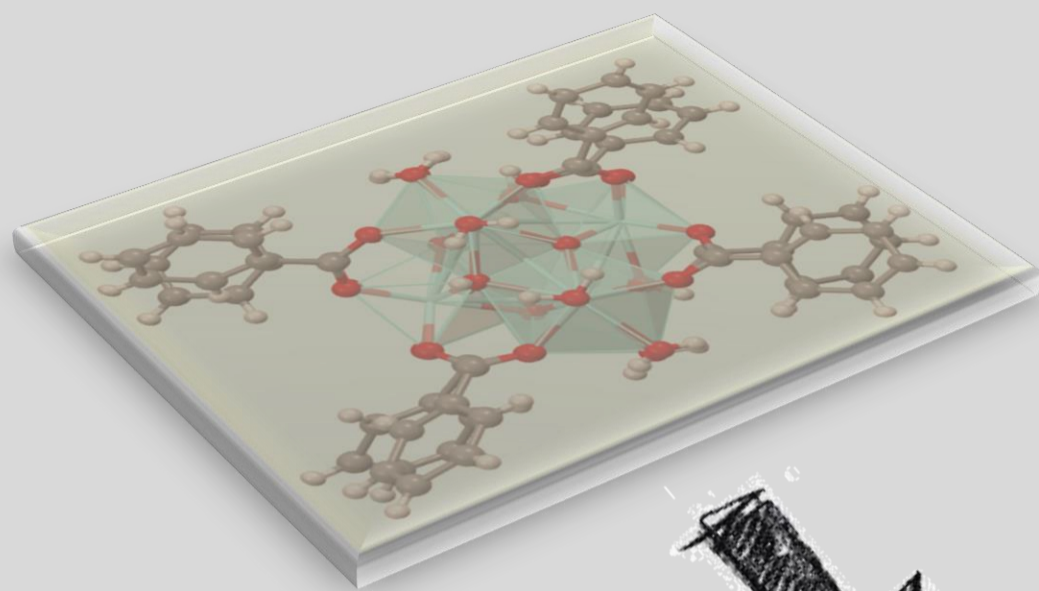
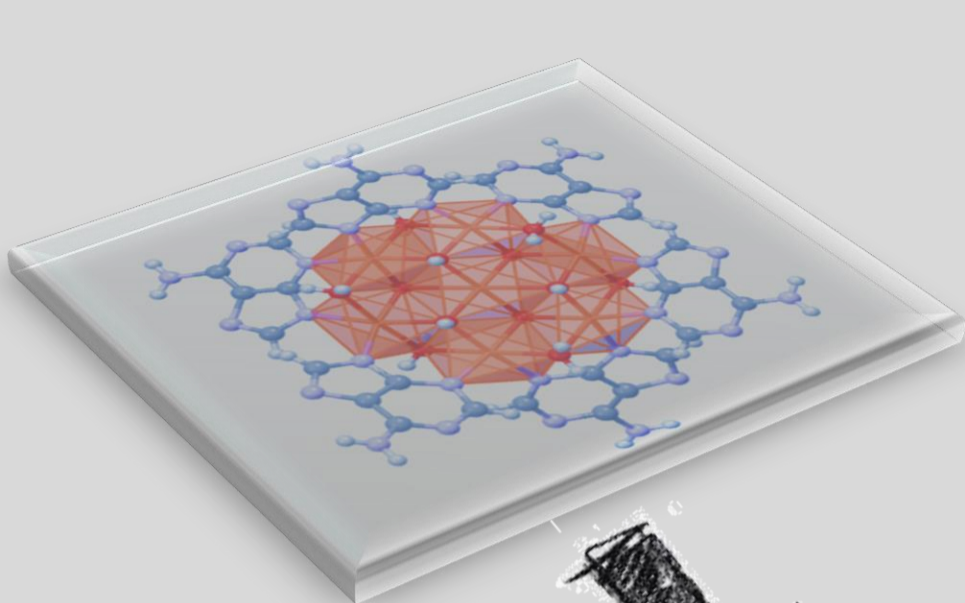


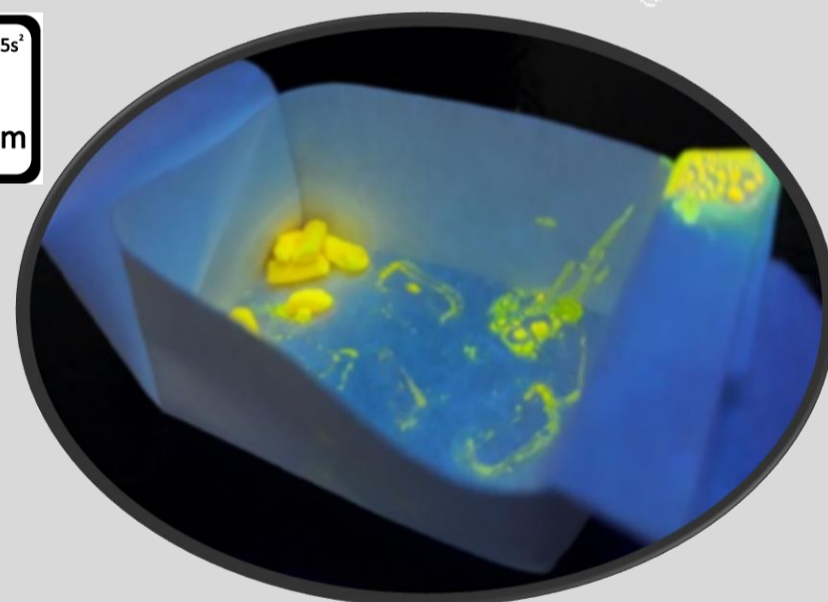
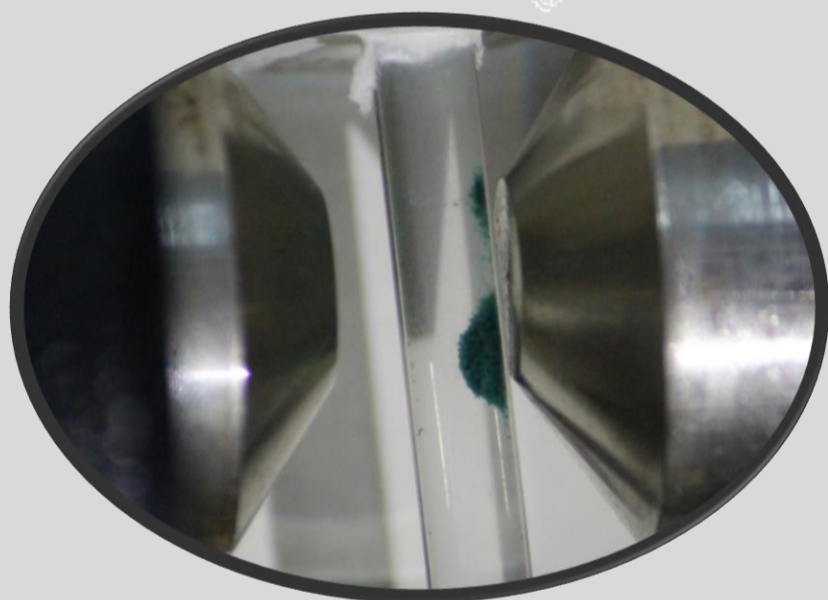
Merging porosity with magnetism and fluorescence in metal-organic materials for sensing purposes



Magnetism



Luminescence



Jon Pascual Colino

Doctoral Thesis

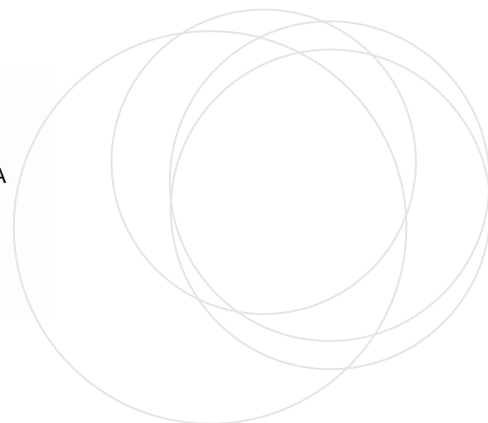
July 2022

eman ta zabal zazu



Universidad
del País Vasco

Euskal Herriko
Unibertsitatea



UPV/EHU
FACULTAD DE CIENCIA Y TECNOLOGÍA
DEPARTAMENTO DE QUÍMICA ORGÁNICA E INORGÁNICA

Merging porosity with magnetism and fluorescence in metal-organic materials for sensing purposes

MEMORIA PRESENTADA POR

Jon Pascual Colino

PARA OPTAR AL GRADO DE DOCTOR EN CIENCIAS QUÍMICAS CON
MENCIÓN DE DOCTOR INTERNACIONAL

Leioa, julio 2022

Dirigida por: Antonio Luque Arrebola
Oscar Castillo García

AGRADECIMIENTOS

Toda historia tiene un inicio y esta comenzó con un grito, ¡futuros químicos en paro, este fin de semana se hace cena de clase!

Cuando empiezas una tesis te explican que es un viaje con bastantes altibajos donde vas a pasar por momentos de desierto total hasta que con suerte encuentres el oasis de los buenos resultados. En mi caso la verdad es que ha sido un viaje enriquecedor hasta el último momento, teniendo la posibilidad de poder viajar, aprender de los mejores tanto fuera como dentro de la Universidad y sobre todo aprender a desenvolverte por ti mismo. Muchas veces se compara con una montaña rusa, pero más bien lo compararía con una en la que tú mismo tienes que subir el vagón para cuando una vez estas en la cima, montarte y disfrutes de lo trabajado.

Cuando envié los datos para mi solicitud de beca para la tesis allá por junio de 2017 fue quizás mi época más solitaria; por temas personales empecé este viaje solo, donde el trabajo era la mejor y única escapatoria. Hoy, junio de 2021, escribo esto desde mi estancia en Arabia Saudí, sí, ¡quién lo diría! Viaje para el cual el camino sí que ha sido una montaña rusa y me ha hecho pasar por los momentos más oscuros de estos últimos años.

En primer lugar, quiero agradecer a mis tutores, Antonio Luque y Oscar Castillo. *Antonio Luque* fue la persona que me “fichó” para el grupo allá por 2015 en la asignatura de tercero que impartías. Durante todos estos años has sido como un padre para mí, ayudándome en todo lo posible, estando en todo momento al inicio de mi andadura con el TFG y TFM y haciéndome ver la suerte que tenía de estar en este grupo y echándome la bronca cuando fuese necesario. Aún me acuerdo del día que nos propusiste a Maite y a mí en tu despacho las dos rutas que había disponibles. Ella eligió la ruta de geles que sonaba tan bien por tener mejor nota, pero visto ahora, gracias por ser tan lista, ya que me ha permitido descubrir el rico mundo de los SMOFs y la cristalografía.

Oscar Castillo, gracias por estar 24/7 para cualquier duda que pudiese tener tanto en la resolución estructural como en el laboratorio, ya fuese fin de semana como en horarios intempestuosas de la tarde/noche, siempre estabas disponible para resolverla. Gracias por todas las horas dedicadas para resolverme todas las dudas de los programas de WINGX y que razón tenías que no aprendería hasta que me pusiese realmente yo solo frente a ellas.

Garikoitz Beobide, idea tuya fue la estancia, durante varias semanas creo que fue la peor decisión de todas por los problemas diarios y quebraderos de cabeza que me generaba, pero antes de ir ya logre un hecho raro, siendo el más joven del grupo, ser de los primeros vacunados. No siendo mi tutor oficial siempre estuviste para cualquier duda y siempre dispuesto a aclarar los conceptos las veces que fuese necesario.

Sonia Pérez, nuestra madre del laboratorio, quizás por ser la más joven nos comprendía la que mejor y sabía realmente los problemas y dudas que rondaban nuestras cabezas. Cuando había algo que no tenías claro sabías que podías acudir a ella, además de tener un ojo clínico por el cual no pasaba ni un ligero error de tu escrito.

A *Mónica Lanchas*, en muchas ocasiones y durante mis momentos más alocados de este último lustro, mi psicóloga de cabecera y siempre dispuesta a echar una mano para dejar el laboratorio como una patena.

No me quiero olvidar de todos los compañeros que he tenido en el laboratorio de MOM como *Jon, Naia, Nerea, Mikel, Rubén* o *Dani*, pero debo destacar a *Maite Perfecto*. Hemos viajado, reído, disfrutado, salvado el culo en muchos momentos; aventuras como perdernos en una huerta del sur de Italia con un coche alquilado, visitar pueblos de nombres impronunciables, conocer Extremadura o recorrerlos Múnich en un día entero. Hemos salido de fiesta mano a mano, te he tenido esclavizada corrigiéndome posts y mira que al inicio de esta aventura éramos casi dos desconocidos de un grupo de amigos de clase, ahora, hasta somos de la misma cuadrilla.

Deseo agradecer a los Servicios Generales de Investigación (SGIker) de la Universidad del País Vasco por su apoyo técnico y humano. En particular a *Javier Sangüesa, Leire San Felices, Aitor Larrañaga* y *Iñaki Orue* por toda su ayuda, los cuales en ciertos momentos les tuve atosigados de trabajo, aunque siempre teníamos momentos para la broma.

También quiero agradecer a todos los compañeros de esta larga maratón que empezamos juntos hace diez años y que hoy en día, de los 12 iniciales, nueve de ellos tras varias vueltas por el mundo seguimos juntos haciendo la tesis: *Carlos Asensio* el listo del grupo, *Lía Campos* la cual nos aporta la cordura necesaria; *Cristian*; *Maite Perfecto* mi apoyo estos cuatro años, *Mikel Rincón* (Mikelon) no cambies nunca; *Carlos Santiago* (Charly) con sus bromas y *Estibaliz Ruiz* (Estitxu) con su alegría y sonrisa permanente que animaba todo el departamento, bendito sea el día que trajiste ese juego de mesa que

tantas risas y anécdotas ha generado o los nuevos fichajes físicos como *Mikel Perez* (Maik) o *Ander Garcia*. No me quiero olvidar de los que ya no están en la universidad como *Lorena Simón*, *Amaia Pereda*, *Aitor Nunes* y *Estela Carballo*. Podría contar mil anécdotas de cenas y quedadas de estos últimos cuatro años, pero sé que las mejores están por llegar. Empecé siendo el calladito del grupo para pasar con los años a ser el pesado organizador de cenas y viajes. Quiero destacar de nuevo a una persona, *Cristian*, inseparables desde segundo de carrera donde nos pasamos todas las tardes estudiando y haciendo esquemas de esquemas de esquemas para mantener las manías. Si no fuese por ti, no creo que hubiese llegado a este punto. Para cuando este defendiendo este trabajo el ya habrá logrado cinco tesis internacionales, 27 orales y 50 papers. Y sí, no te pienso poner el apellido jaja.

Pero en estos cuatro años no ha sido todo trabajar, antes de comenzar el doctorado tuve la suerte de conocer a mi familia de Decathlon. Esos meses finales de 2017 nos juntamos cuatro personas que desde hace años solo ha hecho falta decir “Tengo dos días libres” para preparar una escapada al fin del mundo. Se suele decir que las mejores amistades comienzan cuando chocan o no se caen del todo bien, y así fue con el que ahora tomo como uno de mis mejores amigos, *Alejandro Carrillo*. Quien diría que mi mejor amigo sería Sevillano, pero fue él, el que mayor luz me supo aportar en mi momento más oscuro justo al iniciar el camino de la tesis. Carreras, quedadas y sobre todo humor fue lo que nos hizo conectar, como bien dijo cuándo me denegaron la beca por primera vez, ¡Haber estudiado más! *Amaia Gondra* y *Aitor Oilaskoaga*, juntarnos durante unas horas alrededor de una mesa es dolor de tripa asegurado. Por ese verano de 2019 entero juntos recorriendo Italia, Galicia, Barcelona, Croacia, Asturias... Todos los viajes que la pandemia nos quitó, volverán estos años.

No me quiero olvidar de mi cuadrilla de estos últimos tres años, amigos de hace años que me acogieron como uno más al primer momento. Gracias por esos viernes de Ganeko donde me hacían olvidar lo malos ratos de la semana, los vaciles iban y venían tan pronto dejabas la sudadera. Sobre todo, en la preparación de la estancia donde mi humor no era mi fuerte y estaba lo más huraño posible.

No me quiero olvidar de Sandra, persona muy importante en estos últimos tres años que me ha ayudado y sobretodo soportado en los peores momentos. Los cuales he tenido y mucho hace justo un año. Hubo meses muy negros debido a todos los problemas que me encontré para realizar la tesis, donde no estaba para nada soportable y lograste

alejarme de ese mundo y sacarme una sonrisa. Los fines de semana eran el oasis de la semana donde cogía fuerzas para afrontar los problemas que seguro que me encontraría. Gracias, gracias.

Finalmente me gustaría agradecer a mi familia, a mis padres ya a mi hermana donde durante muchos momentos de la tesis era como un extraño que aparecía y desaparecía. A mis tios y aitites, sobre todo a mi tío Victor, pieza muy importante para mí durante mi infancia y adolescencia y que por fin vuelvo a tenerle cerca y a mi amoma, la más guapa de todas, estés donde estés este tocho va por tí.

Y lejos que suene prepotente quiero agradecerme a mí mismo por no tirar la toalla y por luchar hasta el último momento por sacar la mejor tesis posible, donde se refleje todo el esfuerzo realizado. La vida da muchas vueltas, veamos cual es la siguiente...

Rest in the end, not in the middle

Para mi amoma

De tu nieto más “guapo”

Es lo que tiene ser el único

INDEX

Chapter 1:	1
1.1. INGENIERÍA CRISTALINA: BREVE HISTORIA	3
1.2. REDES METAL ORGÁNICAS (MOFs)	9
1.2.1. Desarrollo de MOFs	14
1.2.2. Estabilidad térmica y química de MOFs	20
1.2.3. Química reticular	22
1.2.4. Métodos de síntesis	26
1.3. REDES METAL BIOMOLÉCULAS (MBioFs)	27
1.4. REDES METAL-ORGÁNICAS SUPRAMOLECULARES (SMOFs).....	31
1.4.1. Ingeniería supramolecular: interacciones	34
1.4.2. Biomoléculas como ligandos en SMOFs (SMBioFs)	38
1.5. GELES METAL ORGÁNICOS (MOGs)	46
1.5.1. Aerogeles Metal-Orgánicos (MOAs).....	50
1.5.2. Secado supercrítico	51
1.6. APLICACIONES DE MATERIALES METAL ORGÁNICOS (MOMs)	52
1.7. OBJETIVOS Y DESARROLLO DEL TRABAJO.....	54
Chapter 2:	59
Homometallic adenine nucleobase based SMOFs	59
2.1. INTRODUCTION.....	61
2.2. SYNTHESIS AND CHEMICAL CHARACTERIZATION	68
2.2.1. Synthesis	68
2.2.2. Infrared spectroscopy	75
2.2.3. Thermal analysis	82
2.2.4. Powder X-ray diffraction	87
2.3. CRYSTALLOGRAPHIC ANALYSIS	93
2.4. Supramolecular architectures based on dimeric metal-adenine entities.....	99
2.4.1. Structural description of compound CU2AD3TB.....	101
2.4.2. Structural description of compound CU2AD2TB.....	107
2.4.3. Structural description of compound CU2ADCAF	111
2.4.4. Structural description of compound CU2ADTP	115
2.5. Crystal structures of compounds containing heptameric units.....	122
2.5.1. Structural description of compounds based on $[\text{Cu}_7(\mu\text{-ade})_6(\mu_3\text{-OH})_6(\mu\text{-H}_2\text{O})_6]^{2+}$ units	126
2.6. Water adsorption	197
2.7. Magnetic properties.....	204

4.3.4. Magnetic sustentation experiments	212
Chapter 3:	219
Heterometallic adenine nucleobase based SMOFs for catalysis	219
3.1. INTRODUCTION.....	221
3.2. SYNTHESIS AND CHEMICAL CHARACTERIZATION	225
3.2.1. Synthesis	225
3.2.2. Infrared spectroscopy	226
3.2.3. Thermal analysis	229
3.2.4 Powder X-ray diffraction	231
3.3. CRYSTALLOGRAPHIC ANALYSIS	234
3.3.1. Structural description of heterometallics compounds	236
3.3.2. Temperature variable XRPD experiments.	244
3.3.3. Catalysis properties	246
Chapter 4:	259
Zr-SMOFs: The chemistry of zirconium/carboxylate clustering	259
4.1. INTRODUCTION.....	261
4.2. SYNTHESIS AND CHEMICAL CHARACTERIZATION	265
4.2.1. Synthesis	265
4.2.2. Infrared spectroscopy	268
4.2.3. Thermal analysis	272
4.2.4. Powder X-ray diffraction	275
4.2.5 Solid state nuclear magnetic resonance (NMR)	279
4.3. CRYSTALLOGRAPHIC ANALYSIS	282
4.4. RESULTS AND DISCUSSION	285
4.4.1. Structural description of compounds.....	285
4.4.2. Mass spectrometry.....	303
4.4.3. Conclusions	313
4.3.4. Further applications.....	317
Chapter 5:	321
Zirconium-polycarboxylate gel systems as substrate to develop advance fluorescence sensing devices.....	321
5.1 INTRODUCTION.....	323
5.2 SYNTHESIS AND CHEMICAL CHARACTERIZATION.....	323
5.2.1 Synthesis	325
5.3 RESULTS AND DISCUSSION	327
5.3.1 Initial MOG optimization.....	327
5.3.2 Zr-BTC-Fluorescein gel optimization.....	327
5.3.3 Zr-BTC-Fluorescein gel qualitative sensing applications	328

5.3.4 Zr-BTC-Fluorescein gel fluorescence measurements	330
5.3.5. Zr-BTC-Fluorophore and quartz-sand composite	331
CONCLUSIONS	341
REFERENCES.....	343
Appendices.....	365
A.1. CHEMICALS.....	367
A.2. INSTRUMENTAL TECHNIQUES	368
A.2.1. Infrared spectroscopy	368
A.2.2. Thermal analysis.....	368
A.2.3. Elemental analyses and inductively coupled plasma (ICP).....	369
A.2.4. Single-crystal X-ray diffraction.....	369
A.2.5. X-ray powder diffraction.....	370
A.2.6. X powder diffraction in mother liquid.....	371
A.2.7. X-Ray Fluorescence (XRF).....	372
A.2.8. X-Ray Photoelectron Spectroscopy.....	372
A.2.9. Transmission Electron Microscopy.....	373
A.2.10. Magnetism measurements	374
A.2.11. Fluorescence measurements	375
A.3. X-RAY FLUORESCENCE (XRF) OF CHAPTER 3.....	¡Error! Marcador no definido.
A.4. MAGNETIC FITTING MODELS	376
A.4. PUBLICATIONS ARISING FROM THIS WORK.....	378

ACRÓNIMOS

ADN	Ácido desoxirribonucleico
ARN	Ácido ribonucleico
BET	Brunauer-Emmett-Teller
BIPY	4,4'-bipiridina
BPDC	Bifenildicarboxilato
CP	Coordination polymer
CSD	Cambridge Structural Database
DHBDC	ácido 2,5-dihidroxi-1,4-bencenodicarboxílico
DMF	N,N-dimetilformamida
EHU-30	Euskal Herriko Unibertsitatea, $[\text{Zr}_6(\mu_3\text{-O})_4(\mu_3\text{-OH})_4(\mu_4\text{-BDC})_6]_n$
ESI-MS	Electrospray ionization–Mass spectrometry
FTIR	Fourier Transform Infrared Spectroscopy
GHSV	Gas hourly space velocity
H	Hoogsteen
H2BDC/BDC	Ácido benceno-1,4-dicarboxílico / Benceno-1,4-dicarboxilato
H3BTC/BTC	Ácido benceno-1,3,5-tricarboxílico / Benceno-1,3,5-tricarboxilato
HF	Fluorescein
HKUST	Hong Kong University of Science and Technology
H4TCPP	4,4',4'',4'''-(Porphine-5,10,15,20-tetrayl)tetrakis(benzoic acid)
HSAB	Hard and soft (Lewis) acids and bases
ICP-OES	Inductively coupled plasma atomic emission spectroscopy
IRMOF-1	Isorecticular metal-organic framework, $\{[\text{Zn}_4(\mu_3\text{-O})(\mu_4\text{-BDC})_3] \cdot (\text{DMF})_8 \cdot (\text{C}_6\text{H}_5\text{Cl})\}_n$
IUPAC	International Union of Pure and Applied Chemistry
LC4	4-(1,8-naphthalimido)benzoate
NMR	Nuclear magnetic resonance
MBioF	Metal-biomolecule framework

M-HOF	Metal Hydrogen Bonded Frameworks
MIL	Materials Institute Lavoisier
MOA	Metal-organic aerogels
MOF	Metal-organic framework
MOG	Metal-organic gels
MOM	Metal-organic materials
PCP	Polímero de coordinación poroso
PDF	Powder diffraction file
SBU	Unidad de construcción secundaria
SMBioF	Supramolecular metal-biomolecule framework
SMOF	Supramolecular metal-organic framework
TEM	Transmission electron microscopy
TOS	Time on stream
UiO	Universitetet i Oslo
W-C	Watson–Crick
XPS	X-ray photoelectron spectroscopy
XRPD	X-ray powder diffraction
XRF	X-ray fluorescence
ZIF	Zeolite Imidazolate Frameworks

Chapter 1:

Introducción

1.1. Ingeniería cristalina: breve historia

1.2. Redes metal orgánicas (MOFs)

1.3. Redes metal biomoléculas (MBioFs)

1.4. Redes metalorgánicas supramoleculares (SMOFs)

1.5. Geles metal orgánicos (MOGs)

1.6. Aplicaciones de materiales metal orgánicos (MOMs)

1.7 Objetivos y desarrollo del trabajo

1.1. INGENIERÍA CRISTALINA: BREVE HISTORIA

Desde la prehistoria, la humanidad ha estado cautivada por su entorno intentando entender y aplicar los elementos que tenemos a nuestro alcance. De esa forma se lograron descubrimientos tan importantes como el fuego, la rueda, las herramientas, etc. La obtención de nuevos materiales mediante una incansable y continua manipulación, modificación y perfeccionamiento ha sido una de las piedras angulares de la evolución humana, ayudándonos en la vida cotidiana y en solucionar o minimizar los problemas de cada época. A lo largo de la historia los avances realizados a través de la observación, ensayo-error y posterior aprendizaje nos ha permitido alterar nuestro entorno con el fin de mejorar nuestra vida en el día a día.

Fue en la Edad Media donde los primeros “químicos” centraron todos sus esfuerzos en lo que hoy se llama la alquimia,¹ al intentar transformar metales pesados en oro. Se encontraron con el problema de la conservación de la materia, pero este incansable esfuerzo de investigación dio lugar al descubrimiento de nuevos elementos y a los conceptos básicos de la Química. Pero no es hasta el siglo XX cuando el ser humano comienza a requerir y desarrollar materiales con una función específica y, de esa forma, sacarles partido a un nuevo nivel. Esto es debido a que las propiedades de un material (físicas, magnéticas, catalíticas, etc.) están correlacionadas con su estructura química.²

El diseño de compuestos con características estructurales específicas que den lugar a las propiedades físico-químicas deseadas ha sido uno de los principales objetivos de los científicos desde el inicio de la química moderna. En 1960, Feynman, ya lanzó la pregunta de “¿cuáles serían las propiedades de los materiales si pudiéramos ordenar los átomos como quisiéramos?”.³ Gracias a las posibilidades que nos ofrece el avance científico se han logrado notables avances en la comprensión y, posteriormente, en el control de la relación entre las propiedades de un material y su estructura. Es este punto donde se puede decir que nace la ciencia de materiales, disciplina que estudia los fundamentos de las propiedades y su relación estructural con un amplio y diverso rango de aplicaciones en el campo de la energía, transporte, alimentación e incluso biosanitario.

¹ Miller, K. P. H. *J. Chem. Educ.* **2015**, 92 (6), 969–970.

² Finn, M. G.; Fokin, V. V. *Chem. Soc. Rev.* **2010**, 39 (4), 1231–1232.

³ (a) Junk, A.; Riess, F. *Am. J. Phys.* **2006**, 74 (9), 825–830. (b) Feynman, R. P. *J. Eng. Sci.* **1960**, 4 (2), 22–36.

La intención de obtener compuestos con propiedades concretas y aplicarlas industrialmente conlleva un gran control estructural de los materiales. Sin embargo, inicialmente no se poseía el control del crecimiento cristalino. Tuvo que pasar cierto tiempo, y tras analizar diversidad de estructuras se llegó a la conclusión de que era necesario la presencia de cierta entidad molecular que ayudase a dirigir el crecimiento de la estructura mediante enlaces covalentes y no covalentes hacia nuestro objetivo final.⁴ De esta forma, la falta de control en la síntesis se eliminaba de la ecuación. Pero no ha sido hasta las últimas décadas, donde un continuo estudio, desarrollo e hincapié en el diseño de estructuras cristalinas, ha dado lugar al término de *ingeniería cristalina*. Este término fue introducido por Pepinsky⁵ en los años 50 y finalmente acuñado por Schmidt en los años 70 tras el estudio de una serie de reacciones en estado sólido de sólidos cristalinos.⁶ Fue Desiraju⁷ quien proporcionó una definición más amplia, describiéndola como “la comprensión de las interacciones intermoleculares en el contexto del empaquetamiento cristalino y la utilización de dicho conocimiento para el diseño de nuevos sólidos con propiedades físicas y químicas deseadas”.

En este sentido, la ingeniería cristalina es un campo que engloba el estudio de las posibles modificaciones o elecciones a realizar en la síntesis molecular y supramolecular y los estudios computacionales de las interacciones intermoleculares para conocer su papel en el empaquetamiento cristalino y generar materiales con unas propiedades determinadas (caracterizadas y cuantificadas por una gran diversidad de técnicas).⁸

Llegado a este punto podemos decir que la correlación entre la forma, simetría y las fuerzas intermoleculares es la clave para el diseño de estructuras cristalinas.⁹ Para llevar a cabo el diseño cristalino de materiales moleculares, sin la presencia de enlaces de coordinación, se hace uso de tectones y sintones, Figura 1.1.¹⁰ Los primeros son moléculas cuyas interacciones están dominadas por fuerzas atractivas específicas y que se enlazan mediante sintones (combinaciones de grupos funcionales o moléculas que se unen

⁴ Pauling, L. *The Nature of the Chemical Bond*, 2nd ed.; University Press: New York, United States of America, **1948**.

⁵ Pepinsky, R. *Phys. Rev.A: At. Mol. Opt. Phys.* **1955**, 100, 971.

⁶ Schmidt, G. M. J. *Pure Appl. Chem.* **1971**, 27 (4), 647–678.

⁷ Desiraju, G. R. *Crystal engineering. The design of organic solids*; Elsevier: Amsterdam Netherlands, **1989**.

⁸ (a) Braga, Dari.; Grepioni, F.; Orpen, G. *Crystal Engineering: From Molecules and Crystals to Materials*, Ed. Springer Science, Erice, Italy, **1999**. (b) Almarsson, Ö.; Zaworotko, M. J. *Chem. Commun.* **2004**, 17, 1889–1896.

⁹ Desiraju, G. R. *J. Am. Chem. Soc.* **2013**, 135 (27), 9952–9967.

¹⁰ Desiraju, G. R. *Angew. Chem. Ed. Engl.* **1995**, 34, 2311–2327.

habitualmente por el mismo tipo de interacciones supramoleculares) dando lugar a estructuras supramoleculares con geometría controlada.¹¹

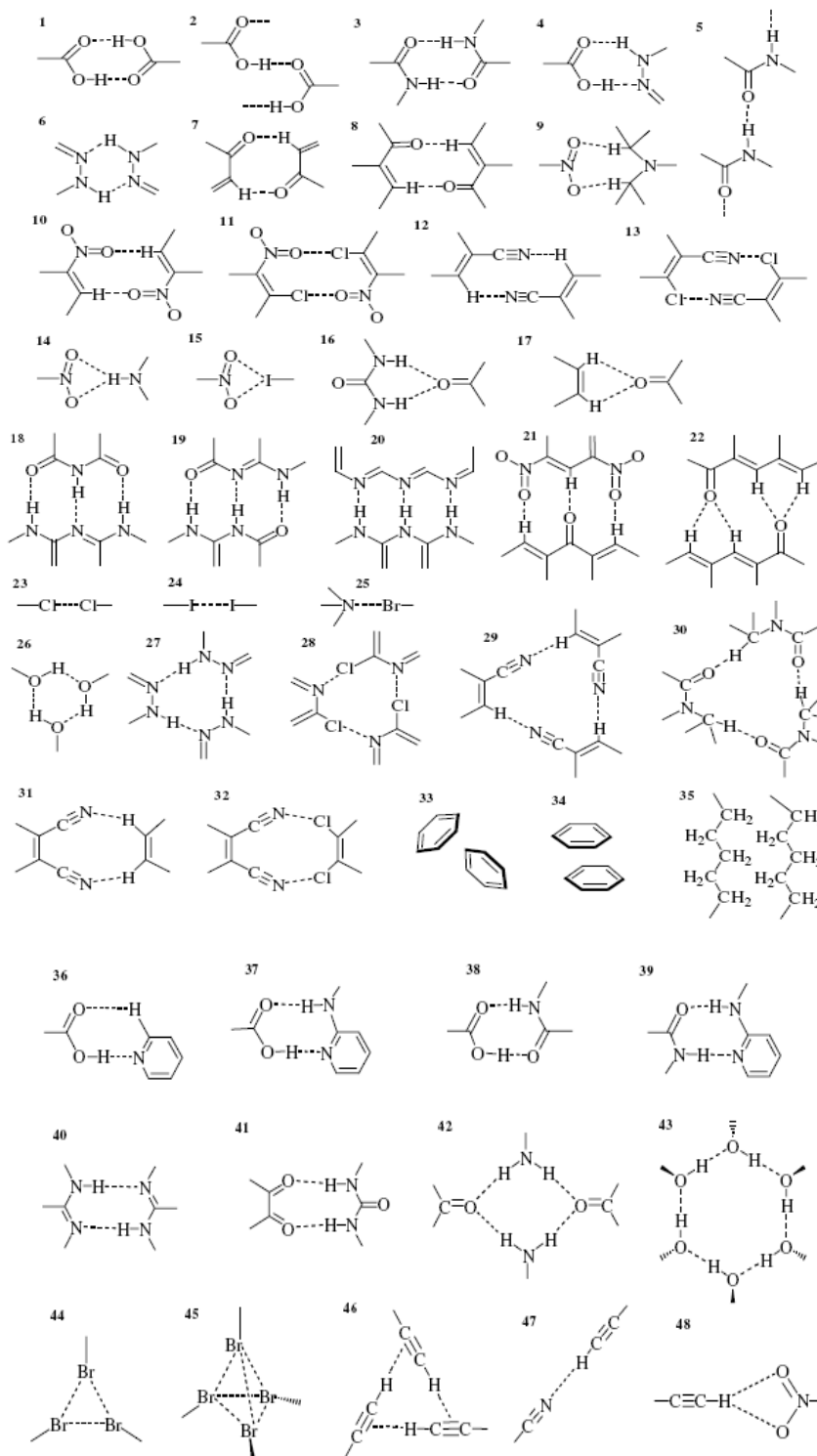


Figura 1.1. Esquema de los diferentes sintones representados por Desiraju en 1995.¹⁰

¹¹ Stang, P. J.; Olenyuj, B. *Acc. Chem. Res.* **1997**, 30, 502–518.

La ingeniería cristalina de los sistemas metal-orgánicos, puede dividirse en dos grandes grupos:

- cristales formados por estructuras extendidas (polímeros de coordinación) que se propagan mediante enlaces de coordinación entre el metal y el ligando.
- cristales formados por bloques de construcción moleculares (neutros o iónicos) que se unen mediante interacciones no covalentes

Este último grupo, comparte características comunes con las estructuras moleculares orgánicas, ya que los bloques de construcción se ensamblan de manera similar fuertemente influenciados por las interacciones intermoleculares. En ambos casos, se logran materiales con porosidad intrínseca o permanente que han despertado un gran interés debido a sus muchas aplicaciones, Figura 1.2.¹²

Los materiales porosos poseen cavidades en sus estructuras que permiten la difusión de distintos tipos de moléculas a través de ellas dando lugar a aplicaciones en áreas como el almacenamiento y separación de gases, intercambio iónico o catálisis, entre otras.¹³ Fue en 1965 cuando se publicaron los primeros polímeros de coordinación porosos, contruidos por metales multivalentes unidos mediante aniones carboxilato (di- y tetratópicos).¹⁴ Estos materiales con una alta área superficial en relación a su peso, se pueden clasificar en tres tipos, según los elementos que lo conformen: orgánicos, inorgánicos e híbridos, Figura 1.3.¹⁵ Históricamente, los materiales porosos inorgánicos como arcillas¹⁶, zeolitas¹⁷ y silicatos¹⁸ mesoporosos han recibido gran atención.¹⁹

¹² (a) Thomas, A. *Nat. Commun.* **2020**, *11* (1), 11–13. (b) Das, S.; Heasman, P.; Ben, T.; Qiu, S. *Chem. Rev.* **2017**, *117* (3), 1515–1563.

¹³ (a) Ishizaki, K.; Komarneni, S.; Nanko, M. *Porous Materials Processing and Applications*; Elsevier Inc., Amsterdam, Netherlands, **1998**, 181–201.

¹⁴ (a) Howarth, A. J.; Peters, A. W.; Vermeulen, N. A.; Wang, T. C.; Hupp, J. T.; Farha, O. K. *Chem. Mater.* **2017**, *29* (1), 26–39. (b) Tomic, E. A. *J. Appl. Polym. Sci.* **1965**, *9* (11), 3745–3752.

¹⁵ (a) Kitagawa, S.; Matsuda, R. *Coord. Chem. Rev.* **2007**, *251* (21–24), 2490–2509. (b) Bravo, L., *Nuevas arquitecturas de MOFs y supraMOFs basadas en la interacción de complejos de cobre con ligandos carboxilato o polioxoaniones*, Tesis doctoral, Euskal Herriko Unibertsitatea (UPV/EHU), 2019.

¹⁶ Gil, A.; Santamaría, L.; Korili, S. A.; Vicente, M. A.; Barbosa, L. V.; de Souza, S. D.; Marçal, L.; de Faria, E. H.; Ciuffi, K. J. *J. Environ. Chem. Eng.* **2021**, *9* (5), 105808.

¹⁷ Rangnekar, N.; Mittal, N.; Elyassi, B.; Caro, J.; Tsapatsis, M. *Chem. Soc. Rev.* **2015**, *44* (20), 7128–7154.

¹⁸ Alothman, Z. A. *Materials (Basel)*. **2012**, *5* (12), 2874–2902.

¹⁹ Gándara, F. *An. R. Soc.* **2012**, *108* (3), 190–196.

Introducción

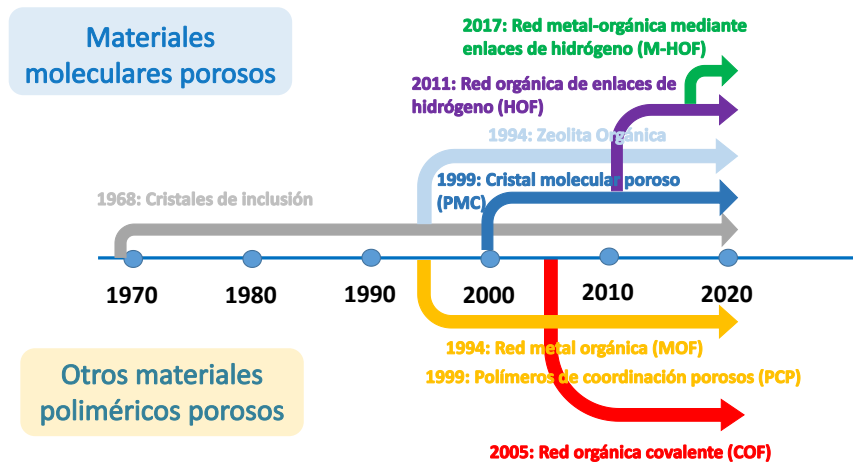


Figura 1.2 Materiales moleculares porosos y sus derivados más representativos.

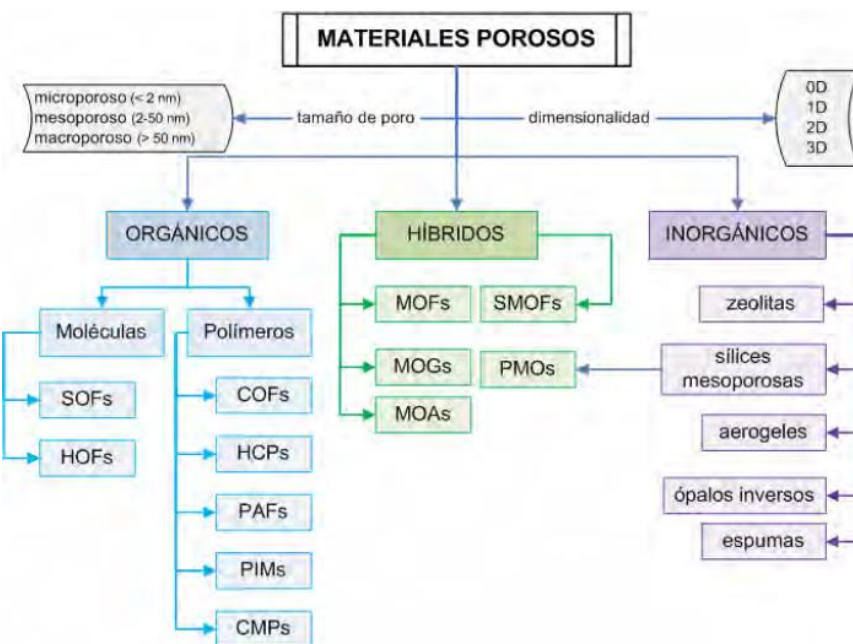


Figura 1.3. Esquema de la nomenclatura empleada para designar a los diferentes materiales porosos más comunes según su naturaleza orgánica, inorgánica o híbrida.¹⁵

Estos materiales también se pueden clasificar por propiedades como el tamaño de las cavidades. Los que tienen tamaños pequeños inferiores a 2 nm se denominan materiales microporosos, mesoporosos en caso de tamaños de 2 a 50 nm y finalmente macroporosos aquellos con diámetros mayores de 50 nm.²⁰ Otra clasificación, acuñada por G. Férey en 2001²¹ se centra en el tipo de cavidades y la intercomunicación entre ellas, existiendo materiales porosos 0D, 1D, 2D y 3D, Figura 1.4.²² Las cavidades 0D, implican que los poros son inaccesibles desde el exterior, las 1D son canales de tamaño de poro

²⁰ Polarz, S.; Smarsly, B. *J. Nanosci. Nanotechnol.* **2002**, *2* (6), 581–612.

²¹ Férey, G. *Chem. Mater.* **2001**, *13* (10), 3084–3098.

²² Little, M. A.; Cooper, A. I. *Adv. Funct. Mater.* **2020**, *30* (41), 1–30.

variable pero no conectado entre ellos; las 2D son cavidades en capas que no se conectan entre diferentes capas y finalmente las 3D, que presentan canales interconectados entre sí tridimensionalmente.

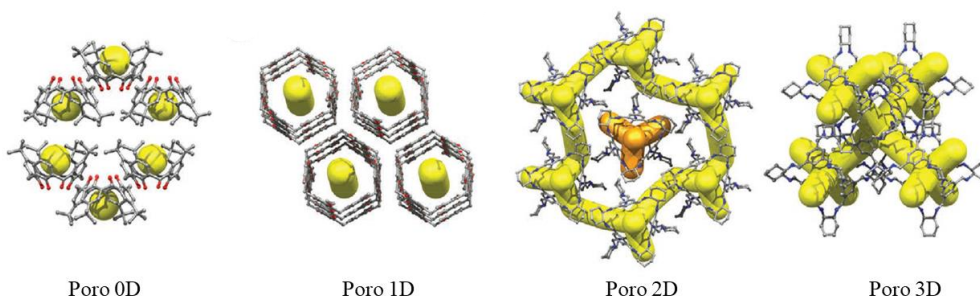


Figura 1.4. Diferentes cavidades de los compuestos porosos con ejemplos de dimensionalidad 0D, 1D, 2D y 3D según Férey.

Como hemos visto anteriormente, existen una gran variedad de materiales porosos, pero nos centraremos en los materiales metal orgánicos (MOM, metal organic materials), y haremos hincapié en los denominados MOFs (metal organic frameworks)²³ SMOFs (supramolecular metal organic frameworks),²⁴ MOGs (metal organic gels)²⁵ o geles metal-orgánicos y MOAs (metal organic aerogels)²⁶ o aerogeles. Los MOFs pertenecen al primer caso de los sistemas metal orgánicos antes descritos, donde los enlaces entre el metal y el ligando que generan la estructura extendida son de tipo covalente. El segundo en cambio, esta constituido por entidades discretas que se unen mediante interacciones intermoleculares. Los MOGs, son sistemas coloidales con agregados de corto alcance y con una fase líquida dispersa en una fase sólida. Cuando se sustituye la parte líquida por un gas como el CO₂ mediante secado supercrítico, se logran materiales con muy baja densidad, MOAs.

²³ Zhou, H-C.; Long, J. R.; Yaghi, O. *Chem. Rev.* **2012**, 112, 673–674.

²⁴ Reger, D. L.; Debreczeni, A.; Smith, M. D.; Jezierska, J.; Ozarowski, A. *Inorg. Chem.* **2012**, 51 (2), 1068–1083.

²⁵ (a) Hou, J.; Sapnik, A. F.; Bennett, T. D. *Chem. Sci.* **2020**, 11 (2), 310–323. (b) Zhang, J.; Su, C. Y. *Coord. Chem. Rev.* **2013**, 257 (7–8), 1373–1408.

²⁶ Hüsing, N.; Schubert, U. *Angew Chem Int Ed Engl* **1998**, 37, 22–45.

1.2. REDES METAL ORGÁNICAS (MOFs)

En ingeniería cristalina un grupo de materiales que han recibido una creciente atención desde su preparación en mitad del siglo XX son los denominados MOFs (metal-organic frameworks)^{23,27} o anteriormente llamados polímeros de coordinación (CPs, coordination polymers).²⁸ Este auge se debe a que autores como Zhou,²⁹ Kitagawa,²⁹ Eddaoudi,³⁰ O’Keeffe,³¹ Robson,³² Yaghi,³³ Lee y Mooreh³⁴ y Férey³⁵ destacaron el gran potencial de estas estructuras con porosidad permanente.

Debido a la enorme cantidad de trabajos publicados sobre estos materiales, el número de estructuras porosas y su terminología se ha incrementado considerablemente, llegándose a nombrar con diferentes nombres al mismo tipo de polímeros de coordinación sin tener en cuenta si eran estructuras porosas o compactas.³⁶ La IUPAC³⁷ con el fin de aclarar la definición de estos materiales, recomendó las siguientes definiciones:

- **Compuestos de coordinación:** Compuesto que consiste en una entidad de coordinación iónica o neutra, formada por un átomo central metálico unido a un grupo de átomos, llamados ligandos.
- **Polímero de coordinación (CP):** Compuesto de coordinación que se expande en 1, 2 ó 3 dimensiones a través de enlaces de coordinación.
- **Redes metal-orgánicas (MOFs):** Polímero (o red) de coordinación con un entramado abierto que presente huecos potencialmente accesibles.

En otras palabras, los MOFs son compuestos cristalinos porosos formados por una parte inorgánica (átomos metálicos o clústeres de los mismos) unidos a moléculas

²⁷ (a) James, S. L. *Chem. Soc. Rev.* **2003**, 32 (5), 276–288. (b) Kitagawa, S.; Kitaura, R.; Noro, S. I. *Angew. Chemie - Int. Ed.* **2004**, 43 (18), 2334–2375.

²⁸ Batten, S. R.; Champness, N. R.; Chen, X. M.; Garcia-Martinez, J.; Kitagawa, S.; Öhrström, L.; O’Keeffe, M.; Suh, M. P.; Reedijk, J. *CrystEngComm* **2012**, 14 (9), 3001–3004.

²⁹ Zhou, H. C. J.; Kitagawa, S. *Chem. Soc. Rev.* **2014**, 43 (16), 5415–5418.

³⁰ Li, H.; Eddaoudi, M.; O’Keeffe, M.; Yaghi, O. M. *Nature* **1999**, 402 (November), 276–279.

³¹ Furukawa, H.; Cordova, K. E.; O’Keeffe, M.; Yaghi, O. M. *Science* **2013**, 341 (6149), 1230444.

³² Batten, S. R.; Hoskins, B. F.; Robson, R. *J. Am. Chem. Soc.* **1995**, 117 (19), 5385–5386.

³³ Yaghi, O. M.; Li, H. *J. Am. Chem. Soc.* **1995**, 117 (41), 10401–10402.

³⁴ Lett, M. A. C. P.; Gardner, G. B.; Venkataramant, D.; Mooreh, J. S.; Lee, S. *Lett. to Nat.* **1995**, 374 (April), 792–795.

³⁵ Cheetham, A. K.; Férey, G.; Loiseau, T. *Angew. Chemie - Int. Ed.* **1999**, 38 (22), 3268–3292.

³⁶ Rowsell, J. L. C.; Yaghi, O. M. *Microporous Mesoporous Mater.* **2004**, 73 (1–2), 3–14.

³⁷ Batten, S. R.; Champness, N. R.; Chen, X. M.; Garcia-Martinez, J.; Kitagawa, S.; Öhrström, L.; O’Keeffe, M.; Suh, M. P.; Reedijk, J. *Pure Appl. Chem.* **2013**, 85 (8), 1715–1724.

orgánicas mediante enlaces de coordinación para dar lugar a redes extendidas.³⁸ Estos compuestos son un punto de encuentro entre la Química Inorgánica, la Química Orgánica y la Ciencia de Materiales.^{31,39} La gran variedad y riqueza que presentan los ligandos orgánicos han permitido obtener redes con poros accesibles tras la eliminación del disolvente, de tamaño y forma ajustable a las necesidades de nuestro interés. Uno de los objetivos más recurrentes es la obtención de materiales con poros suficientemente grandes para ser capaces de incluir moléculas orgánicas, inorgánicas o con interés biológico.

Los MOFs y los otros materiales porosos más empleados hasta la fecha, como las zeolitas, presentan ciertas similitudes, como la porosidad y la formación de las redes estructurales a partir de nodos unidos mediante átomos de oxígeno y nitrógeno (ligandos o aniones óxido, respectivamente). Pero es la direccionalidad estructural de los MOFs lo que les diferencia de las zeolitas o arcillas; es decir, la posibilidad de poder dirigir la estructura final a propiedades específicas mediante la adecuada selección de los componentes del MOF. En el caso de las zeolitas, los nodos son átomos como Si, Al, Ga, Ge, Ti, etc, enlazados tetraédricamente por enlaces covalentes a través de aniones óxido. Los MOFs, al contrario, pueden contener nodos formados por átomos metálicos o clústeres unidos mediante ligandos orgánicos polidentados. Esto hace que las zeolitas presenten unas redes mucho más fuertes y rígidas con mayor estabilidad térmica, llegando a valores de 1000 °C, y estabilidad química; en cambio, los MOFs, muestran una mayor flexibilidad estructural, aunque son térmicamente menos estables.

Por tanto, la elección del nodo metálico correcto y la forma en la que lo conectaremos entre sí es de vital importancia para la preparación de MOFs. La Figura 1.5 nos muestra el número de coordinación más común para diferentes iones metálicos y en la Figura 1.6 se indican algunos ligandos orgánicos y su coordinación más habitual para formar los polímeros de coordinación.

³⁸ Izatt, R. M. *Macrocyclic and Supramolecular Chemistry: How Izatt–Christensen Award Winners Shaped the Field*, John Wiley & Sons, Hoboken, United States of America **2016**. (Schoedel, A.; Yaghi, O. M. Chapter 2: Porosity in Metal-Organic Compounds)

³⁹ (a) Kim, J.; Chen, B.; Reineke, T. M.; Li, H.; Eddaoudi, M.; Moler, D. B.; O’Keeffe, M.; Yaghi, O. M. *J. Am. Chem. Soc.* **2001**, *123* (34), 8239–8247. (b) Férey, G. *Chem. Soc. Rev.* **2008**, *37* (1), 191–214.

Introducción

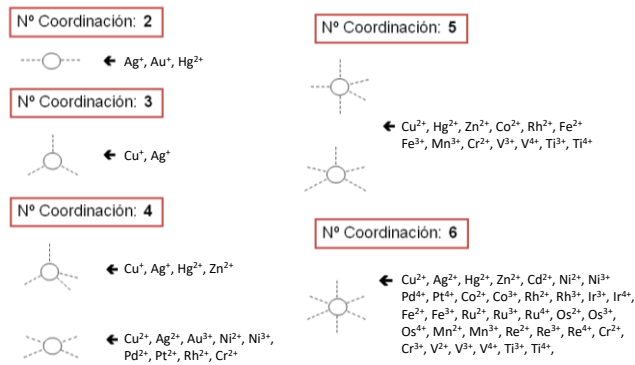


Figura 1.5. Metales de transición que presentan una geometría de coordinación determinada en porcentaje superior al 10%.

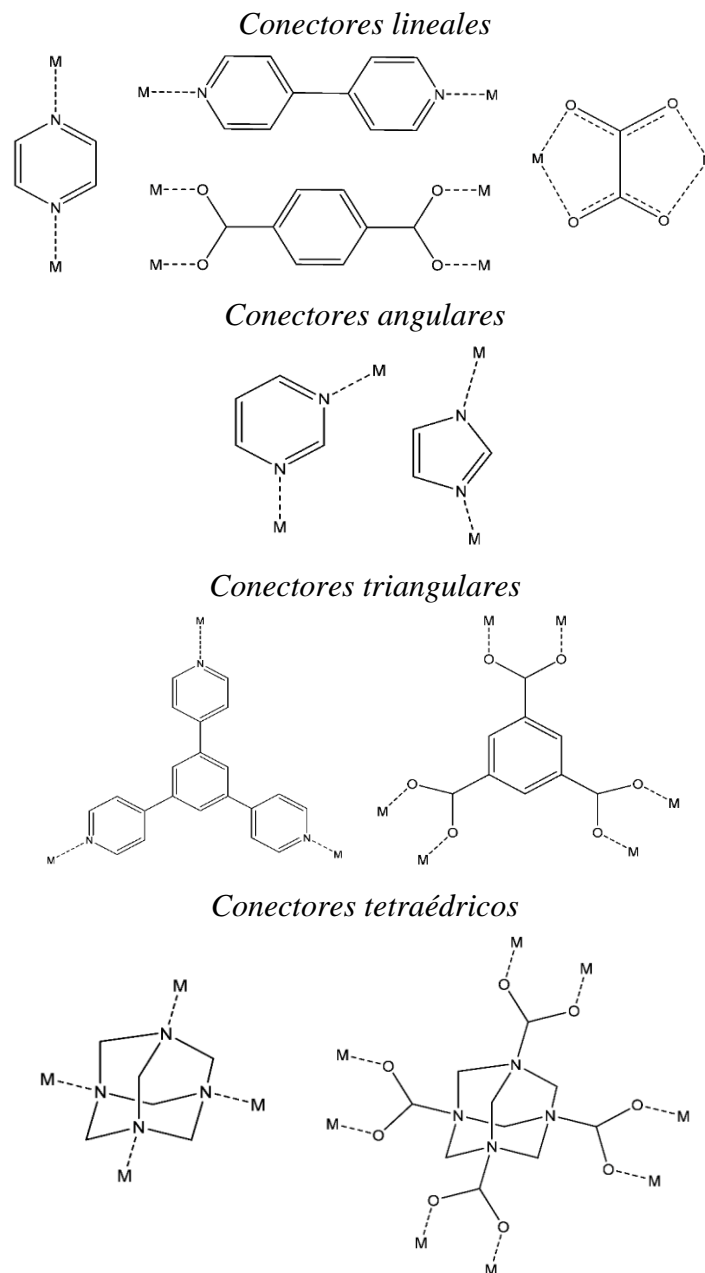


Figura 1.6. Diferentes conectores empleados en ingeniería cristalina de MOFs.

El proceso de autoensamblaje entre los nodos metálicos y los conectores orgánicos del MOF está dirigido por la formación de enlaces de coordinación, aunque también puede aparecer en el edificio cristalino fuerzas supramoleculares, menos fuertes, como son los enlaces de hidrógeno e interacciones de van der Waals. Todo esto conduce a una extensa diversidad estructural que va desde entidades discretas (0D) hasta sistemas extendidos (1D, 2D, 3D). Las Figuras 1.7 y 1.8 esquematizan las diferentes posibilidades.



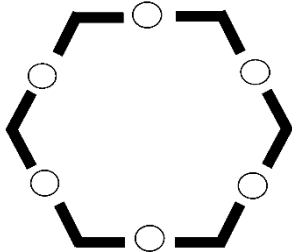





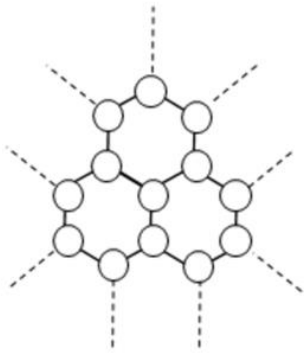
Ligando/Conector	Metal/Nodo	Estructura resultante	Dimensionalidad
 Angular (120 °C)	 Lineal		0D
 Lineal	 Lineal	 Lineal	1D
 Lineal	 Trigonal	 Estructura tipo panal	2D

Figura 1.7. Diferentes combinaciones nodo-conector.

Los ligandos que aparecen en las Figuras 1.7 y 1.8, con conectividad ditópica, tritópica y tetratópica interactúan con el átomo metálico en todas sus posiciones lábiles, saturando así todas las posiciones de coordinación del metal. Pero existen casos donde es necesario bloquear algunas de las posiciones de la esfera de coordinación, imponiendo geometrías del centro metálico que difieren de las comunes para el beneficio sintético. Por tanto, para impedir el crecimiento en todas las dimensiones o al menos reducirla parcialmente se hace uso de ligandos auxiliares o bloqueantes. Partiendo, por ejemplo, como vemos en la Figura 1.9, de un metal con una geometría de coordinación octaédrica, puede ser modificada (a) ocupando las dos posiciones apicales para obtener así un nodo

plano cuadrado y (b) bloqueando tres posiciones en disposición *fac*- al emplear un ligando tridentado quelante, dejando únicamente las otras tres posiciones *fac*- disponibles para un enlace con los conectores orgánicos.


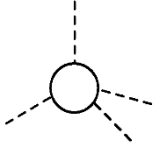
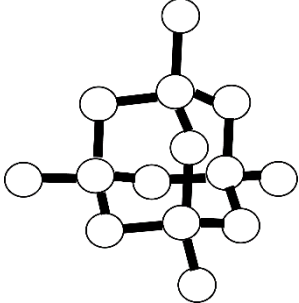
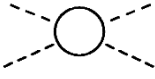
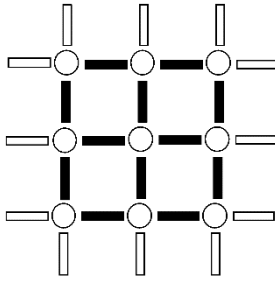
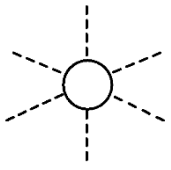
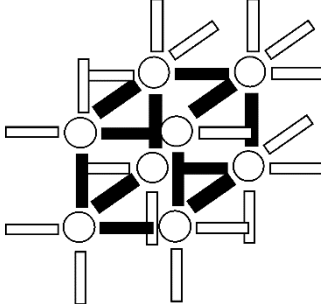

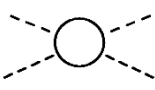
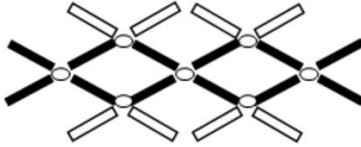
Ligando/Conector	Metal/Nodo	Estructura resultante	Dimensionalidad
			3D
Lineal	Tetraédrico	Tridimensional tipo diamante	
			2D
	Plano cuadrado	Bidimensional cuadrada	
			3D
	Octaédrico	Tridimensional cúbico simple	
			2D
Plano cuadrado	Plano cuadrado	Trenza	

Figura 1.8. Otras combinaciones nodo-conector.


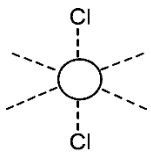
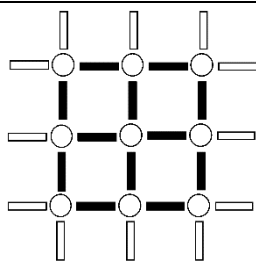
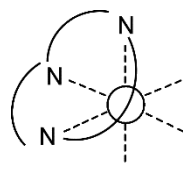

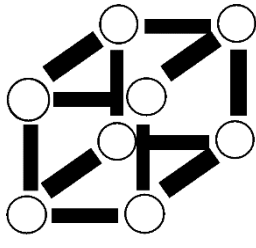
Ligando	Metal	Estructura resultante	Dimensionalidad
 Lineal	 Plano cuadrado	 Plano cuadrado	2D
 Cúbica simple	 Cúbica simple	 Cúbica simple	0D

Figura 1.9. Diferentes estructuras obtenidas utilizando ligandos bloqueantes para generar nodos con nuevas geometrías.

Otro punto, con una gran influencia en la obtención de estos materiales son las condiciones de síntesis. En ellas entran en juego factores como la elección de disolventes, o mezclas de los mismos, o incluso la ausencia de ellos, así como el control del pH, de la temperatura, de la humedad y de la presión. Estas condiciones cobran especial interés en el caso de intentar reproducir diferentes estructuras cristalinas generadas a partir de los mismos bloques de construcción.

1.2.1. Desarrollo de MOFs

El primer MOF tridimensional fue sintetizado en el año 1989 al mezclar en el medio Cu(I) como nodo metálico, tetraédrico, con un ligando de misma geometría como es el 4,4',4'',4'''-tetracianotetrafenilmetano.⁴⁰ El compuesto resultante con entidades $\{\text{Cu}^{\text{I}}(\text{C}(\text{C}_6\text{H}_4\cdot\text{CN}_4))\}_n^{n+}$ y aniones BF_4^- presentaba una estructura tipo diamante con quεδadades en forma de diamante, Figura 1.10a. En 1995, Omar Yaghi y colaboradores publicaron el primer compuesto acuñado como MOF con tipología también de diamante sustituyendo el ligando por 4,4'-bipiridina (BIPY), y con iones nitrato en los huecos para compensar las cargas. De esta forma se lograba el compuesto con formula $\{[\text{Cd}(\text{BIPY})_{1,5}][\text{NO}_3]\}_n$ donde los aniones nitrato se situaban en los huecos para compensar la carga del MOF, Figura 1.10b.³³

⁴⁰ Hoskins, B. F.; Robson, R. *Am. Chem. Soc.* **1989**, *111* (15), 5964–5965.

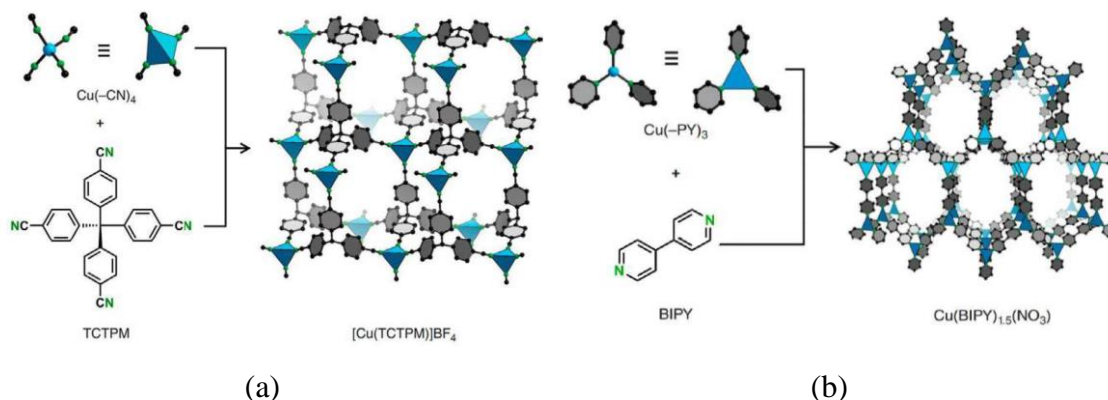


Figura 1.10. Esquemas del (a) primer compuesto 3D extendido y (b) primer compuesto acuñado como MOF.

Más tarde gracias a el estudio realizado por Fujita y colaboradores se sintetizaba el primer material con estructura porosa, con Cd(II) y el ligando rígido 4,4'-bipiridina (BIPY), con aplicaciones catalíticas en reacciones de cianosilaciones de aldehídos y cloración de dihalobencenos.⁴¹

En resumen, los MOFs pueden considerarse materiales altamente ordenados y ensamblados a partir de la combinación nodo-conector. Hasta ahora hemos visto cómo existe una gran riqueza al hablar de los diferentes conectores, con conectividad creciente y tamaño cada vez mayor. Pero existe un cuello de botella a la hora de obtener estructuras porosas complejas empleando únicamente átomos metálicos simples como lo hacía esta primera generación de MOFs. Todos ellos comparten la falta de porosidad permanente en su forma activada (tras la eliminación de las moléculas en los huecos) ya que estas moléculas de disolvente mantenían la estabilidad estructural del sistema. Esto junto con la fragilidad del enlace metal-ligando, hizo que no fuese hasta 1997 cuando se realizaron las primeras medidas experimentales de área superficial para los compuestos con fórmula $\{[M_2(4,4\text{'-BIPY})_3(\text{NO}_3)_4](\text{H}_2\text{O})_x\}_n$ donde M es Co, Ni ($x = 4$) o Zn ($x = 2$) que presentaban porosidad permanente, Figura 1.11.⁴² Como se observa en los ejemplos anteriores, eran los enlaces N–M (átomo metálico), más débiles, los más comunes en este tipo de materiales.

⁴¹ Fujita, M.; Washizu, S.; Ogura, K.; Kwon, Y. J. *J. Am. Chem. Soc.* **1994**, *116* (3), 1151–1152.

⁴² Kondo, M.; Yoshitomi, T.; Seki, K.; Matsuzaka, H.; Kitagawa, S. *Angew Chem Int Ed Engl* **1997**, *36* (16), 1725–1727.

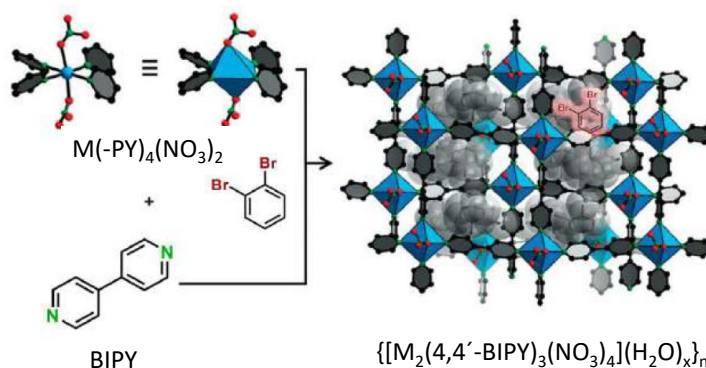


Figura 1.11. Esquema estructural del primer MOF con porosidad permanente empleado para alojar dihalobencenos (molécula en rojo).

Omar Yaghi y colaboradores resolvieron las limitaciones de porosidad permanente de los MOFs de primera generación, empleando como nodos cluster formados por átomos metálicos y grupos funcionales de los ligandos puente que presentan una gran estabilidad y robustez, las denominadas SBUs (de sus siglas en inglés Secondary Building Units), las cuales toma un papel muy destacado para dar lugar a MOFs con porosidad permanente. Estas unidades, concepto introducido por Yaghi en 2003⁴³ e inspirado por un trabajo previo de Robson,⁴⁴ se definen como clusters rígidos de átomos metálicos unidos por los grupos funcionales de ligandos orgánicos rígidos (generalmente ácido carboxílico) que dan lugar a estructuras MOF extendidas con estabilidad estructural y periodicidad. La conectividad de los mismos se define como el número de puntos de anclaje ocupado por un ligando y condiciona la estructura final del MOF. Al incluir el grupo funcional coordinado al metal dentro de la SBU/nodo, el término conector hace referencia únicamente a la parte central del ligando.

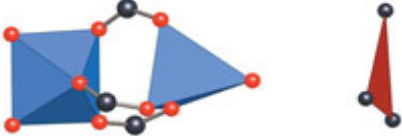

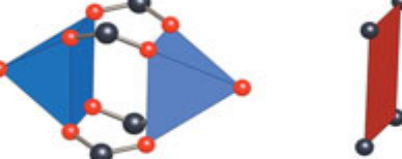
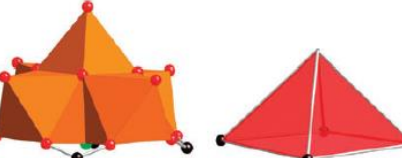

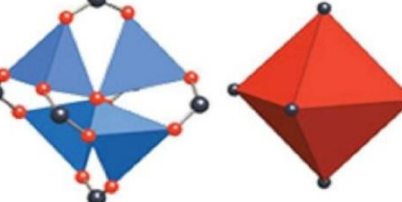
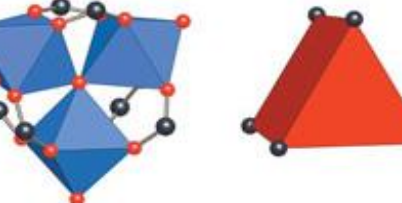
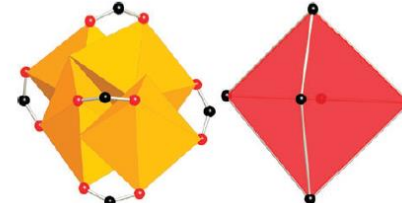
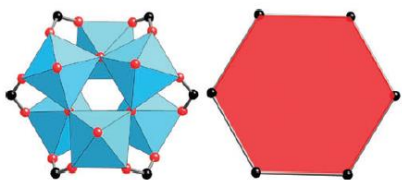
Se han empleado una gran variedad de geometrías SBU en el diseño de estructuras de nuevos MOFs con estructuras robustas y con porosidad permanente.⁴⁵ Las SBUs presentan diferentes números y geometrías de puntos de conexión, como octaédrica, prisma trigonal de seis puntos, tetragonal, *paddle-wheel* (o molino de viento) de cuatro puntos o la triangular de tres, Tabla 1.1.

⁴³ (a) Tranchemontagne, D. J.; Tranchemontagne, J. L.; O’Keeffe, M.; Yaghi, O. M. *Chem. Soc. Rev.* **2009**, 38 (5), 1257–1283. (b) Yaghi, O. M.; O’Keeffe, M.; Ockwig, N. W.; Chae, H. K.; Eddaoudi, M.; Kim, J. *Nature* **2003**, 423 (6941), 705–714.

⁴⁴ Batten, S. R.; Robson, R. *Angew. Chemie - Int. Ed.* **1998**, 37 (11), 1460–1494.

⁴⁵ Kalmutzki, M. J.; Hanikel, N.; Yaghi, O. M. *Sci. Adv.* **2018**, 4 (10), 1-16

Tabla 1.1 Ejemplos de diferentes SBUs.

SBU	Metales	Descripción
	Zn, Co, Cu	<i>Triángulo</i> Un átomo metálico tetraédrico y el otro octaédrico con tres carboxilatos puente
	Mn	<i>Triangular</i> Tres átomos de metal están unidos por un átomo de O central
	Ru, Cu, Rh, Mo, Fe, Ni, Co, Re, Cr, Zn, Mn, W, Tc, Os, Cd, Bi, Rh/Bi, Pt, Al, Mg, In, Pd/Co, Pd/Mn	<i>Paddle-wheel</i> Pirámide de base cuadrada para los dos centros metálicos con cuatro grupos carboxilato puente
	V	<i>Rectangular</i>
	Cd, Zr, Hf, Nb	<i>Tetraedro</i>
	Zn, Co, Be	<i>Octaedro</i> Su estructura consiste en cuatro centros metálicos tetraédricos, cada uno coordinado a tres grupos carboxilato puente y unidos a un O ²⁻ central
	Fe, Cr, Ru, Mn, V, Ni, Sc, Co, Cr/Co, Ir, Al, Fe/Co, Fe/Zn, Cr/Fe/Ni, Zn, Ga, Fe/Ca	<i>Prisma trigonal</i> Tres centros metálicos octaédricos, cada uno coordinado a cuatro grupos carboxilato puente y unidos a un O ²⁻ central
	Ag	<i>Octaedro</i> Cuatro carboxilatos tapan los bordes del cuadrilátero, cada uno puenteano dos Ag. Los dos carboxilatos restantes, perpendiculares, cubren las caras del cuadrilátero.
	Ti, Sn, Ni, Ag	<i>Prisma hexagonal</i> Seis átomos en las esquinas alternantes, completados por seis O ²⁻ . Grupos carboxilatos puentean los metales

Gracias a la introducción de ligandos policarboxílicos, como el ácido benceno-1,4-dicarboxílico (H₂BDC, ácido tereftálico) se logra el compuesto neutro de fórmula [Zn(BDC)(DMF)(H₂O)], nombrado como MOF-2.⁴⁶ El conector es lineal y la SBU está constituida por dos átomos metálicos puenteados por cuatro grupos carboxilato para dar una geometría de paddle-wheel como se puede observar en la Figura 12a. En este caso, el compuesto era estable tras la activación, con un valor de BET (Brunauer-Emmett-Teller) de área específica de $S_{\text{BET}} = 270 \text{ m}^2 \cdot \text{g}^{-1}$. La publicación de este material constituyó el punto de inicio de la obtención de un gran número de MOFs, constituidos por ligandos carboxilatos y SBUs como nodos que presentan porosidad permanente.⁴⁷

Dos de esos compuestos porosos sintetizados según la aproximación de Yaghi fueron los HKUST-1 con fórmula $\{[\text{Cu}_3\text{BTC}_2(\text{H}_2\text{O})_3]\}_n$ donde el ligando trigonal BTC= benceno-1,3,5-tricarboxilato genera una estructura 3D con un 40% de hueco, uniendo clústeres con geometría *paddle-wheel* de Cu(II).⁴⁸ El otro compuesto a destacar, es el [Zn₄O(BDC)₃(DMF)₈(C₆H₅Cl)] sintetizado en 1999 y denominado MOF-5, el primer MOF tridimensional con propiedades adsorbentes, donde el ligando lineal BDC, ácido benceno-1,4-dicarboxílico une clústers de Zn(II) con geometría octaédrica para dar una estructura 3D con poros interconectados de 12 Å de diámetro y ventanas de 8 Å de ancho.³⁰ La fortaleza del enlace M-O entre el metal y los grupos carboxilato en estos dos MOFs les permite mantener su porosidad, cristalinidad y robustez una vez activados a temperaturas de 300 °C, presentando áreas superficiales de 2900 m²·g⁻¹ y 1800 m²·g⁻¹, respectivamente, muy superiores a las de las zeolitas, 560–900 m²·g⁻¹.⁴⁹

El acrónimo empleado para referirse a muchos MOFs deriva de la institución donde se han preparado. HKUST, por ejemplo, proviene de *Hong Kong University of Science and Technology*. En otras ocasiones deriva de alguno de sus constituyentes. Son conocidas varias series de MOFs (Figura 1.12), entre las que podemos citar las siguientes:

- Serie MIL. Los primeros MOFs de esta serie fueron preparados por Férey y colaboradores en Francia en el centro Lavoisier (*Materials Institute Lavoisier*) en

⁴⁶ Li, H.; Eddaoudi, M.; Groy, T. L.; Yaghi, O. M. *J. Am. Chem. Soc.* **1998**, *120* (33), 8571–8572.

⁴⁷ Connolly, B. M.; Aragonés-Anglada, M.; Gandara-Loe, J.; Danaf, N. A.; Lamb, D. C.; Mehta, J. P.; Vulpe, D.; Wuttke, S.; Silvestre-Albero, J.; Moghadam, P. Z.; Wheatley, A. E. H.; Fairen-Jimenez, D. *Nat. Commun.* **2019**, *10* (1), 1–11.

⁴⁸ Chui, S. S. Y.; Lo, S. M. F.; Charmant, J. P. H.; Orpen, A. G.; Williams, I. D. *Science*, **1999**, *283* (5405), 1148–1150.

⁴⁹ Sowunmi, A. R.; Folayan, C. O.; Anafi, F. O.; Ajayi, O. A.; Omisanya, N. O.; Obada, D. O.; Doodoo-Arhin, D. *Data Br.* **2018**, *20*, 90–95.

la década de los 2000. Son materiales estables, de elevadas áreas superficiales, enormes poros y formados por metales trivalentes (Al^{3+} , Fe^{3+} , Cr^{3+}) conectados por ligandos carboxilatos politópicos.⁵⁰ Uno de los más conocidos es el MIL-53(Al) donde el empaquetamiento de cadenas en zigzag de nodos $[\text{Al}(\text{OH})_2(\text{COO})_2]$ genera una estructura porosa y flexible que se adapta a las moléculas huésped que es capaz de adsorber.⁵¹

- Serie ZIF. La estructura de los MOFs de esta serie imita a las zeolitas. Su topología porosa se alcanza mediante el empleo de nodos tetraédricos y ligandos angulares (similares a los enlaces Si–O–Si y Si–O–Al). Los primeros fueron sintetizados en el año 2006 en que se les dio el acrónimo ZIF (*Zeolite Imidazolate Frameworks*), al estar constituidos por agregados de Zn(II) y ligandos imidazolato.⁵² Uno de los más empleado es el ZIF-8, con formula $[\text{Zn}(\text{MeIM})_2(\text{DMF})(\text{H}_2\text{O})_3]_n$ (MeIM: 2-metilimidazol), que presenta porosidad permanente con aplicaciones en separación de CO_2 entre otros.⁵³
- La serie UiO. Su nombre proviene de “*Universitetet i Oslo*” donde en 2008 se publicó el compuesto $[\text{Zr}_6(\mu_3\text{-O}_4)(\mu_3\text{-OH}_4)(\mu_4\text{-BDC})_6]$ (BDC: tereftalato), conocido como UiO-66, con mayor robustez que los anteriores. Su SBU es un clúster hexanuclear $[\text{Zr}_6(\mu_3\text{-O}_4)(\mu_3\text{-OH}_4)(\mu\text{-COO})_{12}]$.⁵⁴ La conectividad del clúster, cada uno está coordinado a 12 ligandos carboxilato y la fortaleza de enlace de Zr–O explican su elevada estabilidad. Se ha empleado en una gran diversidad de aplicaciones como catálisis, adsorción y separación de gases, almacenamiento de H_2 , como sensor e incluso en biomedicina.⁵⁵

⁵⁰ (a) Férey, G.; Serre, C.; Millange, F.; Dutour, J.; Surblé, S. *Science*. **2005**, *309*, 2040–2042. (b) Férey, G.; Serre, C.; Mellot-Draznieks, C.; Millange, F.; Surblé, S.; Dutour, J.; Margiolaki, I. *Angew. Chemie - Int. Ed.* **2004**, *43* (46), 6296–6301.

⁵¹ Serre, C.; Millange, F.; Thouvenot, C.; Noguès, M.; Marsolier, G.; Louër, D.; Férey, G. *J. Am. Chem. Soc.* **2002**, *124* (45), 13519–13526.

⁵² Park, K. S.; Ni, Z.; Côté, A. P.; Choi, J. Y.; Huang, R.; Uribe-Romo, F. J.; Chae, H. K.; O’Keeffe, M.; Yaghi, O. M. *Proc. Natl. Acad. Sci. U. S. A.* **2006**, *103* (27), 10186–10191.

⁵³ Bergaoui, M.; Khalfaoui, M.; Awadallah-F, A.; Al-Muhtaseb, S. *J. Nat. Gas Sci. Eng.* **2021**, *96*, 104289.

⁵⁴ Cavka, J. H.; Jakobsen, S.; Olsbye, U.; Guillou, N.; Lamberti, C.; Bordiga, S.; Lillerud, K. P. *J. Am. Chem. Soc.* **2008**, *130* (42), 13850–13851.

⁵⁵ Zou, D.; Liu, D. *Mater. Today Chem.* **2019**, *12*, 139–165.

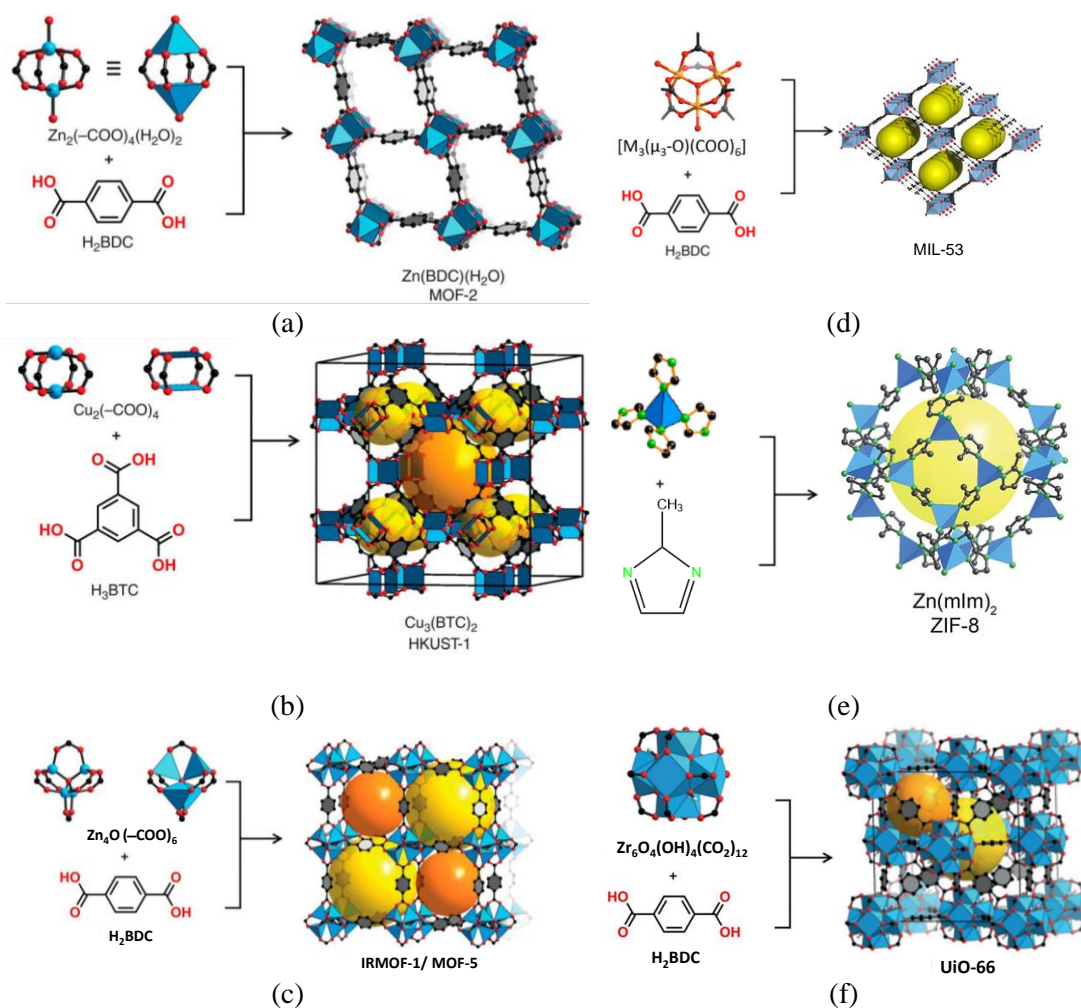


Figura 1.12. Desglose estructural con las SBUs, ligandos y estructura de los compuestos (a) MOF-2, (b) HKUST-1, (c) MOF-5, (d) MIL-53, (e) ZIF-8 y (f) UiO-66.

1.2.2. Estabilidad térmica y química de MOFs

Tal y como se ha comentado anteriormente, los MOFs presentan una menor estabilidad estructural frente a estímulos externos como la temperatura, presión y cambio de pH en comparación con los otros materiales porosos clásicos como las zeolitas. Es por ello, que existe un gran interés en el desarrollo de nuevos materiales MOFs con una mayor resistencia a la temperatura para su uso industrial, mecánica para darles la forma deseada y estabilidad en entornos húmedos o corrosivos.⁵⁶

La estabilidad de los MOFs viene influenciada por múltiples factores, entre los que se encuentran la presencia de defectos estructurales (puntos débiles de la estructura), el tipo de ión metálico o ligando orgánico, la geometría de coordinación metal-ligando o la propia fortaleza del mismo. Pero, mayoritariamente se cree que los enlaces de

⁵⁶ (a) Burch, N. C.; Jasuja, H.; Walton, K. S. *Chem. Rev.* **2014**, *114* (20), 10575–10612. (b) Devic, T.; Serre, C. *Chem. Soc. Rev.* **2014**, *43* (16), 6097–6115.

coordinación relativamente lábiles que soportan las estructuras del MOF son los responsables de la estabilidad limitada de los mismos, siendo el punto donde el compuesto es más sensible frente al ataque del agua y otras especies químicas.⁵⁷

Teniendo en cuenta el concepto de acidez de Pearson, se sabe que la fuerza del enlace metal-ligando con un ligando dado está positivamente correlacionada con las cargas de los cationes metálicos y negativamente correlacionada con el radio iónico. Cuando los ligandos y el entorno de coordinación siguen siendo los mismos, los iones metálicos de alta valencia con altas densidades de carga pueden formar enlaces de coordinación más fuertes y, por lo tanto, un MOF más estable. Esta tendencia está en línea con el principio de ácido/base duro/blando (HSAB) de Pearson y se ha observado en las propiedades físicas de muchos MOFs a lo largo de estas décadas, Figura 1.13. Este principio consiste en que un ligando considerado duro o blando tendrá preferencia y por tanto realizará la unión mediante un enlace fuerte si lo hace con su correspondiente metal duro o blando. Es decir, las interacciones entre ácidos y bases de Lewis duros, o ácidos y bases de Lewis blandos, serán mucho más fuertes que aquellas entre ácidos duros y bases blandas, o ácidos blandos y bases duras. Por ejemplo, los ligandos con grupo funcional carboxilato pueden considerarse bases duras, que forman MOF estables junto con iones metálicos de alta valencia, también denominados ácidos duros, como son los Ti^{4+} , Zr^{4+} , Al^{3+} , Fe^{3+} y Cr^{3+} . Un ejemplo de este tipo de materiales son la familia MIL sintetizada por Ferey con ligandos carboxilatos y metales como el aluminio, cromo y hierro en los MOFs tan estudiados como el MIL-53, MIL-100 o el MIL-101. Otra familia muy importante son los compuestos formados con el metal Zr^{4+} , iniciada en 2008 con el UiO-66.

De acuerdo con el principio HSAB, los MOFs estables también se pueden ensamblar mediante ligandos blandos como el azolato (como imidazolatos, pirazolatos, triazolatos y tetrazolatos) e iones metálicos blandos (como Zn^{2+} , Cu^{2+} , Ni^{2+} , Mn^{2+} y Ag^{+}). En este caso nos encontramos con la familia de los ZIFs con el zinc como metal principal.

Es por ello, que para la obtención de MOF estables, los investigadores optan por construir estructuras con ligandos basados en carboxilatos (bases duras de Lewis) e iones

⁵⁷ (a) Howarth, A. J.; Liu, Y.; Li, P.; Li, Z.; Wang, T. C.; Hupp, J. T.; Farha, O. K. *Nat. Rev. Mater.* **2016**, *1* (15018), 1–16. (b) Morris, R. E.; Brammer, L. *Chem. Soc. Rev.* **2017**, *46* (17), 5444–5462.

metálicos de alta valencia (ácidos duros de Lewis), o ligandos basados en azolatos (bases blandas de Lewis) y metales de transición de baja valencia (ácidos de Lewis blandos).⁵⁸

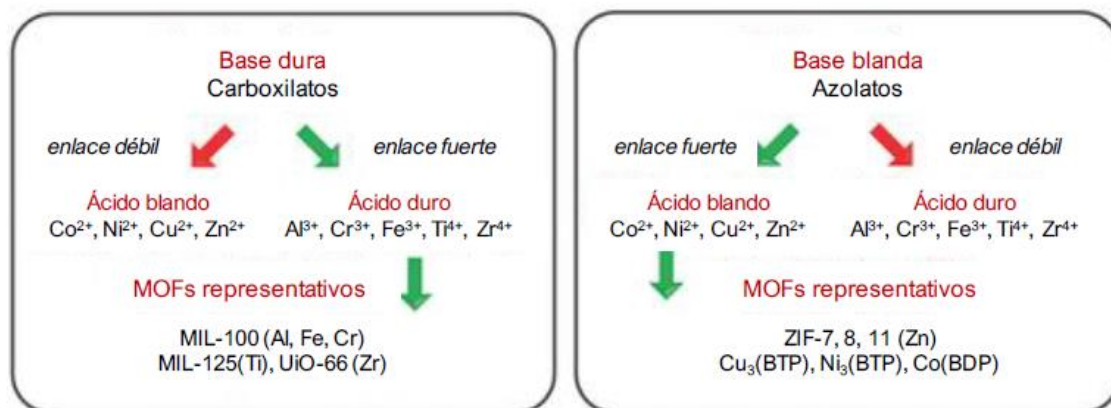


Figura 1.13. Estrategias de construcción según la teoría del principio ácido/base blando/duro de Pearson (HSAB).

1.2.3. Química reticular

La química reticular es el diseño y preparación de materiales a través de la formación de enlaces entre diferentes unidades (clústeres metálicos y ligandos orgánicos) con tamaño y direccionalidad predefinida para dar lugar a estructuras con características topológicas determinadas.⁵⁹ Es decir, la síntesis reticular es la obtención intencionada de una estructura cristalina con una propiedades predeterminadas a partir de bloques de construcción prediseñados. Generalmente la construcción se realiza modificando el tamaño del conector, mientras que los principales grupos funcionales del mismo se mantienen y también la SBU. Aunque se modifique la longitud del conector, siempre que se mantenga su conectividad se obtiene la formación de un mismo tipo de red, pero modificando la distancia entre las SBUs. La aplicación de este principio ha dado lugar al concepto de química isoreticular, donde, por ejemplo, la adición de un anillo aromático al conector, da estructuras con las mismas características geométricas, pero con diferencias en el tamaño de poro, en el área superficial específica y en las propiedades de adsorción. Yaghi y colaboradores han sintetizado 16 MOFs, denominados IRMOFs, isoreticulares. Emplean desde el ligando H_2BDC , hasta el H_2TPC con diferencias de tamaño de hasta 25 angstroms (3,8 a 28,8 Å) con lo que se alcanzan áreas superficiales

⁵⁸ Yuan, S.; Feng, L.; Wang, K.; Pang, J.; Bosch, M.; Lollar, C.; Sun, Y.; Qin, J.; Yang, X.; Zhang, P.; Wang, Q.; Zou, L.; Zhang, Y.; Zhang, L.; Fang, Y.; Li, J.; Zhou, H. C. *Adv. Mater.* **2018**, *30* (37), 1–35.

⁵⁹ (a) Yaghi, O. M.; Kalmutzki, M. J.; Diercks, C. S. *Introduction to Reticular Chemistry: Metal-Organic Frameworks and Covalent Organic Frameworks*; Wiley-VCH Verlag GmbH & Co, Weinheim, Germany **2019**. (b) Lu, W.; Wei, Z.; Gu, Z. Y.; Liu, T. F.; Park, J.; Park, J.; Tian, J.; Zhang, M.; Zhang, Q.; Gentle, T.; Bosch, M.; Zhou, H. C.. *Chem. Soc. Rev.* **2014**, *43* (16), 5561–5593.

superiores a $7000 \text{ m}^2 \cdot \text{g}^{-1}$.⁶⁰ Como se observa en la Figura 1.14, todos mantienen la misma topología cúbica **pcu**. En el caso de los IRMOF-9, -11, -13 y -15 el gran tamaño de hueco da lugar a la interpenetración de las redes y por tanto la reducción de su porosidad potencial.

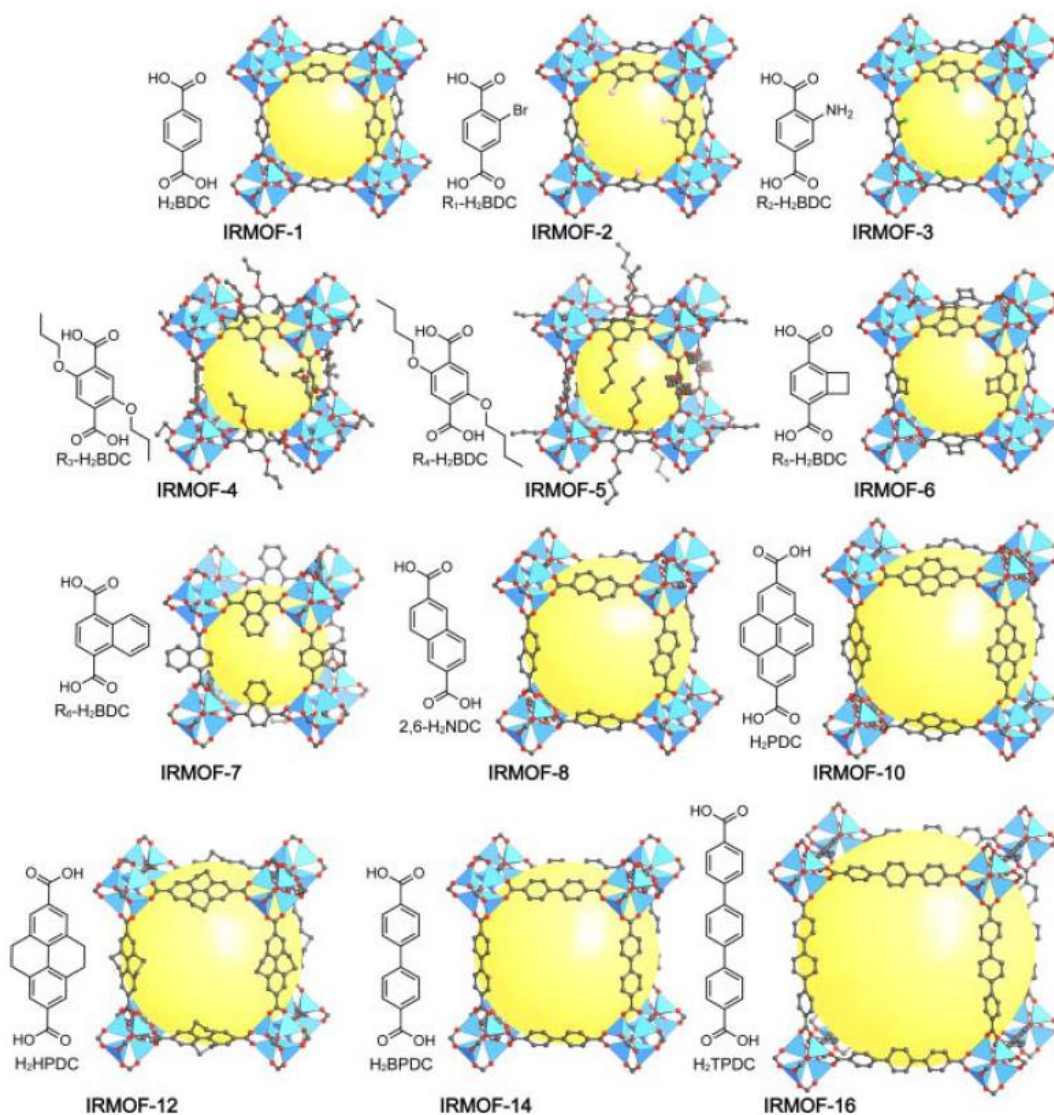


Figura 1.14. Serie de MOFs isoreticulares (IRMOF) basados en el MOF-5 (también denominado IRMOF-1). Los derivados del conector original H_2BDC , junto a la respectiva estructura, se van modificando alargando el tamaño del poro del correspondiente MOF. Código de colores: Zn, azul; O, rojo; C, gris.

Además de modificar el tamaño de poro, en esta serie se aprecia cómo al introducir nuevos sustituyentes en estos ligandos, se pueden incorporar grupos funcionales dentro de los mismos que aportan nuevas funciones o propiedades al material. Con los años, se

⁶⁰ Eddaoudi, M.; Kim, J.; Rosi, N.; Vodak, D.; Wachter, J.; O’Keeffe, M.; Yaghi, O. M. *Science* **2002**, 295 (5554), 469–472.

ha demostrado que este tipo de síntesis es una de las más productivas para la obtención de nuevos MOFs hoy en día.⁶¹

El tamaño de abertura de poro más grande hasta ahora publicado en materiales de tipo MOFs es de unas dimensiones de 85 por 98 Å para el compuesto IRMOF74-XI, sintetizado en el año 2012.⁶² Este compuesto isoreticular del compuesto inicial MOF-74⁶³ con fórmula $\{[Zn_2(\text{DHBDC})] \cdot (\text{DMF})_2 \cdot (\text{H}_2\text{O})_2\}$, donde DHBDC es el ligando ácido 2,5-dihidroxi-1,4-bencenodicarboxílico sustituye el ligando mencionado por uno más grande, pasando de un tamaño de 7 Å a un ligando con diez anillos aromáticos adicionales, llegando a medir 50 Å, este tamaño permite que proteínas atraviesen los poros de compuestos como el IRMOF-74-IV, V, VII y IX, Figura 1.15.

Viendo estos resultados, y el año de su publicación, puede extrañar que no se hayan sintetizado MOFs con tamaños de poro mucho mayores mediante el empleo de ligandos orgánicos de mayor tamaño. El problema surge que, al incrementar excesivamente el hueco vacío, se produce el proceso de interpenetración,^{22,60,64} Figura 1.15, y como resultado, se da una importante disminución del espacio vacío y del poro accesible o se genera una fragilidad estructural, con el consiguiente colapso de la estructura a la hora de eliminar las moléculas de agua de disolvente presentes en esos huecos.⁶⁵ Esto se debe a que los materiales intentan minimizar la energía del sistema mediante el llenado óptimo del espacio vacío, pero la interpenetración estructural sólo puede producirse si el espacio de los poros de una red individual es lo suficientemente grande como para acomodar una red adicional. Además, se cree que varias fuerzas supramoleculares débiles, como los enlaces de hidrógeno, las interacciones de

⁶¹ (a) Yang, Y.; Broto-Ribas, A.; Ortín-Rubio, B.; Imaz, I.; Gándara, F.; Carné-Sánchez, A.; Guillerm, V.; Jurado, S.; Busqué, F.; Juanhuix, J.; MasPOCH, D. *Angew. Chemie - Int. Ed.* **2022**, *61* (4). (b) Jiang, H.; Alezi, D.; Eddaoudi, M. *Nat. Rev. Mater.* **2021**, *6* (6), 466–487. (c) Guillerm, V.; Grancha, T.; Imaz, I.; Juanhuix, J.; MasPOCH, D. *J. Am. Chem. Soc.* **2018**, *140* (32), 10153–10157. (d) Kirchon, A.; Feng, L.; Drake, H. F.; Joseph, E. A.; Zhou, H. C. *Chem. Soc. Rev.* **2018**, *47* (23), 8611–8638. (e) Nguyen, T. T. M.; Le, H. M.; Kawazoe, Y.; Nguyen, H. L. *Mater. Chem. Front.* **2018**, *2* (11), 2063–2069.

⁶² Deng, H.; Grunder, S.; Cordova, K. E.; Valente, C.; Furukawa, H.; Hmadeh, M.; Gándara, F.; Whalley, A. C.; Liu, Z.; Asahina, S.; Kazumori, H.; O’Keeffe, M.; Terasaki, O.; Stoddart, J. F.; Yaghi, O. M.. *Science* **2012**, *336* (6084), 1018–1023.

⁶³ Rosi, N. L.; Kim, J.; Eddaoudi, M.; Chen, B.; O’Keeffe, M.; Yaghi, O. M. *J. Am. Chem. Soc.* **2005**, *127* (5), 1504–1518.

⁶⁴ (a) Lin, X.; Telepeni, I.; Blake, A. J.; Dailly, A.; Brown, C. M.; Simmons, J. M.; Zoppi, M.; Walker, G. S.; Thomas, K. M.; Mays, T. J.; Hubberstey, P.; Champness, N. R.; Schröder, M. *J. Am. Chem. Soc.* **2009**, *131* (6), 2159–2171. (b) Gong, Y. N.; Zhong, D. C.; Lu, T. B. *CrystEngComm* **2016**, *18* (15), 2596–2606.

⁶⁵ Park, Y. K.; Sang, B. C.; Kim, H.; Kim, K.; Won, B. H.; Choi, K.; Choi, J. S.; Ahn, W. S.; Won, N.; Kim, S.; Dong, H. J.; Choi, S. H.; Kim, G. H.; Cha, S. S.; Young, H. J.; Jin, K. Y.; Kim, J. *Angew. Chemie - Int. Ed.* **2007**, *46* (43), 8230–8233.

apilamiento aromático π - π y las fuerzas de van der Waals, desempeñan papeles vitales en la formación de estructuras interpenetradas.⁶⁴

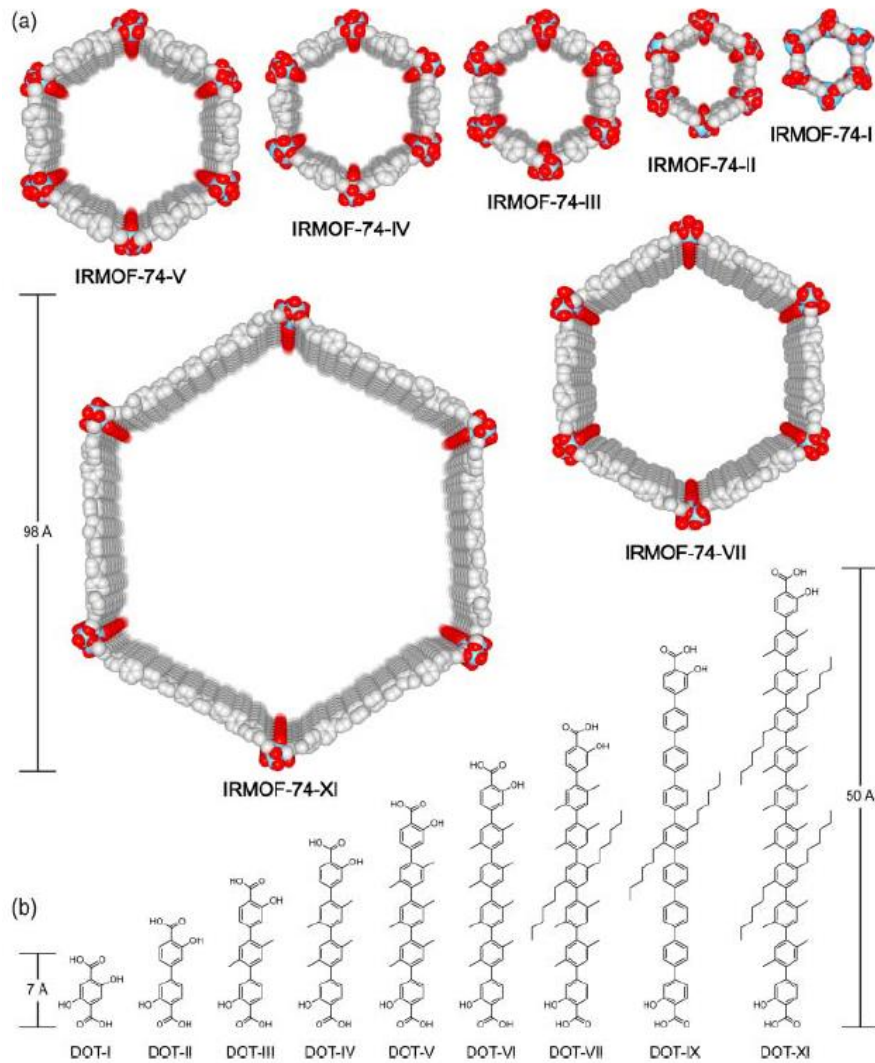


Figura 1.15. Serie isoreticular completa de MOFs a partir del IRMOF-74 con topología **etb** mediante el alargamiento sucesivo del conector palindrómico DOT. En los dibujos de la estructura cristalina se han omitido todas las cadenas laterales alquílicas y los átomos de hidrógeno para mayor claridad. Código de colores: Zn, azul; C, gris; O, rojo.

Un ejemplo de ello es el MOF de fórmula $\{[Zn_4(BTB-NH_2)_3] \cdot x \text{disolvent}\}_n$, también denominado como UPC-98 (donde el ligando empleado es el $H_3BTB-NH_2$: ácido 2'-amino-5'-(4-carboxifenil)-[1,1':3',1''-terfenil]-4,4''-dicarboxílico) con aplicaciones en adsorción y sensorica, Figura 1.16. La presencia de estos poros de gran tamaño, ventanas de $14 \times 17 \text{ \AA}$ facilita este fenómeno muy común en MOFs de Zn. Pero gracias a la funcionalización de dichos poros mediante la presencia de un grupo amino hace que este

compuesto presente un gran rendimiento a la hora de separar mezclas de hidrocarburos C3/C1 y C2/C1.⁶⁶

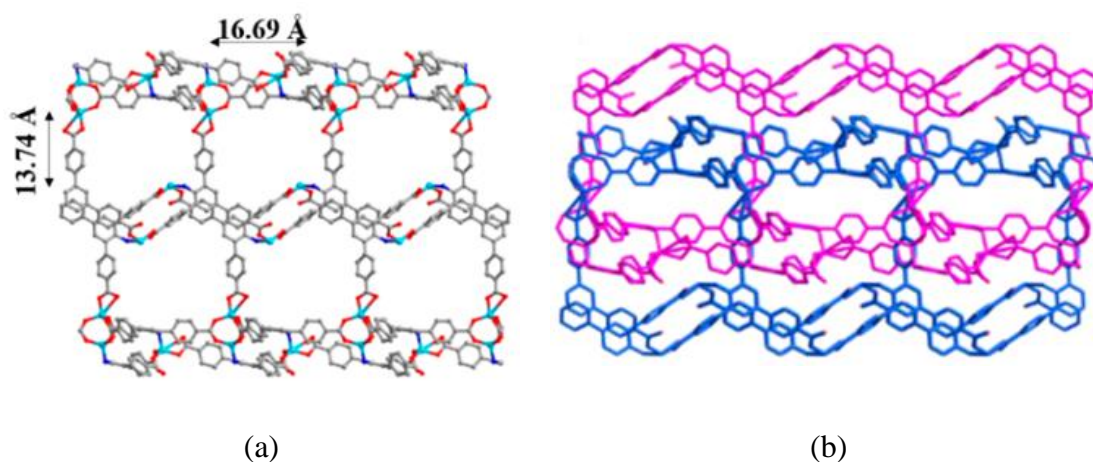


Figura 1.16. (a) Estructura 3D del UPC-98 a lo largo del eje b. (b) Esquema de la doble interpenetración a lo largo del eje b.

1.2.4. Métodos de síntesis

El gran número de aplicaciones de los MOFs con interés industrial ha hecho que sea necesario emplear métodos de síntesis que den lugar a su preparación a gran escala. Las características peculiares de cada familia de MOFs respecto a composición, coordinación y porosidad hace que los métodos de síntesis sean muy diversos y en la mayoría de los casos más complejos que los de las zeolitas,⁶⁷ Entre los problemas que se suelen encontrar destacan:

- Uso de disolventes orgánicos. A gran escala, su costo, toxicidad y, en algunos casos, inflamabilidad se convierten en problemas importantes.
- Acumulación de aniones. Normalmente, las sales metálicas se emplean como precursoras. A gran escala, los nitratos presentan un peligro para la seguridad y otros aniones, como los cloruros, pueden resultar corrosivos. Son preferibles los óxidos e hidróxidos como precursoros.
- Disponibilidad de los ligandos. Muchos MOFs requieren ligandos orgánicos personalizados. Se están desarrollando métodos de producción que también podrían producir estos materiales de partida.

⁶⁶ Wang, X.; Wang, X.; Zhang, X.; Fan, W.; Li, Q.; Jiang, W.; Dai, F.; Sun, D. *Cryst. Growth Des.* **2020**, *20* (9), 5670–5675.

⁶⁷ Rubio-Martinez, M.; Avci-Camur, C.; Thornton, A. W.; Imaz, I.; Maspoch, D.; Hill, M. R.. *Chem. Soc. Rev.* **2017**, *46* (11), 3453–3480.

- Control del tamaño de partícula. Algunas aplicaciones requieren partículas de tamaño nanométrico mientras en otras es deseable partículas más grandes.
- Activación. Para algunas aplicaciones, como la adsorción de gases, se requiere la eliminación de los disolventes y materiales de partida sin reaccionar de sus poros.
- Conformación. También se necesita dar forma a los polvos de MOF producidos para usarlos en aplicaciones industriales reales.

El método más empleado es el *solvothermal*, aunque también se emplean otros métodos de síntesis: microondas, electroquímica, sonoquímica, mecanoquímico. En la síntesis de un MOF, se tienen en cuenta una gran cantidad de parámetros para la optimización de la misma: relación molar entre los reactivos, los disolventes, el pH, la temperatura, la adición de los reactivos, los tiempos/temperatura/presión de reacción. En ocasiones, se añade al medio de reacción una molécula moduladora, que no forma parte de la estructura del MOF, pero que ejerce un efecto plantilla en la construcción de la red, y que sin su presencia es imposible la obtención de la misma.⁶⁸

1.3. REDES METAL BIOMOLÉCULAS (MBioFs)

En muchas de las aplicaciones que presentan los MOFs, como hemos comentado anteriormente, se necesita que sean tanto biológica como medioambientalmente compatibles. La mayoría de las aplicaciones biológicas donde el material está en contacto con el cuerpo humano, como por ejemplo el transporte y posterior liberación de fármacos, requiere que los materiales empleados no sean tóxicos ni liberen compuestos que lo sean al medio.

Por ello que se han empleado biomoléculas como unidades de construcción de MOFs: Redes Metal-Biomolécula (MBioFs, de sus siglas en inglés *Metal-Biomolecule Frameworks*).⁶⁹ Los MBioFs se definen como MOFs constituidos por al menos una biomolécula que ejerce como conector orgánico. El hecho de que las biomoléculas actúen como unidades de construcción aporta varias ventajas:

⁶⁸ (a) Webber, T. E.; Liu, W. G.; Desai, S. P.; Lu, C. C.; Truhlar, D. G.; Penn, R. L.. *ACS Appl. Mater. Interfaces* **2017**, 9 (45), 39342–39346. (b) Morris, W.; Wang, S.; Cho, D.; Auyeung, E.; Li, P.; Farha, O. K.; Mirkin, C. A. *ACS Appl. Mater. Interfaces* **2017**, 9 (39), 33413–33418.

⁶⁹ (a) Beobide, G.; Castillo, O.; Cepeda, J.; Luque, A.; Pérez-Yáñez, S.; Román, P.; Thomas-Gipson, J. *Coord. Chem. Rev.* **2013**, 257 (19–20), 2716–2736. (b) Tamames-Tabar, C.; García-Márquez, A.; Blanco-Prieto, M. J.; Serre, C. Horcajada, P. *In Bio-and Bioinspired Nanomaterials*; Wiley-VCH Verlag GmbH & Co. KGaA, Weinheim, Germany, **2014** (Chapter 4: MOFs in Pharmaceutical technology). (c) Rojas, S.; Devic, T.; Horcajada, P. *Mater. Chem. B* **2017**, 5 (14), 2560–2573. (d) Imaz, I.; Rubio-Martínez, M.; An, J.; Solé-Font, I.; Rosi, N. L.; MasPOCH, D. *Chem. Commun.* **2011**, 47 (26), 7287–7302.

- Las biomoléculas simples, como todos los aminoácidos, las bases nitrogenadas (nucleobases), los azúcares y otros, están disponibles en grandes cantidades de manera rápida, natural y a bajos precios.
- Aumentan la posibilidad de biocompatibilidad del MOF.
- Diversidad estructural, ya que pueden ser tanto rígidas como flexibles. Además, las biomoléculas pueden tener diferentes posiciones de unión al metal, lo cual implica múltiples modos de coordinación, aumentando la diversidad estructural de los MBioFs.
- Muchas biomoléculas tienen propiedades de autoensamblaje intrínsecas, lo que puede usarse para dirigir la estructura y función de los MBioFs.
- Finalmente, algunas biomoléculas son quirales, por lo que pueden obtenerse MBioFs quirales con propiedades y aplicaciones interesantes de reconocimiento, separación y catálisis.

Todas estas características convierten a las biomoléculas como los aminoácidos,⁷⁰ nucleótidos y las bases nitrogenadas (nucleobases)⁷¹ en atractivas unidades de construcción para la obtención de MOFs con nuevas propiedades y aplicaciones que no se podrían alcanzar usando ligandos orgánicos.

En la Figura 1.17a, se muestra un MBioF de fórmula $\{[\text{Cu}_2(\mu_3\text{-ade})_4(\text{H}_2\text{O})_2] \cdot [\text{Cu}(\mu_2\text{-ox})(\text{H}_2\text{O})]_2 \cdot \sim 14\text{H}_2\text{O}\}_n$,⁷² formado por entidades diméricas con forma de molino de viento (*paddle-wheel*) en las que los dos centros metálicos están puenteados mediante ligandos adeninato- $\kappa\text{N}3:\kappa\text{N}9$. El átomo de nitrógeno N7 se conecta a la unidad $[\text{Cu}(\mu_2\text{-ox})(\text{H}_2\text{O})]$ y forma una estructura tridimensional porosa con canales monodimensionales tubulares de 13 Å de diámetro. Como segundo ejemplo en la Figura 17b, se muestra un MOF formado por unidades de construcción secundarias (SBU) zinc-adeninato formado por jaulas octaédricas con una topología **pcu**. Las columnas zinc-

⁷⁰ (a) Ong, T. T.; Kavuru, P.; Nguyen, T.; Cantwell, R.; Wojtas, Ł.; Zaworotko, M. J. *J. Am. Chem. Soc.* **2011**, *133* (24), 9224–9227. (b) Vaidhyanathan, R.; Bradshaw, D.; Rebilly, J. N.; Barrio, J. P.; Gould, J. A.; Berry, N. G.; Rosseinsky, M. J. *Angew. Chemie - Int. Ed.* **2006**, *45* (39), 6495–6499.

⁷¹ (a) Burneo, I.; Stylianou, K. C.; Rodríguez-Hermida, S.; Juanhuix, J.; Fontrodona, X.; Imaz, I.; MasPOCH, D. *Cryst. Growth Des.* **2015**, *15* (7), 3182–3189. (b) Li, T.; Chen, D. L.; Sullivan, J. E.; Kozłowski, M. T.; Johnson, J. K.; Rosi, N. L. *Chem. Sci.* **2013**, *4* (4), 1746–1755. (c) Pérez-Yáñez, S.; Beobide, G.; Bhadbhade, M.; Cepeda, J.; Fröba, M.; Hoffmann, F.; Luque, A.; Román, P. *Chem. Commun.* **2012**, *48* (6), 907–909. (d) Pérez-Yáñez, S.; Beobide, G.; Castillo, O.; Cepeda, J.; Luque, A.; Aguayo, A. T.; Román, P. *Inorg. Chem.* **2011**, *50* (12), 5330–5332. (e) Rachuri, Y.; Kurisingal, J. F.; Chitumalla, R. K.; Vuppala, S.; Gu, Y.; Jang, J.; Choe, Y.; Suresh, E.; Park, D. W. *Inorg. Chem.* **2019**, *58* (17), 11389–11403.

⁷² García-Terán, J. P.; Castillo, O.; Luque, A.; García-Couceiro, U.; Román, P.; Lezama, L. *Inorg. Chem.* **2004**, *43* (15), 4549–4551.

adeninato están interconectadas a través de conectores BPDC (bifenildicarboxilato) dando lugar a una red aniónica que permite el intercambio de los contraiones catiónicos. Los autores demostraron que este compuesto presenta una porosidad permanente con una superficie BET de $1700 \text{ m}^2 \cdot \text{g}^{-1}$, y además, es capaz de almacenar y liberar moléculas de fármacos catiónicos.⁷³

En la figura 1.17c tenemos un MOF de fórmula $[\text{Co}_3(\mu\text{-OH})_4(\mu_5\text{-hipoxantinato-}\kappa\text{N3}:\kappa\text{N7}:\kappa\text{N9}:\kappa\text{O}_6:\kappa\text{O}_6)_2]_n$ con el ligando hipoxantinato (topología **umr**) metamagnético y con capacidad catalítica heterogénea para la oxidación selectiva del cis-cicloocteno. La purina presente en la estructura de los ejemplos anteriores tiene en común que, emplea al menos las posiciones N3, N7 y N9 para unirse a los centros metálicos, proporcionando así un conector rígido que favorece la presencia de huecos en las estructuras resultantes. El compuesto de hipoxantina presenta una porosidad permanente al activarse, capaz de adsorber tanto N_2 ($237 \text{ cm}^3 \cdot \text{g}^{-1}$ a 77 K) como CO_2 ($160 \text{ cm}^3 \cdot \text{g}^{-1}$ a 195 K) con canales 1D de un diámetro de $\sim 4 \text{ \AA}$.⁷⁴

Dentro de este tipo de conectores, los más empleados en la bibliografía son los aminoácidos, Figura 1.18. La gran diversidad de posibilidades de coordinación y gracias al grupo amino y el carboxilato, los hace destacar frente al resto.

⁷³ An, J.; Geib, S. J.; Rosi, N. L. *J. Am. Chem. Soc.* **2009**, *131* (24), 8376–8377.

⁷⁴ Zhang, G.; Li, H.; Zhao, F.; Hu, H.; Huang, H.; Li, H.; Han, X.; Liu, R.; Dong, H.; Liu, Y.; Kang, Z. *Dalt. Trans.* **2013**, *42* (26), 9423–9427.

Introducción

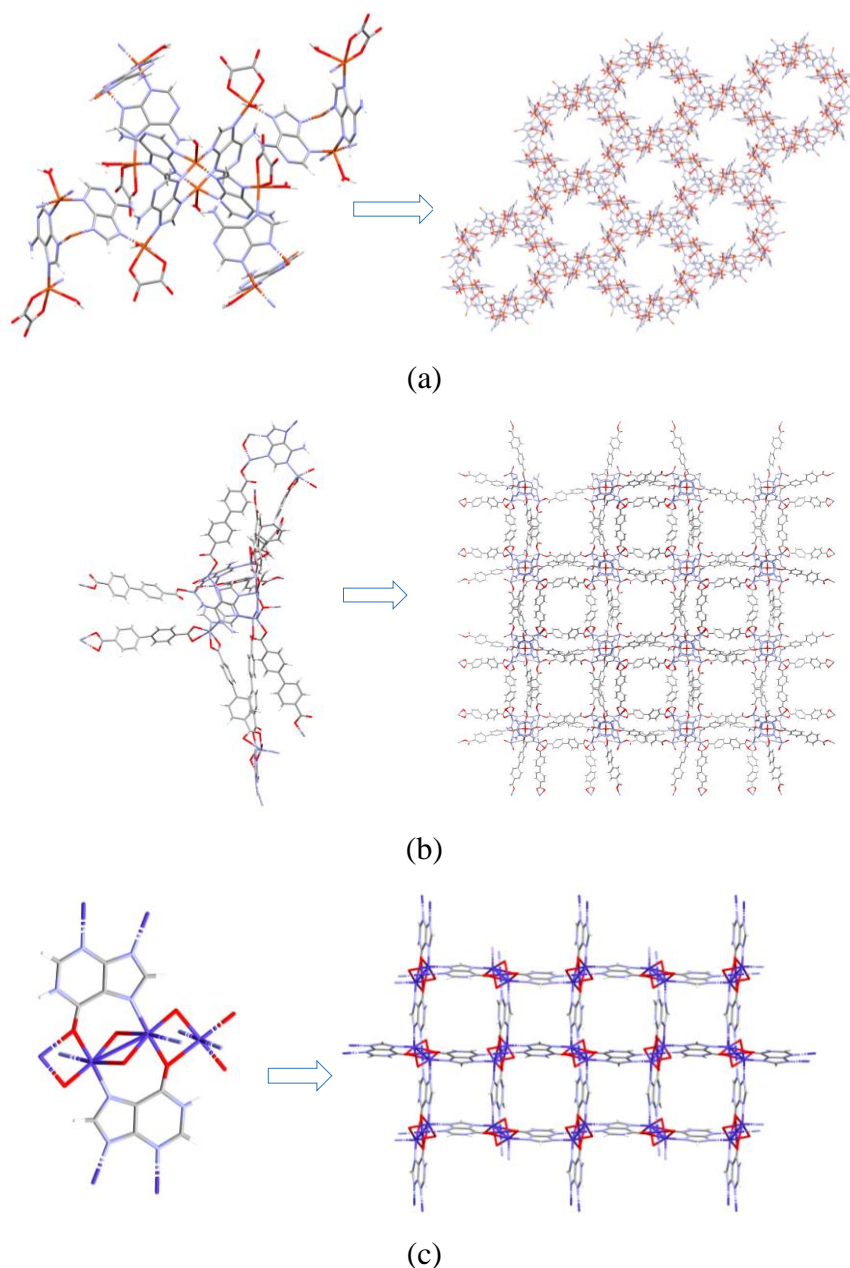


Figura 1.17. Estructura de (a) $\{[\text{Cu}_2(\mu\text{-ade-}\kappa\text{N}3:\kappa\text{N}7:\kappa\text{N}9)_4(\text{H}_2\text{O})_2] \cdot [\text{Cu}(\mu\text{-ox})(\text{H}_2\text{O})_2] \cdot \sim 14\text{H}_2\text{O}\}_n$, (b) $\{(\text{Me}_2\text{NH}_2)_2[\text{Zn}_8(\mu_4\text{-ade-}\kappa\text{N}1:\kappa\text{N}3:\kappa\text{N}7:\kappa\text{N}9)_4(\mu\text{-BPDC})_4(\mu\text{-BPDC})_2(\mu_4\text{-O})] \cdot 8\text{DMF} \cdot 11\text{H}_2\text{O}\}_n$ (BPDC: bifenildicarboxilato) y (c) $\{[\text{Co}_3(\mu\text{-OH})_4(\mu_4\text{-hipoxatinato})_2] \cdot 2\text{H}_2\text{O}\}_n$. Código de colores empleado: H, blanco; C, gris; N, azul; O, rojo; Cu, naranja, Zn, lila, Co, morado.

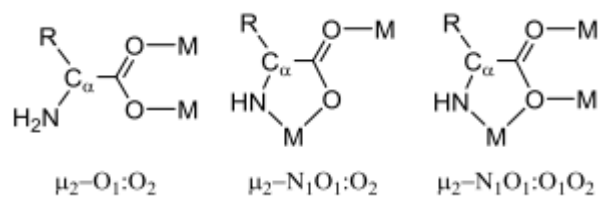


Figura 1.18. Diferentes modos de coordinación de los aminoácidos.

1.4. REDES METAL–ORGÁNICAS SUPRAMOLECULARES (SMOFs)

En los MOFs o MBioFs la conexión entre las unidades estructurales se establece exclusivamente mediante enlaces de coordinación. Sin embargo, también se han publicado compuestos con porosidad permanente donde la conectividad es mantenida por interacciones no covalentes como apilamientos π – π , fuerzas de carácter electrostático, fuerzas de Van der Waals y, fundamentalmente, enlaces de hidrógeno.⁷⁵ De esta forma se obtienen los denominados SMOFs,⁷⁶ término que fue acuñado por Daniel L. Reger,^{24,77} donde las interacciones supramoleculares sustituyen a los enlaces de coordinación en los MOFs, Figura 1.19.

Las interacciones supramoleculares son generalmente más débiles que los enlaces covalentes. Las energías de los enlaces de hidrógeno se encuentran normalmente en el intervalo 10–40 kJ·mol⁻¹, aunque pueden llegar en casos extremos a 170 kJ·mol⁻¹, mientras que los enlaces covalentes que implican a un centro metálico en los compuestos de coordinación oscilan entre 300–600 kJ·mol⁻¹.⁷⁸ La energía de estas interacciones supramoleculares es suficiente para dar cierta estabilidad a la red del SMOF, y su vez le confiere un grado de flexibilidad estructural que puede ser utilizado en ciertas aplicaciones.

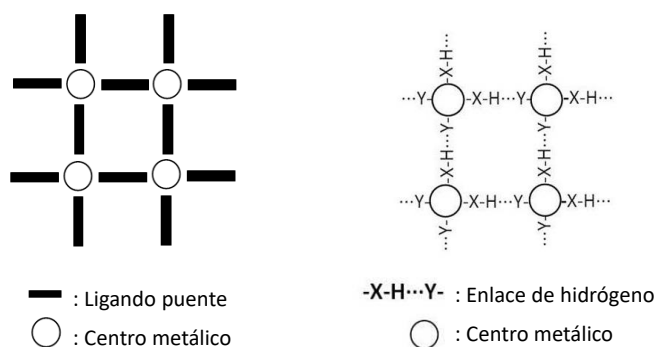


Figura 1.19. Diferencias entre los directores de la estructura cristalina entre los MOFs y los SMOFs: (a) enlaces de coordinación en MOFs y (b) enlaces de hidrógeno en SMOFs.

⁷⁵ (a) Dhotel, A.; Chen, Z.; Delbreilh, L.; Youssef, B.; Saiter, J. M.; Tan, L. *Int. J. Mol. Sci.* **2013**, *14* (2), 2303–2333. (b) He, Y.; Xiang, S.; Chen, B. *J. Am. Chem. Soc.* **2011**, *133* (37), 14570–14573. (c) Kim, H.; Kim, Y.; Yoon, M.; Lim, S.; Park, S. M.; Seo, G.; Kim, K. *J. Am. Chem. Soc.* **2010**, *132* (35), 12200–12202. (d) Fournier, J. H.; Maris, T.; Wuest, J. D.; Guo, W.; Galoppini, E. *J. Am. Chem. Soc.* **2003**, *125* (4), 1002–1006. (e) Cook, T. R.; Zheng, Y. R.; Stang, P. J. *Chem. Rev.* **2013**, *113* (1), 734–777.

⁷⁶(a) Pena, C. *Supramolecular Systems: Chemistry, Types & Applications. Chemistry Research and Applications*; Nova Science Publishers Inc, **2016** New York, United States of America. (b) Pérez-Yañez, S.; Beobide, G.; Castillo, O.; Cepeda, J.; Luque, A. *Supramolecular Metal-Organic Frameworks based on metal-nucleobase entities*; Nova Science Publishers Inc., **2017** New York, United States of America.

⁷⁷ Reger, D. L.; Debreczeni, A.; Smith, M. D. *Eur. J. Inorg. Chem.* **2012**, No. 4, 712–719.

⁷⁸ Jiang, J.; Zhao, Y.; Yaghi, O. M.. *J. Am. Chem. Soc.* **2016**, *138* (10), 3255–3265.

Un ejemplo de SMOF es el sintetizado por Reger y colaboradores con fórmula $[\text{Zn}_2(\text{LC})_4(\text{DMSO})_2]_3 \cdot 2(\text{CH}_2\text{Cl}_2)$ (LC4: 4-(1,8-naftalimido)benzoato), Figura 1.20a, donde SBUs con forma de paddle-wheel de $\text{Zn}_2(\text{O}_2\text{CR})_4$ con dos centros de zinc(II) se encuentran unidos por cuatro ligandos de carboxilato. La posición axial en cada átomo de zinc está ocupada por una molécula de dimetilsulfóxido (DMSO), que está desordenada en dos posiciones. Las SBU diméricas se organizan en una red supramolecular tridimensional abierta mediante dos tipos diferentes de interacciones $\pi-\pi$. Estas interacciones $\pi-\pi$ se forman entre los grupos naftalimida de un dímero que interactúan con cuatro unidades diméricas adyacentes, Figura 1.20b.⁷⁹

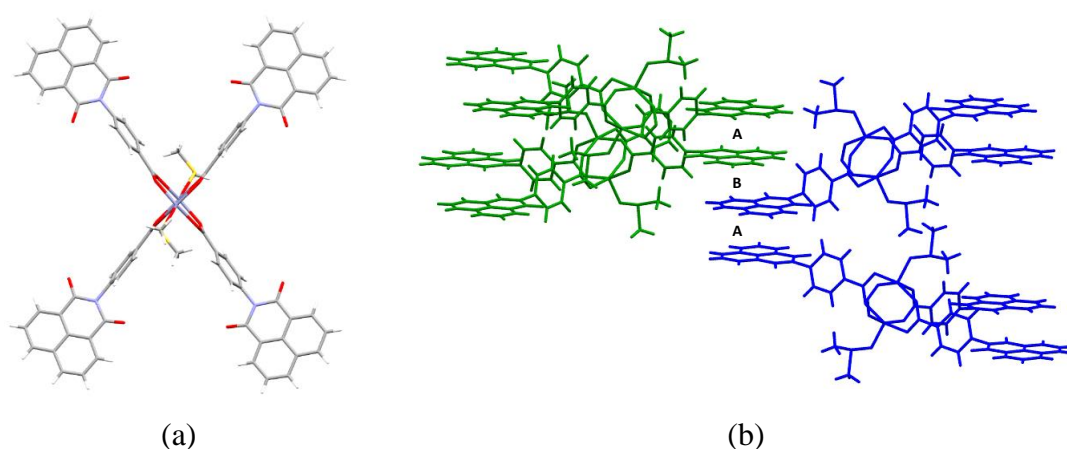


Figura 1.20. (a) Estructura molecular del SMOF (b) Dos pares de dímeros de $[\text{Zn}_2(\text{LC})_4(\text{DMSO})_2]_3 \cdot 2(\text{CH}_2\text{Cl}_2)$ generando la red 3D a través de los apilamientos $\pi-\pi$.

Un inconveniente en cuanto a la aplicabilidad de las estructuras porosas de SMOFs es que, debido a la menor fortaleza de las interacciones entre las unidades estructurales, es habitual que al eliminar las moléculas de disolvente situadas en los poros, la estructura cristalina colapse, perdiendo la porosidad intrínseca, Figura 1.21.⁸⁰ Pero esta desventaja, también permite regenerar la estructura mediante procesos de recristalización mucho más fácilmente que en el caso de los MOFs, donde es necesario una mayor cantidad de energía para modificar los enlaces.⁸¹

⁷⁹ Reger, D. L.; Debreczeni, A.; Smith, M. D. *Inorg. Chem.* **2011**, *50* (22), 11754–11764.

⁸⁰ (a) Lin, R. B.; He, Y.; Li, P.; Wang, H.; Zhou, W.; Chen, B. *Chem. Soc. Rev.* **2019**, *48* (5), 1362–1389. (b) Holst, J. R.; Trewin, A.; Cooper, A. I. *Nat. Chem.* **2010**, *2* (11), 915–920. (c) McKeown, N. B. *J. Mater. Chem.* **2010**, *20* (47), 10588–10597. (d) Barbour, L. J. *Chem. Commun.* **2006**, No. 11, 1163–1168.

⁸¹ (a) Mastalerz, M.; Oppel, I. M. *Angew. Chemie - Int. Ed.* **2012**, *51* (21), 5252–5255. (b) Lauher, J. W. *Science*. **2011**, *333* (6041), 415–416.

Introducción

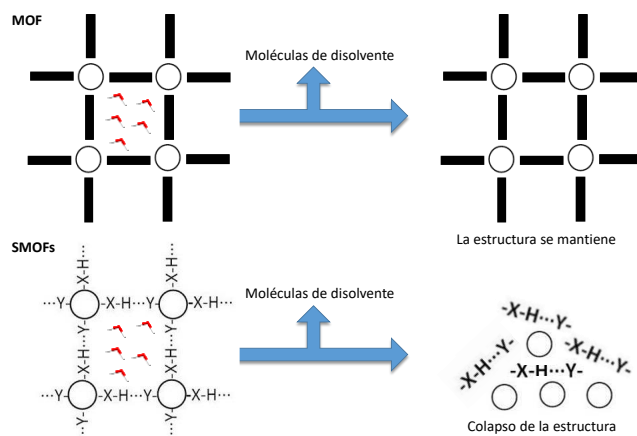


Figura 1.21. Diferencias entre la activación de los MOFs y SMOFs.

El problema anteriormente descrito lleva a la preparación de SMOFs donde la conectividad no se basa en una única interacción supramolecular, como los enlaces de hidrógeno, sino que está reforzada por otras interacciones supramoleculares como los apilamientos π - π . Esta situación se puede observar en el compuesto de fórmula $[\text{Cu}_2(\mu\text{-adenina})_2(\mu\text{-Cl})_2(\text{Cl})_2] \cdot 2\text{MeOH}$, (Figura 1.22) donde los apilamientos π - π entre las adeninas del dímero y los enlaces de hidrógeno entre sus caras Watson-Crick refuerzan la estructura manteniendo la porosidad una vez activada.⁸²

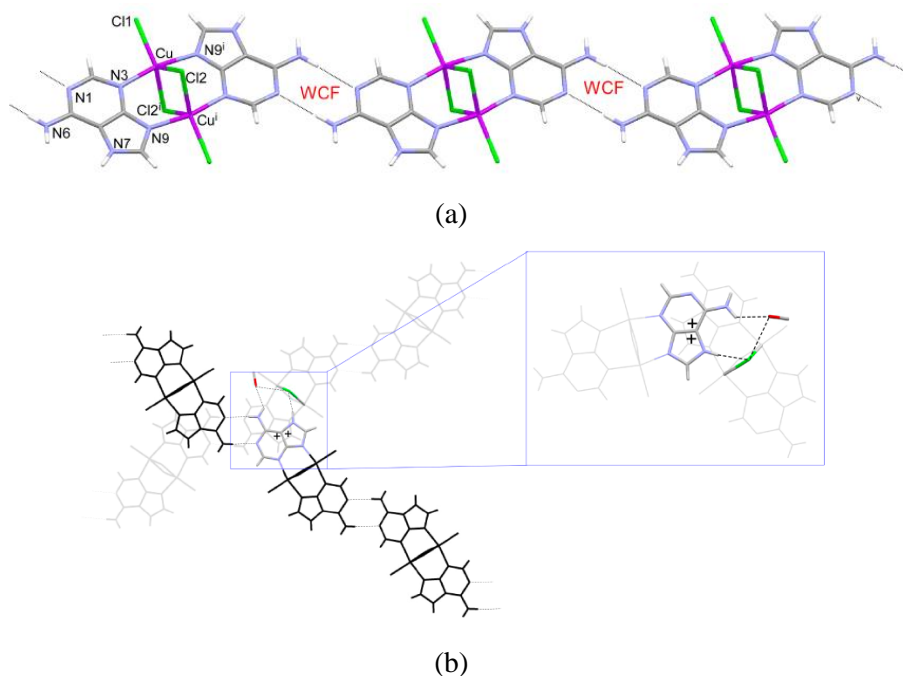


Figura 1.22. (a) Cadenas de enlaces de hidrógeno complementarios entre las adeninas de los dímeros y (b) apilamientos π - π entre los dímeros.

⁸² Thomas-Gipson, J.; Beobide, G.; Castillo, O.; Fröba, M.; Hoffmann, F.; Luque, A.; Pérez-Yáñez, S.; Román, P. *Cryst. Growth Des.* **2014**, 14, 4019–4029

1.4.1. Ingeniería supramolecular: interacciones

El concepto de química supramolecular fue empleado por primera vez en 1978 por el premio Nobel Jean-Marie Lehn, quien la definió como la química de los enlaces supramoleculares.⁸³ Cabe destacar los siguientes tipos de interacciones supramoleculares:

a) Enlaces de hidrógeno:

Son las interacciones supramoleculares predominantes para la formación de SMOFs debido a su direccionalidad. Los primeros estudios fueron llevados a cabo por Linus Pauling en 1931⁸⁴ que la definió como la interacción debida a las diferentes electronegatividades de los átomos del siguiente esquema $A-H^{\delta+} \cdots B^{\delta-}$, donde el átomo de hidrógeno actúa de puente entre los átomos A y B, Figura 1.23a.⁸⁵ Según la IUPAC, el enlace de hidrógeno es una interacción atractiva entre un átomo de hidrógeno de un fragmento molecular X-H, en el que X es más electronegativo que H, y un átomo de la misma molécula o de otra.⁸⁶

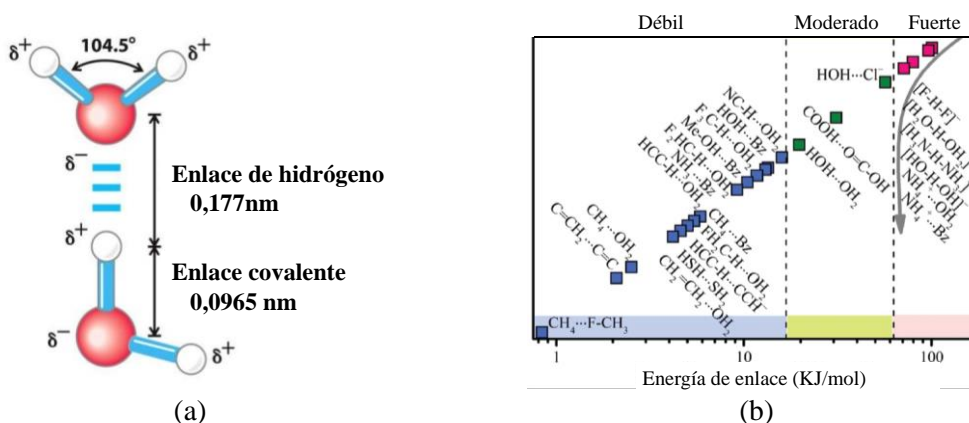


Figura 1.23. (a) Enlace de hidrógeno entre dos moléculas de agua y (b) energías de diferentes enlaces de hidrógeno.

Según los átomos los podemos clasificar en tres tipos: fuertes, moderados y débiles.⁸⁰ Los valores de energía varían entre 0,2 a 165 kcal·mol⁻¹, dependiendo del ángulo de AHB, de la distancia entre los átomos A y B, y la distancia con el átomo de hidrógeno.

⁸³ (a) Cram, D. J.; Cram, J. M. *Science*. **1974**, *183* (4127), 803–809. (b) Lehn, J. M. *Chem., Pure Appl.* **1978**, *50*, 871–892.

⁸⁴ Pauling, L. *J Am. Chem. Soc.* **1931**, 1367, 3225–3237.

⁸⁵ (a) Bernstein, J.; Davis, R. E.; Shimoni, L.; Chang, N. *Angew Chem Int Ed* **1995**, *34*, 1555–1573. (b) Steiner, T. *Angew Chem Int Ed* **2002**, *41*, 48–76.

⁸⁶ Arunan, E.; Desiraju, G. R.; Klein, R. A.; Sadlej, J.; Scheiner, S.; Alkorta, I.; Clary, D. C.; Crabtree, R. H.; Dannenberg, J. J.; Hobza, P.; Kjaergaard, H. G.; Legon, A. C.; Mennucci, B.; Nesbitt, D. J. *Pure Appl. Chem.* **2011**, *83* (8), 1637–1641.

Tabla 2.2. Criterios de enlaces de hidrógeno según Steiner y Jeffrey⁸⁵

Fuerza de enlace	Débil	Moderada	Fuerte
Tipo de interacción A–H···B	Fuerzas electrostáticas y dispersivas	Fuerzas electrostáticas	Fuertemente covalente
Distancia	A–H \approx H···B	A–H < H···B	A–H \ll H···B
H···B (Å)	1,2–1,5	1,5–2,2	2,2–3,2
A···B (Å)	2,2 – 2,5	2,5 – 3,2	> 3,2
Direccionalidad	Fuerte $\approx 180^\circ$	Moderada $> 130^\circ$	Débil $> 90^\circ$
Energía (KJ·mol⁻¹)	< 17	17–63	63–167

Etter y ⁸⁷ Desiraju,⁸⁸ han analizado el ensamblaje que se produce en estructuras orgánicas mediante grupos funcionales compatibles que forman patrones de interacción supramoleculares (sintones).⁸⁹ Este tipo de interacciones es importante ya que, aunque el enlace de hidrógeno tenga una direccionalidad definida, la rotación en torno a dicho enlace es prácticamente libre por lo que un único enlace de hidrógeno no puede considerarse como un sintón rígido. Es necesario la presencia de un segundo enlace de hidrógeno entre los bloques de construcción para lograrlo, como sucede en el ADN entre las bases nitrogenadas.

En la ingeniería supramolecular, la selección correcta de las moléculas que puedan establecer los sintones adecuados para lograr una determinada estructura supramolecular es clave.⁹⁰ Unidos a esta descripción está el concepto "tectón",⁹¹ propuesto por Wuest, que se refiere a una molécula cuyas interacciones están dominadas por fuerzas asociativas

⁸⁷ (a) Etter, M. C. *J Phys. Chem* **1991**, 95 (8), 4601–4610. (b) Etter, M. C. *Acc. Chem. Res.* **1990**, 23 (3), 120–126. (c) Etter, M. C.; Urbakzyk-Lipkowska, Z.; Zia-Ebrahimi, S. M.; Panunto, T. W. *J Am. Chem. Soc.* **1990**, 112 (3), 8415–8426. (d) Panunto, T. W.; Urbakzyk-Lipkowska, Z.; Johnson, R.; Etter, M. C. *J Am. Chem. Soc.* **1987**, 109 (7), 7786–7797.

⁸⁸ Desiraju, G. R. *Prog. Solid State Chem* **1987**, 17, 295–353.

⁸⁹ (a) Pedersen, C. J. *J Am. Chem. Soc.* **1967**, 89 (26), 7017–7036. (b) Pedersen, C. J. *J Am. Chem. Soc.* **1967**, 89 (10), 2495–2496.

⁹⁰ (a) Su, D.; Wang, X.; Simard, M.; Wuest, J. D. *Supramol. Chem.* **1995**, 6 (1–2), 171–178. (b) Brunet, P.; Simard, M.; Wuest, J. D. *J. Am. Chem. Soc.* **1997**, 119 (11), 2737–2738. (c) Wuest, J. D. *Chem. Commun.* **2005**, No. 47, 5830–5837.

⁹¹ Simard, Michel; Su, D.; Wuest, J. D. *J Am. Chem. Soc.* **1991**, 113 (9), 4696–4698.

particulares que inducen el ensamblaje de una red organizada, con características arquitectónicas o funcionales específicas. Para la construcción de arquitecturas moleculares prediseñadas, la selección del sintón (direccionalidad y multiplicidad de enlaces de hidrógeno) y del tectón (geometría, tamaño, rigidez, planaridad, simetría y funcionalidad) es crucial. Los más empleados tienen en común los siguientes grupos funcionales: el ácido carboxílico, urea, heterociclos (como los anillos de piridina, pirazol e imidazol) o la combinación de varios de ellos.⁹² En la Figura 1.24 se muestra algunos sintones. La utilización de algunos de estos sintones ha permitido la preparación de SMOFs con porosidad permanente.⁹³

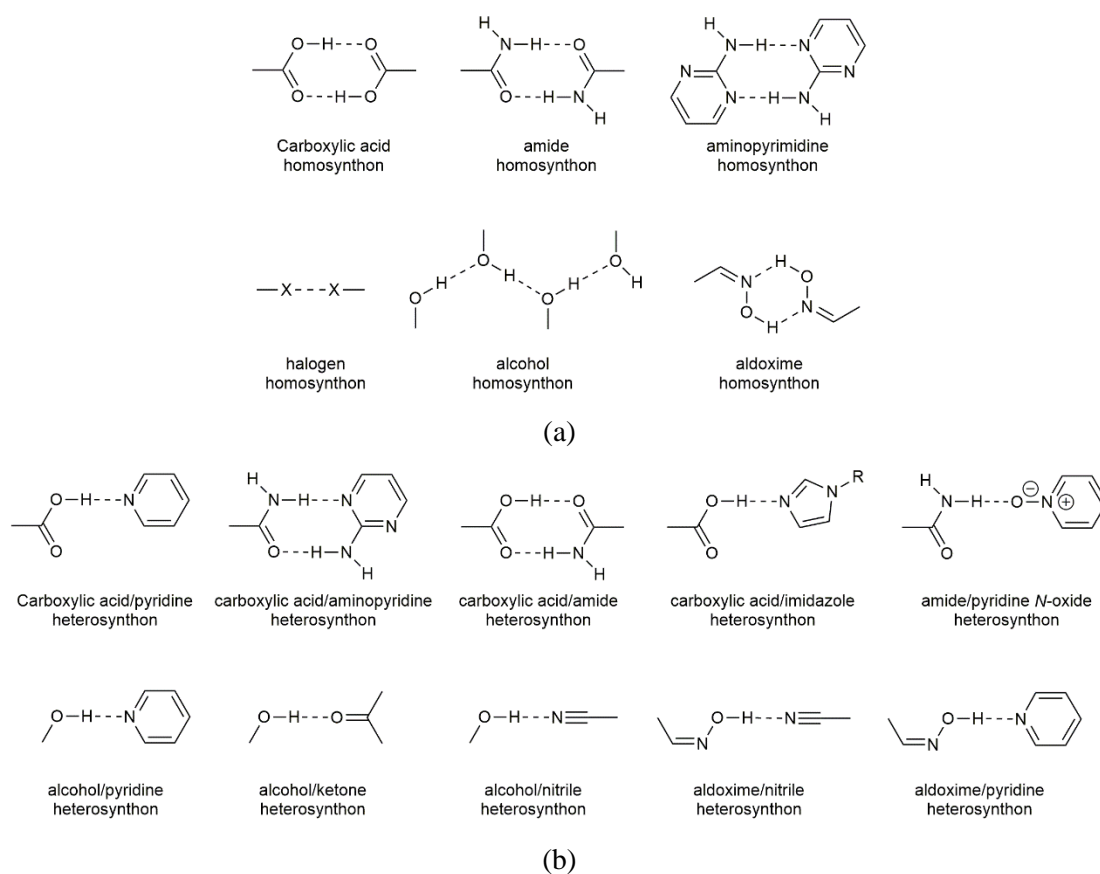


Figure 1.24. Sintones supramoleculares: (a) homosintones y (b) heterosintones.

En este trabajo hemos utilizado el término SMOF, pero algunos autores emplean el acrónimo M–HOF (de sus siglas en inglés Metal Hydrogen Bonded Frameworks)^{75,94} ya que en la mayor parte de los casos la interacción supramolecular dominante son enlaces de hidrógeno entre un ligando de una entidad compleja y una molécula orgánica.

⁹² Hisaki, I.; Xin, C.; Takahashi, K.; Nakamura, T. *Angew. Chemie - Int. Ed.* **2019**, *58* (33), 11160–11170.

⁹³ Zhu, Z. H.; Wang, H. L.; Zou, H. H.; Liang, F. P. *Dalt. Trans.* **2020**, *49* (31), 10708–10723.

⁹⁴ Zhou, M.; Liu, G.; Liu, G.; Ju, Z.; Su, K.; Du, S.; Du, S.; Tan, Y.; Yuan, D.; Yuan, D. *Cryst. Growth Des.* **2020**, *20* (6), 4127–4134.

b) Interacciones π - π :

Estas interacciones se establecen entre anillos aromáticos con una densidad de carga negativa en el centro y positiva centrada en los átomos de hidrógeno. El momento cuadrupolar del benceno puede ser visualizado como una densidad de carga negativa localizada por encima como por debajo del plano del anillo aromático. La magnitud de la interacción depende de múltiples factores como la superposición de los orbitales π en los sistemas conjugados, siendo más fuerte al aumentar el número de electrones π .⁹⁵

Se trata de interacciones débiles que varían su fortaleza en función del ángulo de interacción y de la distancia entre los anillos, tal y como se observa en la Figura 1.25, en la que se representa cómo varía la fortaleza de la interacción π - π entre el uracilo y la citosina. El mínimo de energía (máximo de interacción) se produce con una distancia entre los planos de los anillos aromáticos paralelos de 3,3–3,5 Å.⁹⁶ Por otro lado, la rotación de estas moléculas aromáticas no puede considerarse libre como en el enlace de hidrógeno dado que tal y como aparece en la Figura 1.25b existen varios mínimos locales. Pero tampoco podemos considerarlo rígido al no haber un único mínimo de energía. Es decir, nos encontramos en una situación intermedia que podríamos denominar semirígida.

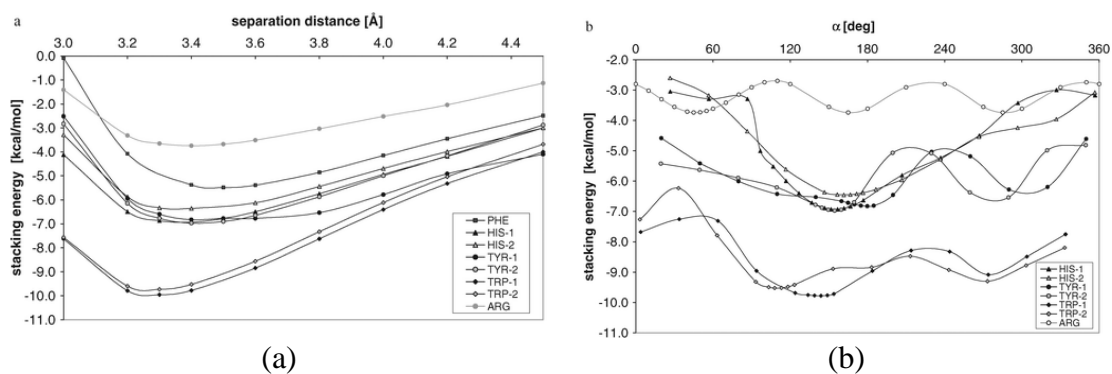


Figura 1.25. Mínimos de energía según (a) la distancia entre anillos y (b) el ángulo.

En esta situación, este sintón probablemente es lo suficiente robusto para generar una estructura porosa pero probablemente no tanto como para resistir el proceso de activación (eliminación de las moléculas de disolvente). Por lo tanto, para generar un sintón completamente rígido sería necesario un doble apilamiento π - π que bloquee dicha rotación.

⁹⁵ (a) Grimme, S. *Angew Chem Int Ed* **2008**, *47*, 3430–3434. (b) Hunter, C. A.; Lawson, K. R.; Urch, C. J. *J. Chem. Soc. Perkin Trans* **2001**, *2*, 651–669. (c) Hunter, C. A.; Sanders, J. K. M. *J Am. Chem. Soc.* **1990**, *112* (2), 5525–5534.

⁹⁶ Cysewski, P. *Phys. Chem. Chem. Phys.* **2008**, *10*, 2636–2645.

Se pueden definir tres formas de interacciones entre anillos, dos de tipo π - π , en las cuales los anillos se disponen paralelamente y una tercera en el que los anillos se posicionan de manera perpendicular, denominada en forma de T (*edge-to-face*), Figura 1.26. En el caso de los paralelamente dispuestos podemos distinguir dos tipos de interacciones según la distancia de desplazamiento lateral entre los anillos, en el caso de que sea casi nula se denomina en forma de sándwich (*face to face*); pero en el caso de que la interacción sufra una desviación lateral se denominará paralelo desplazado (*offset*).⁹⁷ En el caso de los anillos no apilados en paralelo, el ángulo centro-normal (θ) debe ser inferior a 20° . El rango de intensidad de las fuerzas π - π es de 1 a $50 \text{ kJ}\cdot\text{mol}^{-1}$, siendo el de menor energía, y por tanto más débil, la situación en la que los anillos se colocan paralelamente de forma eclipsada (*face to face*).⁹⁸

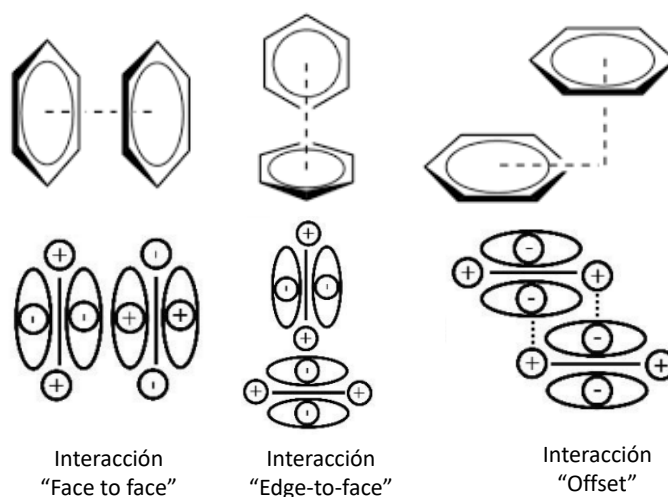


Figura 1.26. Diferentes formas de interacciones entre anillos aromáticos según la distancia y ángulo entre ellos.

1.4.2. Biomoléculas como ligandos en SMOFs (SMBioFs)

La utilización de biomoléculas capaces de establecer patrones de reconocimiento supramolecular específicos, Figura 1.27, ha ampliado los compuestos supramoleculares a los denominados SMBioFs (*supramolecular metal-biomolecule frameworks*).⁹⁹ Este tipo de compuestos, debido a la no toxicidad de las biomoléculas, son excelentes candidatos para aplicaciones en medios biológicos o medioambientalmente compatibles.

⁹⁷ Wheeler, S. E. *Acc. Chem. Res.* 2013, 46 (4), 1029–1038.

⁹⁸ (a) Fidalgo-Marijuan, A.; Barandika, G. *Inorg. Chem.* 2013, 52, 8074–8081. (b) Acharya, P.; Chattopadhyaya, J. *Pure Appl. Chem.* 2005, 77 (1), 291–311.

⁹⁹ Liu, Y.; Wu, H.; Guo, L.; Zhou, W.; Zhang, Z.; Yang, Q.; Yang, Y.; Ren, Q.; Bao, Z. *Angew. Chemie* 2022, 6102, 1–10.

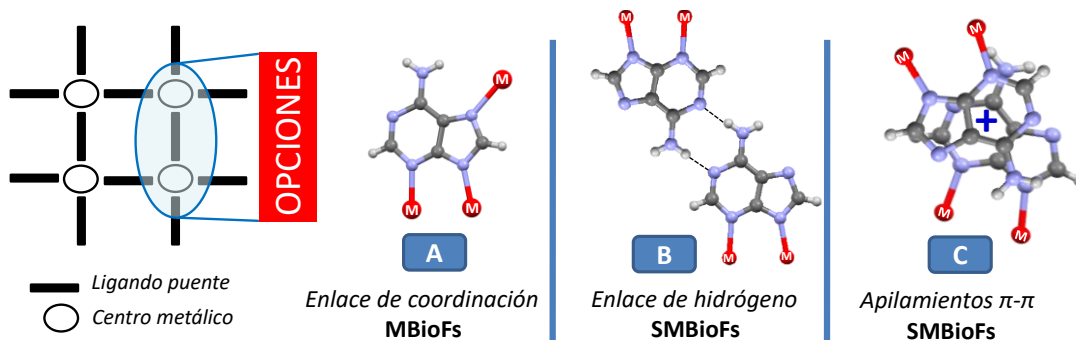


Figura 1.27. Enlaces de coordinación en MBioFs (A), ensamblaje mediante enlaces de hidrógeno (B) y apilamientos π - π (C) en SMBioFs. Se ha empleado la adenina como ejemplo de biomolécula capaz de formar distintos tipos de interacciones supramoleculares.

Un ejemplo de SMBioF es el compuesto $[\text{Co}(\text{6-tioguaninato-}\kappa^2\text{N7,S6})_3]$ en el que cada unidad compleja rígida se conecta con tres adyacentes mediante sintones tioguaninato...tioguaninato consistentes en anillos $\text{R}_2^2(8)$ de enlaces de hidrógeno (Figura 1.28). Este sintón rígido da lugar a capas que se entrelazan mediante enlaces de hidrógeno débiles ($\text{N-H}\cdots\text{S}$ y $\text{C-H}\cdots\text{S}$) e interacciones π - π , para formar una estructura tridimensional porosa con canales de 9 Å. Este compuesto no adsorbe N_2 , pero muestra una alta selectividad de adsorción del CO_2 con una curva no saturada que alcanza un valor de $1,4 \text{ mmol}\cdot\text{g}^{-1}$ a 1 bar y 273 K.¹⁰⁰

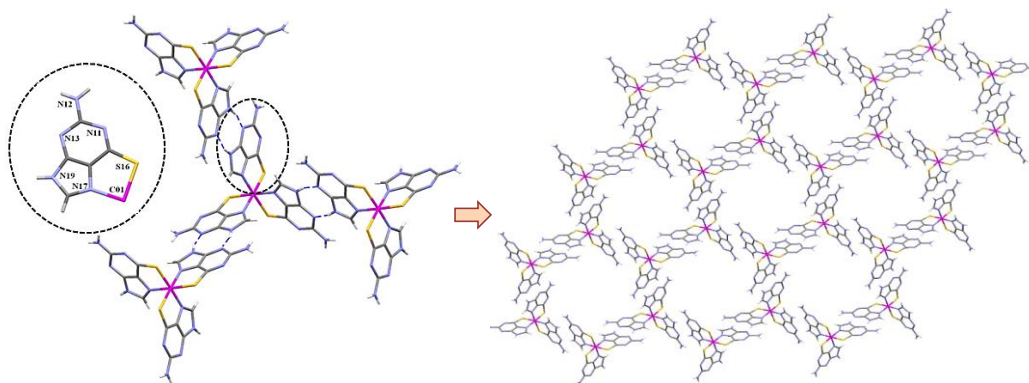


Figura 1.28. Enlaces de hidrógeno en el compuesto $[\text{Co}(\text{6-tioguaninato-}\kappa^2\text{N7,S6})_3]$ (izquierda) y representación de la estructura supramolecular porosa (derecha).¹⁰⁰ Código de colores: S, amarillo, C, gris; N, azul; Co, rosa.

Otro SMOF con una de las SBUs más empleadas, la paddle-wheel, es el compuesto sintetizado por Thomas-Gipson y colaboradores de fórmula $[\text{Cu}_2(\mu\text{-adenina})_4\text{Cl}_2]\text{Cl}_2\cdot 6\text{H}_2\text{O}$. El entramado estructural se basa en dos tipos de enlaces de

¹⁰⁰ Thomas-Gipson, J.; Pérez-Aguirre, R.; Beobide, G.; Castillo, O.; Luque, A.; Pérez-Yáñez, S.; Román, P. *Cryst. Growth Des.* **2015**, *15*, 975–983.

hidrógeno. El primer tipo, como puede observarse en la Figura 1.29a, las entidades dinucleares se conectan entre ellas mediante pares de enlace de hidrógeno N6–H/N1 entre las caras Watson-Crick de dos nucleobases adyacentes para dar un anillo $R_2^2(8)$, un conocido sintón estructural que participa en los procesos de reconocimiento supramolecular. Además, la coordinación al metal de la adenina a través del átomo N9 del anillo de imidazol produce la transferencia del átomo de hidrógeno al átomo N7 del imidazol para dar el tautómero 7H–adenina. Esto favorece la formación de un anillo supramolecular $R_2^1(7)$ entre la cara Hoogsteen [N6H, N7H] de la nucleobase como donante y el anión cloruro como aceptor. Estas interacciones generan una estructura supramolecular 3D, Figura 1.29b, con grandes canales a lo largo del parámetro cristalográfico c de 6,3 Å, que representan, eliminadas las moléculas de solvatación, el 36% del volumen total de la celda. Este compuesto presentaba porosidad permanente con un área superficial mucho más baja que el valor teórico debido a que la estructura colapsaba al activarse.¹⁰¹

Nugent y colaboradores realizaron modificaciones sintéticas en este compuesto al reemplazar el cloruro que queda en dirección hacia el poro por otros aniones más voluminosos como el TiF_6^{2-} y dar el compuesto $[Cu_2(\mu\text{-adenina})_4(TiF_6)_2] \cdot 2CH_3CN$, Figura 1.29c/d. La modificación aumenta la red de enlaces de hidrógeno de un total de 12 contactos (ocho con sus vecinos más cercanos y cuatro con los contraiones Cl^-), a 24 con ocho vecinos. El refuerzo de las interacciones da como resultado una porosidad permanente real, con valores de BET: $840 \text{ m}^2 \cdot \text{g}^{-1}$ en lugar de $30 \text{ m}^2 \cdot \text{g}^{-1}$ como en su predecesor. El porcentaje de huecos vacíos en la estructura es del 49%, mucho mayor que en el caso del compuesto de cloruro, lo que permite la adsorción selectiva de CO_2 a temperatura ambiente con valores mucho más altos que la mayoría de PCPs.¹⁰² Estos dos compuestos han sido estudiados en la separación selectiva de gases (C_2H_2/C_2H_4 ,¹⁰³ gases nobles como el Xe y Kr¹⁰⁴ y CO_2 ¹⁰⁵).

¹⁰¹ Thomas-Gipson, J.; Beobide, G.; Castillo, O.; Cepeda, J.; Luque, A.; Pérez-Yáñez, S.; Aguayo, A. T.; Román, P. *CrystEngComm* **2011**, *13* (10), 3301–3305.

¹⁰² Nugent, P. S.; Rhodus, V. Lou; Pham, T.; Forrest, K.; Wojtas, L.; Space, B.; Zaworotko, M. J. *J. Am. Chem. Soc.* **2013**, *135* (30), 10950–10953.

¹⁰³ Bao, Z.; Xie, D.; Chang, G.; Wu, H.; Li, L.; Zhou, W.; Wang, H.; Zhang, Z.; Xing, H.; Yang, Q.; Zaworotko, M. J.; Ren, Q.; Chen, B. *J. Am. Chem. Soc.* **2018**, *140* (13), 4596–4603.

¹⁰⁴ Liu, Y.; Wu, H.; Guo, L.; Zhou, W.; Zhang, Z.; Yang, Q.; Yang, Y.; Ren, Q.; Bao, Z. *Angew. Chemie - Int. Ed.* **2022**, *61* (11), 1–9.

¹⁰⁵ Forrest, K. A.; Pham, T.; Chen, K. J.; Jiang, X.; Madden, D. G.; Franz, D. M.; Hogan, A.; Zaworotko, M. J.; Space, B. *Langmuir* **2021**, *37* (47), 13838–13845.

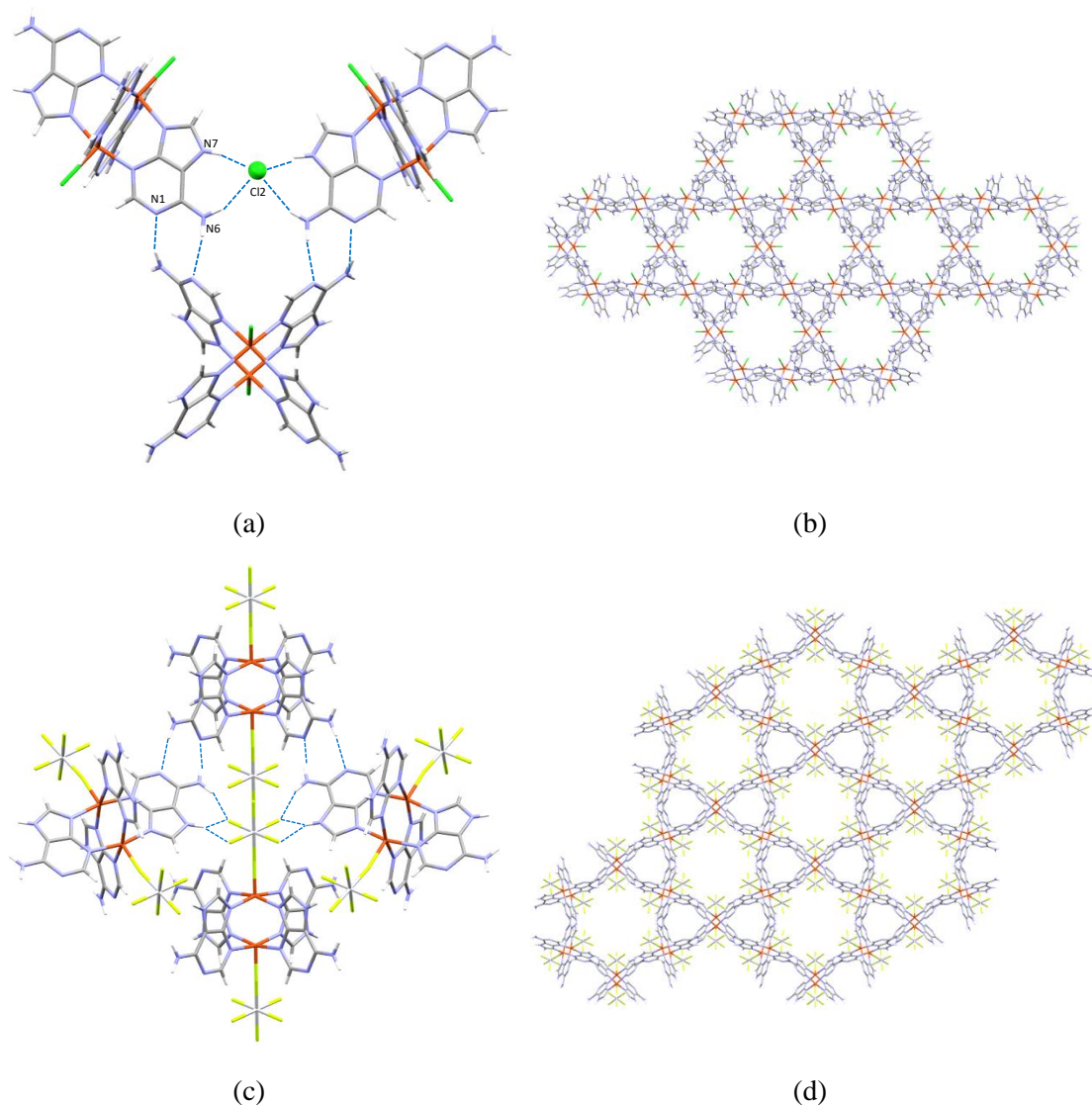


Figura 1.29. (a) Interacciones supramoleculares entre las bases nitrogenadas, (b) entramado supramolecular con el anión cloruro a lo largo del eje c y (c) y (d) interacciones y entramados supramoleculares en el compuesto con el anión TiF_6^{2-} .

El diseño de compuestos SMOFs se debe fundamentar en el cumplimiento de los siguientes puntos clave para la obtención una estructura cristalina potencialmente porosa.^{76b,106}

- La presencia de unidades de construcción discretas y rígidas. Este punto se consigue mediante la coordinación de los ligandos al centro metálico por dos o más posiciones.

¹⁰⁶ Li, P.; Vermeulen, N. A.; Malliakas, C. D.; Gómez-Gualdrón, D. A.; Howarth, A. J.; Mehdi, B. L.; Dohnalkova, A.; Browning, N. D.; O’Keeffe, M.; Farha, O. K. *Science* **2017**, 356 (6338), 624–627.

- La presencia de sintones rígidos que conectan las unidades de construcción rígidas, logrados por enlaces de hidrógeno complementarios y apilamientos π - π .
- La presencia de sintones que se extienden en 3 direcciones no coplanares

Un tipo de moléculas que es capaz de formar estructuras que cumplen estas características son las nucleobases.^{100,101,107} Las nucleobases púricas (adenina y guanina) son las más adecuadas debido al mayor número de posiciones de coordinación. El amplio uso de la adenina, Figura 1.30, en la preparación SMOFs respecto a otras bases nitrogenadas se debe a su solubilidad en agua y a su diversidad de coordinación, además de poder formar parte de diferentes sintones de enlaces de hidrógeno y de interacciones π - π .¹⁰⁸ La guanina en cambio, debido a su baja solubilidad y la inadecuada disposición geométrica de los átomos dadores de enlaces de hidrógeno, tiene un uso más limitado.



Figure 1.30. Diferentes tautómeros de la adenina y numeración empleada para designar los átomos de nitrógeno de esta base nitrogenada.

La presencia de cinco átomos dadores, con el siguiente orden de basicidad: N9 > N1 > N7 > N3 > N6,¹⁰⁹ confiere a la adenina una gran versatilidad como ligando. En la Figura 1.31 se muestran dieciséis diferentes modos de coordinación donde la adenina se coordina al menos a un centro metálico.

¹⁰⁷ (a) Zhang, M.; Lu, W.; Li, J. R.; Bosch, M.; Chen, Y. P.; Liu, T. F.; Liu, Y.; Zhou, H. C. *Inorg. Chem. Front.* **2014**, *1* (2), 159–162. (b) Pérez-Aguirre, R.; Beobide, G.; Castillo, O.; De Pedro, I.; Luque, A.; Pérez-Yáñez, S.; Rodríguez Fernández, J.; Román, P. *Inorg. Chem.* **2016**, *55* (15), 7755–7763.

¹⁰⁸ (a) Verma, S.; Mishra, A. K.; Kumar, J. *Acc. Chem. Res.* **2010**, *43* (1), 79–91. (b) Olea, D.; Alexandre, S. S.; Amo-Ochoa, P.; Guijarro, A.; De Jesús, F.; Soler, J. M.; De Pablo, P. J.; Zamora, F.; Gómez-Herrero, J. *Adv. Mater.* **2005**, *17* (14), 1761–1765. (c) Gupta, R. K.; Riaz, M.; Ashafaq, M.; Gao, Z.-Y.; Varma, R. S.; Li, D.-C.; Cui, P.; Tung, C.-H.; Sun, D. *Coord. Chem. Rev.* **2022**, *464*, 214558.

¹⁰⁹ (a) de Meester, P.; Skapski, A. C. *J. Chem. Soc. Dalt. Trans.* **1972**, No. 424, 424–427. (b) Lippert, B. *Prog. Inorg. Chem.* **2005**, *54*, 385. (c) Rojas-González, P. X.; Castiñeiras, A.; González-Pérez, J. M.; Choquesillo-Lazarte, D.; Niclós-Gutiérrez, J. *Inorg. Chem.* **2002**, *41* (24), 6190–6192.

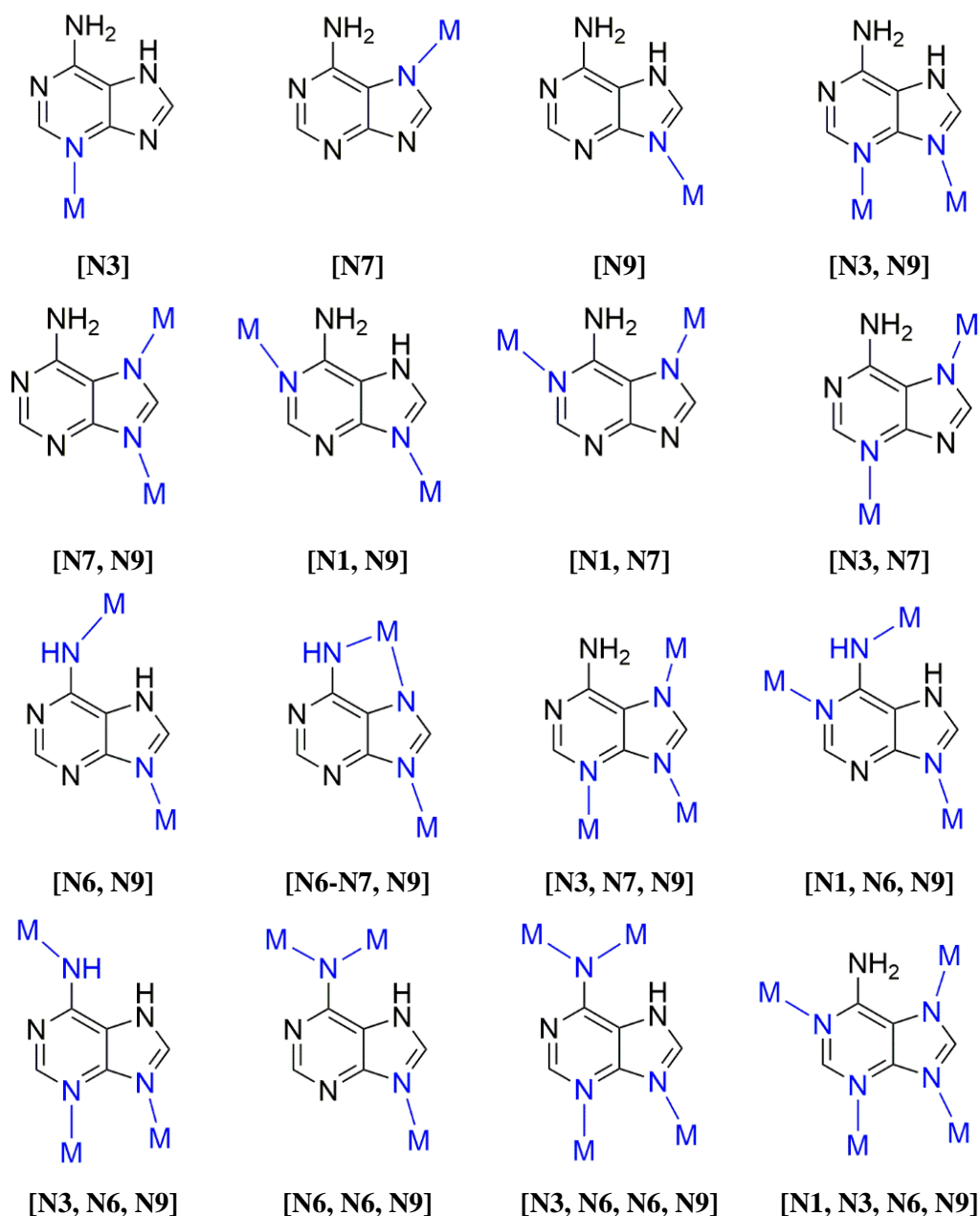


Figure 1.31. Modos de coordinación a átomos metálicos de la adenina.

La adenina puede actuar como ligando monodentado a través de los átomos N3, N7 y N9.^{72,110} También puede unirse como ligando bidentado y tridentado con una gran variedad de combinaciones¹¹¹ siendo el grupo amino exocíclico capaz de conectarse hasta a dos centros metálicos diferentes.^{71,112} Por último, aunque no es muy

¹¹⁰ Pérez-Yáñez, S.; Castillo, O.; Cepeda, J.; García-Terán, J. P.; Luque, A.; Román, P. *Inorganica Chim. Acta* **2011**, 365 (1), 211–219.

¹¹¹ (a) Stylianou, K. C.; Warren, J. E.; Chong, S. Y.; Rabone, J.; Bacsa, J.; Bradshaw, D.; Rosseinsky, M. *J. Chem. Commun.* **2011**, 47 (12), 3389–3391. (b) Gong, Y.; Zhou, Y. C.; Yang, H.; Zhang, H. X.; Proserpio, D. M.; Zhang, J. *Chem. Commun.* **2011**, 47 (20), 5828–5830. (c) Paul, A. K.; Sanyal, U.; Natarajan, S. *Cryst. Growth Des.* **2010**, 10 (9), 4161–4175.

¹¹² Pérez-Yáñez, S.; Beobide, G.; Castillo, O.; Cepeda, J.; Luque, A.; Román, P. *Cryst. Growth Des.* **2012**, 12 (6), 3324–3334.

habitual, también puede coordinarse con cuatro centros metálicos mediante los átomos N1, N3, N6 y N9.¹¹³ De todos estos modos de coordinación polidentados, el más habitual es el bidentado $\kappa N3:\kappa N9$ a través del lado azúcar, el utilizado para unirse a la desoxirribosa en el ADN y a la ribosa en el ARN.¹¹⁴ Este modo de coordinación confiere rigidez a las entidades complejas que se forman, uno de los requisitos para la obtención de SMBioFs, y deja libres sus otras dos caras, las denominadas Watson-Crick (N1/N6) y Hoogsteen (N6/N7), para la formación de enlaces de hidrógeno complementarios con otras moléculas de adenina o con otras especies químicas. (Figura 1.32).

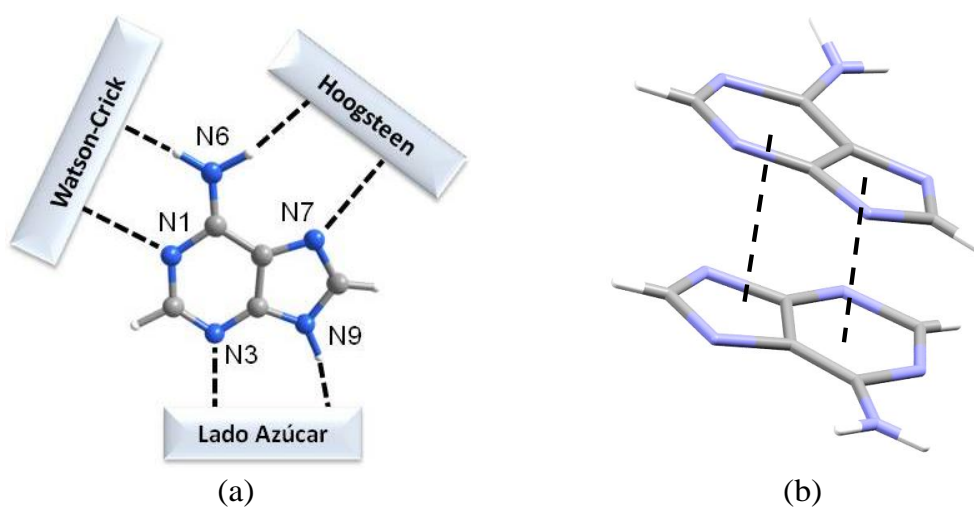


Figura 1.32. Interacciones supramoleculares de la adenina: (a) enlaces de hidrógeno y (b) apilamientos π - π .

La adenina, con valores de pKa de 4,2 y 9,8¹¹⁵ puede encontrarse en forma neutra o iónica en función del pH del medio (Figura 1.33) con la consecuente modificación de sus propiedades de coordinación.¹¹⁶ Con la forma neutra se han preparado monómeros,¹¹⁷ especies polinucleares discretas,¹¹⁸ e incluso cadenas

¹¹³ (a) An, J.; Farha, O. K.; Hupp, J. T.; Pohl, E.; Yeh, J. I.; Rosi, N. L. *Nat. Commun.* **2012**, 3. (b) Yang, E. C.; Zhao, H. K.; Feng, Y.; Zhao, X. J. *Inorg. Chem.* **2009**, 48 (8), 3511–3513.

¹¹⁴ Hadjiliadis, N.; Sletten, E. *Metal Complex- DNA Interactions*; Wiley, Hoboken, New Jersey, (United States), **2009**

¹¹⁵ (a) Gładysiak, A.; Nguyen, T. N.; Anderson, S. L.; Boyd, P. G.; Palgrave, R. G.; Bacsa, J.; Smit, B.; Rosseinsky, M. J.; Stylianou, K. C. *Inorg. Chem.* **2018**, 57 (4), 1888–1900. (b) Taqui Khan, M. M.; Krishnamoorthy, C. R. *J. Inorg. Nucl. Chem.* **1971**, 33, 1417–1425.

¹¹⁶ (a) Gagnon, C.; Hubert, J.; Rivest, R.; Beauchamp, A. L. *Inorg. Chem.* **1977**, 16 (10), 2469–2473.

¹¹⁷ de Meester, P.; Skapski, A. C. *J. Chem. Soc. Dalt. Trans.* **1972**, No. 1596, 2400–2404.

¹¹⁸ Terzis, A.; Beauchamp, A. L.; Rivest, R. *Inorg. Chem.* **1973**, 12 (5), 1166–1170.

poliméricas 1D.¹¹⁹ Con el anión adeninato se han sintetizado compuestos monoméricos,¹²⁰ polinucleares¹²¹ y redes 3D.⁷²



Figura 1.33. Valores de pK_a de la adenina.

Todas estas características, hacen de la adenina uno de los ligandos más valiosos en el diseño y construcción de SMOFs.¹²² Un ejemplo de SMBioF con adenina es el compuesto $[Zn_6(\mu\text{-adeninato-}\kappa N7:\kappa N9)_6(\text{piridina})_6(\text{dimetilcarbamato})_6] \cdot 10.5DMF$ ¹²³ con unidades hexanucleares en forma de anillo que se unen mediante enlaces de hidrógeno complementarios entre los lados Watson-Crick de los ligandos adeninatos. Los huecos generados están obstruidos por moléculas de piridina que se eliminan parcialmente, mediante una activación post sintética, de manera que el compuesto puede ser utilizado para la adsorción de gases, Figura 1.34.

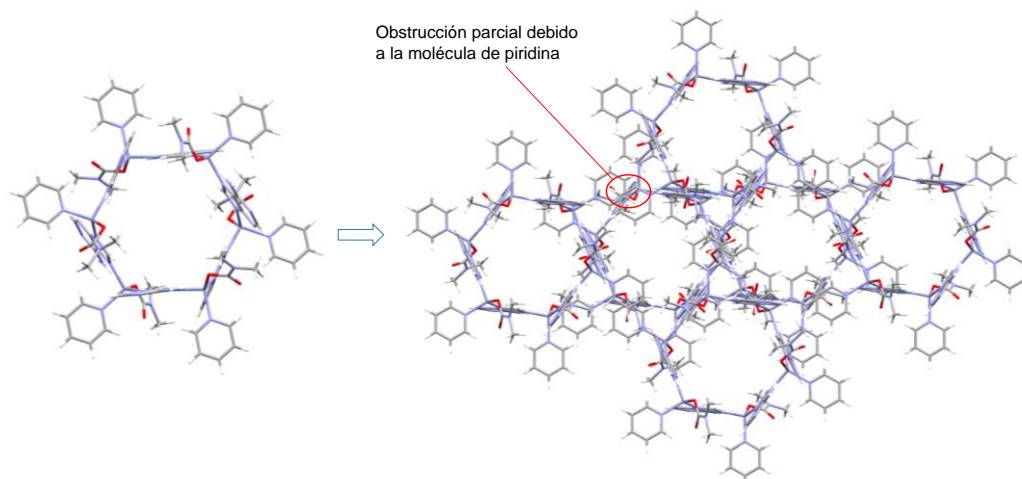


Figura 1.34. Anillo hexanuclear y red supramolecular en el compuesto $[Zn_6(\mu\text{-adeninato-}\kappa N7:\kappa N9)_6(\text{piridina})_6(\text{dimetilcarbamato})_6] \cdot 10.5DMF$.

¹¹⁹ Song, Y.; Yin, X.; Tu, B., Pang, Q., Li, H., Ren, X., Wang, B., Li, Q. *CrystEngComm*, **2014**, *16*, 3082–3085.

¹²⁰ Beck, W. M.; Calabrese, J. C.; Kottmair, N. D. *Inorg. Chem.* **1979**, *18* (1), 176–182.

¹²¹ Hubert, J.; Beauchamp, A. L. *Acta Crystallogr.* **1980**, *B36*, 2613–2616.

¹²² Beobide, G.; Castillo, O.; Luque, A.; Pérez-Yáñez, S. *CrystEngComm* **2015**, *17* (16), 3051–3059.

¹²³ An, J.; Fiorella, R. P.; Geib, S. J.; Rosi, N. L. *J. Am. Chem. Soc.* **2009**, *131* (24), 8401–8403.

Como en el caso de los MOFs, los SMOFs también pueden sufrir la interpenetración de sus redes tridimensionales si el hueco que se genera es muy grande. Un compuesto con interpenetración es el $[\text{Co}(\text{adenina})_2\text{Cl}_2]$, donde un monómero con dos adeninas neutras unidas mediante el N7, deja libre así los lados Watson–Crick y azúcar de la adenina para formar enlaces de hidrógeno complementarios con otras adeninas presentes a su alrededor. Estas interacciones dan lugar a una potencial porosidad del 67% y un área superficial estimada de $3600 \text{ m}^2 \cdot \text{g}^{-1}$. Pero la estructura cristalina real incluye un proceso de interpenetramiento de redes ocupando así el hueco vacío, Figura 1.35.¹²⁴

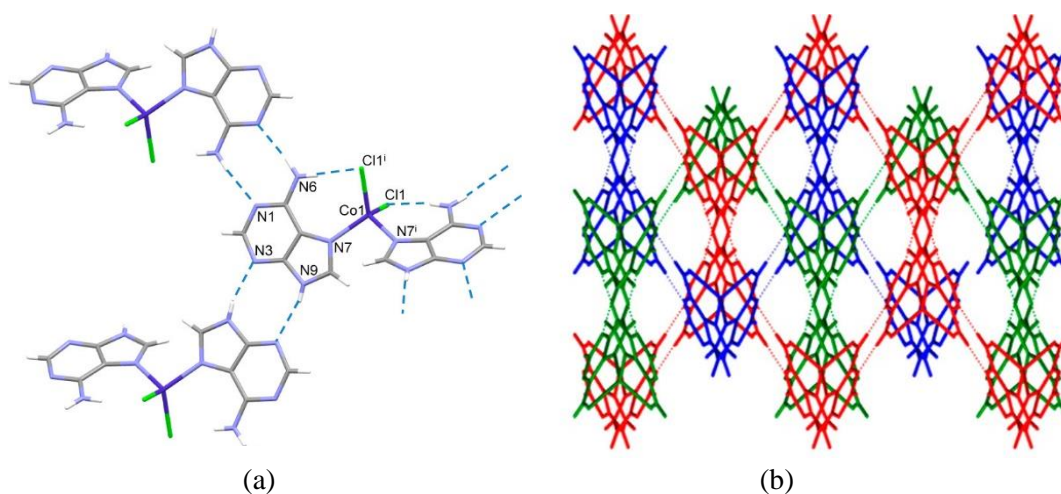


Figura 1.35. (a) Interacciones supramoleculares presentes en el compuesto $[\text{Co}(\text{adenina})_2\text{Cl}_2]$ y (b) interpenetración de la estructura supramolecular.

1.5. GELES METAL ORGÁNICOS (MOGs)

A pesar de las múltiples oportunidades que los materiales anteriores ofrecen en ocasiones presentan problemas generalmente debidos a una mala procesabilidad/conformación.¹²⁵ En el caso de los MOFs, para la obtención de entidades más estables, en 2008, el grupo de Cavka preparó un MOF basado en robustos enlaces $\text{Zr}(\text{IV})\text{-O}$, el famoso UiO-66.⁵⁴ Su estabilidad, junto con las ya relevantes propiedades de los MOFs, hacen de los compuestos basados en Zr una pieza clave en el área de los materiales porosos. La alta estabilidad de los Zr-MOF la proporciona el fuerte enlace formado por la unión de un ácido duro, según el principio HSAB de Pearson, como es el Zr^{4+} y una base dura como es el ligando carboxilato.

¹²⁴ Thomas-Gipson, J.; Pérez-Aguirre, R.; Beobide, G.; Castillo, O.; Luque, A.; Pérez-Yáñez, S.; Román, P. *Cryst. Growth Des.* **2015**, *15* (2), 975–983.

¹²⁵ Chen, Y.; Huang, X.; Zhang, S.; Li, S.; Cao, S.; Pei, X.; Zhou, J.; Feng, X.; Wang, B. *J. Am. Chem. Soc.* **2016**, *138* (34), 10810–10813.

No obstante, un inconveniente en la preparación de estos compuestos, debido a la falta de labilidad metal-ligando y a la formación rápida de enlaces resultantes, es la baja cristalinidad y formación de estructuras con numerosos defectos.⁶¹

Muchos MOFs/SMOFs se obtienen como polvo policristalino y hay que aplicar procedimientos post-sintéticos para conformarlos.¹²⁶ Para intentar superar este problema han surgido una nueva clase de materiales llamados geles metal-orgánicos (MOG) en los que se superan los inconvenientes del conformado, a la vez que se obtienen grandes áreas de superficie interna.¹²⁷

En el año 2013, el grupo de Jung definió un gel como un sistema coloidal en que coexisten una fase líquida dispersa en una fase sólida. Se dividen en dos grupos dependiendo de la naturaleza del disolvente usado: si el disolvente es agua, es un hidrogel y si el disolvente es orgánico, es un organogel.¹²⁸

Cuando en una solución se mezclan iones metálicos y moléculas orgánicas que actúan de ligandos puente, se pueden obtener tres tipos de materiales: (i) agregados metal-orgánicos altamente ordenados con un orden tanto de largo como de corto alcance, MOFs; (ii) agregados aleatorios sin orden de largo ni de corto alcance, polímeros de coordinación amorfos; y (iii) agregados con orden de corto alcance, pero sin orden de largo alcance, los MOGs. Existe una clara relación entre los MOFs y los MOG, ya que estos últimos habitualmente utilizan los elementos de partida de los primeros, pero mientras el tiempo necesario para formar la estructura cristalina en los MOFs ronda entre dos días y una semana, en el caso de los MOGs es de minutos. Es este hecho, el que hace que estos materiales no presenten cristalinidad, ni orden estructural.

Los MOGs son materiales mesoporosos (con tamaños de poro entre 2–50 nm), que contienen moléculas de disolvente (agua, etanol,...) atrapadas en su interior, y presentan una matriz esponjosa constituida por la mínima cantidad de nanopartículas sólidas trabadas entre sí para conformar un entramado tridimensional aleatoria y altamente poroso.¹²⁹ Son materiales viscoelásticos que se ensamblan mediante

¹²⁶ Bazer-Bachi, D.; Assié, L.; Lecocq, V.; Harbuzaru, B.; Falk, V. *Powder Technol.* **2014**, *255*, 52–59.

¹²⁷ Nune, S. K.; Thallapally, P. K.; McGrail, B. P. *J. Mater. Chem.* **2010**, *20* (36), 7623–7625.

¹²⁸ Jung, J. H.; Lee, J. H.; Silverman, J. R.; John, G. *Chem. Soc. Rev.* **2013**, *42* (3), 924–936.

¹²⁹ Wang, H.; Chen, B. H.; Liu, D. J. *Adv. Mater.* **2021**, *33* (25), 1–41.

enlaces de coordinación, además de otras interacciones supramoleculares como el apilamiento π - π , enlace de hidrógeno, interacciones hidrofóbicas, etc.²⁵

En la preparación de estos geles, el compuesto crece en forma de nanopartículas que se van entrecruzando hasta formar una red tridimensional. El MOG adopta la forma del recipiente en el que se prepara, por lo que se evita el proceso de conformación anteriormente mencionado, Figura 1.36.

La estabilidad de los MOGs depende de factores como el propio material metal-orgánico y su concentración, el tiempo de reacción, la temperatura y las condiciones de procesamiento. Dada la elevada estabilidad química y térmica de los compuestos metal-orgánicos de circonio, muchos de los MOGs han sido preparados basados con este centro metálico.¹³⁰

En la síntesis de estos materiales podemos destacar cuatro etapas: hidrólisis, condensación, gelificación y curado.

- **Hidrólisis:** En este punto es primordial la presencia de disolventes como el etanol o el agua que facilitan la hidrólisis y la condensación. El proceso puede estar favorecido por el pH, los grupos funcionales orgánicos y la relación molar agua/precursor.
- **Condensación:** es un proceso que comienza antes de que finalice la hidrólisis.
- **Gelificación:** En esta etapa se conforma la estructura del sólido final, donde se unen las partículas dando un gel. Este proceso se detecta con el incremento repentino de la viscosidad.
- **Curado:** En esta etapa el gel se mantiene inmerso en el líquido lo que favorece las reacciones de entrecruzamiento que dan fortaleza a la estructura y deja el tiempo necesario para completar la reacción entre los centros metálicos y los ligandos orgánicos. En este punto el MOG va a tomar su forma final, lo que hay que tener en cuenta para emplear el recipiente adecuado.

¹³⁰ (a) Bueken, B.; Van Velthoven, N.; Willhammar, T.; Stassin, T.; Stassen, I.; Keen, D. A.; Baron, G. V.; Denayer, J. F. M.; Ameloot, R.; Bals, S.; De Vos, D.; Bennett, T. D.. *Chem. Sci.* **2017**, 8 (5), 3939–3948. (b) Zhang, J.; Hu, Y.; Li, Y. *Gel Chemistry Interactions, Structures and Properties*; Springer, Singapore, (Singapore), 2018. (c) Vallejo-Sánchez, D.; Amo-Ochoa, P.; Beobide, G.; Castillo, O.; Fröba, M.; Hoffmann, F.; Luque, A.; Ocón, P.; Pérez-Yáñez, S. *Adv. Funct. Mater.* **2017**, 27 (15), 1605448. (d) Tam, A. Y. Y.; Yam, V. W. W.. *Chem. Soc. Rev.* **2013**, 42 (4), 1540–1567.

Aunque algunos MOGs se preparan por sonicación o simplemente por la mezcla de los reactivos a temperatura ambiente, lo más habitual es el empleo de métodos solvotermales, es decir, a través de una ruta energéticamente exigente y con disolventes tóxicos como N,N–dimetilformamida, N,N–dimetilacetamida o ácido clorhídrico. En los últimos años, se han desarrollado procesos que intentan evitar los problemas medioambientales en la síntesis de MOGs.

Ejemplos de geles metal-orgánicos son los compuestos MOG-1 y MOG-2 sintetizados en base a los MOF-808 y UiO-66, respectivamente, con Zr(IV) y con ácido trimésico y tereftálico como parte orgánica. Al contrario de los MOFs, los MOGs suelen ser amorfos y no presentan una composición estequiométrica, con fórmulas del tipo $Zr_6O_4(OH)_4(BTC)_{2.13}(HBTC)_{2.81} \cdot n(\text{disolvente})$ y $Zr_6O_4(OH)_4(BDC)_{5.38}(HBDC)_{1.25} \cdot n(\text{disolvente})$, respectivamente. En la preparación de estos dos geles se comprobó la importancia de la relación agua/disolvente analizando la variación del tiempo de gelificación en función del agua añadida. Se obtiene un mínimo de tiempo de gelificación (minutos) en un intervalo de relación H₂O/Zr entre 3,4 y 13,4. Fuera de este rango, el tiempo de gelificación se puede llegar a alargar hasta 12 horas.¹³¹



Figura 1.36. Esquema del tamaño de poro representativo para cada tipo de material.

Una etapa adicional en la síntesis de los MOGs es el secado, en la que el disolvente ocluido en los poros del material se elimina para obtener dos tipos de materiales según el procedimiento empleado. Cuando el secado se realiza en condiciones de presión atmosférica y con un tratamiento térmico se obtienen los xerogeles (MOXs). Cuando se lleva a cabo en condiciones supercríticas en las que se intercambia el disolvente por aire, se forman los aerogeles (MOAs). En este último caso se intercambia el disolvente por un fluido que se lleva a su estado supercrítico, como el CO₂, el etanol o la acetona.¹³² Uno de los principales problemas a la hora de preparar los monolitos de MOAs es evitar la fractura del gel durante el secado en condiciones atmosféricas debido a las tensiones

¹³¹ Santos-Lorenzo, J.; San José-Velado, R.; Albo, J.; Beobide, G.; Castaño, P.; Castillo, O.; Luque, A.; Pérez-Yáñez, S. *Microporous Mesoporous Mater.* **2019**, 284, 128–132.

¹³² Maleki, H.; Durães, L.; Portugal, A. *J. Non. Cryst. Solids* **2014**, 385, 55–74.

provocadas por las fuerzas capilares asociadas a las interfaces líquido-vapor. Esta fractura hace que, aunque se mantenga la composición química del MOG, la estructura colapse cambiando la porosidad y las propiedades que ésta proporciona.

1.5.1. Aerogeles Metal-Orgánicos (MOAs)

En 1931 Kistler preparó un aerogel al eliminar el disolvente de un gel mediante secado supercrítico y obtener un material sólido lleno de aire con unas dimensiones muy parecidas a las originales.¹³³ Esta terminología general se refiere a cualquier material derivado de precursores moleculares orgánicos, inorgánicos o híbridos que normalmente se prepara mediante un proceso sol-gel y una tecnología de secado adecuada con la que se conserva la red tridimensional altamente porosa, Figura 1.37. Pero no fue hasta la década de los 70 cuando se empezó a trabajar de nuevo en aerogeles, en este caso basados en sílice (SiO₂), gracias a los nuevos modos de síntesis y a la mejora en el secado supercrítico.¹³⁴

La combinación de propiedades únicas como baja densidad ($\sim 0,003\text{--}0,5\text{ g}\cdot\text{cm}^{-3}$), alta área superficial ($\sim 500\text{--}1200\text{ m}^2\cdot\text{g}^{-1}$), elevada porosidad ($\sim 80\text{--}99,8\%$), baja conductividad térmica ($\sim 0,015\text{ W}\cdot\text{mK}^{-1}$) y baja velocidad de sonido ($100\text{ m}\cdot\text{s}^{-1}$), con una química superficial modificable y la capacidad para obtenerlos en una variedad de morfologías y tamaños, permite aplicar estos materiales en catalísis, en electródica, en sensórica, y como adsorbentes para la limpieza medioambiental. Una aplicación es como aislamientos térmicos en los sectores aeroespacial. La NASA ha llevado a cabo misiones espaciales utilizando aerogeles como aislante térmico, por su baja conductividad y para la captura de partículas de alta velocidad.¹³⁵ Es su baja conductividad lo que lo hace perfecto para su empleo como aislante térmico, y se ha empleado en misiones como la Mars Rover, Mars Exploration Rovers, Spirit y Opportunity para la protección de baterías u otros elementos eléctricos ya que la diferencia de temperatura entre la noche y el día en Marte puede variar entre $-99\text{ }^\circ\text{C}$ y $+20\text{ }^\circ\text{C}$. Otra aplicación es el uso de estos materiales en una de las cinco capas del traje espacial empleado por los astronautas cuando salen al espacio exterior.¹³⁶

¹³³ (a) Kistler, S. S. *Nature* **1931**, 127, 741, 3211. (b) Kistler, S. S. *J. Phys. Chem.* **1932**, 36 (1), 52–64.

¹³⁴ Maleki, H. *Chem. Eng. J.* **2016**, 300, 98–118.

¹³⁵ Bheekhun, N.; Abu Talib, A. R.; Hassan, M. R. *Adv. Mater. Sci. Eng.* **2013**, 2013, 1–19.

¹³⁶ Trevino, L.; Orndoff, E. *Advanced Space Suit Insulation Feasibility Study*; American Institute of Physics: Tucson, Arizona, (United States), **2000**.

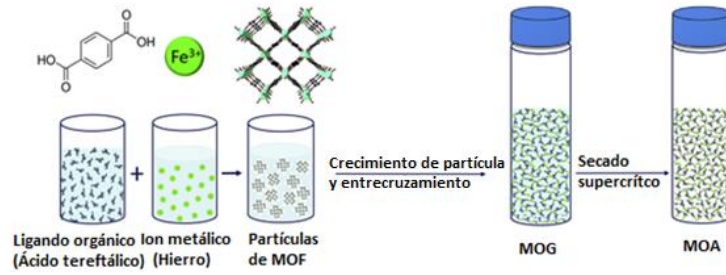


Figura 1.37. Esquema de la formación de MOG y su posterior modificación a MOA a partir del secado supercrítico.

1.5.2. Secado supercrítico

El secado supercrítico es un método por el cual el líquido de un material se transforma en gas, en ausencia de tensión superficial y de estrés capilar, sin destruir la delicada red de poros nanoestructurados de dicho material. Es el proceso más comúnmente utilizado para transformar geles en aerogeles. También se emplea para conservar muestras biológicas, descafeinar el café, etc.

Todas las sustancias puras que no se descomponen de otro modo poseen un punto crítico, una temperatura y una presión específicas en las que la fase líquida y la gaseosa se vuelven indistinguibles. En ese momento se le denomina fluido supercrítico, Figura 1.38. Este es denso como un líquido, conduce el calor como un líquido (si pudieras tocar un fluido supercrítico, se sentiría como un líquido), pero al mismo tiempo, se expande y comprime como un gas. Los fluidos supercríticos a menudo poseen la capacidad de disolver sustancias que en forma líquida no pueden. Por ejemplo, el dióxido de carbono supercrítico disuelve hidrocarburos fluorados, como algunos tipos de Teflon que se usan en lubricantes. Los fluidos supercríticos son infinitamente comprimibles en el punto crítico y, como resultado, exhiben un gradiente de densidad significativo debido al peso del fluido que empuja hacia abajo sobre sí mismo (son más densos en la parte inferior que en la parte superior).

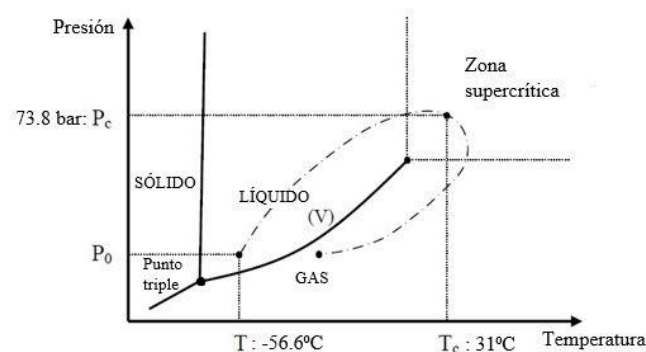


Figura 1.38. Esquema del proceso de secado supercrítico del dióxido de carbono.

Cuando se aplica a un gel, se siguen los siguientes pasos para lograr el aerogel:

1. Inicialmente se prepara el gel usando el procedimiento sol-gel, donde el gel contiene una mezcla de disolvente orgánico y agua en sus poros.
2. El gel se puede sumergir en un disolvente orgánico puro varias veces durante varios días para eliminar el agua de los poros.
3. Finalmente, el gel se seca supercríticamente en un recipiente a presión de dos maneras diferentes, Figura 1.39:
 - a) El gel se coloca en un recipiente a presión lleno hasta la mitad con el mismo líquido contenido en sus poros. Luego, el recipiente se sella, se calienta más allá de su temperatura y presión críticas y posteriormente se despresuriza isotérmicamente para dar lugar al aerogel.
 - b) El gel se coloca en un recipiente a presión que se llena con dióxido de carbono líquido. El gel se empapa en dióxido de carbono líquido para reemplazar el disolvente presente en los poros, expulsando y añadiendo dióxido de carbono nuevo cada 2 a 4 h. Después el dióxido de carbono se calienta más allá de su temperatura y presión críticas. A continuación, el recipiente se despresuriza isotérmicamente para dar lugar al aerogel.

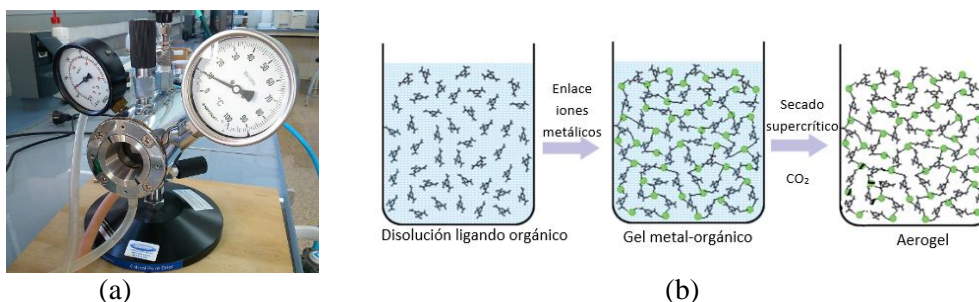


Figura 1.39. (a) Ejemplo de reactor empleado en el procedimiento de secado supercrítico y (b) representación esquemática de la formación de un aerogel.

1.6. APLICACIONES DE MATERIALES METAL ORGÁNICOS (MOMs)

Las condiciones sintéticas de los compuestos porosos influyen significativamente en las aplicaciones de los productos obtenidos. Aunque el tipo de ligando, el metal y el modo de coordinación son puntos muy importantes a considerar, el fin de la elección de estos es la obtención de compuestos de naturaleza porosa, piedra angular para modelar sus propiedades. De hecho, su elevada y permanente porosidad, su microporosidad y la flexibilidad estructural son unas de las

características más importantes de las redes metal-orgánicas. Destacan también su baja densidad y su alto valor de área superficial.¹³⁷

Además, el progreso que ha supuesto el uso de estos materiales para fines industriales y las mejoras en sus aplicaciones ha llevado al desarrollo de nuevas metodologías químicas para funcionalizar sus áreas internas.¹³⁸ Los MOMs presentan aplicaciones derivadas de sus características estructurales como son la adsorción de agua¹³⁹ por sus porosos flexibles,¹⁴⁰ el empleo en procesos de intercambio iónico¹⁴¹, el transporte y liberación de fármacos,¹⁴² el almacenamiento de gases,¹⁴³ el magnetismo,¹⁴⁴ la fluorescencia/sensórica,¹⁴⁵ etc. Se han desarrollado diversos métodos para su obtención en forma de película delgada¹⁴⁶ o como nanopartículas.¹⁴⁷ Y se han puesto a punto métodos sintéticos sencillos para escalar la producción de estos compuestos a cantidades industriales, lo que ha ayudado a ampliar sus aplicaciones.¹⁴⁸

¹³⁷ (a) Long, J. R.; Yaghi, O. M. *Chem. Soc. Rev.* **2009**, *38* (5), 1213–1214. (b) Furukawa, H.; Ko, N.; Go, Y. B.; Aratani, N.; Choi, S. B.; Choi, E.; Yazaydin, A. Ö.; Snurr, R. Q.; O’Keeffe, M.; Kim, J.; Yaghi, O. M. *Science*. **2010**, *329* (5990), 424–428.

¹³⁸ (a) Cai, M.; Qin, L.; You, L.; Yao, Y.; Wu, H.; Zhang, Z.; Zhang, L.; Yin, X.; Ni, J. *RSC Adv.* **2020**, *10* (60), 36862–36872. (b) Baumann, A. E.; Burns, D. A.; Liu, B.; Thoi, V. S. *Commun. Chem.* **2019**, *2* (1), 1–14. (c) Deria, P.; Bury, W.; Hod, I.; Kung, C. W.; Karagiari, O.; Hupp, J. T.; Farha, O. K. *Inorg. Chem.* **2015**, *54* (5), 2185–2192. (d) Wang, Z.; Cohen, S. M. *Chem. Soc. Rev.* **2009**, *38* (5), 1315–1329.

¹³⁹ Furukawa, H.; Gándara, F.; Zhang, Y. B.; Jiang, J.; Queen, W. L.; Hudson, M. R.; Yaghi, O. M. *J. Am. Chem. Soc.* **2014**, *136* (11), 4369–4381.

¹⁴⁰ (a) Formalik, F.; Neimark, A. V.; Rogacka, J.; Firlej, L.; Kuchta, B. *J. Colloid Interface Sci.* **2020**, *578*, 77–88. (b) Parent, L. R.; Pham, C. H.; Patterson, J. P.; Denny, M. S.; Cohen, S. M.; Gianneschi, N. C.; Paesani, F. *J. Am. Chem. Soc.* **2017**, *139* (40), 13973–13976. (c) Férey, G.; Serre, C. *Chem. Soc. Rev.* **2009**, *38* (5), 1380–1399.

¹⁴¹ Liu, Y.; Dai, J.; Zhang, Z.; Yang, Y.; Yang, Q.; Ren, Q.; Bao, Z. *Chem. - An Asian J.* **2021**, *16* (23), 3978–3984.

¹⁴² Sun, Y.; Zheng, L.; Yang, Y.; Qian, X.; Fu, T.; Li, X.; Yang, Z.; Yan, H.; Cui, C.; Tan, W. *Nano-Micro Lett.* **2020**, *12* (1), 1–29.

¹⁴³ Li, H.; Wang, K.; Sun, Y.; Lollar, C. T.; Li, J.; Zhou, H. C. *Mater. Today* **2018**, *21* (2), 108–121.

¹⁴⁴ Terzopoulou, A.; Nicholas, J. D.; Chen, X. Z.; Nelson, B. J.; Pane, S.; Puigmartí-Luis, J. *Chem. Rev.* **2020**, *120* (20), 11175–11193.

¹⁴⁵ Yang, J.; Ni, W.; Ruan, B.; Tsai, L.-C.; Ma, N.; Shi, D.; Jiang, T.; Tsai, F.-C. *ECS J. Solid State Sci. Technol.* **2021**, *10* (5), 056003.

¹⁴⁶ Shekhah, O.; Liu, J.; Fischer, R. A.; Wöll, C. *Chem. Soc. Rev.* **2011**, *40* (2), 1081–1106.

¹⁴⁷ (a) Spokoiny, A. M.; Kim, D.; Sumrein, A.; Mirkin, C. A. *Chem. Soc. Rev.* **2009**, *38* (5), 1218–1227. (b) Carné, A.; Carbonell, C.; Imaz, I.; Maspoch, D. *Chem. Soc. Rev.* **2011**, *40* (1), 291–305.

¹⁴⁸ Rubio-Martinez, M.; Avci-Camur, C.; Thornton, A. W.; Imaz, I.; Maspoch, D.; Hill, M. R. *Chem. Soc. Rev.* **2017**, *46* (11), 3453–3480.

1.7. OBJETIVOS Y DESARROLLO DEL TRABAJO

El trabajo recogido en esta memoria se enmarca dentro del campo de los materiales metal-orgánicos (MOMs). La investigación realizada ha consistido en el diseño, preparación y posterior caracterización química y estructural de nuevos MOMs y sus correspondientes SBUs (secondary building units): SMOFs cristalinos, geles y composites basados en MOFs. El estudio se ha completado con el análisis de las propiedades y su utilización en distintas aplicaciones.

El objetivo general e inicial de este trabajo ha sido la obtención de materiales metal-orgánicos porosos sustentados por interacciones de naturaleza supramolecular (SMOFs). El grupo de investigación en el que se ha llevado a cabo esta tesis doctoral tiene experiencia previa en el desarrollo y estudio de materiales metal-orgánicos supramoleculares porosos formados por bloques de construcción moleculares discretos y sustentados por la presencia de moléculas con grupos funcionales que dirigen el proceso de ensamblaje mediante sintones robustos, formados fundamentalmente por enlaces de hidrógeno. En este caso, nuestro interés es estudiar la formación de materiales que presenten propiedades magnéticas significativas, y cuyas unidades estructurales se ensamblen además por interacciones π - π y hacer especial hincapié en la química subyacente para la obtención de estos materiales. Para ello, se ha elegido como SBU una entidad heptamérica formada por Cu(II) y la base nitrogenada (nucleobase) adenina. La elección del metal se ha debido a la plasticidad de la esfera de coordinación del cobre(II) y a su dureza intermedia de Pearson que lo hace muy adecuado para interactuar con átomos dadores como el N y el O. La presencia de este metal ha permitido modificar las propiedades magnéticas de los compuestos obtenidos mediante la sustitución de uno de los centros metálicos de la SBU por otro metal de transición [Co(II), Ni(II), Zn(II)] dando lugar a compuestos heterometálicos con gran variabilidad de comportamientos magnéticos. El análisis en profundidad de las estructuras cristalinas de los compuestos obtenidos nos permite comprender cómo las características de los bloques de construcción moleculares gobiernan el empaquetamiento cristalino y la porosidad de los compuestos preparados.

Una vez realizada la modelización y síntesis de este tipo de materiales, el siguiente objetivo ha sido comprobar su capacidad para adsorber agua de la atmósfera u otro tipo de moléculas en disolución. En este último caso, se han empleado las propiedades magnéticas intrínsecas de estos materiales para monitorizar el proceso de adsorción de

diferentes analitos moleculares. Debido a que las estructuras cristalinas de los compuestos SMOFs son sustentados por enlaces supramoleculares no tan rígidos como los enlaces covalentes de los MOFs, éstas son más flexibles lo que puede permitir la eliminación del disolvente situado en los poros, pero también la incorporación/reemplazamiento por otras moléculas.

La preparación de compuestos heterometálicos adicionalmente ha permitido que mediante su degradación térmica en atmósfera inerte se obtengan especies metálicas nanométricas de composición controlada que pueden ser utilizadas como catalizadores en procesos de conversión térmica de CO₂ a moléculas de valor añadido.

En la bibliografía se han descrito varios MOFs basados en entidades polinucleares de Zr(IV)-óxido-hidróxido (UiO-66, EHU-30, PCN-224...)^{54,149} que se conectan entre sí mediante ligandos orgánicos puente tipo policarboxilato, para formar compuestos con estructuras tridimensionales covalentes que se emplean en una gran diversidad de aplicaciones.¹⁵⁰ Desde el punto de vista químico y térmico un punto muy importante de estos materiales es la estabilidad que les proporciona la fortaleza del enlace Zr–O/OH. Aunque estructuralmente la naturaleza covalente tridimensional les confiere una cierta rigidez. Por ello, en esta familia de materiales la diversidad estructural y, por ende, la porosidad se basa en la variabilidad de los ligandos orgánicos puente utilizados, siendo por el contrario el estudio de la variación y la formación de nuevas SBUs un tema mucho menos estudiado. Por ello, en nuestro trabajo hemos planteado extender la preparación de SMOFs empleando como SBUs entidades Zr–O similares a las de los MOFs anteriormente citados, pero de naturaleza discreta, es decir, que la interacción en la estructura cristalina entre ellas, o con otras unidades estructurales, sea de carácter supramolecular. El objetivo de esta parte del trabajo ha sido obtener las entidades discretas y analizar la reactividad de su formación, ya que estudios de este tipo no son abundantes en la bibliografía. Se han utilizado para ello, ligandos monocarboxílicos (tales como el ácido benzoico y sus derivados, y también aminoácidos), en lugar de ligandos

¹⁴⁹ (a) Feng, D.; Chung, W. C.; Wei, Z.; Gu, Z. Y.; Jiang, H. L.; Chen, Y. P.; Darensbourg, D. J.; Zhou, H. C. *J. Am. Chem. Soc.* **2013**, *135* (45), 17105–17110. (b) Perfecto-Irigaray, M.; Beobide, G.; Castillo, O.; Da Silva, I.; García-Lojo, D.; Luque, A.; Mendia, A.; Pérez-Yáñez, S. *Chem. Commun.* **2019**, *55* (42), 5954–5957.

¹⁵⁰ Bai, Y.; Dou, Y.; Xie, L. H.; Rutledge, W.; Li, J. R.; Zhou, H. C. *Chem. Soc. Rev.* **2016**, *45* (8), 2327–2367.

policarboxílicos, con el fin de no extender covalentemente la conectividad de las unidades estructurales y poder obtener unidades de construcción aisladas.

El estudio nos ha permitido conocer la química subyacente en la formación de estos clústeres discretos Zr–O–carboxilato y que factores como el pH, la presencia limitada de H₂O, el orden de adición y el uso de una sal de Zr sin presencia de oxígeno en los contraiones, parecen jugar un papel clave. Teniendo en cuenta estos conocimientos, se ha podido favorecer el control cinético en la formación de estas entidades metal-orgánicas de circonio para conseguir una formación muy rápida. Es decir, el SBU final obtenida es controlada por factores cinéticos más que por un aspecto termodinámico.

El parámetro termodinámico es el que hasta ahora generalmente prevalece en la preparación de los MOFs de Zr(IV), con el empleo de condiciones solvotermales y tiempos largos de reacción, lo que da lugar a estructuras ordenadas y con alta simetría debido a la óptima organización estructural para la obtención de un mínimo energético. Sin embargo, las condiciones de síntesis empleadas en nuestro trabajo, donde se favorece el factor cinético y la rápida construcción de los SBUs, han permitido la preparación de materiales en forma de gel, donde partículas de tamaño nanométrico se entrelazan entre sí albergando una cantidad muy elevada de disolvente en el gel y ocupando la totalidad del volumen del medio de reacción. Esto permite pasar de la común microporosidad de los MOFs a materiales con tamaños de poro de dimensiones nanométricas, es decir, de mesoporos. El proceso se ha logrado con la utilización de ligandos policarboxílicos (di-, tri-, tetra-) que unen los clústeres Zr–O de forma exponencial en un periodo de tiempo muy corto. Este control cinético permite, de una manera sencilla, la incorporación de otras moléculas orgánicas, con propiedades específicas, al entramado Zr-ligando policarboxílico que forma el gel. En concreto, se han adicionado moléculas fluorescentes con grupos carboxílicos que permitan el anclaje a las entidades de Zr y de esa manera lograr distintos materiales luminiscentes. Se ha estudiado la posibilidad de aplicar estos materiales como sensores, al disponer de forma simultánea varias moléculas fluorescentes en un mismo material que permite una señal selectiva con respecto a un analito presente en el medio en el cual se encuentra el material. Esta aplicación ha sido uno de los objetivos principales al inicio de este trabajo, pero no se puede desarrollar con las SBUs heptaméricas Cu(II)–adenina ya que los elementos metálicos con la capa de electrones incompleta, anulan (quenching) la luminiscencia. Es por ello, además de las razones

Introducción

anteriormente citadas, que se han diseñado y preparado compuestos de Zr(IV), elemento con la capa de valencia completa, en este caso vacía.

Los geles de Zr(IV) preparados son muy deformables y su manipulación es difícil, lo que afecta gravemente a la reproducibilidad de la señal luminiscente que se emite. Para solucionar este problema se han preparado los geles en presencia de una elevada cantidad de partículas micrométricas de sílice de cuarzo. El gel se disgrega en aglomerados submicrométricos que se alojan entre los huecos de las partículas de sílice indeformables. Esto ha permitido que el material tenga propiedades mecánicas más robustas, sea más manejable y la señal luminiscente no dependa de su manipulación mecánica sino únicamente del analito presente en el medio donde se emplea este composite.

Introducción

Chapter 2:

Homometallic adenine nucleobase based SMOFs

2.1. Introduction

2.2. Synthesis and chemical characterization

2.3. Crystallographic analysis

2.4. Supramolecular architectures based on dimeric metal-adenine entities

2.5. Crystal structures of compounds containing heptameric units

2.6. Water adsorption

2.7. Magnetic properties

2.1. INTRODUCTION

The folding, assembly, and hierarchical structures of biological systems is largely dictated by a combination of non-covalent interactions such as London and/or van der Waals forces, and hydrogen bonds.¹⁵¹ Thus, the access to manipulate these supramolecular interactions will allow the control of the structure and function of soft materials containing biologically interesting molecules.

Our group has been a pioneer in the synthesis and characterization of nucleobase based metal-organic materials (Figure 2.1).⁸² This research line started with the development of a material based in discrete paddle wheel shaped copper(II)-adenine dimeric entities in which the porous 3D structural building is sustained by complementary and predictable hydrogen bonds.¹⁵² These compounds as described in chapter one, have been called supramolecular metal-organic frameworks (SMOFs) due to their analogy with the well-known metal-organic frameworks (MOFs)¹⁵³ with which they show close resemblance.^{76b}

A key factor to afford the porous and robust 3D architectures of SMOFs is the use of rigid and discrete units entangled by predictable supramolecular synthons.¹⁵¹ The adenine is characterized by its acid-base balance, which allows it to be found both as neutral nucleobase and as conjugated adeninate anion, depending on the pH of the medium with the consequent modification of its coordinative properties. However, both forms are well suited to generate this kind of material owing to its predominant coordination mode (μ - $\kappa N3$: $\kappa N9$). This coordination mode leaves the Watson-Crick (W-C) and Hoogsteen (H) faces of the nucleobase decorating the external surface of the metal-adenine entities and enables to establish complementary hydrogen bonding interactions between adjacent units (Figure 2.2 and Figure 2.3).

¹⁵¹ Uhlenheuer, D. A.; Petkau, K.; Brunsveld, L. *Chem. Soc. Rev.* **2010**, *39* (8), 2817–2826.

¹⁵² Thomas-Gipson, J.; Beobide, G.; Castillo, O.; Luque, A.; Pascual-Colino, J.; Pérez-Yáñez, S.; Román, P. *CrystEngComm* **2018**, *20* (18), 2528–2539.

¹⁵³ (a) Cepeda, J.; Pérez-Yáñez, S. *EKAIA* **2017**, *31* (31), 105–116. (b) Villegas-Fernández, M. H.; Carpio-Granillo, M.; Vargas-Hernández, E.; Zuno-Cruz, F. J.; Sánchez-Cabrera, G. *Pädi Boletín Científico Ciencias Básicas e Ing. del ICBI* **2021**, *8* (16), 18–29, (c) Gándara, F.; Bennett, T. D. Crystallography of Metal-Organic Frameworks. *IUCrJ* **2014**, *1*, 563–570 .

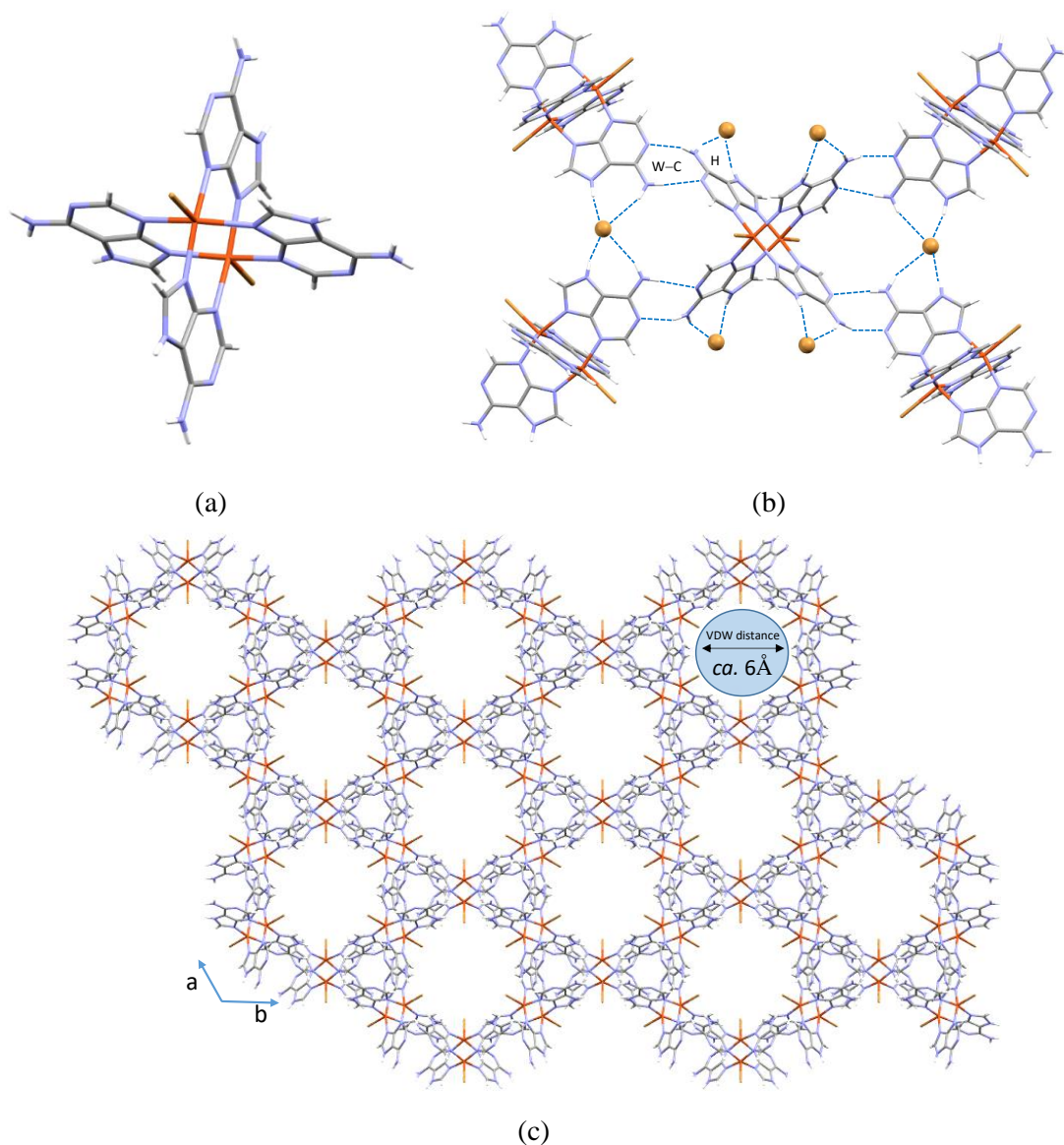


Figure 2.1. (a) Paddle wheel shaped SBU, (b) details of the adenine...adenine and adenine...bromide interactions, and (c) crystal packing of $[\text{Cu}_2(\mu\text{-Hade})_4\text{Br}_2]\text{Br}_2 \cdot \sim 2\text{MeOH}$.

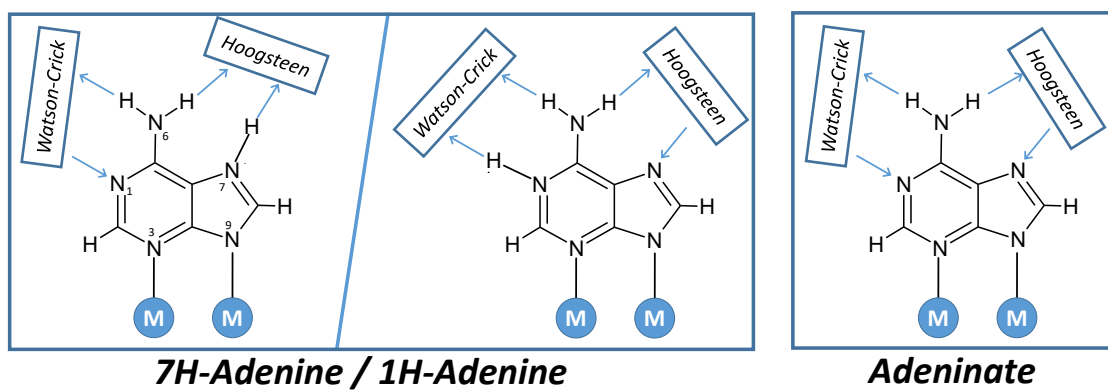


Figure 2.2. Hydrogen bonding capabilities of the $\mu\text{-}\kappa\text{N}3:\kappa\text{N}9$ adenine and adeninate.

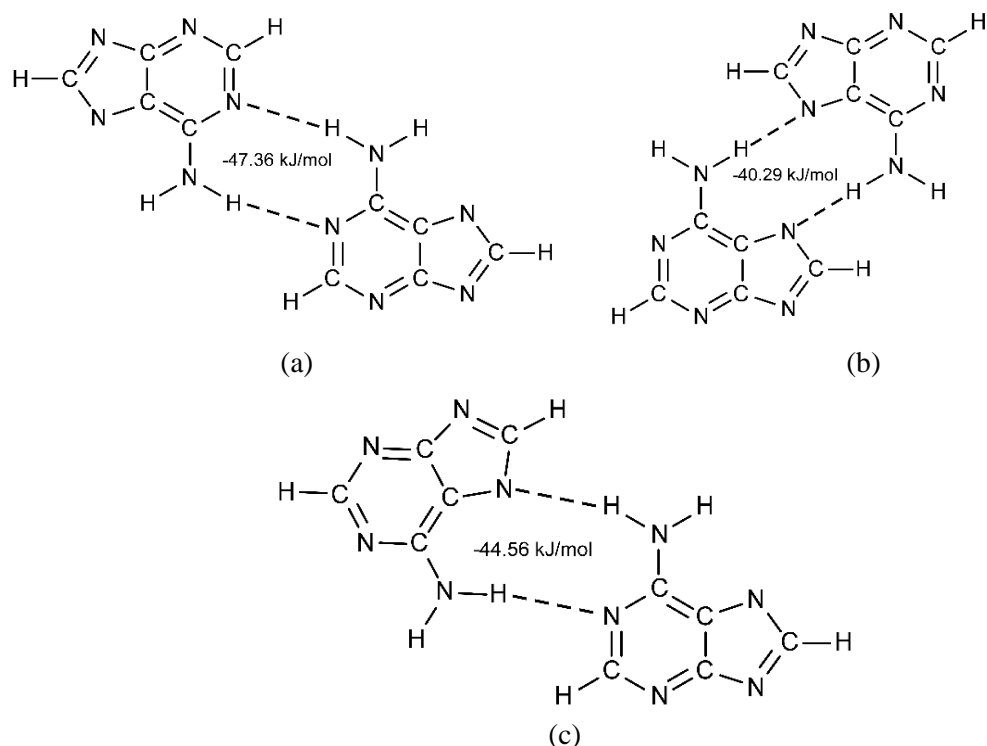


Figure 2.3. Hydrogen-bonding patterns of the adenine dimers and their binding energy of (a)/(c) Watson-Crick and (b) Hoogsteen synthons.

Based on the previous developments, the primary objective at the beginning of this work was to increase the amount of these porous supramolecular metal–organic frameworks based on first row transition metals and nucleobases such as adenine. However, we tried to take a step forward and integrate a second nucleobase or a derivative of it that could provide a higher degree of complexity to the supramolecular structure by the establishment of complementary interactions between the adenines themselves and the other nucleobases that do not have the ability to coordinate to the metal center. At this point theobromine, caffeine and theophylline were used (Figure 2.4) in order to obtain supramolecular interactions such as those shown in Figure 2.5.

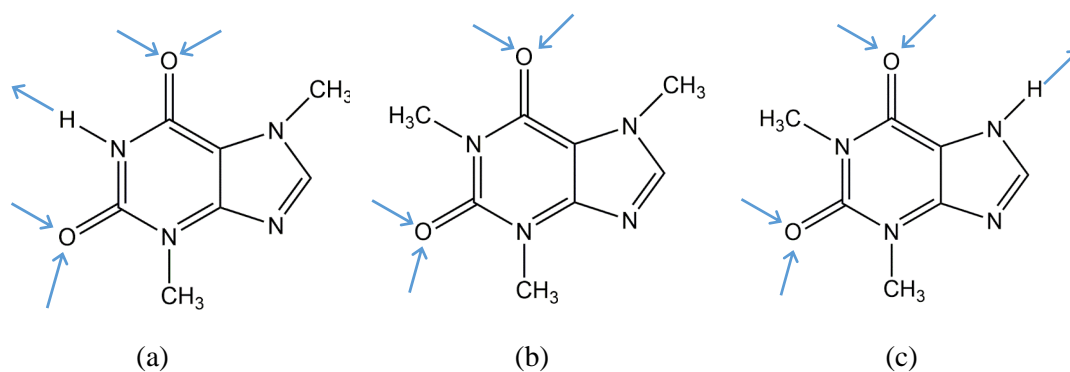


Figure 2.4. Non DNA nucleobases employed in this work: (a) theobromine, (b) caffeine and (c) theophylline.

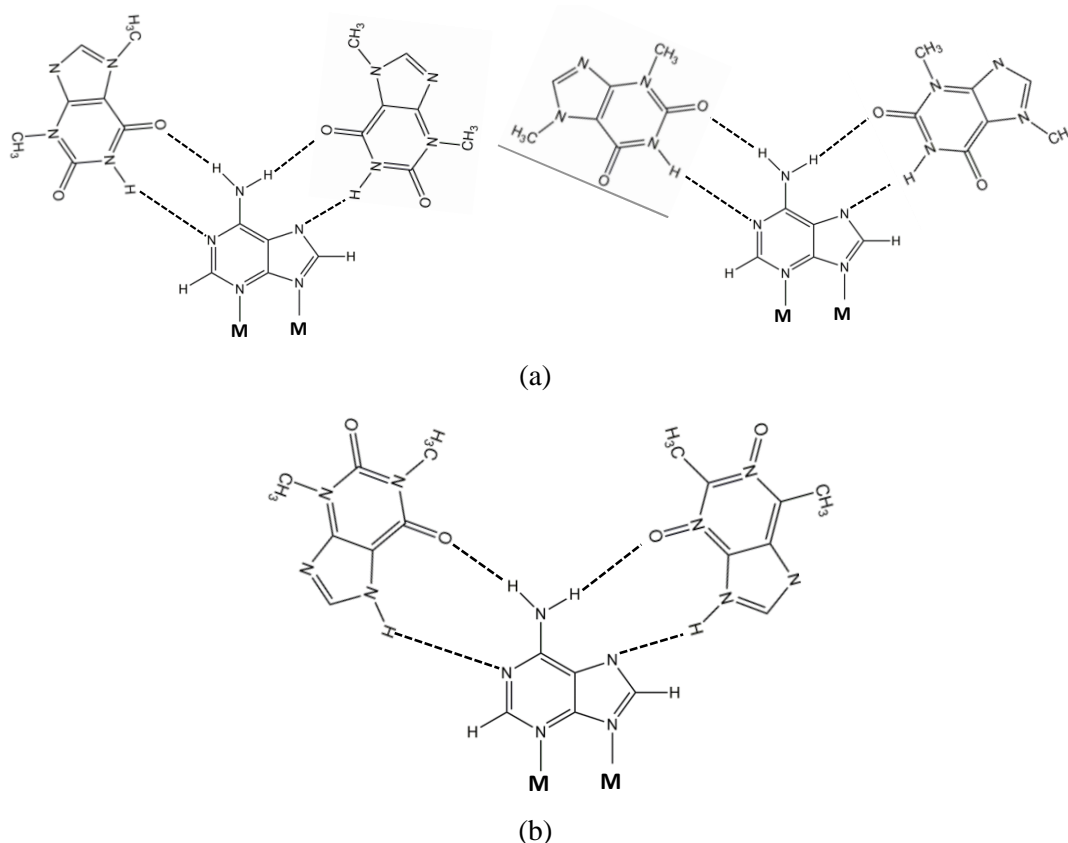


Figure 2.5. Possible hydrogen-bonding patterns between the adeninato ligand and (a) theobromine and (b) theophylline pairs.

A series of dinuclear compounds were obtained containing the paddle wheel SBU $[\text{Cu}_2(\mu\text{-ade-}\kappa\text{N3}:\kappa\text{N9})_4(\text{H}_2\text{O})_2]$, and presenting hydrogen bonds with the theobromine and caffeine (Figure 2.4a and 2.4b) to give rise to a moderate porosity: 13 and 33%, respectively. However, once the compounds are activated, they lose their crystalline nature and are not able to absorb N_2 or CO_2 . The higher coordination capacity of theophylline gives to a 1D polymeric compound in which $[\text{Cu}_2(\mu\text{-ade})_4(\text{H}_2\text{O})_2]$ entities cocrystallized with monomeric $[\text{Cu}(\text{theoph})_2]$ units.

Later, I employed a more voluminous metal-nucleobase entity¹⁵⁴ with formula $[\text{Cu}_7(\mu\text{-ade-}\kappa\text{N3}:\kappa\text{N9})_6(\mu_3\text{-OH})_6(\mu\text{-H}_2\text{O})_6]^{2+}$ to increase the porosity of the supramolecular compounds. This wheel-shaped heptameric entity is cationic which allows to diversify the resulting supramolecular structures using different counterions to balance the charge.

¹⁵⁴ Leite Ferreira, B.J.M.; Brandão, P.; Dos Santos, A.M.; Gai, Z.; Cruz, C.; Reis, M.S.; Santos, T. M.; Félix, V. *J. Coord. Chem.* **2015**, *68*, (16), 2770-2787.

It deserves to note that the pH plays an important role in the formation of this heptameric secondary building (Figure 2.6). At lower pH value, the paddle-wheel binuclear unit is formed due to the lack of hydroxido co-ligands. But at more basic pH values, where the hydroxide anion is more abundant, it can act as co-ligand and a more extended building blocks, the heptameric unit is obtained. In previous works of our research group, UV-vis spectroscopy was employed to obtain information on the acid–base behaviour of the dimeric entity. The dimeric entity in its cationic form (with adenine ligands) is present at pH low values (below 6), but when we increase the pH value at higher values of 9, the corresponding neutral entity, $[\text{Cu}_2(\mu\text{-adeninato})_4(\text{H}_2\text{O})_2]$, is predominant. Naturally, this information about the pH speciation is crucial in order to fix the synthetic conditions.^{69a}

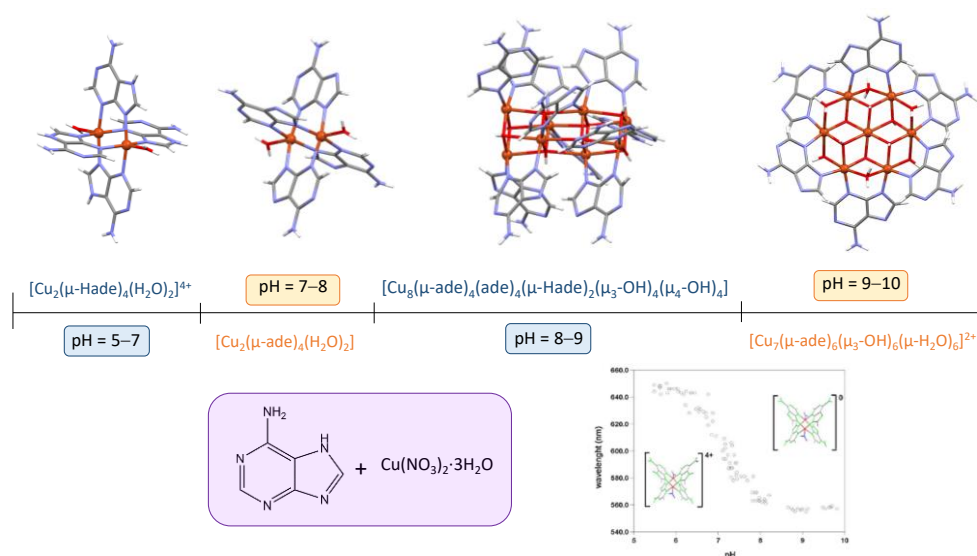


Figure 2.6. Scheme of pH variation in the synthetic route of copper-adenine complexes.

In a previous work, our group published a supramolecular compound in which the discrete heptameric entity is counterbalanced by sulfate anions. The supramolecular interactions (mainly π – π stacking between the coordinated adenine molecules) leads to an apparently porous 3D structure, but the presence of SO_4^{2-} counterions in the channels drastically reduces its potential porosity, Figure 2.7.^{107b} Additionally, the compounds losses their crystallinity as the solvation water molecules are removed. In order to increase the complexity of the supramolecular interactions between the structural units we have used in this work, the theobrominate anion. It was able to replace the sulfate counterions and incorporating the non DNA nucleobase within the framework of the supramolecular structure, by π – π stacking interactions and leaving their channels occupied only by crystallization water molecules.

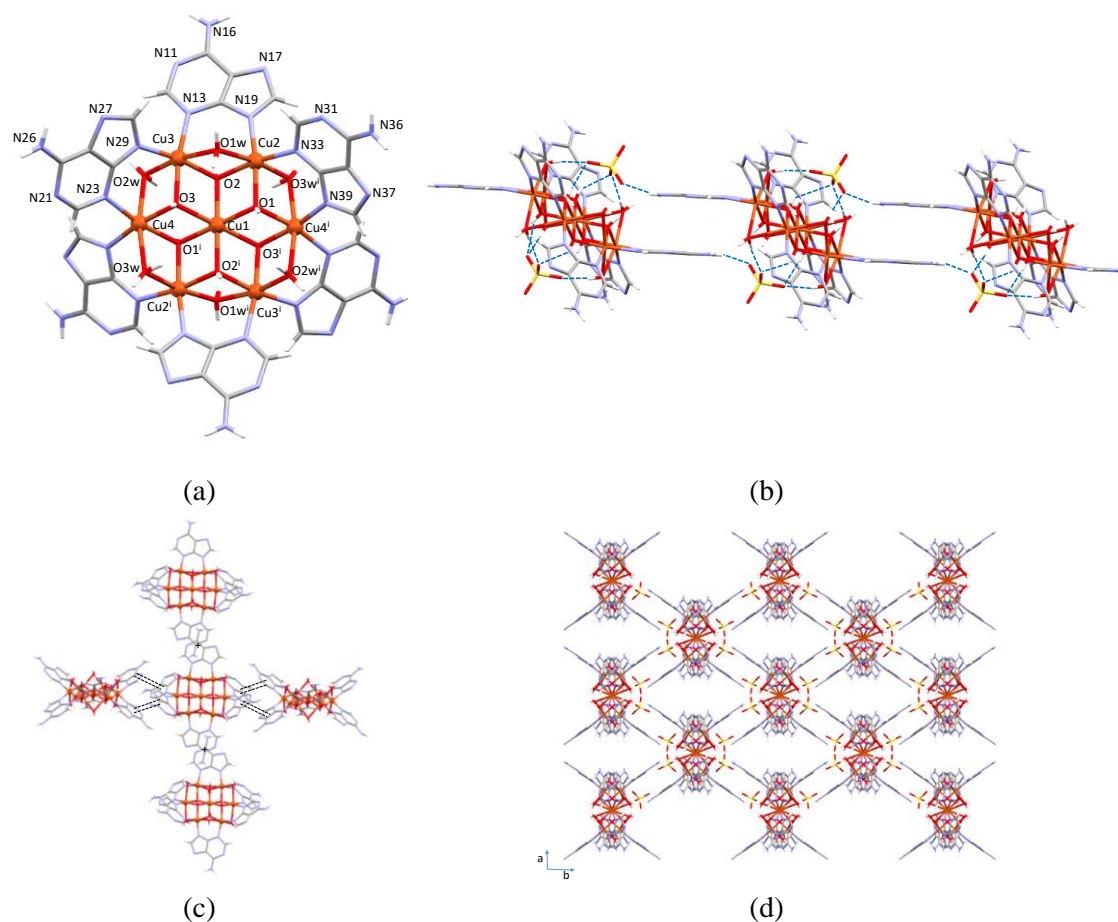


Figure 2.7. (a) Schematic image of the heptameric entity, (b) hydrogen bond of the anionic sulfate inorganic counterion with the cluster, (c) supramolecular π - π stacking interactions connecting each $[\text{Cu}_7(\mu\text{-ade-}\kappa\text{N}3:\kappa\text{N}9)_6(\mu_3\text{-OH})_6(\mu\text{-H}_2\text{O})_6]^{2+}$ heptanuclear entity to four adjacent ones, and (d) crystal packing of $[\text{Cu}_7(\mu\text{-ade-}\kappa\text{N}3:\kappa\text{N}9)_6(\mu_3\text{-OH})_6(\mu\text{-H}_2\text{O})_6](\text{SO}_4) \cdot 18\text{H}_2\text{O}$.

We decided to extend this study to some other organic planar anions not necessarily related to nucleobases. In this sense, we focused on carboxylate containing aromatic anions. Initially, we explore the use of benzoate anion (with a single carboxylate group) and terephthalate dianion (with two carboxylate groups). The presence of a single carboxylate group means that it cannot hold together the heptameric entities through the π - π stacking interactions and its structural role is reduced to be located in the inner surface of the channels, reducing in this way the potentially available free space. However, with a negative charge located at opposite sides of the terephthalate dianion it can play that role, integrating itself within the 3D framework and leaving the pores fully available.

Finally, we decided to exploit the previous results in the development of a series of isorecticular porous SMOFs based on linear dicarboxylate dianions, in which the basic

features of the crystal structure are retained but increasing the size and volume of the pores with the lengthening of the central part of dicarboxylate anion. In addition to all this crystal engineering work, the magnetic properties of these compounds were thoroughly characterize in all cases.

This type of compounds, prepared and stable in aqueous media with a very flexible but reversible structure against the activation process, have various applications thanks to their intrinsic porosity. Among them, the adsorption of water has recently generated great interest due to the drinkable water scarcity that affects a large part of the world population.

In this sense, works have recently began to study the use of MOFs to alleviate the lack of drinking water and shortages in many remote areas of the planet. Although it can also be used for various purposes such as dehumidifying specific areas or thermal batteries. There are several criteria to meet to achieve high values of effectiveness in the process such as the condensation pressure of the water in the pores, the absorption capacity, the recyclability, its dynamics and the stability of the material.^{139,155}

A prototypical example of this kind of materials for these applications is the aluminum-based MOF MOF-303, with the formula $[Al(OH)(PZDC)]$ where (PZDC is 1H-pyrazole-3,5-dicarboxylate). This compound was used in order to adsorb water from the atmosphere in environments with a lack of resources. For this, a water collector was built, capable of generating $1.3 \text{ Lkg}_{\text{MOF}}^{-1} \cdot \text{day}^{-1}$ in an arid environment (32% relative humidity, 27 °C) and $0.7 \text{ Lkg}_{\text{MOF}}^{-1} \cdot \text{day}^{-1}$ in the Mojave Desert (as extreme as 10% relative humidity, 27 °C). These results emphasize that a rapid water sorption dynamic, rather than simply focusing on high water capacities, is crucial to achieving water production on a scale that matches human consumption.¹⁵⁶

Going back to the materials developed by us, the water-stability, the porosity and the relatively flexible nature of the supramolecular frameworks of the synthesized compounds, encouraged us to try to incorporate, in an aqueous solution, different molecules such as solvents, monosaccharides, and drugs. It led to the development of a new method to quantify the adsorption based on the response of these materials towards an external magnetic field.

¹⁵⁵ Liu, X.; Wang, X.; Kapteijn, F. *Chem. Rev.* **2020**, *120* (16), 8303–8377.

¹⁵⁶ Hanikel, N.; Prévot, M. S.; Fathieh, F.; Kapustin, E. A.; Lyu, H.; Wang, H.; Diercks, N. J.; Glover, T. G.; Yaghi, O. M. *ACS Cent. Sci.* **2019**, *5* (10), 1699–1706.

2.2. SYNTHESIS AND CHEMICAL CHARACTERIZATION

2.2.1. Synthesis

We report herein the synthesis and characterization of compounds listed in Table 2.1. In all compounds, suitable single-crystals have been obtained to carry out their structural characterization by X-ray diffraction.

It is worth mentioning that compounds labelled with the number “two”, except in the case of the naphthalen-2,6-dicarboxylate, do not have a specific synthesis process, since they appear in the mother liquid after the crystal bellowing to the compound with the label “one” are removed. In the case of CU7ADNAPH-1/2, they show different arrangement of the structure units, CU7ADNAPH-1 can be considered as the kinetically favoured and CU7ADNAPH-2 is the thermodynamically stable one. As the size of the organic anion increases, its solubility is reduced, which generates the need to use DMF as a co-solvent mixed with water; this causes it to be introduced into the structure of compounds CU7ADBYD and CU7ADSD. In addition, all the chemical characterization of these compounds have been carried out with the samples with label “2”, as they are obtained with a greater yield than those with label “1”.

The homogeneity and purity of the bulk samples was checked by elemental analysis and by comparison of the experimental X-ray powder diffractogram with the simulated one from the single-crystal X-ray data.

Table 2.1. Formula and code used along this work for the compounds synthesized with the dimeric and heptameric copper-adenine entities.

Compound	Code
$[\text{Cu}_2(\mu\text{-ade})_4(\text{H}_2\text{O})_2] \cdot 3\text{Htheo} \cdot \sim 7\text{H}_2\text{O}$	CU2AD3TB
$[\text{Cu}_2(\mu\text{-ade})_4(\text{H}_2\text{O})_2] \cdot 2\text{Htheo} \cdot \sim 18\text{H}_2\text{O}$	CU2AD2TB
$[\text{Cu}_2(\mu\text{-ade})_4(\text{H}_2\text{O})_2] \cdot \text{caf} \cdot \sim 6\text{H}_2\text{O}$	CU2ADCAF
1D- $\{[\text{Cu}_2(\mu\text{-ade})_4(\text{H}_2\text{O})_2] \cdot [\text{Cu}(\text{theoph})_2] \cdot \sim 10\text{H}_2\text{O}\}$	CU2ADTP
$[\text{Cu}_7(\mu\text{-ade})_6(\mu_3\text{-OH})_6(\mu\text{-H}_2\text{O})_6](\text{theobr})_2 \cdot \sim 28\text{H}_2\text{O}$	CU7ADTB
$[\text{Cu}_7(\mu\text{-ade})_6(\mu_3\text{-OH})_6(\mu\text{-H}_2\text{O})_6](\text{benzoate})_2 \cdot \sim 28\text{H}_2\text{O}$	CU7ADBZ
$[\text{Cu}_7(\mu\text{-ade})_6(\mu_3\text{-OH})_6(\mu\text{-H}_2\text{O})_6]\text{fumarate} \cdot \sim 25\text{H}_2\text{O}$	CU7ADFA-1
$[\text{Cu}_7(\mu\text{-ade})_6(\mu_3\text{-OH})_6(\mu\text{-H}_2\text{O})_6]\text{fumarate} \cdot \sim 18\text{H}_2\text{O}$	CU7ADFA-2
$[\text{Cu}_7(\mu\text{-ade})_6(\mu_3\text{-OH})_6(\mu\text{-H}_2\text{O})_6]\text{fumarate} \cdot \sim 23\text{H}_2\text{O}$	CU7ADF-1
$[\text{Cu}_7(\mu\text{-ade})_6(\mu_3\text{-OH})_6(\mu\text{-H}_2\text{O})_6]\text{fumarate} \cdot \sim 16\text{H}_2\text{O}$	CU7ADF-2
$[\text{Cu}_7(\mu\text{-ade})_6(\mu_3\text{-OH})_6(\mu\text{-H}_2\text{O})_6]\text{acety} \cdot \sim 22\text{H}_2\text{O}$	CU7ADAC-1
$[\text{Cu}_7(\mu\text{-ade})_6(\mu_3\text{-OH})_6(\mu\text{-H}_2\text{O})_6]\text{acety} \cdot \sim 17\text{H}_2\text{O}$	CU7ADAC-2
$[\text{Cu}_7(\mu\text{-ade})_6(\mu_3\text{-OH})_6(\mu\text{-H}_2\text{O})_6]\text{thereph} \cdot \sim 24\text{H}_2\text{O}$	CU7ADTEP-1
$[\text{Cu}_7(\mu\text{-ade})_6(\mu_3\text{-OH})_6(\mu\text{-H}_2\text{O})_6]\text{thereph} \cdot \sim 12\text{H}_2\text{O}$	CU7ADTEP-2
$[\text{Cu}_7(\mu\text{-ade})_6(\mu_3\text{-OH})_6(\mu\text{-H}_2\text{O})_6]\text{naph} \cdot \sim 32\text{H}_2\text{O}$	CU7ADNAPH-1
$[\text{Cu}_7(\mu\text{-ade})_6(\mu_3\text{-OH})_6(\mu\text{-H}_2\text{O})_6]\text{naph} \cdot \sim 32\text{H}_2\text{O}$	CU7ADNAPH-2
$[\text{Cu}_7(\mu\text{-ade})_6(\mu_3\text{-OH})_6(\mu\text{-H}_2\text{O})_6]\text{biph} \cdot \sim 44\text{H}_2\text{O}$	CU7ADBP
$[\text{Cu}_7(\mu\text{-ade})_6(\mu_3\text{-OH})_6(\mu\text{-H}_2\text{O})_6]\text{biph} \cdot \text{DMF} \cdot \sim 24\text{H}_2\text{O}$	CU7ADBPD
$[\text{Cu}_7(\mu\text{-ade})_6(\mu_3\text{-OH})_6(\mu\text{-H}_2\text{O})_6]\text{Stil} \cdot \sim 24\text{H}_2\text{O}$	CU7ADS
$[\text{Cu}_7(\mu\text{-ade})_6(\mu_3\text{-OH})_6(\mu\text{-H}_2\text{O})_6]\text{Stil} \cdot 2\text{DMF} \cdot \sim 23\text{H}_2\text{O}$	CU7ADSD

2.2.1.1. Synthesis of compound CU2AD3TB

0.0489 g (0.2 mmol) of $\text{Cu}(\text{NO}_3)_2 \cdot 3\text{H}_2\text{O}$ dissolved in 10 mL of water were added to 0.0676 g (0.5 mmol) of adenine dissolved in 15 mL of an aqueous methanolic 1:1 hot solution at 60 °C. The resulting blue solution (pH~4.0) was basified to pH~8.8 with NaOH while the mixture was continuously stirred. The obtained purple solution was added to 0.0540 g of theobromine (0.3 mmol) dissolved in 20 mL of hot water, 70 °C, basified with NaOH (pH~8.8). The purple solution was left in a crystallizer for evaporation at room temperature. Black single-crystals suitable for X-ray diffraction were obtained and separated after four days.

2.2.1.2. General synthesis of compounds

All the compounds were synthesized following the above described method but changing the employed anion and the quantities of the reagents as listed in Table 2.2.

The X-ray powder diffraction data in compound CU2AD2TB indicates that it corresponds to a mixture of CU2AD3TB and CU2AD2TB, Figure 2.8. As both compounds were indistinguishable by means of colour or shape, crystals were randomly selected from the mixture until a specimen of CU2AD2TB was found and used for single-crystal X-ray study. There are some other examples in the literature for concomitant crystal formation.¹⁵⁷



Figure 2.8. Crystals corresponding to (a) CU2AD3TB and (b) CU2AD2TB.

Single-crystals of CU2ADCAF were obtained after two weeks using test tube diffusion technique in which over a caffeine aqueous solution, the aquo-methanolic solution containing the copper(II) nitrate and adenine mixture is layered carefully.

The counterion containing solution of CU7ADTEP compound was basified with NaOH up to pH~11 and added to the copper-adeninato mixture. The pH was adjusted to

¹⁵⁷ Husain, A., Parveen, R. Dastidar, P. *Cryst. Growth Des.* **2015**, 15, 5075–5085.

~9.2 by adding dilute HNO₃ solution (1:3) dropwise. The final purple solution was covered with parafilm and allowed to stand at room temperature. All the organic counterions were dissolved using this procedure. Blue single-crystals of CU7ADTEP-1 and CU7ADTEP-2 were obtained after one month using test tube diffusion technique in which over the aquo-methanolic solution containing the copper(II) nitrate and adenine mixture, an aqueous solution of the terephthalic acid is layered carefully. Depending on the handling of the crystals: directly picking them from the mother liquor or storing them under room conditions, specimens at different hydration stages, CU7ADTEP-1 and CU7ADTEP-2 were achieved.

A single-crystal of CU7ADFA-1 was selected, removed from the solution, covered with Paratone oil and used for data collection in the single-crystal X-ray diffractometer. The polycrystalline samples were introduced into a capillary with their mother liquor, to obtain their XRPD data, using a Debye-Scherrer geometry and check the purity of the sample. Crystals from another synthesis with the same procedure were filtered for ~20 min and selected for study by single-crystal X-ray diffraction. Data shows that during the filtration process in air, the crystals of CU7ADFA-1 undergo partial dehydration to give CU7ADFA-2 but they preserve the crystalline nature, Figure 2.9.

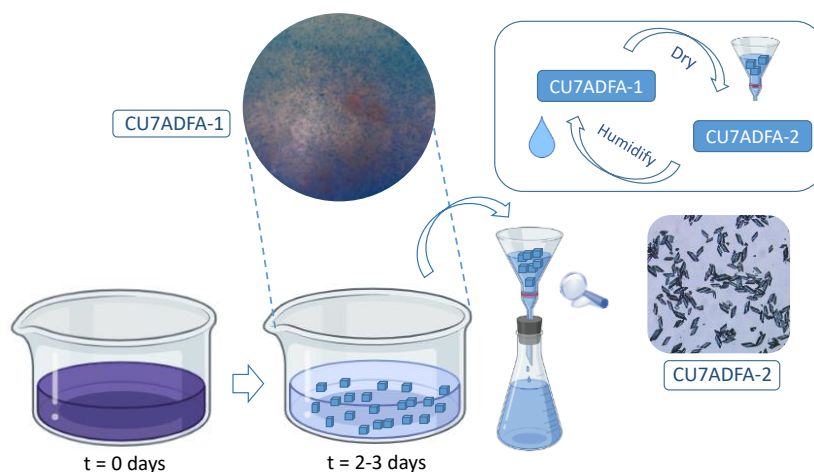


Figure 2.9. Synthesis process of compounds CU7ADFA-1 and CU7ADFA-2 containing fumarate dianion.

Table 2.2. Synthesis conditions employed for dimeric and heptameric compounds.

Compound	Cu(NO ₃) ₂	Adenine	Anion	Yield	pH	Crystal
CU2AD2TB	0.0489 g	0.0676 g	0.0360 g	55	8.8	Black plate
	0.20 mmol	0.50 mmol	0.20 mmol			Two days
CU2ADCAF	0.0489 g	0.0541 g	0.0360 g	35	8.8	Purple plate
	0.20 mmol	0.40 mmol	0.20 mmol			Two weeks
CU2ADTEP	0.0489 g	0.0390 g	0.0540 g	20	9.0	Black prism
	0.20 mmol	0.30 mmol	0.30 mmol			Two months
CU7ADTB	0.0489 g	0.0390 g	0.0540 g	55	8.8	Blue plate
	0.20 mmol	0.30 mmol	0.30 mmol			Four days
CU7ADBZ	0.0489 g	0.0390 g	0.1221 g	60	8.8	Blue square
	0.20 mmol	0.30 mmol	1.0 mmol			Four days
CU7ADTEP	0.0489 g	0.0390 g	0.0997 g	40	8.8	Blue plate
	0.20 mmol	0.30 mmol	0.60 mmol			One month
CU7ADFA	0.1700 g	0.0810 g	0.0360 g	75	9.1	Blue plate
	0.70 mmol	0.60 mmol	0.20 mmol			Two days
CU7ADF	0.1223 g	0.0810 g	0.1160 g	80	9.2	Blue cubic
	0.50 mmol	0.60 mmol	1.0 mmol			Three days
CU7ADAC	0.1223 g	0.0810 g	0.1206 g	60	9.2	Blue cubic
	0.50 mmol	0.60 mmol	0.90 mmol			Four days
CU7ADNAPH	0.1223 g	0.0810 g	0.1405 g	85	9.2	Blue square
	0.50 mmol	0.60 mmol	0.65 mmol			Seven days
CU7ADBP	0.0489 g	0.0603 g	0.1090 g	15	8.8	Blue cubic
	0.20 mmol	0.45 mmol	0.45 mmol			Two weeks
CU7ADBPD	0.1130 g	0.0810 g	0.031 g	55	9.1	Blue plate
	0.45 mmol	0.60 mmol	0.13 mmol			Three weeks
CU7ADS	0.1326 g	0.0810 g	0.1630 g	40	9.1	Blue Needle
	0.55 mmol	0.60 mmol	0.60 mmol			Ten days
CU7ADSD	0.0489 g	0.0603 g	0.1630 g	65	9.0	Blue needle
	0.20 mmol	0.45 mmol	0.60 mmol			Five days

When crystals of CU7ADFA-2 are totally dehydrated at 100 °C or under vacuum, they lose brightness and their colour changes from blue to dark/bright green. Powder X-ray diffraction data indicates a loss of crystallinity with broader peaks shifted to higher 2θ values. This bulk dehydrated sample adsorbs ambient moisture upon air exposure and after 24 hours, it reverts back to blue colour and the XRPD diffractogram is coincident with that of the totally hydrated compound CU7ADFA-1.

Although the heptameric entity and the anion is analogous to that present in the compounds CU7ADF-1/2, the synthesis of compounds CU7ADFA was done during my thesis stay of three months in KAUST (King Abdullah University of Science and Technology). The laboratory temperature and humidity conditions at this University are

extremely controlled at 18 °C and 60% of humidity, giving this type of compound where the single-crystal takes a plate shape, instead of the cubic one obtained in my own laboratory. This fact gives rise to different patterns of supramolecular interactions influencing its thermal stability and the 3D assembly of the building units.

In CU7ADNAPH synthesis procedure, a visual observation of the crystals that appeared in the solution after two days showed a mixture formed by a majority of thick block crystals CU7ADNAPH-1 and a few thinner and elongated crystals CU7ADNAPH-2, both of them blue. One crystal of each type was selected, covered with Paratone oil, placed under the N₂ stream of the diffractometer and quenched to 151 K to proceed to the full X-ray data acquisition. The rest of crystals were allowed to evolve in the mother liquor for another 6–7 days. Visual inspection after this time showed that the thin crystals CU7ADNAPH-1 had disappeared and only the block crystals of CU7ADNAPH-2 remained, Figure 2.10. The composition of the initial mixture of crystals and the purity of the final sample were checked by means of X-ray data taken on polycrystalline samples introduced in a capillary with the mother liquor, and comparing them with the simulated XRPD data from the X-ray structural determination.

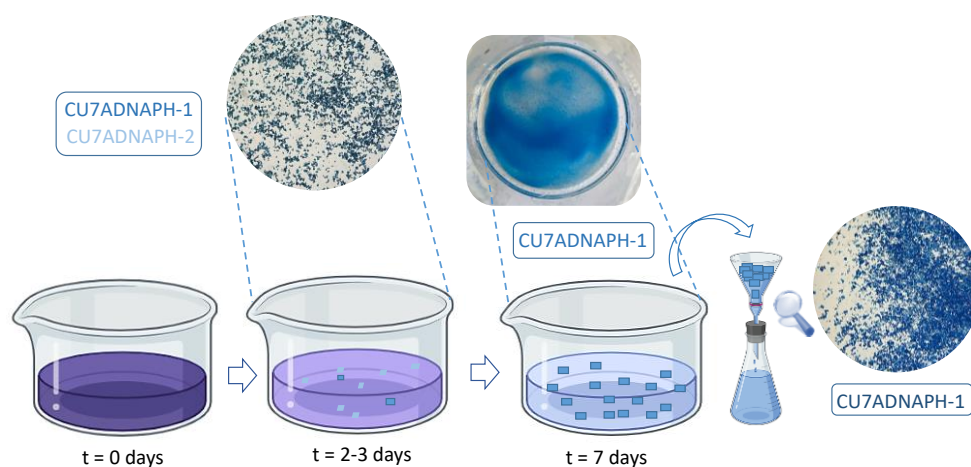


Figure 2.10. Synthesis of compounds CU7ADNAPH-1 and CU7ADNAPH-2.

The crystals of CU7ADNAPH-2 were filtered for ~20 min. As in the compounds with fumarate and acetylenedicarboxylate anions, drying the crystals produces its partial dehydration but, in this case, the process affects their external appearance with a significant loss of brightness and the presence of cracks. It means that every crystal has been fragmented into a multitude of microdomains. The XRPD shows the peaks shift to higher 2θ values than those corresponding to the CU7ADNAPH-2 crystal, indicating that the partial release of the crystallization water molecules leads to a significant shrinkage

of the unit cell. The sample exposed to a 90% saturated atmosphere in water for 24 hours recovers crystallinity and its XRPD is consistent with that corresponding to compound CU7ADNAPH-2.

In compounds CU7ADBP and CU7ADS, the final purple solution was covered with parafilm and immediately a highly insoluble and non crystalline pale blue powder appears. A few block-like crystals of CU7ADBP suitable for X-ray diffraction were isolated after two weeks using test tube diffusion technique in which over the aquo-methanolic solution containing the copper(II) nitrate and adenine mixture, an aqueous solution of the organic acid is layered carefully. Crystal of CU7ADS are obtained after the basification of the cooper-adenine mixture until pH~11.5, the final purple solution is acidified with HNO₃ (1:3 acid/water) until a pH of 9.2. In the case of CU7ADBPD and CU7ADSD, due to the length of the anion employed, a mixture of 10/10 mL of warm water and DMF basified with NaOH (pH~9.1) was employed to dissolve it. The purple solution was left to evaporate at room temperature and blue single-crystals were obtained after ten and five days, respectively.

Table 2.3. Elemental analysis of compounds after they are removed from the mother liquid.

Compound	Experimental				Calculated			
	C (%)	N (%)	H (%)	Cu (%)	C (%)	N (%)	H (%)	Cu (%)
CU2AD2TB	23.10	22.16	4.28	20.20	22.76	22.92	4.86	19.15
CU2ADCAF	33.43	32.77	4.09	12.30	33.57	33.55	4.23	12.69
CU2ADTEP	33.05	29.43	3.95	14.86	33.45	29.26	3.98	14.75
CU7ADTB	23.10	22.16	4.28	20.20	22.76	22.92	4.86	19.15
CU7ADBZ	26.20	20.97	4.35	22.24	26.32	20.92	4.31	22.15
CU7ADTEP	24.72	22.76	3.78	24.17	24.80	22.84	3.83	24.18
CU7ADFA	21.38	22.12	4.10	23.40	21.52	22.14	4.25	23.44
CU7ADF	23.82	23.64	3.80	25.06	23.95	23.71	3.75	25.10
CU7ADAC	21.66	22.31	3.92	23.72	21.74	22.38	4.08	23.69
CU7ADNAPH	22.49	18.60	4.83	19.80	22.42	18.67	5.02	19.77
CU7ADBPD	25.33	19.50	4.73	19.97	25.39	19.53	4.85	20.01
CU7ADS	25.84	19.65	4.53	20.80	25.60	19.47	4.67	20.61
CU7ADSD	26.99	19.50	4.80	19.30	26.89	19.30	5.03	19.15

2.2.2. Infrared spectroscopy

Infrared spectroscopy has turned out to be a useful technique for the initial characterization of the synthesized compounds, as it allows verifying the existence of the bands corresponding to adenine and the different anions. Figures 2.11–2.13 show the infrared spectra of the compounds. Tables 2.4–2.6 show the wavenumbers of the most relevant observed bands,¹⁵⁸ their relative intensity and the assignment that has been proposed in each case.

All spectra exhibit the bands corresponding to the stretching vibration of the C–H and N–H bonds of the purine bases in the region of the spectrum between 3400 and 3100 cm^{-1} , altogether with the O–H bonds of the water molecules. Between 1700 and 1600 cm^{-1} are the bands of the nucleobase ligands for the imino and ketone groups. Around 1640 cm^{-1} , the antisymmetric tension of the carboxylate group of anions are observed. The presence of the peak located around 1600 cm^{-1} corresponding to the vibration of the C=C bond and the deformation of the NH_2 group is noteworthy, which allows the identification of adenine in all the compounds.¹⁵⁹ In the case of the compound CU7ADAC-2, the band associated with the triple bond around 2200 cm^{-1} has been used to verify its presence. The vibrational bands of the M–N bonds appear below 550 cm^{-1} .

¹⁵⁸ Ghose, R. *Inorganica Chim. Acta* **1989**, 156 (2), 303–306. (b) Nakamoto, K. *Infrared and Raman Spectra of Inorganic and Coordination Compounds: Part A: Theory and Applications in Inorganic Chemistry*; John Wiley & Sons, Inc.: New York, (United States), **2008**.

¹⁵⁹ Mohamed, T. A.; Shabaan, I.A., Zoghaib, W. M., Husband, J., Farag, R. S., Alajhaz, A. E. N. M. A., *Journal of molecular structure* **2009**, 938, 263-276.

Chapter 2: Homometallic adenine nucleobase based SMOFs

Table 2.4. Infrared spectra bands (cm^{-1})¹⁶⁰ of the compounds described in chapter 2.^a

Adenine	Theobromine	Caffeine	Theophylline	CU2AD3TB	CU2ADCAF	CU2ADTP	CU7ADTB	Assignment ^b
				3455w	3435s	3446s	3434vs	ν O-H
3354s	—	—	—	3351s	3350s	3360s	3358s	ν_{as} N—H
3123s	3114m	3110m	—	3187s	3170vs	3200s	3199w	N—H
2982s	2954m	2954w	3001w	2951s	2949s	2995w	2944s	ν (C8—H)
1670s	1692vs	1697s	1710s	1700vs	1691s	1681s	1695s	ν C8=N9
—	1665vs	1651s	1664s	1645vs	1654m	1660w	1655vs	ν_{as} C=O
1605m	1593m	1597vs	1622m	1594m	1604vs	1622s	1598w	ν C4=C5, δ NH ₂
—	1548s	1550s	1568s	1551s	1556m	1572s	1546vs	ν_{s} C=O
1504s	—	—	—	1486w	1487w	1496w	1492s	δ C—NH ₂
1420vs	1410s	1404s	—	1401vs	1395vs	1400s	1402vs	δ_{ring} + δ C—H
	1224s	1237vs	1240m	1229s	1238s	1225m	1226w	ν C4—N9
1156m	1141d	1130d	1125w	1144s	1151s	1151m	1145m	ν_{as} C—N
—	1041m	1026vs	980s	1036w	1028m	985w	1032m	ν_{s} N3—CH ₃
—	941m	973vs	—	936m	976m	—	—	ν_{as} N7—CH ₃
—	—	923s	925vs	—	931w	935w	—	ν_{s} N1—CH ₃
790vs	—	—	—	786m	794m	792m	790m	δ NH ₂ (flapping)
720s/640vs	684m	746s, 646m	744s, 643s	737m, 672s	735m, 655s	746s, 648m	730m, 662m	Ring deformation, δ NH ₂
620m	618m	610s	610m	614m	616w	615w	616w	δ C=C—C
—	—	—	—	550m/444s	552m/480w	549m	549m, 451m	ν M—N

^avs: very strong, s: strong, m: medium, w: weak. ^bs: symmetric, as: antisymmetric, ν : stretching vibration, δ : bending vibration, γ : rocking, ω : wagging, ip = in plane, oop = out of plane.

¹⁶⁰ Brown, D. *The Chemical Bond in Inorganic Chemistry. The Bond Valence Model*; Oxford science publications: Oxford, (England), 2006

Chapter 2: Homometallic adenine nucleobase based SMOFs

Table 2.5. Infrared spectra bands (cm^{-1}) of the compounds described in chapter 2.^a

Adenine	Benzoic acid	Fumaric acid	Therephthalic acid	CU7ADBZ	CU7ADFA-2	CU7ADF-2	CU7ADTEP-2	Assignment ^b
				3465vs	3430vs	3450vs	3410vs	ν O—H,
3354s	—	—	—	3360vs	3210s	3350vs		ν_{as} N—H
3123s	3080s	3088m	3110m	3180s	2920w	3210s	3220vs	ν C—H
1670vs	1690vs	1699vs	1690vs	1640vs	1640vs	1640vs	1640vs	ν_{as} C=O + δ NH ₂
1600vs	1590vs	1620s	1570vs	1610s	1610m	1600m	1604s	ν C=C + ν C=N
—	1555vs	1540w	1540s	1545s	1550s	1550s	1546s	ν_{s} C=O
1504s	—	—	—	1500w	1500w	1500w	1502m	ν C—NH ₂
—	1460vs	1496vs	1500vs	1462s	1470s	1460vs	1462s	ν_{as} COO
1420vs	1420vs	1406m	1420vs	1395s	1400s	1400vs	1400vs	δ_{ring} + δ C—H
—	1340s	1382vs	1380vs	1380vs	1380m	1370s	1375s	ν_{s} COO
—	1290vs/1130vs	1296s/1152s	1290vs/1110s	1275s/1145s	1306m/1150m	1280s/1140vs	1275m/1142m	ν_{s} C—O
1230s	1190vs	1202s	1180m	1200s	1195s	1190vs	1200m	δ_{ip} CCH
1020vs	1020vs	1050s	1020s	1025m	1031m	1040m	1040m	γ C—H + γ NH ₂ + ν C—C _{arom}
930vs	930vs	933m	940m	935m	970m	930w	935w	δ C—H, δ C—C
790vs	810s	782m	790vs	790m	795m	800m	795m	δ_{ip} C—H, ω NH ₂
720s/640vs	670s	740m/660s	730s/680m	725m/665m	740m/655m	740m/670s	740m/650m	δ_{ip} ring defor., δ_{oop} COO ⁻
—	—	—	—	550m/460m	560m/455m	520vs, 470m	555w/455w	ν M—N

^avs: very strong, s: strong, m: medium, w: weak. ^bs: symmetric, as: antisymmetric, ν : stretching vibration, δ : bending vibration, γ :rocking, ω : wagging, ip = in plane, oop = out of plane.

Chapter 2: Homometallic adenine nucleobase based SMOFs

Table 2.6. Infrared spectra bands (cm^{-1}) of the compounds described in chapter 2.^a

Adenine	Acetylenedicarboxylic acid	Naphthalen-2,6-dicarboxylic acid	Biphenyl-4,4'-dicarboxylic acid	Stilbidene-4,4'-dicarboxylic acid	CU7ADAC-2	CU7ADNAPH-2	CU7ADBPD	CU7ADS	CU7ADSD	Assignment ^b
					3420vs	3440vs	3550vs	3440vs	3440vs	ν O—H,
3296s	—	—	—	—	3350w	3340w	3360vs	3380vs	3340w	ν N—H
3123s	—	3100w	3220s	3240w	—	3190vs	3200vs	3210vs	3210vs	ν C—H
—	2232m	—	—	—	2130m	—	—	—	—	ν C \equiv C
1670vs	1680vs	1694vs	1680vs	1670vs	1640vs	1640vs	1640vs	1640vs	1640vs	ν_{as} C=O + δ NH ₂
1600vs	1620m	1605m	1600vs	1602vs	1600m	1600m	1600s	1605m	1600w	ν C=C + ν C=N
—	1520m	1570w	1560m	1560m	1550s	1540s	1550s	1545s	1540s	ν_{s} C=O
1504s	—	—	—	—	1500m	1490m	1490w	1500w	1500w	ν C—NH ₂
—	1440s	1504s	1496w	1480vs	1460vs	1460vs	1460vs	1460s	1460s	ν_{as} COO ⁻
1420vs	—	1420vs	1420s	1420vs	—	1400vs	1380vs	1400s	1420vs	δ_{ring} + δ C—H
—	1375s	1344vs	1370s	1384s	1340s	1340s	1350s	1380s	1380vs	ν_{s} COO ⁻
—	1283s/1120m	1290vs/1140s	1300vs/1130m	1290vs/1130m	1280m/1150s	1270m/1140s	1280s/1150m	1270m/1145m	1270m/1140s	ν_{s} C—O
1230ss	1200s	1993s	1180s	1185vs	1200s	1200s	1200s	1195m	1200m	δ_{ip} CCH
1020vs	1060w	1090m	1000s	1020m	1030w	1040m	1030m	1030w	1040m	γ C—H + γ NH ₂ + ν C—C _{arom}
930vs	930w	920m	930m	930w	940w	930w	930w	940w	930w	δ C—H, δ C—C
790vs	820m	780m	780w	780s	780m	790m	770w	795w	790m	δ_{ip} C—H, ω NH ₂
720s/640vs	750vs/650vs	750vs/630m	750s/670m	770s/700s	740m/660m	740m/650m	740m/660m	740m/650m	740m/650m	δ_{ip} ring defor., δ_{oop} COO ⁻
—	—	—	—	—	550m/450m	550m/450m	550m/450m	555m/450m	550m/450m	ν M—N

^avs: very strong, s: strong, m: medium, w: weak. ^bs: symmetric, as: antisymmetric, ν : stretching vibration, δ : bending vibration, γ :rocking, ω : wagging, ip = in plane, oop = out of plane.

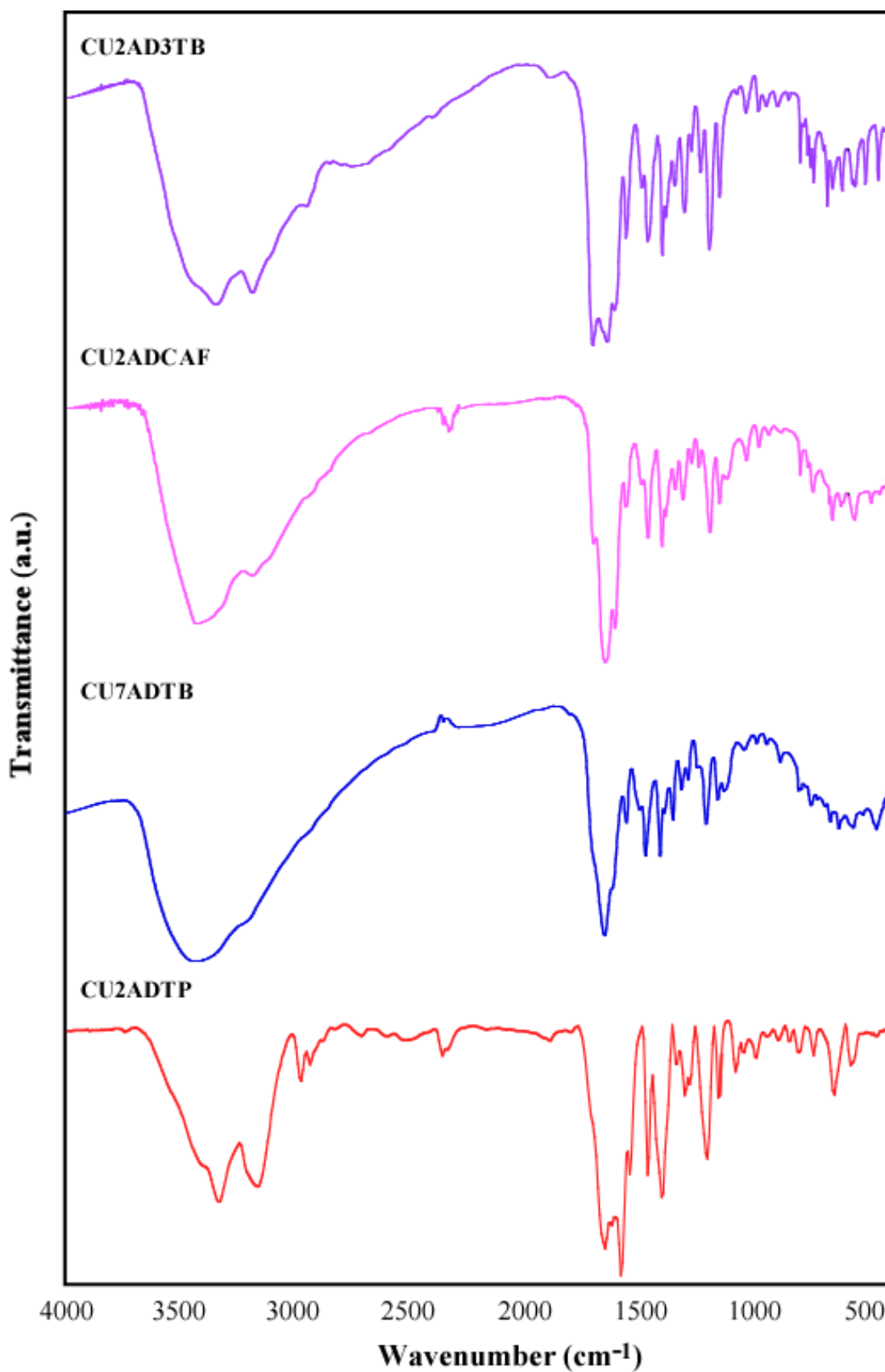


Figure 2.11. Infrared spectra of compounds CU2AD3TB (purple), CU2ADCAF (pink), CU2ADTP (blue) and CU7ADTB (red).

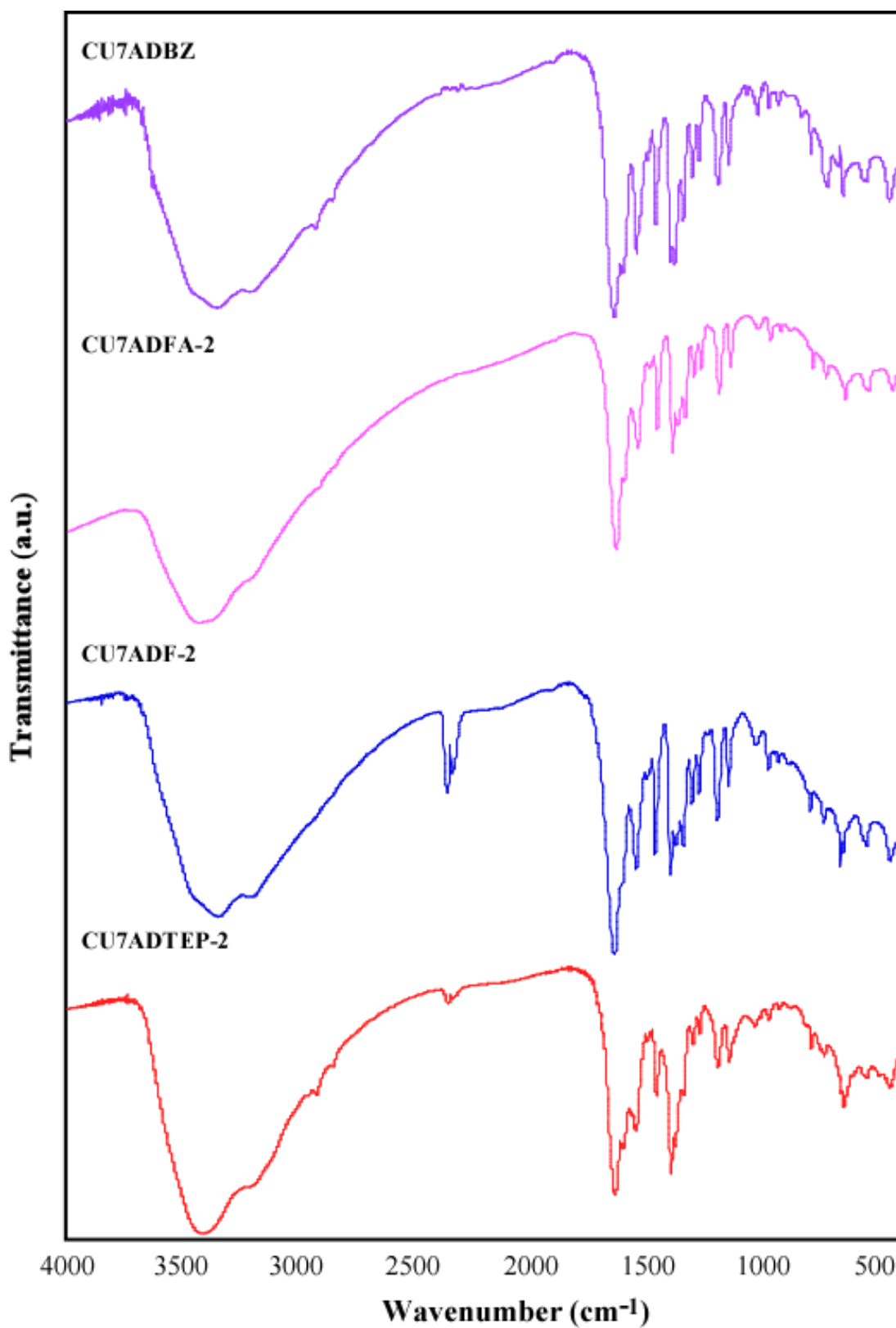


Figure 2.12. Infrared spectra of compounds CU7ADBZ (purple), CU7ADFA-2 (pink), CU7ADF-2 (blue) and CU7ADTEP-2 (red).

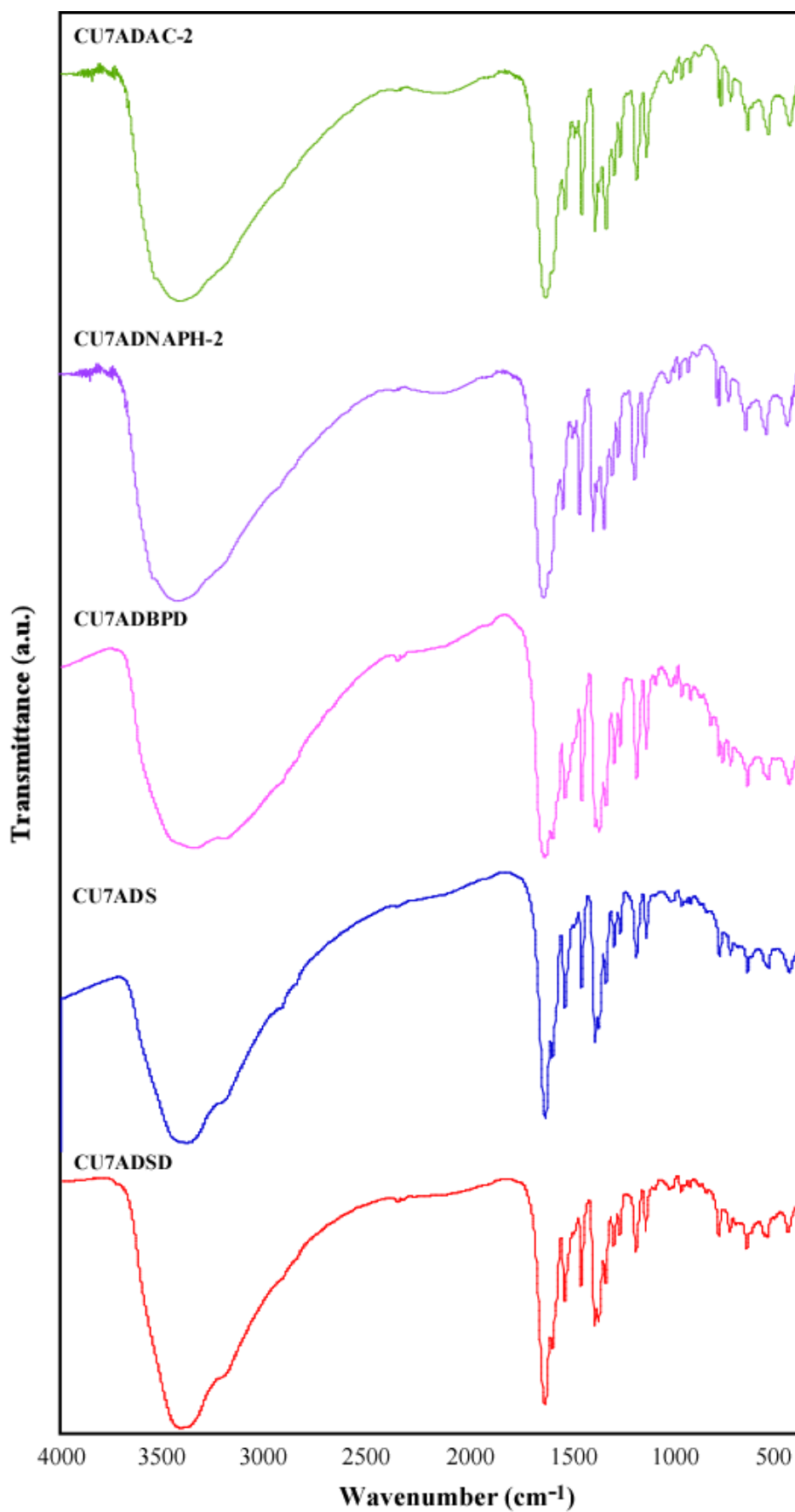


Figure 2.13. Infrared spectra of compounds CU7ADAC-2 (green), CU7ADNAPH-2 (purple) CU7ADBDP (pink), CU7ADS (blue) and CU7ADSD (red).

2.2.3. Thermal analysis

Thermogravimetric analyses (TG/ATD curves) of the compounds are plotted in Figures 2.14–2.15, while the processes occurring in each degradation stage are gathered in Tables 2.7–2.9. Note that all experimental mass losses fit fairly well with those expected from the chemical formula of the compounds. The measurements were run using synthetic air (79% N₂, 21% O₂) as atmosphere from 30 °C to 600 °C with a temperature increase rate of 5 °C/min.

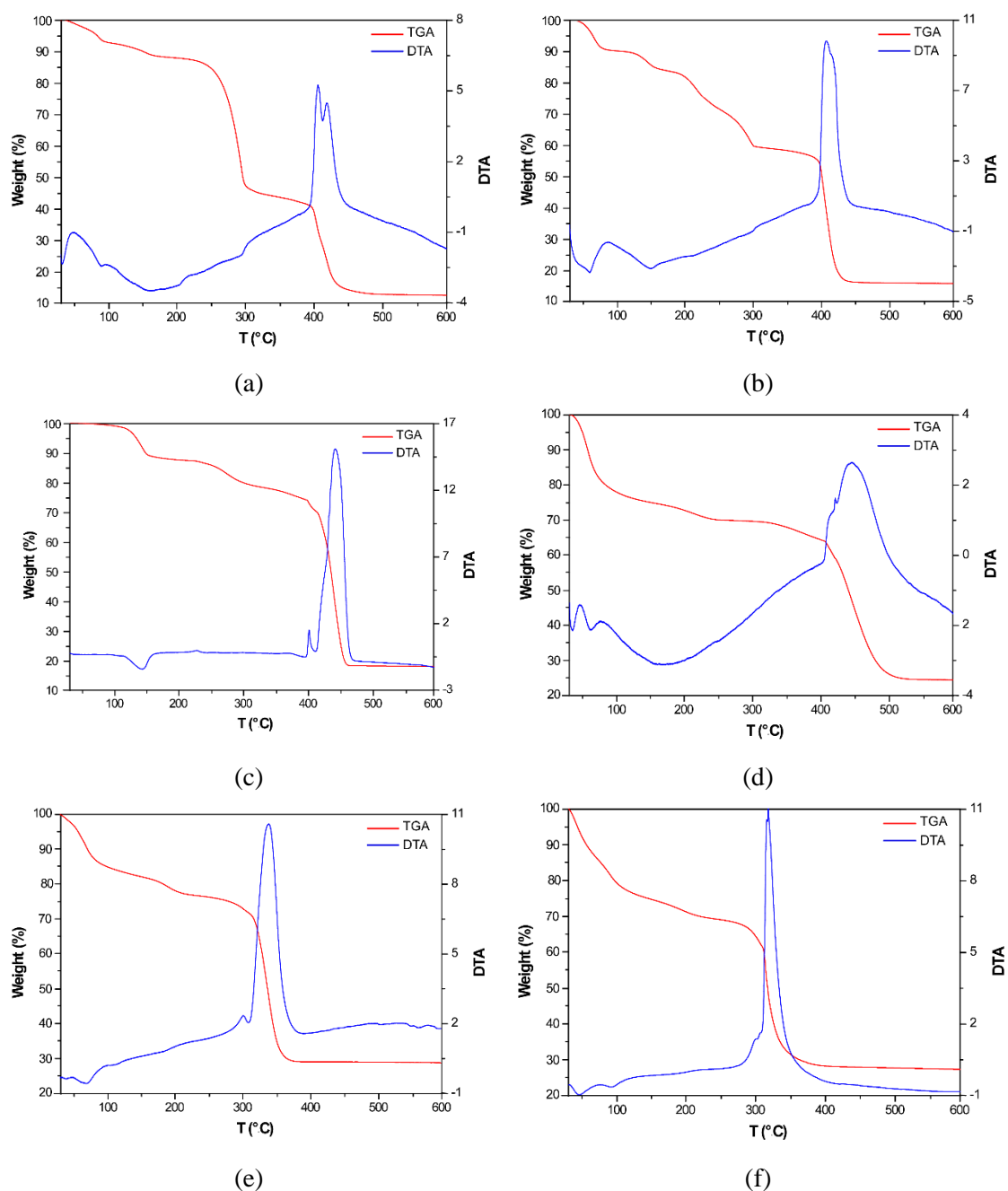


Figure 2.14. Thermogravimetric data (TGA-DTA curves) for compounds (a) CU2AD3TB, (b) CU2ADCAF, (c) CU2ADTP, (d) CU7ADTB, (e) CU7ADBZ and (f) CU2ADTEP-1.

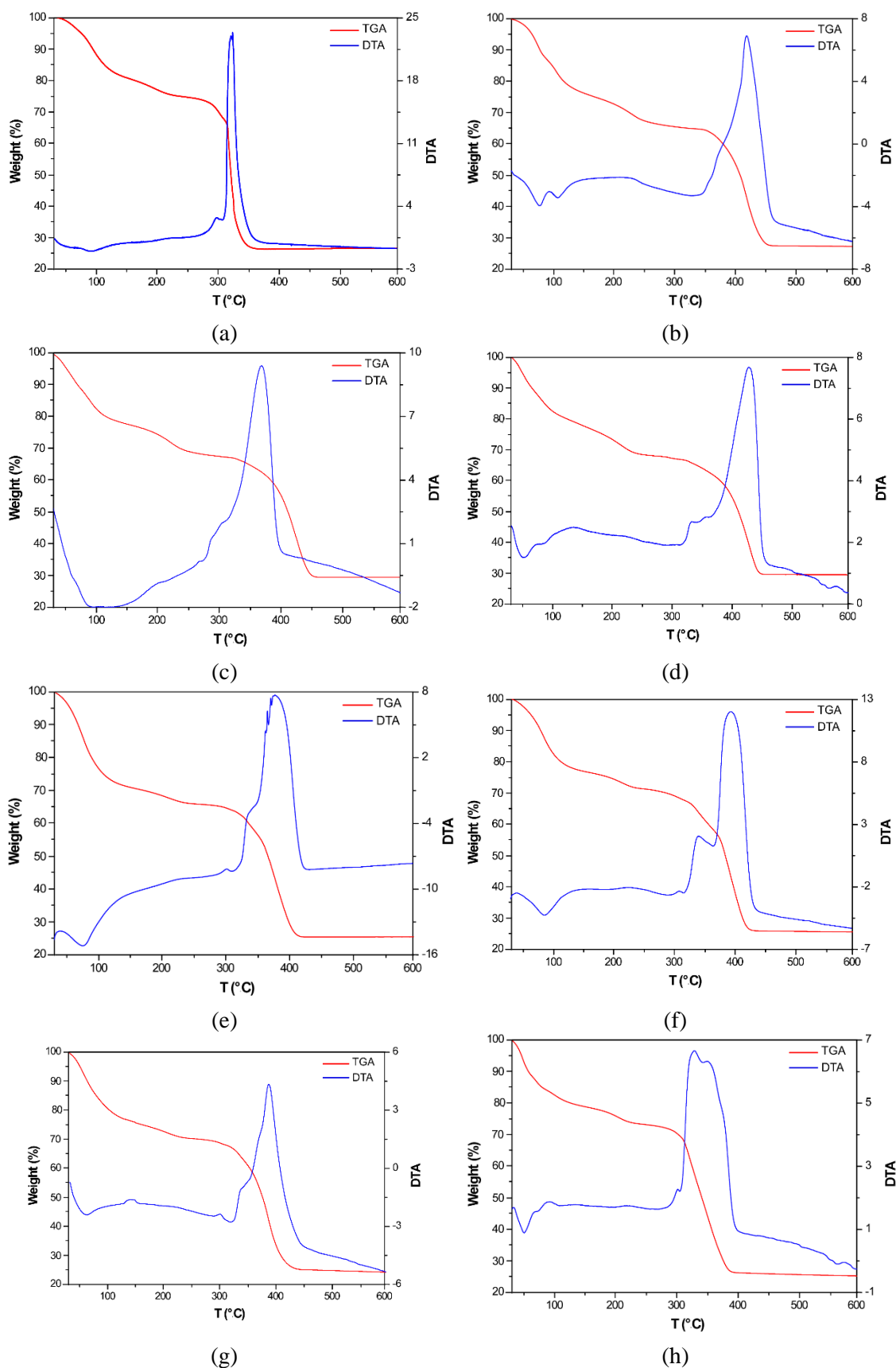


Figure 2.15. Thermogravimetric data (TGA-DTA curves) for (a) CU7ADTEP-2, (b) CU7ADFA-2, (c) CU7ADF-2, (d) CU7ADAC-2, (e) CU7ADNAPH-2, (f) CU7ADBPD, (g) CU7ADS and (h) CU7ADSD.

Table 2.7. Thermoanalytic data for copper-adenine compounds.^a

Step	T _i	T _{peak}	T _f	ΔH	Δm(%)	ΣΔm(%)	ΣΔm(%) _{theor}
CU2AD3TB							
1	25	80	100	Endo	7.34	7.34	7.91 (−6 H ₂ O)
2	100	150	180	Endo	4.47	11.81	11.87 (−3 H ₂ O)
3	220	295	320	Endo	43.59	55.40	55.75 (−3 x C ₇ H ₇ N ₄ O ₂ + −4 x NH ₂)
4	370	415	600	Exo	32.80	88.20	88.36 (CuO)
CU2ADCAF							
1	25	55	80	Endo	9.16	9.16	8.99 (−5 H ₂ O)
2	110	140	150	Endo	5.95	15.11	14.38 (−3 H ₂ O)
3	180	220	300	Endo	25.11	40.22	40.15 (C ₈ H ₁₀ N ₄ O ₂ and −4 NH ₂)
4	370	425	600	Exo	43.74	83.96	84.13 (CuO)
CU2ADTP							
1	25	145	210	Endo	12.50	12.50	12.54 (−12 H ₂ O)
2	230	240	335		10.36	22.86	22.94 (− C ₇ H ₇ N ₄ O ₂)
3	350	380	400	Endo	3.59	26.45	26.65 (−4 NH ₂)
4	400	450	600	Exo	55.15	81.60	81.54 (CuO)
CU7ADTB							
1	25	28/58	95	Endo	21.90	21.90	21.71 (−28 H ₂ O)
2	95	165	180	Endo	4.41	26.31	26.36 (−6 H ₂ O)
3	180		240	Endo	3.59	29.90	30.49 (−6 NH ₂)
4	310	445	600	Exo	46.13	76.03	76.02 (CuO)
CU7ADBZ							
1	25	65	85	Endo	14.98	14.98	15.25 (−17 H ₂ O)
2	85	140	160		5.38	20.36	20.63 (−6 H ₂ O)
3	160	207	240		4.93	25.29	25.42 (−6 NH ₂)
4	300	330	600	Exo	46.95	72.24	72.32 (CuO)
CU7ADTEP-1							
1	25	45	100	Endo	20.78	20.78	20.98 (−24 H ₂ O)
2	100	135	170		5.46	26.24	26.23 (−6 H ₂ O)
3	170	200	245		4.67	30.91	30.89 (−6 NH ₂)
4	285	335	600	Exo	42.07	72.98	72.92 (CuO)

^a T_i = initial temperature; T_{peak} = DTA peak temperature; T_f = final temperature; ΔH = type of process according to DTA, Δm(%) = mass loss percentage for each process; ΣΔm(%) = total mass loss percentage; ΣΔm(%)_{theor} = theoretical total mass loss percentage.

Table 2.8. Thermoanalytic data for heptameric compounds of chapter 2.^a

Step	T _i	T _{peak}	T _f	ΔH	Δm(%)	ΣΔm(%)	ΣΔm(%) _{theor}
CU7ADTEP-2							
1	25	70	100	Endo	15.20	15.20	15.11 (−9 H ₂ O)
2	100		150		2.86	18.06	18.14 (−3 H ₂ O)
3	150	170	220		5.45	23.51	23.51 (−6 NH ₂)
4	280	320	600	Exo	45.33	68.84	68.84 (CuO)
CU7ADFA-2							
1	25	70/105	130	Endo	22.10	22.10	22.25 (−25 H ₂ O)
2	130	150	200	Exo	5.20	27.30	27.59 (−6 H ₂ O)
3	200	230	250	Exo	4.91	32.21	32.27 (−6 NH ₂)
4	250		350		2.87	35.08	35.00 (−3 H ₂ O)
5	350	421	600	Exo	37.39	72.47	72.49 (CuO)
CU7ADF-2							
1	25	125	140	Endo	21.82	21.82	21.82 (−17 H ₂ O − 6 H ₂ O)
2	140		190		3.12	24.94	24.91 (−3 H ₂ O)
3	200	220	240	Endo	5.19	30.13	30.02 (−6 NH ₂)
4	330	440	600	Exo	40.26	70.39	70.39 (CuO)
CU7ADAC-2							
1	25	50	100	Endo	17.14	17.14	17.10 (−18 H ₂ O)
2	100	135	195	Exo	8.58	25.72	25.69 (−9 H ₂ O)
3	200	225	240	Exo	4.93	30.65	30.75 (−6 NH ₂)
4	250	435	600	Exo	40.00	70.65	70.64 (CuO)
CU7ADNAPH-2							
1	25	75	125	Endo	27.54	27.54	27.52 (−27 H ₂ O − 6 H ₂ O)
2	125		180		2.59	30.13	30.02 (−3 H ₂ O)
3	180	230	290	Exo	4.17	34.30	34.46 (−6 NH ₂)
4	300	380	600	Exo	39.92	74.22	74.22 (CuO)
CU7ADBDP							
1	25	80	105	Endo	19.50	19.50	19.59 (−25 H ₂ O)
2	105	150	170	Exo	4.92	24.42	24.48 (−6 H ₂ O)
3	180	229	235	Exo	4.42	28.84	28.83 (− C ₃ H ₇ NO + H ₂ O)
4	260	305	335	Endo	5.45	34.29	34.59 (−2 H ₂ O + −6 NH ₂)
5	330	400	600	Exo	40.67	74.96	74.96 (CuO)

^a T_i = initial temperature; T_{peak} = DTA peak temperature; T_f = final temperature; ΔH = type of process according to DTA, Δm(%) = mass loss percentage for each process; ΣΔm(%) = total mass loss percentage; ΣΔm(%)_{theor} = theoretical total mass loss percentage.

Table 2.9. Thermoanalytic data for stilbene-4,4'-dicarboxylate anion compounds.^a

Step	T _i	T _{peak}	T _f	ΔH	Δm(%)	ΣΔm(%)	ΣΔm(%) _{theor}
CU7ADS							
1	25	55	100	Endo	20.28	20.26	20.03 (–24 H ₂ O)
2	100	135	160	Exo	4.68	24.94	25.04 (–6 H ₂ O)
3	160	220	240	Exo	4.46	29.40	29.49 (–6 NH ₂)
4	270	300	315	Exo	2.25	31.95	31.99 (–3 H ₂ O)
5	315	385	600	Exo	42.24	74.19	74.20 (CuO)
CU7ADSD							
1	25	50	75	Endo	14.03	14.03	14.06 (–17 H ₂ O)
2	75	95	115	Exo	4.96	18.99	19.02 (–6 H ₂ O)
3	115	150	225		6.89	25.88	25.91 (–6 NH ₂ + – 3 H ₂ O)
4	230		300		3.35	29.23	29.26 (–C ₃ H ₇ NO)
5	300	340/350	600	Exo	45.14	74.37	74.44 (–C ₃ H ₇ NO, CuO)

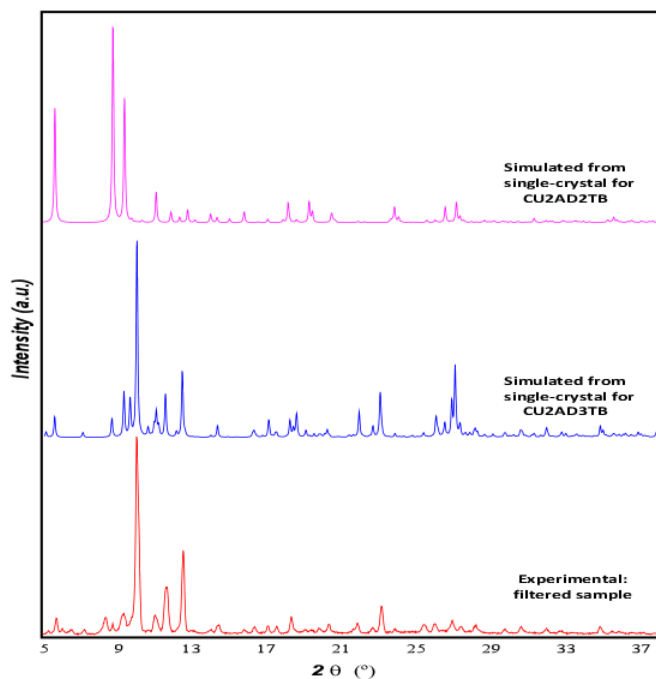
[a] T_i = initial temperature; T_{peak} = DTA peak temperature; T_f = final temperature; ΔH = type of process according to DTA, Δm(%) = mass loss percentage for each process; ΣΔm(%) = total mass loss percentage; ΣΔm(%)_{theor} = theoretical total mass loss percentage.

The thermograms of compounds containing the dimeric entity show four main weight loss stages. First, in two overlapped stages crystallization solvent and coordination water molecules are released at a temperature range of 25–200 °C. Thereafter, the deamination stage occurred at a value range of 180–320 °C. In the case of compounds CU2AD3TB and CU2ADCAF, in this stage the compounds also lose the cocrystallized nucleobase derivative.

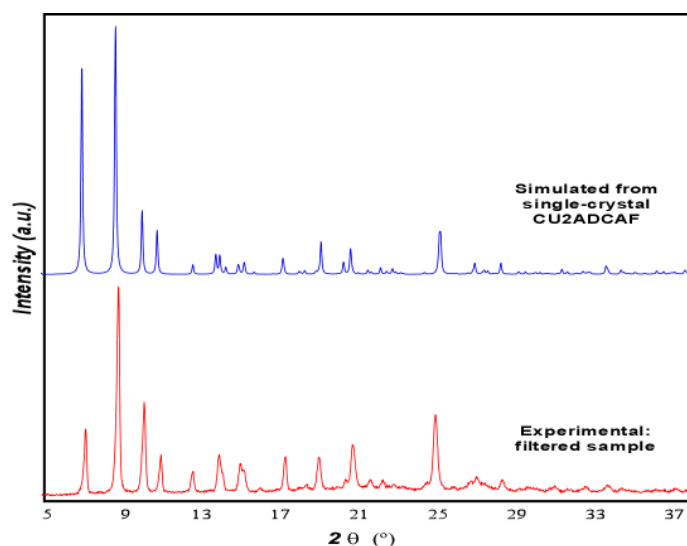
In heptameric entities, crystallization solvent molecules are released at a temperature range of 25–100 °C. Thereafter, the compounds lose the six coordination water molecules at 75–195 °C range. This stage is overlapped with the release of three additional water molecules due to the dihydroxylation of three hydroxide groups of the cluster in the range 140–250 °C. After that, the deamination stage occurred at 180–290 °C. For compounds CU7ADBPD and CU7ADSD, there is another step where a dimethylformamide is lost *ca.* 200 °C. Finally, in all the compounds a very exothermic final decomposition step takes place to lead to CuO (PDF: 48-1548) as final residue at 450 °C.

2.2.4. Powder X-ray diffraction

Crystals of some of these compounds loss crystallinity upon their removal from the mother liquid, therefore, their purity was ensured by means of X-ray powder diffraction performed over samples introduced in a Lindemann capillary and immersed in the synthesis mother liquid. A Rigaku Smartlab automatic diffractometer with a capillary fixation head was used and the diffraction data was collected in continuous rotation in the range $5^\circ < 2\theta < 65^\circ$.



(a)



(b)

Figure 2.16. Experimental X-ray diffraction pattern of the sample and their simulated diffraction patterns for (a) mixture of compounds CU2AD2TB / CU2AD3TB and (b) CU2ADCAF.

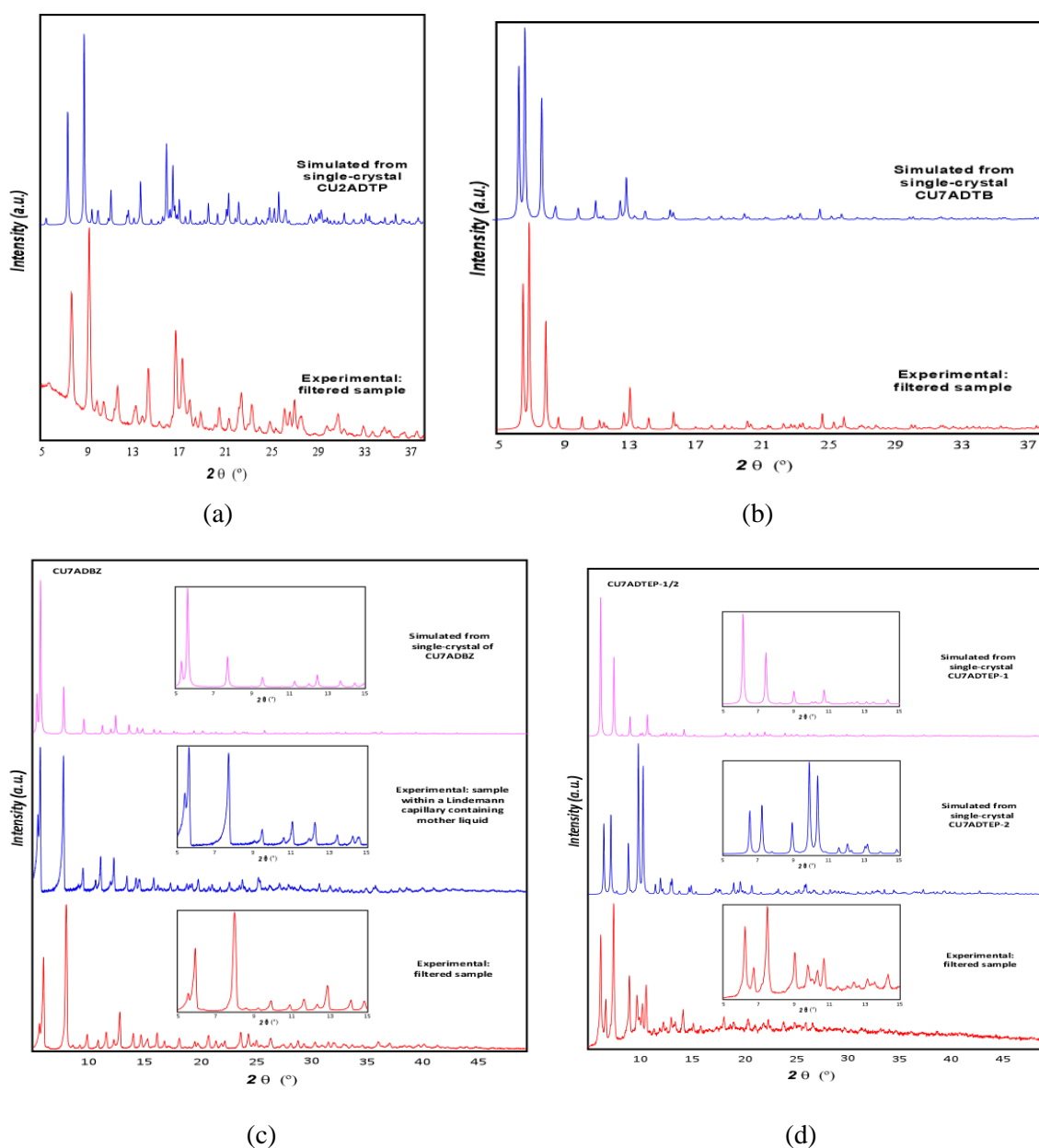


Figure 2.17. Experimental X-ray diffraction pattern of the sample obtained from the synthesis and their simulated diffraction patterns corresponding to compounds: (a) CU2ADTP, (b) CU7ADTB, (c) CU7ADBZ, and (d) CU7ADTEP-1 and CU7ADTEP-2.

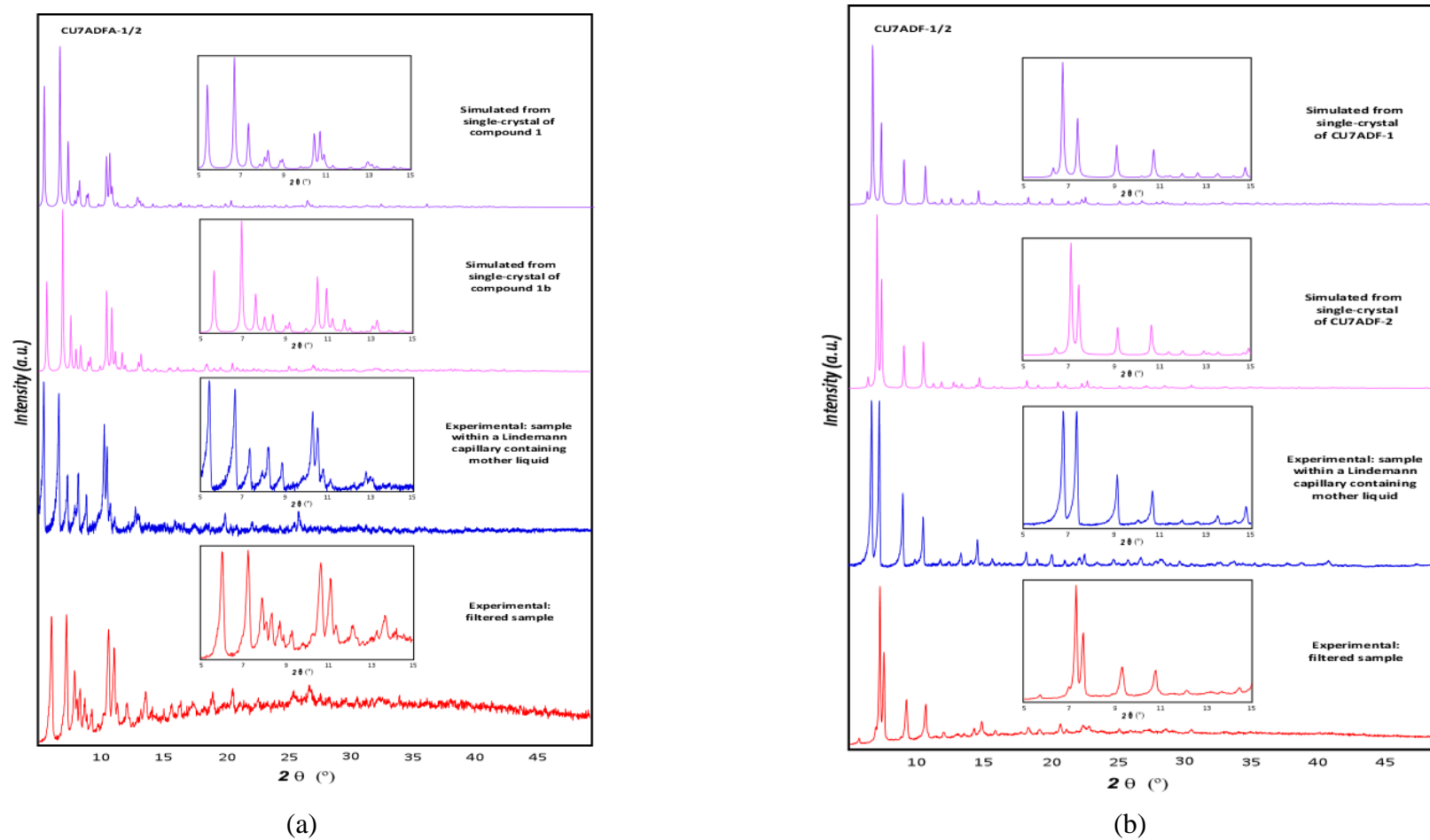


Figure 2.18. Powder X-ray diffraction patterns: simulated pattern from single-crystal of compounds (a) CU7ADFA-1/2 and (b) CU7ADF-1/2 (top), experimental pattern (middle) and experimental pattern measured on filtered sample (bottom). Depicted in the insets an amplification of the 5–15 $^{\circ}$ area for a better comparison.

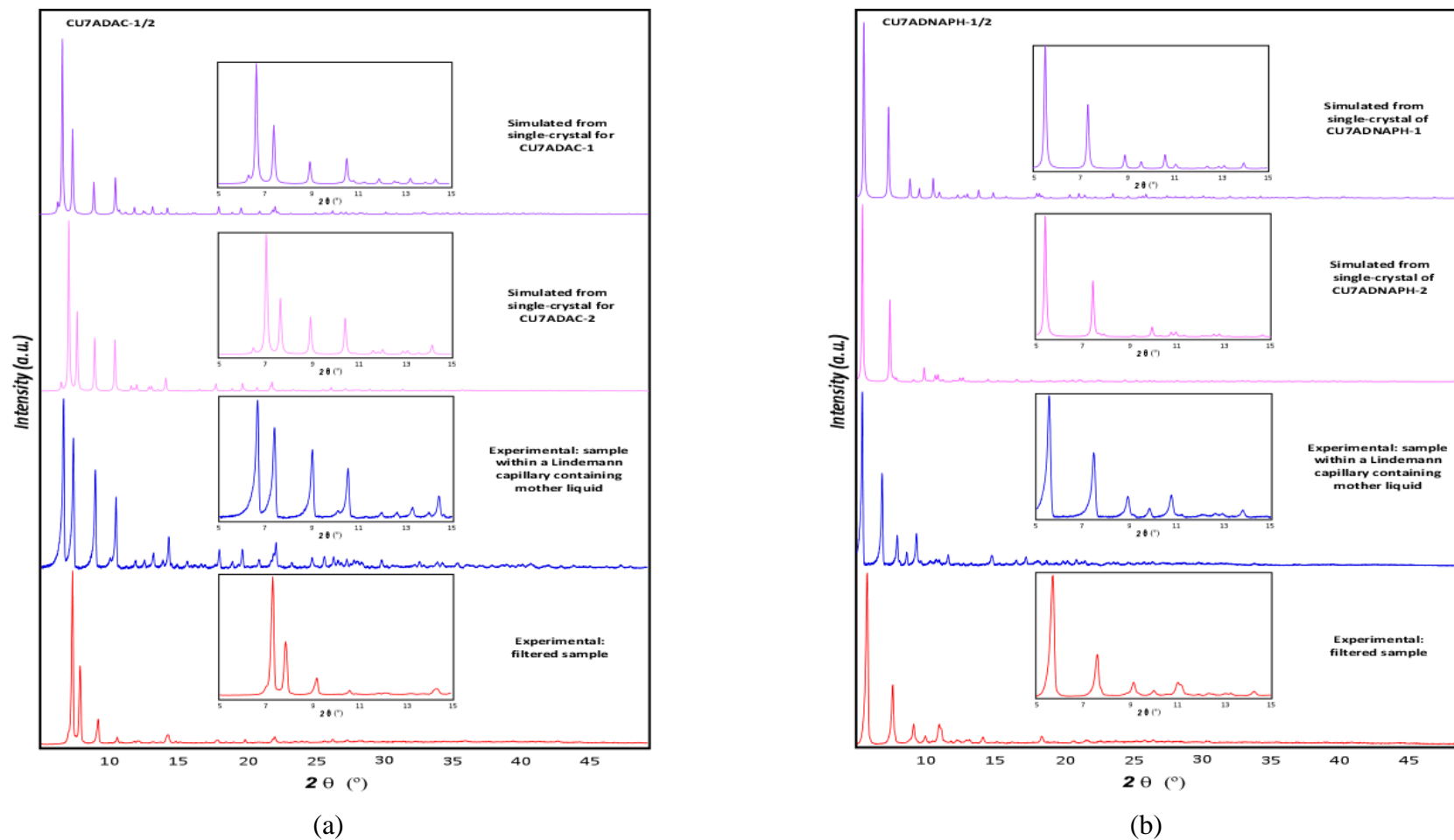


Figure 2.19. Powder X-ray diffraction patterns: simulated pattern from single-crystal of compounds (a) CU7ADAC-1/2 and (b) CU7ADNAPH-1/2 (top), experimental pattern (middle) and experimental pattern measured on filtered sample (bottom). Depicted in the insets an amplification of the 5–15° area for a better comparison.

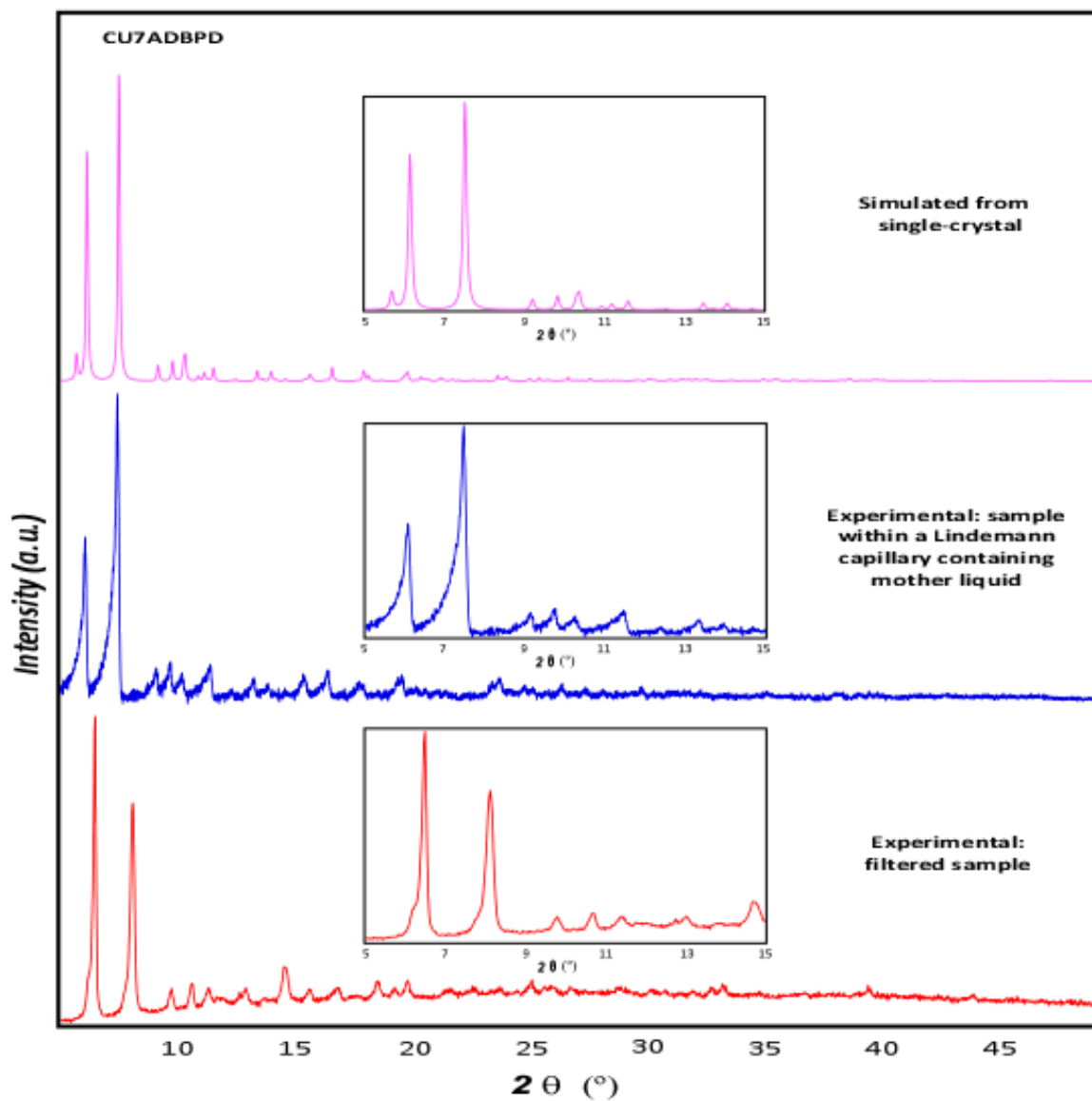


Figure 2.20. Powder X-ray diffraction patterns: simulated pattern from single-crystal of compounds CU7ADBPD (top), experimental pattern (middle) and experimental pattern measured on filtered sample (bottom). Depicted in the insets an amplification of the 5–15° area for a better comparison.

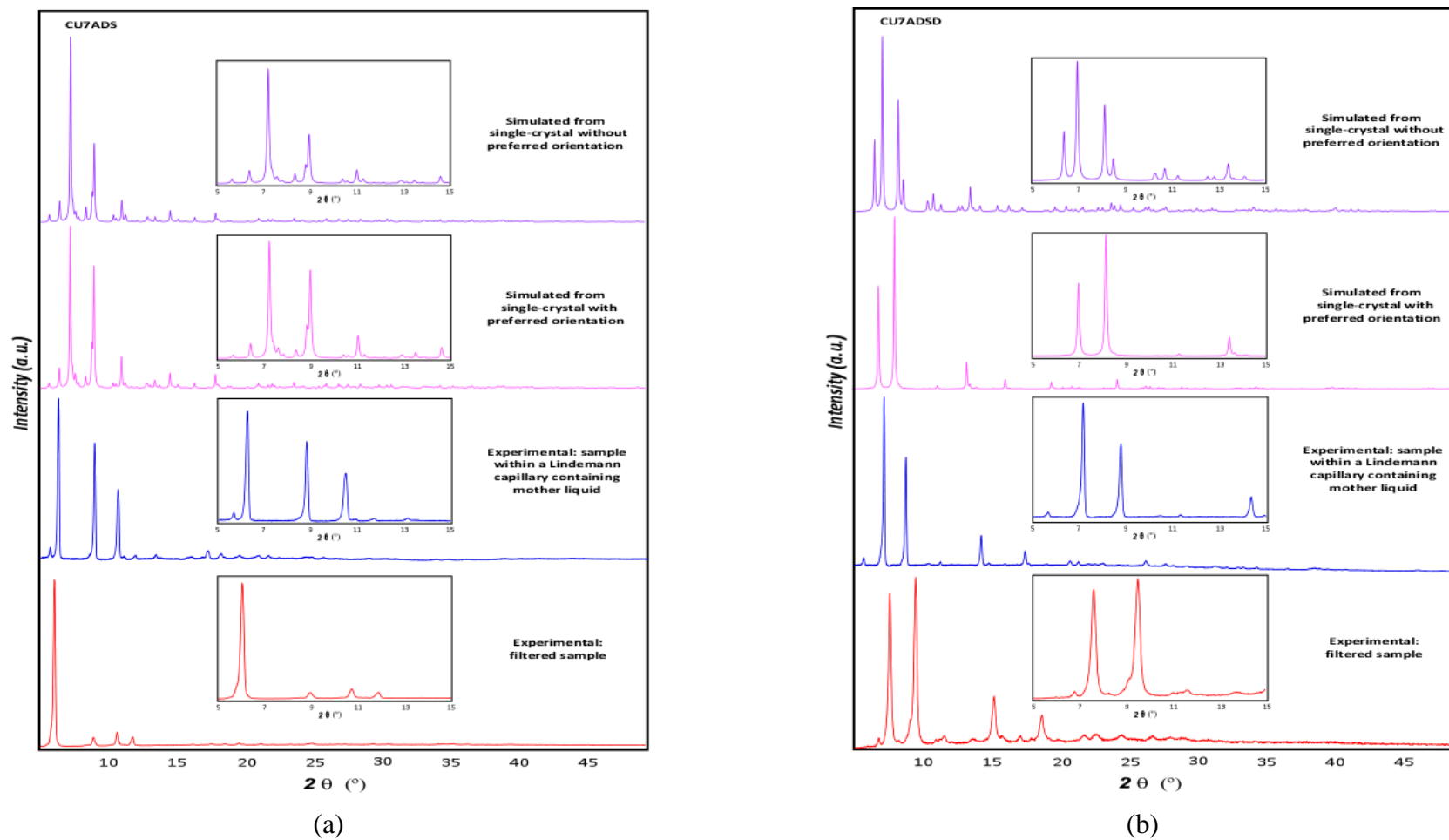


Figure 2.21. Powder X-ray diffraction patterns: simulated pattern from single-crystal of compounds CU7ADS and CU7ADSD (top), experimental pattern (middle) and experimental pattern measured on filtered sample (bottom). Depicted in the insets an amplification of the 5–15 $^{\circ}$ area for a better comparison.

2.3. CRYSTALLOGRAPHIC ANALYSIS

The crystallographic data, the refinement conditions, and parameters of the resolution of compounds have been gathered in Tables 2.10–2.13. All non-hydrogen atoms were refined anisotropically, except those corresponding to disordered atoms. The hydrogen atoms belonging to organic entities have been geometrically fixed and refined according to a riding model with an isotropic thermal parameter linked to the atom to which they are attached (120%). In most of the cases, the hydrogen atoms of the ligands and anions have been located in the difference Fourier map, while in the coordination water molecules cases the routine CALC-OH¹⁶¹ implemented in WinGX¹⁶² interface has been employed. The refinement of water hydrogen atoms has been performed using an isotropic thermal parameter of 150% regarding their parent atom. It has not been possible to position geometrically the hydrogen atoms of all crystallization water molecules due to the disorder that some of them present.

During the structural resolution of the compounds, the existence of a static disorder in the adenine molecules with an unusually high thermal motion of some atoms and nearby peaks in the Fourier map differences with high electron density was observed. This disorder corresponds to the existence of two coplanar positions of the nucleobase base with inverted orientation with respect to the coordination mode (μ - $\kappa N3$: $\kappa N9$ / μ - $\kappa N9$: $\kappa N3$). The disorder was modelled including the peaks observed as atoms split in two positions (A and B), to which common free occupancy factors were assigned to each of the subgroups with the condition that the two occupancy factors add up to 100%, Figure 2.22.

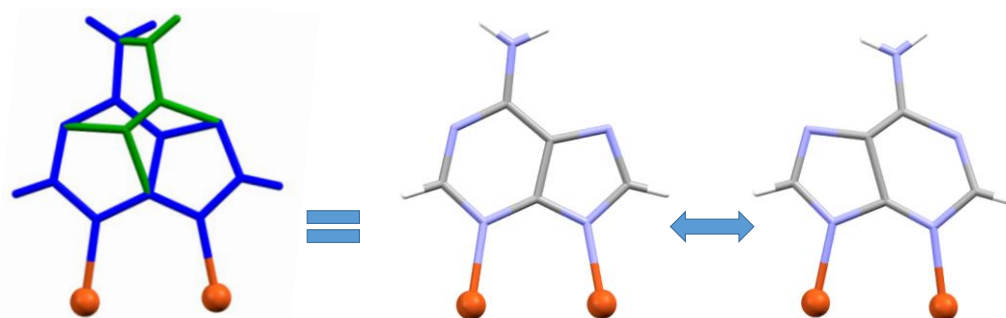


Figure 2.22. Disorder of the adeninato ligand with two coplanar orientations coloured in blue and green.

¹⁶¹ Nardelli M., *J. Appl. Crystallogr.* **1999**, 32, -571.

¹⁶² (a) Farrugia, L. J. *J. Appl. Crystallogr.* **2012**, 45 (4), 849–854, (b) Sheldrick, G. M. *Acta Crystallogr. Sect. C Struct. Chem.* **2015**, 71, 3–8.

Single-crystal X-ray diffraction data were collected on Agilent Technologies Supernova diffractometers. The data reduction was done with the CrysAlisPro program.¹⁶³ Crystal structures were solved by direct methods using the SIR92¹⁶⁴ for CU2AD3TB, CU2AD2TB, CU2ADCAF, CU2ADTP, CU7ADTB, CU7ADBZ, CU7ADFA-2, CU7ADF-1, CU7ADF-2, CU7ADAC-1, CU7ADTEP-1 CU7ADNAPH-1, CU7ADNAPH-2, CU7ADS and CU7ADBPD or SUPERFLIP¹⁶⁵ for CU7ADFA-1, CU7ADAC-2, CU2ADTEP-2, CU7ADBP and CU7ADSD. SHELXS¹⁶⁶ programs and refined by full-matrix least-squares on F^2 including all reflections (WinGX).

As previously stated, in many of these structures some of the adeninato ligands appear disordered as well as some of the organic counterions. In addition to that, the diffraction data quality of the specimen belonging to the partially dehydrated samples is quite poor and as a consequence the refinement of organic parts required the use of several restraints (DFIX, SADI and FLAT).

The crystal structure of compounds show the presence of great channels in which the solvent molecules ions are placed highly disordered. It precluded their modeling and, therefore, the electron density at the voids of the crystal structure was subtracted from the reflection data by the SQUEEZE method¹⁶⁷ as implemented in PLATON.¹⁶⁸ The representation of the crystal structures has been made by MERCURY.¹⁶⁹

¹⁶³ CrysAlisPRO, Oxford Diffraction /Agilent Technologies UK Ltd, Yarnton, England.

¹⁶⁴ A. Altomare, G. Cascarano, C. Giacovazzo, A. Guagliardi, M. C. Burla, G. P. & M. C. *J. Appl. Crystallogr.* **1994**, No. 1978, 8898.

¹⁶⁵ Palatinus, L.; Chapuis, G. *J. Appl. Crystallogr.* **2007**, *40* (4), 786–790.

¹⁶⁶ Sheldrick, G. M. A. *Acta Crystallogr. Sect. A Found. Crystallogr.* **2008**, *64* (1), 112–122.

¹⁶⁷ Spek, A. L. *Acta Crystallogr. Sect. C Struct. Chem.* **2015**, *71*, 9–18.

¹⁶⁸ Spek, A. L. *J. Appl. Crystallogr.* **2003**, *36* (1), 7–13.

¹⁶⁹ (a) Macrae, C. F.; Edgington, P. R.; McCabe, P.; Pidcock, E.; Shields, G. P.; Taylor, R.; Towler, M.; Van De Streek, J. *J. Appl. Crystallogr.* **2006**, *39* (3), 453–457. (b) MacRae, C. F.; Sovago, I.; Cottrell, S. J.; Galek, P. T. A.; McCabe, P.; Pidcock, E.; Platings, M.; Shields, G. P.; Stevens, J. S.; Towler, M.; Wood, P. A. *J. Appl. Crystallogr.* **2020**, *53*, 226–235.

Table 2.10. Crystallographic data and refinement details of compounds CU2AD3TB, CU2AD2TB, CU2ADCAF, CU2ADTEP, CU7ADTB and CU7ADBZ.

	CU2AD3TB	CU2AD2TB	CU2ADCAF	CU2ADTEP	CU7ADTB	CU7ADBZ
formula	C ₄₁ H ₅₈ Cu ₂ N ₃₂ O ₁₅	C ₃₄ H ₇₂ Cu ₂ N ₂₈ O ₂₄	C ₂₈ H ₄₂ Cu ₂ N ₂₄ O ₁₀	C ₄₈ H ₆₈ Cu ₄ N ₃₆ O ₂₀	C ₄₄ H ₁₁₂ Cu ₇ N ₃₈ O ₄₄	C ₄₄ H ₈₆ Cu ₇ N ₃₀ O ₃₃
formula weight	1366.20	1384.20	1001.88	1723.47	2322.49	2008.15
crystal system	Triclinic	Triclinic	Monoclinic	Triclinic	Monoclinic	Trigonal
space group	<i>P</i> $\bar{1}$ (2)	<i>P</i> $\bar{1}$ (2)	<i>C</i> 2/c (15)	<i>P</i> $\bar{1}$ (2)	<i>C</i> 2/c (15)	<i>R</i> $\bar{3}$ (148)
<i>a</i>	10.2142(5)	9.4687(7)	16.0977(8)	9.1184(5)	22.6236(14)	31.2961(8)
<i>b</i>	15.9877(8)	9.8967(6)	19.7853(7)	11.9896(6)	15.3261(7)	31.2961(8)
<i>c</i>	17.5772(11)	15.9452(9)	13.7487(6)	16.3784(9)	27.5588(14)	20.9992 (3)
α	94.837(4)	88.697(5)	90	90.665(4)	90	90
β	98.162(5)	76.994(6)	100.785(4)	105.760(5)	105.705(6)	90
γ	96.355(4)	86.031(6)	90	103.134(4)	90	120
V (Å ³)	2809.2	1452.34(17)	4301.6(3)	1673.05(16)	9198.8(9)	17812.0(9)
Z	2	1	4	1	4	9
T (K)	100.1(2)	150.0(1)	100.1(2)	100.0(2)	100.0(2)	150.0(2)
λ (Å)	0.71073	1.54184	0.71073	0.71073	0.71073	1.54184
Sizes (mm)	0.36, 0.16, 0.04	0.14, 0.12, 0.08	0.32, 0.06, 0.04	0.06, 0.05, 0.04	0.11, 0.06, 0.05	0.13, 0.12, 0.11
Shape	Plate	Plate	Needle	Prism	Plate	Square
Colour	Black	Purple	Purple	Black	Blue	Blue
Max. and medium Δ/σ	0.000 / 0.000	0.000 / 0.000	0.000 / 0.000	0.001 / 0.000	0.000 / 0.000	0.000 / 0.001
Θ interval (°)	1.831 – 28.208	2.844 – 76.221	1.649 – 28.269	2.592 – 27.347	1.625 – 24.999	3.882 – 60.000
hkl interval	-13 <h<math>\leq13; -21<hmath>\leq21; -22<hmath>\leq22</hmath></hmath></h<math>	-7 <hmath>\leq11; -12<hmath>\leq12; -18<hmath>\leq20</hmath></hmath></hmath>	-10 <hmath>\leq21; -25<hmath>\leq26; -17<hmath>\leq17</hmath></hmath></hmath>	-10 <hmath>\leq10; -15<hmath>\leq15; -20<hmath>\leq18</hmath></hmath></hmath>	-26 <hmath>\leq6; -17<hmath>\leq18; -32<hmath>\leq32</hmath></hmath></hmath>	-35 <hmath>\leq27; -27<hmath>\leq34; -17<hmath>\leq23;</hmath></hmath></hmath>
ρ_c (g·cm ⁻³)	1.615	2.180	1.380	1.709	1.677	1.684
μ (cm ⁻¹)	0.853	2.412	1.051	1.351	1.696	2.907
<i>F</i> (000)	1412	1012	1824	784	4788	9243
<i>S</i> ^a	1.042	1.039	1.066	1.088	0.980	1.120
<i>R</i> _{int}	0.0308	0.0415	0.0351	0.0326	0.1725	0.0528
Parameters	768	320	215	446	450	428
Weight scheme ^c	Shelx	Shelx	Shelx	Shelx	Shelx	Shelx
final R indices						
[<i>I</i> > 2 σ (<i>I</i>)] <i>R</i> ₁ ^b / <i>wR</i> ₂ ^c	0.0882/0.2149	0.0706/0.1901	0.0786/0.2142	0.0554/0.1115	0.0962/0.2231	0.0775/0.2148
all data <i>R</i> ₁ ^b / <i>wR</i> ₂ ^c	0.1185/0.2379	0.0811/0.2009	0.1161/0.2435	0.0676/0.1167	0.1879/0.2715	0.1385/0.2772
^a <i>S</i> =[$\sum w(F_o^2 - F_c^2)^2 / (N_{obs} - N_{param})$] ^{1/2} . ^b <i>R</i> ₁ = $\sum F_o - F_c / \sum F_o $. ^c <i>wR</i> ₂ = [$\sum w(F_o^2 - F_c^2)^2 / \sum wF_o^2$] ^{1/2} ; <i>w</i> = 1/[$\sigma^2(F_o^2) + (aP)^2 + b$] where <i>P</i> = (max(<i>F</i> _o ² , 0) + 2 <i>F</i> _c ²)/3; CU2AD3TB (<i>a</i> = 0.0930, <i>b</i> = 14.2495); CU2AD2TB (<i>a</i> = 0.0972, <i>b</i> = 2.7145); CU2ADCAF (<i>a</i> = 0.1088, <i>b</i> = 18.6618); CU2ADTEP (<i>a</i> = 0.0267, <i>b</i> = 5.5757), CU7ADTB (<i>a</i> = 0.1180, <i>b</i> = 0) and CU7ADBZ (<i>a</i> = 0.1202, <i>b</i> = 198.4934).						

Table 2.11. Crystallographic data and refinement details.

	CU7ADTEP-1	CU7ADTEP-2	CU7ADFA-1	CU7ADFA-2	CU7ADF-1	CU7ADF-2
formula	C ₃₈ H ₉₄ N ₃₀ O ₄₀ Cu ₇	C ₃₈ H ₇₀ Cu ₇ N ₃₀ O ₂₈	C ₃₄ H ₉₄ Cu ₇ N ₃₀ O ₄₁	C ₃₄ H ₈₀ Cu ₇ N ₃₀ O ₃₄	C ₃₄ H ₈₈ Cu ₇ N ₃₀ O ₃₈	C ₃₄ H ₇₆ Cu ₇ N ₃₀ O ₃₂
formula weight	2056.21	1839.97	2024.17	1898.06	1970.12	1862.02
crystal system	Monoclinic	Triclinic	Monoclinic	Monoclinic	Monoclinic	Monoclinic
space group	<i>P</i> 2 ₁ / <i>c</i> (14)	<i>P</i> $\bar{1}$ (2)	<i>C</i> 2/ <i>c</i> (15)	<i>C</i> 2/ <i>c</i> (15)	<i>C</i> 2/ <i>c</i> (15)	<i>C</i> 2/ <i>c</i> (15)
<i>a</i>	14.636(1)	10.530(3)	52.419(4)	52.134(3)	28.462(5)	35.805(7)
<i>b</i>	16.079(6)	13.979(5)	17.574(9)	16.758(6)	16.489(1)	16.417(1)
<i>c</i>	17.929(1)	24.763(3)	20.366(2)	19.903(1)	17.881(2)	17.887(3)
α	90	94.114(18)	90	90	90	90
β	100.961(9)	97.132(17)	123.949(1)	122.401(7)	113.016(11)	136.27(4)
γ	90	103.66(3)	90	90	90	90
<i>V</i> (Å ³)	4142.0(5)	3495.3(17)	15563(3)	14681.1(15)	7723.6(18)	7265(4)
<i>Z</i>	2	2	8	8	4	4
<i>T</i> (K)	100.0(1)	100.0(1)	101.5(5)	170.0(1)	150.0(1)	170.0(1)
λ (Å)	0.71073	0.71073	1.54184	0.71073	0.71073	0.71073
Sizes (mm)	0.12/0.11/0.06	0.11, 0.09, 0.05	0.07, 0.03, 0.02	0.06, 0.02, 0.01	0.08/0.06/0.04	0.03/0.02/0.02
Shape	Plate	Plate	Plate	Plate	Cubic	Cubic
Colour	Blue	Blue	Blue	Blue	Blue	Blue
Max. and medium Δ/σ	0.000 / 0.000	0.001 / 0.000	0.001 / 0.000	0.000 / 0.000	0.000 / 0.000	0.000 / 0.000
Θ interval (°)	1.715 – 24.998	2.787 – 24.000	2.032 – 48.728	1.845 – 24.200	1.649 – 28.269	2.114 – 29.960
hkl interval	-17 ≤ h ≤ 17; -19 ≤ k ≤ 19; -15 ≤ l ≤ 21	-12 ≤ h ≤ 12; -15 ≤ k ≤ 15; -28 ≤ l ≤ 28	-50 ≤ h ≤ 50; -17 ≤ k ≤ 17; -15 ≤ l ≤ 19	-60 ≤ h ≤ 60; -19 ≤ k ≤ 18; -22 ≤ l ≤ 22	-33 ≤ h ≤ 21; -19 ≤ k ≤ 19; -17 ≤ l ≤ 21	-48 ≤ h ≤ 44; -22 ≤ k ≤ 22; -25 ≤ l ≤ 24
ρ_c (g·cm ⁻³)	1.649	1.585	1.728	1.717	1.694	1.702
μ (cm ⁻¹)	1.866	2.152	3.306	2.091	1.995	2.110
<i>F</i> (000)	2110	1628	8312	7752	4036	3796
<i>S</i> ^a	1.169	1.141	1.534	1.212	0.957	1.249
<i>R</i> _{int}	0.1128	0.1728	0.0853	0.0691	0.1702	0.0668
Parameters	409	459	747	734	400	410
Weight scheme ^c	Shelx	Shelx	Shelx	Shelx	Shelx	Shelx
final R indices						
[<i>I</i> > 2σ(<i>I</i>)] <i>R</i> ₁ ^b / <i>wR</i> ₂ ^c	0.1327/0.3572	0.1728/0.4180	0.1282/0.3704	0.1564/0.4484	0.1043/0.2863	0.1678 / 0.4568
all data <i>R</i> ₁ ^b / <i>wR</i> ₂ ^c	0.2424/0.4332	0.3372/0.4765	0.1681/0.4147	0.2445/0.4926	0.2336/0.3764	0.3247 / 0.5238
^a <i>S</i> = [Σw(F _o ² - F _c ²) ² / (N _{obs} - N _{param})] ^{1/2} . ^b <i>R</i> ₁ = Σ F _o - F _c / Σ F _o . ^c <i>wR</i> ₂ = [Σw(F _o ² - F _c ²) ² / ΣwF _o ²] ^{1/2} ; w = 1/[σ ² (F _o ²) + (aP) ² + b] where P = (max(F _o ² , 0) + 2F _c ²) / 3; CU7ADTEP-1 (a = 0.2000, b = 0); CU7ADTEP-2 (a = 0.2000, b = 0); CU7ADFA-1 (a = 0.2000, b = 0); CU7ADFA-2 (a = 0.2000, b = 0); CU7ADF-1 (a = 0.1718, b = 0); CU7ADF-2 (a = 0.2000, b = 0),						

Table 2.12. Crystallographic data and refinement details.

	CU7ADAC-1	CU7ADAC-2	CU7ADNAPH-1	CU7ADNAPH-2	CU7ADBP	CU7ADBDP
formula	C ₃₄ H ₈₆ N ₃₀ O ₃₈ Cu ₇	C ₃₄ H ₇₆ Cu ₇ N ₃₀ O ₃₃	C ₄₂ H ₁₁₂ Cu ₇ N ₃₀ O ₄₈	C ₄₂ H ₁₁₂ Cu ₇ N ₃₀ O ₄₈	C ₄₄ H ₁₃₈ Cu ₇ N ₃₀ O ₆₀	C ₄₇ H ₁₀₇ Cu ₇ N ₃₀ O ₄₂
formula weight	1968.10	1878.02	2250.39	2250.33	2492.62	2223.41
crystal system	Monoclinic	Monoclinic	Orthorhombic	Monoclinic	Monoclinic	Orthorhombic
space group	<i>C2/c</i> (15)	<i>C2/c</i> (15)	<i>Pbcn</i> (60)	<i>P21/c</i> (14)	<i>I2/c</i> (15)	<i>Pccn</i> (56)
<i>a</i>	28.4832(5)	26.3048(16)	16.0999(4)	15.9866(12)	18.2720(6)	28.7356(8)
<i>b</i>	16.4538(2)	16.2582(7)	17.8124(7)	15.8405(7)	15.9298(5)	18.4350(5)
<i>c</i>	17.9449(3)	17.7037(12)	32.9353(9)	18.4074(9)	37.2369(16)	17.9382(4)
α	90	90	90	90	90	90
β	111.355(2)	107.089(7)	90	95.424(5)	93.503(3)	90
γ	90	90	90	90	90	90
V (Å ³)	7832.6(2)	7237.0(8)	9445.1(5)	4640.5(5)	10825.1(7)	9502.6(4)
Z	4	4	4	2	4	4
T (K)	150.1(3)	150.1(1)	150.0(1)	151.0(2)	100.0(1)	150.0(1)
λ (Å)	1.54184	0.71073	1.54184	1.54184	0.71073	0.71073
Sizes (mm)	0.10, 0.10, 0.05	0.13, 0.12, 0.11	0.08, 0.07, 0.03	0.07, 0.07, 0.02	0.08, 0.07, 0.03	0.07, 0.03, 0.02
Shape	Cubic	Square	Square	Cubic/Square	Cube	Plate
Colour	Blue	Blue	Blue	Blue	Blue	Blue
Max. and medium Δ/σ	0.000 / 0.000	0.001 / 0.000	0.001 / 0.000	0.000 / 0.000	0.000 / 0.000	0.000 / 0.000
Θ interval (°)	4.496 – 73.126	2.407 – 28.729	3.701 – 62.996	3.688 – 72.697	1.983 – 23.999	1.735 – 23.997
hkl interval	-35 ≤ h ≤ 34; -20 ≤ k ≤ 18; -20 ≤ l ≤ 22	-25 ≤ h ≤ 34; -21 ≤ k ≤ 21; -22 ≤ l ≤ 23;	-18 ≤ h ≤ 14; -20 ≤ k ≤ 20; -38 ≤ l ≤ 38	-18 ≤ h ≤ 19; -18 ≤ k ≤ 19; -14 ≤ l ≤ 22	-20 ≤ h ≤ 20; -18 ≤ k ≤ 16; -42 ≤ l ≤ 42	-32 ≤ h ≤ 32; -18 ≤ k ≤ 21; -20 ≤ l ≤ 20
ρ_c (g·cm ⁻³)	1.669	1.724	1.583	1.611	1.529	1.544
μ (cm ⁻¹)	2.969	2.120	2.622	2.669	1.456	1.635
<i>F</i> (000)	4028	3828	4644	2322	5180	4580
S ^a	1.050	0.921	1.093	1.003	0.977	1.172
R _{int}	0.0317	0.0786	0.0821	0.1037	0.0628	0.1131
Parameters	417	286	456	444	471	447
Weight scheme ^c	Shelx	Shelx	Shelx	Shelx	Shelx	Shelx
final R indices						
[I > 2 σ (I)] R ₁ ^b /wR ₂ ^c	0.0832/0.2408	0.1397/0.3863	0.1334/0.3931	0.1166/0.3157	0.0630/0.1806	0.1098/0.3293
all data R ₁ ^b /wR ₂ ^c	0.0929/0.2408	0.2977/0.4355	0.1621/0.4204	0.2030/0.3700	0.1021/0.1931	0.1783/0.3802
^a S = [$\sum w(F_o^2 - F_c^2)^2 / (N_{obs} - N_{param})$] ^{1/2} . ^b R ₁ = $\sum F_o - F_c / \sum F_o $. ^c wR ₂ = [$\sum w(F_o^2 - F_c^2)^2 / \sum wF_o^2$] ^{1/2} ; w = 1/[$\sigma^2(F_o^2) + (aP)^2 + b$] where P = (max(F _o ² , 0) + 2F _c ²)/3; CU7ADAC-1 (a = 0.1351, b = 38.8421), CU7ADAC-2 (a = 0.2000, b = 0), CU7ADNAPH-1 (a = 0.1997, b = 40.7961), CU7ADNAPH-2 (a = 0.2000, b = 0); CU7ADBP (a = 0.1090, b = 0).						

Table 2.13. Crystallographic data and refinement details.

	CU7ADS	CU7ADSD
formula	C ₄₆ H ₁₀₀ Cu ₇ N ₃₀ O ₄₀	C ₅₂ H ₁₁₆ Cu ₇ N ₃₂ O ₄₃
formula weight	2158.33	2322.54
crystal system	Monoclinic	Monoclinic
space group	<i>P</i> 2 ₁ / <i>c</i> (14)	<i>C</i> 2/ <i>c</i> (15)
<i>a</i>	15.9667(6)	16.0981(3)
<i>b</i>	19.6541(5)	21.7161(6)
<i>c</i>	28.1700(1)	28.4683(7)
α	90	90
β	102.150(4)	103.393(2)
γ	90	90
V (Å ³)	8642.0(5)	9681.5(4)
Z	4	4
T (K)	170.0(1)	150.0(1)
λ (Å)	0.71073	0.71073
Sizes (mm)	0.14, 0.03, 0.02	0.13, 0.03, 0.02
Shape	Needle	Needle
Colour	Blue	Blue
Max. and medium Δ/σ	0.001 / 0.000	0.000 / 0.000
Θ interval (°)	1.931 – 29.990	1.876 – 24.497
hkl interval	-19 ≤ h ≤ 21; -27 ≤ k ≤ 27; -37 ≤ l ≤ 37	-20 ≤ h ≤ 20; -27 ≤ k ≤ 26; -36 ≤ l ≤ 36
ρ_c (g·cm ⁻³)	1.659	1.593
μ (cm ⁻¹)	1.793	1.609
<i>F</i> (000)	4436	4796
S ^a	1.190	1.044
R _{int}	0.0782	0.1029
Parameters	857	532
Weight scheme	Shelx	Shelx
final R indices		
[I > 2 σ (I)] R ₁ ^b /wR ₂ ^c	0.1251/0.3722	0.1087/0.3042
all data R ₁ ^b /wR ₂ ^c	0.2391/0.4281	0.2308/0.3961
^a S = $[\sum w(F_o^2 - F_c^2)^2 / (N_{obs} - N_{param})]^{1/2}$. ^b R ₁ = $\sum F_o - F_c / \sum F_o $. ^c wR ₂ = $[\sum w(F_o^2 - F_c^2)^2 / \sum wF_o^2]^{1/2}$; w = $1/[\sigma^2(F_o^2) + (aP)^2 + b]$ where P = (max(F _o ² , 0) + 2F _c ²)/3; CU7ADS (a = 0.2000, b = 0), CU7ADSD (a = 0.2000, b = 0).		

2.4. Supramolecular architectures based on dimeric metal-adenine entities

A key factor to afford porous and robust 3D architectures of SMOFs is the use of rigid and discrete units entangled by predictable supramolecular synthons. The adenine nucleobase (Hade) and its conjugated adeninato ligands (ade) are well suited to generate this kind of material owing to its predominant coordination mode (μ - $\kappa N3:\kappa N9$), Figure 2.23. In these compounds, the Watson-Crick (W-C) and Hoogsteen (H) faces of the nucleobases are decorating the external surface of the metal-adenine entities and they are available to establish complementary hydrogen bonding interactions. In principle, it should provide a hydrogen bonded robust porous supramolecular network.

In some cases the great tendency of water molecules in which the synthesis is accomplished to stablish hydrogen bonds disrupts the predicted hydrogen bonding interactions.^{107b} This phenomena has been also reported for compound $[\text{Cu}_2(\mu\text{-Hade})_4\text{Cl}_2]\text{Cl}_2$ in which, depending on the solvent employed, these complementary hydrogen bonding interactions are present (methanol, ethanol, acetonitrile) or not (water).⁸² In fact, the product obtained upon crystallization of the latter dimeric compound in a non-aqueous solvent represented the first example of a robust porous 3D architecture based on adenine-containing complexes in which the self-assembling of the structural units is essentially driven by non-covalent interactions: hydrogen bonds between the W-C faces of adeninato ligands and between the chloride ions and the Hoogsteen faces of the nucleobases.

We aim to explore the possibilities of self-assembly of neutral $[\text{Cu}_2(\mu\text{-ade})_4(\text{H}_2\text{O})_2]$ complex entities and theobromine (Htheo) or caffeine (caf) neutral molecules as a source of structural diversity for the synthesis of supramolecular porous materials. As in adenine molecule, the biochemical activity¹⁷⁰ of theobromine and caffeine (derivates of the non DNA xanthine) is dominated by the supramolecular recognition patterns that they can establish.

Keeping all the above in mind, in this section the reaction between copper(II) nitrate, adenine and theobromine/caffeine give rise to compounds $[\text{Cu}_2(\mu\text{-ade})_4(\text{H}_2\text{O})_2] \cdot 3\text{Htheo} \cdot \sim 7\text{H}_2\text{O}$ (CU2AD3TB), and $[\text{Cu}_2(\mu\text{-ade})_4(\text{H}_2\text{O})_2] \cdot 2\text{Htheo} \cdot \sim 18\text{H}_2\text{O}$ (CU7AD2TB) and $[\text{Cu}_2(\mu\text{-ade})_4(\text{H}_2\text{O})_2] \cdot (\text{caf}) \cdot \sim 6\text{H}_2\text{O}$ (CU2ADCAF).

¹⁷⁰ (a) Martínez-Pinilla, E.; Oñatibia-Astibia, A.; Franco, R. *Front. Pharmacol.* **2015**, *6*, 1–5. (b) Van Den Bogaard, B.; Draijer, R.; Westerhof, B. E.; Van Den Meiracker, A. H.; Van Montfrans, G. A.; Van Den Born, B. J. H. *Hypertension* **2010**, *56* (5), 839–846.

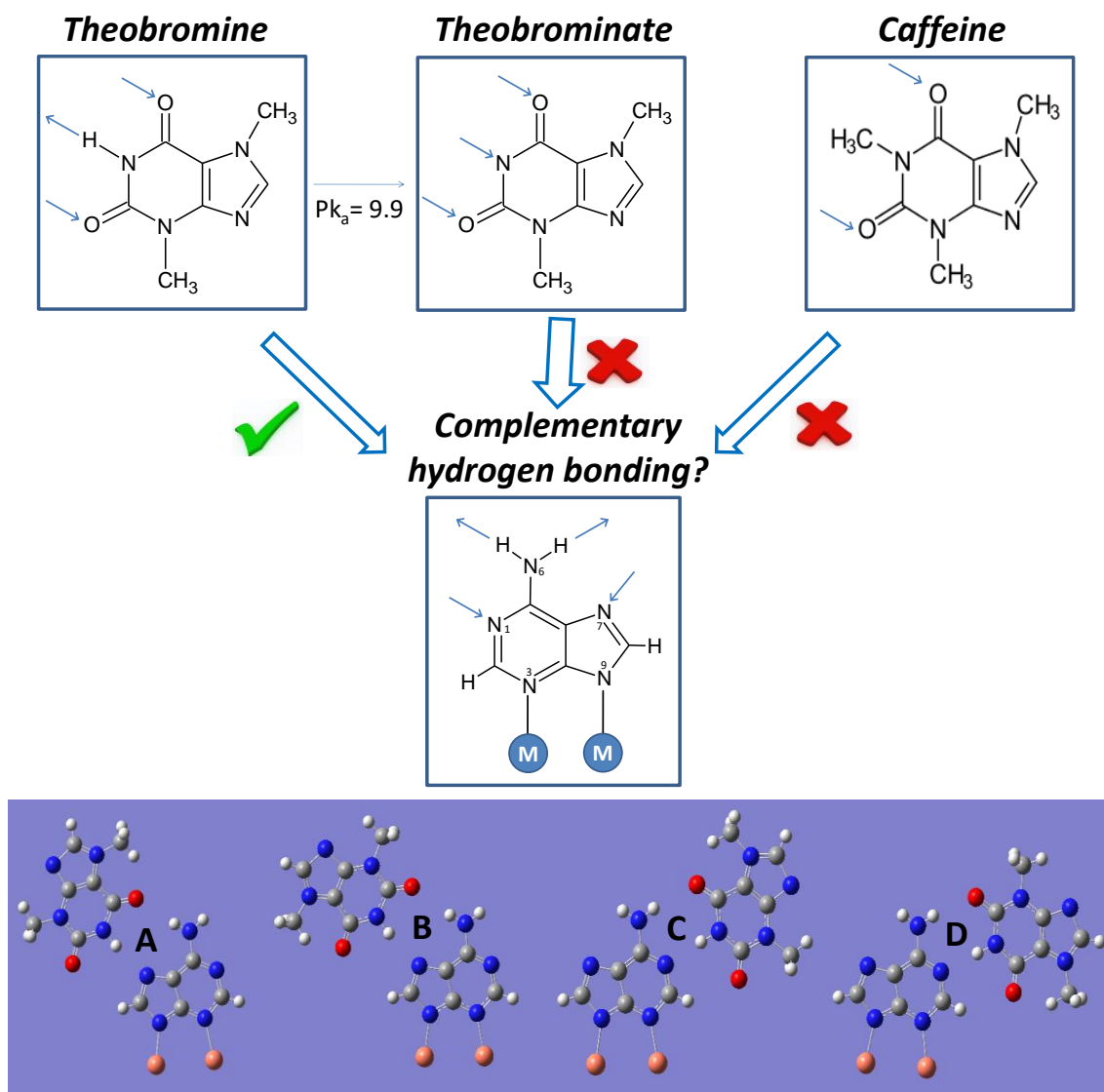


Figure 2.23. Upper: Hydrogen bonding capabilities of the theobromine and caffeine molecules with the μ - $\kappa\text{N}3:\kappa\text{N}9$ adeninato ligand. Bottom: Detail on the potential complementary hydrogen bonding interactions of the μ - $\kappa\text{N}3:\kappa\text{N}9$ adeninato with the theobromine molecule.

2.4.1. Structural description of compound CU2AD3TB

The neutral $[\text{Cu}_2(\mu\text{-ade})_4(\text{H}_2\text{O})_2]$ entity of compound CU2AD3TB is similar to the paddle-wheel unit found in the SMOF $[\text{Cu}_2(\mu\text{-ade})_4\text{Cl}_2]\text{Cl}_2 \cdot 2\text{MeOH}$, replacing the apical chloride ligands by water molecules.¹⁰¹ The two copper(II) atoms are coordinated to the N3 pyrimidinic and N9 imidazolic nitrogen atoms of two adeninato ligands (Figure 2.24) and the apical position of the square pyramidal environment of the metal is occupied by a water molecule with a Cu–O_w distance longer than those involving the nitrogen atoms (Table 2.14).

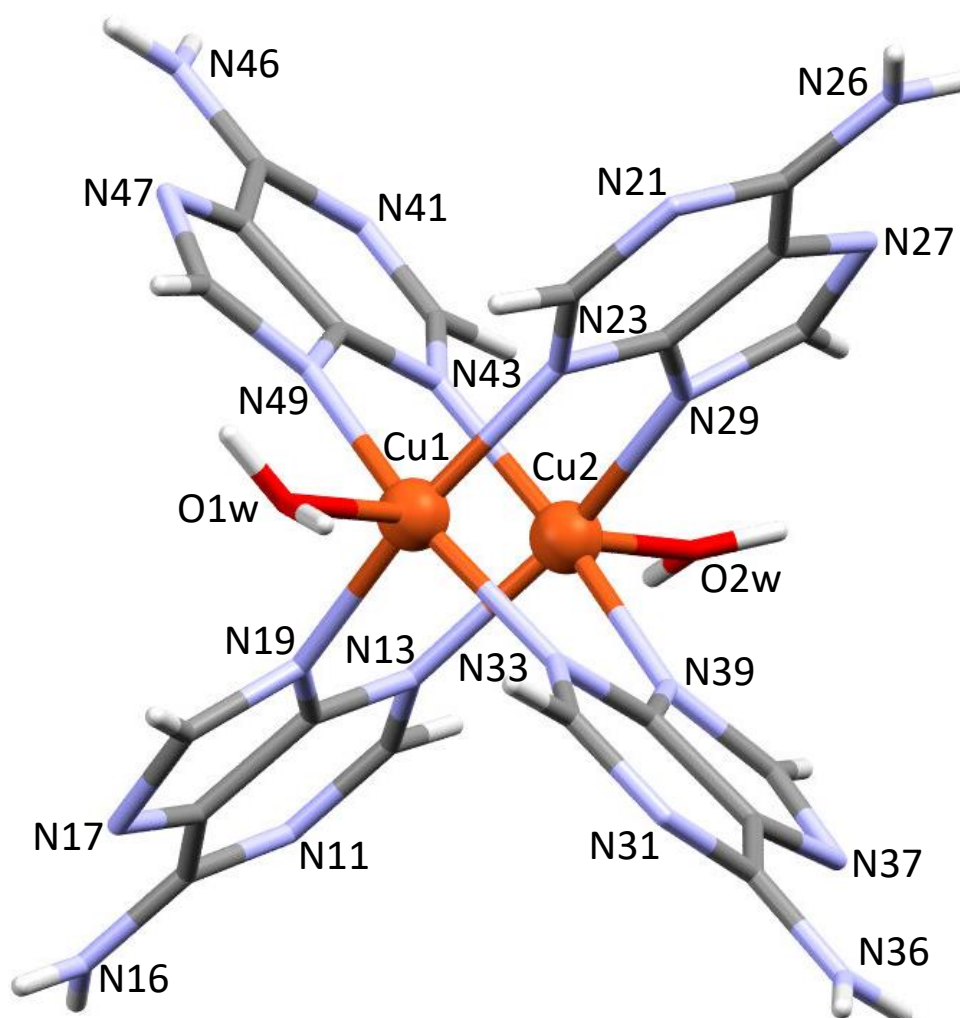


Figure 2.24. Dimeric entity of compound CU2AD3TB showing the labeling scheme.

The dihedral angles between adjacent adeninato ligands in the paddle-wheel unit are *ca.* 90° with a copper···copper distance of 2.956(1) Å. Two of the adeninato ligands transverse to each other (N31 and N41 containing ligands) also show the previously described static disorder with $\mu\text{-}\kappa\text{N3}:\kappa\text{N9}/\mu\text{-}\kappa\text{N9}:\kappa\text{N3}$ inverted coordination.

Table 2.14. Distances and angles (Å, deg) for compound **CU2AD3TB**.

Cu1—N19	1.998(5)	Cu1—N49	2.023(5)	Cu2—N29	2.007(5)
Cu1—N23	2.031(4)	Cu1—O1w	2.189(4)	Cu2—N39	1.999(5)
Cu1—N33	2.025(5)	Cu2—N13	2.037(5)	Cu2—N43	2.009(5)
Cu2—O2w	2.176(5)	Cu1...Cu2	2.956(1)		
N19—Cu1—N23	166.2(2)	N23—Cu1—O1w	98.2(2)	N39—Cu2—N43	166.7(2)
N19—Cu1—N33	89.5(2)	N33—Cu1—O1w	98.7(2)	N13—Cu2—N43	88.4(2)
N19—Cu1—N49	89.8(2)	N49—Cu1—O1w	98.5(2)	N13—Cu2—O2w	99.5(2)
N23—Cu1—N33	87.6(2)	N13—Cu2—N29	162.9(2)	N29—Cu2—O2w	97.6(2)
N23—Cu1—N49	89.0(2)	N29—Cu2—N43	89.0(2)	N39—Cu2—O2w	96.8(2)
N33—Cu1—N49	162.7(2)	N13—Cu2—N39	89.7(2)	N43—Cu2—O2w	96.6(2)
N19—Cu1—O1w	95.6(2)	N29—Cu2—N39	89.0(2)		

In the crystal structure of compound CU2AD3TB the presence of solvent water and theobromine molecules disrupt the direct complementary hydrogen bonding interactions between the adeninato ligands from adjacent dimeric entities. However, they are able to self-assemble by means of a combination of π - π stacking and N-H...aromatic interactions involving two *trans* arranged adeninato ligands (Figures 2.25 and 2.26, Table 2.15). These interactions are geometrically less demanding than the more common complementary hydrogen bonding synthons and it allows the presence of the above described static disorder of these two adeninato ligands. The remaining two adeninato ligands, which are not disordered, interact with three theobromine molecules by means of rigid hydrogen bonds interactions (Figure 2.24a). In this sense, Watson-Crick side of one of the ordered adeninato ligands establishes a $R_2^2(8)$ hydrogen bonds ring with a molecule of theobromine: the exocyclic N16 amino group interacts with the O72 atom of the ketone group, and the pyrimidinic N11 with the theobromine N71 atom (synthon D in Figure 2.23). This synthon is similar to the pattern of molecular recognition that takes place between adenine and thymine in the DNA double helix. In addition, the Hoogsteen (N16 / N17) side of the same adenine ligand forms a $R_2^2(9)$ ring with the O66 atom of the ketone group of another theobromine as acceptor and the adjacent N61 nitrogen as donor (synthon A). The CSD¹⁷¹ database does not register any structure in which the adenine (or

¹⁷¹ Groom, C. R.; Bruno, I. J.; Lightfoot, M. P.; Word, S. C. *Acta Cryst.* **2016**, B72, 171–179.

derivatives) and theobromine bases coexist. However, a simultaneous interaction of adenine with its Watson–Crick (W–C) and Hoogsteen (H) sides has been found for a 2:1 adenine-isopropyluracil compound (CSD code: BERNAP).¹⁷²

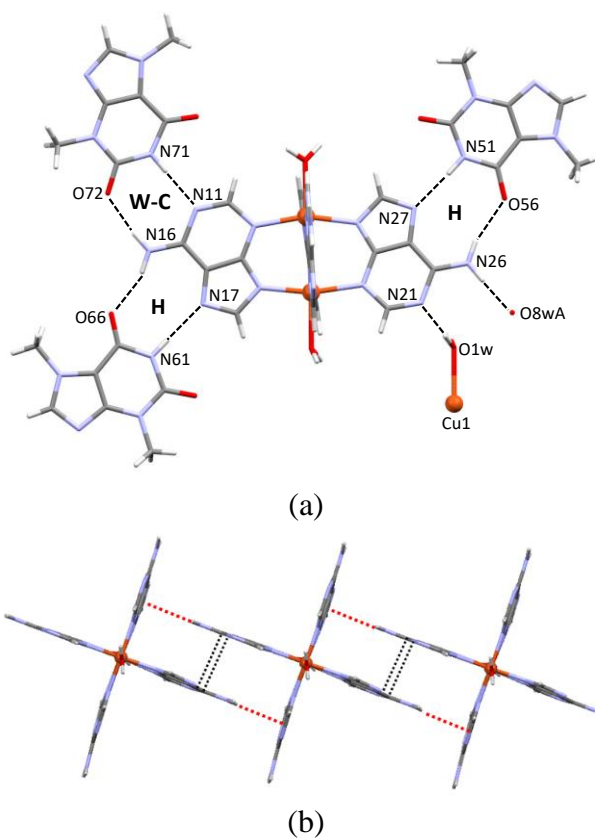


Figure 2.25. (a) Theobromine molecules anchored to the dimeric entities by means of complementary hydrogen bonding interactions and (b) dimeric entities assembled through π – π stacking (double dashed lines) and N–H...aromatic (red dotted lines) interactions.

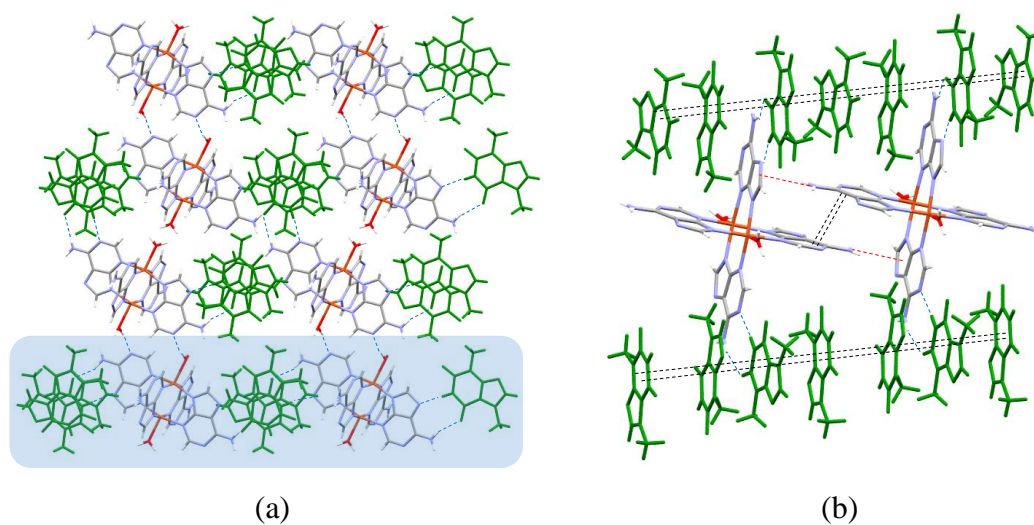


Figure 2.26. Crystal packing showing the supramolecular interactions in CU2AD3TB.

¹⁷² Radhakrishnan, K.; Burgula, L.N.; Kundu, L. M. *RSC Advances* **2013**, *3*, 7282.

Table 2.15. Structural parameters (Å, °) of the supramolecular interactions.^a

D–H...A ^b	H...A	D...A	D–H...A		
N16–H16A...O66 ⁱ	2.07	2.891(7)	158		
N16–H16B...O72 ⁱⁱ	2.04	2.872(7)	164		
N26–H26A...O56	2.09	2.932(7)	165		
N26–H26B...O8wA ⁱⁱⁱ	2.33	3.002(13)	135		
N36A–H36A...O3w ^{iv}	2.07	2.770(13)	138		
N36A–H36B...O7wA	2.33	3.170(11)	164		
N51–H51...N27	1.94	2.795(6)	177		
N61–H61...N17 ^v	2.03	2.886(7)	179		
N71–H71...N11 ⁱⁱ	2.00	2.861(6)	175		
O1w–H11w...O4w ^{vi}	1.86	2.664(9)	154		
O1w–H12w...N21 ^{vi}	2.02	2.861(6)	167		
O2w–H21w...O6w	1.88	2.729(8)	172		
O2w–H22w...O7wA ⁱⁱ	1.96	2.740(8)	151		

π – π interactions ^c					
ring–ring	packing	angle	DC	DZ	DXY
1pa...5pt ⁱ	A...T	6.6	3.83	3.11	1.86
2pa...6pt	A...T	2.2	3.86	3.35	1.88
3ha...4ha ⁱⁱ	A...A	5.1	4.22	3.24	2.56
5pt...7ht ⁱⁱⁱ	T...T	1.9	3.51	3.34	1.09
5ht...7ht ⁱⁱⁱ	T...T	2.5	3.55	3.29	1.19
6pt...2pa	T...A	2.2	3.85	3.37	1.92
6pt...7pt	T...T	5.2	3.69	3.43	1.37
6pt...7ht	T...T	4.9	3.71	3.30	1.74
6ht...5ht	T...T	3.6	4.06	3.08	2.50
6ht...7pt	T...T	5.6	3.65	3.44	1.22
6ht...5pt	T...T	5.2	3.56	3.35	1.47
7pt...5pt ^{iv}	T...T	2.3	3.83	3.27	1.86
7pt...5ht ^{iv}	T...T	3.0	3.74	3.25	1.78
7pt...6pt	T...T	5.2	3.69	3.43	1.65
7pt...6ht	T...T	5.6	3.65	3.44	1.46
7ht...5pt ^{iv}	T...T	1.9	3.51	3.34	1.08
7ht...5ht ^{iv}	T...T	2.5	3.55	3.34	1.32
7ht...6ht	T...T	5.2	3.56	3.25	1.21

X –H... π interactions ^d					
	packing	H–Perp	H...Cg	X–H...Cg	X–H...ring
N36–H...2pa ^{iv}	A...A	2.9	2.9	120	36
N46–H...1pa ⁱⁱⁱ	A...T	2.8	2.9	110	35

^aSymmetry codes: (i) $x, -1 + y, z$; (ii) $x + 1, y, z$; (iii) $x - 1, y, z$; (iv) $x + 1, y, z$. ^bD: donor; A: acceptor. ^cAngle: dihedral angle between the planes (deg), DC: distance between the centroids of the rings (Å), DZ: interplanar distance (Å), DXY: lateral displacement (Å), pa: adenine pentagonal ring, ha: adenine hexagonal ring, pt: theobrominate

pentagonal ring, ht: theobrominate hexagonal ring. ⁴H-Perp: Perpendicular distance of H to ring plane; H...Cg: distance of H to the centroid of the ring; X-H...Cg: X-H-Cg angle; X-H...ring: angle of the X-H bond with the aromatic ring.

Several reports have been published on the interaction established by xanthines,¹⁷³ such as theophylline and theobromine, with biological systems such as DNA, RNA and ATP inside the cellular structure and it has been suggested that anchoring with deoxyribonucleic acid may be produced with the adenine-thymine pair, in a similar molecular recognition pattern observed in the crystal structure of compound CU2AD3TB. The second non-disordered adeninato ligand of the dimeric structure only interacts through its Hoogsteen face with a theobromine molecule through a $R_2^2(9)$ ring of hydrogen bonds, while its W-C side forms hydrogen bonds with a crystallization water molecule and the coordinated O1w water molecule of an adjacent dimeric entity.

Additionally, the theobromine molecules form columns along the crystallographic [100] direction in which they are arranged parallel to each other with interplanar distances of 3.2–3.4 Å, indicative of the presence of offset face-to-face π - π interactions, Figure 2.27. Complex entities and the theobromine molecules form layers, propagating along the *ab* plane, which are sustained by the above-described supramolecular interaction, Figure 2.25a. Crystallization water molecules are inserted between the layers and joined to them by means of the hydrogen bonds with the coordination water molecules and with the nitrogen atoms of the adeninato ligands. The cohesion between the layers is further sustained by a direct Ow-H...N hydrogen bond that involves the coordination water molecule O1w and the N21 atom of an adeninato ligand from the adjacent layer.

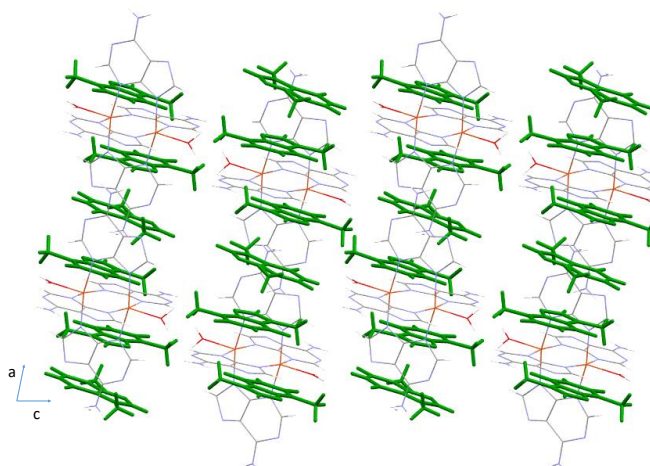


Figure 2.27. π - π stacking of remarked theobromine molecules depicted in green.

¹⁷³ (a) Gattuso, G.; Manfredi, G.; Sammartano, S. *Fluid Phase Equilib.* **2011**, *308* (1–2), 47–54. (b) Johson, I. M.; Prakash, H. Prathiba, J.; Raghunathan, R.; Malathi, R. *PLoS One* **2012**, *7*, 1–11.

The variable-temperature X-ray powder diffraction data (Figure 2.28) show that the crystallinity is retained after the release of the crystallization water molecules (*ca.* 100 °C) and even after the removal of the coordination ones (*ca.* 180 °C), remaining stable up to 180 °C.

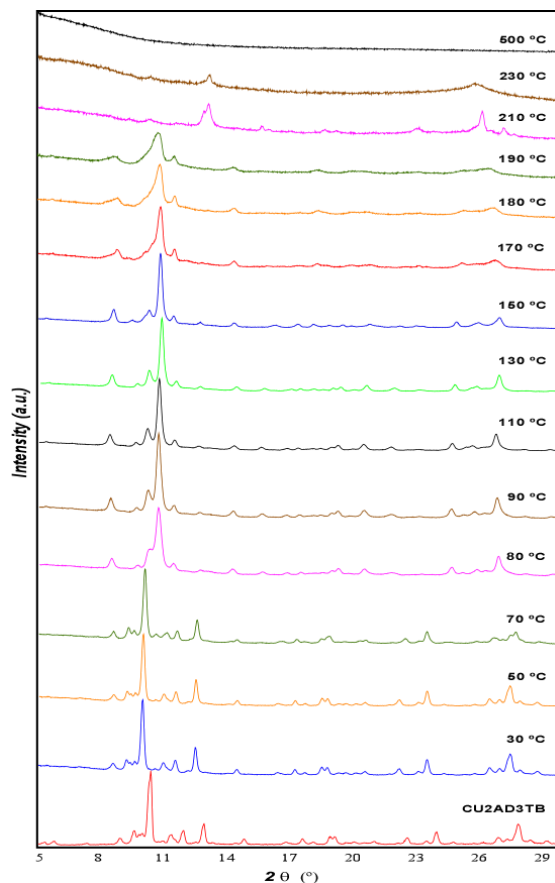


Figure 2.28. Thermodiffractometric data compared with fresh sample (bottom) of CU2AD3TB.

The volume occupied by the water molecules located between the layers is 365 Å³ (13% of the total volume of the unit cell) and it reaches 490 Å³ (18% of the unit cell) if the space occupied by coordinating water molecules is also taken into account. In order to analyze the pore size distribution in CU2AD3TB, a procedure implemented in a code developed by Sarkisov¹⁷⁴ has been used, in which the Lennard–Jones universal force field parameters are used to describe the adsorbent atoms, while a probe that increases its size gradually analyses the free volume. It indicates the existence of some isolated cavities with a maximum diameter of 3.8 Å (mode: 2.9 Å). According to their isolated nature, these pores are not accessible either for N₂ or for CO₂, as checked by adsorption measurements.

¹⁷⁴ (a) Herdes, C.; Sarkisov, L. *Langmuir* **2009**, 25 (9), 5352–5359. (b) Topos Main Page <http://www.topospro.com> (accessed: 2022/05/15).

2.4.2. Structural description of compound CU2AD2TB.

Crystal structure of compound CU2AD2TB contains the above described neutral $[\text{Cu}_2(\mu\text{-ade})_4(\text{H}_2\text{O})_2]$ paddle-wheel unit, but it is located on an inversion center. Distances and angles are listed in Table 2.16. The different complex/theobromine ratio in the formulae (1/3 in CU2AD3TB versus 1/2 in CU2AD2TB) leads to each centrosymmetric complex to be only surrounded by two theobromine molecules anchored to two *trans* arranged adeninato ligands by a hydrogen bonding $R_2^2(9)$ ring involving the N1H and ketone O6 sites of the theobromine and the Hoogsteen face of the nucleobase ligands (Figure 2.29, Table 2.17). The W–C faces of these adeninato ligands and the W–C and H sides of the adeninato ligands not involved in the interaction just described, form hydrogen bonds with water molecules like the one between the coordinated water molecule O1w and the nitrogen N11 of the W–C face of an adeninato ligand from an adjacent dimeric entity.

This hydrogen bonding interaction is similar to that found in compound CU2AD3TB but lacking the third theobromine ligand that was interacting with the Watson–Crick face belonging to one of the adeninato ligands. It seems to indicate a greater preference of the theobromine molecule for the Hoogsteen face of adenine.

On the other hand, the methyl groups of the theobromine molecule preclude further propagation of the hydrogen bonding interactions. Therefore, the supramolecular architecture is built up by the presence of aromatic interactions that spread in two almost perpendicular directions to generate a 2D arrangement. The first one involves the π – π interactions between the theobromine molecules and the second one takes place between the adeninato ligands not involved in the hydrogen bonding. These sheets are connected among them by means of additional double $\text{Ow}\cdots\text{N1}$ hydrogen bonds between the coordinated water molecules and the N1 nitrogen atom of the adeninato ligands. All these supramolecular interactions lead to an interconnected network of one-dimensional channels along the crystallographic *a* axis, which are occupied by crystallization water molecules, that are connected by small windows with a diameter of less than 2.1 Å.

The volume of the channels is 479 Å³ (represents the 33% of the total volume, almost the double of the previous compound with one more theobromine ligand) with a pore diameter ranging from 3.5 Å to 4.5 Å, and a pore volume of 0.26 cm³·g⁻¹. This allows the number of water molecules to increase from seven in CU2AD3TB to the

eighteen observed in this compound. On the other hand, using a 3.341 Å N₂ probe,¹⁷⁵ a potentially accessible surface area value of 58 m²·g⁻¹ has been computed.

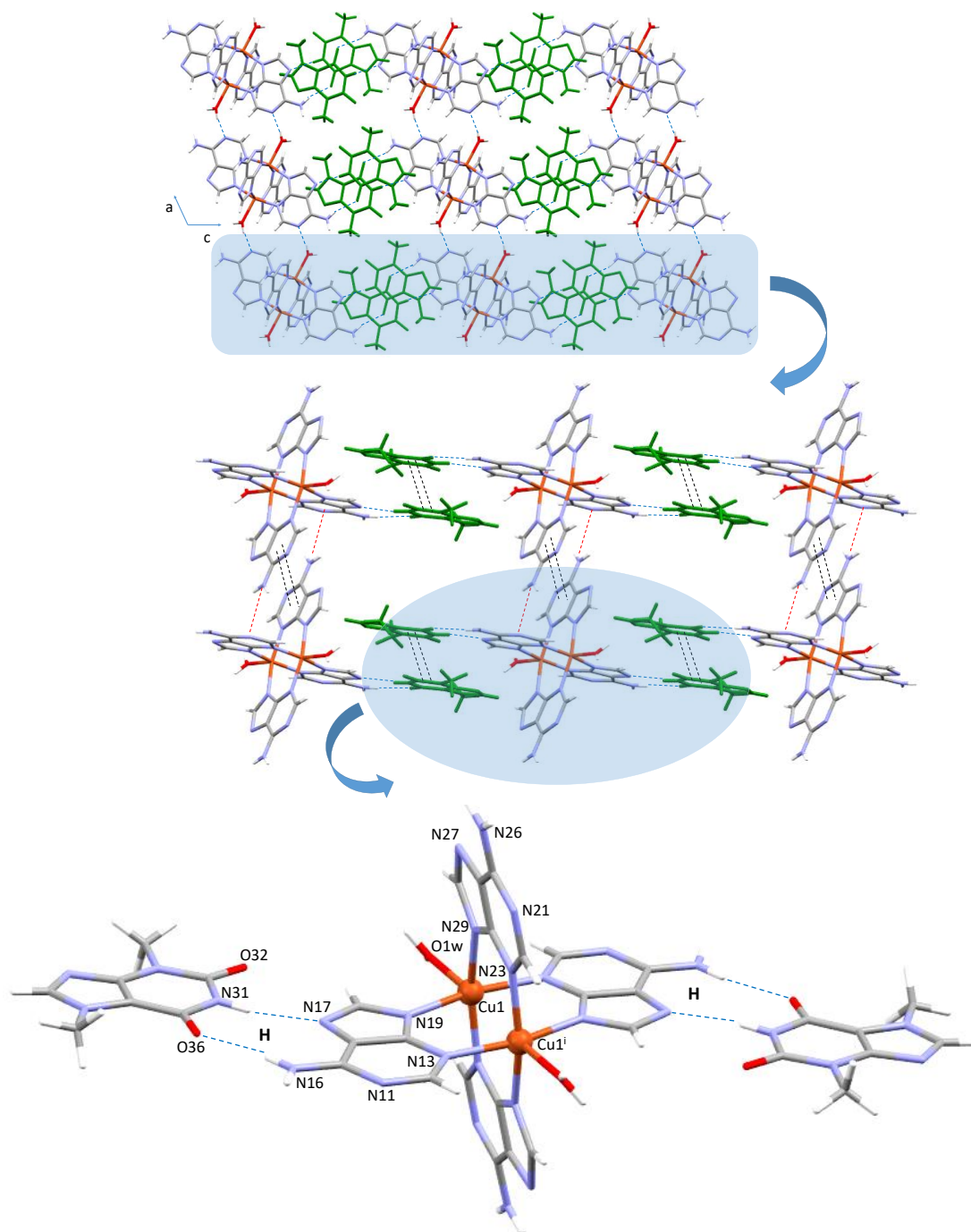


Figure 2.29. Crystal packing showing the supramolecular sheets sustained by complementary hydrogen bonds (dashed lines), π - π stacking (double dashed lines) and N-H...aromatic (red dotted lines) interactions between the dimeric entities and theobromine molecules. (c) Theobromine molecules anchored to the dimeric entities by means of complementary hydrogen bonding interactions.

¹⁷⁵ Du, T.; Walton, K. S.; Snurr, R. Q. *J. Phys. Chem. C* **2007**, 111, 15350–15356.

Table 2.16. Distances and angles (Å, deg) for compound CU2AD2TB.^a

Cu1–N13 ⁱ	2.026(3)	Cu1–N19	2.004(3)	Cu1–N23 ⁱ	2.024(3)
Cu1–N29	2.015(3)	Cu1–O1w	2.183(3)	Cu1...Cu1 ⁱ	2.954(1)
N19–Cu1–N29	89.2(1)	N19–Cu1–N23 ⁱ	90.5(1)	N29–Cu1–N23 ⁱ	164.5(1)
N19–Cu1–N13 ⁱ	164.7(2)	N29–Cu1–N13 ⁱ	88.7(1)	N23 ⁱ –Cu2–N13 ⁱ	87.6(1)
N19–Cu1–O1w	96.1(2)	N29–Cu1–O1w	97.9(1)	N23 ⁱ –Cu1–O1w	97.5(1)
N13 ⁱ –Cu1–O1w	99.2(2)				

^aSymmetry: (i) $-x + 3/2, -y + 1/2, -z$ **Table 2.17.** Structural parameters (Å, °) of the supramolecular interactions in CU2AD2TB.^a

D–H...A ^b	H...A	D...A	D–H...A		
N16–H16A...O36	2.05	2.887(5)	163		
N31–H31...N17	2.03(6)	2.838(5)	173(5)		
O1w–H11w...N11 ⁱ	2.18	3.004(6)	160		
π-π interactions^c					
ring - ring	packing	angle	DC	DZ	DXY
2pa...2ha ⁱⁱ	A...A	1.0	4.21	3.30	2.66
1pa...3pt ⁱⁱⁱ	A...T	4.2	3.77	3.19	1.87
3ht...3ht ⁱⁱⁱ	T...T	0.0	3.96	3.16	2.38
X–H...π interactions^d					
	packing	H–Perp	H...Cg	X–H...Cg	X–H...ring
N26–H...1ha ^{iv}	A...A	3.0	3.1	117	35

^aSymmetry codes: (i) $x - 1, y, z$ (ii) $-x, -y + 2, -z + 2$; (iii) $-x, -y + 1, -z + 3$; (iv) $x, y + 1, z$. ^bD: donor; A: acceptor. ^cAngle: dihedral angle between the planes (deg), DC: distance between the centroids of the rings (Å), DZ: interplanar distance (Å), DXY: lateral displacement (Å), pa: adenine pentagonal ring, ha: adenine hexagonal ring, pt: theobrominate pentagonal ring, ht: theobrominate hexagonal ring. ^dH–Perp: Perpendicular distance of H to ring plane; H...Cg: distance of H to the centroid of the ring; X–H...Cg: X–H–Cg angle; X–H...ring: angle of the X–H bond with the aromatic ring.

The crystal structure of CU2AD2TB can be also described as that generated from CU2AD3TB by the removal of the theobromine molecule interacting with the Watson-Crick side of the adeninato ligand (Figure 2.30).

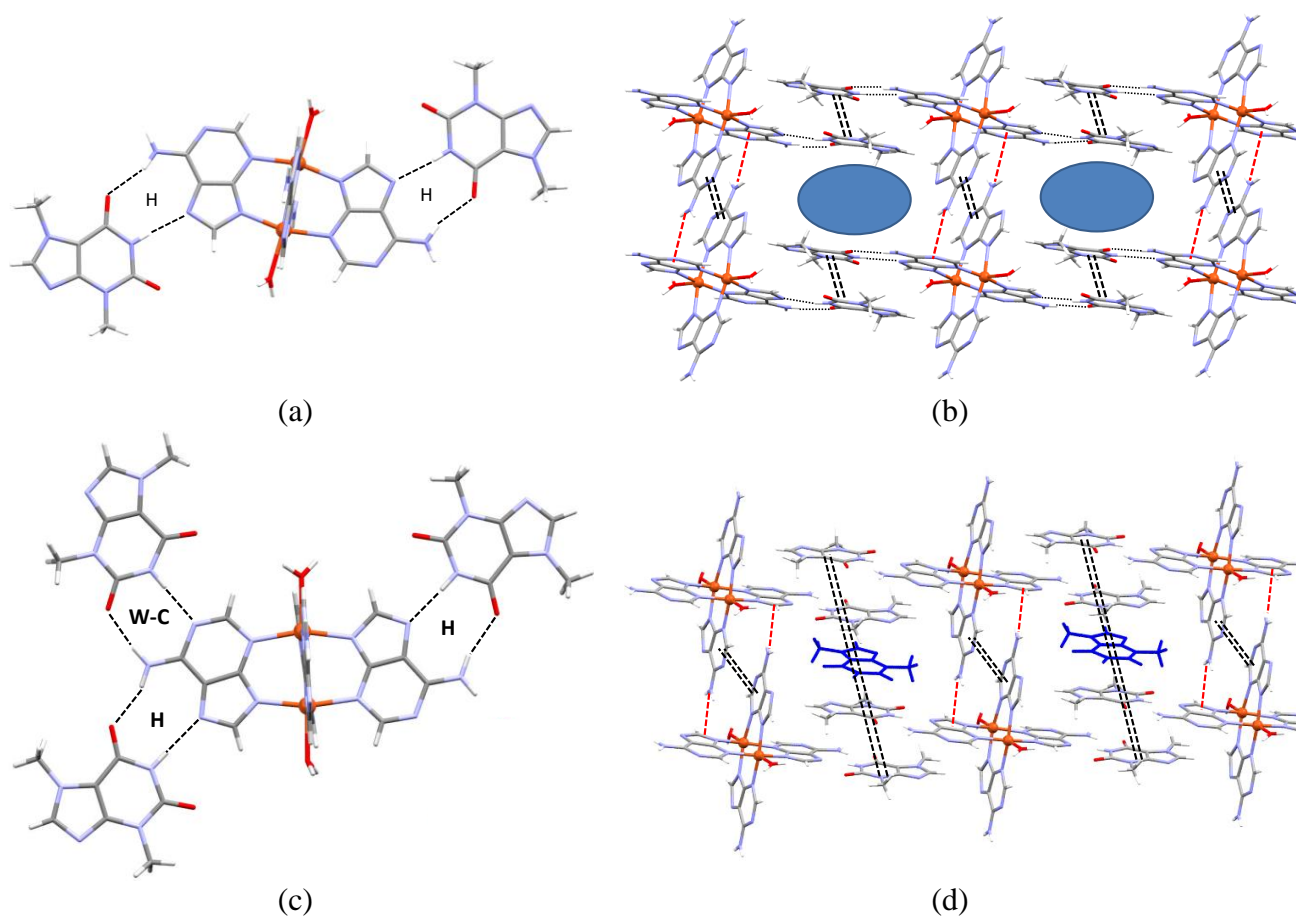


Figure 2.30. Complementary hydrogen bond interactions and voids in compounds CU2AD2TB (a, b) and CU2AD3TB (c, d) where it can be seen the space occupied by the third molecule.

2.4.3. Structural description of compound CU2ADCAF

The N-methylation of caffeine precludes its involvement in hydrogen bonding synthons with the adenine ligands or the non-DNA nucleobase as theobromine described in Figure 2.23. As a consequence, the supramolecular architecture of compound CU2ADCAF is sustained by means of adenine···adenine supramolecular complementary hydrogen bonds and π -stacking interactions with the caffeine molecule, Tables 2.18 and 2.19. The neutral $[\text{Cu}_2(\mu\text{-ade})_4(\text{H}_2\text{O})_2]$ paddle-wheel units form chains held together by means of hydrogen bonding rings between the Hoogsteen faces of two neighboring adeninato ligands. The dihedral angles between adjacent adeninato ligands in the paddle-wheel unit are *ca.* 84° with a copper···copper distance of 2.948(1) Å. These supramolecular ribbons are intertwined to give boxes whose walls are formed by eight adeninato ligands of four dimeric entities. In the center of each box a caffeine molecule is placed, disordered in two positions related by a two-fold axis (Figure 2.31).

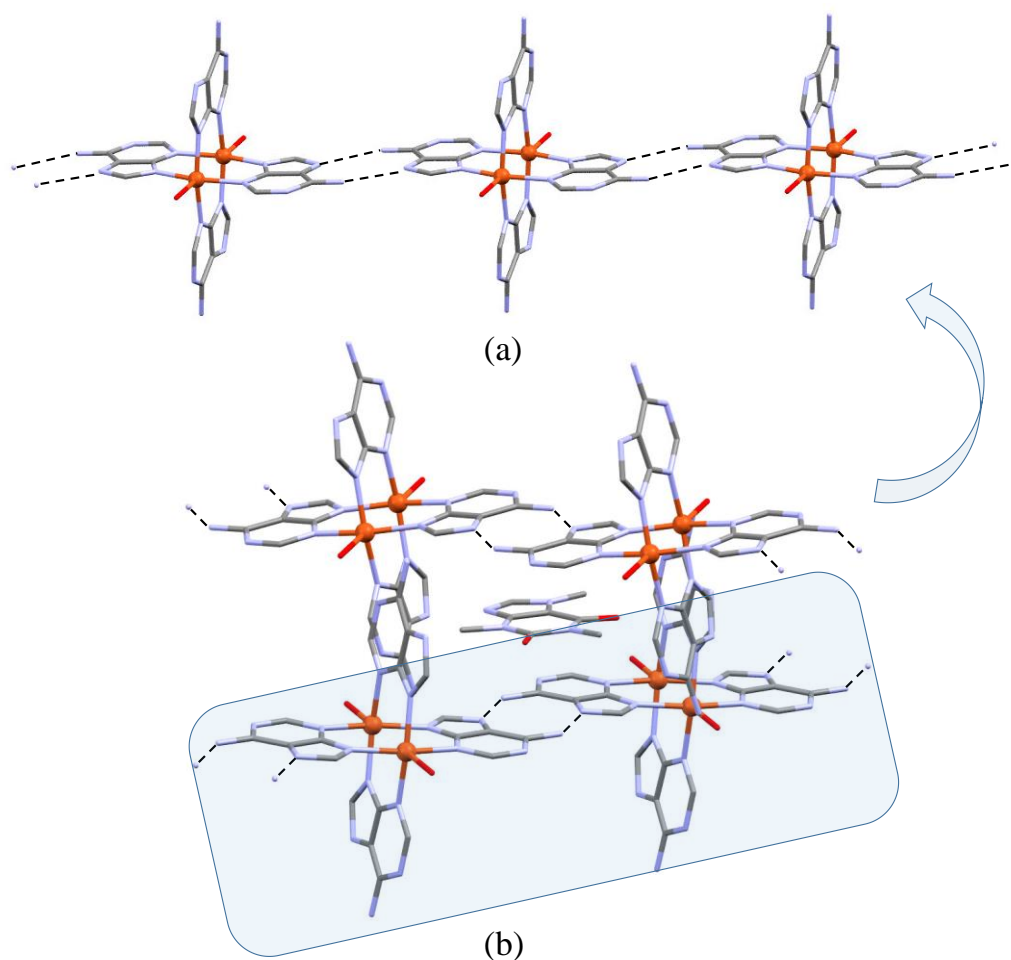


Figure 2.31. (a) Supramolecular chains sustained by adeninato···adeninato interactions, and (b) insertion of the caffeine molecule in the square shaped supramolecular box in CU2ADCAF.

Table 2.18. Distances and angles (Å, deg) for compound CU2ADCAF.^a

Cu1—N13ⁱ	2.024(5)	Cu1—N19	1.991(5)	Cu1—N23ⁱ	2.026(5)
Cu1—N29	1.995(5)	Cu1—O1w	2.202(5)	Cu1...Cu1 ⁱ	2.948(1)
N19—Cu1—N29	90.0(2)	N19—Cu1—N23 ⁱ	87.8(2)	N29—Cu1—N23 ⁱ	164.9(2)
N19—Cu1—N13ⁱ	164.8(2)	N29—Cu1—N13 ⁱ	89.9(2)	N23 ⁱ —Cu2—N13 ⁱ	88.3(2)
N19—Cu1—O1w	99.2(2)	N29—Cu1—O1w	99.3(2)	N23 ⁱ —Cu1—O1w	95.8(2)
N13ⁱ—Cu1—O1w	95.8(2)				

^aSymmetry: (i) $-x, -y + 1, -z + 2$.**Table 2.19.** Structural parameters (Å, °) of the hydrogen bonding interactions in CU2ADCAF.^a

D—H...A ^a	H...A	D...A	D—H...A
N26A—H26A...N27 ⁱ	2.20	3.02(1)	161
O1w—H1w2...N11 ⁱⁱ	2.05	3.89(7)	169

^aSymmetry codes: (i) $-x + 2, -y + 1, -z$; (ii) $1/2 + x, 1/2 - y, z$

Caffeine molecule is disposed parallel to two hydrogen bonded adeninato...adeninato moieties with an interplanar distance of *ca.* 3.7 Å, and perpendicular to the other four adeninato ligands with the methyl groups of the methylxanthine molecule pointing to the center of the pyrimidinic rings of three adeninato ligands (carbon...centroid average distance of 3.5 Å). It suggests the existence of similar CH₃... π interactions to those described for compound [Pt₂L₄](NO₃)₄·2(caf) {L: 1,3-bis(10-(pyridin-3-yl)-9-anthryl)-4,5,6-tris(2-methoxyethoxy)benzene} in which caffeine molecules are occluded in spherical cavities formed by eight anthracene rings.¹⁷⁶

The above-described supramolecular assembly generates channels along the [001] direction with a volume of 800 Å³ which imply the 19% of the unit cell volume and host the crystallization water molecules (Figure 2.32). The pore diameter of these channels ranges from 3.1 to 4.5 Å with a pore volume of 0.13 cm³·g⁻¹.

The variable-temperature X-ray powder diffraction data (Figure 2.33) show that the crystallinity is retained after the release of the crystallization water molecules (*ca.* 80 °C) and even after the removal of part of the coordination ones (*ca.* 130 °C), remaining stable up to 150 °C.

¹⁷⁶ Düren, T.; Millange, F.; Férey, G.; Walton, K. S.; Snurr, R. Q. *J. Phys. Chem.* **2007**, *111*, 15350–15356.

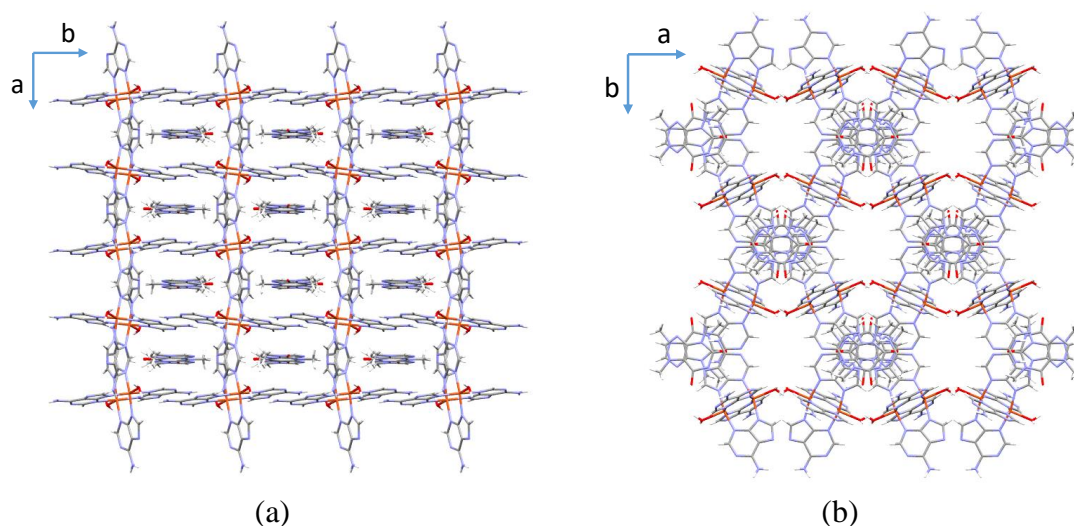


Figure 2.32. Views of the crystal packing of compound CU2ADCAF showing (a) the insertion of the caffeine molecules and (b) the channels running along the [001] direction.

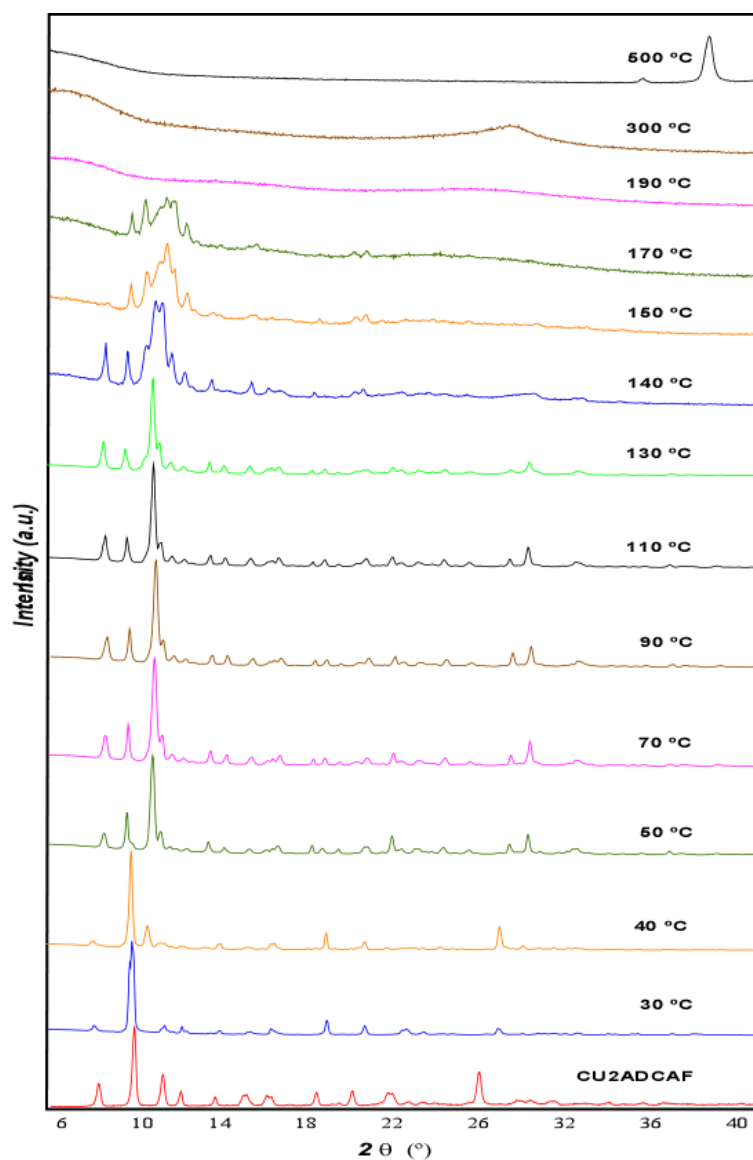


Figure 2.33. Thermodiffractometric data compared with fresh sample (bottom) of CU2ADCAF.

Regarding the gas adsorption experiment, despite the outgassed sample of CU2ADCAF (at 80 °C during 6h) shows a mass loss of 10.6% (corresponding to all crystallization water molecules), it does not adsorb N₂ at 77 K. The CO₂ adsorption measurements at 273 K between 0 and 5 bar show a significant gas uptake curve of type I, with a saturation value of 0.88 mmol of CO₂·g⁻¹ of compound (Figure 2.34).

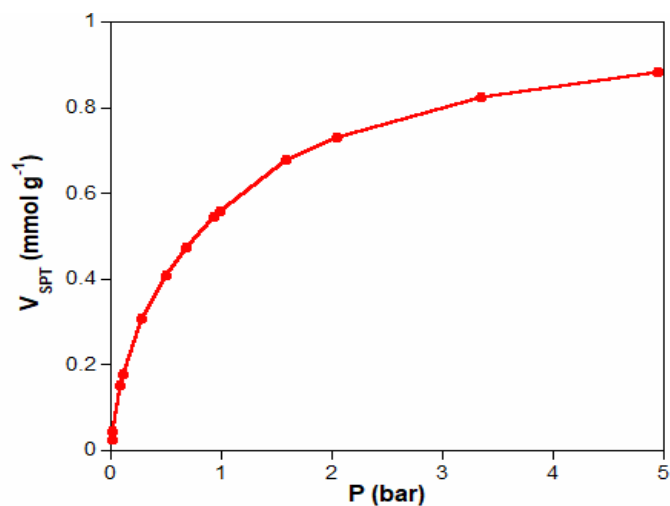


Figure 2.34. CO₂ adsorption curve at 273 K (0–5 bar) for CU2ADCAF.

2.4.4. Structural description of compound CU2ADTP

The greater coordination capacity of theophylline, Figure 2.35, with respect to theobromine and obviously to caffeine due to the latter higher methylation grade, Figure 2.36, has given rise to the formation of a one-dimensional coordination biopolymer, $\{[\text{Cu}_2(\mu\text{-ade})_4(\text{H}_2\text{O})_2] \cdot 2[\text{Cu}(\text{theoph})_2] \cdot \sim 10\text{H}_2\text{O}\}_n$, CU2ADTP, in which the adeninato ligand exhibits a tridentate coordination mode ($\mu_3\text{-}\kappa\text{N}3:\kappa\text{N}7:\kappa\text{N}9$)¹⁷⁷ and the theophylline (1,3-dimethyl-3,7-dihydro-1H-purine-2,6-dione) acts as peripheral ligand. This alkaloid is a methylxanthine, with a moderate solubility in water, found in common food products such as cocoa and tea, and it is commercially available as a bronchodilator in the treatment of asthma due to its diuretic and anti-inflammatory effects.¹⁷⁸

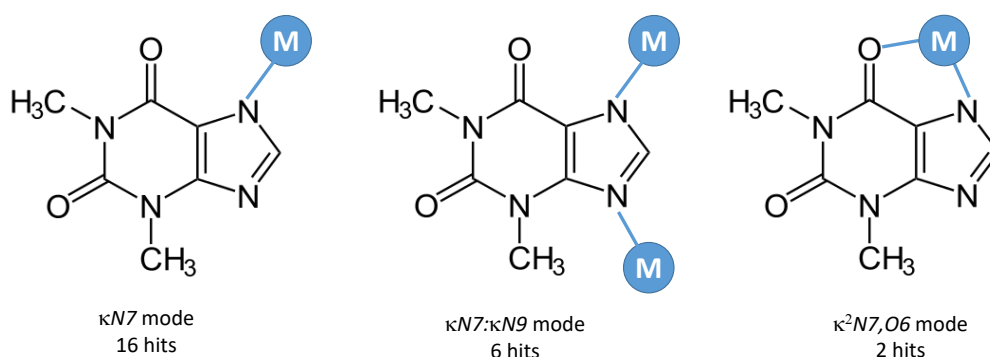


Figure 2.35. Coordination modes of the theophyllinate anion.

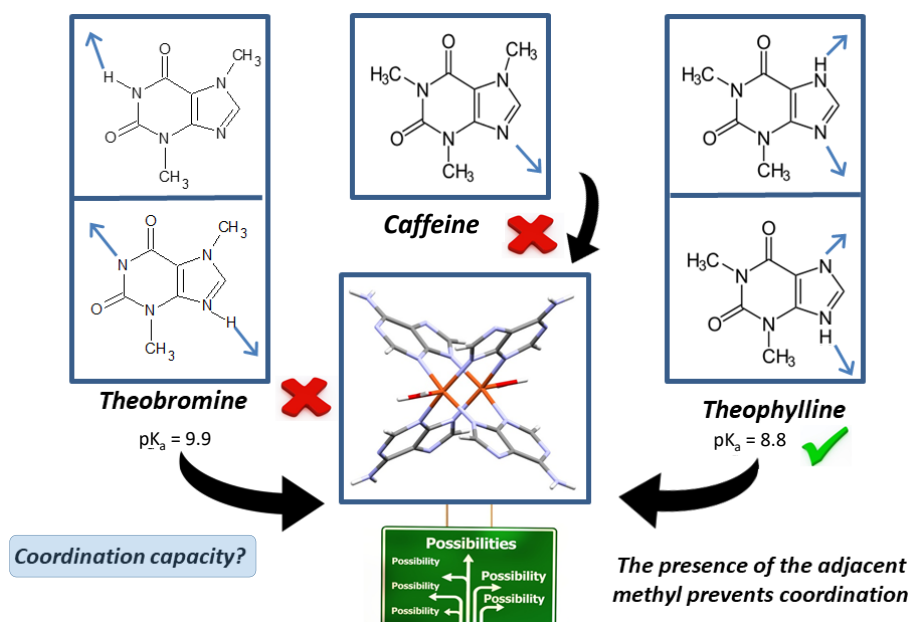


Figure 2.36. Scheme of the coordination capacity of different nucleobase derivatives.

¹⁷⁷ Giles-Mazón, E. A.; Germán-Ramos, I.; Romero-Romero, F.; Reinheimer, E.; Toscano, R. A.; Lopez, N.; Barrera-Díaz, C. E.; Varela-Guerrero, V.; Ballesteros-Rivas, M. F. *Inorganica Chim. Acta* **2018**, *469*, 306–311.

¹⁷⁸ Persson, C. G. A. *J. Allergy Clin. Immunol.* **1986**, *78*, 780–787.

Figure 2.37 represents a fragment of the polymeric structure showing the dimeric neutral $[\text{Cu}_2(\mu\text{-ade})_4(\text{H}_2\text{O})_2]$ nodes with a paddle wheel shape being doubly bridged by bis(theophyllinato)copper(II) entities by means of the bridging adeninato ligand. Table 2.20 lists the most relevant bond distances in the polymeric chain.

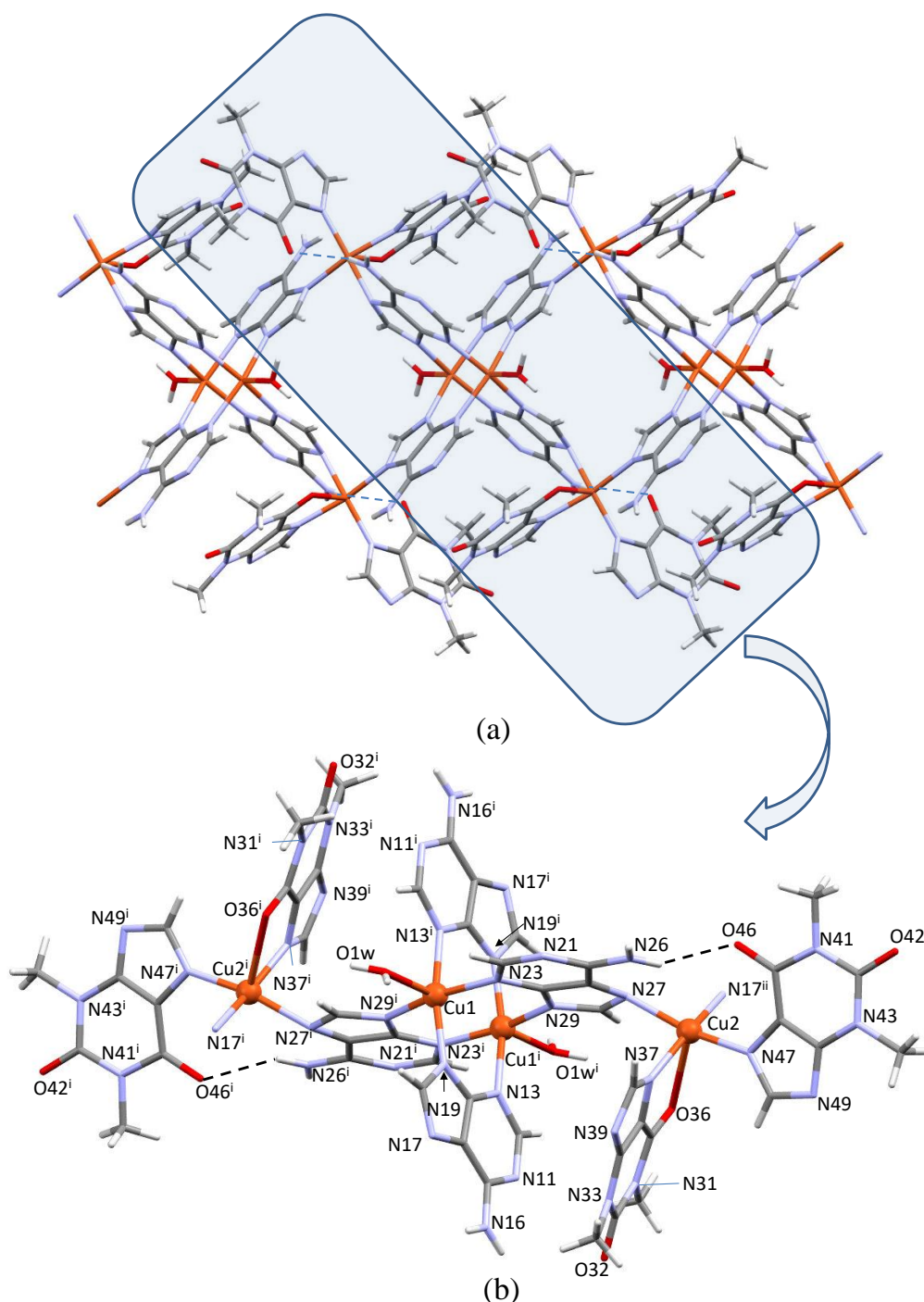


Figure 2.37. (a) Polymeric chain in compound CU2ADTP showing the intramolecular hydrogen bond $\text{N-H}\cdots\text{O}$ (dashed line) and (b) detail with the numbering scheme used.

Table 2.20. Selected bond lengths (Å).^a

Cu1—N13 ⁱ	2.034(3)	Cu2—N17 ⁱⁱ	2.032(3)	Cu1...Cu1 ⁱ	2.956(7)
Cu1—N19	1.997(3)	Cu2—N27	1.988(3)	Cu1 ⁱ ...Cu2	5.755(7)
Cu1—N23	2.024(4)	Cu2—O36	2.766(3)	Cu1...Cu2 ⁱⁱⁱ	5.924(7)
Cu1—N29 ⁱ	1.998(4)	Cu2—N37	1.991(3)		
Cu1—O1w	2.172(3)	Cu2—N47	1.941(3)		

^aSymmetry codes: (i) $-x + 3, -y + 1, -z + 1$; (ii) $-1 + x, y, z$; (iii) $x + 1, y, z$.

The centrosymmetric dimeric fragment is built up by two copper atoms bridged by four adeninato ligands through the pyrimidine NX3 and imidazolic NX9 nitrogen atoms ($x = 1$ or 2) to provide a paddle-wheel shaped core with a Cu1...Cu1ⁱ distance of 2.956(7) Å. The dimeric unit has a paddle-wheel entity with a dihedral angle between two adjacent adeninato ligands of 79°. The square-based pyramidal environment around the Cu1 atom is completed by a water molecule in the apical position with a Cu1—Ow distance longer than those involving the nitrogen atoms. The structural parameters of this building block are similar to those previously reported for analogous dimeric entities.^{102,179} Each dimeric fragment is linked to four neighboring [Cu(theoph)₂] entities via the Nx7 atom from the imidazole ring of adeninato ligand with Cu1...Cu2 distances of 5.755(7) and 5.924(7) Å, Figure 2.38. The square-based pyramidal N₄O donor set of the Cu2 atom is filled by the NX7 atoms from two adeninato bridges, the imidazolic N47 nitrogen atom of one peripheral monodentate theophyllinate anion and a five-membered chelating ring formed by a second alkaloid molecule attached to the metal by the N37 nitrogen atom and the adjacent ketonic O36 oxygen atom with a Cu2—O36 distance, 2.766(3) Å, substantially greater than the Cu—N but slightly shorter than the sum of the van der Waals radii (1.52 Å for O, 1.43 Å for Cu).¹⁸⁰ The non-coordination of the carboxyl O46 oxygen atom of the monodentated theophyllinato ligand is stabilized by an interligand N26—H26B...O46 hydrogen bond with the exocyclic amino group of an adjacent adeninato ligand [N...O: 3.099(6) Å and H...O: 2.30 Å, <N—H...O: 155°].

A perusal analysis in the crystallographic CSD database¹⁶⁸ of the crystal structures corresponding to theophylline/theophyllinato transition metal complexes shows that the

¹⁷⁹ (a) Cepeda, J.; Castillo, O.; García-Terán, J. P.; Luque, A.; Pérez-Yáñez, S.; Roman, P. *Eur. J. Inorg. Chem.* **2009**, 2344–2353. (b) Sletten, E. *Acta Crystallogr. Sect. B Struct. Crystallogr. Cryst. Chem.* **1970**, 26 (10), 1609–1614. (c) Sletten, E. *Acta Crystallogr. Sect. B Struct. Crystallogr. Cryst. Chem.* **1969**, 25 (8), 1480–1491.

¹⁸⁰ Li, W. K.; Zhou, G. D.; Mak, T. C. W. *Advanced Structural Inorganic Chemistry*; Oxford University Press: Oxford, (England), **2008**.

$\kappa N7$ -monodentate coordination mode is predominant and the chelating $\kappa^2 N7, O6$ binding is only observed in the compounds $[\text{Ti}(\text{theoph})(\eta^5\text{-C}_5\text{H}_5)_2]$ ¹⁸¹ and $[\text{Cu}(\text{theoph})(\text{L})]$ (L = N-3,4-benzosalicylidine-N',N'-dimethylethylenediamine).¹⁸² The titanium(III) complex exhibits a relatively symmetric coordination mode [Ti–N7: 2.211(3) Å, Ti–O6: 2.278(2) Å] whereas the copper(II) complex shows an asymmetric binding [Cu–N7: 1.939(3) Å, Cu–O6: 2.919(2) Å] similar to that presented in this compound.

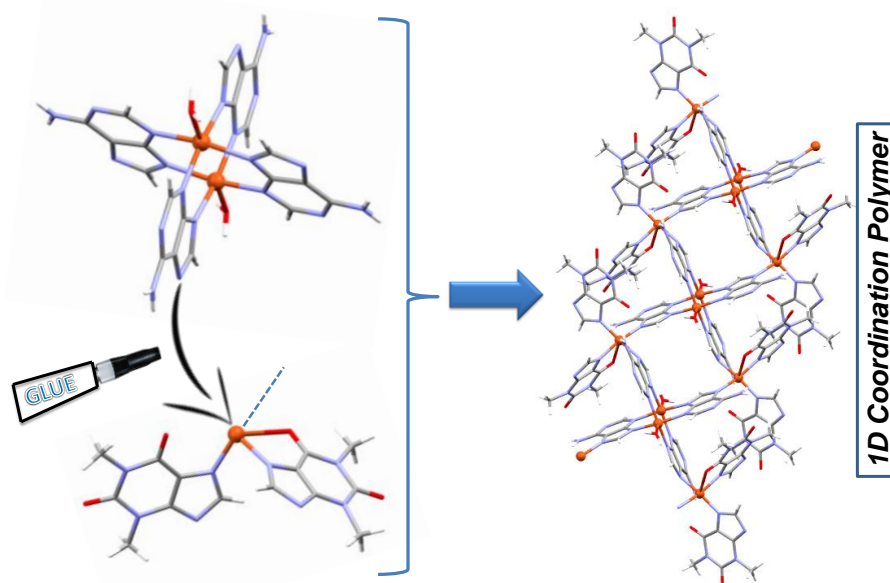


Figure 2.38. Schematic description of the structure of compound CU2ADTP.

An analogous alternation of dimeric and monomeric units has been previously described in the three-dimensional compound $\{[\text{Cu}_2(\mu\text{-ade})_4(\text{H}_2\text{O})_2] \cdot 2[\text{Cu}(\text{ox})(\text{H}_2\text{O})] \cdot \sim 14\text{H}_2\text{O}\}_n$ ⁷² (ox = oxalate dianion) where the tridentate $\mu_3\text{-}\kappa N3:\kappa N7:\kappa N9$ binding of the adeninato ligands generates a helical network and channels along the direction [001] with a diameter of 13 Å. However, in compound CU2ADTP, the greater volume of the theophyllinate anion with respect to the oxalate, and the coordination of two anions in the monomer unit are probably crucial in preventing the developing of a covalent three-dimensional architecture. The crystalline building is maintained by Van der Waals forces between these ribbons and probably by hydrogen bonds involving the crystallization molecules located in the gaps left by the ribbons.

The water interconnected rhomboid $[\text{Cu}_6(\text{ad})_4]$ subunits of this compound gives rise to ribbons by alternating centrosymmetric dimeric (Cu1) and monomeric (Cu2) entities as vertices and a quartet of adenine ligands perpendicularly arranged to the plane of the

¹⁸¹ Cozak, D.; Mardhy, A.; Olivier, M. J.; Beauchamp, A. L. *Inorg. Chem.* **1986**, 25 (15), 2600–2606.

¹⁸² Szalda, D. J.; Kistenmacher, T. J.; Marzilli, L. G. *J. Am. Chem. Soc.* **1976**, 98 (26), 8371–8377.

rhombus as sides. There are no π - π interactions between the adeninato ligands since, although they are almost parallel arranged to each other, the nucleobases sited in front are directed towards opposite sides of the chain. In fact, there are not relevant direct supramolecular interactions among the polymeric chains, nor hydrogen bonding nor π -stacking interactions, that could direct the crystal building into an open architecture as observed for compounds where complementary nucleobase...nucleobase interactions are present.¹²⁴ In our case, the crystallization water molecules prevail on the competition to establish hydrogen bonds and disrupt the expected direct interactions among the chains. However, the irregular shape and rigidity of the polymeric chain due to the coordination mode of the adeninato ligands, and the presence of intramolecular hydrogen bonds preclude their compact packing. In fact, the resulting inefficient packing generates occluded voids with a volume of the pores of 271 Å³ (18% of the total cell) occupied by the crystallization water molecules with a diameter between 2.1 and 3.7 Å and a pore volume of 0.11 cm³·g⁻¹, (Fig. 2.39 and 2.40).

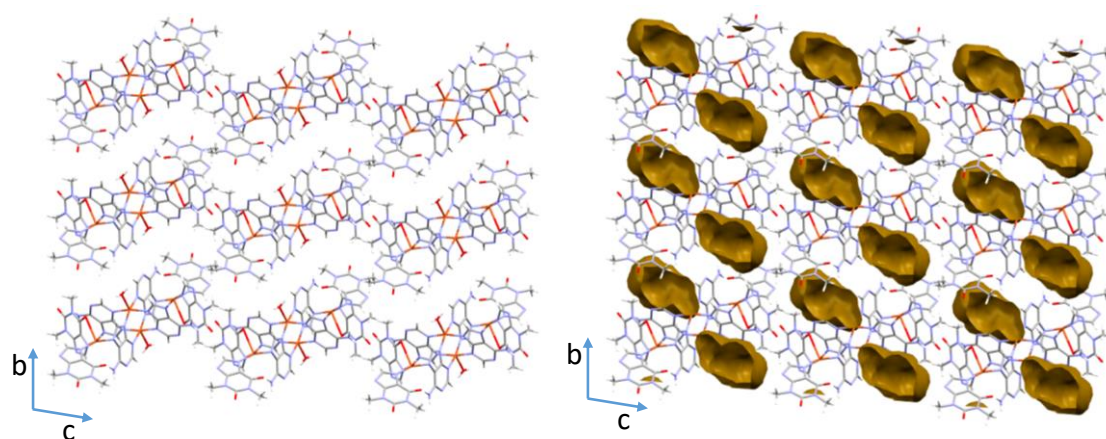


Figure 2.39. Projection in the *bc* plane of the crystal packing of compound showing the voids between the polymeric chains.

In order to assess the adsorption properties of compound CU2ADTP, a sample was activated in vacuum at 50 °C for 4 h. The outgassed sample undergoes a mass loss of 10.4% (corresponding to all crystallization water molecules), and shows a moderate adsorption of 0.35 mmol CO₂·g⁻¹ (Figure 2.41a) in agreement with its low pore volume percentage. The activated sample retains the crystallinity upon activation process as it can be seen in Figure 2.41b.

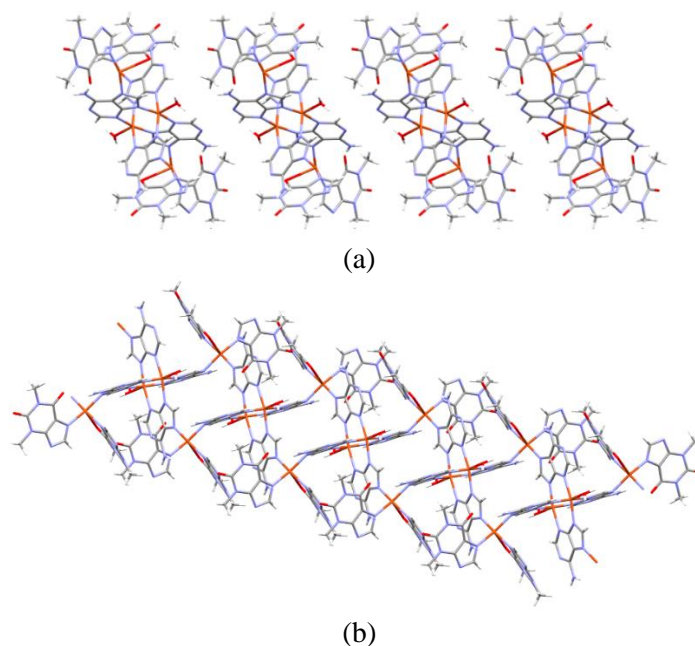


Figure 2.40. Irregular shape of 1D coordination polymer view along (a) *a* axis, (b) *b* axis crystallographic direction.

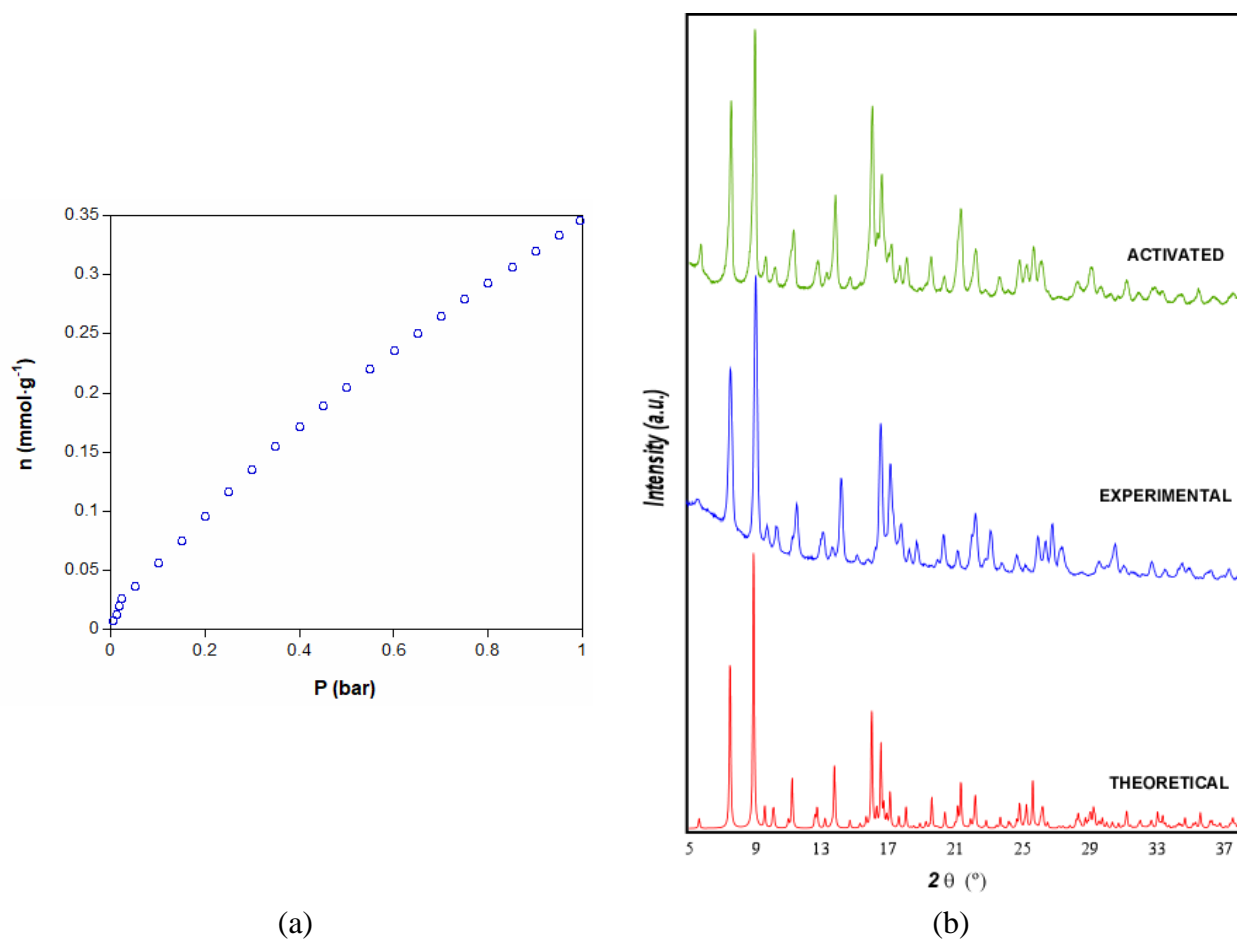


Figure 2.41. (a) CO₂ adsorption curve at 273 K (0–1 bar) for compound CU₂ADTP and (b) DRX comparison of fresh sample, theoretical and activated one.

Despite the absence of robust supramolecular synthons between the chains, the X-ray thermodiffractogram, shown in Figure 2.42, indicates that the CU2ADTP compound maintains its crystallinity unchanged up to 120 °C and only above this temperature, at which the coordination water molecules begin to get lost, there is a significant decrease in the intensity of the diffraction peaks with the disappearance of several of them. The anhydrous product remains thermally stable up to 195 °C after which it undergoes several decomposition processes to provide CuO as the final residue above 500 °C.

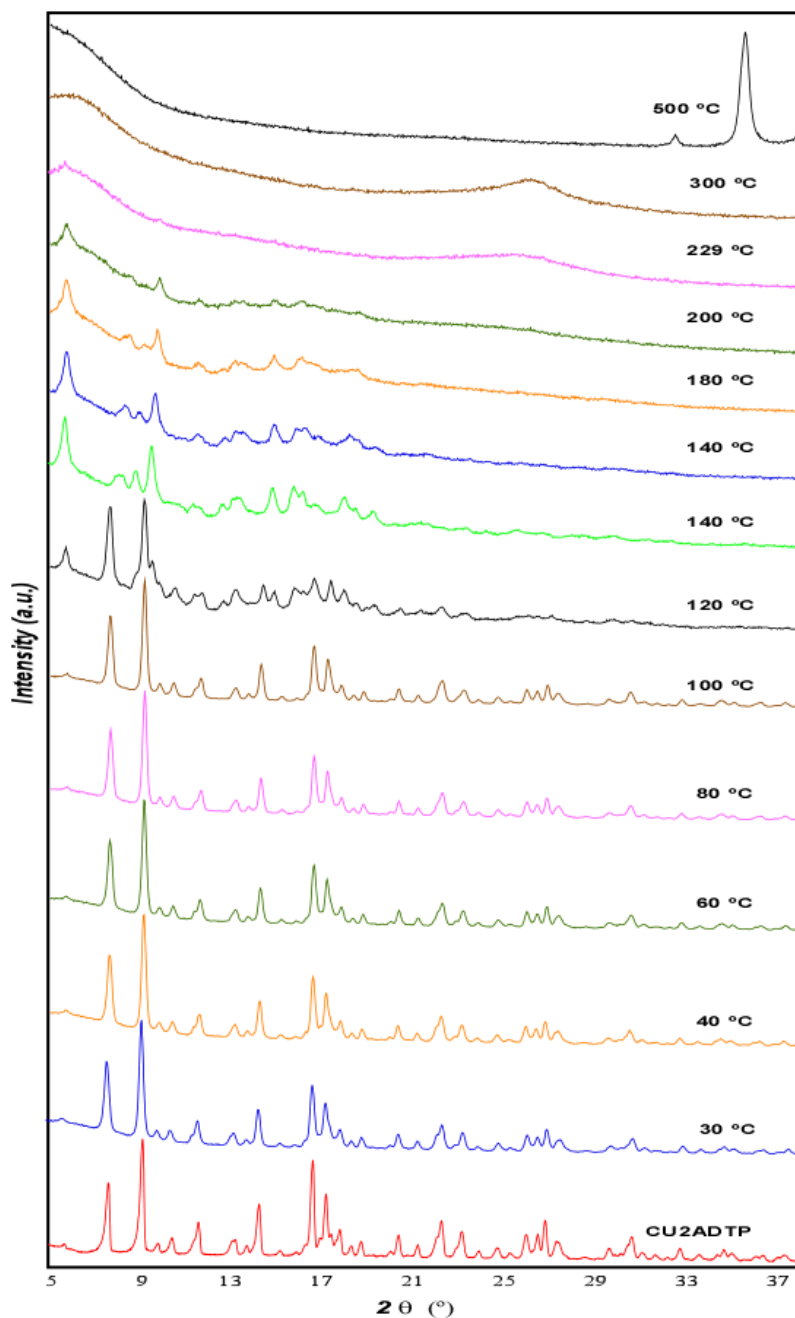


Figure 2.42. Variable-temperature powder X-ray diffractogram of CU2ADTP.

2.5. Crystal structures of compounds containing heptameric units.

As we have seen, nucleobases are key structure directing agents to build up ordered porous structures known as SMOFs (supramolecular metal-organic frameworks).^{76b} However, supramolecular recognition capability of the nucleobases does not lie only on hydrogen-bonding interactions but also on its ability to establish π - π stacking interactions.^{104, 122} These latter interactions are less directional than the hydrogen bonds but can play a crucial role on the resulting supramolecular architecture. In fact, calculations on the stability of the DNA indicate that these π - π stacking interactions are crucial to provide stability to the double helix.¹⁸³

Therefore, we aimed at getting a deeper insight on the resulting supramolecular assembling coming from the latter interactions and the $[\text{Cu}_7(\mu\text{-ade})_6(\mu_3\text{-OH})_6(\mu\text{-H}_2\text{O})_6]^{2+}$ heptameric entity. The cationic nature of these discrete entities provides a rich source for novel compounds just by replacing the counterion, as it has been previously reported when this cationic entity crystallizes with sulfate^{107b} and nitrate¹⁵⁴ counterions. These inorganic anions lack the capacity to establish π - π stacking interactions and reduce the accessible volume. Contrarily, if the counterion can be intercalated within the 3D supramolecular architecture, the pores remain accessible with an increase of the robustness of these systems.

For this purpose we have employed the planar/aromatic theobrominate anion that gave rise to a flexible porous material, in which the negatively charged nucleobase derivatives, the theobrominate anions (theo), are sandwiched between the π - π stacking adenines CU7ADTB. The steric hindrance of the theobrominate methyl groups difficults its coordination to the copper atoms and, as a consequence, does not alter the rigid metal-adenine entities. The structural flexibility taking place in this compound is highly unusual for complementary hydrogen bond sustained porous architectures based on rigid discrete entities.^{101,102} The less directional π - π stacking interactions seem to be the source of this behavior as reported for some other π -stacking sustained structures.^{107b} It is worth noticing that the theobrominate anion cannot establish complementary hydrogen bonds with μ -adeninato- $\kappa\text{N}3:\kappa\text{N}9$ ligand as it lacks of adjacent donor and acceptor positions (Figure 2.24).

¹⁸³ Yakovchuk, P.; Protozanova, E.; Frank-Kamenetskii, M. D. *Nucleic Acids Res.* **2006**, *34* (2), 564–574.

Once we were sure that this type of interaction that gave rise to new porous structures was possible, we selected two planar organic anions, benzoate and benzene-1,4-dicarboxylate (terephthalate), in order to analyze the effect of the charge density distribution on the π - π stacking interactions and, as a consequence, on the supramolecular architecture. Indeed, the π - π stacking interaction is usually described as an electrostatic attraction between partial opposite charges located in the interacting molecules.^{96,184}

Once understood the interaction that provides the double negative charge of the dicarboxylic anions, a reticular study is carried out where the length of those is modified, Table 2.21. Reticular chemistry,¹⁸⁵ the rational combination of inorganic nodes and organic linkers to afford extended framework structures with predictable and precise architectural arrangements, has made metal-organic frameworks (MOFs) the most fruitful and the fastest growing area of inorganic chemistry¹⁸⁶ with more than 100,000 crystal structures of MOFs in the structural CSD database records.¹⁸⁷

In this sense, the development of the concept of isorecticular chemistry played a key role in the success of these materials as it provided to the experimentalist a straightly forward control on the pores size and inner surface chemistries while retaining the network topology.¹⁸⁸ This approach has been fruitful providing families of isorecticular MOF families such as the pioneering IRMOFs of Omar Yaghi⁶⁰ and later, the Zr-based MOFs, named UiO-66, -67, and -68 prepared by Lillerud and co-workers (UiO= University of Oslo)⁵⁴, the large analogues of MIL-88 from the Christian Serre laboratory (MIL= Materials Institute Lavoisier),¹⁸⁹ and the PCN-61, PCN-66, PCN-68 and PCN-610

¹⁸⁴ Martinez, C. R.; Iverson, B. L. *Chem. Sci.* **2012**, *3* (7), 2191–2201.

¹⁸⁵ (a) Freund, R.; Canossa, S.; Cohen, S. M.; Yan, W.; Deng, H.; Guillerm, V.; Eddaoudi, M.; Madden, D. G.; Fairen-Jimenez, D.; Lyu, H.; Macreadie, L. K.; Ji, Z.; Zhang, Y.; Wang, B.; Haase, F.; Wöll, C.; Zaremba, O.; Andreato, J.; Wuttke, S.; Diercks, C. S. *Angew. Chemie - Int. Ed.* **2021**, *60* (45), 23946–23974. (b) Chen, Z.; Kirlikovali, K. O.; Li, P.; Farha, O. K. *Acc. Chem. Res.* **2022**, *55* (4), 579–591.

¹⁸⁶ Gropp, C.; Canossa, S.; Wuttke, S.; Gándara, F.; Li, Q.; Gagliardi, L.; Yaghi, O. M. *ACS Cent. Sci.* **2020**, *6* (8), 1255–1273.

¹⁸⁷ Moghadam, P. Z.; Li, A.; Wiggin, S. B.; Tao, A.; Maloney, A. G. P.; Peter, A.; Ward, S. C.; Fairen-jimenez, D. *Chem. Mater.* **2017**, *29* (7), 2618–2625.

¹⁸⁸ (a) Furukawa, H.; Go, Y. B.; Ko, N.; Park, Y. K.; Uribe-Romo, F. J.; Kim, J.; O’Keeffe, M.; Yaghi, O. M. *Inorg. Chem.* **2011**, *50* (18), 9147–9152. (b) Schukraft, G. E. M.; Ayala, S.; Dick, B. L.; Cohen, S. M. *Chem. Commun.* **2017**, *53* (77), 10684–10687.

¹⁸⁹ Surblé, S.; Serre, C.; Mellot-Draznieks, C.; Millange, F.; Férey, G. A. *Chem. Commun.* **2006**, *3*, 284–286.

named MOFs based on hexacarboxylate ligands and developed by Hong-Cai Zhou (PCN= Porous Coordination Network).¹⁹⁰

Herein, the features of isorecticular series in MOFs, retaining the topology but modifying the size of the pores by means of the organic linkers with different length, Table 2.21, is reproduced in a family of SMOFs with general formula $[\text{Cu}_7(\mu\text{-adeninato})_6(\mu_3\text{-OH})_6(\mu\text{-OH}_2)_6](\text{OOC-R-COO})_n(\text{H}_2\text{O})$ based on wheel shaped heptameric cations and dicarboxylate organic anions: fumarate (CU7ADFA-1, CU7ADFA-2, CU7ADF-1, CU7ADF-2), acetylendicarboxylate (CU7ADNAC-1, CU7ADNAC-2), terephthalate (CU7ADTEP-1), naphthalene-2,6-dicarboxylate (CU7ADNAPH-1, CU7ADNAPH-2), biphenyl-4,4'-dicarboxylate (CU7ADBP) and stilbene-4,4'-dicarboxylate (CU7ADS). The assembly of the structural units takes place, in addition to the electrostatic forces, by recurrent $\pi\text{-}\pi$ interactions between the adeninato ligands of the cationic entities and also by means of hydrogen-bonded synthons involving the carboxylate groups of the organic anions and a HO-Cu-OH₂ fragment of the complex cations. This last interaction is reinforced by $\pi\text{-}\pi$ stacking between the adeninato ligands and the aromatic rings of the anions. The overall supramolecular arrangement gives rise to isorecticular cavities whose inner volume, occupied by solvent molecules, increases with the size of the organic anion. The compounds, synthesized in aqueous media, are stable and highly insoluble in water and the supramolecular architecture is flexible allowing a pore shrinkage during the solvent molecules release and recovering the initial porous structure upon exposure to a water-saturated atmosphere.

The water adsorption capabilities of compounds have been measured showing also dependence of the total amount of adsorbed water and the partial pressure onset with respect to the length of the dicarboxylate counterion.¹⁹¹ Furthermore, the paramagnetic behavior of the heptameric entities at room temperature has been employed to monitorize the adsorption of different molecules (including conventional drugs) from aqueous solution, as previously made for $[\text{Cu}_6\text{Cr}(\mu\text{-adeninato-}\kappa\text{N3}:\kappa\text{N9})_6(\mu_3\text{-OH})_6(\mu\text{-H}_2\text{O})_6](\text{SO}_4)_{1.5}$.¹⁹² The results indicate size limiting selectivity that can be tailored again through the length of the dicarboxylate anion. Two compounds based in the same

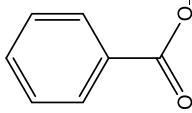
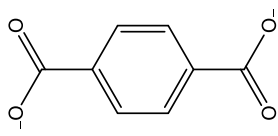
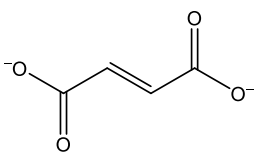
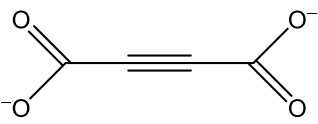
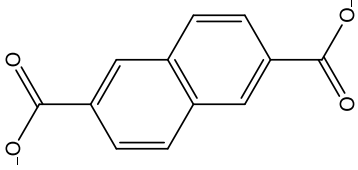
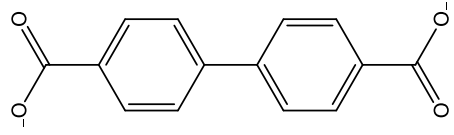
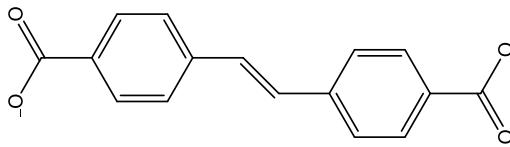
¹⁹⁰ Yuan, D.; Zhao, D.; Sun, D.; Zhou, H. C. *Angew. Chemie - Int. Ed.* **2010**, *49* (31), 5357–5361.

¹⁹¹ Gong, W.; Xie, H.; Idrees, K. B.; Son, F. A.; Chen, Z.; Sha, F.; Liu, Y.; Cui, Y.; Farha, O. K. *J. Am. Chem. Soc.* **2022**, *144* (4), 1826–1834.

¹⁹² Pérez-Aguirre, R.; Artetxe, B.; Beobide, G.; Castillo, O.; de Pedro, I.; Luque, A.; Pérez-Yáñez, S.; Wuttke, S. *Cell Reports Phys. Sci.* **2021**, *2* (5), 100421.

heptameric unit has been prepared using DMF as solvent and the biphenyl-4,4'-dicarboxylate (CU7ADBPD), and stilbene-4,4'-dicarboxylate (CU7ADSD) anions, but the presence DMF in the voids of their supramolecular crystal structures leads to a different reticular topology with an important decrease of the potential porosity.

Table 2.21. Organic anions used in the isorecticular SMOF series.

Molecule	Abreviation	Scheme
Benzoate (Benzenecarboxylic acid)	<i>benzoate</i>	
Terephthalate (Benzene-1,4-dicarboxylic acid)	<i>tereph</i>	
Fumarate (<i>(2E)</i> -But-2-enedioic acid)	<i>fumarate</i>	
Acetylenedicarboxylate (But-2-ynedioic acid)	<i>acety</i>	
Naphthalen-2,6-dicarboxylate (Naphthalene-2,6-dicarboxylic acid)	<i>naph</i>	
Biphenyl-4,4'-dicarboxylate ([1,1'-biphenyl]-4,4'-dicarboxylic acid)	<i>biph</i>	
Stilbene-4,4'-dicarboxylate (4,4'-(1,2-Ethenediyl)bisbenzoic acid)	<i>stil</i>	

2.5.1. Structural description of compounds based on $[\text{Cu}_7(\mu\text{-ade})_6(\mu_3\text{-OH})_6(\mu\text{-H}_2\text{O})_6]^{2+}$ units

The cationic $[\text{Cu}_7(\mu\text{-ade})_6(\mu_3\text{-OH})_6(\mu\text{-H}_2\text{O})_6]^{2+}$ entity of all the later described compounds consists of a central $[\text{Cu}(\text{OH})_6]^{4-}$ core, located on an inversion center, that is connected to six additional external copper(II) metal centers in a radial and planar arrangement. Those are further bridged through six hydroxide which adopt a μ_3 -bridging mode, in such a way that they connect the central metal atom to two external ones (Figure 2.43). This bridging generates a wheel-shaped entity in which six semicoordinated bridging water molecules and six μ -adeninato- $\kappa\text{N}3:\kappa\text{N}9$ ligands bridge the peripheral copper atoms.

All the copper centers present an octahedral geometry with the usual Jahn-Teller tetragonal elongation, see Table 2.22 for CU7ADTB, which is more pronounced for the peripheral copper(II) centers because of the rigidity of the heptanuclear entity. The elongation at the peripheral copper atoms takes place along the metal-water coordination bonds, in such a way that the coordinated water molecules are loosely held, with longer coordination bonds than for the adeninato ligand.

Table 2.22. Distances and angles (\AA , deg) for compound CU7ADTB.^a

Cu1–O1	1.995(6)	Cu1–O2	2.001(6)	Cu1–O3	2.247(7)
Cu2–O1	1.972(7)	Cu2–O2	1.966(6)	Cu2–N13	1.999(10)
Cu2–N33	1.991(9)	Cu2–O2w	2.501(9)	Cu2–O3w	2.470(9)
Cu3–O1	1.985(7)	Cu3–O3	1.951(6)	Cu3–N13	2.018(10)
Cu3–N29	1.958(9)	Cu3–O1w	2.706(10)	Cu3–O3w	2.384(7)
Cu4–O2	1.992(7)	Cu4–O3	1.954(6)	Cu4–N29	2.008(10)
Cu4–N39 ⁱ	1.971(9)	Cu4–O1w	2.558(1)	Cu4–O2w ⁱ	2.429(7)
Cu1...Cu2 ⁱ	3.038(1)	Cu1...Cu4	3.152(1)	Cu2...Cu4 ⁱ	3.125(2)
Cu1...Cu3	3.123(1)	Cu2...Cu3	3.114(2)	Cu3...Cu4	3.074 (2)
Cu1–O1–Cu2	100.0(3)	Cu1–O1–Cu3	103.4(3)	Cu2–O1–Cu3	103.8(3)
Cu1–O2–Cu2 ⁱ	100.0(3)	Cu1–O2–Cu4	104.2(3)	Cu4–O2–Cu2 ⁱ	104.3(3)
Cu1–O3–Cu3	95.9(3)	Cu1–O3–Cu4	97.0(3)	Cu3–O3–Cu4	103.8(3)
Cu3–O1w–Cu4	71.4(3)	Cu2–O2w–Cu4 ⁱ	78.7(3)	Cu2–O3w–Cu3	79.6(3)

^aSymmetry: (i) – x, – y, – z.

In the case of CU7ADTB, as it happens with the rest of herein described heptanuclear compounds, the heptameric entity is analogous to that found in the

crystalline structures of the compounds $[\text{Cu}_7(\mu\text{-ade})_6(\mu_3\text{-OH})_6(\mu\text{-H}_2\text{O})_6](\text{NHEt}_3)_2(\text{SO}_4)_2 \cdot n\text{H}_2\text{O}$ ($n = 23, 42$)¹⁵⁴ and $[\text{Cu}_7(\mu\text{-ade})_6(\mu_3\text{-OH})_6(\mu\text{-H}_2\text{O})_6](\text{NO}_3)_2 \cdot 6\text{H}_2\text{O}$ ^{107b} and resembles that present in the compound $2\text{D}-\{[\text{Cu}_7(\mu\text{-ade})_2(\mu_3\text{-OH})(\mu\text{-sip})_2(\mu\text{-H}_2\text{O})_6] \cdot 2.5\text{H}_2\text{O}\}_n$ where four of the adeninate bridges are replaced by two 5-sulphoisophthalate anions.¹⁹³

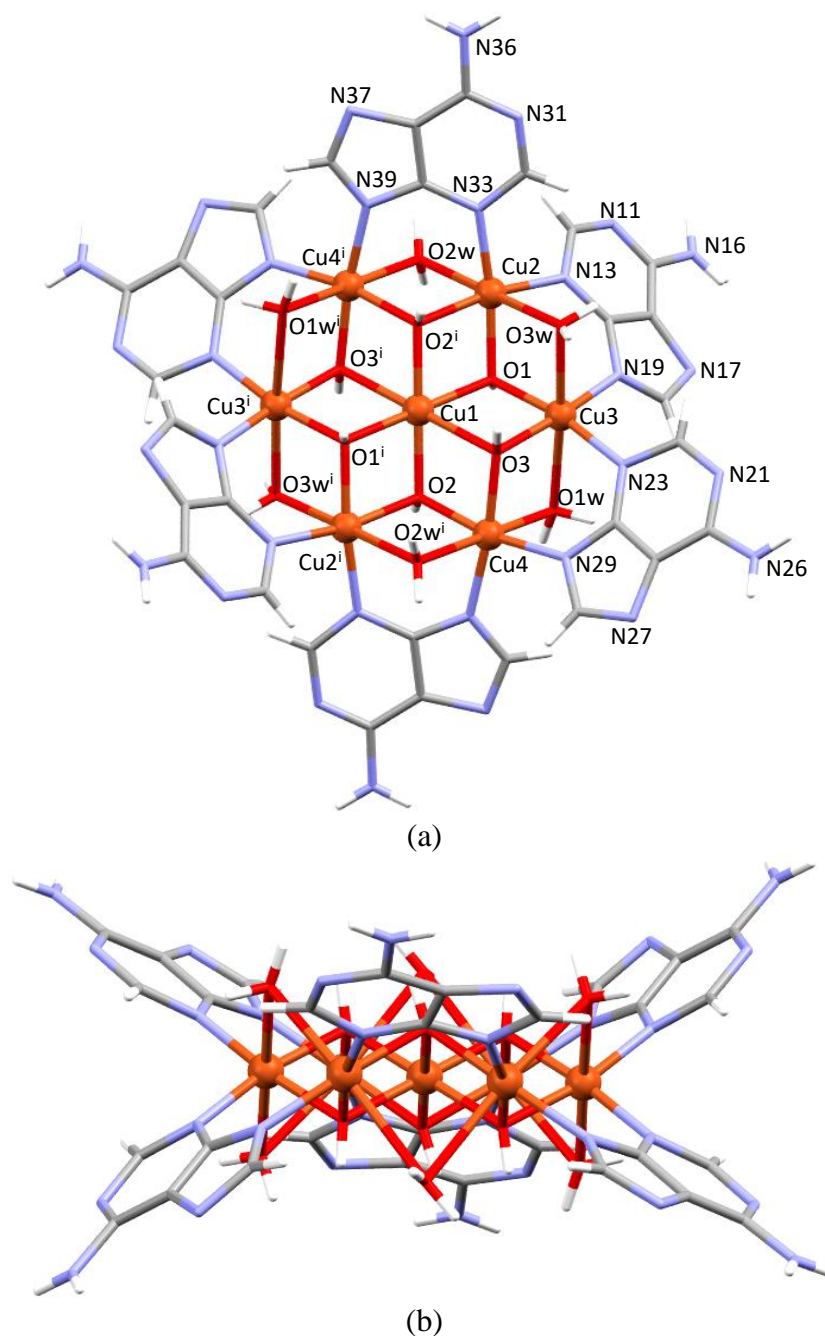


Figure 2.43. (a) and (b) The $[\text{Cu}_7(\mu\text{-ade})_6(\mu_3\text{-OH})_6(\mu\text{-H}_2\text{O})_6]^{2+}$ heptanuclear cationic entity in all the compounds.

¹⁹³ Liu, Z.-Y.; Zhang, H.-Y.; Yang, E.-C.; Liu, Z.-Y.; Zhao, X.-J. *A. Dalt. Trans.* **2015**, *44*, 5280–5283.

The crystal building of these previously reported compounds is maintained by a combination of supramolecular π - π stacking and hydrogen bonding interactions in addition to the electrostatic forces taking place between the charged entities. In the sulfate containing compounds, the arrangement of the heptameric entities generates voids where sulfate and triethylammonium counterions are sited, together with the crystallization water molecules. The thermal release of these water molecules collapses the crystal building and the compounds loss their crystallinity during the dehydration process. The shape of the cluster $\text{Cu}_7\text{O}_{12}\text{N}_{12}$ of these complex entities is reminiscent of the so-called Anderson structure observed for some heteropolyoxometalate anions with the general formula $[\text{XM}_6\text{O}_{24}]$, Figura 2.44.¹⁹⁴

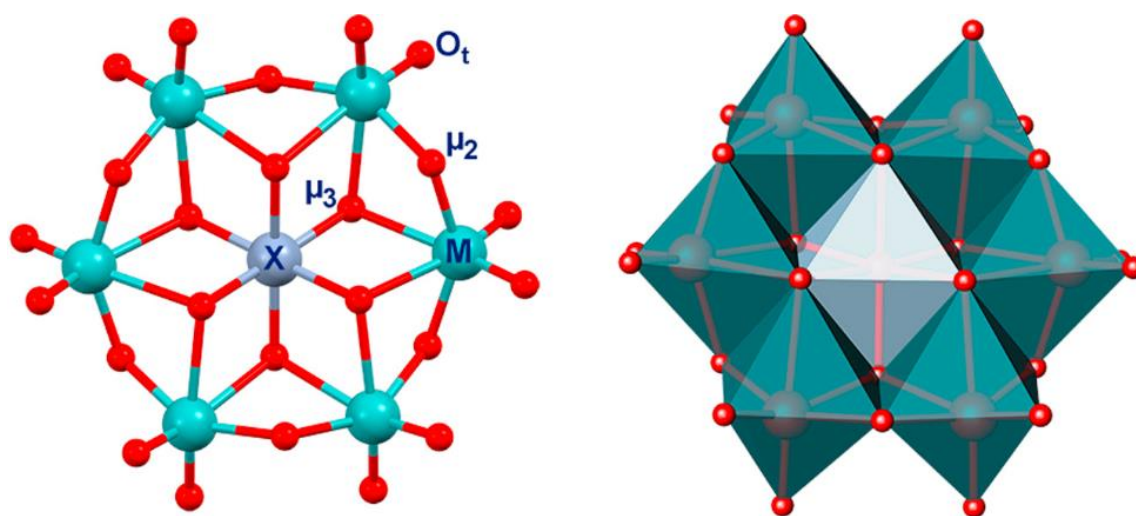


Figure 2.44. Anderson type complex structure.

The use of water as solvent hinders the presence of direct hydrogen bonding interactions between the adeninato ligands. Therefore, the crystal structure is dominated by π - π stacking interactions, Figures 2.45 and 2.46. In the crystal building, each cationic complex is surrounded by four others and attached to them through three different rigid synthons (Figure 2.45b). The first one (A) comes from double adeninato \cdots adeninato π - π stacking interactions to provide a synthon that spreads along the crystallographic c -axis, Figure 2.45a. The second one (B) involves a single adeninato \cdots adeninato stacking between metal-adenine complexes placed in the same ab -plane. The third one consist of pairs of theobrominate anions parallel to each other and to the adeninato ligands to give

¹⁹⁴ (a) Kurmoo, M. *Chem. Soc. Rev.* **2009**, 38 (5), 1353–1379. (b) Blazevic, A.; Rompel, A. *Coord. Chem. Rev.* **2016**, 307, 42–64.

a ...A...T...T...A... sequence of supramolecular π - π interactions (C) that spreads along the crystallographic *ab*-plane.

Finally, the three-dimensional cohesiveness of the crystal structure is reinforced with several hydrogen bonds, for example that involving the hydroxyl group O3 and the nitrogen N41 of the theobrominate anion and that established between the exocyclic amino group of the adeninato ligand (X= 3) and the carbonylic C=O42 of the theobrominate anion. The structural parameters of the above-described supramolecular interactions are gathered in the Table 2.23.

Table 2.23. Structural parameters (\AA , deg) of more relevant noncovalent interactions.^a

Hydrogen-bonding interactions					
	D-H...A ^b	H...A	D...A	D-H...A	
	O1-H1... O6w ^{iv}	1.98	2.80(3)	171	
	O2-H2...O5w	1.97	2.75(1)	151	
	O3-H3... N41 ⁱⁱ	2.28	3.12(1)	155	
	N16A-H16A1...O4w	2.33	3.07(2)	140	
	N16A-H16A2...O10w	2.39	3.23(3)	160	
	N26A-H26A...O10w ⁱⁱⁱ	1.98	2.82(3)	158	
	N26A-H26B...O11w	2.27	3.12(3)	162	
	N36A-H36A...O5w ^{iv}	1.94	2.71(2)	145	
	N36A-H36B...O42A ⁱ	2.63	3.35(2)	140	
π-π interactions^c					
ring-ring	packing	angle	DC	DZ	DXY
1ha...1ha ⁱⁱⁱ	A...A	2.0	4.37	3.62	2.45
2pa...2pa ⁱⁱⁱ	A...A	3.0	3.70	3.40	1.46
3ha...3har ^{iiiv}	A...A	0.0	4.07	3.34	2.32
pt...1pa ⁱ	T...A	9.8	3.80	3.69	0.93
ht...ht ^v	T...T	0.0	3.52	3.34	0.73

^aSymmetry codes: (i) $-x, 1-y, -z$; (ii) $-1/2+x, -1/2+y, z$; (iii) $-x, 1+y, 1/2-z$; (iv) $-1/2+x, 1/2+y, z$; (v) $1/2-x, 1/2-y, -z$. ^bD: donor; A: acceptor. ^cAngle: dihedral angle between the planes (deg), DC: distance between the centroids of the rings (\AA), DZ: interplanar distance (\AA), DXY: lateral displacement (\AA), pa: adenine pentagonal ring, ha: adenine hexagonal ring, pt: theobrominate pentagonal ring, ht: theobrominate hexagonal ring.

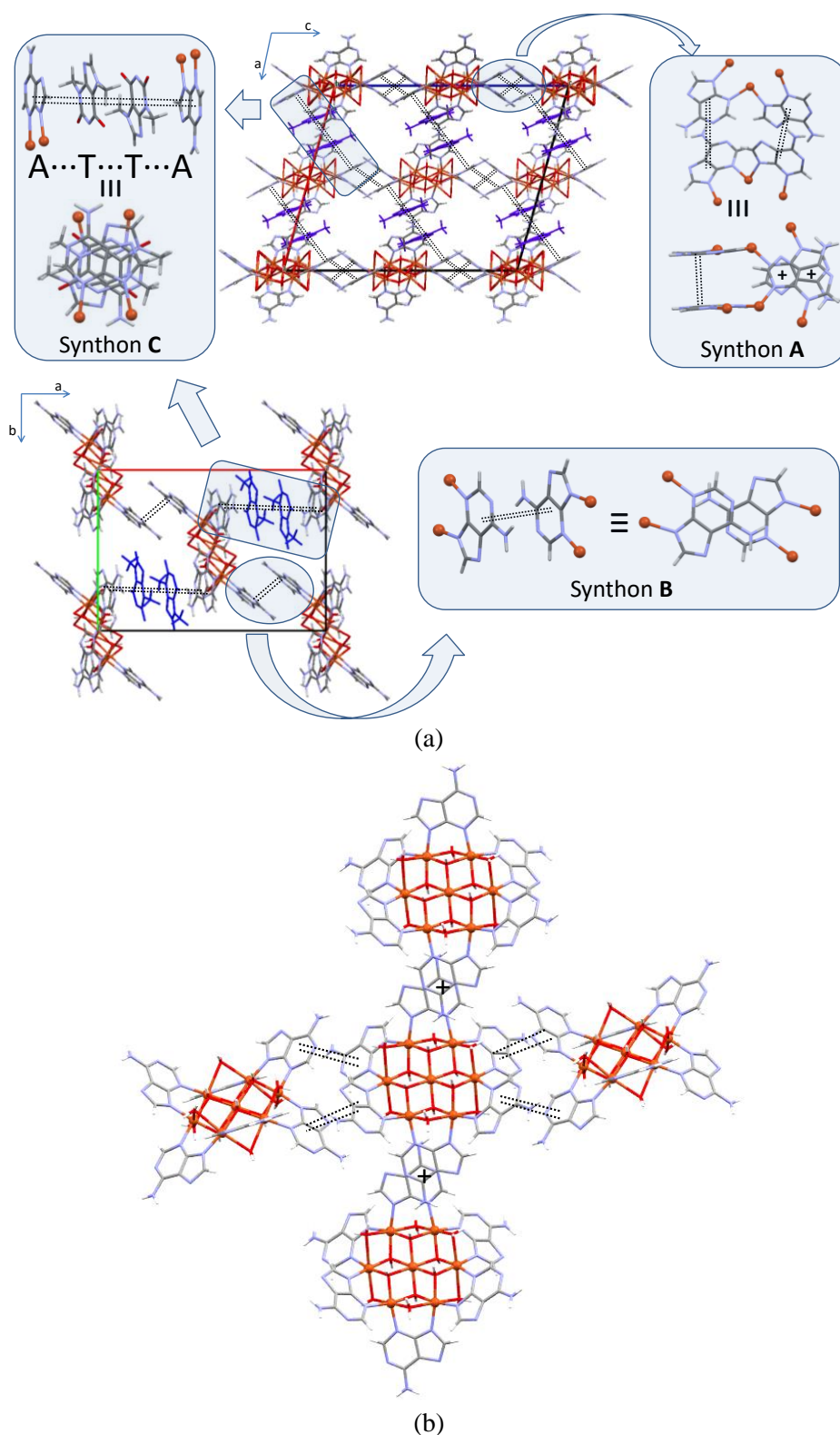


Figure 2.45. (a) CU7ADTB compound: supramolecular interactions connecting heptanuclear entities in the *ac* (top) and *ab* (bottom) crystallographic planes. Insight show the π - π interactions based rigid synthon along the crystallographic *c* axis (top right) and the more flexible ones in the *ab* plane (top left and bottom right). Double dotted lines and plus signal indicate π - π stacking interactions and (b) supramolecular interactions connecting each $[\text{Cu}_7(\mu\text{-ade-}\kappa\text{N}3:\kappa\text{N}9)_6(\mu_3\text{-OH})_6(\mu\text{-H}_2\text{O})_6]^{2+}$ heptanuclear entity to four adjacent ones.

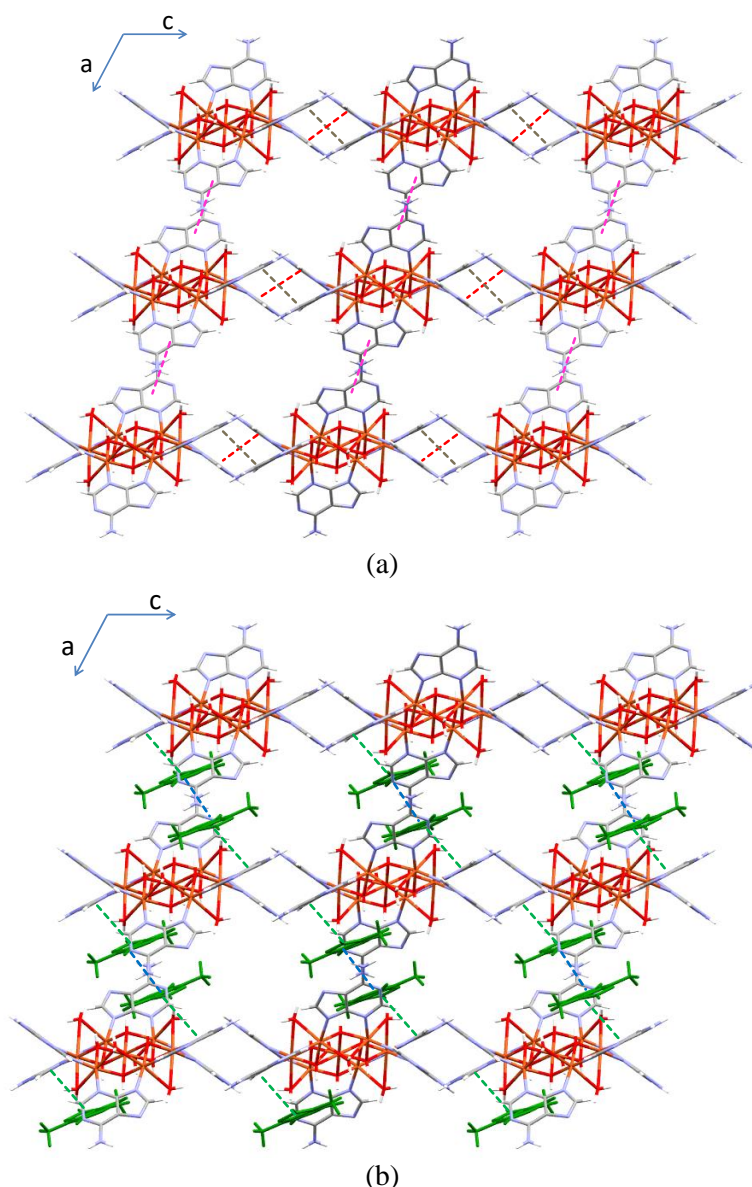


Figure 2.46. π - π stacking interactions connecting heptanuclear entities in the ac between (a) the adeninato ligands coloured in red, grey and pink and (b) adeninato and theobrominate ligands.

The voluminous heptameric entity is a rigid construction unit since all its components establish at least two coordination bonds and, therefore, it meets the first of the structural requirements necessary for the construction of supramolecular porous structures.¹²² On the other hand, the synthons connecting the heptameric units are relatively rigid, especially synthon A, which accounts for the second requirement. The third requirement is also accomplished as these synthons propagate in three noncoplanar directions. As a consequence, the just described packing of the complex entities and theobrominate anions generates an open structure with channels representing 37% of the unit cell. In these channels a large number of water molecules are placed establishing hydrogen bonding interactions among them and with the $-\text{NH}_2$ and $-\text{OH}$ groups of the

complex entities located in the walls of the channels. The involvement of the theobrominate counterions in the supramolecular packing generates an increase in the void volume percentage in comparison to that reported for the analogous $[\text{Cu}_7(\mu\text{-ade})_6(\mu_3\text{-OH})_6(\mu\text{-H}_2\text{O})_6](\text{NHEt}_3)_2(\text{SO}_4)_2 \cdot 42\text{H}_2\text{O}$ compound (3106 \AA^3 , 33% of the unit cell).

In order to analyze the pore size distribution, a procedure implemented in a code developed by L. Sarkisov¹⁸⁰ has been used, in which the Lennard-Jones universal force field parameters are used to describe the adsorbent atoms while a probe that increases its size gradually analyses the free volume. The results of this analysis show the existence of a network of interconnected channels with a pore diameter ranging from 4.3 to 5.5 Å (mode: 5.1 Å), upon the subtraction of the crystallization water molecules. These larger channels along the crystallographic *b* axis are interconnected by smaller channels along *a* and *c* directions (Figure 2.47). On the other hand, a theoretical accessible surface area value of $256 \text{ m}^2 \cdot \text{g}^{-1}$ and a pore volume of $0.22 \text{ cm}^3 \cdot \text{g}^{-1}$ has also been computed using a Monte Carlo-based integration code,¹⁷⁴ where a molecule with a parameter equal to the Lennard-Jones diameter of N_2 [3.681 Å] probes the structure of the compound.

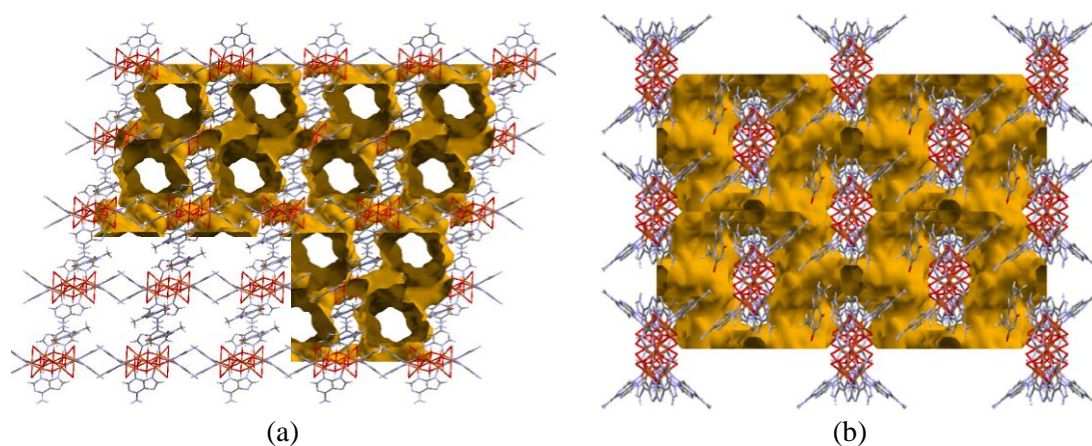


Figure 2.47. Image showing the channels contact surface along the crystallographic (a) *b* axis and (b) *c* axis for compound CU7ADTB.

It is interesting to note that compound CU7ADTB and the above-cited $[\text{Cu}_7(\mu\text{-ade})_6(\mu_3\text{-OH})_6(\mu\text{-H}_2\text{O})_6](\text{NHEt}_3)_2(\text{SO}_4)_2 \cdot 42\text{H}_2\text{O}$ compound show the same CdSO_4 -like *cds* topology with a $(6^5.8)$ point symbol (nodes being the heptameric units and connector being the π - π stacking interaction between the adeninato ligands).¹⁹⁵ Nonetheless, the exchange of sulfate anions by the theobrominate anions implies the presence of the above-

¹⁹⁵ (a) O’Keeffe, M.; Yaghi, O. M. *Chem. Rev.* **2012**, *112* (2), 675–702. (b) Blatov, V. A. *IUCr CompComm Newsl.* **2006**, *7*, 4–38.

described additional π - π interactions, which strengthens the crystal structure stability of compound CU7ADTB. In fact, whereas the thermal removal of the water molecules in the sulfate containing compound produces the collapse of the crystal structure, the thermal degradation study (Figure 2.14d and Table 2.7) and the variable-temperature X-ray powder diffraction data (Figure 2.48) show that the crystallinity is retained after the release of the crystallization water molecules (*ca.* 100 °C) and even after the removal of the coordination ones (*ca.* 180 °C), remaining stable up to 300 °C.

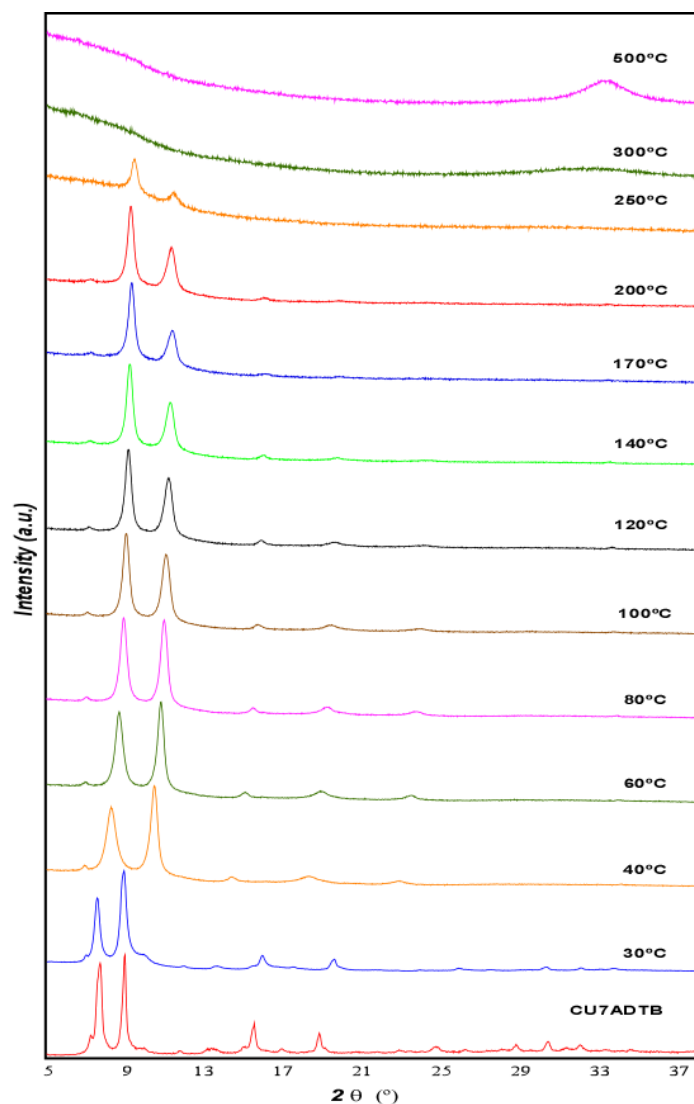


Figure 2.48. Thermodiffractometric data compared with fresh sample (bottom) of CU7ADTB.

However, the X-ray diffraction peaks shift toward higher 2θ angles, and the indexation on the variable-temperature X-ray powder diffraction patterns (Figure 2.49 and Table 2.24) based on the crystal structure parameters obtained from the single-crystal data show a progressive decreasing of the unit cell volume from 9199 Å³ for the pristine compound to 7142 Å³ at 100 °C (loss of the crystallization water molecules) and to 6417

\AA^3 at 180 °C (loss of coordination water molecules). This unit cell shrinkage implies an 80% reduction of the void volume present in the pristine sample (3489\AA^3).

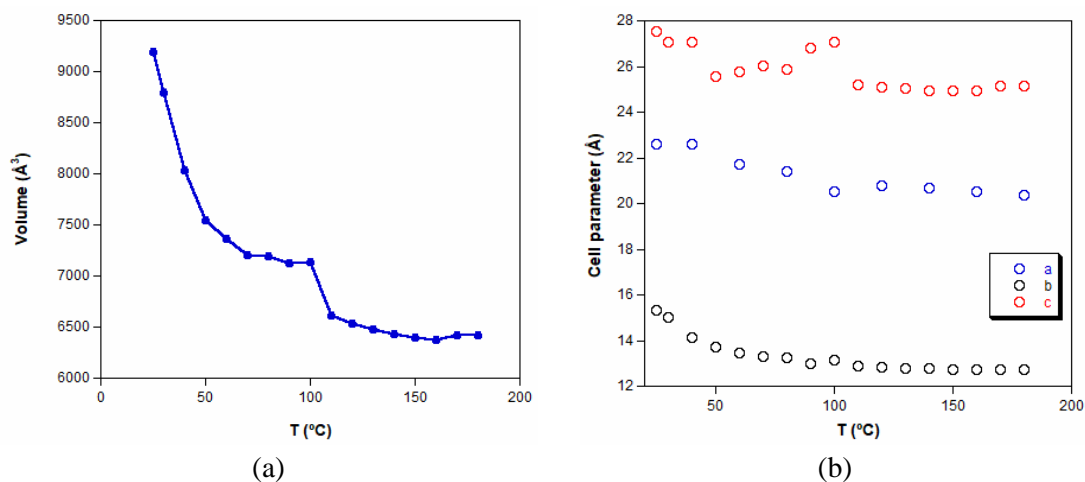


Figure 2.49. Variation of (a) cell volume and (b) cell parameter with the temperature for compound CU7ADTB.

Table 2.24. Variation of cell parameters a , b , c and β with the temperature for CU7ADTB.

Temperature	a (\AA)	b (\AA)	c (\AA)	β ($^{\circ}$)	Volume (\AA^3)
25	22.62	15.33	27.56	105.71	9200
30	22.65	15.00	27.09	107.18	8793
40	22.58	14.11	25.91	103.21	8037
50	22.06	13.70	25.59	102.79	7542
60	21.70	13.46	25.75	102.05	7355
70	21.40	13.32	26.03	101.12	7280
80	21.41	13.23	25.88	101.31	7188
90	20.75	13.01	26.82	100.17	7127
100	20.52	13.15	27.09	102.32	7142
110	20.88	12.87	25.22	102.51	6616
120	20.79	12.82	25.12	102.52	6536
130	20.75	12.79	25.03	102.60	6483
140	20.67	12.77	24.96	102.42	6434
150	20.61	12.75	24.92	102.16	6401
160	20.55	12.78	24.95	101.93	6411
170	20.37	12.74	25.12	99.99	6420
180	20.36	12.74	25.12	99.99	6417

In fact, an activated sample (80 $^{\circ}\text{C}$, 6h) of CU7ADTB (whose X-ray diffraction pattern is equal to those corresponding to the thermally obtained anhydrous compound at

180 °C) is not able to adsorb neither N₂ at 77K nor CO₂ at 273 K. So that, the dehydration process implies the loss of the porous nature of the compound but heptameric entity persists (as it will be discussed below by means of magnetic measurements) and the plasticity of the supramolecular interactions is flexible enough to allow the complete reversible contraction of the porous crystal structure of the unit cell shrinkage upon exposure to a water-saturated atmosphere for 24 hours (Figure 2.50).

The outgassing, precludes the adsorption of gas molecules, but allows a complete reversal to the initial open structure upon exposure to a water-saturated atmosphere.

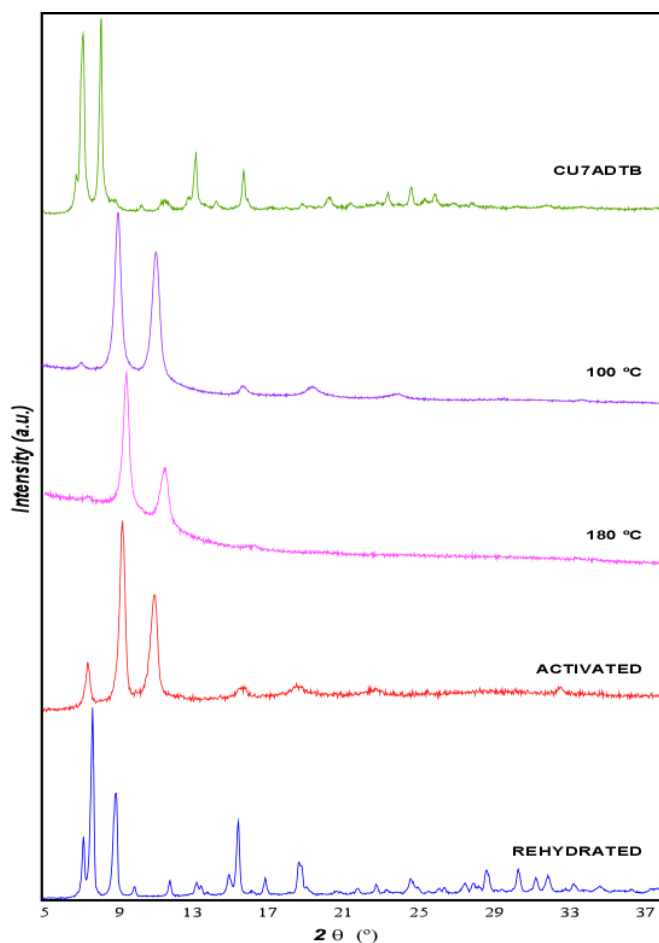


Figure 2.50. X-ray diffraction patterns of the fresh synthesized compound CU7ADTB (top), at 100, at 180 °C, of the sample activated under vacuum and moderate heating, and of the rehydrated sample upon exposure of the activated sample to humidity saturated atmosphere for 24 h. (bottom).

Although the heptameric entity is analogous to that present in the previously described CU7ADTB compound, in CU7ADBZ (Table 2.25) the presence of different anions give rise to different patterns of supramolecular interactions influencing its thermal stability and the 3D assembly of the structure.

Table 2.25. Distances and angles (Å, deg) for compound CU7ADBZ.^a

Cu1–O1	1.987(6)	Cu1–O2	1.963(8)	Cu1–O3	2.328(8)
Cu2–O1	2.000(8)	Cu2–O3 ⁱ	1.958(7)	Cu2–N19	1.957(9)
Cu2–N33 ⁱ	1.976(12)	Cu2–O2w	2.415(11)	Cu2–O3w	2.612(10)
Cu3–O1	1.967(8)	Cu3–O2	1.985(6)	Cu3–N13	1.982(9)
Cu3–N23	1.977 (11)	Cu3–O1w	2.422(8)	Cu3–O2w	2.514(11)
Cu4–O2	2.001(8)	Cu4–O3	1.947(8)	Cu4–N29	1.993(11)
Cu4–N39	1.987(11)	Cu4–O1w	2.431(7)	Cu4–O3w ⁱ	2.685(8)
Cu1···Cu2	3.185(1)	Cu1···Cu4	3.190(2)	Cu2···Cu4 ⁱ	3.083(2)
Cu1···Cu3	3.008(2)	Cu2···Cu3	3.133(3)	Cu3···Cu4	3.170(2)
Cu1–O1–Cu2	106.0(4)	Cu1–O1–Cu3	99.0(3)	Cu2–O1–Cu3	104.4(4)
Cu1–O2–Cu3	99.2(3)	Cu1–O2–Cu4	107.2(4)	Cu3–O2–Cu4	105.4(4)
Cu1–O3–Cu4	96.1(3)	Cu1–O3–Cu2 ⁱ	95.6(3)	Cu2 ⁱ –O3–Cu4	104.3(3)
Cu3–O1w–Cu4	81.6(2)	Cu2–O2w–Cu3	78.9(3)	Cu2–O3w–Cu4 ⁱ	71.2(2)

^aSymmetry: (i) 1 – x, – y, 2 – z.

According to our expectations the planar benzoate anions establish π – π stacking interactions with some of the coordinated adeninato ligands. However, as Figure 2.51 describes, the charge distribution does not allow a propagation of this interaction as the approach of a second adeninato ligand from an adjacent heptameric entity is sterically hindered, and sandwich arrangement of the benzoate anion between two adeninato ligands is not observed. As a consequence, the 3D supramolecular architecture of compound CU7ADBZ differs greatly from the previously reported theobrominate analogous. In fact, there are not additional π – π stacking interactions among the adeninato ligands and, instead of that, they are assembled together through quite unusual complementary hydrogen bonds (Table 2.26). Four of the adeninato ligands of each heptameric entity form a hydrogen bonded R₂²(8) ring involving the Hoogsteen face of a nucleobase moiety (exocyclic N16 amino group, imidazolic N17 site) and the imidazolic N37 and C38 atoms of an adeninato ligand belonging to an adjacent heptameric entity (Figure 2.52). These connections between heptameric units are reinforced with an additional hydrogen bond involving the imidazolic C28–H28 group and the pyrimidinic N21 site of two adjacent heptameric units.

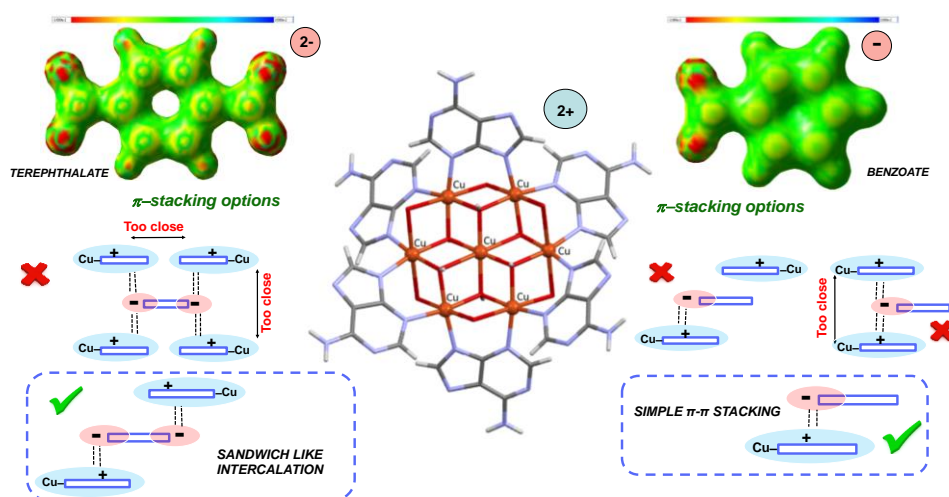


Figure 2.51. Potential supramolecular π - π stacking interactions between the adeninato ligands and the carboxylate anions.

Table 2.26. Structural parameters (\AA , deg) of hydrogen bonding interactions in CU7ADBZ.^a

Hydrogen-bonding interactions					
D-H...A ^b	H...A	D...A	D-H...A		
N16-H16...N37 ⁱ	2.35	3.05(3)	139		
C38-H38...N17 ⁱⁱ	2.57	3.41(2)	149		
C28-H28...N21 ⁱⁱⁱ	2.62	3.49(1)	156		
O1-H1...O49A	1.66	2.63(2)	175		
O1w-H11w...O48A ⁱⁱ	1.75	2.61(2)	167		
O3w-H31w...O48A	1.94	2.74(1)	153		
π - π interactions ^c					
ring-ring	packing	angle	DC	DZ	DXY
1pa...2pa ^{iv}	A...A	0.0	5.56	3.32	4.46
2pa...3pa ⁱⁱⁱ	A...A	0.0	5.72	5.23	2.18
1pa...hd ^v	A...B	2.7	4.64	3.62	2.81

^aSymmetry codes: (i) $1/3 + x - y, -2/3 + x, 7/3 - z$; (ii) $2/3 + y, 1/3 - x + y, 7/3 - z$; (iii) $4/3 - x + y, 2/3 - x, -1/3 + z$, (iv) $2/3 - y, -2/3 + x - y, 1/3 + z$; (v) x, y, z . ^bD: donor; A: acceptor. ^cAngle: dihedral angle between the planes (deg), DC: distance between the centroids of the rings (\AA), DZ: interplanar distance (\AA), DXy: lateral displacement (\AA), pa: adenine pentagonal ring, ha: adenine hexagonal ring, hd: anion hexagonal ring.

Considering the above described supramolecular interactions, the 3D arrangement of the complex units can be topologically described as a uninodal 4-connected **nbo**-net, in which the nodes are ascribed to the heptameric units and the linkers correspond to the above described hydrogen bonding interactions.^{180,196} This topology, found on the niobium oxide structure, can be also found in one of the first reported bioMOFs in which each

¹⁹⁶ Blatov, V. A.; Shevchenko, A. P.; Proserpio, D. M.. *Cryst. Growth Des.* **2014**, *14* (7), 3576–3586.

paddle-wheel dimeric $[\text{Cu}_2(\mu\text{-adeninato})_4]$ unit is linked to four equivalent ones by means of $[\text{Cu}(\mu\text{-oxalate})(\text{H}_2\text{O})]$ entities leading to a porous coordination polymer.⁷²

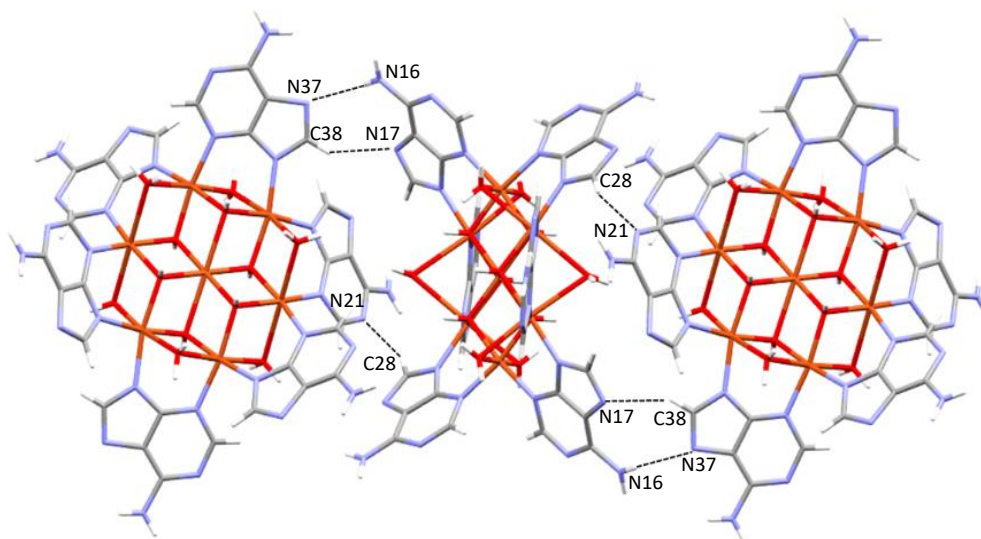


Figure 2.52. Hydrogen bonding interactions connecting heptanuclear entities in CU7ADBZ.

The three dimensional packing in CU7ADBZ allows the occurrence of channels that are partially occupied by the benzoate anions (Figure 2.53) whose phenyl rings are parallel stacked with respect to an adeninato ligand (interplanar distance of 3.60 Å, lateral offset of 1.34 Å). This interaction is reinforced by the presence of hydrogen bonds between the benzoate carboxylate group as acceptor, and one hydroxide group and two coordinated water molecules of neighbouring heptameric units as donors.

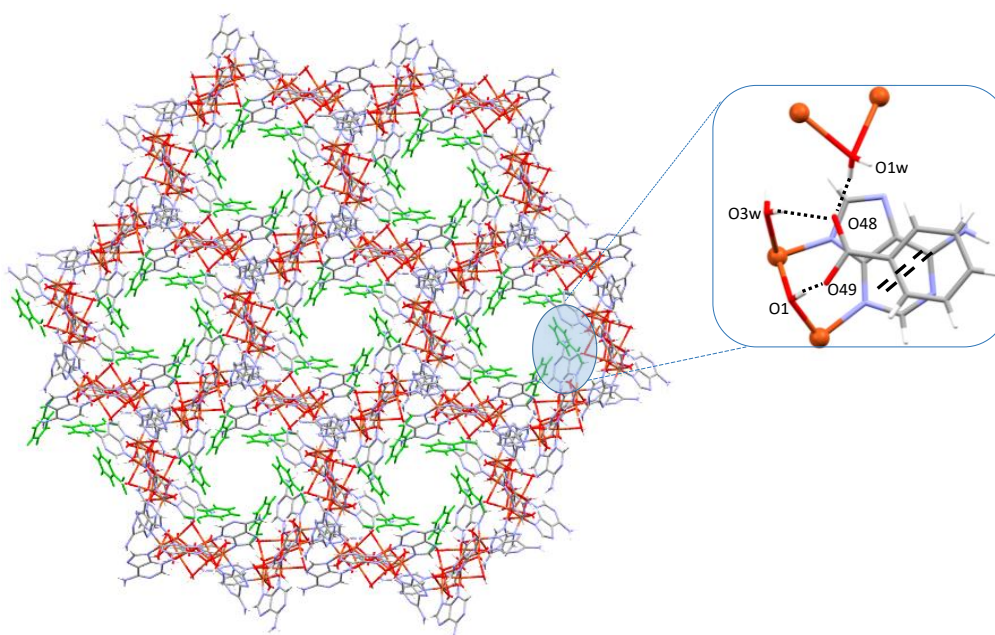


Figure 2.53. Arrangement of the organic anions (green colour) and the heptameric complex units in compound CU7ADBZ. Supramolecular benzoate \cdots adeninato interactions are highlighted.

The benzoate anions do not completely occlude the channels that run along the crystallographic [001] direction. These channels present a quite irregular shape with ovoid holes of a maximum radius of 6 Å (surrounded by the exocyclic N-site of the adeninato ligands) connected through tube-shaped corridors with an approximate radius of 3 Å on whose walls are located the phenyl rings of the benzoate anions (Figure 2.54). The volume of these channels, occupied by the crystallization water molecules, is 5098 Å³ with diameter of a range of 5.5 and 6.1 Å (29 % of the total volume of the unit cell as calculated by PLATON). A computational analysis reveals an accessible surface area value of 205 m²·g⁻¹ and a pore volume of 0.200 cm³·g⁻¹.

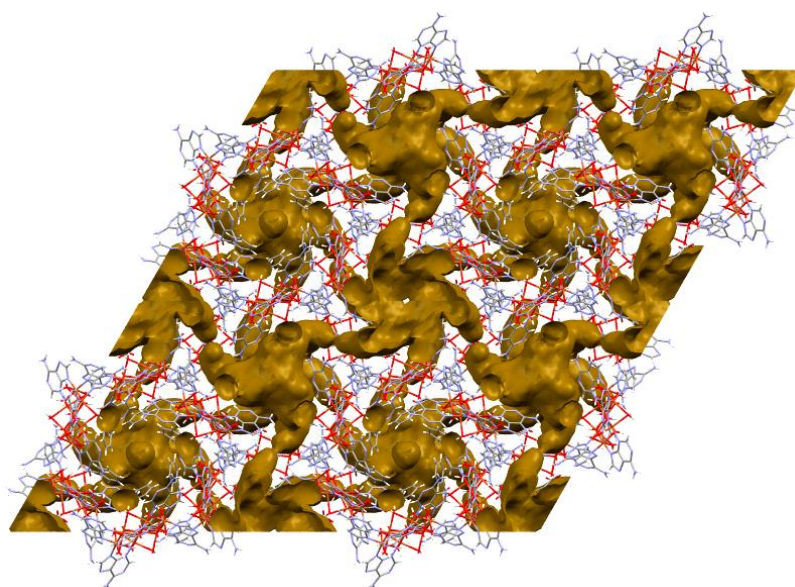


Figure 2.54. Representation of the voids present in compound CU7ADBZ

The thermogravimetric (Table 2.7, Figure 2.14e) and variable-temperature X-ray powder diffraction data of compound CU7ADBZ (Figure 2.55) indicate that upon heating it retains the crystallinity but shows a significant structural change after the removal of crystallization (*ca.* 85 °C) and coordination (*ca.* 160 °C) water molecules. The shift of diffraction peaks toward higher 2θ angles and the indexation of the variable-temperature X-ray powder diffraction patterns (Table 2.27) show a marked and progressive decrease of the unit cell volume from 17812 Å³ for the pristine compound to 13064 Å³ at 85 °C (loss of the crystallization water molecules), Figure 2.56. Interestingly, the rehydrated sample shows unit cell parameter values close to those of the pristine compound.

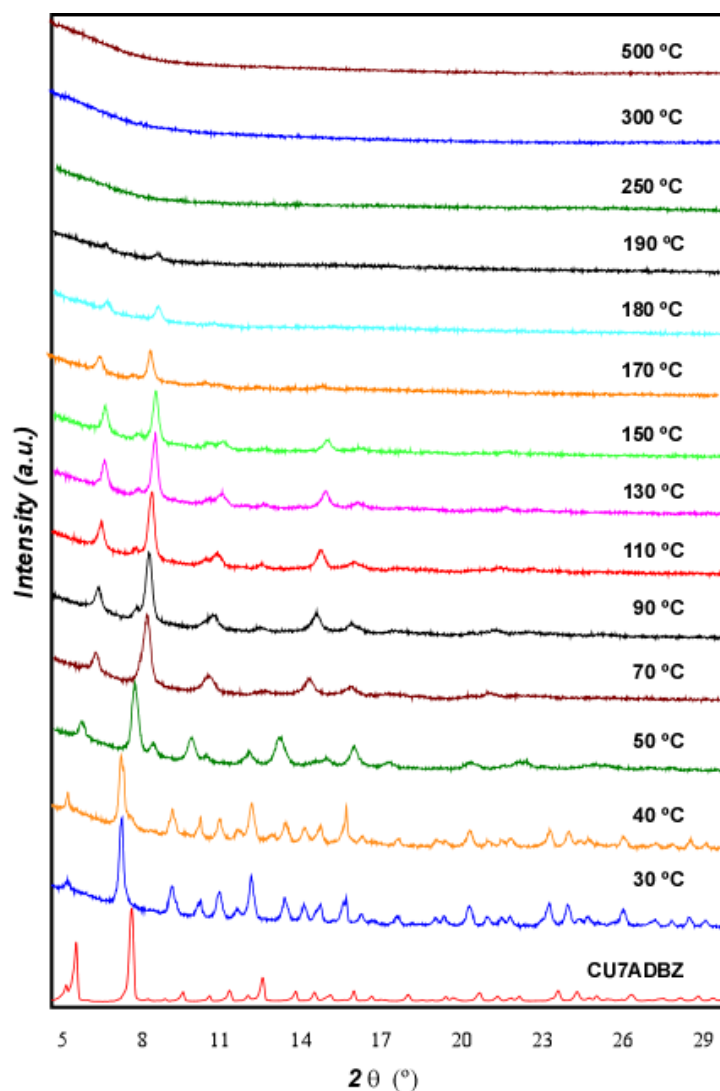


Figure 2.55. Variable-temperature X-ray diffraction patterns for CU7ADBZ.

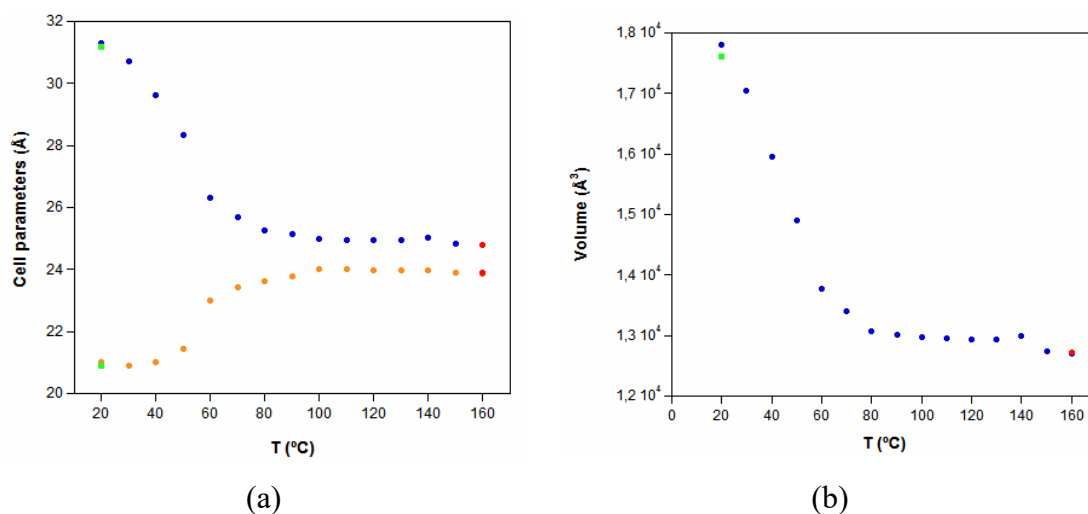


Figure 2.56. Variation of unit cell (a) parameters and (b) volume with the temperature for compound CU7ADBZ. (green dots represent the initial values of the cell parameters, blue the a cell parameters in a and the volume values in b and orange c cell parameter).

Table 2.27. Unit cell values obtained from the indexation of the variable-temperature X-ray powder diffraction patterns for CU7ADBZ.

Temperature (°C)	a (Å)	c (Å)	Volume (Å ³)
20	31.296	20.999	17812
30	30.698	20.890	17049
40	29.606	21.009	15948
50	28.335	21.440	14907
60	26.309	22.987	13779
70	25.685	23.449	13397
80	25.274	23.616	13064
90	25.134	23.798	13020
100	24.990	24.006	12984
110	24.946	24.026	12948
120	24.959	23.980	12937
130	24.952	23.991	12935
140	25.014	23.982	12996
150	24.817	23.902	12749
160	24.798	23.868	12711
Activated	24.782	23.904	12713
Rehydrated	31.189	20.899	17606

This unit cell shrinkage implies a 93% of the void volume present in the pristine sample (5098 Å³). The loss of coordination water molecules up to 160 °C only implies an additional decrease of 353 Å³. Accordingly to this sharp void volume reduction, this compound is not able to adsorb neither N₂ at 77 K nor CO₂ at 273 K. During the outgassing procedure (by vacuuming at 30 °C for 6 h) the colour of the sample changes from blue to deep dark green. It undergoes a weight loss mass of 21.0% which fits the expected value for the removal of both crystallization and coordination water molecules (20.6%). The X-ray diffraction pattern of this activated sample (Figure 2.57) is equal to that corresponding to the compound heated at 160 °C.

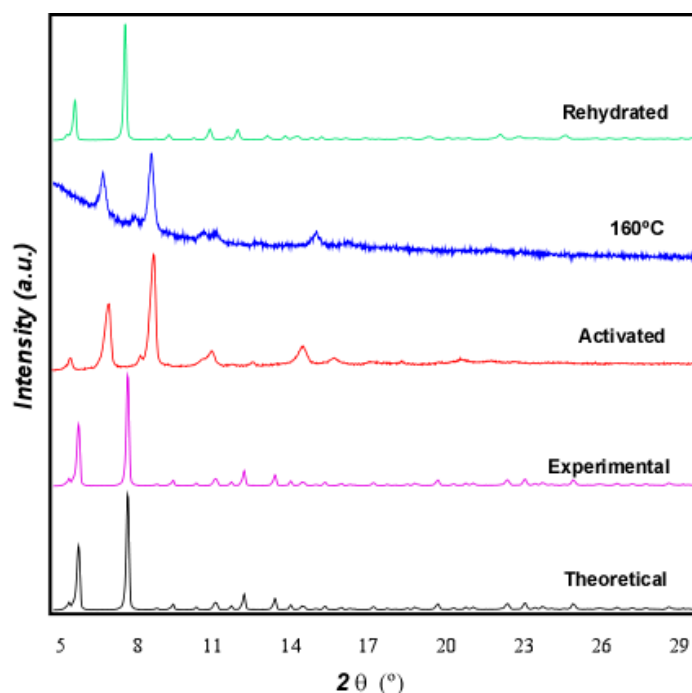


Figure 2.57. Powder X-ray diffraction patterns from samples of compound CU7ADBZ.

Employing the dianionic benzene-1,4-dicarboxylate (terephthalate) anion, compounds CU7ADTEP-1 and -2 were obtained. In the case of CU7ADTEP-1, as reported in the synthesis section, this compound corresponds to a more hydrated phase in comparison to CU7ADTEP-1, where the asymmetric unit consist in a half-centrosymmetric heptameric cation, half dicarboxylate anion and there are 24 crystallization water molecules inside the channels, Table 2.28. The presence of those water molecules leads to a volume of unit cell of 4142 \AA^3 (Figure 2.58a, Table 2.29).

Each heptameric cation is surrounded by four other ones, which interacts through offset face-to-face π - π stacking interactions established by four of their adeninato ligands (Figure 2.58a). The supramolecular architecture is completed by direct hydrogen bonding interactions between the amino N36 groups of the adeninato ligands of adjacent heptameric entities with a hydroxide group and the coordination water molecules with the nitrogen N31 atom of the six member ring of the adeninato, both nitrogen atoms as acceptor, $\text{O-H}\cdots\text{N}$, Figure 2.58b. The other two adeninato ligands interacts with the dicarboxylate dianions.

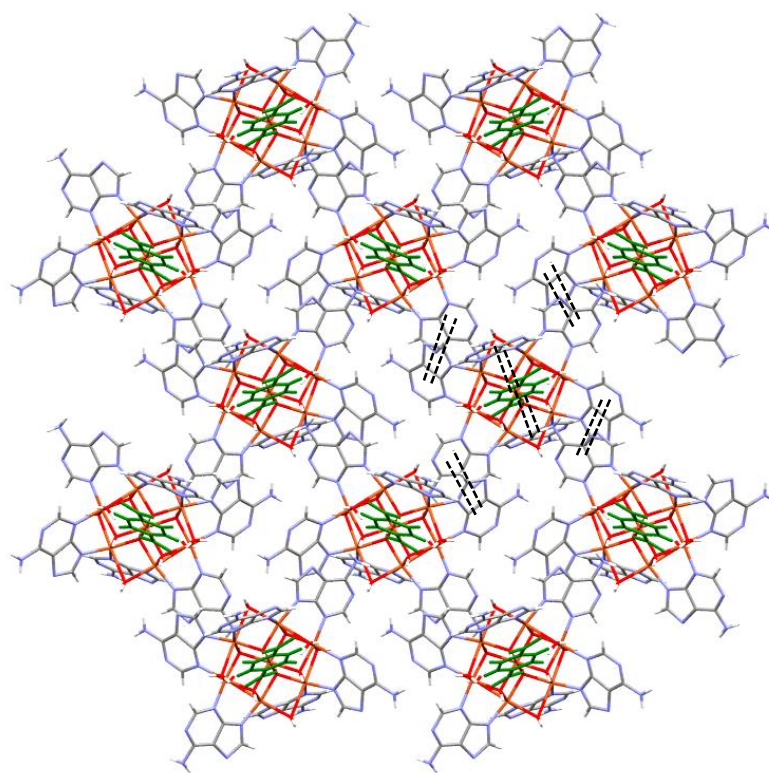
Table 2.28. Distances and angles (Å, deg) for compound CU7ADTEP-1.^a

Cu1–O1	2.061(10)	Cu1–O2	1.963(10)	Cu1–O3	2.141(9)
Cu2–O1	1.922(12)	Cu2–O2	1.960(8)	Cu2–N23	1.977(17)
Cu2–N19 ⁱ	2.045(17)	Cu2–O2w	2.499(11)	Cu2–O1w ⁱ	2.436(11)
Cu3–O1 ⁱ	1.989(9)	Cu3–O3	1.974(8)	Cu3–N13	1.993(15)
Cu3–N33	1.986(16)	Cu3–O1w	2.400(12)	Cu3–O3w	2.596(14)
Cu4–O2	2.025(9)	Cu4–O3	1.971(10)	Cu4–N29	2.010(2)
Cu4–N39	1.990(14)	Cu4–O2w	2.380(10)	Cu4–O3w	2.590(12)
Cu1⋯Cu2	3.082(2)	Cu1⋯Cu4	3.094(2)	Cu2⋯Cu3 ⁱ	3.065(3)
Cu1⋯Cu3	3.108(2)	Cu2⋯Cu4	3.122(3)	Cu3⋯Cu4	3.097 (3)
Cu1–O1–Cu2	101.3(5)	Cu1–O1–Cu3 ⁱ	100.2(4)	Cu2–O1–Cu3 ⁱ	103.2(5)
Cu1–O2–Cu2	103.6(4)	Cu1–O2–Cu4	101.8(4)	Cu2–O2–Cu4	103.2(4)
Cu1–O3–Cu3	98.0(4)	Cu1–O3–Cu4	97.5(4)	Cu3–O3–Cu4	103.5(5)
Cu2 ⁱ –O1w–Cu4	78.6(3)	Cu2–O2w–Cu4	79.5(3)	Cu3–O3w–Cu4	73.3(2)

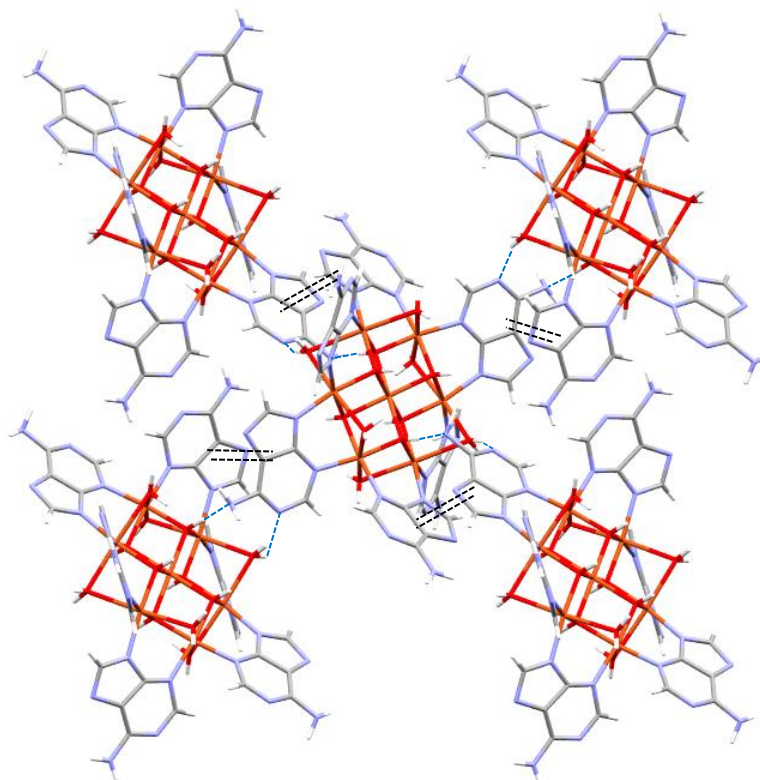
^a Symmetry: (i) 1 – x, – y, 1 – z.**Table 2.29.** Structural parameters (Å, deg) of hydrogen bonding interactions in CU7ADTEP-1.^a

Hydrogen-bonding interactions					
D–H⋯A ^b	H⋯A	D⋯A	D–H⋯A		
O1–H1⋯N36 ⁱ	1.87	2.85(2)	175		
O2–H2⋯O471	1.65	2.61(2)	164		
O3–H3⋯O4w	1.85	2.82(2)	174		
O1w–H11w⋯O9w ⁱⁱ	1.90	2.74(2)	165		
O1w–H12w⋯O472 ⁱⁱⁱ	1.93	2.77(2)	162		
N16A–H16A⋯O9w ^{iv}	1.97	2.81 (3)	171		
O2w–H21w⋯N31 ⁱ	1.98	2.80(2)	158		
O2w–H22w⋯O6w	1.96	2.84(2)	170		
N26B–H26C⋯O11w ^v	2.05	2.89(4)	165		
O3w–H32w⋯O471	2.20	3.02(2)	162		
N36–H36B⋯O4w ⁱⁱ	2.43	3.19(2)	137		
C32–H32⋯O9w ⁱⁱ	2.50	3.40(2)	163		
π – π interactions ^c					
ring–ring	packing	angle	DC	DZ	DXY
1pa⋯3pa ^{iv}	A⋯A	8.0	4.17	3.59	1.99
2pa⋯hd ^{vi}	A⋯T	4.0	4.1	3.67	1.82

^aSymmetry codes: (i) 1 – x, 1/2 + y, 1/2 – z; (ii) 1 – x, – 1/2 + y, 1/2 – z; (iii) 1 – x, – y, 1 – z; (iv) x, – 1/2 – y, 1/2 + z; (v) – 1 + x, 1/2 – y, – 1/2 + z, (vi) x, y, z. ^bD: donor; A: acceptor. ^cAngle: dihedral angle between the planes (deg), DC: distance between the centroids of the rings (Å), DZ: interplanar distance (Å), DXY: lateral displacement (Å), pa: adenine pentagonal ring, ha: adenine hexagonal ring, hd: anion hexagonal ring.



(a)



(b)

Fig. 2.58. (a) Layer of heptameric entities in the *bc*-plane of CU7ADTEP-1, (b) supramolecular interactions of the heptameric entity. Dashed lines represent the π - π interactions connecting the structural entities.

The ditopic charge distribution of the terephthalate anion allows its insertion between two adeninato ligands with an interplanar distance of 3.50 Å. Interestingly, the carboxylate groups do not lie just above the adenine aromatic rings but over the adenine chelating ring with the metal centers where the positive charge density is higher. The anchorage of the organic dianion is reinforced by hydrogen bonds involving its carboxylate oxygen atoms as acceptor and one hydroxide, a coordination water molecule and the exocyclic amino group of the adeninato ligands as donors, Figure 2.59.

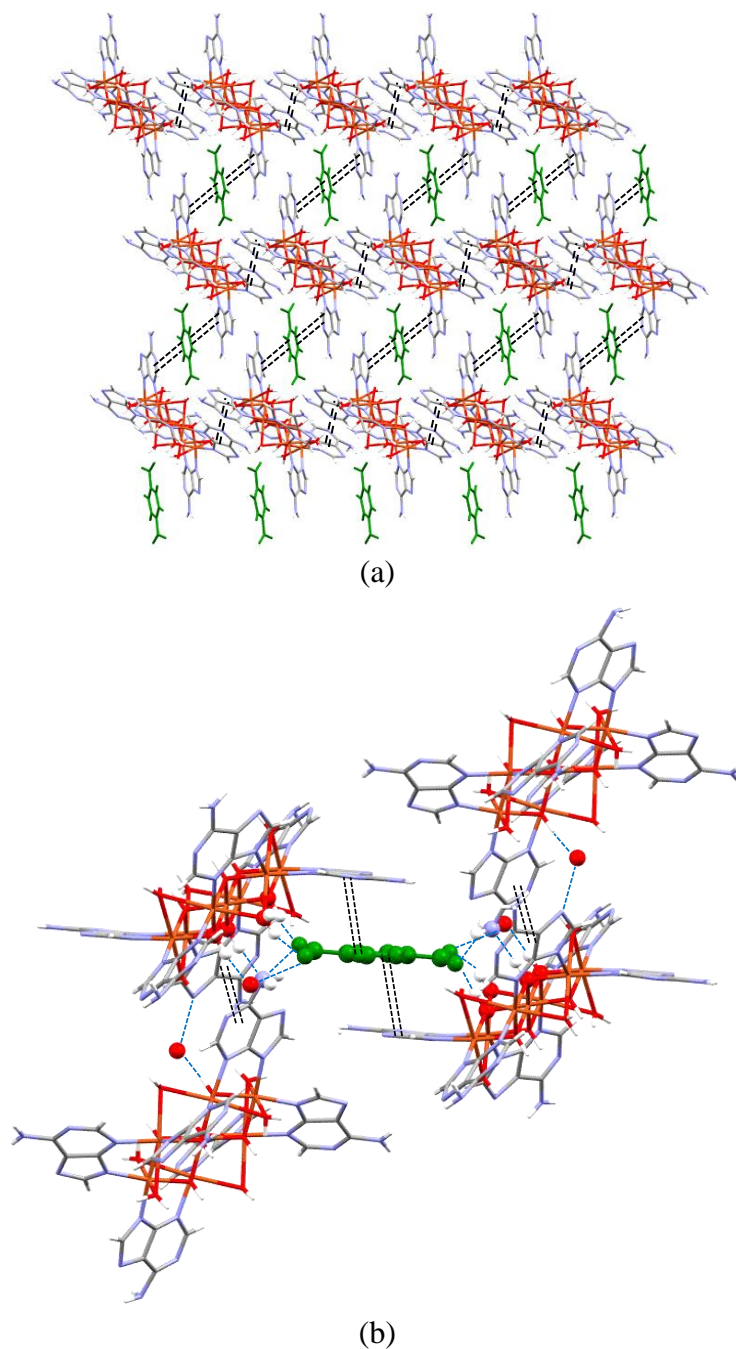


Figure 2.59. (a) View along the crystallographic *b*-axis (b) insertion of the dicarboxylate organic anion (green colour).

The resulting supramolecular architecture shows a two-dimensional system of voids channels with ovoid holes values of $7 \times 6 \text{ \AA}$ surrounded by the N-site of the adeninato ligands belonging to heptameric cations, as well as the corridors connecting them with an approximate radius of 3 \AA (Figure 2.60). The volume of these channels, occupied by the crystallization water molecules, is 1541 \AA^3 per unit cell (37% of the total volume as calculated by PLATON). A computational analysis shows an accessible surface area value of $1048 \text{ m}^2 \cdot \text{g}^{-1}$ and a pore volume of $0.290 \text{ cm}^3 \cdot \text{g}^{-1}$.

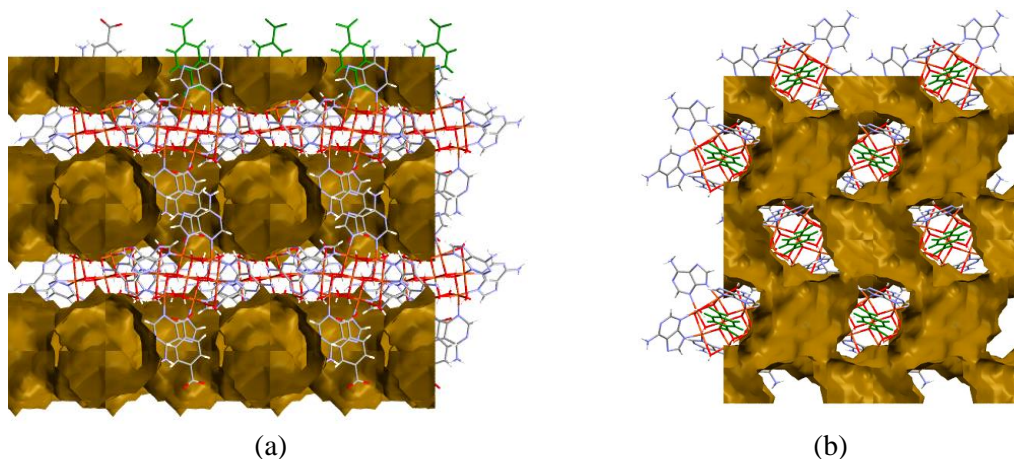


Figure 2.60. Views of contact surface of the 2D channels along the *c*-axis (a) and the *a*-axis (b).

The asymmetric unit of compound CU7ADTEP-2, at this stage of hydration, consists of two half-centrosymmetric crystallographic independent heptameric cations, one terephthalate dianion and twelve crystallization water molecules (Table 2.30, Figure 2.61).

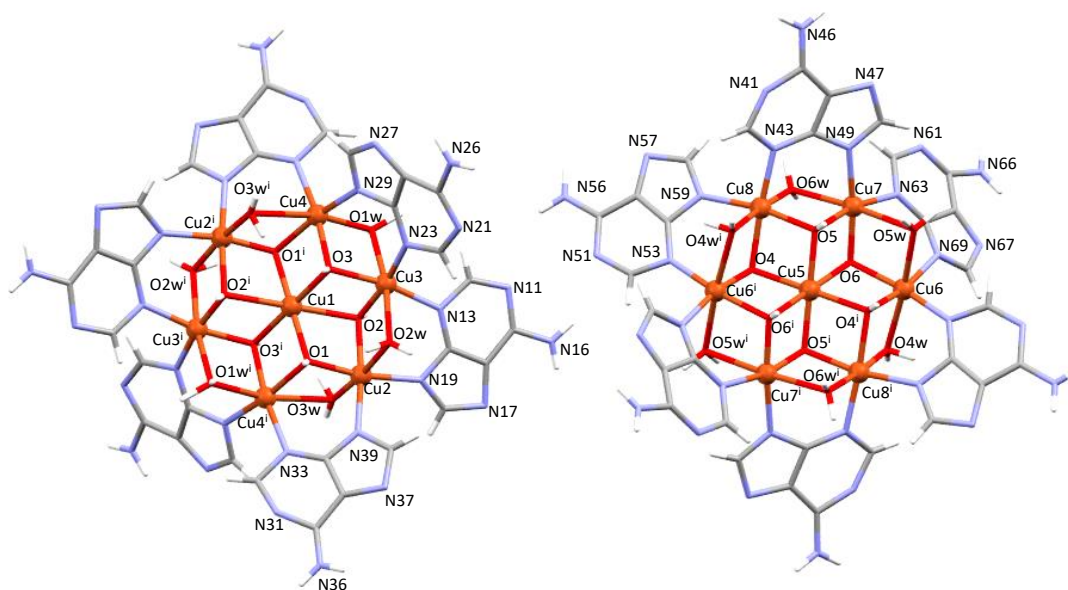


Figure 2.61. Scheme of the two crystallographically different heptameric entities present in compound CU7ADTEP-2 with the corresponding labelling scheme.

Table 2.30. Distances and angles (Å, deg) for compound CU7ADTEP-2.^a

Cu1–O1	1.98(3)	Cu1–O2	2.29(3)	Cu1–O3	2.10(3)
Cu2–O1	1.90(3)	Cu2–O2	1.98(3)	Cu2–N39	2.01(2)
Cu2–N19	1.99(2)	Cu2–O2w	2.54(3)	Cu2–O3w	2.34(4)
Cu3–O2	1.86(3)	Cu3–O3	2.01(3)	Cu3–N13	1.99(3)
Cu3–N23	1.87(3)	Cu3–O1w	2.34(3)	Cu3–O2w	2.53(3)
Cu4–O1 ⁱ	2.08(3)	Cu4–O3	2.00(3)	Cu4–N29	2.08(3)
Cu4–N33 ⁱ	2.09(16)	Cu4–O1w	2.21(3)	Cu4–O3w ⁱ	2.71(4)
Cu5–O4	2.05(2)	Cu5–O5	2.00(2)	Cu5–O6	2.24(3)
Cu6–N69	2.02(4)	Cu6–O4w	2.41(2)	Cu6–O5w	2.40(3)
Cu7–O5	2.04(2)	Cu7–O6	1.90(3)	Cu7–N49	2.03(2)
Cu7–N63	2.02(3)	Cu7–O5w	2.54(3)	Cu7–O6w	2.41(3)
Cu8–O4	2.08(2)	Cu8–O5	1.95(2)	Cu8–N43	2.00(3)
Cu8–N59	2.03(2)	Cu8–O6w	2.49(3)	Cu8–O4w ⁱⁱ	2.50(2)
Cu1···Cu2	3.141(5)	Cu1···Cu3	3.158(6)	Cu1···Cu4	3.049(7)
Cu2···Cu3	3.073(1)	Cu2···Cu4 ⁱ	3.165(1)	Cu3···Cu4	3.114 (7)
Cu5···Cu6	3.139(6)	Cu5···Cu7	3.160(7)	Cu5···Cu8	3.065(5)
Cu6···Cu7	3.114(7)	Cu6···Cu8 ⁱⁱ	3.150(9)	Cu7···Cu8	3.101 (9)
Cu1–O1–Cu2	108.0(13)	Cu1–O1–Cu4 ⁱ	97.4(11)	Cu2–O1–Cu4 ⁱ	105.3(15)
Cu1–O2–Cu2	94.5(11)	Cu1–O2–Cu3	98.9(14)	Cu2–O2–Cu3	106.4(13)
Cu1–O3–Cu3	100.6(14)	Cu1–O3–Cu4	96.3(11)	Cu3–O3–Cu4 ⁱ	77.4(10)
Cu3–O1w–Cu4	86.5(10)	Cu2–O2w–Cu3	74.5(8)	Cu2–O3w–Cu4	73.3(2)
Cu5–O4–Cu6 ⁱⁱ	102.3(10)	Cu5–O4–Cu8	95.8(10)	Cu8–O4–Cu6 ⁱⁱⁱ	101.8(10)
Cu5–O5–Cu7	102.9(9)	Cu5–O5–Cu8	101.8(10)	Cu7–O5–Cu8	101.9(8)
Cu5–O6–Cu6	94.1(10)	Cu5–O6–Cu7	99.2(14)	Cu6–O6–Cu7	104.3(13)
Cu6–O4w–Cu8 ⁱⁱ	79.8(7)	Cu6–O5w–Cu7	104.3(13)	Cu7–O6w–Cu8	78.5(8)

^aSymmetry: (i) 1 – x, 2 – y, 1 – z, (ii) – x, – y, – z.

Table 2.31 Structural parameters (Å, deg) of hydrogen bonding interactions in CU7ADTEP-2.^a

Hydrogen-bonding interactions					
D–H···A ^b		H···A	D···A	D–H···A	
N16–H16B···N31		2.47	3.25(6)	151	
N56–H56B···N21 ⁱ		2.70	3.53(5)	159	
C42–H42···N37 ⁱⁱ		2.58	3.32(4)	138	
C48–H48···N67 ⁱⁱⁱ		2.60	3.36(5)	139	
O5w–H51w···N66 ⁱⁱⁱ		2.09	2.85(5)	149	
O1–H1···O771 ^{iv}		1.94	2.90(3)	168	
O4–H4···O781		1.92	2.86(3)	161	
O1w–H12w···O772 ^v		1.80	2.71(4)	161	
O2w–H22w···O771 ^{iv}		2.55	3.43(4)	160	
N66–H66B···O782 ⁱ		2.12	2.96(4)	166	
π – π interactions ^c					
ring–ring	packing	angle	DC	DZ	DXY
1pa···4pa ^v	A···A	7.0	5.51	3.43	4.38
2pa···2pa ^{vi}	A···A	0.0	4.51	3.44	2.91
3pa···5pa ^v	A···A	4.0	4.08	3.53	1.82
3pa···ha ^{vii}	A···T	7.0	3.86	3.49	1.96
5pa···hd ^{viii}	A···T	3.0	3.73	3.52	1.37

^aSymmetry codes: (i) $x, -1 + y, z$; (ii) $-1 + x, -1 + y, z$; (iii) $-x, 1 - y, -z$; (iv) $x, 1 + y, z$; (v) $1 + x, 1 + y, z$; (vi) $-x, 1 - y, 1 - z$; (vii) $x, 1 + y, z$; (viii) x, y, z . ^bD: donor; A: acceptor. ^cAngle: dihedral angle between the planes (deg), DC: distance between the centroids of the rings (Å), DZ: interplanar distance (Å), DXY: lateral displacement (Å), pa: adenine pentagonal ring, ha: adenine hexagonal ring, hd: anion hexagonal ring.

The presence of only twelve crystallization additional water molecules leads to a significant unit cell volume decrease (from 4142 to 3495 Å³) and some relevant changes on the supramolecular interactions. The supramolecular assembly of the heptameric cations generates a new pattern of interactions, the clusters are closer and some of the interactions between these clusters that were previously impossible, due to the greater number of water molecules, are now possible.

The origin of the change comes from the competition on the hydrogen bonds of the adeninato ligands with the adjacent nucleobases or with the crystallization water molecules. This is not the first case in which the presence of water has disrupted the direct hydrogen bonding interactions between the nucleobases. For example, compounds of formula [Cu₂(μ -adenine)₄(Cl)₂]₂Cl₂·~2CH₃OH¹⁹¹ and [Cu₂(μ -adenine)₄(Cl)₂]₂Cl₂·6H₂O¹⁹⁷ greatly differ in their crystal structure (porous and non-porous, respectively) just due to the presence or not of water solvent molecules.

¹⁹⁷ De Meester, P.; Skapski, A. C. *Inorg. Phys. Theor.* **1970**, A13, 2167–2169.

Each heptameric cation is surrounded by four other ones which interacts through offset face-to-face π - π stacking interactions established by four of their adeninato ligands (Figure 2.62). The supramolecular architecture is completed by direct hydrogen bonding interactions between the amino N66 groups of the adeninato ligands of adjacent heptameric entities with a coordination water molecules that act as donor, O-H \cdots N. The other two adeninato ligands interacts with crystallization water molecules.

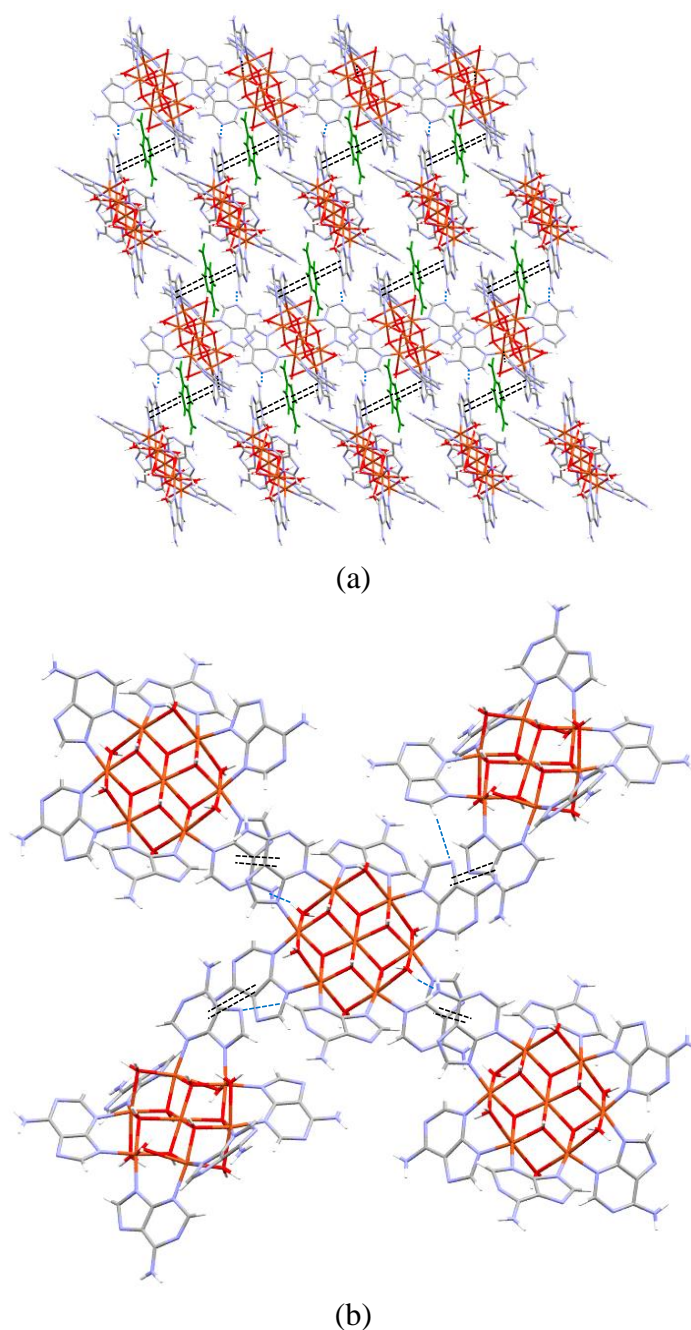


Figure 2.62. (a) Crystal packing of compound CU7ADTEP-2 along the crystallographic *b*-axis and (b) supramolecular interactions between the heptameric entities (hydrogen bond: dotted lines; π - π interaction: double dashed lines).

The dicarboxylate anion is inserted as in compound CU7ADTEP-1, but some of the hydrogen bonding interactions are modified. The anchorage of the organic dianion is reinforced by hydrogen bonds involving its carboxylate oxygen atoms as acceptor and one hydroxide, a coordination water molecule and only in one of them, with the exocyclic amino group of the adeninato ligands as donors, $N-H\cdots O$, Figure 2.63.

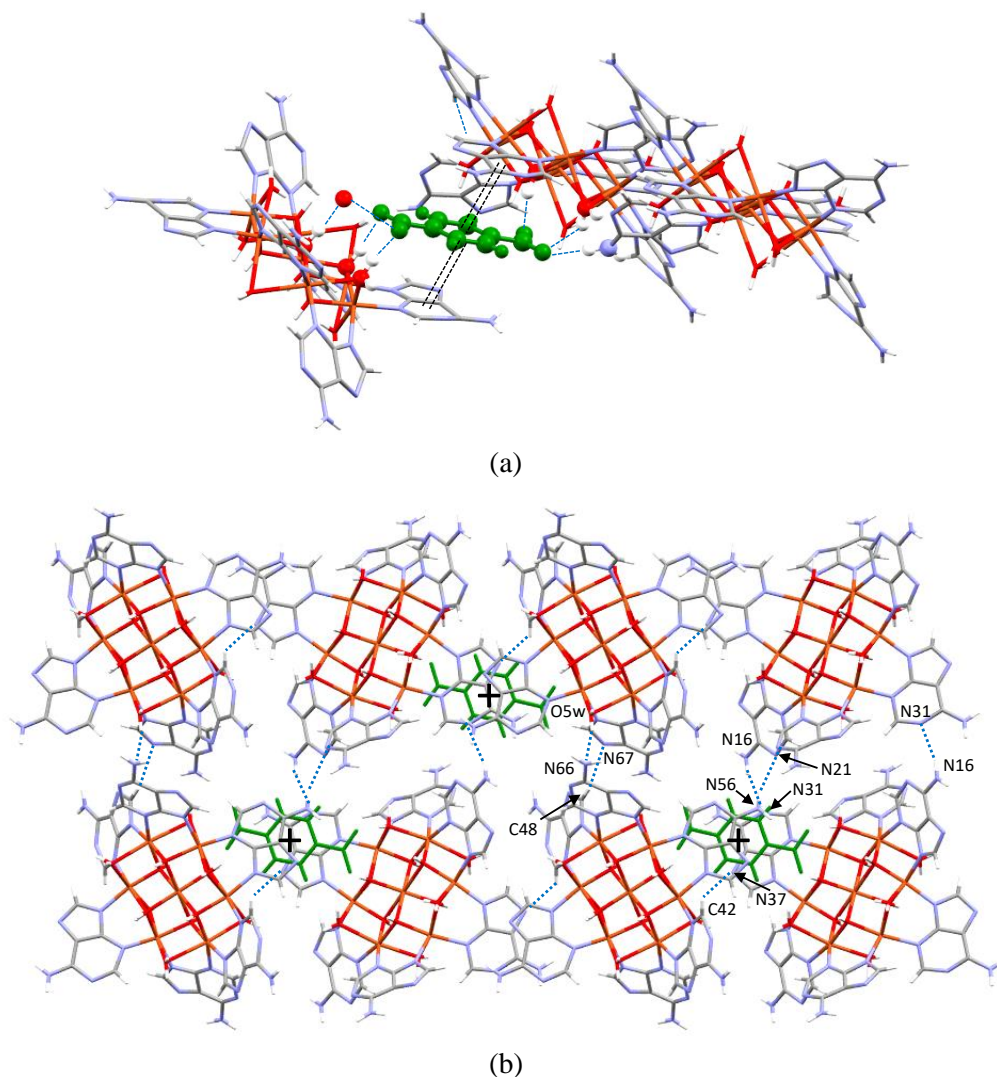


Figure 2.63. (a) Insertion of the dicarboxylate organic anion (green colour) and (b) supramolecular interactions connecting the structural entities (π - π interaction: + symbol).

At low water content, the nucleobases involved in the π - π stacking interaction with the terephthalate anion are tilted in such a way that they are able to establish direct hydrogen bonds, involving Watson-Crick face, with adjacent adenines (Figure 2.64).

However, at a higher content of water, these interactions break up and the adenines align linearly (they become being related by a symmetry center) to expose the Watson-Crick faces to the water molecules located inside the channels. This subtle modification

of the dominating hydrogen bonding interactions is also responsible of the observed crystal system change (from monoclinic to triclinic) and a longer distance between the centroids of the two heptameric units related by these π - π interactions (14.6 Å vs 12.8 Å).

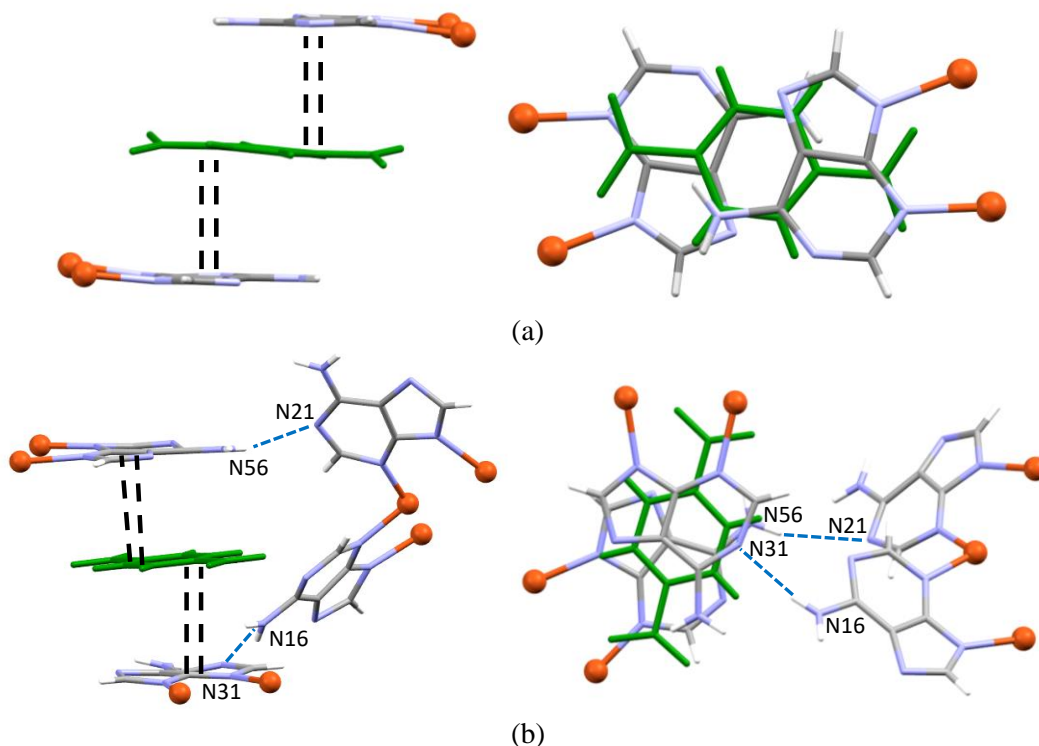


Figure 2.64. Arrangement of the terephthalate anion between the adeninato ligands in (a) CU7ADTEP-1 and (b) CU7ADTEP-2. Dotted lines indicate hydrogen bonds and double dashed lines represent π - π interactions.

To sum up, the cationic nature of the discrete heptameric entity imposes a net positive density on the coordinated adeninato ligands (in spite of their formal anionic nature). This fact favours their interactions with the negative charge density of the organic anion, mainly located on the carboxylate groups. Therefore, depending on the presence of two carboxylate groups (terephthalate) or one (benzoate) the organic anion would be able to be sandwiched between π - π stacking adenines or not (Figure 2.51). Accordingly, the ligand with just one carboxylate would imply such an approach of the heptameric entities that this option is sterically hindered. As a consequence, the benzoate anions are displaced into the channels reducing the accessible volume. On the contrary, the two carboxylate groups located at opposite sites in the terephthalate anion do not present this steric hindrance and allow a sandwich arrangement of the terephthalate anion between the interacting π - π stacking adenines. This arrangement provides a more open porous

supramolecular structure than that obtained using the benzoate anion, but both of them share the fact that their supramolecular crystal structures are flexible.

The comparison between the porosity and the size of the holes generated in the structure of these three compounds can be seen in Figure 2.65. The difference between the two structures containing the terephthalate anion is due to the difference in the supramolecular interactions and leads to a different distribution of pores.

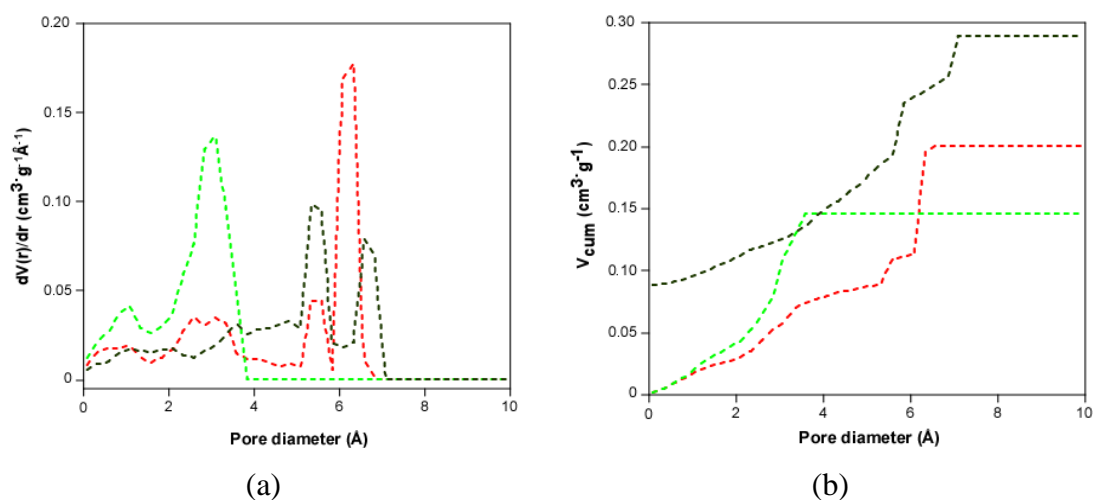


Figure 2.65. (a) Derivative representation of the geometric pore volume and (b) cumulative representation of the geometric pore volume of compound CU7ADBZ (red), CU7ADTEP-1 (dark green) and CU7ADTEP-2 (light green).

As is above commented, the resulting supramolecular architecture shows the same two-dimensional network described for CU7ADTEP-1 but the oval holes are smaller, giving a 2D dimensional voids. The radii of the voids have a main value of 3.1 \AA and they are surrounded by the site of the adeninato ligands belonging to heptameric cations and connected by corridors with an approximate radius of 2.5 \AA (Figure 2.66). The volume of these channels, occupied by the crystallization water molecules, is 783 \AA^3 ($0.145 \text{ cm}^3 \cdot \text{g}^{-1}$) per unit cell (22% of the total volume as calculated by PLATON).

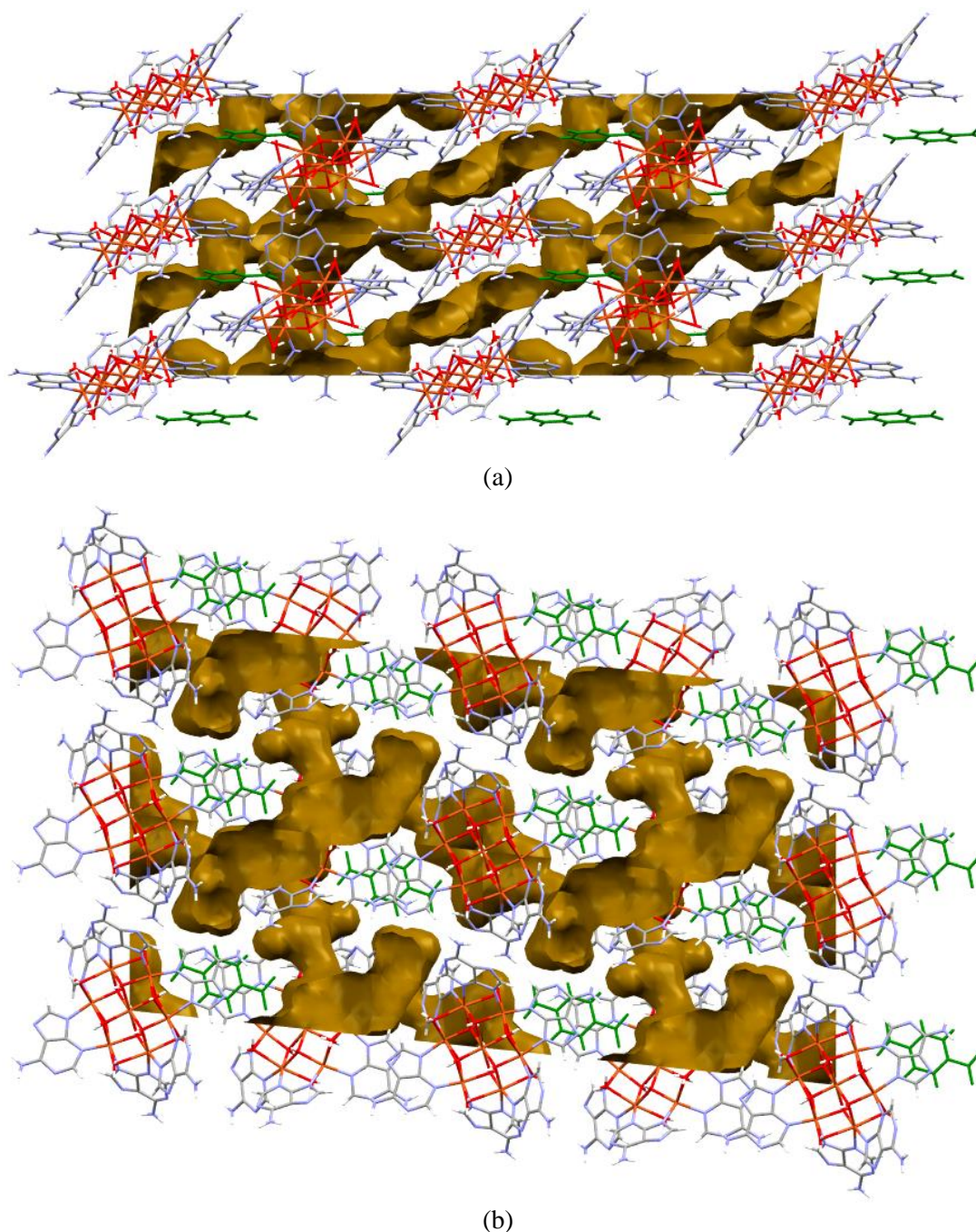


Fig. 2.66. Views of contact surface of the 2D network of channels in CU7ADTEP-2 along (a) the *b*-axis and (b) the *a*-axis.

The thermoanalytical (Figure 2.14f and 2.15a and Table 2.7 and 2.8) and variable-temperature X-ray diffraction data of terephthalate containing compounds show that the release of the crystallization water molecules implies a substantial decrease of crystallinity, as revealed by the widening of the diffraction maxima, which is even more notorious with the loss of coordination water molecules (Figure 2.67).

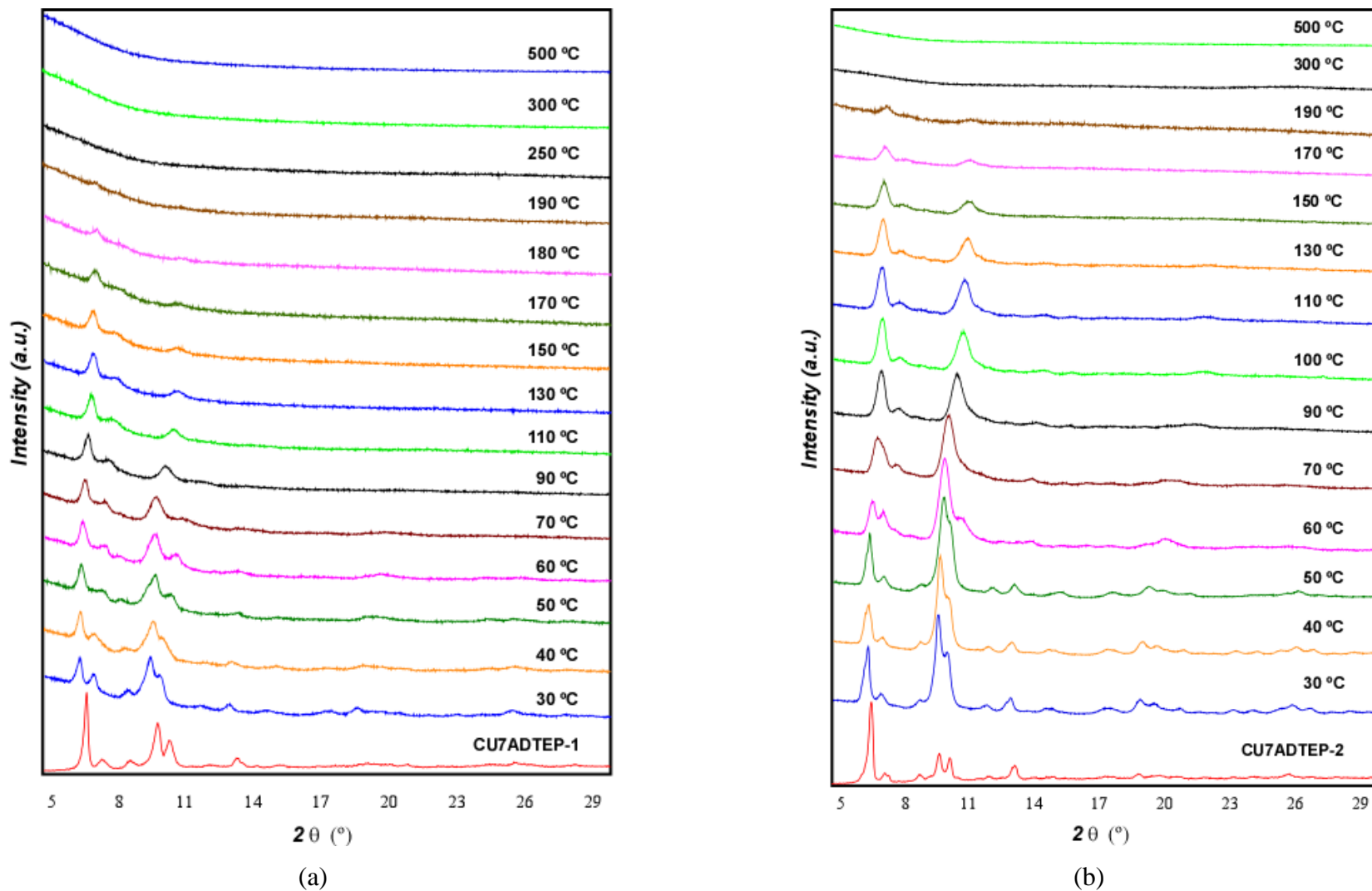


Figure 2.67. Variable-temperature X-ray diffraction patterns for (a) CU7ADTEP-1 (the fully hydrated terephthalate compound) and (b) -2.

Crystal structure of CU7ADFA-1 and CU7ADFA-2 consists of two half-centrosymmetric crystallographic different heptameric cations, one fumarate dianion and different amount of crystallization water molecules with 25 and 18, respectively, Figure 2.68 and Table 2.32 and 2.33.

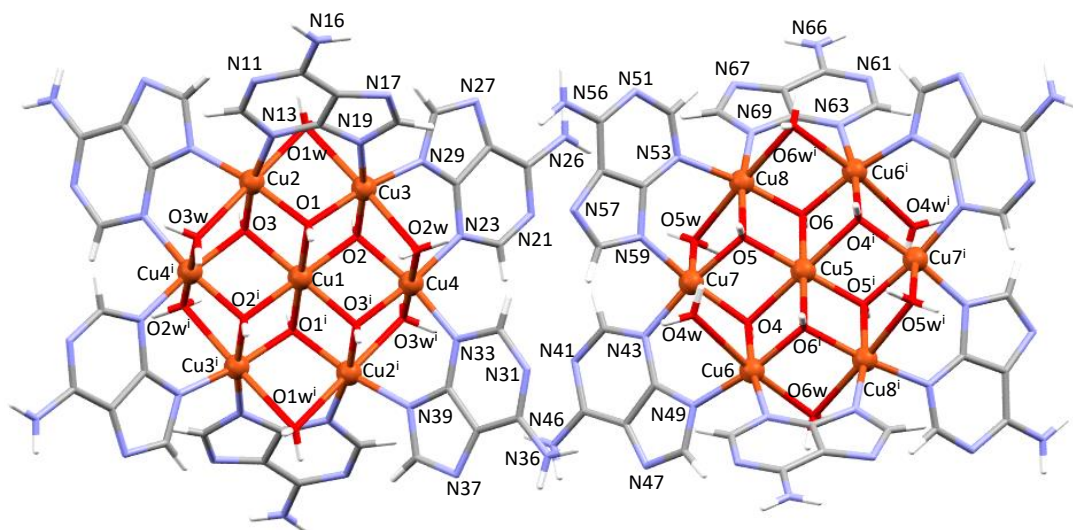


Figure 2.68. Scheme of the two crystallographically independent heptameric cluster of compound CU7ADFA-2 with the atom labelling scheme.

The different water solvent molecule content in the polymorph compounds CU7ADFA-1/2 has a crucial paper in their crystal building. Due to the great amount of water molecules in CU7ADFA-1 there are not direct π - π stacking interactions between adjacent heptameric entities, which generates the observed non-stability of these crystals when they are removed from the mother liquor, Figure 2.69a/b. The crystal structure of CU7ADFA-1 is maintained by a sandwich π - π stacking interaction, where the dicarboxylate anion is inserted parallel to the cationic sheets and sited between two adeninato ligands holding together the supramolecular heptameric entities. These interactions are extended by a F...A...A...F...A...A...F scheme along the crystallographic *c*-axis, Figure 2.69c/d. These chains are reinforced with the interactions established by each carboxylate group of the organic anion, which are attached to the nearest cationic layer by two $O_{\text{anion}} \cdots H-O_{\text{cation}}$ hydrogen bonds, one with a hydroxide group and the other one with a water molecule coordinated to the same copper atom, to form a supramolecular $R_2^2(8)$ synthon (Figure 2.71a/b, Table 2.34).

The adeninato ligands that do not take part in the previous interaction present hydrogen bond interactions with another two adjacent heptamers: N66-H66B...N56 and N56-H56B...N31.

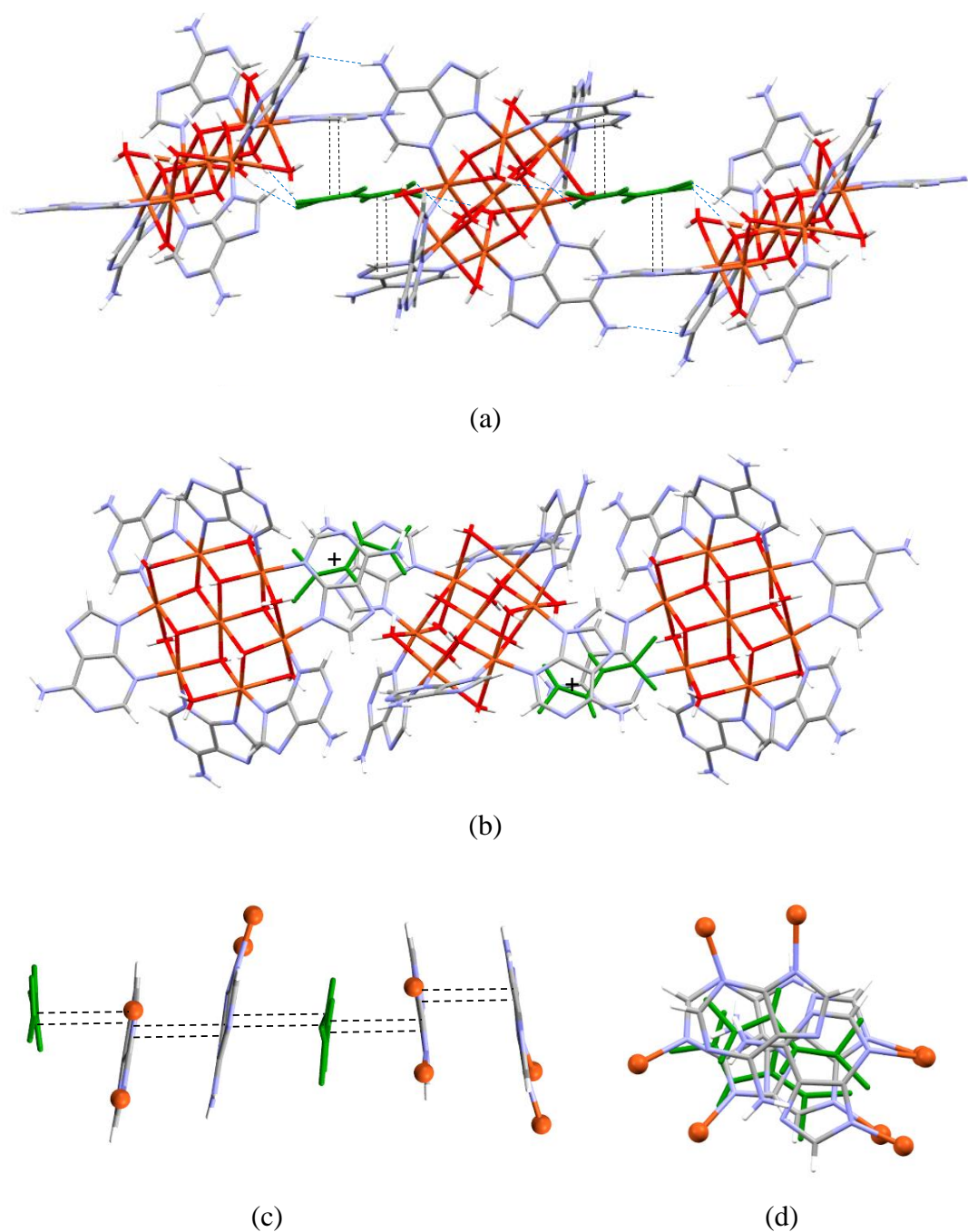


Figure 2.69. (a) and (b) Crystal packing of compound CU7ADFA-1 (double dashed lines: π - π stacking, and blue dashed line: H-bonding interactions), (c) and (d) Supramolecular interactions of the dicarboxylate anion.

When the crystals are removed from the liquid where they crystallize a partial dehydration takes place, and the CU7ADFA-2 compound is obtained. The heptameric clusters approach each other in such a way that they are able to establish π - π interactions through offset face-to-face π - π stacks between adeninato ligands, already seen in previous cases such as CU7ADTEP-1/2 (Figure 2.70). Each unit is connected to the adjacent ones by a double π - π stacking interaction between adeninato ligands, Table

2.35. These stacking interactions are reinforced by a hydrogen-bond ring formed by a double N–H···N interaction between the pyrimidinic exocyclic N66 nitrogen atoms of the previously no interacting adeninato ligand and the N17 of an adjacent adeninato as acceptor.

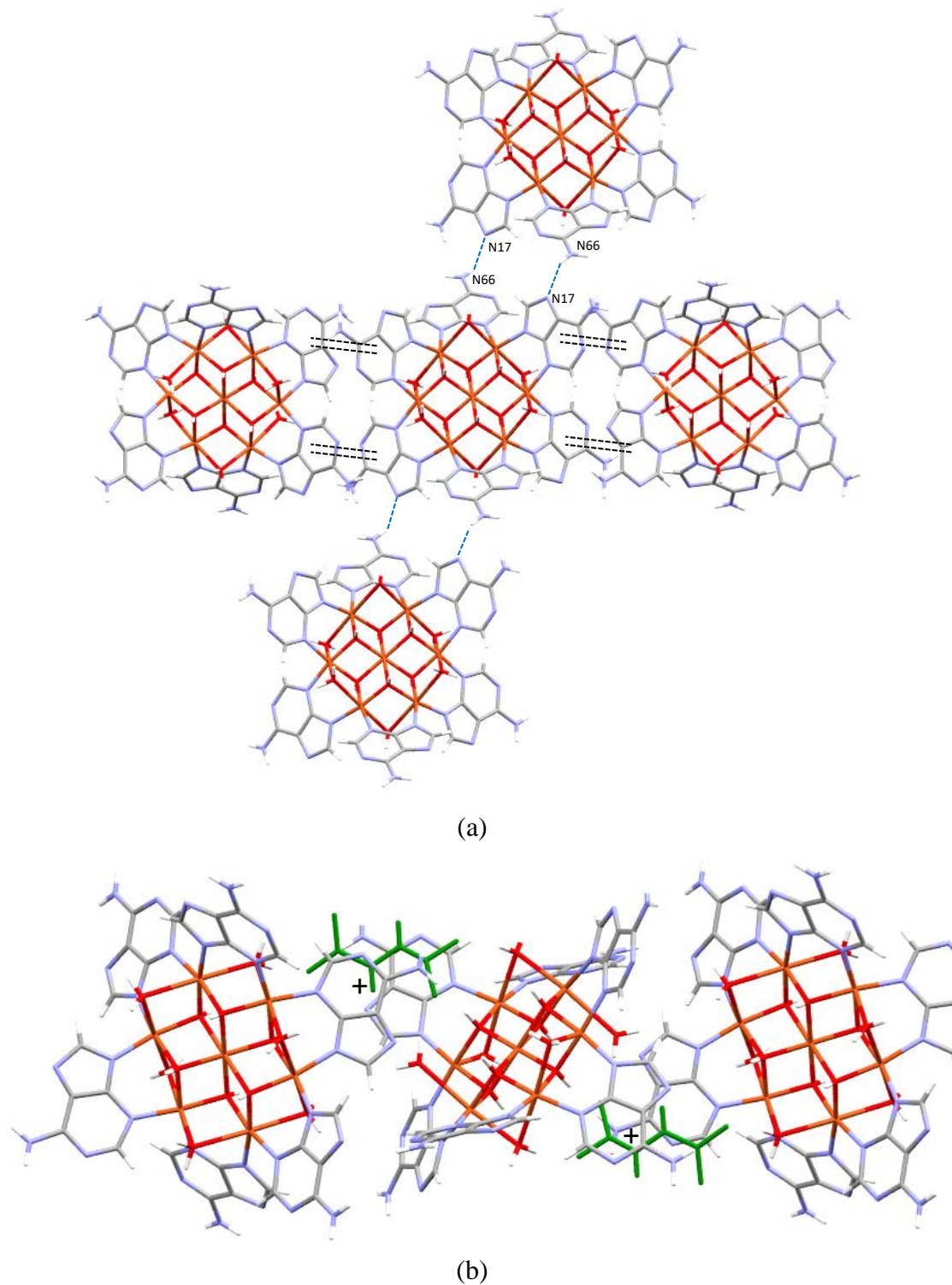


Figure 2.70. Crystal packing fragments of compound CU7ADFA-2 (double dashed lines: π - π stacking, and blue dashed line: hydrogen-bonding interactions).

Table 2.32. Distances and angles (Å, deg) for compound CU7ADFA-1.^a

Cu1–O1	2.030(12)	Cu1–O2	2.051(11)	Cu1–O3	2.211(10)
Cu2–O1	1.983(10)	Cu2–O3	1.933(11)	Cu2–N19	1.955(17)
Cu2–N33	2.032(14)	Cu2–O1w	2.442(11)	Cu2–O3w	2.577(14)
Cu3–O1	1.974(11)	Cu3–O2	1.974(12)	Cu3–N13	1.959(17)
Cu3–N23	1.959(17)	Cu3–O1w	2.412(11)	Cu3–O2w	2.486(11)
Cu4–O2	1.971(11)	Cu4–O3 ⁱ	1.949(11)	Cu4–N29	2.000(2)
Cu4–N39 ⁱ	2.010(18)	Cu4–O2w	2.429(12)	Cu4–O3w ⁱ	2.588(15)
Cu5–O4	1.954(11)	Cu5–O5	2.200(10)	Cu5–O6	2.061(12)
Cu6–O4	1.994(13)	Cu6–O6	1.947(12)	Cu6–O4w	2.372(10)
Cu6–N49	1.962(19)	Cu6–O6w ⁱⁱ	2.587(12)	Cu6–N63 ⁱⁱ	2.001(17)
Cu7–O4	1.990(10)	Cu7–O5	1.930(12)	Cu7–N43	1.990(2)
Cu7–N59	1.943(16)	Cu7–O4w	2.457(16)	Cu7–O5w	2.852(18)
Cu8–O5	1.929(13)	Cu8–O6 ⁱⁱ	1.980(11)	Cu8–N53	1.978(16)
Cu8–N69	2.030(2)	Cu8–O5w	2.604(15)	Cu8–O6w	2.445(13)
Cu1…Cu2	3.131(3)	Cu1…Cu3	3.056(3)	Cu1…Cu4	3.154(3)
Cu2…Cu3	3.121(4)	Cu2…Cu4 ⁱ	3.098(4)	Cu3…Cu4	3.123(4)
Cu5…Cu6	3.056(3)	Cu5…Cu7	3.139(3)	Cu5…Cu8	3.158(3)
Cu6…Cu7	3.145(4)	Cu6…Cu8 ⁱⁱ	3.129(4)	Cu7…Cu8	3.082(4)
Cu1–O1–Cu2	102.6(5)	Cu1–O1–Cu3	99.5(4)	Cu2–O1–Cu3	104.2(5)
Cu1–O2–Cu3	98.8(5)	Cu1–O2–Cu4	103.3(5)	Cu3–O2–Cu4	104.7(5)
Cu1–O3–Cu2	97.9(4)	Cu1–O3–Cu4 ⁱ	98.4(4)	Cu2–O3–Cu4 ⁱ	105.9(4)
Cu2–O1w–Cu3	80.1(3)	Cu3–O2w–Cu4	78.9(3)	Cu2–O3w–Cu4 ⁱ	73.7(3)
Cu5–O4–Cu6	101.4(5)	Cu5–O4–Cu7	105.5(5)	Cu6–O4–Cu7	104.3(5)
Cu5–O5–Cu7	98.7(5)	Cu5–O5–Cu8	99.6(5)	Cu7–O5–Cu8	106.0(5)
Cu5–O6–Cu6	99.3(5)	Cu5–O6–Cu8 ⁱⁱ	102.8(5)	Cu6–O6–Cu8 ⁱⁱ	105.6(5)
Cu6–O4w–Cu7	81.3(4)	Cu7–O5w–Cu8	72.9(4)	Cu8–O6w–Cu6 ⁱⁱ	76.8(4)

^a Symmetry: (i) 2 – x, – y, 2 – z, (ii) 3/2 – x, 1/2 – y, 1 – z.

Table 2.33. Distances and angles (Å, deg) for compound CU7ADFA-2.^a

Cu1–O1	2.251(9)	Cu1–O2	1.978(9)	Cu1–O3	2.010(9)
Cu2–O1	1.976(9)	Cu2–O3	2.028(9)	Cu2–13	2.018(13)
Cu2–N39 ⁱ	1.984(15)	Cu2–O1w	2.549(10)	Cu2–O3w	2.470(10)
Cu3–O1	1.966(10)	Cu3–O2	1.999(9)	Cu3–N19	1.958(13)
Cu3–N29	1.952(13)	Cu3–O1w	2.568(10)	Cu3–O2w	2.450(10)
Cu4–O2	1.966(9)	Cu4–O3 ⁱ	1.944(10)	Cu4–N23	1.961(13)
Cu4–N33	2.007(16)	Cu4–O2w	2.454(10)	Cu4–O3w ⁱ	2.483(10)
Cu5–O4	2.171(10)	Cu5–O5	1.929(8)	Cu5–O6	2.116(8)
Cu6–O4	1.972(9)	Cu6–O4w	2.750(11)	Cu6–O6w	2.427(11)
Cu6–N49	1.961(12)	Cu6–O6 ⁱⁱ	1.953(10)	Cu6–N63 ⁱⁱ	1.997(10)
Cu7–O4	1.941(9)	Cu7–O5	1.987(9)	Cu7–N43	1.999(12)
Cu7–N59	1.935(12)	Cu7–O4w	2.862(12)	Cu7–O5w	2.359(9)
Cu8–O5	1.995(7)	Cu8–O6	1.949(9)	Cu8–N53	2.028(12)
Cu8–N69	1.957(12)	Cu8–O5w	2.483(10)	Cu8–O6w ⁱⁱ	2.474(12)
Cu1…Cu2	3.182(2)	Cu1…Cu3	3.135(2)	Cu1…Cu4	3.023(2)
Cu2…Cu3	3.071(3)	Cu2…Cu4 ⁱ	3.134(3)	Cu3…Cu4	3.136(3)
Cu5…Cu6	3.161(2)	Cu5…Cu7	3.077(2)	Cu5…Cu8	3.073(2)
Cu6…Cu7	3.109(2)	Cu6…Cu8 ⁱⁱ	3.086(3)	Cu7…Cu8	3.120(2)
Cu1–O1–Cu2	97.5(4)	Cu1–O1–Cu3	95.8(4)	Cu2–O1–Cu3	102.4(4)
Cu1–O2–Cu3	104.1(4)	Cu1–O2–Cu4	100.1(3)	Cu3–O2–Cu4	104.6(4)
Cu1–O3–Cu2	104.0(4)	Cu1–O3–Cu4 ⁱ	99.7(4)	Cu2–O3–Cu4 ⁱ	104.2(4)
Cu2–O1w–Cu3	73.8(2)	Cu3–O2w–Cu4	79.5(3)	Cu2–O3w–Cu4 ⁱ	78.5(3)
Cu5–O4–Cu6	99.4(4)	Cu5–O4–Cu7	96.7(4)	Cu5–O5–Cu7	103.6(3)
Cu5–O5–Cu8	103.1(4)	Cu5–O6–Cu6 ⁱⁱ	101.9(4)	Cu6–O4–Cu7	105.3(4)
Cu7–O5–Cu8	103.2(4)	Cu5–O6–Cu8	98.2(4)	Cu8–O6–Cu6 ⁱⁱ	104.5(3)
Cu6–O4w–Cu7	67.3(3)	Cu7–O5w–Cu8	80.2(3)	Cu6–O6w–Cu8 ⁱⁱ	78.1(3)

^a Symmetry: (i) $-x, -y, 1-z$, (ii) $1/2-x, 1/2-y, 1-z$.

In compound CU7ADFA-2, the dicarboxylate anions are inserted in the same way that in CU7ADFA-1 by a π -stacking interaction A…A…F…A…A scheme along the crystallographic c -axis, Figure 2.69c. However, the reinforcing hydrogen-bonding interactions differ. One carboxylate group of the organic anion is attached to the nearest cationic layer by two O_{anion}…H–O_{cation} hydrogen bonds, one with a hydroxide group and the other one with a water molecule coordinated to the same copper atom, to form a

supramolecular $R_2^2(8)$ synthon as in CU7ADFA-1, but the other one is attached to another cluster by a coordination water molecule and to a crystallization one located in the void (Figure 2.71 c/d). The labelling scheme for the fumarate anions in compounds CU7ADFA-1 and -2 is depicted in Figure 2.72.

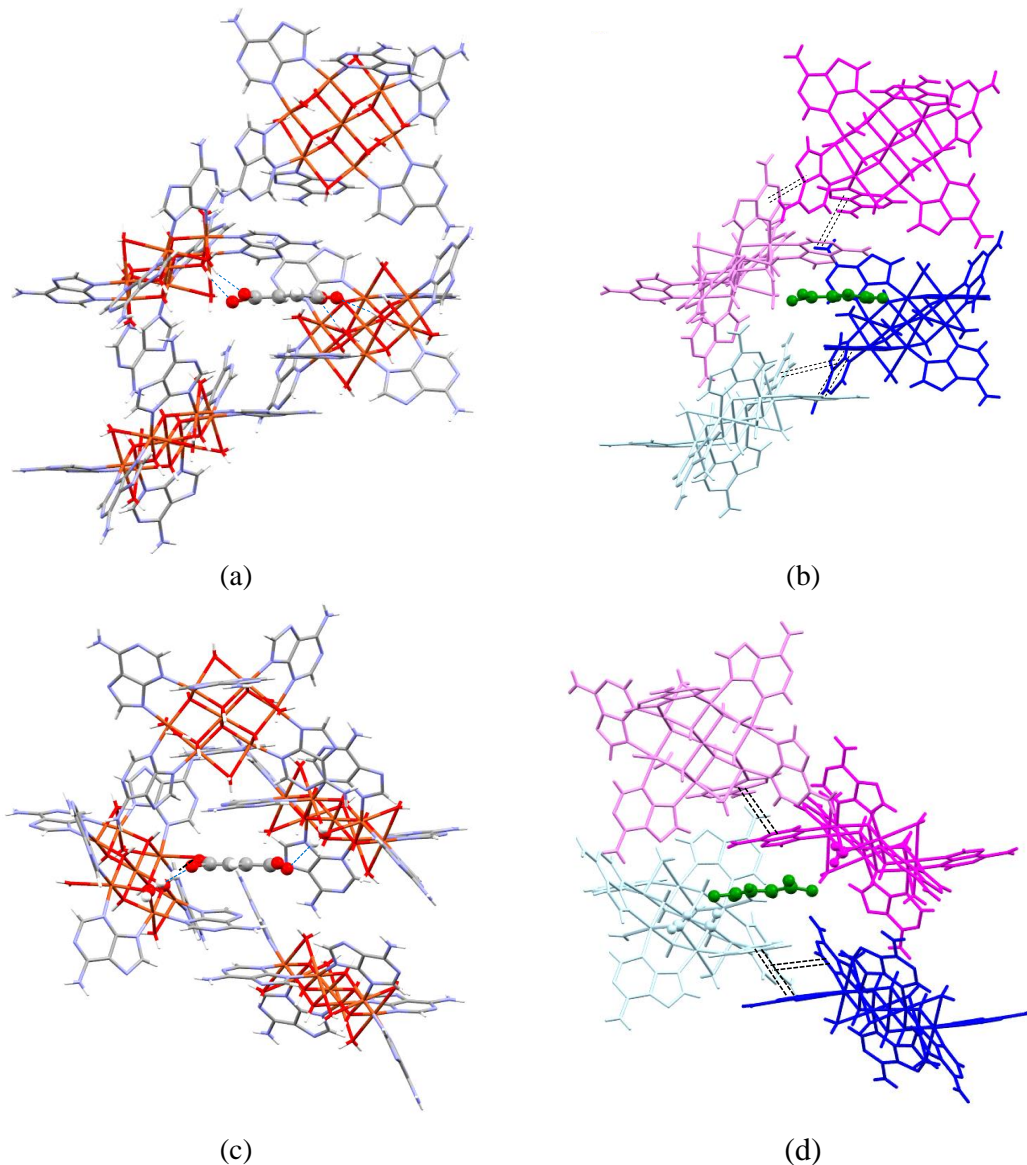


Figure 2.71. Supramolecular interactions of the dicarboxylate anion in (a) and (b) CU7ADFA-1, and (c) and (d) in CU7ADFA-2. Heptameric cluster that interacts between them are coloured with the same colour and different shades to clarify the fumarate packing.



Figure 2.72. Labels of the fumarate anions in compounds: (a) CU7ADFA-1/2, (b) CU7ADF-1/2.

Table 2.34. Structural parameters (Å, deg) of supramolecular interactions in CU7ADFA-1.^a

Hydrogen-bonding interactions					
D-H...A ^b	H...A	D...A	D-H...A		
O1-H1...O78 ⁱ	1.88	2.85(2)	171		
O4-H4...O76 ⁱⁱ	1.80	2.64(2)	168		
O2w-H21w...O79 ⁱ	2.03	2.90(3)	164		
O5w-H51w...O77 ⁱⁱ	2.23	3.03(4)	168		
O6w-H62w...O76 ⁱ	1.99	2.83(2)	162		
N56-H16B...N31 ⁱⁱ	2.40	3.18(3)	151		

π - π interactions ^c					
ring-ring	packing	angle	DC	DZ	DXY
1pa...4pa ⁱⁱⁱ	A...A	1.0	5.08	3.41	3.79
2pa...6pa ^{iv}	A...A	8.0	5.73	3.04	4.42

^aSymmetry codes: (i) $3/2 - x, 1/2 - y, 1 - z$; (ii) x, y, z , (iii) $3/2 - x, -1/2 + y, 3/2 - z$; (iv) $x, -y, -1/2 + z$. ^bD: donor; A: acceptor. ^cAngle: dihedral angle between the planes (deg), DC: distance between the centroids of the rings (Å), DZ: interplanar distance (Å), DX Y: lateral displacement (Å), pa: adenine pentagonal ring, ha: adenine hexagonal ring.

Table 2.35. Structural parameters (Å, deg) of supramolecular interactions in CU7ADFA-2.^a

Hydrogen-bonding interactions					
D-H...A ^b	H...A	D...A	D-H...A		
O5-H5...O78	1.69	2.67(2)	164		
O3w-H31w...O76 ⁱ	2.20	3.02(2)	171		
O4w-H31w...O78	1.96	2.77(2)	163		
O6w-H62w...O79 ⁱⁱ	2.05	2.87(2)	165		
N16-H16B...N37 ⁱⁱⁱ	2.22	3.01(2)	149		
N66-H66A...N17 ^{iv}	2.34	3.17(2)	156		

π - π interactions ^c					
ring-ring	packing	angle	DC	DZ	DXY
2pa...5pa ^v	A...A	3.0	4.76	3.28	3.39
3pa...4pa ^v	A...A	7.0	5.99	3.23	4.68

^aSymmetry codes: (i) $-x, y, 1/2 - z$; (ii) $1/2 - x, 1/2 - y, 1 - z$; (iii) $x, -1 + y, z$; (iv) $1/2 - x, 1/2 + y, 3/2 - z$; (v) x, y, z . ^bD: donor; A: acceptor. ^cAngle: dihedral angle between the planes (deg), DC: distance between the centroids of the rings (Å), DZ: interplanar distance (Å), DX Y: lateral displacement (Å), pa: adenine pentagonal ring, ha: adenine hexagonal ring.

The thermoanalytical (Figure 2.15b and Table 2.8) and variable-temperature X-ray diffraction data of fumaric containing compound show that the release of the crystallization water molecules not means a substantial decrease of crystallinity, maintaining the crystallinity of the structure even after losing the coordination water molecules around 200 °C (Figure 2.73).

The resulting supramolecular architecture in CU7ADFA-1/2 shows a two-dimensional voids with ovoid holes values of 3.6×5.3 and 3.6 \AA respectively surrounded by the N-site of the adeninato ligands belonging to heptameric cations. The corridors connecting them have an approximate radius of 3.3 and 3.0 \AA (Figure 2.74). The volume of these channels, occupied by the crystallization water molecules, is 5313 and 4307 \AA^3 per unit cell (34 and 29 % of the total volume as calculated by PLATON), respectively. A computational analysis shows an accessible surface area value of 625 and $6.21 \text{ m}^2 \cdot \text{g}^{-1}$ and a pore volume of 0.508 and $0.206 \text{ cm}^3 \cdot \text{g}^{-1}$, respectively, Figure 2.75.

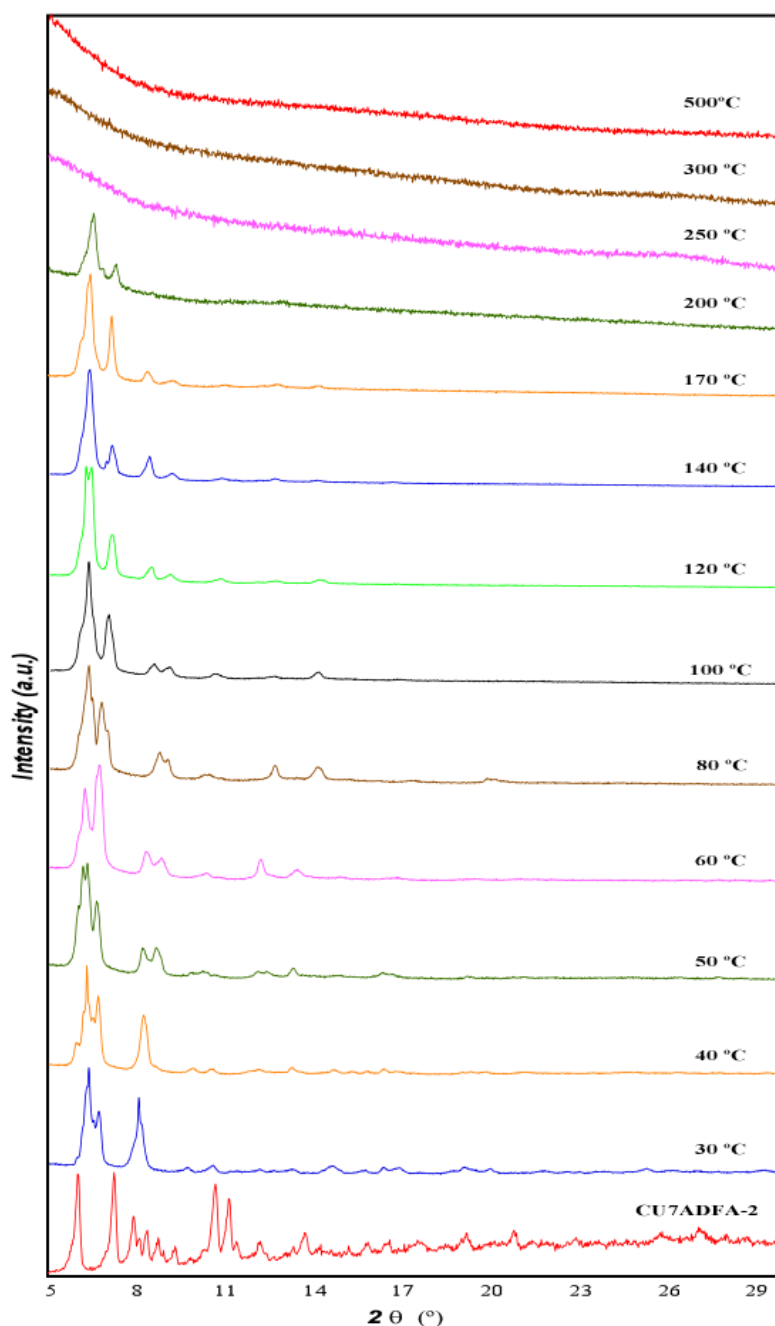


Figure 2.73. Variable-temperature X-ray diffraction patterns for CU7ADFA-2.

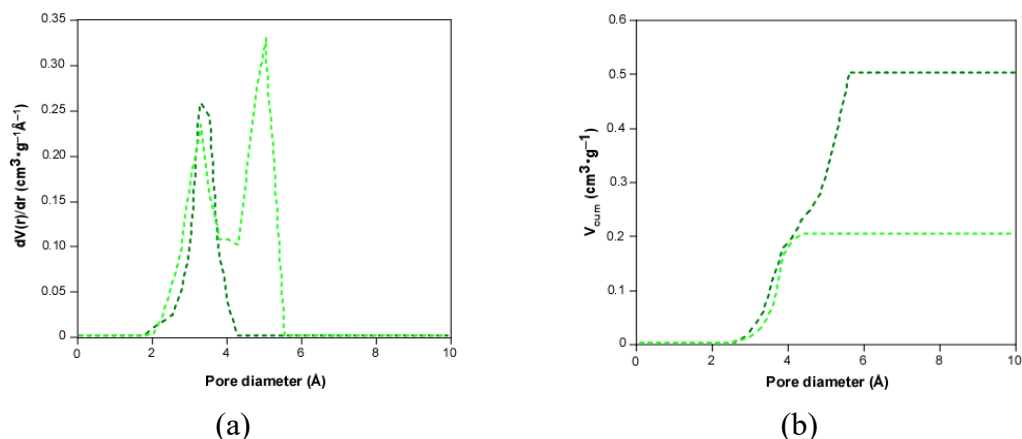


Figure 2.74. (a) Derivative representation of the geometric pore volume and (b) cumulative representation of the geometric pore volume of compound CU7ADFA-1 (dark green) and CU7ADFA-2 (light green).

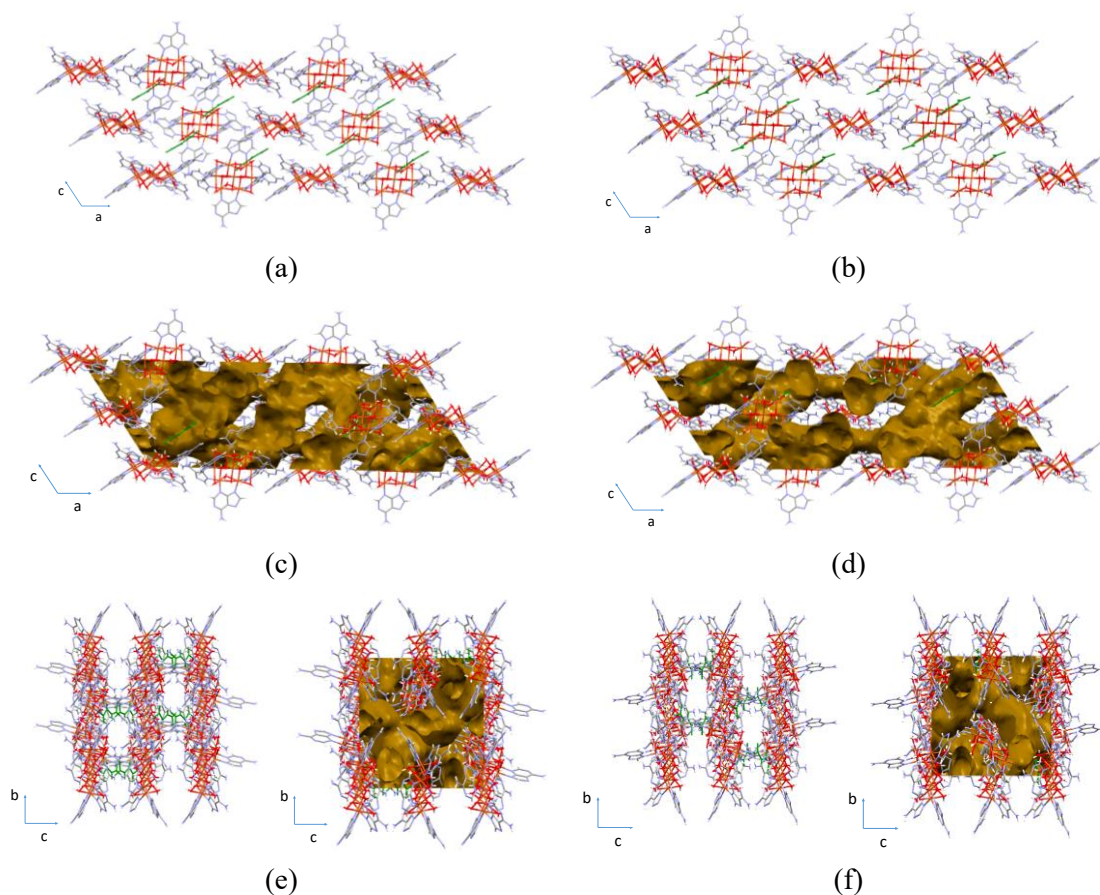


Figure 2.75. Crystal packing of (a), (c), (e) of CU7ADFA-1 and (b), (d) and (f) of CU7ADFA-2.

The remaining fumarate containing compounds, i.e. CU7ADF-1/2 bear a close resemblance with compounds CU7ADAC-1/2, CU7ADNAPH-2, CU7ADTEP-1/2 and CU7ADBP. Specifically, they are isoreticular compounds, where the structural difference relies in the employed dicarboxylate counterion. All the reticular dicarboxylate compounds contain the same $[Cu_7(\mu\text{-ade})_6(\mu_3\text{-OH})_6(\mu\text{-H}_2\text{O})_6]^{2+}$ cationic wheel-shaped

entity with the usual Jahn-Teller tetragonal elongation which is more pronounced for the external copper(II) atoms than for the inner one because of the rigidity of the heptanuclear entity (Tables 2.36–2.42).

Table 2.36. Distances and angles (Å, deg) for compound CU7ADF-1.^a

Cu1–O1	2.079(9)	Cu1–O2	2.095(8)	Cu1–O3	2.001(8)
Cu2–O1	1.976(9)	Cu2–O3	2.017(9)	Cu2–N13	1.997(1)
Cu2–N39 ⁱ	2.011(1)	Cu2–O1w	2.508(1)	Cu2–O3w ⁱ	2.497(1)
Cu3–O1	1.973(8)	Cu3–O2	1.957(9)	Cu3–N19	1.966(2)
Cu3–N29	1.961(2)	Cu3–O1w	2.466(1)	Cu3–O2w	2.475(1)
Cu4–O2	1.961(9)	Cu4–O3 ⁱ	1.995(8)	Cu4–N23	2.000(1)
Cu4–N33	2.026(1)	Cu4–O2w	2.339(1)	Cu4–O3w	2.500(1)
Cu1···Cu2	3.073(2)	Cu1···Cu3	3.149(2)	Cu1···Cu4	3.093(2)
Cu2···Cu3	3.101(3)	Cu2···Cu4 ⁱ	3.142(3)	Cu3···Cu4	3.073(3)
Cu1–O1–Cu2	98.5(4)	Cu1–O1–Cu3	102.0(4)	Cu2–O1–Cu3	103.5(4)
Cu1–O2–Cu3	101.9(4)	Cu1–O2–Cu4	99.3(4)	Cu3–O2–Cu4	103.3(4)
Cu1–O3–Cu2	99.8(4)	Cu1–O3–Cu4 ⁱ	101.4(4)	Cu2–O3–Cu4 ⁱ	103.1(4)
Cu2–O1w–Cu3	77.1(3)	Cu3–O2w–Cu4	79.3(3)	Cu3–O3w–Cu2 ⁱ	77.9(4)

^aSymmetry: (i) $1/2 - x, 1/2 - y, -z$.

Table 2.37. Distances and angles (Å, deg) for compound CU7ADF-2.^a

Cu1–O1	1.961(1)	Cu1–O2	2.210(1)	Cu1–O3	2.108(1)
Cu2–O1	1.997(1)	Cu2–O3	1.913(1)	Cu2–N13	2.020(2)
Cu2–N39 ⁱ	2.040(3)	Cu2–O1w	2.469(2)	Cu2–O3w ⁱ	2.540(3)
Cu3–O1	1.965(1)	Cu3–O2	1.962(1)	Cu3–N19	2.150(2)
Cu3–N29	1.860(2)	Cu3–O1w	2.500(2)	Cu3–O2w	2.590(2)
Cu4–O2	1.972(2)	Cu4–O3 ⁱ	2.012(1)	Cu4–N23	2.080(2)
Cu4–N33	1.970(2)	Cu4–O2w	2.410(3)	Cu4–O3w	2.510(3)
Cu1···Cu2	3.067(2)	Cu1···Cu3	3.093(3)	Cu1···Cu4	3.132(2)
Cu2···Cu3	3.107(4)	Cu2···Cu4 ⁱ	3.109(4)	Cu3···Cu4	3.078(4)
Cu1–O1–Cu2	101.6(8)	Cu1–O1–Cu3	104(8)	Cu2–O1–Cu3	103.3(7)
Cu1–O2–Cu3	98.5(7)	Cu1–O2–Cu4	99.8(7)	Cu3–O2–Cu4	103.0(8)
Cu1–O3–Cu2	99.3(8)	Cu1–O3–Cu4 ⁱ	98.9(6)	Cu2–O3–Cu4 ⁱ	104.7(8)
Cu2–O1w–Cu3	77.4(6)	Cu3–O2w–Cu4	76.0(8)	Cu4–O3w–Cu2 ⁱ	75.9(8)

^aSymmetry: (i) $1/2 - x, 1/2 - y, 1 - z$.

Table 2.38. Distances and angles (Å, deg) for compound CU7ADAC-1.^a

Cu1–O1	2.012(4)	Cu1–O2	2.125(3)	Cu1–O3	2.048(4)
Cu2–O1	1.991(4)	Cu2–O3 ⁱ	1.962(4)	Cu2–N13	1.982(7)
Cu2–N39 ⁱ	2.015(7)	Cu2–O1w	2.473(4)	Cu2–O3w	2.531(6)
Cu3–O1	1.989(3)	Cu3–O2	1.957(5)	Cu3–N19	1.970(6)
Cu3–N29	1.992(6)	Cu3–O1w	2.490(4)	Cu3–O2w	2.496(4)
Cu4–O2	1.960(4)	Cu4–O3	1.980(3)	Cu4–N23	2.016(6)
Cu4–N33	2.012(6)	Cu4–O2w	2.369(5)	Cu4–O3w ⁱ	2.510(6)
Cu1···Cu2	3.079(9)	Cu1···Cu3	3.126(9)	Cu1···Cu4	3.110(8)
Cu2···Cu3	3.119(1)	Cu2···Cu4 ⁱ	3.123(1)	Cu3···Cu4	3.072(1)
Cu1–O1–Cu2	100.5(2)	Cu1–O1–Cu3	102.8(2)	Cu2–O1–Cu3	103.2(2)
Cu1–O2–Cu3	99.8(2)	Cu1–O2–Cu4	99.1(2)	Cu3–O2–Cu4	103.3(2)
Cu1–O3–Cu2 ⁱ	100.3(2)	Cu1–O3–Cu4	101.1(2)	Cu4–O3–Cu2 ⁱ	104.8(2)
Cu2–O1w–Cu3	77.9(1)	Cu3–O2w–Cu4	78.3(1)	Cu2–O3w–Cu4 ⁱ	76.6(2)

^aSymmetry: (i) 1/2 – x, 1/2 – y, 1 – z.**Table 2.39.** Distances and angles (Å, deg) for compound CU7ADAC-2.^a

Cu1–O1	2.004(1)	Cu1–O2	2.096(1)	Cu1–O3	2.084(8)
Cu2–O1	2.012(1)	Cu2–O3 ⁱ	1.990(1)	Cu2–N19	1.999(8)
Cu2–N39 ⁱ	1.994(7)	Cu2–O1w	2.502(1)	Cu2–O3w ⁱ	2.583(1)
Cu3–O1	1.982(1)	Cu3–O2	1.934(1)	Cu3–N13	1.978(6)
Cu3–N29	2.092(1)	Cu3–O1w	2.477(1)	Cu3–O2w	2.530(1)
Cu4–O2	1.969(9)	Cu4–O3	1.949(9)	Cu4–N23	1.918(1)
Cu4–N33	1.963(5)	Cu4–O2w	2.570(1)	Cu4–O3w	2.291(1)
Cu1···Cu2	3.071(2)	Cu1···Cu3	3.096(2)	Cu2···Cu4	3.129(2)
Cu2···Cu3	3.142(3)	Cu2···Cu4 ⁱ	3.080(3)	Cu3···Cu4	3.075(3)
Cu1–O1–Cu2	99.8(5)	Cu1–O1–Cu3	102.0(5)	Cu2–O1–Cu3	103.8(5)
Cu1–O2–Cu3	100.4(4)	Cu1–O2–Cu4	100.6(4)	Cu3–O2–Cu4	104.0(5)
Cu1–O3–Cu2 ⁱ	97.8(4)	Cu1–O3–Cu4	101.7(4)	Cu4–O3–Cu2 ⁱ	102.8(4)
Cu2–O1w–Cu3	78.3(3)	Cu3–O2w–Cu4	74.2(4)	Cu4–O3w–Cu2 ⁱ	78.1(4)

^aSymmetry: (i) 3/2 – x, 1/2 – y, – z.

Table 2.40. Distances and angles (Å, deg) for compound CU7ADNAPH-2.^a

Cu1–O1	1.997(8)	Cu1–O2	2.012(8)	Cu1–O3	2.243(7)
Cu2–O1	1.974(8)	Cu2–O3 ⁱ	1.959(8)	Cu2–N13	2.006(1)
Cu2–N33 ⁱ	1.968(9)	Cu2–O1w	2.367(8)	Cu2–O3w ⁱ	2.627(1)
Cu3–O1	1.990(8)	Cu3–O2	1.997(7)	Cu3–N19	1.972(1)
Cu3–N29	2.010(1)	Cu3–O1w	2.416(7)	Cu3–O2w	2.583(8)
Cu4–O2	1.998(7)	Cu4–O3	1.972(8)	Cu4–N23	1.962(1)
Cu4–N39	1.988(9)	Cu4–O2w	2.412(8)	Cu4–O3w	2.582(1)
Cu1···Cu2	3.104(2)	Cu1···Cu3	3.062(2)	Cu1···Cu4	3.164(2)
Cu2···Cu3	3.116(3)	Cu2···Cu4 ⁱ	3.080(2)	Cu3···Cu4	3.136(2)
Cu1–O1–Cu2	102.8(3)	Cu1–O1–Cu3	100.4(4)	Cu2–O1–Cu3	103.6(4)
Cu1–O2–Cu3	99.6(3)	Cu1–O2–Cu4	104.2(3)	Cu3–O2–Cu4	103.4(3)
Cu1–O3–Cu2 ⁱ	95.0(3)	Cu1–O3–Cu4	97.1(3)	Cu4–O3–Cu2 ⁱ	103.2(4)
Cu2–O1w–Cu3	81.3(2)	Cu3–O2w–Cu4	77.7(2)	Cu4–O3w–Cu2 ⁱ	72.5(3)

^aSymmetry: (i) 2 – x, – y, 2 – z.**Table 2.42.** Distances and angles (Å, deg) for compound CU7ADBP.^a

Cu1–O1	2.226(4)	Cu1–O2	2.014(5)	Cu1–O3	1.984(4)
Cu2–O1	1.943(5)	Cu2–O2 ⁱ	1.968(4)	Cu2–N13	1.981(6)
Cu2–N33	2.051(7)	Cu2–O1w	2.366(4)	Cu2–O3w	2.632(5)
Cu3–O1	1.959(5)	Cu3–O3	1.986(4)	Cu3–N19	1.997(6)
Cu3–N23	1.989(6)	Cu3–O2w	2.387(5)	Cu3–O3w	2.559(5)
Cu4–O2	1.970(4)	Cu4–O3	1.984(5)	Cu4–N29	1.973(6)
Cu4–N39 ⁱ	2.031(7)	Cu4–O1w ⁱ	2.406(4)	Cu4–O2w	2.563(4)
Cu1···Cu2	3.112(8)	Cu1···Cu3	3.147(8)	Cu1···Cu4	3.060(9)
Cu2···Cu3	3.0879(1)	Cu2···Cu4 ⁱ	3.098(1)	Cu3···Cu4	3.135(1)
Cu1–O1–Cu2	96.3(2)	Cu1–O1–Cu3	97.3(2)	Cu2–O1–Cu3	104.6(2)
Cu1–O2–Cu4	100.4(2)	Cu1–O2–Cu2 ⁱ	102.8(2)	Cu4–O2–Cu2 ⁱ	103.7(2)
Cu1–O3–Cu3	104.9(2)	Cu1–O3–Cu4	100.9(2)	Cu3–O3–Cu4	104.3(2)
Cu2–O1w–Cu4 ⁱ	80.9(1)	Cu3–O2w–Cu4	78.5(1)	Cu2–O3w–Cu3	72.9(1)

^aSymmetry: (i) 2 – x, – y, 1 – z.

In the crystal building of all compounds, except those containing DMF (CU7ADBPD and CU7ADSD) as solvation molecule, each heptameric cation is surrounded by four other ones with which interacts through offset face-to-face π - π stacking interactions established by four of their adeninato ligands (Figure 2.76). These stacking interactions, except in CU7ADNAPH-1 and CU7ADS, are reinforced by a hydrogen-bonded $R_2^2(8)$ ring formed by two O-H \cdots N interactions between the pyrimidinic N1 and exocyclic N6 nitrogen atoms of the Watson-Crick face of an adeninato ligand as acceptor, and a HO-Cu-OH₂ fragment of a cationic unit as donor. These supramolecular interactions give rise to cationic layers from which the adeninato ligands not involved in them are arranged perpendicularly. The dicarboxylate anions are inserted perpendicular to the cationic shells and sited between these two pendant adeninato ligands (Figure 2.77).

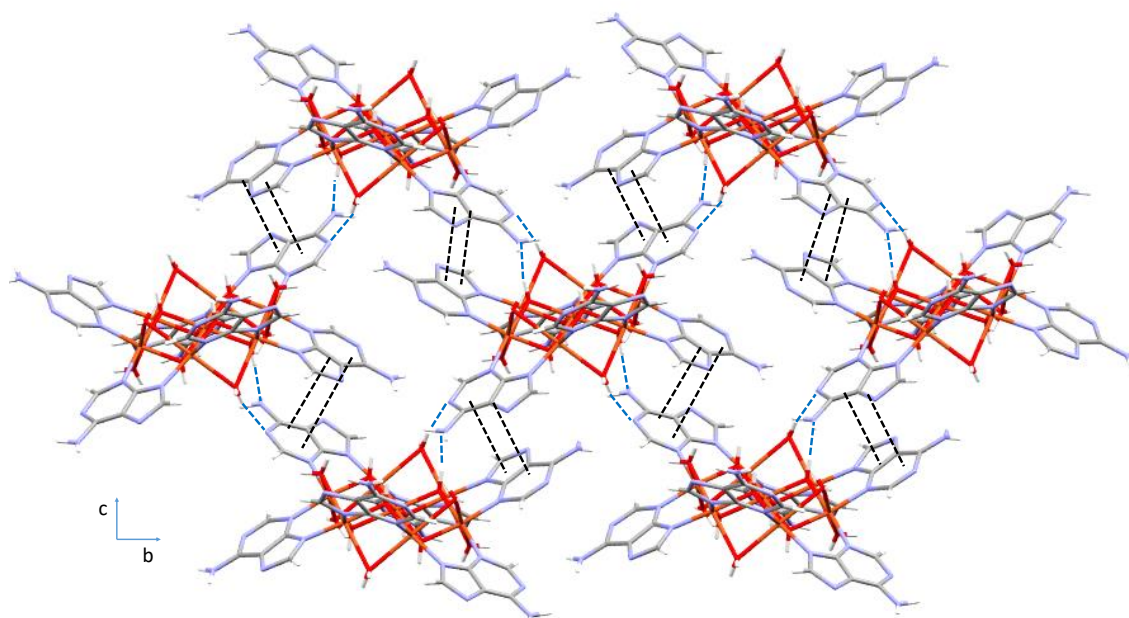


Figure 2.76. Supramolecular cationic layer formed by heptameric complexes in isorecticular compounds; π - π interaction (double black line) and hydrogen bonds (dashed blue line).

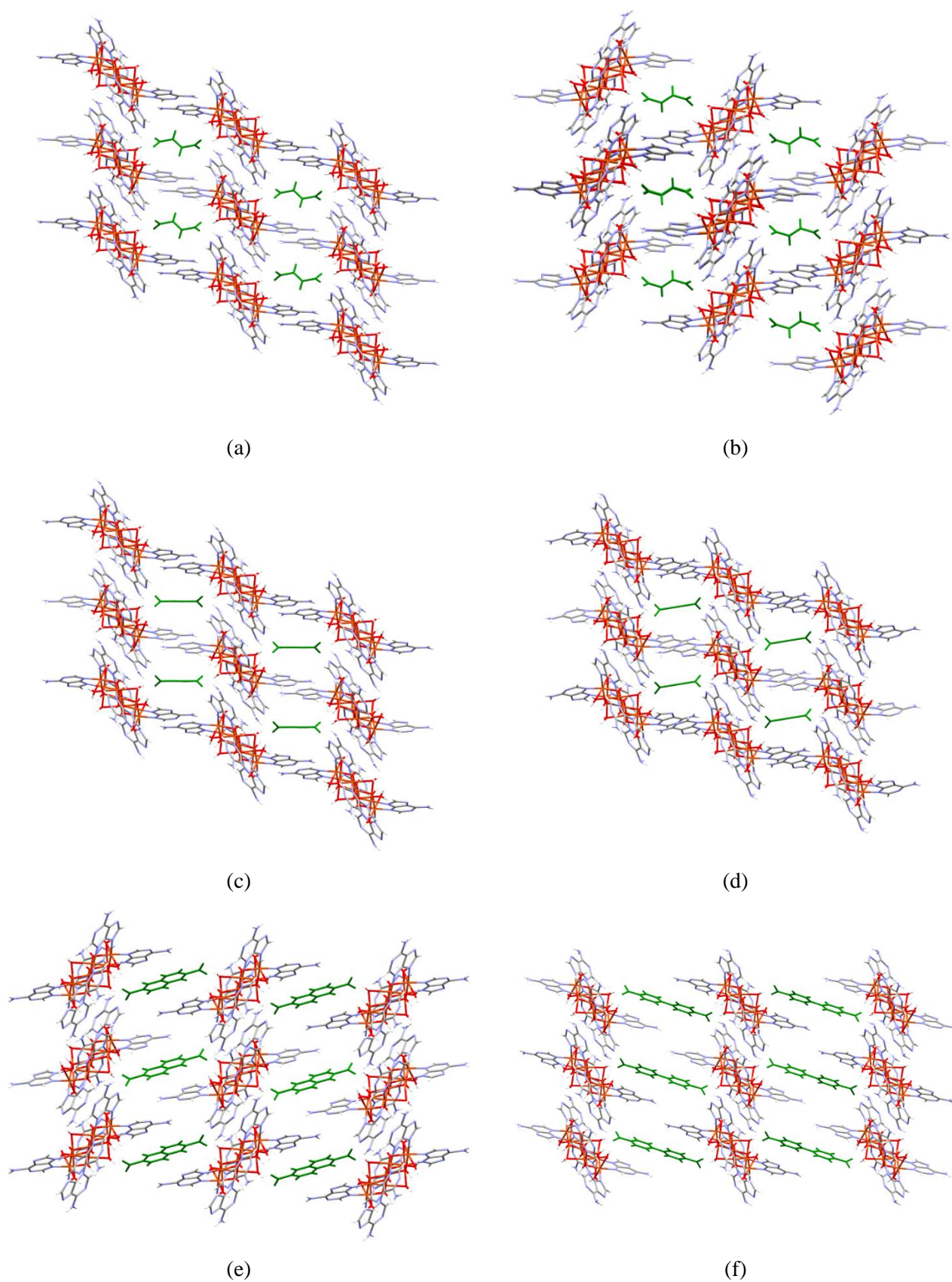


Figure 2.77. Insertion of the dicarboxylate dianion (green colour) in the crystal structure along *b* axis view in (a) CU7ADF-1, (b) CU7ADF-2, (c) CU7ADAC-1, (d) CU7ADAC-2, (e) CU7ADNAPH-2 and (f) CU7ADBP.

Each carboxylate group of the organic anion is attached to the nearest cationic layer by two $O_{\text{anion}} \cdots H-O_{\text{cation}}$ hydrogen bonds, one with a hydroxide group and the other one with a water molecule coordinated to the same copper atom, to form a supramolecular $R_2^2(8)$ synthon. Additionally, the aromatic rings of the terephthalate (CU7ADTEP-1) naphthalene-2,6-dicarboxylate (CU7ADNAPH-2) and biphenyl-4,4'-dicarboxylate anions (CU7ADBP) establish offset face-to-face $\pi-\pi$ interactions with both adeninato moieties (Figure 2.78), Table 2.43–2.47.

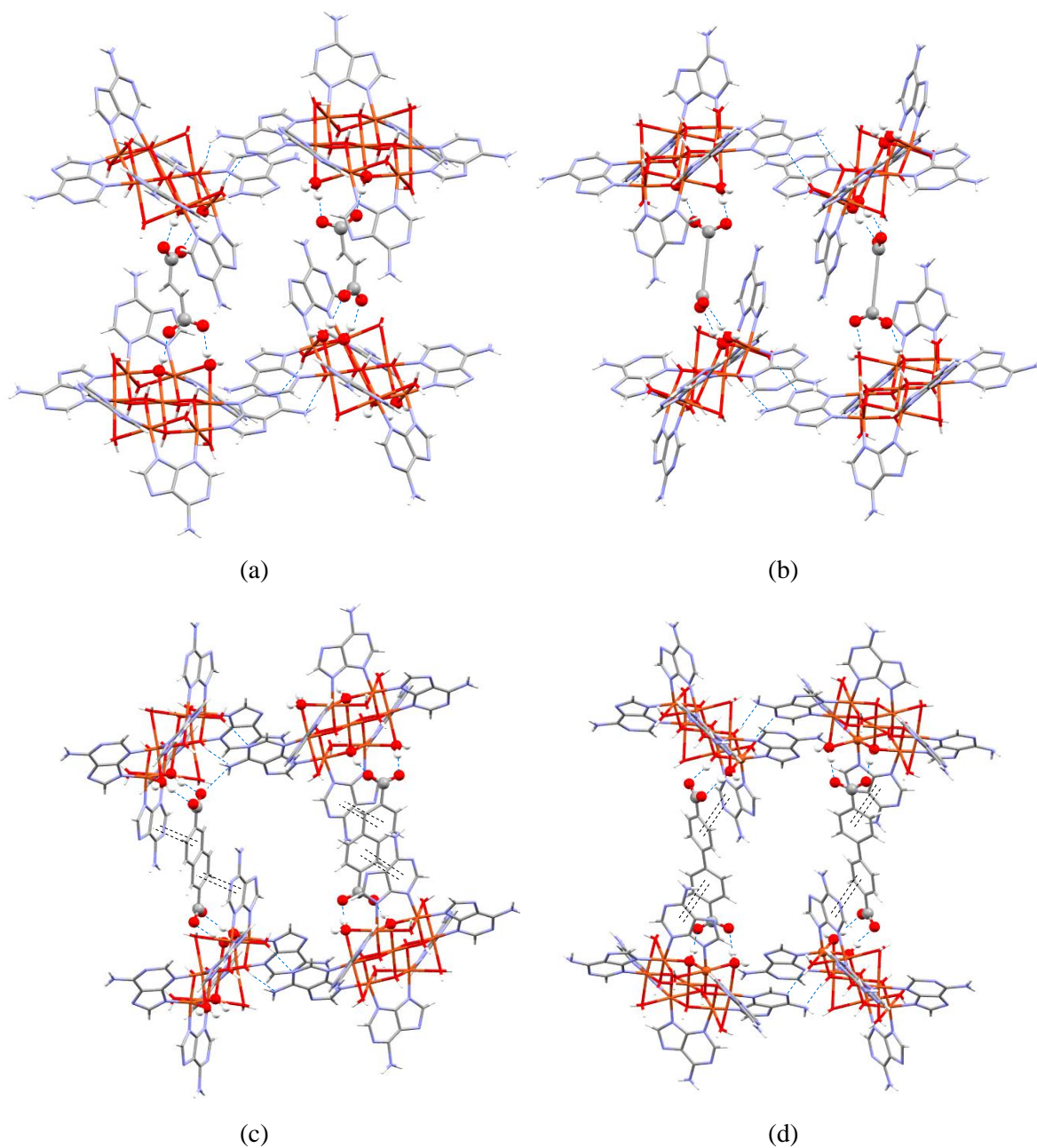


Figure 2.78. Details of the supramolecular interactions between the organic anion and the cationic complexes in compound: (a) CU7ADF-1, (b) CU7ADAC-1, (c) CU7ADNAPH-2 and (d) CU7ADBP.

Table 2.42. Structural parameters (Å, deg) of hydrogen bonding interactions in CU7ADF-1.^a

Hydrogen-bonding interactions					
D-H...A ^b		H...A	D...A	D-H...A	
O1-H1...O48		1.78	2.76(2)	171	
O2-H2...N36A ⁱ		1.92	2.90(2)	177	
O3-H3...O4w ⁱⁱ		1.76	2.74(1)	172	
O1w-H12w...O5w		1.91	2.78(2)	171	
O2w-H21w...O49		1.87	2.76(2)	174	
O2w-H22w...O10w ⁱ		2.05	2.85(2)	164	
N16A-H16B...O9w ⁱⁱⁱ		1.77	2.62(3)	172	
N26A-H26B...O10w ^{iv}		2.18	3.04(2)	176	
π - π interactions ^c					
ring-ring ^a	packing	angle	DC	DZ	DXY
1pa...1pa ⁱ	A...A	0.0	5.32	2.86	4.49
2pa...3pa ^v	A...A	4.0	4.13	3.65	1.92

^aSymmetry codes: (i) $x, -y, 1/2 + z$; (ii) $-1/2 - x, 1/2 + y, -1/2 - z$; (iii) $-x, -y, -z$; (iv) $-1/2 - x, -1/2 + y, -1/2 - z$, (v) $x, -y, 1/2 + z$. ^bD: donor; A: acceptor. ^cAngle: dihedral angle between the planes (deg), DC: distance between the centroids of the rings (Å), DZ: interplanar distance (Å), DXY: lateral displacement (Å), pa: adenine pentagonal ring, ha: adenine hexagonal ring.

Table 2.43. Structural parameters (Å, deg) of hydrogen bonding interactions in CU7ADF-2.^a

Hydrogen-bonding interactions					
D-H...A ^b		H...A	D...A	D-H...A	
O1-H1...O48		1.70	2.70(4)	172	
O2-H2...N36 ⁱ		1.84	2.84(4)	179	
O3-H3...O6w		1.72	2.70(3)	168	
O1w-H11w...N31 ⁱ		2.12	2.93(4)	159	
O1w-H12w...O5w ⁱⁱ		1.97	2.86(2)	173	
O2w-H21w...O49		1.74	2.55(4)	168	
O2w-H22w...O7w ⁱⁱⁱ		2.23	3.01(3)	168	
N26-H26B...O7w ^{iv}		2.16	3.03(3)	171	
π - π interactions ^c					
ring-ring ^a	packing	angle	DC	DZ	DXY
1pa...1pa ⁱⁱ	A...A	0.0	4.76	3.06	3.65
2pa...3pa ⁱ	A...A	4.0	4.23	3.78	1.89

^aSymmetry codes: (i) $x, 1 - y, -1/2 + z$; (ii) $-x, 1 - y, -z$; (iii) $-x, y, 1/2 - z$; (iv) $1/2 + x, 3/2 - y, 1/2 + z$. ^bD: donor; A: acceptor. ^cAngle: dihedral angle between the planes (deg), DC: distance between the centroids of the rings (Å), DZ: interplanar distance (Å), DXY: lateral displacement (Å), pa: adenine pentagonal ring, ha: adenine hexagonal ring.

Table 2.44. Structural parameters (Å, deg) of hydrogen bonding interactions in CU7ADAC-1.^a

Hydrogen-bonding interactions					
D–H...A ^b		H...A	D...A	D–H...A	
O1–H1...O48		1.82	2.78(7)	168	
O2–H2...N36 ⁱ		1.93	2.91(8)	176	
O3–H3...O4W ⁱⁱ		1.82	2.80(6)	174	
O1W–H12W...N31 ⁱ		2.03	2.88(7)	167	
O2W–H21W...O49		1.88	2.73(8)	173	
O2W–H22W...O6W		1.95	2.78(7)	172	
N26A–H26B...O6W ⁱⁱⁱ		2.22	3.07(2)	173	
N36–H36B...O4W ⁱⁱⁱ		2.27	3.15(1)	173	
π - π interactions ^c					
ring–ring ^a	packing	angle	DC	DZ	DXY
1pa...1pa ^{iv}	A...A	0.0	5.42	2.93	4.56
2pa...3pa ⁱ	A...A	4.6	4.09	3.64	1.94

^aSymmetry codes: (i) $x, -y, 1/2 + z$; (ii) $x, -y, -1/2 + z$; (iii) $1/2 - x, 1/2 - y, 1 - z$; (iv) $x, -y, 1 - z$. ^bD: donor; A: acceptor. ^cAngle: dihedral angle between the planes (deg), DC: distance between the centroids of the rings (Å), DZ: interplanar distance (Å), DXY: lateral displacement (Å), pa: adenine pentagonal ring, ha: adenine hexagonal ring.

Table 2.45. Structural parameters (Å, deg) of hydrogen bonding interactions in CU7ADAC-2.^a

Hydrogen-bonding interactions					
D–H...A ^b		H...A	D...A	D–H...A	
O1–H1...O49 ⁱ		1.79	2.64(2)	164	
O2–H2...O6 ⁱⁱ		1.89	2.81(2)	168	
O3–H3...N26 ⁱⁱⁱ		1.83	2.70(3)	173	
O1W–H11W...N21 ^{iv}		2.14	3.01(1)	170	
O1W–H12W...O4W		2.07	2.85(2)	166	
O2W–H21W...O7W		2.07	2.87(2)	168	
O3W–H31W...O48		1.78	2.72(2)	169	
O3W–H32W...O8W		1.99	2.84(2)	163	
N36A–H36A...O8W ⁱ		2.08	2.92(2)	163	
π - π interactions ^c					
ring–ring ^a	packing	angle	DC	DZ	DXY
1pa...1pa ^v	A...A	0.0	4.82	2.97	3.79
2pa...3pa ⁱⁱ	A...A	9.7	4.20	3.66	1.78

^aSymmetry codes: (i) $3/2 - x, 1/2 - y, -z$; (ii) $x, -y, 1/2 + z$; (iii) $x, -y, -1/2 + z$; (iv) $3/2 - x, 1/2 + y, 1/2 - z$; (v) $1 - x, 1 - y, z$. ^bD: donor; A: acceptor. ^cAngle: dihedral angle between the planes (deg), DC: distance between the centroids of the rings (Å), DZ: interplanar distance (Å), DXY: lateral displacement (Å), pa: adenine pentagonal ring, ha: adenine hexagonal ring.

Table 2.46. Structural parameters (Å, deg) of H-bonding interactions in CU7ADNAPH-2.^a

Hydrogen-bonding interactions					
D–H...A ^b		H...A	D...A	D–H...A	
O1–H1...N36 ⁱ		2.05	2.87(2)	163	
O2–H2...O48		1.66	2.63(1)	172	
O3–H3...O4w ⁱⁱ		1.83	2.81(1)	175	
O1W–H11W...O49		1.86	2.70(1)	174	
O1W–H12W...O5w		1.94	2.78(1)	174	
O2W–H21W...N31 ⁱ		1.93	2.78(2)	166	
O2W–H22W...O6w		1.97	2.81(1)	164	
O3W–H31W...O8w ⁱⁱⁱ		2.06	2.91(1)	170	
O3W–H32W...O12w		2.08	2.92(2)	169	
N16A–H16A...O5w ^{iv}		2.12	2.97(2)	167	
π - π interactions ^c					
ring–ring ^a	packing	angle	DC	DZ	DXY
1pa...3pa ⁱⁱ	A...A	6.4	4.28	3.64	2.25
2pa...1hd ^v	A...N	4.0	3.86	3.60	1.65
2pa...2hd ^{vi}	A...N	4.0	3.86	3.59	1.65

^aSymmetry codes: (i) $2 - x, 1/2 + y, 5/2 - z$; (ii) $2 - x, -1/2 + y, 5/2 - z$; (iii) $x, -1/2 - y, -1/2 + z$; (iv) $2 - x, 1 - y, 2 - z$, (v) x, y, z , (vi) $3 - x, -y, 2 - z$. ^bD: donor; A: acceptor. ^cAngle: dihedral angle between the planes (deg), DC: distance between the centroids of the rings (Å), DZ: interplanar distance (Å), DXY: lateral displacement (Å), pa: adenine pentagonal ring, ha: adenine hexagonal ring, hd: anion hexagonal ring.

Table 2.47. Structural parameters (Å, deg) of hydrogen bonding interactions in CU7ADBP.^a

Hydrogen-bonding interactions					
D–H...A ^b		H...A	D...A	D–H...A	
O1–H1...O5w		1.89	2.86(6)	171	
O2–H2...N16 ⁱ		2.05	2.88(7)	164	
O3–H3...O48		1.73	2.70(6)	170	
O1w–H11w...O49 ⁱⁱ		1.91	2.77(6)	179	
O1w–H12w...O7w ⁱⁱⁱ		1.91	2.75(7)	171	
O2w–H21w...N11i		1.96	2.82(8)	170	
O2w–H22w...O6w		2.02	2.87(7)	169	
N16–H16A...O5w ^{iv}		2.22	3.08(8)	160	
N36–H36B...O7w		1.93	2.77(1)	165	
π - π interactions ^c					
ring – ring ^a	packing	angle	DC	DZ	DXY
2pa...hd ^v	A...B	3.9	4.04	3.57	2.04
1pa...3pa ^{vi}	A...A	5.2	4.21	3.66	2.14

^aSymmetry codes: (i) $3/2 - x, 1/2 + y, 1 - z$; (ii) $2 - x, -y, 1 - z$; (iii) $2 - x, -1 - y, 1 - z$; (iv) $3/2 - x, -1/2 + y, 1 - z$, (v) x, y, z , (vi) $1/2 + x, -1/2 - y, z$. ^bD: donor; A: acceptor. ^cAngle: dihedral angle between the planes (deg), DC: distance between the centroids of the rings (Å), DZ: interplanar distance (Å), DXY: lateral displacement (Å), pa: adenine pentagonal ring, ha: adenine hexagonal ring, hd: anion hexagonal ring.

The above-described supramolecular interactions generate rectangular structural boxes (Figure 2.79), where the crystallization water molecules are hosted, resembling the reticular topology of the well-known IRMOF metal-organic series. Heptameric units are located at the eight vertices of these boxes. The edges of the upper and lower faces of these boxes are defined by the adeninato \cdots adeninato π -stacking interactions with no left empty space, whereas the lateral edges imply the adenine sandwiched organic anions. The distance between the heptameric clusters connected through the direct adeninato \cdots adeninato π -stacking are *ca.* 12.1 Å in all cases but the lateral edges distance increase with the size of the dicarboxylate anion ranging from 13.5 Å for CU7ADF-1 to 18.6 Å for CU7ADBP.

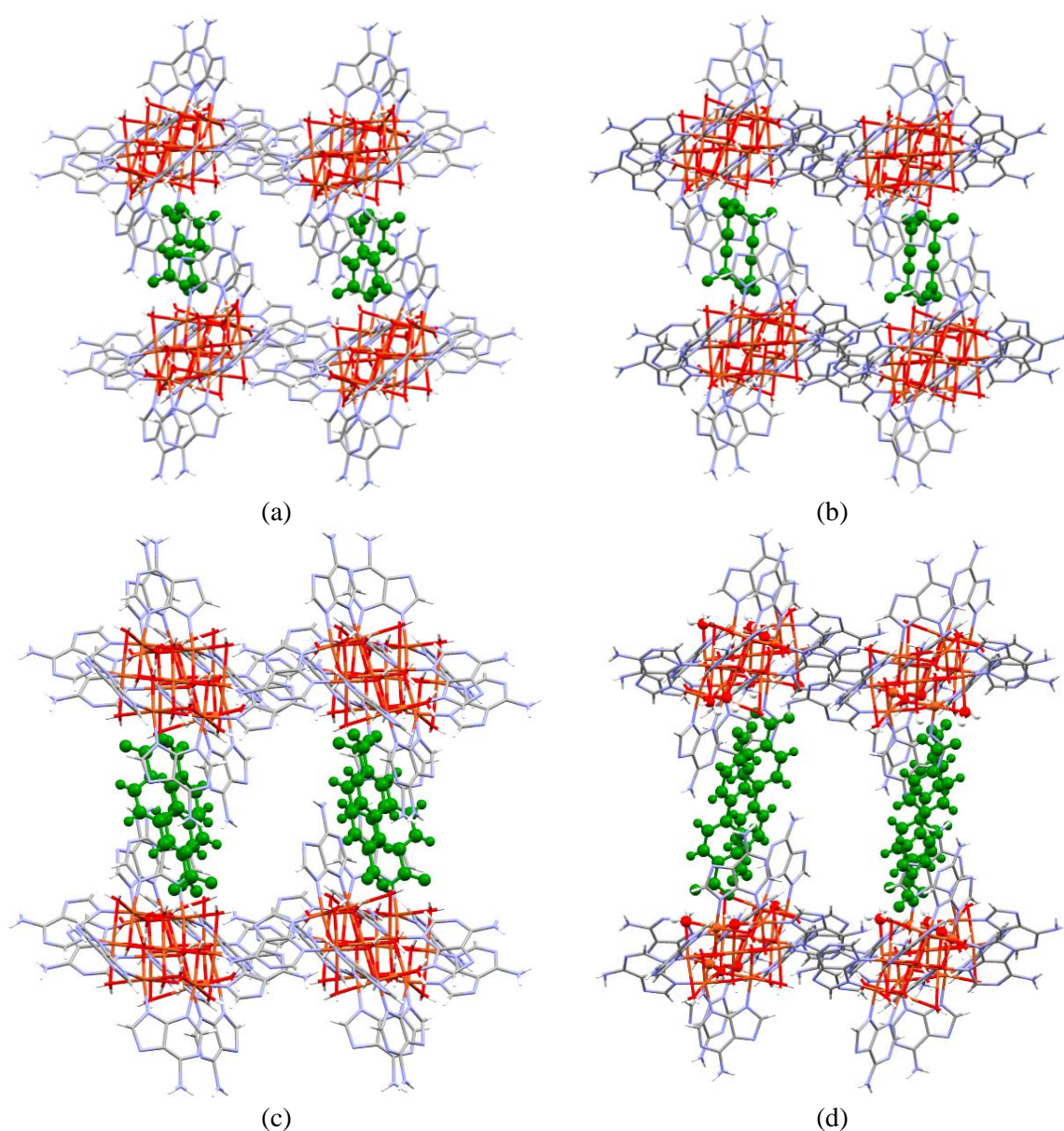


Figure 2.79. Supramolecular boxes present in the isorecticular crystal structure of compounds (a) CU7ADF-1, (b) CU7ADAC-1, (c) CU7ADNAPH-2 and (d) CU7ADBP.

The resulting porous supramolecular network corresponds to a 6-connected unimodal net with **pcu** α -Po primitive cubic topology and $(4^{12}\cdot 6^3)$ point symbol considering the heptameric clusters as nodes and the π - π interactions among the adeninato ligands together with the hydrogen bonding interactions between the carboxylate group of the dicarboxylic anion and the cluster as connectors. The resulting supramolecular architecture of the above described compounds shows a 2D system of void with big ovoid pores connected by thinner corridors. In Figure 2.80 are represented the void distributions of all the isorecticular compounds (Table 2.48, Figures 2.81 and 2.82).

Table 2.48. Voids information in heptameric isorecticular compounds.

Compounds	Pore (Å)	Corridor min/max (Å)	Void volume (Å ³)	Void (%)	Surface area (m ² /g)	Pore volume (cm ³ /g)
CU7ADF-1	5.1 x 6.4	4.4 x 7.1	2791	36	411	0.267
CU7ADF-2	4.4 x 5.6	3.2 x 5.8	2137	29	242	0.204
CU7ADAC-1	5.1 x 6.4	3.6 x 6.7	2788	36	449	0.267
CU7ADAC-2	4.3 x 5.4	3.0 x 5.7	2198	30	216	0.210
CU7ADNAPH-1	7.1 x 7.9	4.1 x 8.1	4171	44	877	0.375
CU7ADNAPH-2	9.5 x 11.2	8.5 x 11.5	1994	43	1477	0.359
CU7ADBP	7.1 x 9.1	6.8 x 9.9	5380	50	1153	0.476

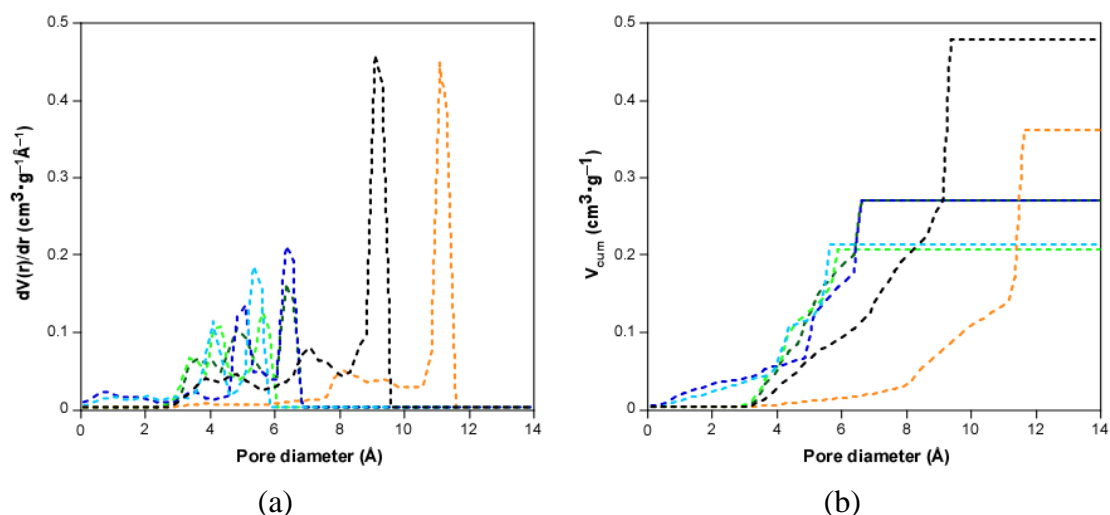


Figure 2.80. (a) Derivative representation of the geometric pore volume of compounds (b) Cumulative representation of the geometric pore volume of compound CU7ADF-1/2 (dark and light green), CU7ADAC-1/2 (dark and light blue), CU7ADNAPH-2 (orange) and CU7ADBP (black).

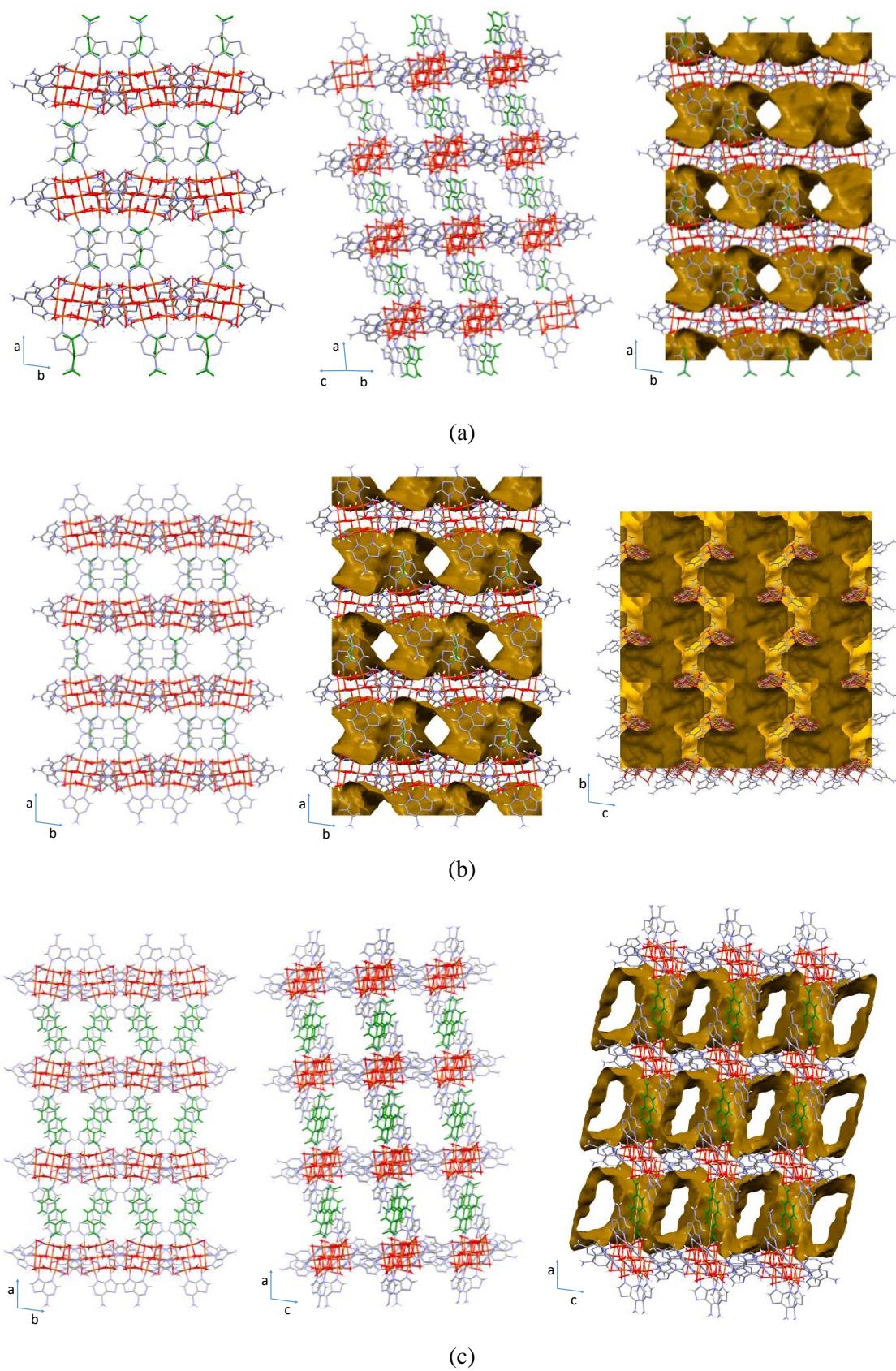


Figure 2.81. Image showing the channels for the squeezed form of compound (a) CU7ADF-1, (b) CU7ADAC-1 and (c) CU7ADNAPH-2.

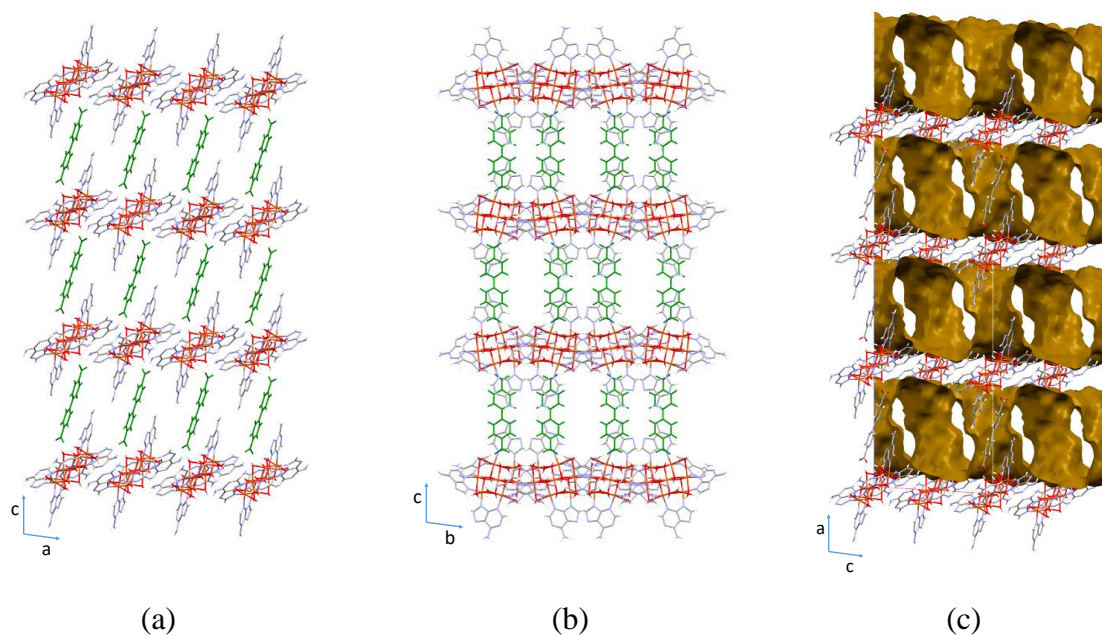


Figure 2.82. Different projections of the crystal structure of compound CU7ADBP (a, b) and the inner surface of the porous system (c).

The inner cavity, the size of the molecular boxes and the porosity of the crystal structures increase with the distance between the carbon atoms in the carboxylate groups as represented in Figures 2.83.

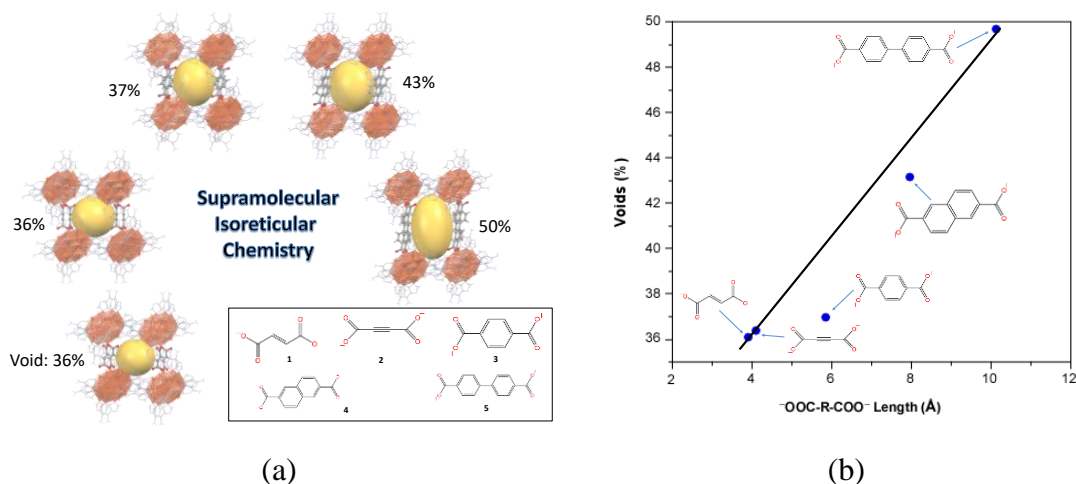


Figure 2.83. (a) Supramolecular boxes in the crystal structure of CU7ADF-1 to CU7ADBP, all the anions employed are listed in the box and (b) Relation between the void value and the anion length in isoreticular compounds.

The thermoanalytical (Figure 2.15c-e and Table 2.8) and variable-temperature X-ray diffraction data of CU7ADF-2, CU7ADAC-2 and CU7ADNAPH-2, Figure 2.84 and 2.85 show that in all of compounds except CU7ADNAPH-2, the release of the crystallization water molecules implies a substantial structural change at a value around

60 °C. The crystallinity remains until a value of 210 °C except for the compound with acetylendicarboxylic anion, that only show peaks until a value of 170 °C. In the case of the naphthalendicarboxylic compound, the data are similar for the compound CU7ADTB, where the crystallinity peaks keeps with a great intensity values until high temperatures.

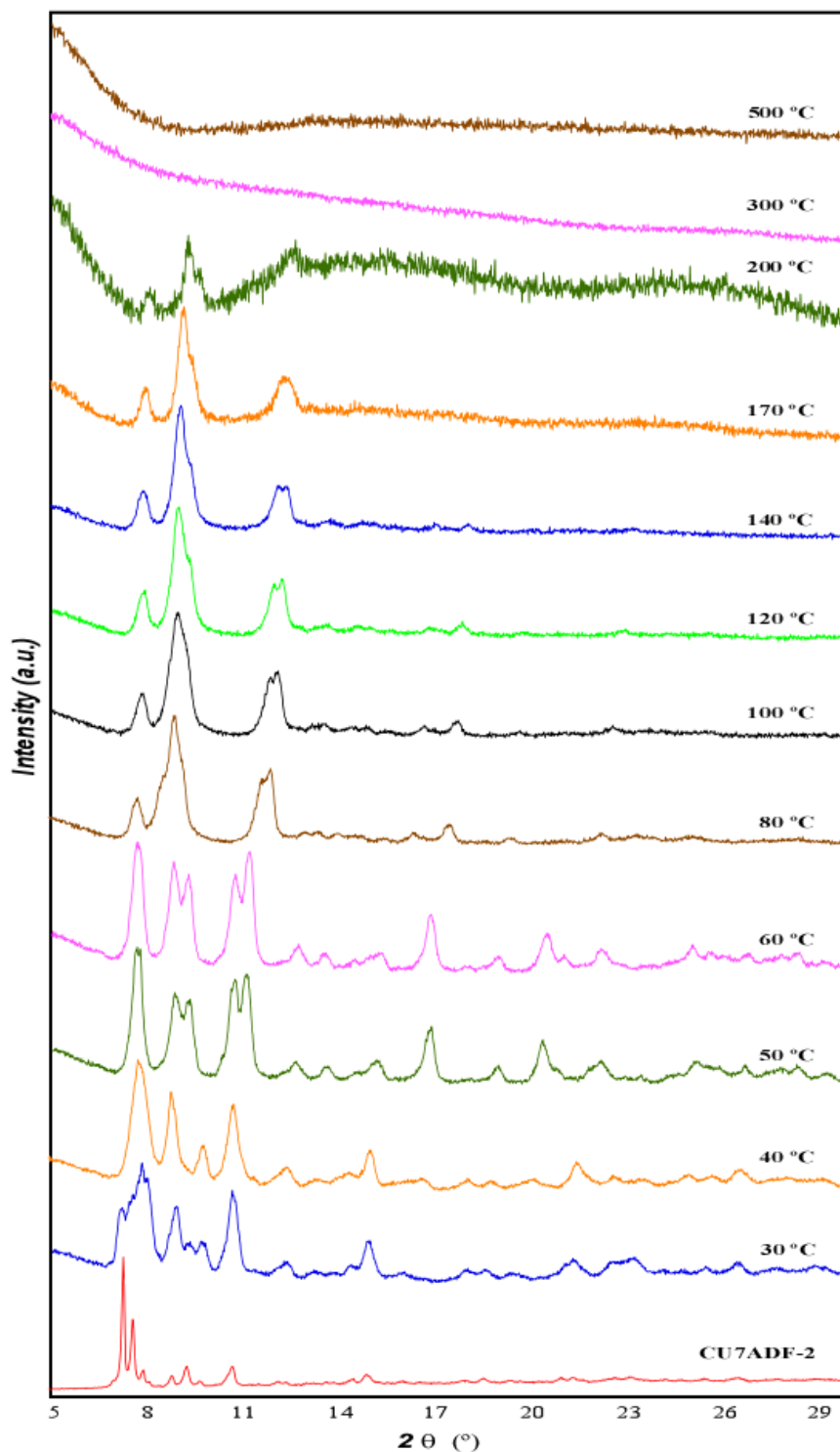
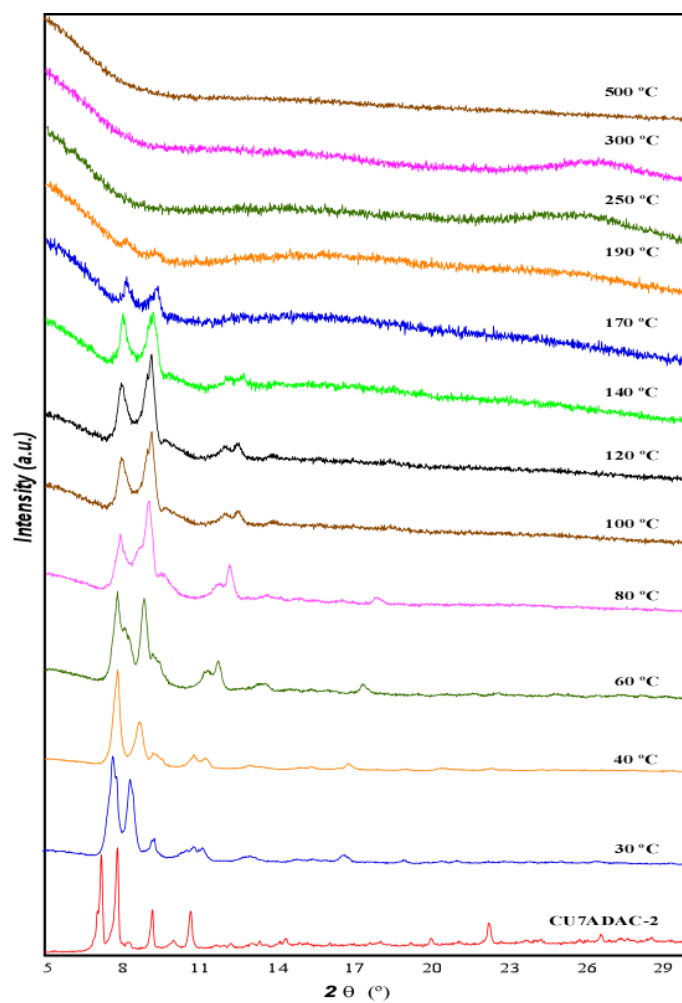
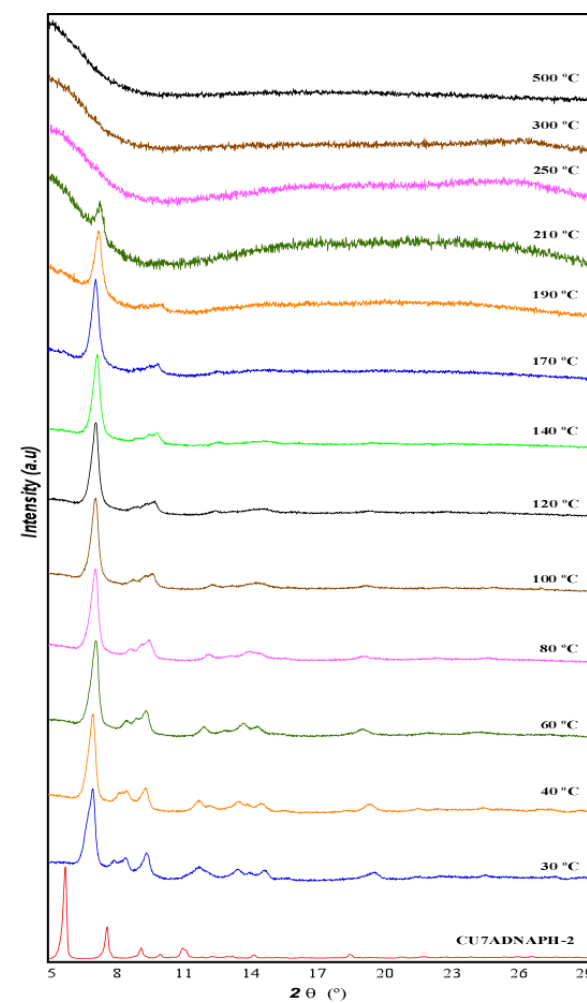


Figure 2.84. Variable-temperature X-ray diffraction patterns for CU7ADF-2.



(a)



(b)

Figure 2.85. Variable-temperature X-ray diffraction patterns for (a) CU7ADAC-2 and (b) CU7ADNAPH-2.

A small amount of crystals of CU7ADNAPH-1 initially appear during the crystallization process of CU7ADNAPH-2, which disappear over time, Table 2.49. Cationic layers sustained by π - π adeninato \cdots adeninato stacking of four adjacent adeninato entities are also present in metastable CU7ADNAPH-1 compound, but their pendant adeninato ligands interact with each other through a double N-H \cdots N hydrogen bond involving the Hoogsteen face of the nucleobase, Figure 2.86. Dicarboxylate anion is parallel stacked to both ligands and the hydrogen bonding rings R₂²(8) between its carboxylate groups and the O-H sites of the heptameric entity are still present. These supramolecular interactions also generate supramolecular boxes, with an inner cavity filled by solvation water molecules to give again a **pcu** topology and a structural porosity very similar to that found for the stable compound CU7ADNAPH-1.

Table 2.49. Distances and angles (Å, deg) for compound CU7ADNAPH-1.^a

Cu1–O1	2.099(8)	Cu1–O2	2.126(7)	Cu1–O3	1.972(6)
Cu2–O1	1.966(7)	Cu2–O3 ⁱ	1.965(7)	Cu2–N13	2.004(1)
Cu2–N29	2.015(1)	Cu2–O1w	2.423(9)	Cu2–O3w ⁱ	2.494(9)
Cu3–O1	1.957(9)	Cu3–O2	1.978(7)	Cu3–N23	2.042(1)
Cu3–N33	1.949(1)	Cu3–O1w	2.377(7)	Cu3–O2w	2.677(1)
Cu4–O2	1.969(6)	Cu4–O3	2.022(7)	Cu4–N19 ⁱ	1.979(1)
Cu4–N39	2.014(12)	Cu4–O2w	2.556(1)	Cu4–O3w	2.442(8)
Cu1 \cdots Cu2	3.101(2)	Cu1 \cdots Cu3	3.109(2)	Cu2 \cdots Cu4	3.096(2)
Cu2 \cdots Cu3	3.056(2)	Cu2 \cdots Cu4 ⁱ	3.117(2)	Cu3 \cdots Cu4	3.133(2)
Cu1–O1–Cu2	99.4(3)	Cu1–O1–Cu3	100.0(4)	Cu2–O1–Cu3	102.3(4)
Cu1–O2–Cu3	98.5(3)	Cu1–O2–Cu4	98.2(3)	Cu3–O2–Cu4	105.1(3)
Cu1–O3–Cu2 ⁱ	104.0(3)	Cu1–O3–Cu4	101.6(3)	Cu4–O3–Cu2 ⁱ	102.8(3)
Cu2–O1w–Cu4	79.1(2)	Cu3–O2w–Cu4	73.5(3)	Cu4–O3w–Cu2 ⁱ	78.3(3)

^a Symmetry: (i) 2 –x, –y, 1 –z.

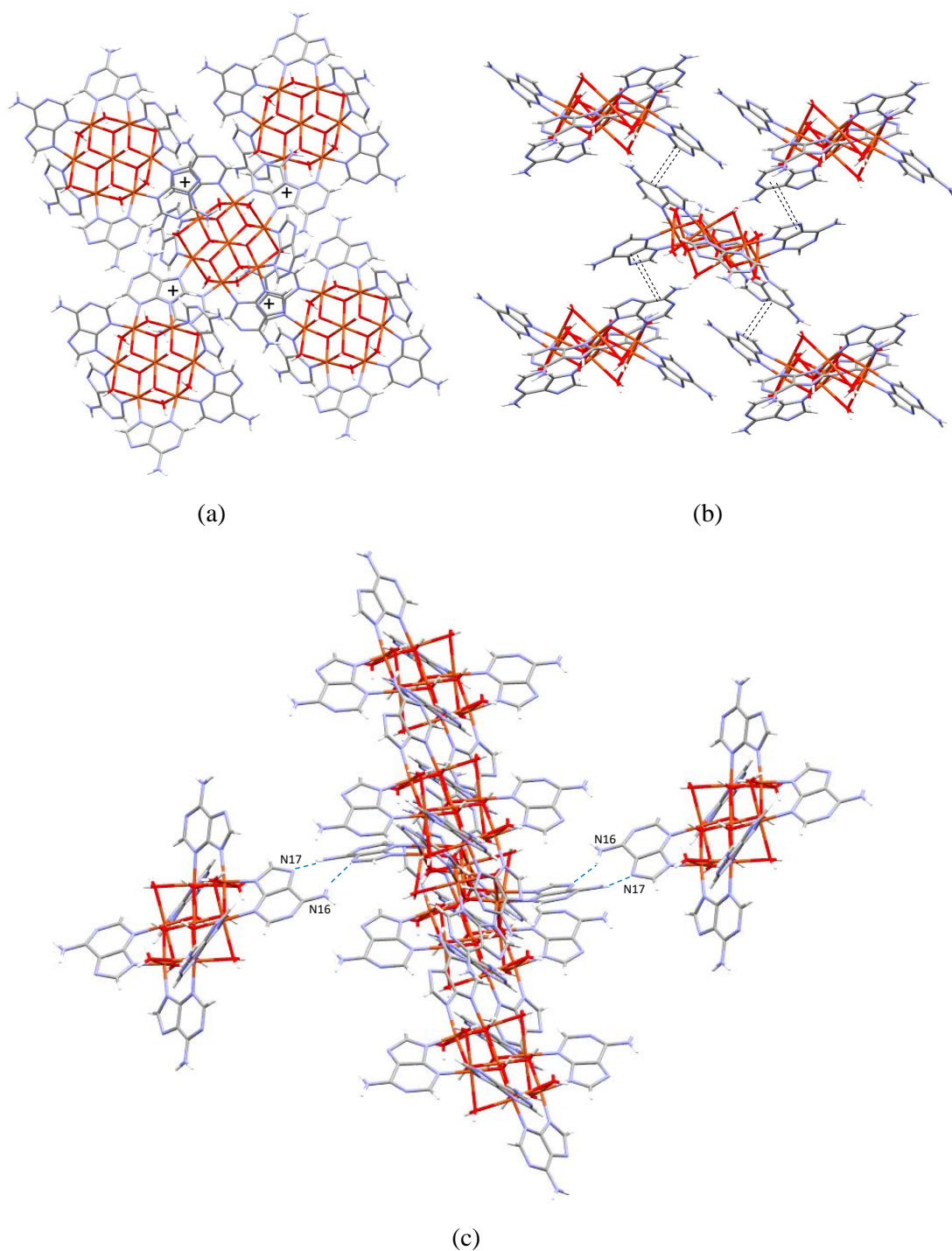


Figure 2.86. (a, b) adeninato...adeninato π -stacking interactions in CU7ADNAPH-1 and (c) hydrogen bonding interactions sustaining the porous architecture.

The carboxylate groups of the naphthalene-2,6-dicarboxylate anion are attached to the nearest cationic layer by two $O_{\text{anion}} \cdots H-O_{\text{cation}}$ hydrogen bonds, one with a hydroxide group and the other one with a water molecule coordinated to the same copper atom, to form a supramolecular $R_2^2(8)$ synthon. Additionally, the aromatic rings establish offset face-to-face π - π interactions with both adeninato moieties Figure 2.87.

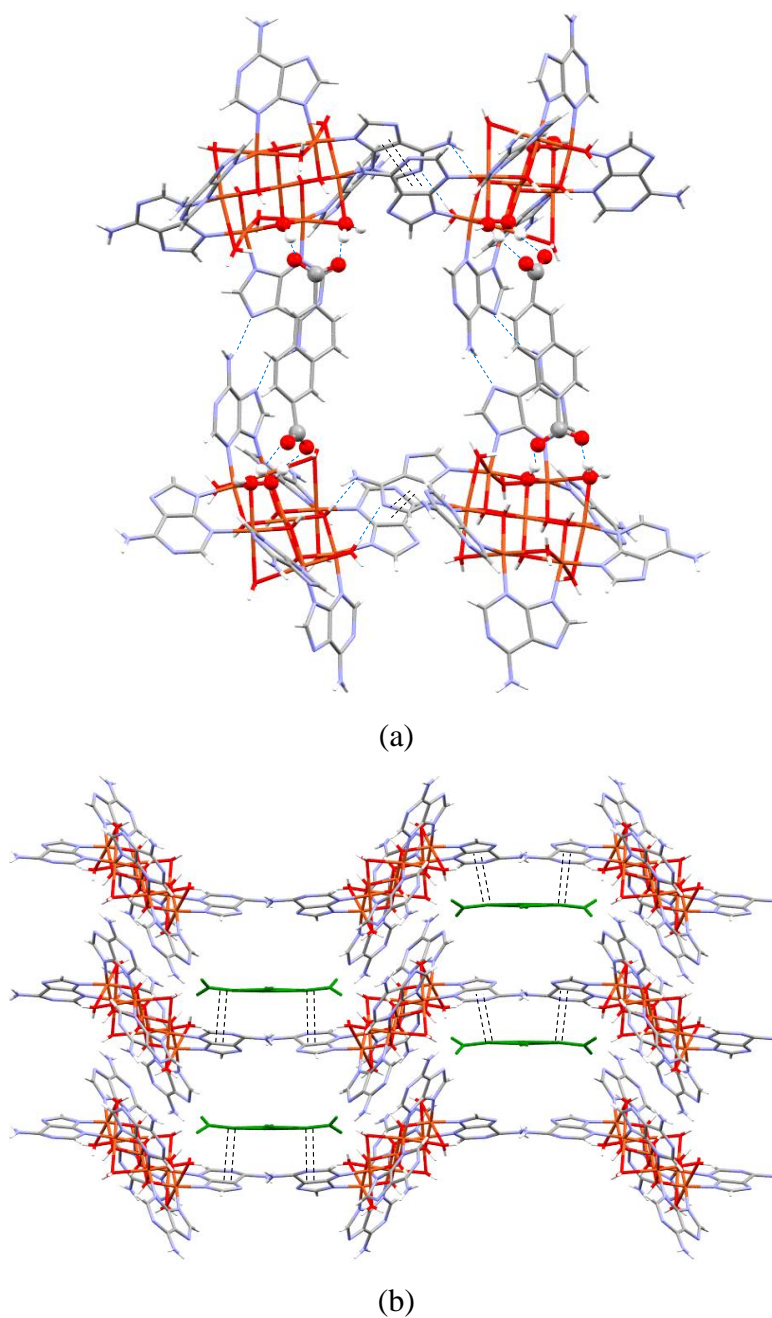


Figure 2.87. Details of the supramolecular interactions between the organic anion (green colour) and the cationic complexes in CU7ADNAPH-1.

As the compounds above described, the supramolecular interactions generate rectangular structural boxes (Figure 2.88), where the crystallization water molecules are hosted. Cationic entities are located in all the vertices of these boxes, two opposite faces are filled by the $\pi \cdots \pi$ adeninato \cdots adeninato interactions and the edges that connect them are formed by the organic anions and the adeninato hanging from the cation layers, Table 2.50. The distance between the heptameric clusters in the filled faces is *ca.* 12.1 Å as prior cases, with a longitudinal distance of 14.9 Å.

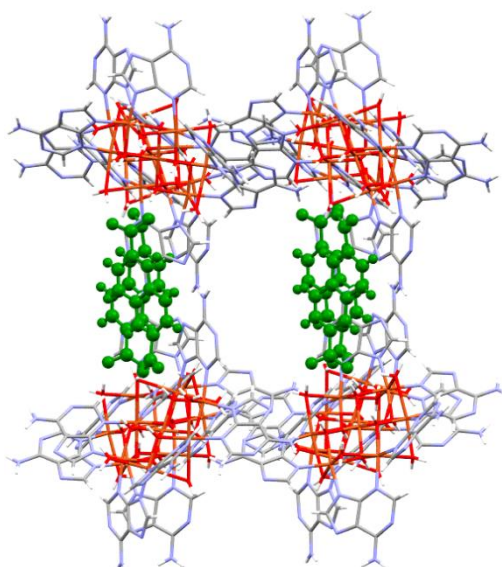


Figure 2.88. Supramolecular box in the crystal structure of CU7ADNAPH-1.

Table 2.50. Structural parameters (Å, deg) of H-bonding interactions in CU7ADNAPH-1.^a

Hydrogen-bonding interactions					
D–H···A ^b	H···A	D···A	D–H···A		
O1–H1···N36 ⁱ	2.00	2.85(2)	173		
O2–H2···O5w ⁱⁱ	1.84	2.81(1)	170		
O3–H3···O48 ⁱⁱⁱ	1.67	2.63(1)	164		
O1W–H11W···O49	1.88	2.72(1)	175		
O1W–H12W···O4w	1.88	2.77(1)	177		
O2W–H22W···O48 ⁱⁱⁱ	2.17	2.98(2)	171		
O3W–H31W···O8w ^{iv}	1.99	2.86(1)	172		
O3W–H32W···N31 ^{iv}	2.02	2.86(2)	177		
N16A–H16A···N17 ^v	2.30	3.11(2)	156		
N26A–H16A···O4w ^{vi}	1.98	2.84(2)	171		
N36–H36A···O5w ^{vi}	2.31	3.03(2)	141		
π - π interactions ^c					
ring – ring ^a	packing	angle	DC	DZ	DXY
1pa···3pa ^{vii}	A···A	6.4	4.28	3.65	2.34
2pa···1hd ^{viii}	A···A	4.0	3.86	3.60	1.65
2pa···2hd ^{ix}	A···A	4.0	3.86	5.49	1.42

^aSymmetry codes: (i) $3/2 - x, -1/2 + y, z$; (ii) $3/2 - x, 1/2 + y, z$; (iii) $2 - x, -y, 1 - z$; (iv) $1/2 + x, 1/2 - y, 1 - z$; (v) $2 - x, y, 1/2 - z$; (vi) $1 - x, -y, 1 - z$; (vii) $2 - x, 1/2 + y, 5/2 - z$; (viii) x, y, z ; (ix) $3 - x, -y, 2 - z$. ^bD: donor; A: acceptor. ^cAngle: dihedral angle between the planes (deg), DC: distance between the centroids of the rings (Å), DZ: interplanar distance (Å), DXY: lateral displacement (Å), pa: adenine pentagonal ring, ha: adenine hexagonal ring.

The resulting supramolecular architecture of CU7ADNAPH-1 follows the lead of the isorecticular series with some minimal changes as shown in Figure 2.89. The pores of $7.1 \times 7.9 \text{ \AA}$ with 4.1 \AA corridors form a 2D network that correspond to 4171 \AA^3 per unit cell (44%) and a calculated accessible surface area of $877 \text{ m}^2 \cdot \text{g}^{-1}$ with a void volume of $0.375 \text{ cm}^3 \cdot \text{g}^{-1}$, Figure 2.90.

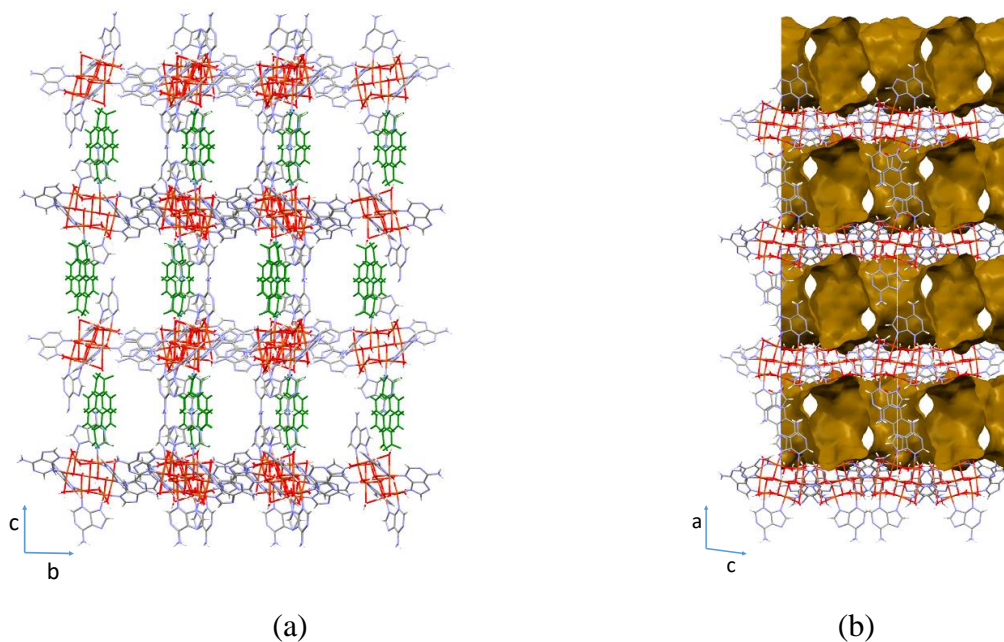


Figure 2.89. Image showing the channels of CU7ADNAPH-1.

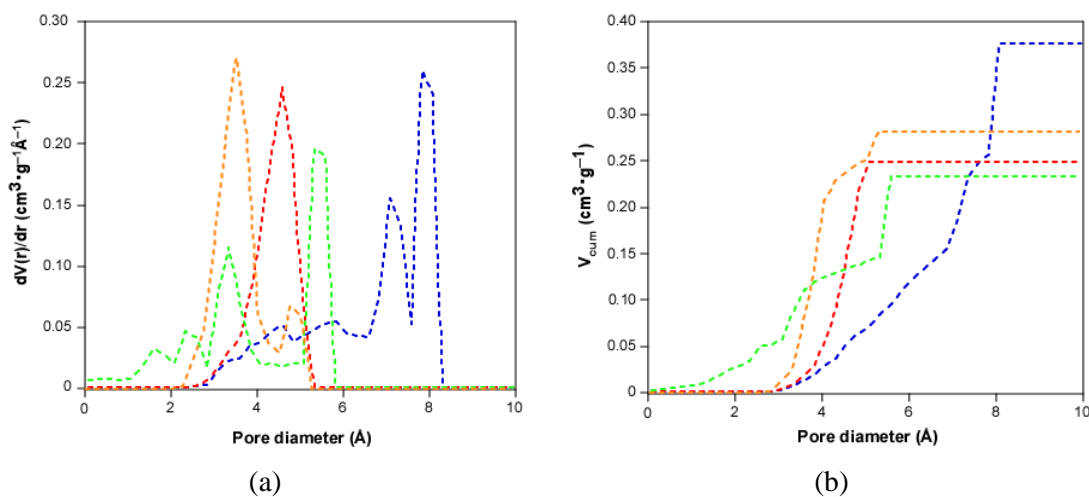


Figure 2.90. (a) Derivative representation of the geometric pore volume and (b) cumulative representation of the geometric pore volume of compounds CU7ANAPH-1 (blue), CU7ADS (orange), CU7ADBPD (red) and CU7ADSD (green).

Compound CU7ADS with the stilbene-4,4'-dicarboxylate anion does not exhibit the above described isorecticular framework, Table 2.51. Cationic chains sustained by π - π adeninato \cdots adeninato stacking of four adjacent adeninato entities, two adeninato ligands generate a double π - π stacking interactions with an adjacent cluster, and the remaining pendant adeninato generate a offset face-to-face π - π stacks with another two cluster belonging to adjacent chains. This last interaction is reinforced by a double hydrogen bonding interactions between the amino N66 group and the O5w coordination water molecule of the cluster in one side and with the N36 group and a hydroxide and coordination water molecule of another cluster, Figure 2.91.

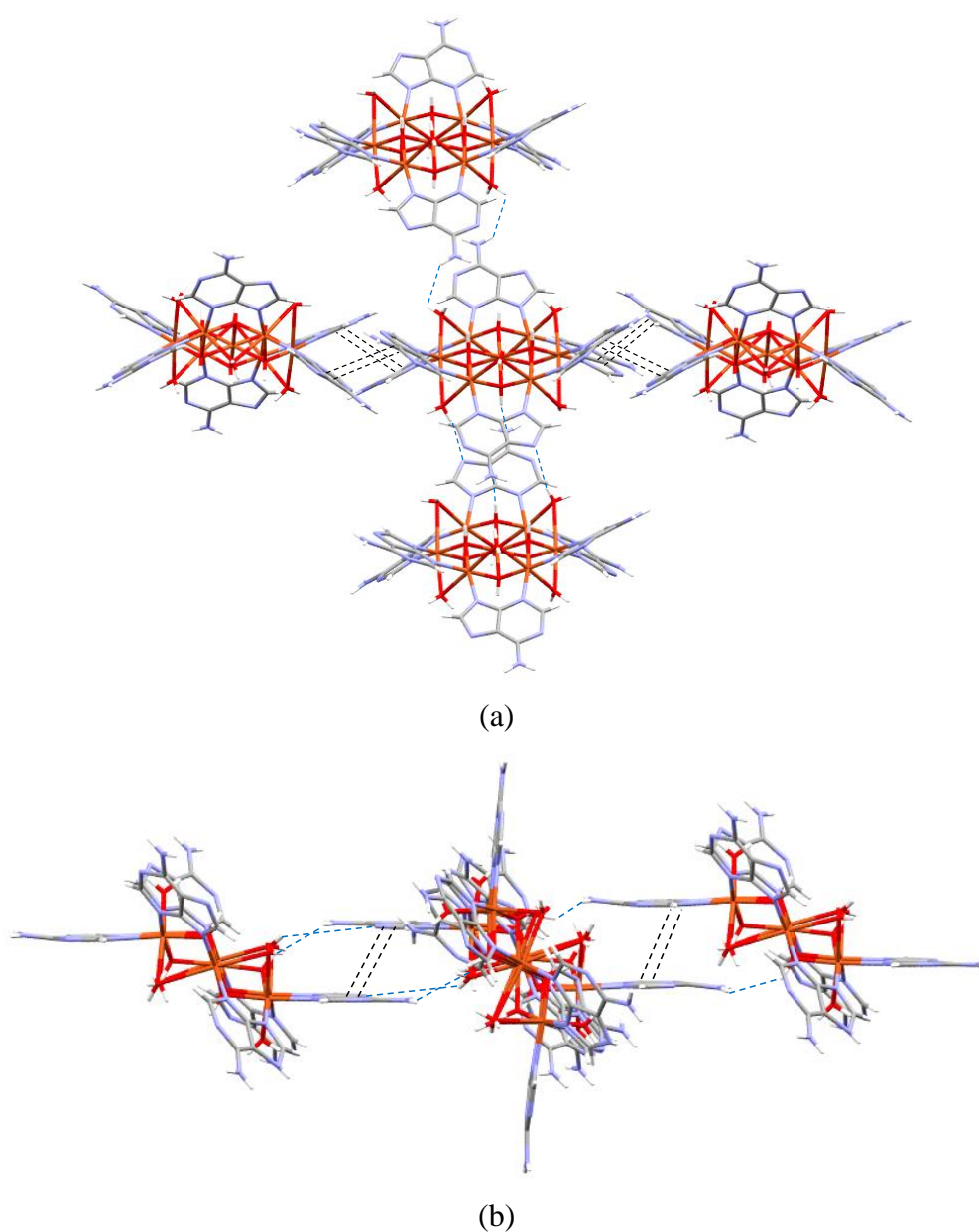


Figure 2.91. Supramolecular interaction sustaining the porous architecture and adeninato \cdots adeninato π -stacking interactions in CU7ADS.

Table 2.51. Distances and angles (Å, deg) for compound CU7ADS.^a

Cu1–O1	2.044(8)	Cu1–O2	2.160(6)	Cu1–O3	2.011(6)
Cu1–O4	2.104(6)	Cu1–O5	2.091(8)	Cu1–O6	2.023(6)
Cu2–O1	1.973(7)	Cu2–O6	1.978(8)	Cu2–N13	1.991(1)
Cu2–N69	1.981(9)	Cu2–O1w	2.530(7)	Cu2–O6w	2.469(7)
Cu3–O1	1.961(8)	Cu3–O2	1.915(6)	Cu3–N19	1.933(1)
Cu3–O23	2.007(1)	Cu3–O1w	2.413(8)	Cu3–O2w	2.772(8)
Cu4–O2	2.011(6)	Cu4–O3	1.954(5)	Cu4–N29	1.969(1)
Cu4–O39	2.009(8)	Cu4–O2w	2.649(8)	Cu4–O3w	2.471(8)
Cu5–O3	1.976(6)	Cu5–O4	1.982(6)	Cu5–N33	2.026(8)
Cu5–O43	2.006(1)	Cu5–O3w	2.437(7)	Cu5–O4w	2.537(7)
Cu6–O4	1.950(6)	Cu6–O5	1.968(8)	Cu6–N49	2.000(1)
Cu6–O53	1.989(1)	Cu6–O4w	2.668(6)	Cu6–O5w	2.397(6)
Cu7–O5	1.960(7)	Cu7–O6	1.956(7)	Cu7–N59	1.982(1)
Cu7–O63	2.002(9)	Cu7–O5w	2.498(6)	Cu7–O6w	2.490(8)
Cu1···Cu2	3.091(2)	Cu1···Cu3	3.127(2)	Cu1···Cu4	3.119(2)
Cu1···Cu5	3.101(2)	Cu1···Cu6	3.130(2)	Cu1···Cu7	3.092(2)
Cu2···Cu3	3.125(2)	Cu2···Cu7	3.137(2)	Cu3···Cu4	3.089(2)
Cu4···Cu5	3.133(2)	Cu5···Cu6	3.099(2)	Cu6···Cu7	3.082(2)
Cu1–O1–Cu2	100.6(4)	Cu1–O1–Cu3	102.7(3)	Cu2–O1–Cu3 ⁱ	105.2(4)
Cu1–O2–Cu3	100.1(3)	Cu1–O2–Cu4	96.7(2)	Cu3–O2–Cu4	103.8(3)
Cu1–O3–Cu4	103.8(3)	Cu1–O3–Cu5	102.1(3)	Cu4–O3–Cu5	105.7(2)
Cu1–O4–Cu5	98.7(3)	Cu1–O4–Cu6	101.0(3)	Cu5–O4–Cu6	104.1(3)
Cu1–O5–Cu6	100.9(3)	Cu1–O5–Cu7	99.5(4)	Cu6–O5–Cu7	103.4(4)
Cu1–O6–Cu2	101.1(3)	Cu1–O6–Cu7	102.0(3)	Cu2–O6–Cu7	105.8(3)
Cu2–O1w–Cu3	78.4(2)	Cu3–O2w–Cu4	69.4(2)	Cu4–O3w–Cu5	79.3(2)
Cu5–O4w–Cu6	73.1(2)	Cu6–O5w–Cu7	78.1(2)	Cu2–O6w–Cu7	78.49(2)

The organic anion is located between four clusters that are held together by a combination of complementary hydrogen bonding and π – π stacking interactions. Dicarboxylate anion is parallel stacked to both adeninato ligands and the hydrogen bonding rings $R_2^2(8)$ between its carboxylate groups and the O–H sites of the heptameric entity are still present in one of the side on the anion. The other carboxylate group interacts with a hydroxide group of the cluster and with a crystallization water molecule, Figure 2.90a. Thanks to its flexible shape, the anion is rotated as necessary to be able to interact with two adeninato ligands from two different clusters, Figure 2.92b.

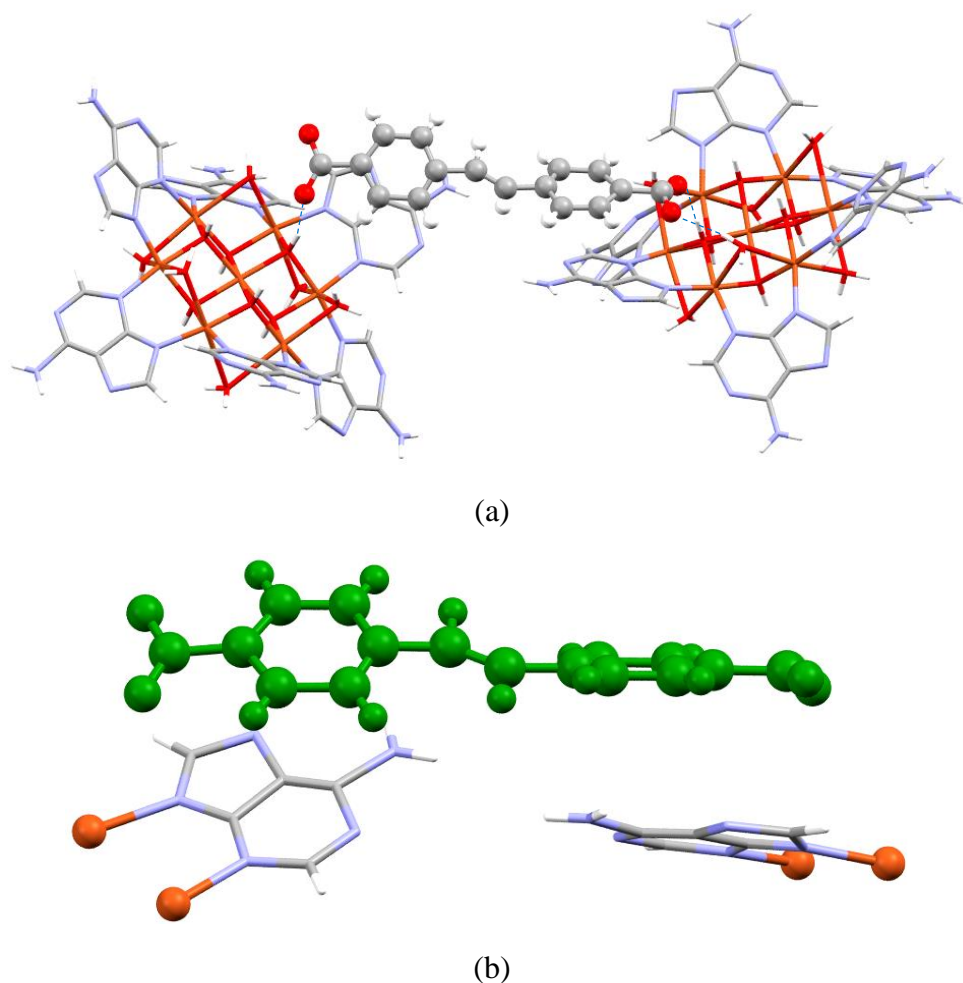


Figure 2.92. Interactions of the stilbene-4, 4'-dicarboxylate anion with the adeninato ligands.

The previously described sandwich adeninato...organic anion...adeninato is not present in this compound. Instead of that, as in the previous compound CU7ADNAPH-2, the two adeninato ligands are placed at the same side of the dicarboxylate anions (Figure 2.93), Table 2.52.

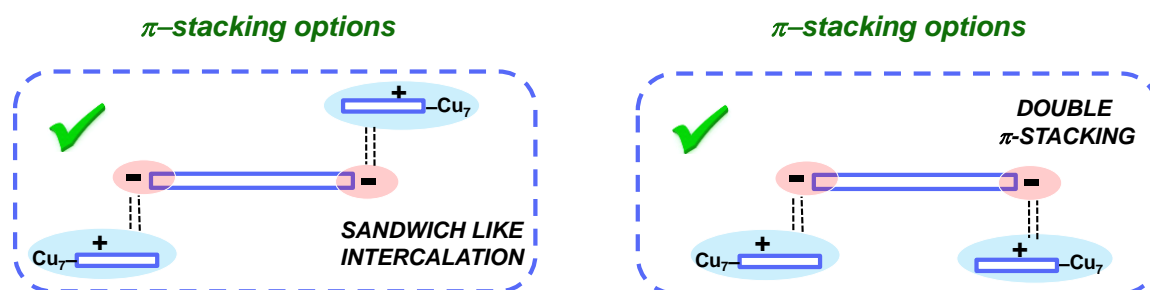


Figure 2.93. Scheme of the different π -stacking interactions between isorecticular compounds and those ones with flexible dicarboxylate anions.

Table 2.52. Structural parameters (\AA , deg) of hydrogen bonding interactions in CU7ADS.^a

Hydrogen-bonding interactions					
D–H...A^b		H...A	D...A	D–H...A	
O1–H1...O78		1.76	2.73(2)	168	
O3–H3...N36A ⁱ		1.96	2.92(1)	166	
O4–H4...O89 ⁱⁱ		1.83	2.77(2)	159	
O2W–H22W...O79		2.23	3.03(2)	160	
O4W–H42W...N37 ⁱ		2.36	3.12(1)	146	
O5W–H52W...O88 ⁱⁱ		2.44	3.14(2)	139	
O5W–H52W...O88 ⁱⁱ		2.24	3.07(2)	159	

π–π interactions^c					
ring–ring^a	packing	angle	DC	DZ	DXY
1pa...5pa ⁱⁱⁱ	A...A	8.3	5.34	3.14	3.84
1pa...7hd ^{iv}	A...S	15.7	4.30	3.19	2.68
2pa...4pa ⁱⁱⁱ	A...A	6.9	5.34	3.15	3.91
3pa...3pa ⁱ	A...A	0.0	4.40	3.58	2.56
4pa...8hd ⁱⁱⁱ	A...S	4.9	4.06	3.43	1.90

^aSymmetry codes: (i) $2 - x, -y, 2 - z$; (ii) $1 + x, 1/2 - y, 1/2 + z$; (iii) $x, 1/2 - y, -1/2 + z$; (iv) x, y, z . ^bD: donor; A: acceptor. ^cAngle: dihedral angle between the planes (deg), DC: distance between the centroids of the rings (\AA), DZ: interplanar distance (\AA), DXY: lateral displacement (\AA), pa: adenine pentagonal ring, ha: adenine hexagonal ring, hd: anion hexagonal ring.

The crystal building presents a two-dimensional network of channels, (Figure 2.94) filled by crystallization water molecules, with a degree of porosity (excluding water molecules) of 34%, not as much that we could expect with the presence of this anion if we extrapolate the value of the isorecticular compounds. The voids consist of pores of dimensions $3.6 \times 5.1 \text{ \AA}$ connected by smaller windows of 3.1 \AA that accounts for 2943 \AA^3 . Computational analyses indicate a theoretical surface area of $80.6 \text{ m}^2 \cdot \text{g}^{-1}$ and a pore volume of $0.282 \text{ cm}^3 \cdot \text{g}^{-1}$, Figure 2.90.

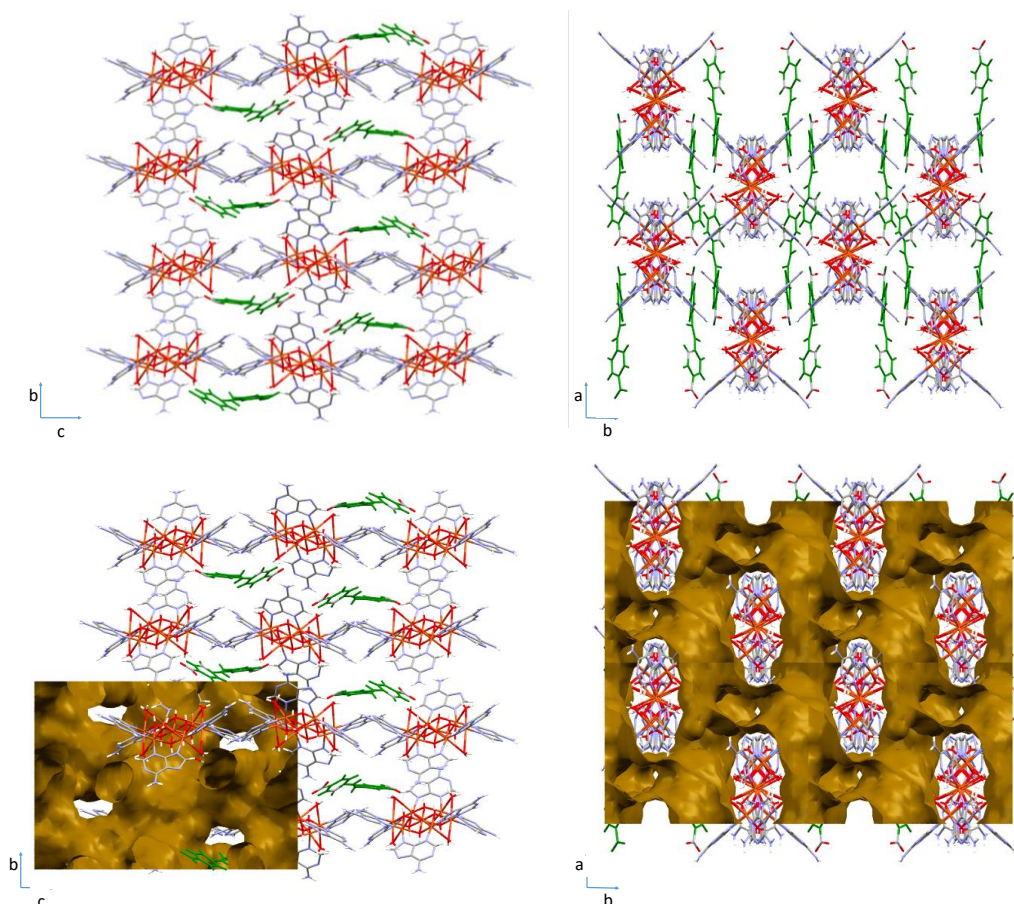


Figure 2.94. Images showing the channels of CU7ADS.

Compounds CU7ADBPD and CU7ADSD maintain the above-described supramolecular interactions with some differences due to the presence of DMF molecules, Table 2.53 and 2.54. Each heptameric cation of CU7ADBPD compound is surrounded by six other ones; four of them interacting through offset face-to-face π - π stacks (Figure 2.95a). These stacking interactions are reinforced by a hydrogen-bonded $R_2^2(8)$ ring formed by two N-H \cdots N interactions between the pyrimidinic N1 and exocyclic N6 nitrogen atoms of the Watson-Crick face of both adeninato ligands not included in prior π - π interactions. The amino group of these *trans* adeninato ligands of the cluster also establish hydrogen bond interactions with the oxygen atom of the DMF molecule, Figure 2.95b, Tables 2.55 and 2.56. Both dicarboxylate anions follow the above described situation where the sandwich interaction is described in Figure 2.93.

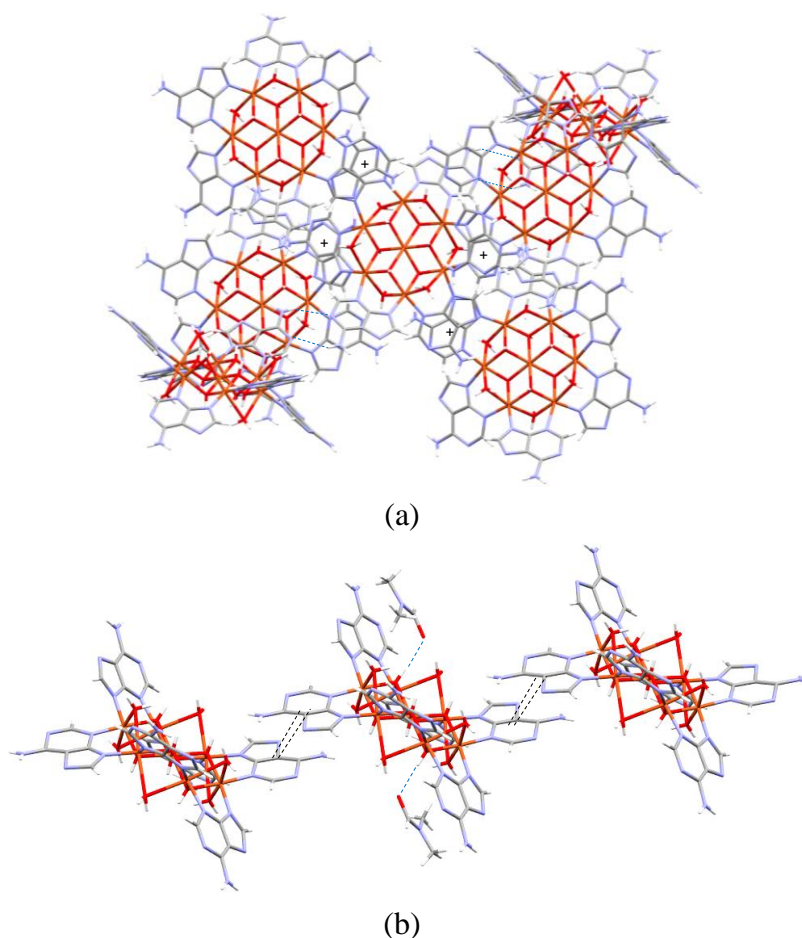


Figure 2.95. Supramolecular cationic layer formed by heptameric complexes in compounds CU7ADBPD (a) and CU7ADSD (b).

Table 2.53. Distances and angles (Å, deg) for compound CU7ADBPD.^a

Cu1–O1	2.047(7)	Cu1–O2	1.994(7)	Cu1–O3	2.110(9)
Cu2–O2 ⁱ	1.979(9)	Cu2–O3	1.926(8)	Cu2–N19	1.937(1)
Cu2–N23 ⁱ	2.199(2)	Cu2–O1w	2.523(9)	Cu2–O3w	2.505(1)
Cu3–O1	1.954(9)	Cu3–O3	1.986(8)	Cu3–N29A	1.910(1)
Cu3–N33	2.000(1)	Cu3–O1w	2.578(9)	Cu3–O2w	2.436(1)
Cu4–O1	1.967(7)	Cu4–O2	1.938(8)	Cu4–N13 ⁱ	2.001(1)
Cu4–N39	1.970(1)	Cu4–O2w	2.479(9)	Cu4–O3w ⁱ	2.547(1)
Cu1⋯Cu2	3.097(2)	Cu1⋯Cu3	3.149(2)	Cu1⋯Cu4	3.076(2)
Cu2⋯Cu3	3.085(3)	Cu2⋯Cu4 ⁱ	3.148(2)	Cu3⋯Cu4	3.090(2)
Cu1–O1–Cu3	103.8(3)	Cu1–O1–Cu4	100.0(3)	Cu3–O1–Cu4	104.0(4)
Cu1–O2–Cu4	101.3(3)	Cu1–O2–Cu2 ⁱ	102.4(4)	Cu4–O2–Cu2 ⁱ	105.2(4)
Cu1–O3–Cu2	100.2(4)	Cu1–O3–Cu3	100.5(3)	Cu2–O3–Cu3	104.1(3)
Cu2–O1w–Cu3	74.4(2)	Cu3–O2w–Cu4	77.9(3)	Cu2–O3w–Cu4 ⁱ	77.1(3)

^aSymmetry: (i) 1 – x, – y, 1 – z.

Table 2.54. Distances and angles (Å, deg) for compound CU7ADSD.^a

Cu1–O1	2.268(6)	Cu1–O2	1.970(6)	Cu1–O3	1.978(7)
Cu2–O1	1.942(7)	Cu2–O3 ⁱ	1.980(6)	Cu2–N19	1.988(1)
Cu2–N33 ⁱ	1.974(1)	Cu2–O1w	2.577(9)	Cu2–O3w ⁱ	2.471(8)
Cu3–O1	1.935(6)	Cu3–O2	1.989(6)	Cu3–N13	2.028(1)
Cu3–N29	1.958(1)	Cu3–O1w	2.456(9)	Cu3–O2w	2.515(1)
Cu4–O2	1.957(7)	Cu4–O3	1.978(6)	Cu4–N23	2.004(1)
Cu4–N39	1.926(1)	Cu4–O2w	2.541(9)	Cu4–O3w	2.469(8)
Cu1···Cu2	3.149(1)	Cu1···Cu3	3.178(1)	Cu1···Cu4	3.011(1)
Cu2···Cu3	3.044(2)	Cu2···Cu4 ⁱ	3.145(2)	Cu3···Cu4	3.152(2)
Cu1–O1–Cu2	96.6(3)	Cu1–O1–Cu3	97.9(3)	Cu2–O1–Cu3	103.5(3)
Cu1–O2–Cu3	106.8(3)	Cu1–O2–Cu4	100.1(3)	Cu3–O2–Cu4	106.0(3)
Cu1–O3–Cu2 ⁱ	105.5(3)	Cu1–O3–Cu4	99.1(3)	Cu4–O3–Cu2 ⁱ	105.2(3)
Cu2–O1w–Cu3	74.4(2)	Cu3–O2w–Cu4	77.1(3)	Cu4–O3w–Cu2 ⁱ	79.1(2)

^a Symmetry: (i) 1 – x, – y, – z.**Table 2.55.** Structural parameters (Å, deg) of hydrogen bonding interactions in CU7ADBPD.^a

Hydrogen-bonding interactions					
D–H···A ^b	H···A	D···A	D–H···A		
O1–H1···O5w ⁱ	1.92	2.78(1)	168		
O2–H2···O4w ⁱⁱ	1.95	2.79(1)	168		
O3–H3···O48	2.12	2.96(2)	169		
O1W–H11W···O4w ⁱⁱⁱ	2.20	2.91(1)	143		
O1W–H12W···O6w	2.03	2.89(2)	170		
O2W–H21W···O48	2.04	2.87(2)	160		
O2W–H22W···O7w	1.91	2.74(3)	171		
O3W–H31W···O8w	1.74	2.53(3)	156		
O3W–H32W···O5w ^{iv}	2.05	2.91(2)	161		
N16–H16A···O5w	2.48	3.26(2)	152		
N26A–H16A···N21A ^v	2.53	3.30(3)	148		
π – π interactions ^c					
ring–ring ^a	packing	angle	DC	DZ	DXY
1pa···3pa ⁱⁱⁱ	A···A	11	4.13	3.69	2.18
2pa···1hd ^{vi}	A···B	71	5.36	0.04	0
2pa···1hd ^{vii}	A···B	72	5.87	4.99	0

^aSymmetry codes: (i) 1 – x, 1/2 + y, 1/2 – z; (ii) x, 1/2 – y, – 1/2 + z; (iii) 1 – x, – 1/2 + y, 1/2 – z; (iv) x, – 1/2 – y, 1/2 + z, (v) 3/2 – x, – 1/2 – y, z, (vi) x, y, z, (vii) 3/2 – x, y, – 1/2 + z. ^bD: donor; A: acceptor. ^cAngle: dihedral angle between the planes (deg), DC: distance between the centroids of the rings (Å), DZ: interplanar distance (Å), DXY: lateral displacement (Å), pa: adenine pentagonal ring, ha: adenine hexagonal ring, hd: anion hexagonal ring.

Table 2.56. Structural parameters (Å, deg) of hydrogen bonding interactions in CU7ADSD.^a

Hydrogen-bonding interactions					
D–H...A ^b		H...A	D...A	D–H...A	
O1–H1...O52		2.13	2.99(2)	171	
O2–H2...O48 ⁱ		1.84	2.69(1)	172	
O3–H3...O4w ⁱⁱ		1.91	2.79(1)	168	
O1W–H11W...O8w ⁱⁱⁱ		1.94	2.77(2)	168	
O1W–H12W...O49 ⁱ		1.99	2.86(1)	175	
O2W–H21W...O52		2.04	2.86(2)	159	
O2W–H22W...O5w		1.89	2.82(2)	160	
O3W–H31W...O48 ⁱ		2.10	2.93(1)	168	
O3W–H32W...O6w		1.84	2.73(2)	163	
N16–H16A...O12w		2.29	3.12(3)	162	
N16–H16B...O13w ^{iv}		2.13	2.87(3)	144	
N26–H26A...O11w		2.32	3.15(3)	161	
π – π interactions ^c					
ring – ring ^a	packing	angle	DC	DZ	DXY
1pa...2pa ⁱⁱⁱ	A...A	5.6	5.62	3.10	4.39
3pa...3pa ^v	A...A	0	5.62	3.43	4.46
2pa...2hd ⁱ	A...S	12.7	4.65	3.72	2.80

^aSymmetry codes: (i) $1/2 + x, -1/2 + y, z$; (ii) $1/2 - x, 1/2 - y, -z$; (iii) $1 - x, y, 1/2 - z$; (iv) $2 - x, y, 1/2 - z$; (v) $3/2 - x, 1/2 - y, -z$; (vi) $1 - x, -y, 1 - z$; (vii) $2 - x, 1/2 + y, 5/2 - z$; (viii) x, y, z ; (ix) $3 - x, -y, 2 - z$. ^bD: donor; A: acceptor. ^cAngle: dihedral angle between the planes (deg), DC: distance between the centroids of the rings (Å), DZ: interplanar distance (Å), DXY: lateral displacement (Å), pa: adenine pentagonal ring, ha: adenine hexagonal ring, hd: anion hexagonal ring.

The carboxylate groups of the biphenyl-4,4'-dicarboxylate anion are attached to the nearest cationic layer by two O_{anion}...H–O_{cation} hydrogen bonds, one with a hydroxide group and the other one with a water molecule coordinated to the same copper atom, to form a supramolecular R₂²(6) synthon, Figure 2.96a. In this interaction only takes part one of the two oxygen atoms of each carboxylate group instead of both of them. Moreover, the aromatic rings of the dicarboxylate anions are not longer parallel arranged with respect to the adeninato ligands, instead of that they are perpendicularly oriented and establish C–H– π interactions with two adeninato moieties from two adjacent heptameric entity, Figure 2.97. The other two *trans* adeninato ligands that do not interact with other clusters, establish π – π stacking interactions with the dicarboxylate anion. Due to the lack of rigidity in the central part of this ligand, it can be flexed in order to interact with adeninato ligands, Figure 2.96b.

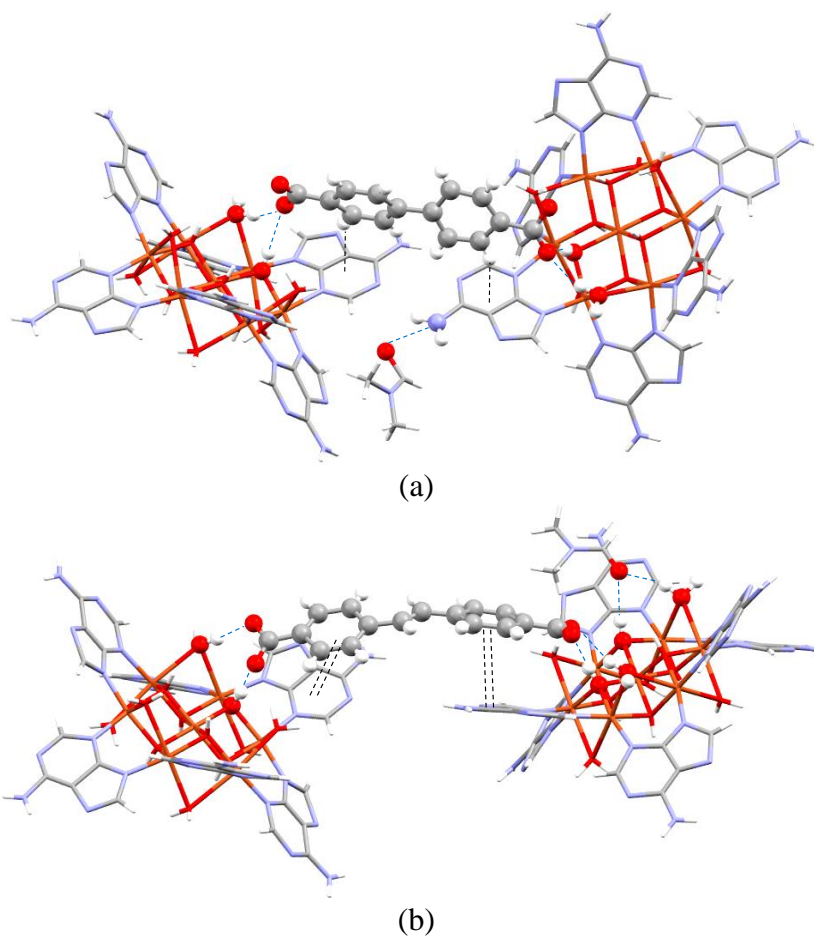


Figure 2.96. Details of the supramolecular interactions between the organic anion and the cationic complexes in compounds: (a) CU7ADBPD and (b) CU7ADSD.

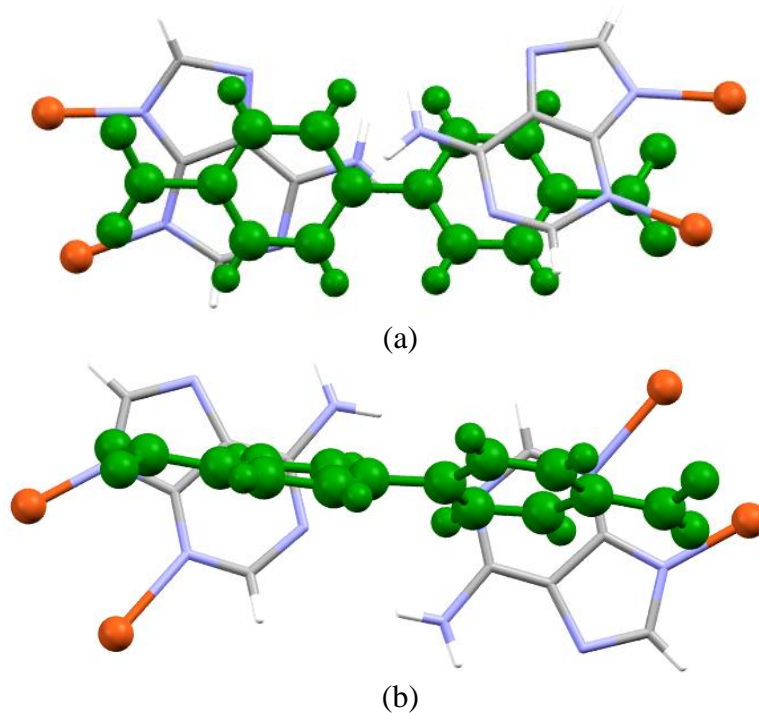


Figure 2.97. Interactions of the biphenyl-4, 4'-dicarboxylate anion with the adeninato ligands in compounds (a) CU7ADBP and (b) CU7ADBP.

This new arrangement of the dicarboxylate anions prevent the boxes described for previous compounds. In CU7ADBPD, the anion is located between four clusters that are held together by a combination of complementary hydrogen bonding interactions between the adenines and π - π stacking interactions, Figure 2.98. The crystal building presents a two-dimensional network of channels, (Figure 2.99 and 2.100) filled by water and DMF molecules, with a degree of porosity (excluding water molecules) of 31 and 32%, respectively. This porosity increases up to 40 and 42% if the DMF molecules are excluded. In any case, these values are much lower than would be expected for the isorecticular structure taking into account the size of the corresponding organic anion. The voids consist of pores of dimensions 4.6 and 3.4 x 5.6 Å connected by smaller windows of 4.1 and 3.0 Å that accounts for 2916 and 3125 Å³, respectively. Computational analyses indicate a theoretical surface area of 438 and 177 m²·g⁻¹ and a pore volume of 0.247 and 0.251 cm³·g⁻¹ respectively, Figure 2.90.

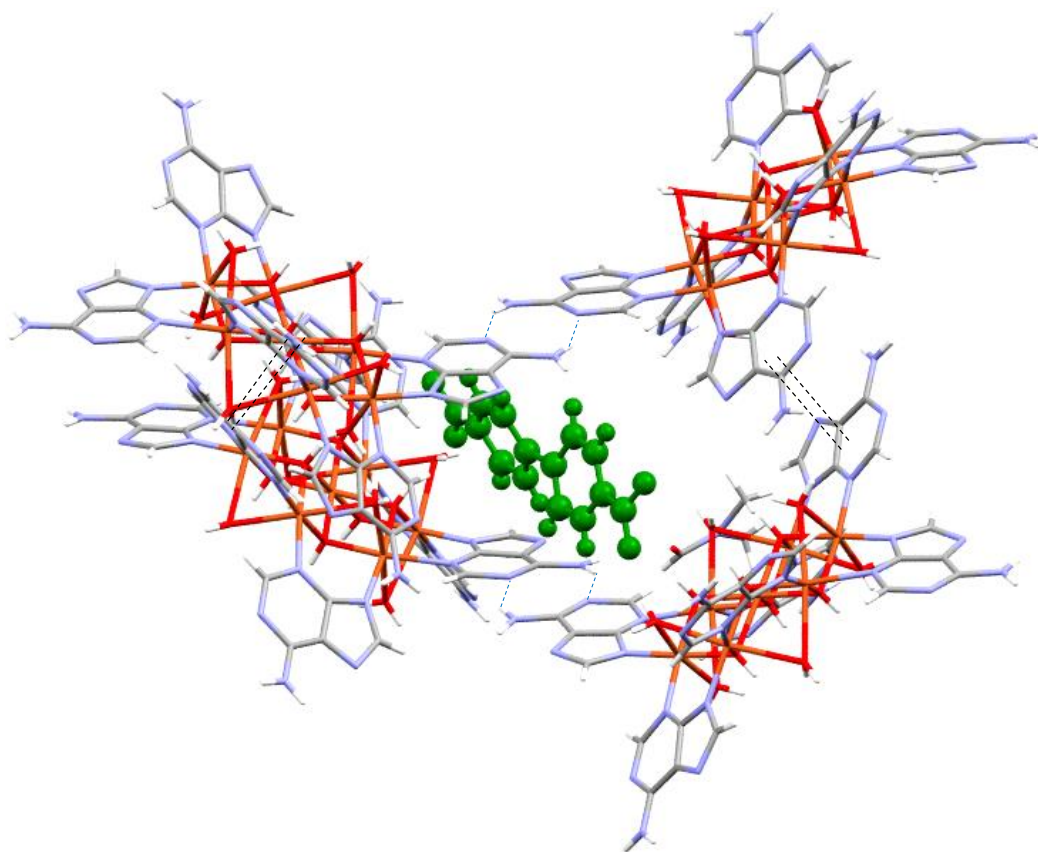


Figure 2.98. Supramolecular box present in the crystal structure of CU7ADBPD in which the dicarboxylate anion is encapsulated.

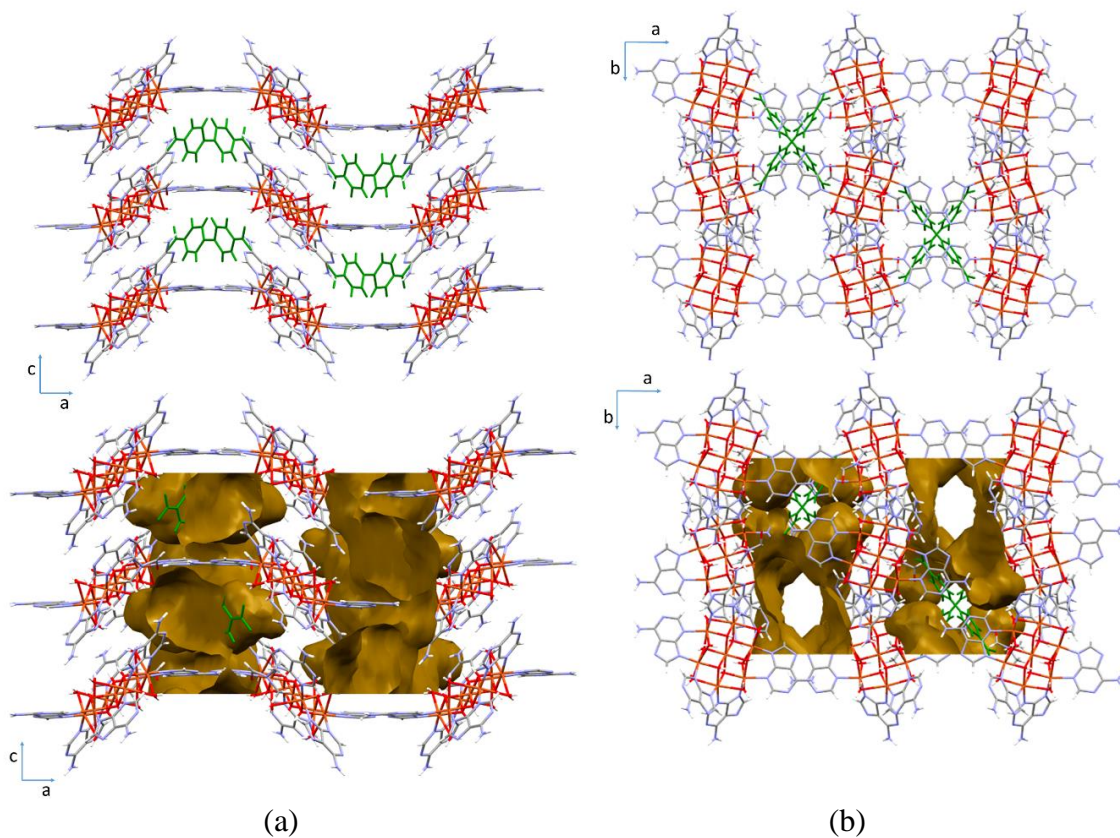


Figure 2.99. Images showing the channels of CU7ADBPD.

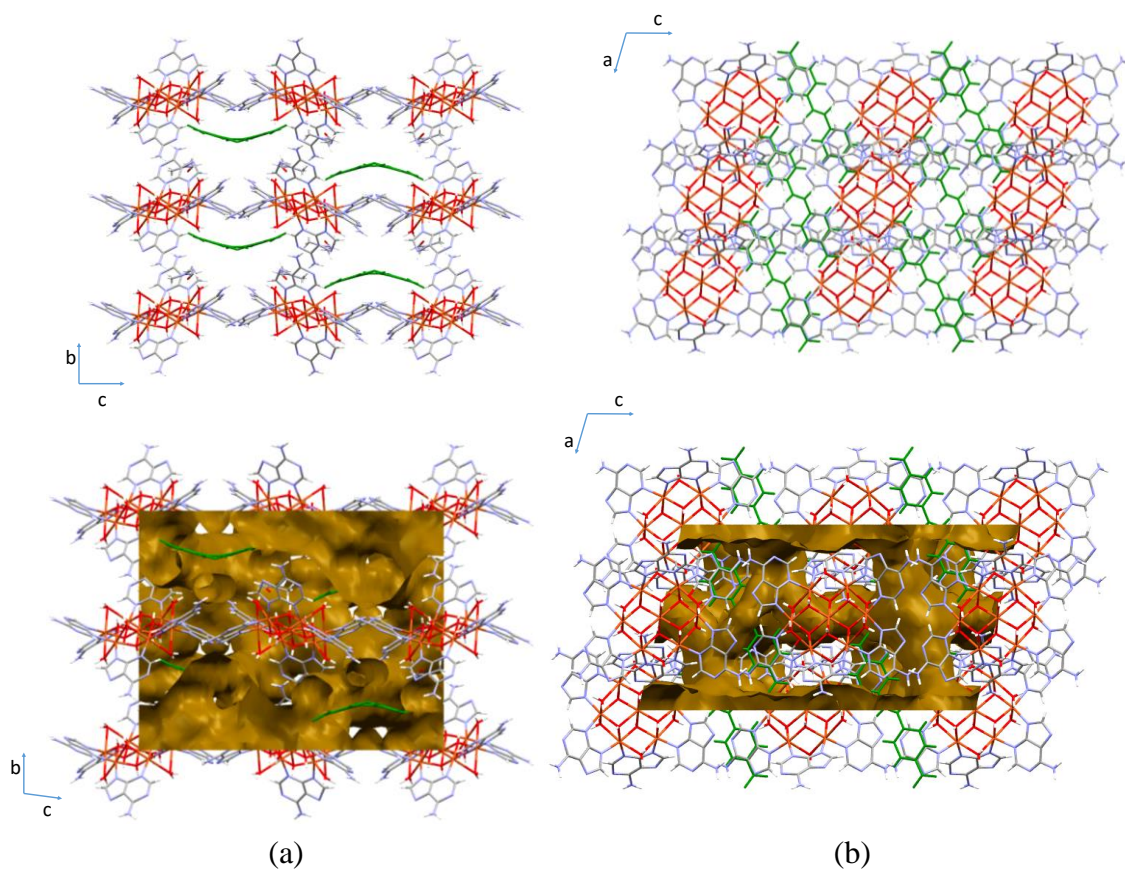


Figure 2.100. Images showing the channels of CU7ADSD.

The thermoanalytical (Figure 2.15 f-h and Table 2.8 and 2.9) and variable-temperature X-ray diffraction data of CU7ADBPD and CU7ADSD, Figure 2.101 and 2.102, show that the release of the crystallization water molecules implies a substantial structural change at a value around 50 °C. In all the compounds the crystallinity remains until a value greater than 200 °C. In the case of the compound without the dimethylformamide solvent molecule CU7ADS (figure 2.102a), the crystallinity keeps with a great intensity values until high temperatures and the peaks remain almost unchanged.

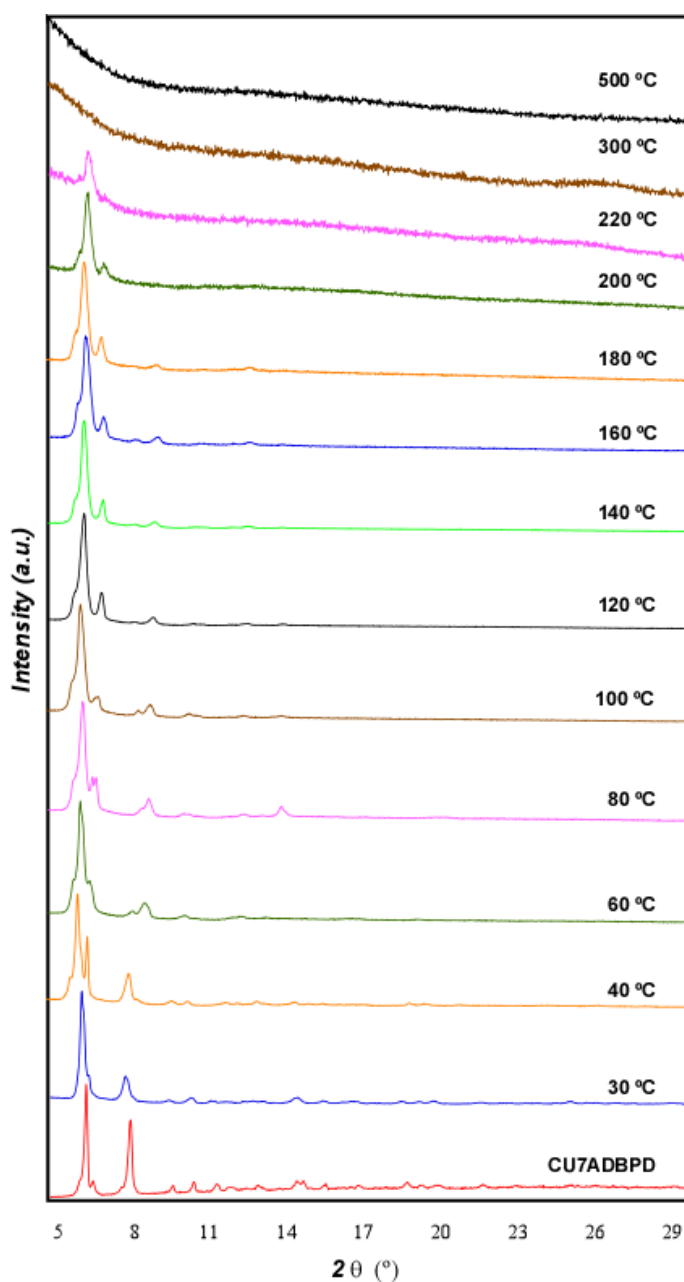


Figure 2.101. Variable-temperature X-ray diffraction patterns for compound CU7ADBPD.

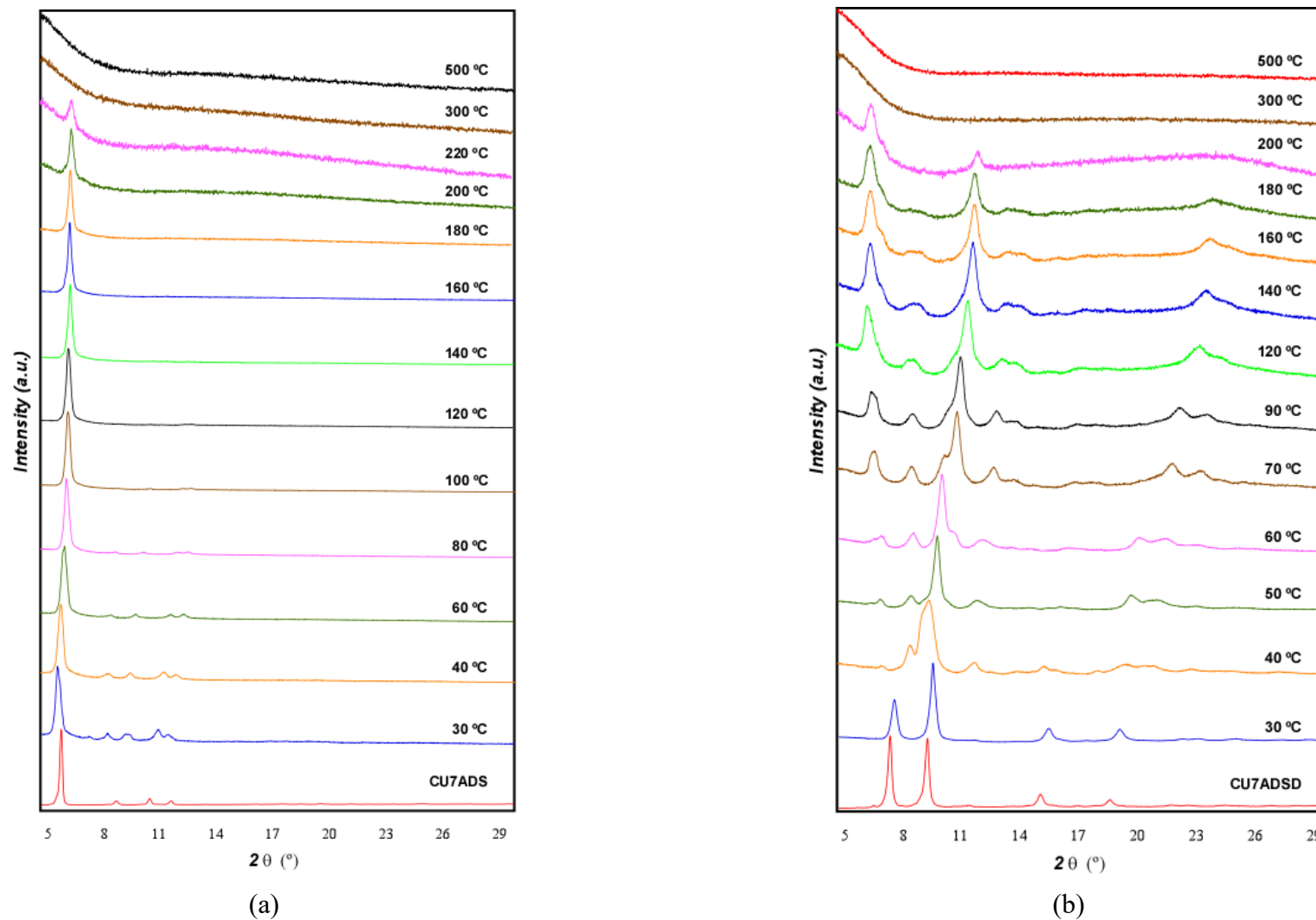


Figure 2.102. Variable-temperature X-ray diffraction patterns for stilbene-4,4'-dicarboxylate anion compounds (a) CU7ADS and (b) CU7ADSD.

2.6. Water adsorption

As previously stated, the dehydration process of the compounds implies the shrinkage of the pores but the crystal structure is flexible enough to allow the total rehydration of the sample upon exposure to a water-saturated atmosphere for 24 h to recover the original open crystal structure. This behavior is in good agreement with the water vapour adsorption/desorption curves shown in Figure 2.103.

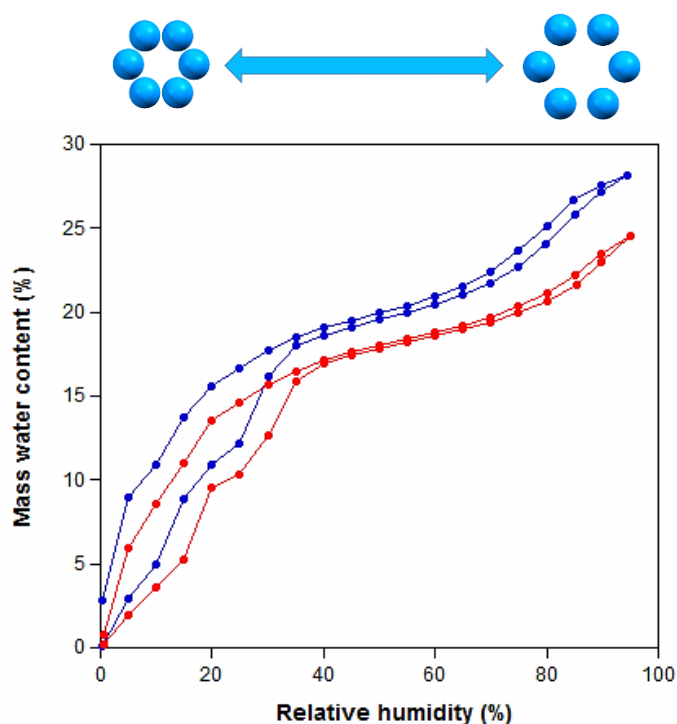


Figure 2.103. Water vapour adsorption/desorption isotherm for compound CU7ADBZ at 20 °C (blue) and 35 °C (red). The schematic image appearing at the top of the graphic tries to emphasize the structural flexible nature of these compounds.

The adsorption/desorption isotherms at 20 and 35 °C show some unusual features such as the presence of three different segments on the adsorption curve: i) a relative increase at low humidity values (0–40%) which corresponds to the adsorption of a water mass content of 19%; ii) an apparent plateau at intermediate humidity values (40–60%) with a small increase on the water intake up to 21% and iii) a steeper final segment in which water adsorption rapidly increases again with a maximum water uptake of 28% at a relative humidity value of 95%. In addition to that, the desorption curve shows a thin hysteresis at humidity values above 40% that widens noticeably at lower humidity values. These features are attributed to the flexible nature of the supramolecular architecture. At low humidity values, the pores are collapsed prone to “bottle-neck” like structure for which wide hysteresis curves are expected. However, as the humidity increases and more

water molecules are incorporated into the channels widening them, the “bottle-neck” effect disappears and a thinner hysteresis loop is achieved.

The measurement at 35 °C shows essentially the same features but with a lower amount of water being adsorbed, as expected for a temperature increase. However, it allows, by comparison with the data obtained at 20 °C, to determine the apparent isosteric adsorption heats (Figure 2.104). The values, calculated through Clausius–Clapeyron equation,¹⁹⁸ at low coverage value (*ca.* 68 kJ·mol⁻¹) compare well with other reported values for MOFs.¹⁹⁹ It is important to have in mind that due to the flexible nature of the crystal structure the obtained value does not only reflect the adsorption enthalpy value but also the contribution coming from the structural change that water adsorption implies (apparently of endothermic nature). Therefore, the real isosteric adsorption heat would be probably greater. Many works have pointed out that the presence of strongly polar groups on the surface of the voids help improving the adsorbate-substrate interaction. In this sense, the terephthalate carboxylate groups, the amino site of the adeninato and the hydroxido ligand of this compound point out in this way. This phenomenon has been also reported for other flexible porous materials.⁵⁶

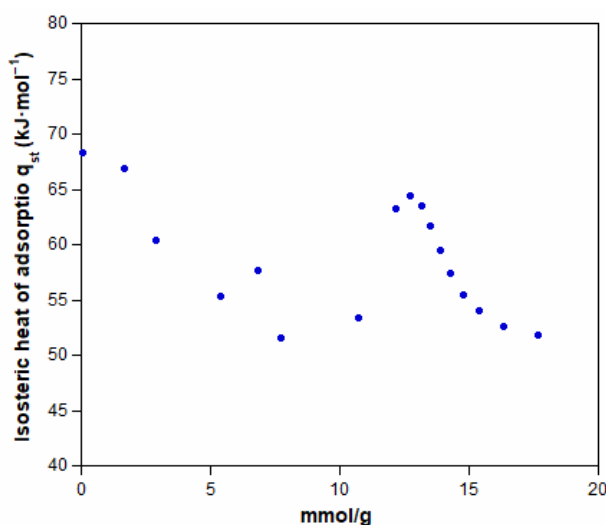


Figure 2.104. Isosteric enthalpy of adsorption values calculated through Clausius-Clapeyron equation.

¹⁹⁸ Brown, O. L. I. *J. Chem. Educ.* **1950**, 2 (6), 1950–1951.

¹⁹⁹ (a) Boström, H. L. B.; Burrows, A.; Cass, M.; Chanteux, G.; Laybourn, A.; Li, Y.; Papathanasiou, K.; Patel, K.; Yaghi, O.; Yang, S. *RSC Faraday Discuss.* **2021**, 231, 150–151. (b) Kim, H.; Cho, H. J.; Narayanan, S.; Yang, S.; Furukawa, H.; Schiffres, S.; Li, X.; Zhang, Y. B.; Jiang, J.; Yaghi, O. M.; Wang, E. N. *Sci. Rep.* **2016**, 6 (January), 1–8. (c) Canivet, J.; Fateeva, A.; Guo, Y.; Coasne, B.; Canivet, J.; Fateeva, A.; Guo, Y.; Coasne, B.; Water, D. F.; Canivet, J.; Fateeva, A.; Guo, Y. *Chem. Soc. Rev.* **2014**, 43 (16), 5594–5617.

As described, compound CU7ADTEP-1 suffers a crystal system change from monoclinic to triclinic during the release of the water molecules. It implies a twinning phenomenon of the initial single-crystal. In fact, all the crystals selected for the structural characterization were twinned, and all the efforts made for avoiding this twinning were unfruitful. In addition to that, during the water release, the border between the generated domains is getting highly disordered in such a way that they may not be able to come back to the water rich monoclinic phase (CU7ADTEP-1), giving rise to the observed amorphization of the sample. In addition, a vacuum activated sample, shows in its X-ray powder diffraction pattern the same loss of crystallinity and a change on the colour from blue to a deep green. This sample was not able to adsorb CO₂ (298 K), neither N₂ (77 K) but it adsorbed water vapour (Figure 2.105). It is notorious the presence of pronounced hysteresis curves that do not close at low humidity values. There is still a 6% of water retained, at zero humidity value, a value close to that expected for the coordination water molecules. Despite the adsorption capacity is reduced after the second cycle the starting first points of the adsorption curve are almost the same up to this value, which implies that the amorphization hindered adsorption capability only applies on the crystallization water molecules but not on the coordination ones. The latter conclusion is also reinforced by the fact that desorption curves finish at the same water content in both compounds studied in this section, Figure 2.105b. As stated, the partial amorphization of the sample probably contributes to the pronounced hysteresis loops Figure 2.106.

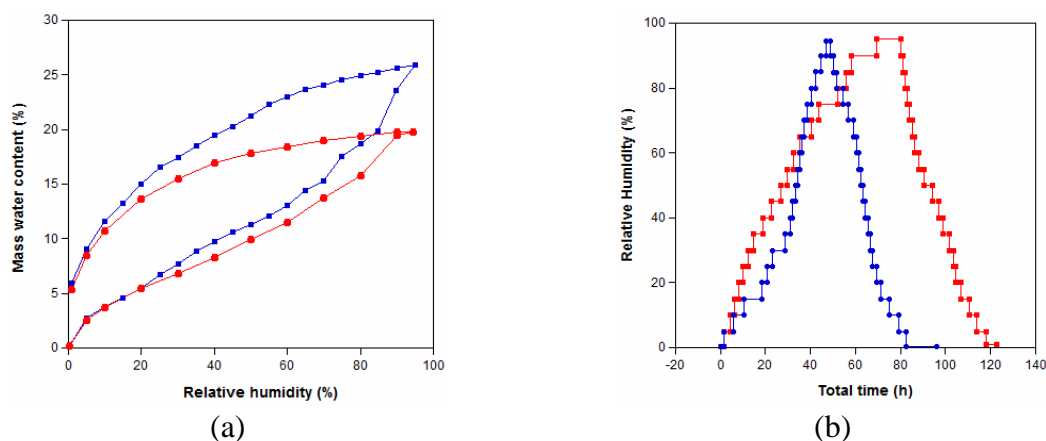


Figure 2.105. (a) Water cycling of adsorption/desorption isotherms at 20 °C for an activated sample (first cycle: blue, second cycle: red). (b) Data acquisition times for the adsorption/desorption curves of compound CU7ADBZ (blue) and CU7ADTEP (red). Note that at these experiment the difference between CU7ADTEP-1 and -2 losses its meaning as they only differ in their water content.

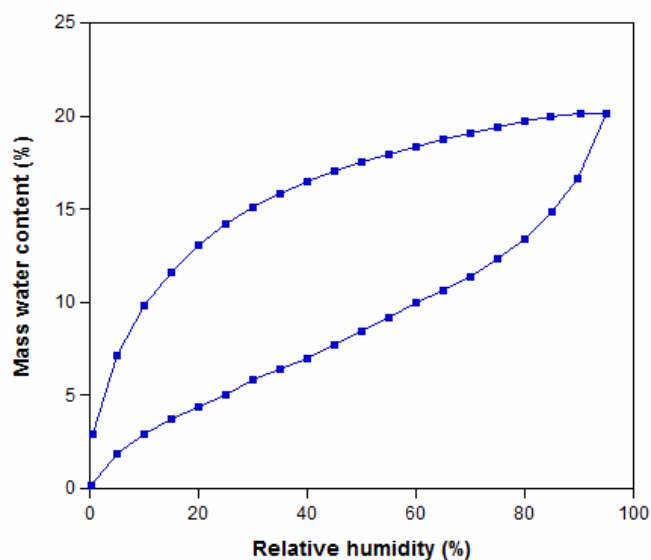


Figure 2.106. Water adsorption/desorption isotherms for activated sample of compound CU7ADTEP at 35 °C.

The X-ray diffraction pattern of this activated/rehydrated sample (Figure 2.107) confirmed the return to the initial structure but losing some crystallinity compared to the pristine sample.

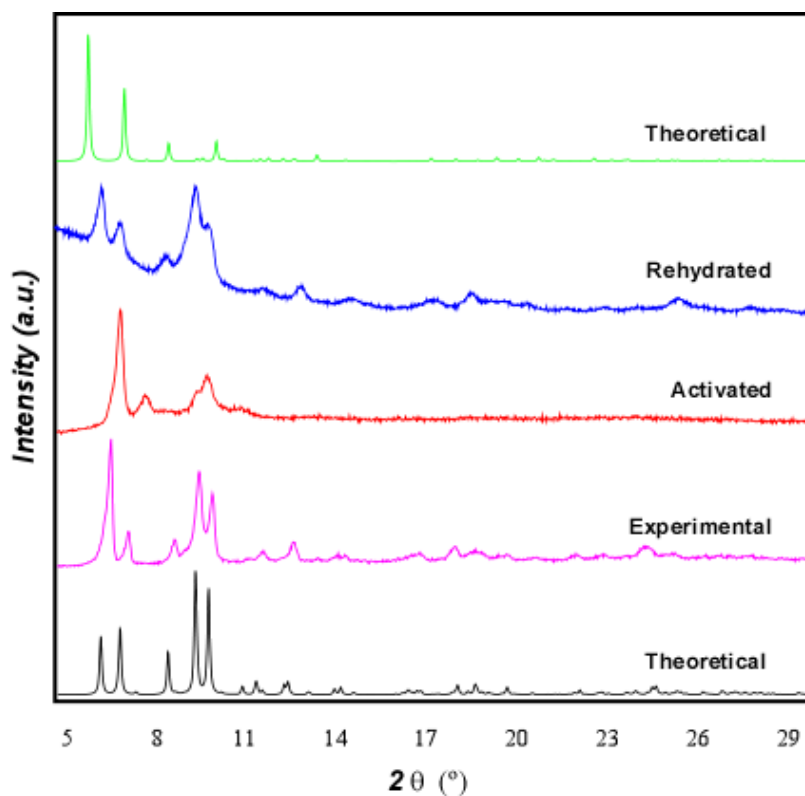


Figure 2.107. Powder X-ray diffraction patterns from samples of compound CU7ADTEP-2.

Performing the same water adsorption experiments for the isorecticular series show a remarkable feature for the more extended naphthalene-2,6-dicarboxylic counterion

(Figure 2.108). The remaining samples present the same feature of the above described terephthalic compound.

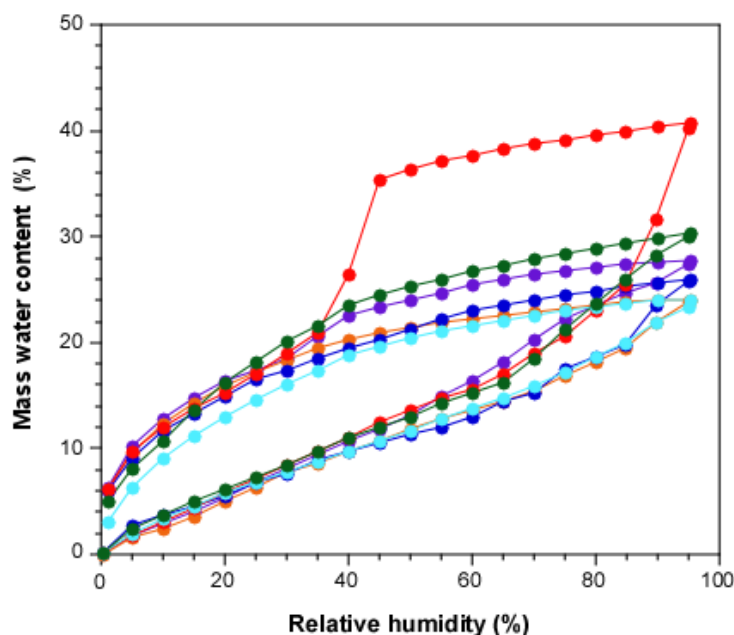


Figure 2.108. First water cycling of adsorption/desorption isotherms at 20 °C for an activated sample of CU7ADF-2 (purple), CU7ADAC-2 (orange), CU7ADTEP-2 (blue), CU7ADNAPH-2 (red), CU7ADBPD (light blue) and CU7ADSD (green).

All compounds show a water adsorption pronounced hysteresis curve that do not close at low humidity values. There is still a 5.6% of water retained, at zero humidity value, a value close to that expected for the coordination water molecules. The source of this broad hysteresis curve comes from the structural flexibility that these compounds show, in which the pores collapse upon the removal of the solvent molecules and expand upon their adsorption. It means that there is not a sudden adsorption step as the adsorption must be followed by a structural rearrangement, nor there is that sudden step in the desorption curve for the same reason. However, CU7ADNAPH-2 shows a different desorption curve with the presence of a sudden drop around humidity values of 40%. The adsorption curve follows the same tendency described for the rest of the compounds with the exception of a greater amount of adsorbed water at its maximum (*ca.* 40%) which agrees with the void volume present in its crystal structure. The sharp decrease in the desorption curve is characteristic of well-defined and rigid voids. It seems that the elimination of the coordination water molecules induces a structural transformation but the removal of the crystallization water molecules does not produce strong structural changes on the contrary to the other compounds tested in this work. This explanation becomes more evident when we analyze the second and third adsorption/desorption cycles (Figure 2.109) where the

sample is not further activated and the coordination water molecules are not removed. In these new cycles, we can observe not only that sharp step in desorption curve but also in adsorption. Apart from that, there is a great mismatch between the adsorption step (humidity: ~70%) and the desorption step (humidity: ~40%) that arrives from the bottle neck effect. The crystal structure of this compound shows huge ellipsoidal pores (diameter: 11.2 Å) that are connected by relatively narrow windows (8.5 Å). It means that the area surrounding these window will adsorb a moderate amount of water at lower humidity values, as the water molecules interact more strongly, but the big pores to be filled requires higher humidity values. However when performing the desorption, the water molecules present in the pores are only going to be released when the water molecules in these necks/windows are released. The latter being the cause for this hysteresis which is the key feature that researchers look for in compounds with potential application harvesting water from the atmosphere humidity.

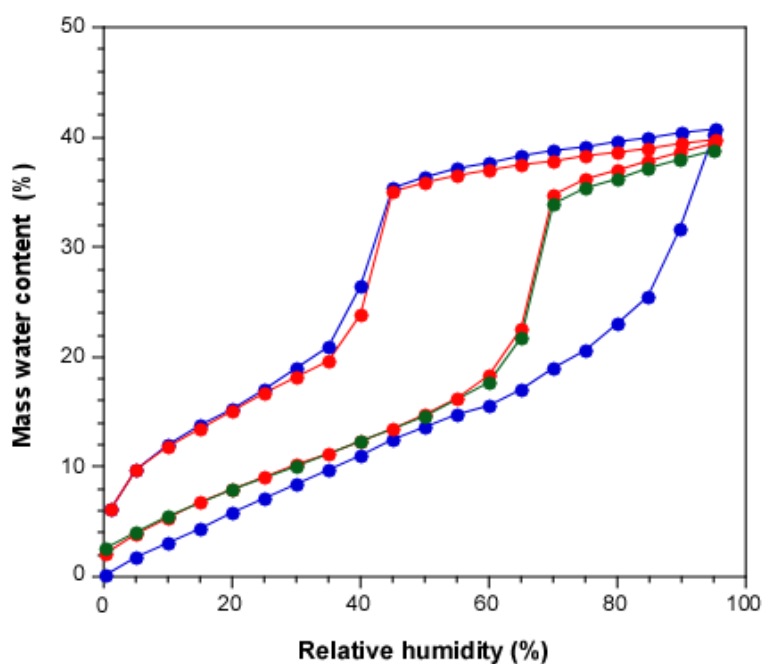


Figure 2.109. Consecutive adsorption/desorption cycling at 20 °C for CU7ADNAPH-2 (1st cycle: blue dots; 2nd cycle: red dots and 3rd cycle: green dots).

The successive cycles for the remaining compounds only show a progressive decrease in the water adsorption capacity (Figure 2.110), probably due to an increasing amorphization during these structural modifications accompanying the water adsorption cycling.

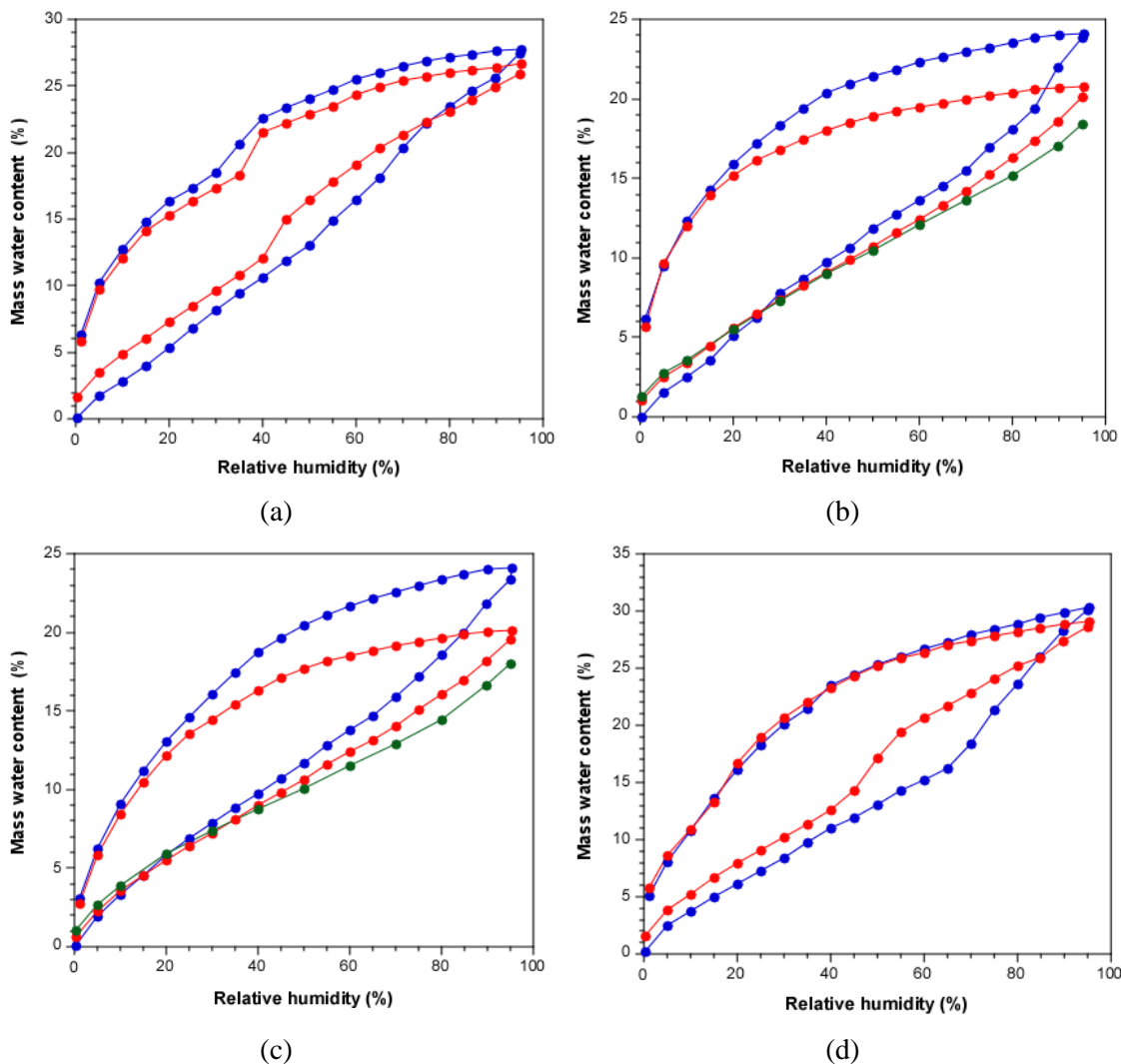


Figure 2.110. Consecutive adsorption/desorption cycling (1st cycle: blue dots; 2nd cycle: red dots and 3rd cycle: green dots) at 20 °C for (a) CU7ADF-2, (b) CU7ADAC-2, (c) CU7ADBPD, (d) CU7ADSD.

2.7. Magnetic properties

All the compounds reported in this chapter contain copper(II) paramagnetic centers bridged by ligands that impose a short distance between them and levels to interesting magnetic properties.

For the compounds CU2AD3TB, CU2ADCAF and CU2ADTP (Figure 2.111), the magnetic data (Figure 2.112) indicates a strong antiferromagnetic interaction between the copper atoms of the dimeric entity mediated by the four μ - $\kappa N3$: $\kappa N9$ adeninato ligands.

In fact, $\chi_M T$ at room temperature (0.64 and 0.75 $\text{cm}^3\text{K}\cdot\text{mol}^{-1}$ for compounds CU2AD3TB and CU2ADCAF, respectively), is slightly below the expected value for two uncoupled paramagnetic ($S = 1/2$ centers with $g = 2.0$) copper(II) centers (0.83 $\text{cm}^3\text{K}\cdot\text{mol}^{-1}$, $g = 2.10$) and continuously decreases upon cooling, Figure 2.112a/b. The χ_M curve shows the typical maximum for these systems around 240 and 200 K, respectively. It then decreases and reaches a minimum near 45 and 70 K, respectively. However, the χ_M curve also shows an increase of its value at low temperatures indicative of the presence of paramagnetic impurities. The susceptibility data have been fitted using the Bleaney-Bowers equation ($H = -JS_1S_2$) for a modified copper(II) dinuclear complex to take into account the paramagnetic impurities (ρ) present in the compound.²⁰⁰ The best fitting values are $g = 2.11$, $J = -271 \text{ cm}^{-1}$, and $\rho = 0.4\%$ for CU2AD3TB and $g = 2.11$, $J = -256 \text{ cm}^{-1}$, and $\rho = 4.4\%$ for compound CU2ADCAF. The obtained superexchange parameters are within the range observed for compounds with the $[\text{Cu}_2(\mu\text{-ade-}\kappa N3:\kappa N9)_4(\text{X})_2]^{n+}$ ($n = 0, 2, 4$; $\text{X} = \text{H}_2\text{O}, \text{Cl}^-, \text{Br}^-$; $\text{ade} = \text{adenine or adeninato}$), with J ranging from -211 to -316 cm^{-1} .¹⁷⁷

In the case of the theophyllinato containing compound (CU2ADTP), the room temperature $\chi_M T$ value (1.38 $\text{cm}^3\text{K}\cdot\text{mol}^{-1}$) is also lower than that expected for four uncoupled Cu(II) ions (1.50 $\text{cm}^3\text{K}\cdot\text{mol}^{-1}$, considering a $g = 2.00$) and decreases rapidly up to 70 K, reaching a plateau with a value of 0.90 $\text{cm}^3\text{K}\cdot\text{mol}^{-1}$. Below 30 K, the curve decreases again to 0.52 $\text{cm}^3\text{mol}^{-1}\text{K}$ at 2 K, which is lower than the value corresponding to the presence of two uncoupled Cu(II) atoms (0.75 $\text{cm}^3\text{K}\cdot\text{mol}^{-1}$, $g = 2.00$). The magnetic behavior of this compound is dominated by the presence of two magnetic exchange pathways, Figure 2.112c, one resulting from the four Cu1–Nx3–Cx4–Nx9–Cu1ⁱ bridges

²⁰⁰ Bleaney, B.; Bowers, K. D.; A, P. R. S. L. *Proc. R. Soc. London. Ser. A.* **1952**, 214 (1119), 451–465.

in the dimeric nucleus (J) and the other from the adeninato bridges that join the dimeric entity and four adjacent monomeric entities ($\text{Cu1-N29}^i\text{-C28}^i\text{-N27}^i\text{-Cu2}^i$). We have to take into account that the distances between the monomeric and the dimeric copper entities $\text{Cu1}\cdots\text{Cu2}$ is substantially longer in comparison with the intradimeric distance (5.755/5.924 vs 2.956 Å). Additionally, it has been previously reported that the longer imidazolic pathway involves a very weak antiferromagnetic coupling in comparison with the one involving the dimeric core.^{71d,72,112} As far as we know, there is no magnetic model that could account for the complex magnetic coupling scheme present in this coordination polymer. Therefore, dismissing the weaker magnetic interaction, the susceptibility data have been adjusted using the Bleaney-Bowers equation¹⁹⁹ $H = -JS_1S_2$ modified to take into account the presence of a dimeric entity and two copper monomer entities per formula. The fitting was made with the data above 30 K, obtaining values of $J = -267 \text{ cm}^{-1}$ and $g = 2.13$. These values are in the range found for compounds containing paddle-wheel $[\text{Cu}_2\text{L}_4\text{X}_2]$ entities (L = $\kappa\text{N}3:\kappa\text{N}9$ -coordinated purine derivatives, X = Cl^- , Br^- , H_2O)³⁴ which show J values from -210 to -320 cm^{-1} and the coupling is slightly weaker than that observed for the three-dimensional compound $\{[\text{Cu}_2(\mu\text{-ade})_4(\text{H}_2\text{O})_2] \cdot 2[\text{Cu}(\text{ox})(\text{H}_2\text{O})] \cdot \sim 14\text{H}_2\text{O}\}_n$ ($J = -316 \text{ cm}^{-1}$).⁷² The further decrease of the χ_{MT} value upon cooling below 30 K indicates the weaker but also antiferromagnetic nature of the magnetic exchange between the dimeric (Cu1) and monomeric (Cu2) entities through the imidazole ring of the adeninato ligands. This discrepancy and the one between the experimental data and those calculated at low temperatures suggest that the magnetic exchange between the dimeric and monomeric entities (by means of the N7 coordination of the imidazole ring of the adeninato ligands) is relevant at these temperatures.

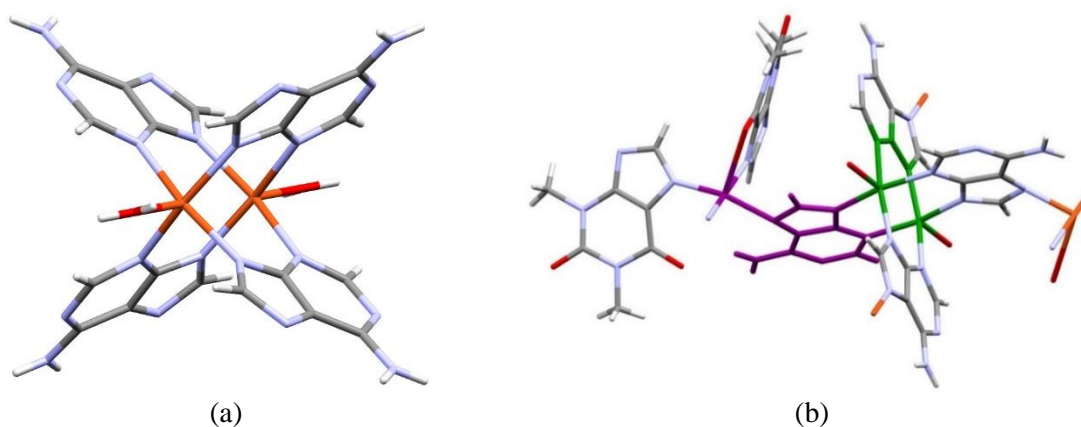


Figure 2.111. Dimeric entity of compounds (a) CU2AD3TB and (b) CU2ADCAF. Representation of the two exchange pathways represented in two different colours (purple and green) for the compound CU2ADTP.

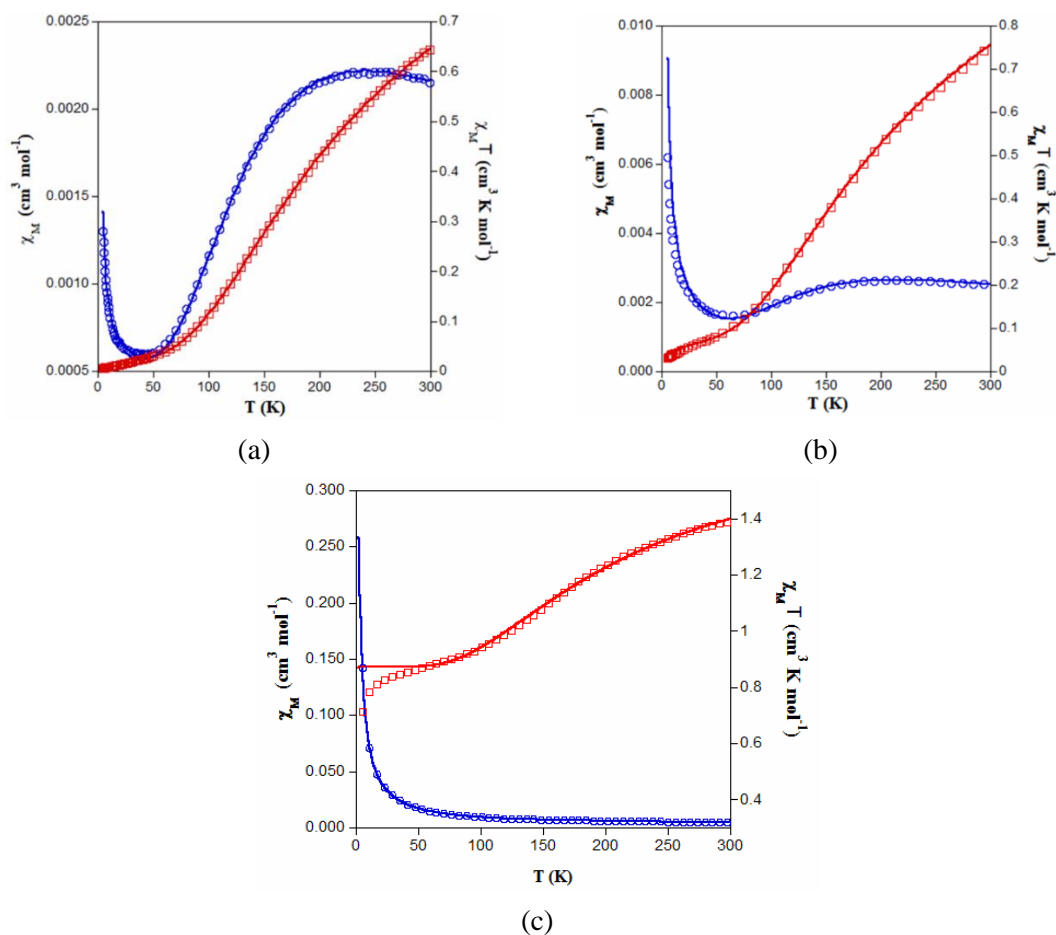


Figure 2.112. ZFC thermal evolution of the molar magnetic susceptibility (χ_M) (blue points) and $\chi_M T$ (red square) product for (a) CU2AD3TB, (b) CU2ADCAF and (c) CU2ADTP. The line shows the fitting of the experimental data.

Figure 2.113a shows the temperature dependence of the molar magnetic susceptibility (χ_M , blue circles) and $\chi_M T$ (red squares) curves for compound CU7ADTB. The $\chi_M T$ value per heptameric unit at 300 K is $3.12 \text{ cm}^3 \text{K} \cdot \text{mol}^{-1}$, which agrees fairly well with the expected value for seven magnetically non-interacting Cu^{2+} ions (with $S = 1/2$ and $g = 2.00$ ($2.63 \text{ cm}^3 \text{K mol}^{-1}$)).²⁰¹ This value remains nearly constant upon cooling up to 100 K with a slight increase, but below this temperature a sharp increase is observed to reach a maximum of $4.73 \text{ cm}^3 \text{K} \cdot \text{mol}^{-1}$ at 6 K. The field dependence of the magnetization at 2 K displays a linear dependence, from 0 to 15 kOe, which slowly tends to saturate at 20 kOe ($5.3 \mu_B/\text{heptamer}$). This value is less than the theoretical saturation for seven ferromagnetically coupled Cu^{II} atoms with magnetic spin $S = 1/2$ and $g \approx 2$ ($7.0 \mu_B$) but is consistent with a ground state $S = 5/2$. The magnetization at 2 K shows no hysteresis (have neither coercivity nor remanence) at this temperature. This behaviour

²⁰¹ Boca, R. *A Handbook of Magnetochemical Formulae*; Elsevier: Amsterdam, (Netherlands), **2012**.

seems to indicate the presence of ferromagnetic heptameric entities in which the central copper(II) atom is antiferromagnetically coupled to the external ferromagnetic hexanuclear ring to provide a $S = 5/2$ ground state.^{107b}

Taking into account the molecular structure of the $[\text{Cu}_7(\mu\text{-adeninato-}\kappa\text{N3}:\kappa\text{N9})_6(\mu_3\text{-OH})_6(\mu\text{-H}_2\text{O})_6]^{2+}$ heptanuclear entities and the Jahn-Teller elongated octahedron of the central copper(II) atom, the following Hamiltonian (Equation 1) was employed to fit the experimental data of this complex includes three superexchange magnetic parameters (J_1, J_2, J_3) that take into account the different couplings between the copper atoms.

$$H = -J_1(\vec{S}_1 \cdot \vec{S}_3 + \vec{S}_1 \cdot \vec{S}_4 + \vec{S}_1 \cdot \vec{S}_{3'} + \vec{S}_1 \cdot \vec{S}_{4'}) - J_2(\vec{S}_1 \cdot \vec{S}_2 + \vec{S}_1 \cdot \vec{S}_{2'}) - J_3(\vec{S}_2 \cdot \vec{S}_3 + \vec{S}_3 \cdot \vec{S}_4 + \vec{S}_4 \cdot \vec{S}_{2'} + \vec{S}_{2'} \cdot \vec{S}_{3'} + \vec{S}_{3'} \cdot \vec{S}_{4'} + \vec{S}_{4'} \cdot \vec{S}_2) - g\mu_B \vec{B} \cdot \vec{S} \quad (\text{equation 1})$$

J_1 and J_2 are assigned to the superexchange interactions between the central and the external copper ions taking place through double $\mu\text{-OH}$ bridges, J_1 involves a mixture of equatorial-equatorial, with Cu–O short distance ($< 2.0 \text{ \AA}$) and equatorial-axial coordinated with short and long distance (Cu4–O3: $1.954(6) \text{ \AA}$ and Cu1–O3: $2.247(7) \text{ \AA}$, respectively), whereas J_2 presents only an equatorial-equatorial arrangement of short distance bridging hydroxides. J_3 represents the superexchange interaction between the external Cu^{II} ions bridged by adeninato, hydroxide and semicoordinated water molecules. The fitting of the χ_{mT} experimental data (Figure 2.113b) to this model was performed using the MagProp software tool distributed with DAVE.²⁰² The best fitting parameters (red continuous line in Figure 2.113a) are $J_1 = 25$, $J_2 = -158$, $J_3 = 86 \text{ cm}^{-1}$ and $g = 2.11$.

The fitting of the data gives significant differences in the coupling constants involving the central atom and the outer copper atoms (J_1 and J_2). In the case of J_2 , involving two $\mu\text{-hydroxo}$ bridges with short distances and Cu–O–Cu angles of 99.7 and 100.1° , it is antiferromagnetic which is in agreement with that described by Hatfield for symmetrically bridged dinuclear $\mu\text{-hydroxo}$ complexes, where angles larger than 98.5° give antiferromagnetic coupling, while smaller angles are set give ferromagnetic couplings.²⁰³ The weakly ferromagnetic J_1 interaction is related to two different superchannel paths, the one involving a hydroxide bridge with two short distances and

²⁰² Azuah, R. T.; Kneller, L. R.; Qiu, Y.; Tregenna-Piggott, P. L. W.; Brown, C. M.; Copley, J. R. D.; Dimeo, R. M. *J. Res. Natl. Inst. Stand. Technol.* **2009**, *114* (6), 341–358.

²⁰³ Van Crawford, H.; Richardson, H. W.; Wasson, J. R.; Hodgson, D. J.; Hatfield, W. E. *Inorg. Chem.* **1976**, *15* (9), 2107–2110.

another with one short and one long distance. In this case the energy difference between the SOMOs orbitals resulting from the overlap between the magnetic orbitals is about a quarter of that corresponding to two hydroxide bridges with short copper-hydroxide distances. This weakens the antiferromagnetic component and allows the ferromagnetic component of the coupling constant to dominate. The value of J_1 is within the range (between +10 and +90 cm^{-1}) observed for other ferromagnetic compounds with a similar bridge between copper(II) atoms.²⁰⁴

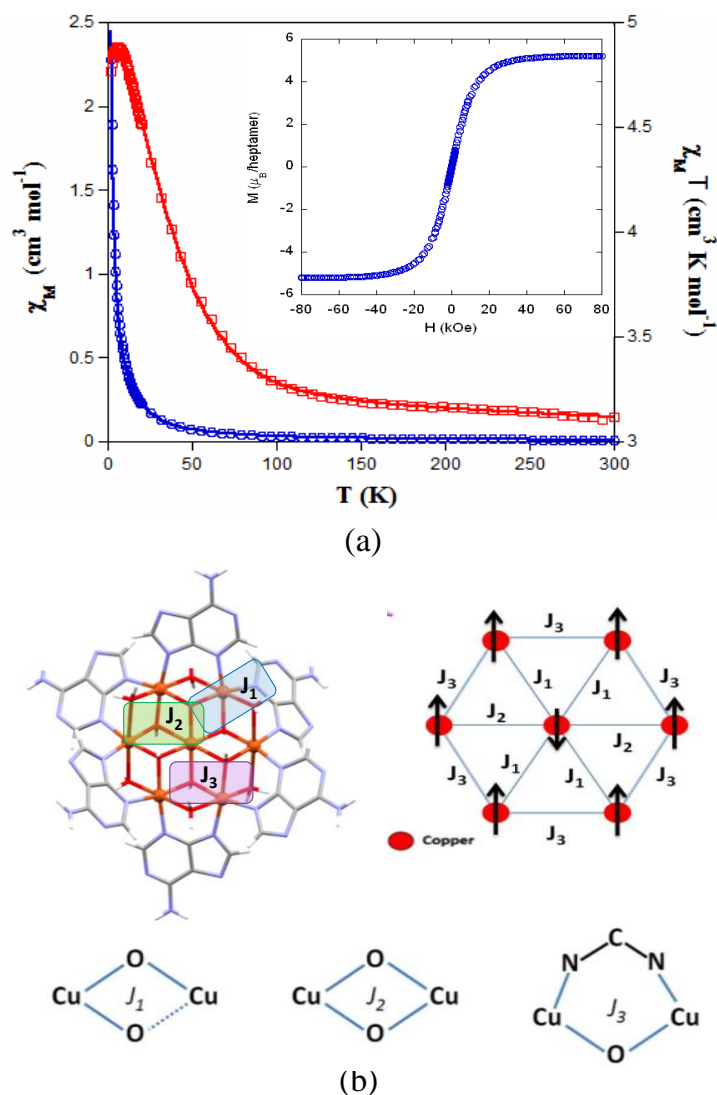


Figure 2.113 (a) ZFC thermal evolution of the molar magnetic susceptibility (χ_m) and $\chi_m T$ product for compound CU7ADTB. Magnetization curve at 2 K (inset). The line shows the best fitting of the experimental data. (b) $[\text{Cu}_7(\mu\text{-ade-}\kappa\text{N}3:\kappa\text{N}9)_6(\mu_3\text{-OH})_6(\mu\text{-H}_2\text{O})_6]^{2+}$ entity emphasizing the relationship of the magnetic topology and 3-J coupling scheme for the local Cu^{II}_7 cluster.

²⁰⁴ Tercero, J.; Ruiz, E.; Alvarez, S.; Rodríguez-Fortea, A.; Alemany, P. *J. Mater. Chem.* **2006**, *16* (26), 2729–2735.

The fit gives a ferromagnetic value for the coupling constant J_3 , corresponding to the interaction between the outer metal centers through the adeninate and hydroxide bridging ligands and water molecules. Normally, the presence of nonlinear NCN ligands or a high value of the μ -oxide ligand angle (ca. 104°) causes strong antiferromagnetic couplings.²⁰⁵ However, in certain cases, the existence of two different types of bridges that individually give an antiferromagnetic interaction, when acting simultaneously reverse their effects generating a ferromagnetic interaction in an effect called orbital countercomplementarity.^{71c,d,206} The splitting of the magnetic molecular orbitals is reversed for each type of bridging ligand, leading to an almost negligible energy difference between them and, as a consequence, the resulting interaction is ferromagnetic.

This behavior and the obtained superexchange values are similar to those published for other similar wheel-shaped copper(II) heptameric entities in which the outer metal atoms are ferromagnetically coupled to each other and antiferromagnetically coupled to the central atom.^{107b,154}

As previously stated, the dehydration procedure gives rise to a substantial reorganization of the crystal structure of compound CU7ADTB. In order to get some insight on the persistence of the heptanuclear entity after this structural rearrangement, the magnetic characterization of an activated sample of this compound was accomplished (Figure 2.114). It shows a similar magnetization curve at 2 K but without reaching to saturation at 65 kOe. In a similar way, the $\chi_{\text{M}}T$ curve is similar to that of the fresh sample, but its maximum at higher temperatures (15 K) with a lower $\chi_{\text{M}}T$ value of $3.41 \text{ cm}^3 \text{ K mol}^{-1}$. Both facts suggest the presence of the heptameric entities in the activated sample, which establish stronger supramolecular antiferromagnetic interactions between them in agreement with the observed shrinkage of the unit cell upon the activation process.

²⁰⁵ Pasán, J.; Sanchiz, J.; Ruiz-Pérez, C.; Lloret, F.; Julve, M. *Inorg. Chem.* **2005**, *44* (22), 7794–7801.

²⁰⁶ (a) Gonzalez-Pérez, J. M.; Alarcon-Payer, C.; Castiñeiras, A.; Pivetta, T.; Lezama, L.; Choquesillo-Lazarte, D.; Crisponi, G.; Niclós-Gutiérrez, J. *Inorg. Chem.* **2006**, *139* (2), 877–882. (b) Pérez-Yáñez, S.; Castillo, O.; Cepeda, J.; García-Terán, J. P.; Luque, A.; Román, P. *Eur. J. Inorg. Chem.* **2009**, *2* (26), 3889–3899.

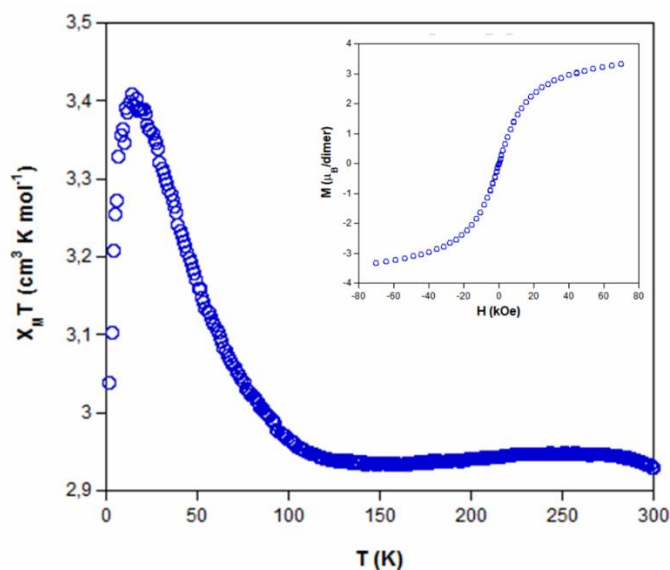


Figure 2.114. ZFC thermal evolution of the $\chi_M T$ product for compound CU7ADTB upon desolvation. Inset: magnetization curve at 2 K.

The magnetic measurements of the remaining $[\text{Cu}_7(\mu\text{-ade})_6(\mu_3\text{-OH})_6(\mu\text{-H}_2\text{O})_6]^{2+}$ clusters also indicate an overall ferrimagnetic behavior (Figure 2.115). The $\chi_M T$ value at room temperature agrees with the expect value for seven paramagnetic copper(II) metal centers with J values listed in Table 2.57. Due to the similarity of the results of the magnetic adjustment of the dicarboxylate anion containing compounds, only some of them are described as examples.

Despite the supramolecular rearrangements induced by such counterions, they have little impact on the intramolecular magnetic behaviour, they only give rise to noticeably dissimilar supramolecular magnetic properties which are only appreciable at very low temperatures, where the magnetic ordering through non-covalent interaction pathways is more relevant.²⁰⁷

²⁰⁷ (a) Mondal, K. C.; Mereacre, V.; Kostakis, G. E.; Lan, Y.; Anson, C. E.; Prisecaru, I.; Waldmann, O.; Powell, A. K. *Chem. - A Eur. J.* **2015**, *21* (30), 10835–10842. (b) Zheng, Y.-Z.; Tong, M.-L.; Xue, W.; Zhang, W.-X.; Chen, X.-M.; Grandjean, F.; Long, G. J. *Angew. Chemie* **2007**, *119* (32), 6188–6192. (c) Sharples, J. W.; Collison, D.; McInnes, E. J. L.; Schnack, J.; Palacios, E.; Evangelisti, M. *Nat. Commun.* **2014**, *5*, 3–8.

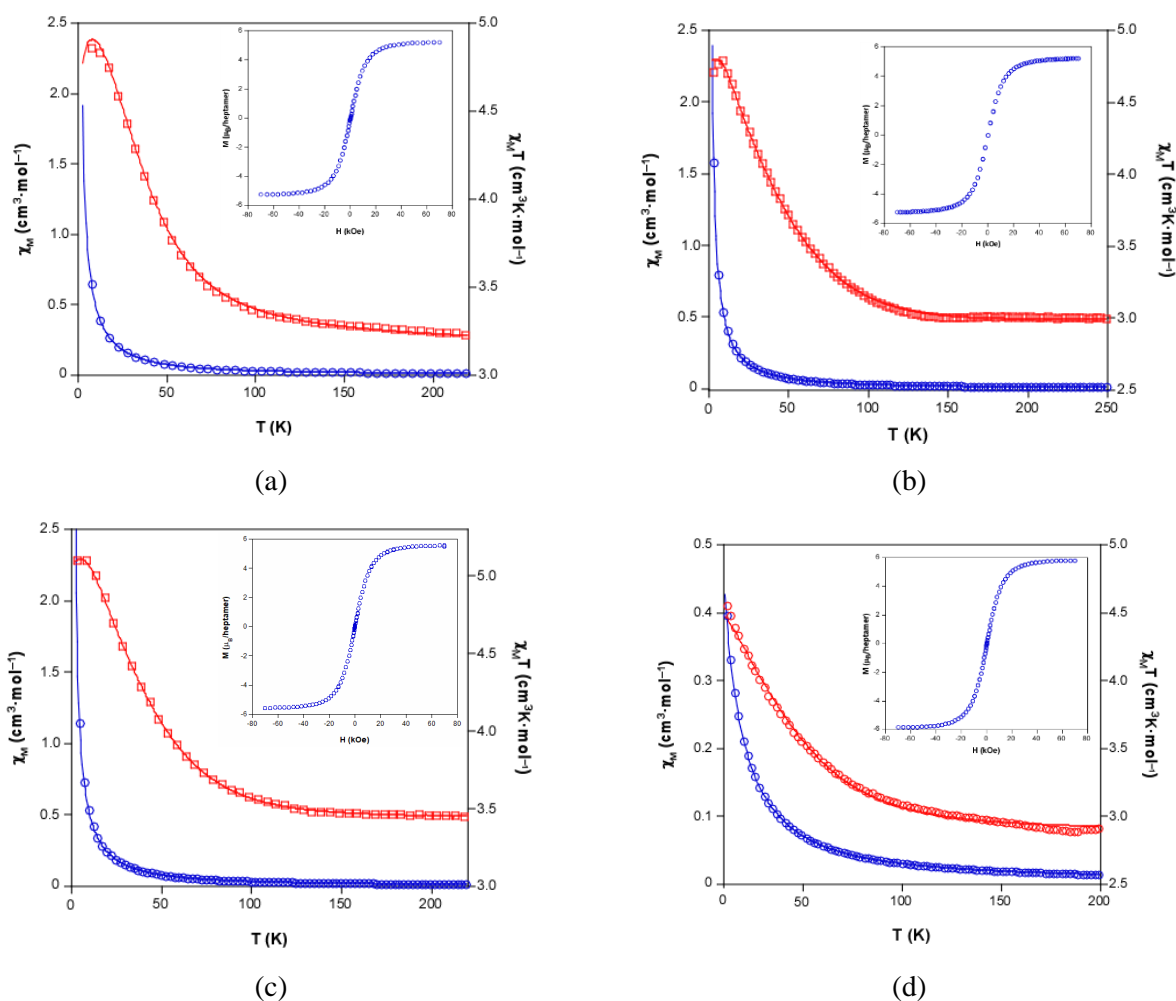


Figure 2.115. Thermal evolution of the molar magnetic susceptibility χ_m (o) and $\chi_m T$ (\square) product for compound (a) CU7ADBZ, (b), CU7ADAC-2, (c) CU7ADTEP-2, (d) CU7ADNAPH-2. Magnetization curve at 2 K (inset). The line shows the best fitting of the experimental data.

Table 2.57. Magnetic properties of heptameric compounds.

Compound	J_1	J_2	J_3	g	$\chi_m T_{\max}$ value ($\text{cm}^3 \cdot \text{K} \cdot \text{mol}^{-1}$)
CU7ADBZ	-2	-100	67	2.13	4.85
CU7ADTEP-2	35	-180	100	2.11	5.09
CU7ADAC-2	44	-229	97	2.10	4.79
CU7ADNAPH-2	27	-178	94	2.03	4.82

2.7.1. Magnetic sustentation experiments.

Usually, the reported studies on this kind of polynuclear materials containing paramagnetic centres are focused in the analysis of their magnetic ordering that takes place well below room temperature.²⁰⁸ Instead of that, we herein address the challenge of using the room temperature paramagnetic response of this kind of compounds towards an external magnetic field to prompt a driven motion of its particles while immersed in a liquid and even to accomplish sensing through the quantification of this response. Related to the latter, recently our research group reported the use of compound $[\text{Cu}_6\text{Cr}(\mu\text{-adeninato})_6(\mu_3\text{-OH})_6(\mu\text{-H}_2\text{O})_6](\text{SO}_4)_{1.5}$, to capture anti-inflammatory anionic drugs from aqueous effluents and to quantify them through this new magnetic sensing approach.¹⁹² This work is focused on performing a more specific adsorption selectivity study using a broader selection of drug molecules and the CU7ADNAPH-2 SMOF that contain voids big enough to be feasible the incorporation of these molecules.

As previously stated, these compounds establish complex magnetic interactions at low temperatures but at room temperature they are well placed in the paramagnetic regime as it can be deduced from their $\chi_{\text{M}}T$ product at room temperature. Therefore, the attraction force exerted by a relatively strong external magnetic field (i.e. that of magnets or electromagnets) on their particles is not strong enough to overcome the earth gravity attraction under normal conditions and, as a consequence, no displacement takes place on these particles. Contrarily, under attenuated gravity force, such as it occurs for particles suspended in a liquid, the magnetic field attraction is capable to sustain the particles avoiding their deposition at the bottom and even to induce their motion upon magnetic field shifts. In order to apply this phenomenon for sensing purposes, a double pole electromagnet was employed to get a fine control on the applied magnetic field. It required a complete characterization of electromagnet in which the profile of the magnetic field and its gradient was measured on the pole surface of the electromagnet at different current I values. Figure 2.116 depicts the magnetic field measured along the plane corresponding to the surface of the magnetic pole in the vertical z -axis. The magnetic data were fitted to a fourth order polynomial expression and ∇H and $H \cdot \nabla H$ were computed.

²⁰⁸ (a) Shao, D.; Wang, X. Y. *Chinese J. Chem.* **2020**, *38* (9), 1005–1018. (b) Cai, W.; Bocarsly, J. D.; Gomez, A.; Letona Lee, R. J.; Metta-Magaña, A.; Seshadri, R.; Echegoyen, L. *Chem. Sci.* **2020**, *11* (48), 13129–13136.

Figure 2.117 shows the dependence of the most negative $H \cdot \nabla H$ product for each current value with the magnetic field measured in the center of the pole.

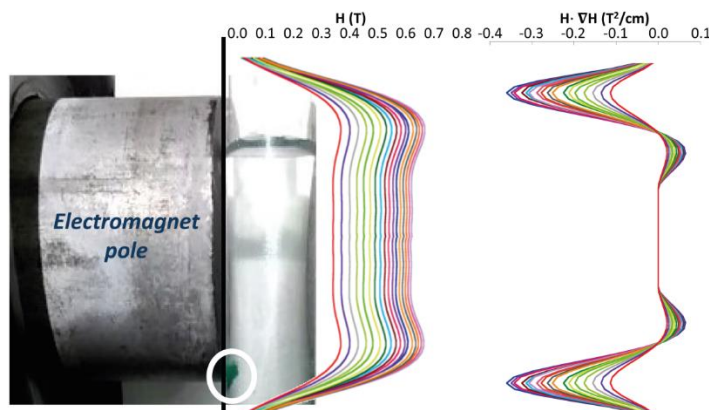


Figure 2.116. Magnetic field profile (H and $H \cdot \nabla(H)$) on the electromagnet pole along the dashed line. The different colours refer to the applied intensity current: increasing from 0.0 to 2.5 A (step: 0.1 A).

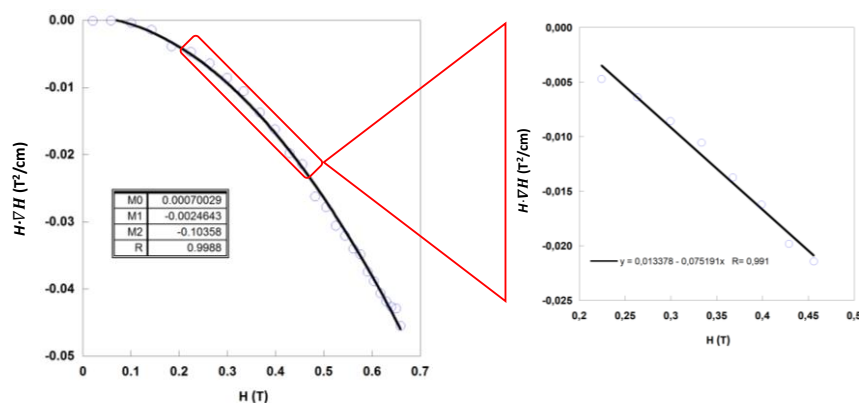


Figure 2.117. $H \cdot \nabla(H)$ dependence on the magnetic field at the center of the pole. Left: second order polynomial fitting of the entire magnetic field range and right: linear fit within the range at which the experimental data appear for these compounds.

The equation that accounts for the attraction between the paramagnetic particles and the magnetic field is: $F = \nabla(m \cdot H)$, where the gradient ∇ is the change of the quantity $m \cdot H$ per unit distance (m : magnetic dipole of the particle and H : external magnetic field), and the direction is that of maximum increase of $m \cdot H$. If m is aligned with H , as it is the case for paramagnetic particles, the gradient brings the particles towards the regions of maximum H -field.

The paramagnetic nature of the particles implies their magnetic dipole is related to the external magnetic field and assuming the particles are small, it can be considered constant and taken away from the gradient (equation 2):

$$F_p = \mu_0 \frac{\chi_M}{MW} \cdot \rho_p \cdot V_p \cdot H \cdot \nabla(H_p) \quad (2)$$

being F_p the magnetic attraction force on particle, μ_0 the permeability of vacuum, χ_M molar susceptibility, MW the molecular weight of the compound framework (excluding the solvent molecules hosted in the pores), ρ_p the density of the compound framework, V_p particle volume, H and $\nabla(H_p)$ magnetic field and field gradient in the centre of the particle.

The particles are sustained at the position where the upwards force is maximum, according to equation (2) it corresponds to the position of most negative $H \cdot \nabla H$ product: close to the lower end of the pole (Figure 2.118).

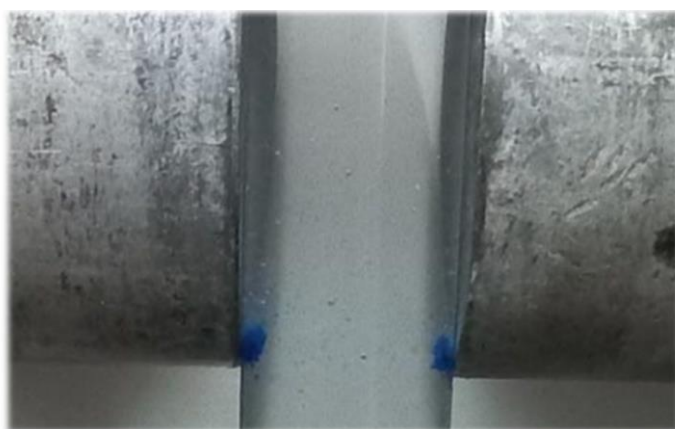


Figure 2.118. Heptameric compound particles immersed in water attached to the poles of an electromagnet.

The use of an electromagnet that allows dialling the magnetic field at the expense of the experimentalist, facilitates determining the critical magnetic field or more precisely the $H \cdot \nabla(H_p)$ at which the particles fall from the pole bottom edge. At this critical value, the forces exerted by the magnetic field and the gravity reduced by the flotation effect of being immersed in a liquid (Equation 3)

$$F_{magnetism} = F_{gravity} - F_{flotation} \quad (3)$$

This equilibrium can be employed for the quantification of adsorbed molecules within the channels of these materials. In other words, any increase of the particle weight (due to adsorption phenomena for example) will have a profound effect on the subtle balance between the magnetic attraction, gravity and flotation forces that determine the critical magnetic field at which the particles are detached from the poles of the electromagnet. Therefore, according to the previous equations the modification of this critical value towards higher magnetic fields will indicate the adsorption of the adsorbate

molecules within the pores of the material. It has been exemplified placing 15 mg of CU7ADNAPH-2 compound, in 1.5 mL of an aqueous solution containing 15 mg (or 15 μL if the adsorbate is liquid) of different adsorbates, some of them drugs, for an entire night (24 h) while gently stirred. The next day these particles were placed in a test-tube containing distilled water and the critical magnetic field is determined. The results are depicted in Figure 2.120, where we can observe a size exclusion based selectivity with greater deviation of the critical magnetic field for the smaller butan-1-ol and 5-fluorouracil.

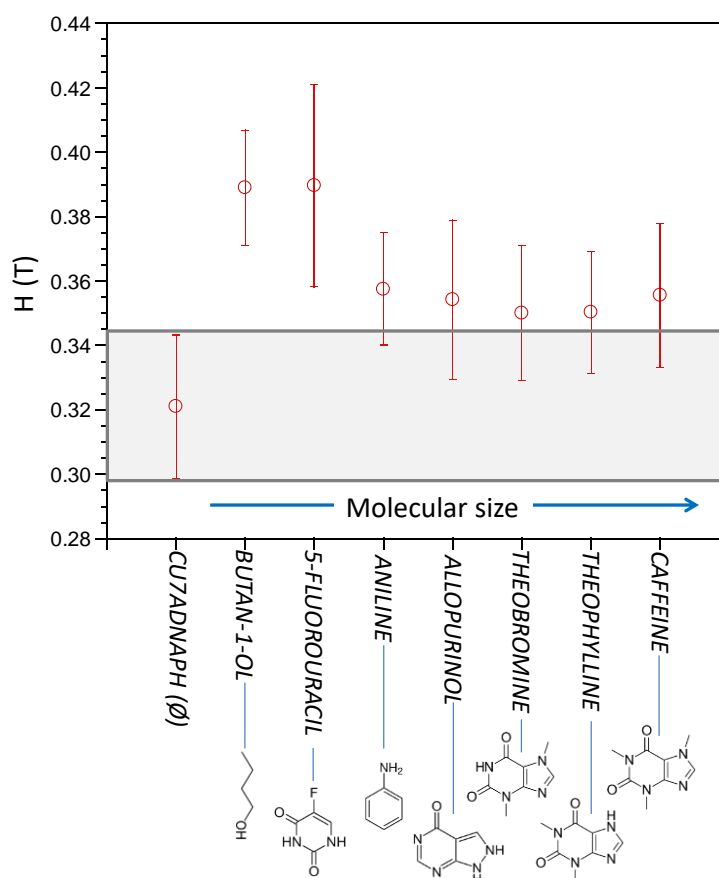


Figure 2.120. Measured critical magnetic field at which the **CU7ADNAPH-2** particles are detached from the pole of the electromagnet after the adsorption experiment in aqueous solutions of a series of substances. \emptyset indicates control experiment using pure water.

As below described, the equations governing this phenomena indicate a linear correlation between the adsorbed mass of guest molecules and H (more precisely the $H \cdot \nabla(H)$ product), in such a way that the greater the deviation with respect to the pristine critical magnetic value, the greater mass of adsorbate captured by the porous material. To demonstrate this relation we must separate the magnetic attraction force, gravitation and

flotation in terms accounting for the framework of the compound (the heptameric entity plus the organic counterion) and for the adsorbates.

$$\frac{\chi_M}{MW_F} \cdot \rho_F \cdot V_F \cdot H \cdot \nabla H = (V_F \cdot \rho_F + V_{Ads} \cdot \rho_{Ads}) \cdot g - (V_F \cdot \rho_{H_2O} + V_{Ads} \cdot \rho_{H_2O}) \cdot g \quad (4)$$

$$\frac{\chi_M}{MW_F} \cdot \rho_F \cdot H \cdot \nabla H = (\rho_F - \rho_{H_2O}) \cdot g + (\rho_{Ads} - \rho_{H_2O}) \cdot \frac{V_{Ads}}{V_F} \cdot g \quad (5)$$

with V_F (ρ_F) and V_{Ads} (ρ_{Ads}) being the volume (density) occupied by the framework and the adsorbate in the particle. As $V_F = \frac{M_F}{\rho_F} = \frac{n \cdot MW_F}{\rho_F}$ and $V_{Ads} = \frac{M_{Ads}}{\rho_{Ads}} = \frac{n \cdot x \cdot MW_{Ads}}{\rho_{Ads}}$, then $\frac{V_{Ads}}{V_F} = \frac{x \cdot MW_{Ads} \cdot \rho_F}{MW_F \cdot \rho_{Ads}}$ (n being the times the framework formula is repeated in the particle and x is the relative ratio between the adsorbed guest molecules and the compound framework formula). As a consequence equation 5 becomes :

$$H \cdot \nabla H = \frac{(\rho_F - \rho_{H_2O})}{\chi_M} \cdot \frac{MW_F}{\rho_F} \cdot g + \frac{(\rho_{Ads} - \rho_{H_2O})}{\chi_M} \cdot \frac{x \cdot MW_{Ads}}{\rho_{Ads}} \cdot g \quad (6)$$

In this latter equation, all parameters except " $H \cdot \nabla H$ " and " $x \cdot MW_{Ads}$ " are constants (we assume that the ρ of the different adsorbates are nearly the same), the above equation can be simplified to:

$$H \cdot \nabla H = A + B \cdot x \cdot MW_{Ads} = A + B \cdot M_{Ads} \quad (7)$$

M_{Ads} being the mass of drug adsorbed per formula of the framework compound. Therefore, there should be a linear relation between the adsorbed mass and the $H \cdot \nabla H$ parameter at which the particles are detached from the pole of the electromagnet. Having in mind the linear dependence between $H \cdot \nabla H$ and H , at least in the region where these experiments have been performed, the latter expression can be rewritten as equation 8:

$$H = A' + B' \cdot x \cdot MW_{Ads} = A' + B' \cdot M_{Ads} \quad (8)$$

Therefore we have quantified some of these adsorbates by means of $^1\text{H-NMR}$ measurement in which we determined the amount of the adsorbate in solution after repeating the same adsorption experiment but using D_2O and tertbutanol as internal reference (Figures 2.121). The obtained adsorption results are depicted in Figure 2.122 as red circles (corresponding to the pristine CU7ADNAPH-2 with its voids only filled by water, caffeine and butan-1-ol). It has allowed us determining the A' and B' parameters of equation 8 to determine the adsorbed mass (in percentage with respect to the mass of the adsorbent, CU7ADNAPH in this case) of the rest of the adsorbate molecules. These values correspond to the blue circles depicted in Figure 2.121.

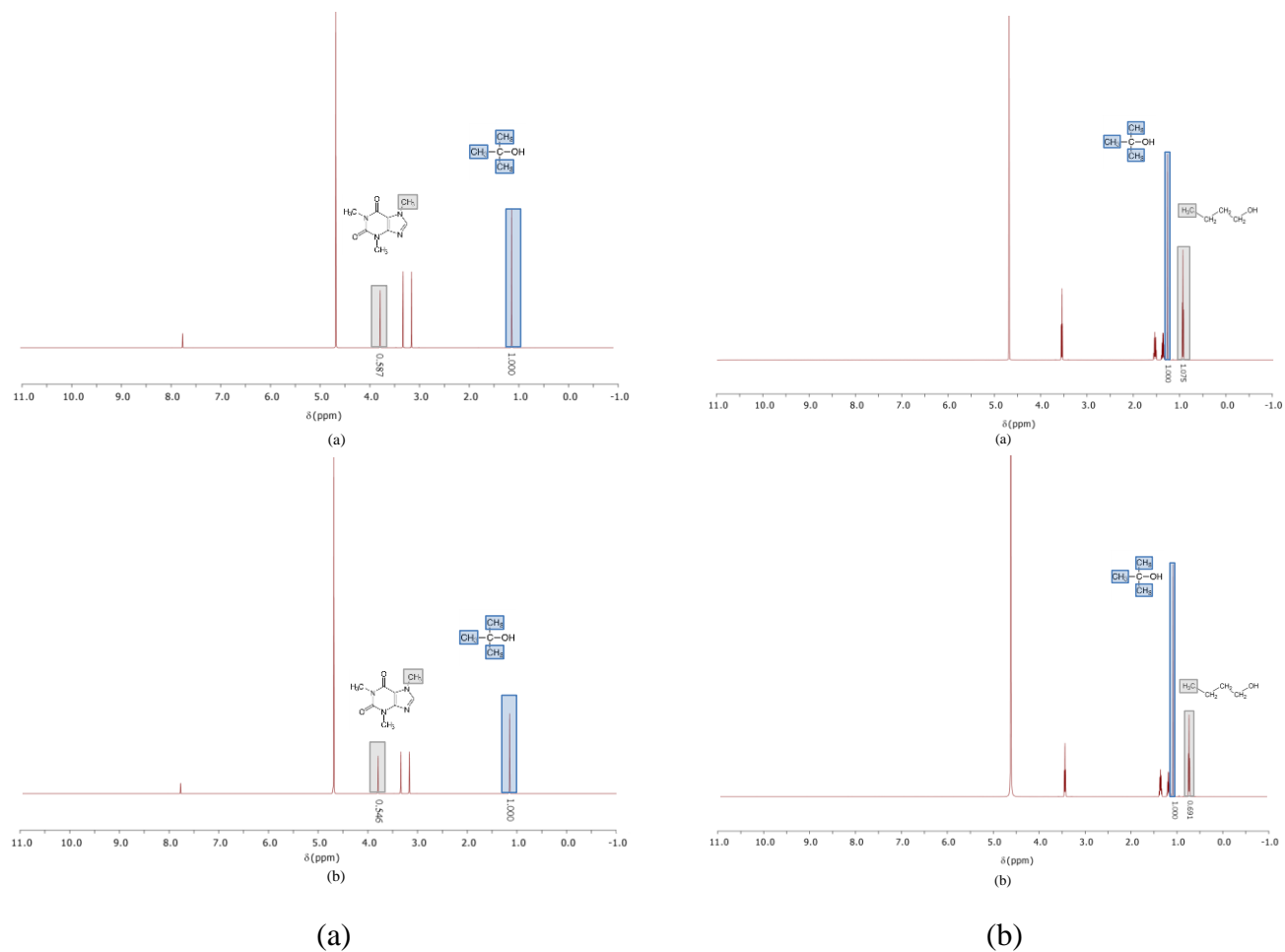


Figure 2.121. ¹H-NMR spectra of the blank solution (top) and of the filtered sample (bottom) containing the compound CU7ADNAPH-2 and (a) caffeine and (b) 1-butanol coloured in grey after 24h of continuous stirring..

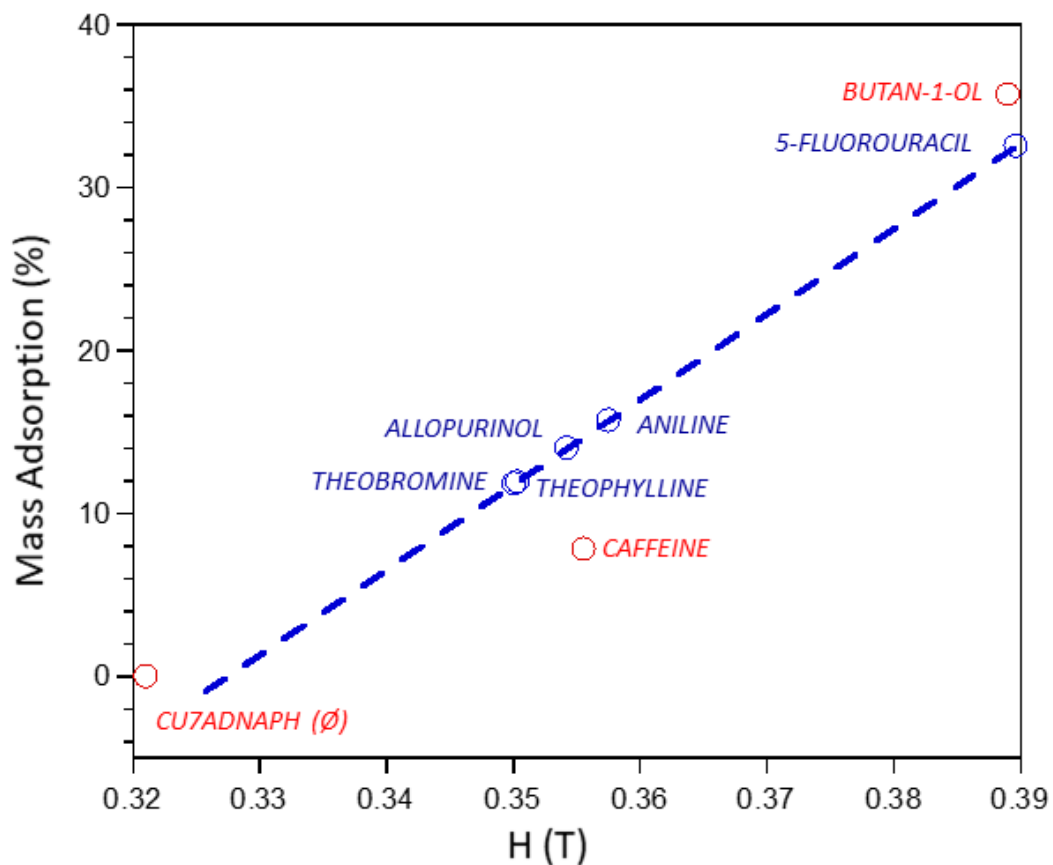


Figure 2.122. Percentage of adsorbed mass of the different adsorbates calculated by means of ^1H -NMR spectroscopy (red circles) with their linear fitting (dashed blue line) and the extrapolated values for the remaining adsorbates (blue circle).

Chapter 3:

Heterometallic adenine nucleobase based SMOFs for catalysis

3.1. Introduction

3.2. Synthesis and chemical characterization

3.3. Crystallographic analysis

3.4. Results and discussion

3.1. INTRODUCTION

In recent years, the unremitting increase in the concentration of CO₂ in our atmosphere has motivated an intense search for remediation industrial processes or strategies. The most studied options involve storage, separation and the valorization of this gas. The last option is the most desirable one and thanks to increasingly promising new developments in electroreduction, photoreduction and thermoreduction technologies, it is possible to transform CO₂ into value added species such as, CO, CH₄, HCOOH, H₂C₂O₄, CH₃OH, etc.²⁰⁹ Here we explore the opportunities arising from combining magnetic and catalyst properties and porosity in metal-organic materials.

All the above-described technologies require the use of catalysts: usually metal oxide or metallic nanoparticles in order to reduce the energy penalty for these transformations.²¹⁰ The use of metal-organic precursors to obtain these catalytically active nanoparticles has been well documented in the literature since long time ago.²¹¹ In that sense, sol-gel resins with a stochastic distribution of the metals and metal-organic precursors with an ordered crystal structure and a well-defined formula had been the most developed approaches.^{211b,212} The porous nature of the metal-organic precursor and the amount of organic matter incorporated in the starting material plays a crucial role in determining the final size of the particles and the amount of carbon resulting from the thermolysis. However, although there are studies carried out to implement the latter methodology to provide nanoparticles from heterometallic systems, it is more complicated and less

²⁰⁹ (a) Pajares, A.; Prats, H.; Romero, A.; Viñes, F.; de la Piscina, P. R.; Sayós, R.; Homs, N.; Illas, F. *Appl. Catal. B Environ.* **2020**, 267 (January), 118719. (b) Yang, L.; Pastor-Pérez, L.; Gu, S.; Sepúlveda-Escribano, A.; Reina, T. R. *Appl. Catal. B Environ.* **2018**, 232 (March), 464–471. (c) Zhuang, Y.; Currie, R.; McAuley, K. B.; Simakov, D. S. A. *Appl. Catal. A Gen.* **2019**, 575, 74–86. (d) Williamson, P. *Nature* **2016**, 530, 153–155.

²¹⁰ (a) Zhao, J.; Teng, Y. L.; Dong, B. X. *Energy and Fuels* **2020**, 34 (9), 11210–11218. (b) Juneau, M.; Vonglis, M.; Hartvigsen, J.; Frost, L.; Bayerl, D.; Dixit, M.; Mpourmpakis, G.; Morse, J. R.; Baldwin, J. W.; Willauer, H. D.; Porosoff, M. D. *Energy Environ. Sci.* **2020**, 13 (8), 2524–2539. (c) Zhou, H.; Chen, Z.; Kountoupi, E.; Tsoukalou, A.; Abdala, P. M.; Florian, P.; Fedorov, A.; Müller, C. R. *Nat. Commun.* **2021**, 12 (1), 1–10. (d) Williamson, D. L.; Herdes, C.; Torrente-Murciano, L.; Jones, M. D.; Mattia, D. *ACS Sustain. Chem. Eng.* **2019**, 7 (7), 7395–7402.

²¹¹ (a) Liu, W.; Zhai, P.; Li, A.; Wei, B.; Si, K.; Wei, Y.; Wang, X.; Zhu, G.; Chen, Q.; Gu, X.; Zhang, R.; Zhou, W.; Gong, Y. *Nat. Commun.* **2022**, 13 (1), 1–12. (b) Zhao, S.; Jin, R.; Jin, R. *ACS Energy Lett.* **2018**, 3 (2), 452–462.

²¹² (a) Li, D.; Kassymova, M.; Cai, X.; Zang, S.; Jiang, H. *Coord Chem Rev.* **2020**, 412, 213262. (b) Li, R.; Zhang, W.; Zhou, K. *Adv. Mater.* **2018**, 30 (35), 1–31. (c) Shah, S. S. A.; Najam, T.; Wen, M.; Zang, S.-Q.; Waseem, A.; Jiang, H.-L. *Small Struct.* **2021**, 2100090, 2100090. (d) Tseng, I.; Chang, W.; Wu, J. C. S. *Appl. Catal. B Environ.* **2002**, 37, 37–48. (e) Kornienko, N.; Zhao, Y.; Kley, C. S.; Zhu, C.; Kim, D.; Lin, S.; Chang, C. J.; Yaghi, O. M.; Yang, P. *J. Am. Chem. Soc.* **2015**, 137 (44), 14129–14135.

common.²¹³ In this chapter, we use an emerging class of porous metal-organic compound, known as SMOF (supramolecular assembled metal—organic framework), to yield homo- and heterometallic nanosized catalyst materials. Precisely, the metal-organic precursor consists of wheel shaped heptanuclear $[\text{Cu}_6\text{M}(\mu\text{-adeninato})_6(\mu_3\text{-OH})_6(\mu\text{-H}_2\text{O})_6]^{n+}$ cationic discrete entities $[\text{M}^{\text{II}}: \text{Cu}, \text{Co}, \text{Ni}, \text{Zn}]$ and organic carboxylate counterions that assemble together by means of π -stacking interactions and hydrogen bonds. The homometallic Cu_7 entities described in the last chapter presents the peculiarity that it contains two well-differentiated metallic environments: the central one with a regular MO_6 environment and the six peripheral ones with a CuO_4N_2 coordination sphere showing a notable Jahn-Teller tetragonal distortion. Due to this difference between the two environments, it is possible to obtain heterometallic compounds where we can locate several transition metals such as Cu(II) , Co(II) , Ni(II) , or Zn(II) in the central position but only Cu(II) is allowed to be placed in the six external positions, Figure 3.1.¹⁹²

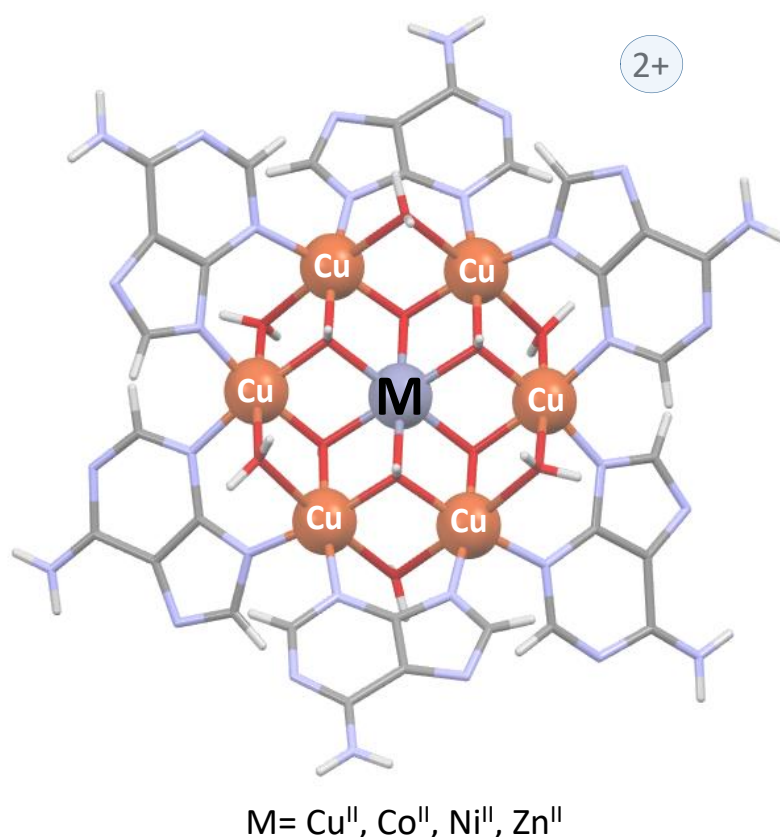


Figure 3.1. (a) Heptameric cluster depicting the targeted replacement of the central metal center where the grey atom is Cu, Co, Ni or Zn.

²¹³ Oar-Arteta, L.; Wezendonk, T.; Sun, X.; Kapteijn, F.; Gascon, J. *Mater. Chem. Front.* **2017**, *1* (9), 1709–1745.

Apart from those structural features, these compounds present two especially well suited characteristics for their use as precursors of metallic nanoparticles. The first one is the presence of the adenine nucleobase, which is a good reducing agent, facilitating the obtaining of the metallic nanoparticles by simple thermolysis under inert atmosphere (such as He, N₂, Ar). The second one is the porosity these compounds present that makes the metal clusters to be well separated among them to discourage the aggregation of the particles resulting from the thermolysis procedure. This fact removes the necessity to incorporate a great amount of organic material in the composition of the precursor to avoid that phenomena which also leads to the formation of a vast amount of carbonous matrix, whose relevance on the CO₂ thermal reduction will be discussed later. Related to the organic content of the precursor, the cationic nature of these entities requires the incorporation of counterions to compensate the (2+) charge of the heptameric entities. In this work, mono- and dicarboxylic organic counterions of different size and mass such as fumarate (C₄H₂O₄²⁻), naphthalene-2,6-dicarboxylate (C₁₂H₆O₄²⁻) and benzoate (C₇H₅O₂⁻) anions have been selected, Figure 3.2.

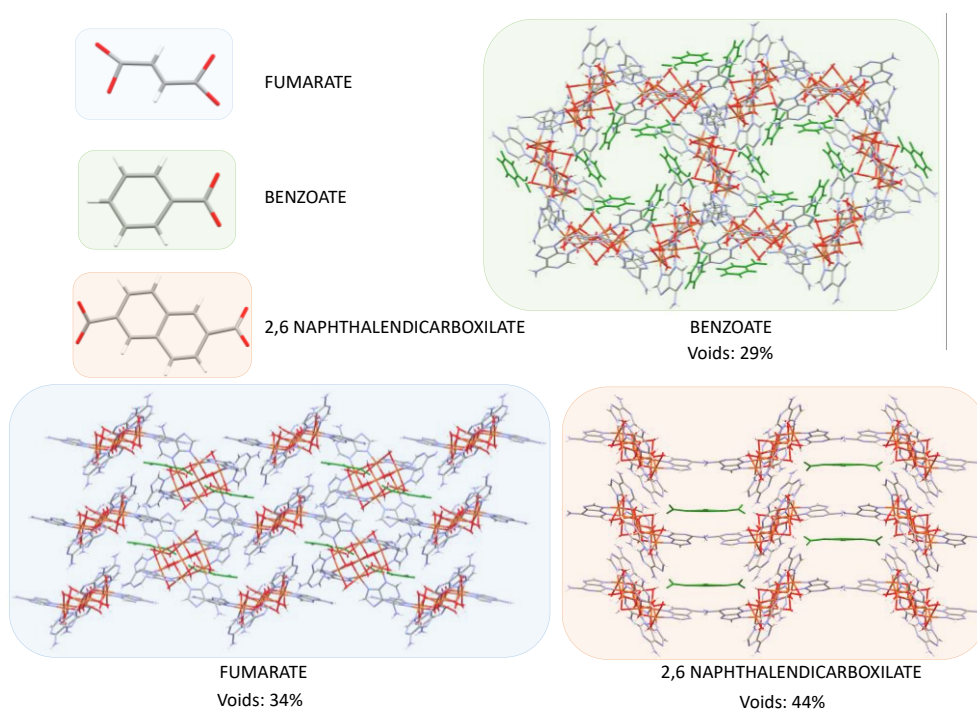


Figure 3.2. Scheme of the employed organic counterions with the porous packing of the heptameric entities with the organic counterions colored in green.

These features will allow to analyze the effect of the increase in organic content of the precursor on the final product and its influence on its catalytic properties. It is common when the thermal decomposition is carried out in an inert atmosphere that part of the

organic matter end up in final product as more or less graphitized carbon.²¹⁴ The presence of this carbon could play a positive or negative effect on the catalytic activity. This fact has been highly discussed, since the surface of the final product increases with the amount of carbon present, and it redounds in a better dispersion of the metallic nanoparticles with a lower sintering. However, there is also the risk of blocking the access to these catalytically active metallic nanoparticles.

In this sense, three copper homometallic compounds based on the previously mentioned heptanuclear entity and containing increasingly bulkier counterions before described have been used: CU7ADFA-2, CU7ADNAPH-2 and CU7ADBZ. They have been selected to analyze the influence the carbon content in the final thermolysis products has on their catalytic performance. Once this parameter has been analyzed a new three heterometallic compound has been synthesized with the fumarate counterion: CU6COADF, CU6NIADF and CU6ZNADF. These latter ones are aimed to analyze the possible synergic effects carried out on the CO₂ thermal reduction performance by the presence of a second transition metal in the nanoparticles.

²¹⁴ Ren, J.; Huang, Y.; Zhu, H.; Zhang, B.; Zhu, H.; Shen, S.; Tan, G.; Wu, F.; He, H.; Lan, S.; Xia, X.; Liu, Q. *Carbon Energy* **2020**, 2 (2), 176–202.

3.2. SYNTHESIS AND CHEMICAL CHARACTERIZATION

3.2.1. Synthesis

We report herein the synthesis and the chemical and structural characterization of the compounds listed in Table 3.1. The presence of the other transition metals, apart of Cu, it has been probe with surface techniques such as XRF (X-ray fluorescence) and bulk techniques such as ICP (Inductively coupled plasma).

Table 3.1. Formula and code use along this work of the compounds synthetized in this chapter.

Compound	Code
$[\text{Cu}_6\text{Co}(\mu\text{-ade})_6(\mu_3\text{-OH})_6(\mu\text{-H}_2\text{O})_6]\text{fumarate}\cdot\sim 24\text{H}_2\text{O}$	CU6COADF
$[\text{Cu}_6\text{Ni}(\mu\text{-ade})_6(\mu_3\text{-OH})_6(\mu\text{-H}_2\text{O})_6]\text{fumarate}\cdot\sim 19\text{H}_2\text{O}$	CU6NIADF
$[\text{Cu}_6\text{Zn}(\mu\text{-ade})_6(\mu_3\text{-OH})_6(\mu\text{-H}_2\text{O})_6]\text{fumarate}\cdot\sim 24\text{H}_2\text{O}$	CU6ZNADF

3.2.1.2. Synthesis of compound CU6COADF, CU6NIADF and CU6ZNADF

The synthesis of these heterometallics compounds follows a similar procedure than that previously described for the homometallic Cu_7 compounds using a mixture of 0.1700 g (0.7 mmol) of $\text{Cu}(\text{NO}_3)_2\cdot 3\text{H}_2\text{O}$ and (0.6 mmol) of $\text{Co}(\text{NO}_3)_2\cdot 6\text{H}_2\text{O}$, $\text{Ni}(\text{NO}_3)_2\cdot 6\text{H}_2\text{O}$, and $\text{Zn}(\text{NO}_3)_2\cdot 6\text{H}_2\text{O}$ for Co, Ni and Zn compound, respectively. At the first moment, a powdered sample was obtained and after 4-7 days green (CU6COADF), light blue (CU6NIADF) and dark blue (CU6ZNADF) crystals were obtained. All the final mixtures were basified to a higher pH, pH~9.4. Yield: 45%, 48% and 55%, respectively (based on metal).

The presence of the heterometallic atom was corroborated with an XRF and ICP study of the filtered samples, with values *ca.* 12%, 18% and 14% respectively in fresh samples. Due to the type of metallic atom substitution expected, only the central atom of the heptameric entity, the expected value is 14.3%.

3.2.2. Infrared spectroscopy

Figure 3.3 shows the infrared spectra for the compounds and Table 3.2 lists the wavenumbers of the most relevant observed bands,¹⁵⁸ their relative intensity and the assignment that has been proposed in each case.

Spectra exhibit the bands corresponding to the strain vibration of the C–H and N–H bonds of the purine bases in the region of the spectrum between 3400 and 3100 cm^{-1} , in addition to that due to the O–H bonds of the water molecules. Between 1700 cm^{-1} are the bands of the nucleobase ligands for the groups of amino. Around 1640 cm^{-1} , the asymmetric tension of the carboxylate group of the carboxylate anions are observed.¹⁵⁹ The presence of the peak located around 1600 cm^{-1} corresponding to the vibration of the C=C bond and the deformation of the NH_2 group is noteworthy, which allows the identification of adenine in all the compounds. The vibrational bands of the M–N bonds appear in all compounds below 550 cm^{-1} .

Heterometallic adenine nucleobase based SMOFs in catalyst

Table 3.2. Infrared spectra bands (cm^{-1})¹⁵⁷ of the compounds described in chapter 3.^a

Adenine	Fumaric acid	CU6COADF	CU6NIADF	CU6ZNADF	Assignment ^b
		3360vs	3360vs	3350vs	ν O—H,
3296s	—	3210vs	3200vs	3200vs	ν N—H
2930w	2925w	2920w	2920w	2920w	ν_{as} C—H
1670vs	1699vs	1640vs	1640vs	1640vs	ν_{as} C=O + δ NH ₂
1600vs	1620s	1610s	1600w	1600w	ν C=C+ ν C=N
—	1540w	1550s	1550vs	1550vs	ν_{s} C=O
1504s	—	1500w	1500w	1500w	ν C—NH ₂
—	1496vs	1460vs	1460vs	1460vs	ν_{as} COO
1420vs	1406m	1390vs	1400vs	1400vs	δ_{ring} + δ C—H
—	1382vs	1370s	1340s	1340s	ν_{s} COO
—	1296s/1152s	1300m/1150s	1310m/1150m	1310m/1140s	ν_{s} C—O
1230ss	1202s	1200vs	1200s	1200vs	δ_{ip} CCH
1020vs	1050s	1030m	1030m	1030m	γ C—H + γ NH ₂ + ν C—C _{arom}
—	990m	980m	980m	980m	ν_{s} COO
930vs	933m	930w	940w	940w	δ C—H, δ C—C
790vs	782m	790m	800m	800m	δ_{ip} C—H, ω NH ₂
720s/640vs	740m/660s	740m/660m	740m/660m	740m/660m	δ_{ip} ring defor., δ_{oop} COO ⁻
—	—	560m/460m	560m/440m	550m/420m	ν M—N

^avs: very strong, s: strong, m: medium, w: weak. ^bs: symmetric, as: antisymmetric, ν : stretching vibration, δ : bending vibration, γ : rocking, ω : wagging, ip = in plane, oop = out of plane..

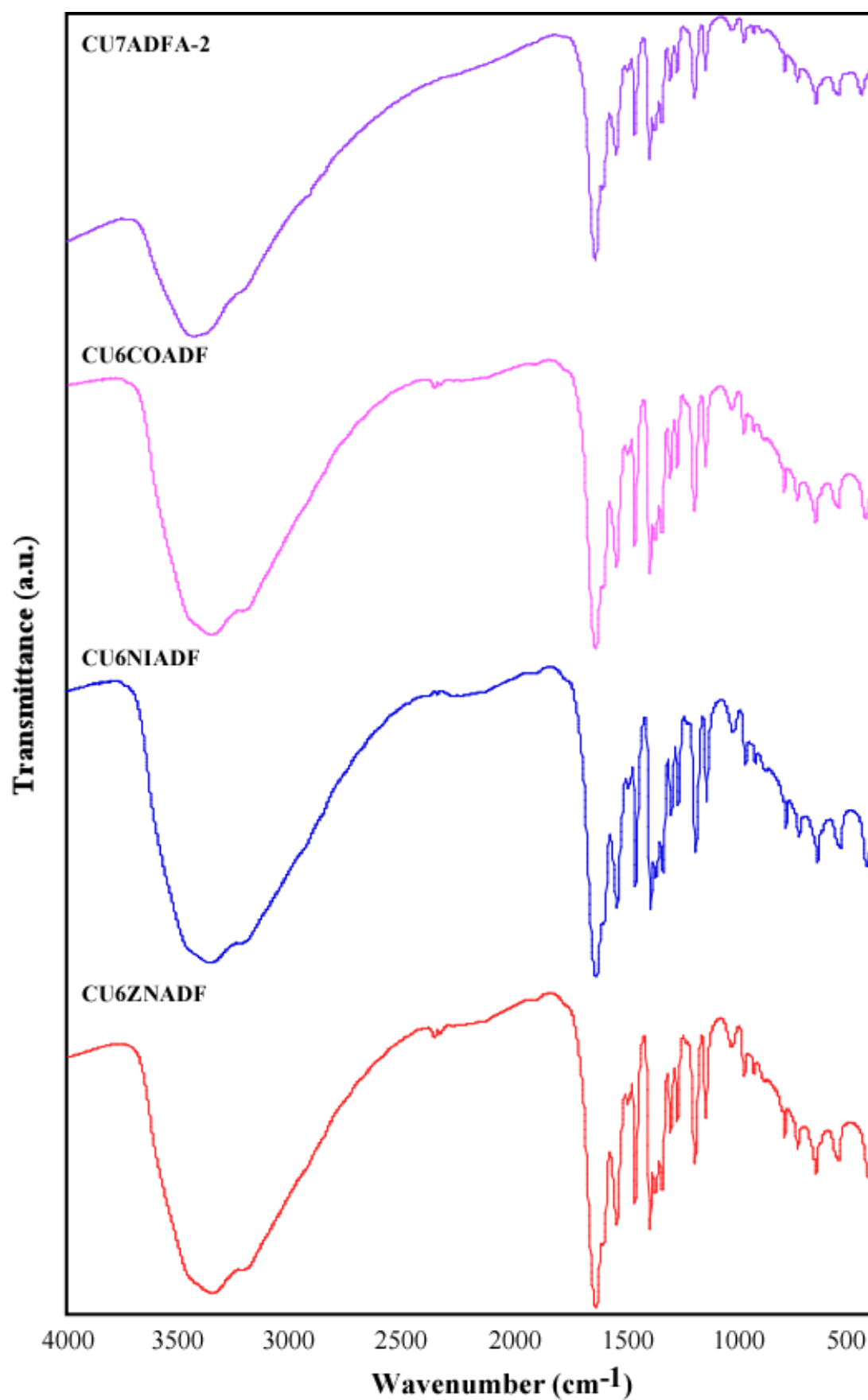


Figure 3.3. Infrared spectrum of compounds CU7ADFA-2 (purple), CU6COADF (pink), CU6NIADF (blue) and CU6ZNADF (red).

3.2.3. Thermal analysis

The results of the thermogravimetric analyses (TG/DTA curves) are plotted in Figure 3.3, while the processes occurring in each degradation stage are gathered in Table 3.3. Experimental mass losses fit fairly well with those expected from the chemical formula of the compounds.

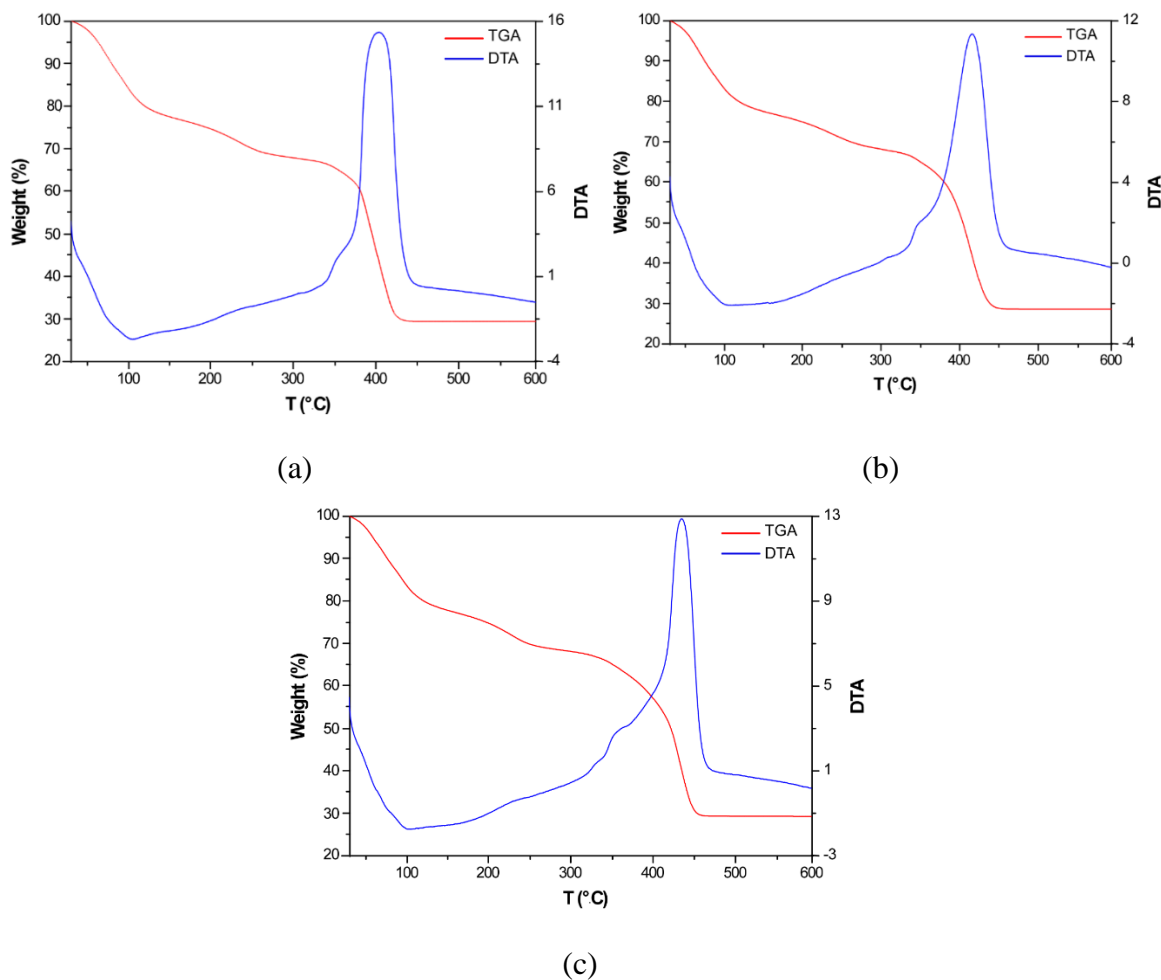


Figure 3.4. Thermogravimetric data (TGA-DTA curves) for compounds (a) CU₆COADF, (b) CU₆NIADF and (c) CU₆ZNADF.

Table 3.3. Thermoanalytic data.^a

Step	T _i	T _{peak}	T _f	ΔH	Δm(%)	ΣΔm(%)	ΣΔm(%) _{theor}
CU6COADF							
1	25	100	135	Endo	21.90	21.90	22.09 (-17 H ₂ O + -6 H ₂ O)
2	135	145	190	Endo	3.04	24.94	24.97 (-3 H ₂ O)
3	190	230	250	Exo	5.19	30.13	30.09 (-6 NH ₂)
4	335	405	600	Exo	40.26	70.39	70.60 (CuO, CoO)
CU6NIADF							
1	25	100	160	Endo	23.38	23.38	23.56 (-19 H ₂ O + -6 H ₂ O)
2	160		210		2.60	25.98	26.39 (-3 H ₂ O)
3	210		280		5.22	31.20	31.41 (-6 NH ₂)
4	330	420	600	Exo	39.70	70.90	71.12 (CuO, NiO)
CU6ZNADF							
1	25	95	115	Endo	20.00	20.00	20.01 (-27 H ₂ O + -3 H ₂ O)
2	115	160	200	Endo	5.72	25.72	25.54 (-3 H ₂ O + -3 H ₂ O)
3	200	230	260	Exo	4.93	30.65	30.59 (-6 NH ₂)
4	325	440	600	Exo	40.08	70.73	70.60 (CuO, ZnO)

^a T_i = initial temperature; T_{peak} = DTA peak temperature; T_f = final temperature; ΔH = type of process according to DTA, Δm(%) = mass loss percentage for each process; ΣΔm(%) = total mass loss percentage; ΣΔm(%)_{theor} = theoretical total mass loss percentage.

The fumarate anion, the thermograms show four main weight loss stages. First, in two overlapped stages crystallization solvent and coordination water molecules are released at a temperature range of 25–200 °C. Thereafter, in two overlapped stages the deamination of the adeninato ligands and the loss of three more water molecules due the deshydroxilation of three hydroxide group of the cluster at a range of dehydration occurred at a value range of 135–210 °C and 115–200 °C, respectively. Finally, the framework decomposition takes place to lead to a mixture of CuO and M^{II}O (M: Co, Ni or Zn) as final residue at 450 °C. Finally, the identification of the final product was performed by XRPD analysis on powder sample of all the above compounds. In all the compounds a very exothermic final decomposition stop takes place to lead to (CuO PDF: 48-1548) as final residue at 450 °C with the correspondent metal oxide (Co₃O₄: PDF 80-1541; NiO: PDF 47-1049; ZnO: PDF 36-1451), respectively.

3.2.4 Powder X-ray diffraction

The purity of the samples was checked by means of X-ray powder diffraction performed over samples introduced a Lindemann capillary and immersed in the synthesis mother liquid, Figure 3.5–3.7.

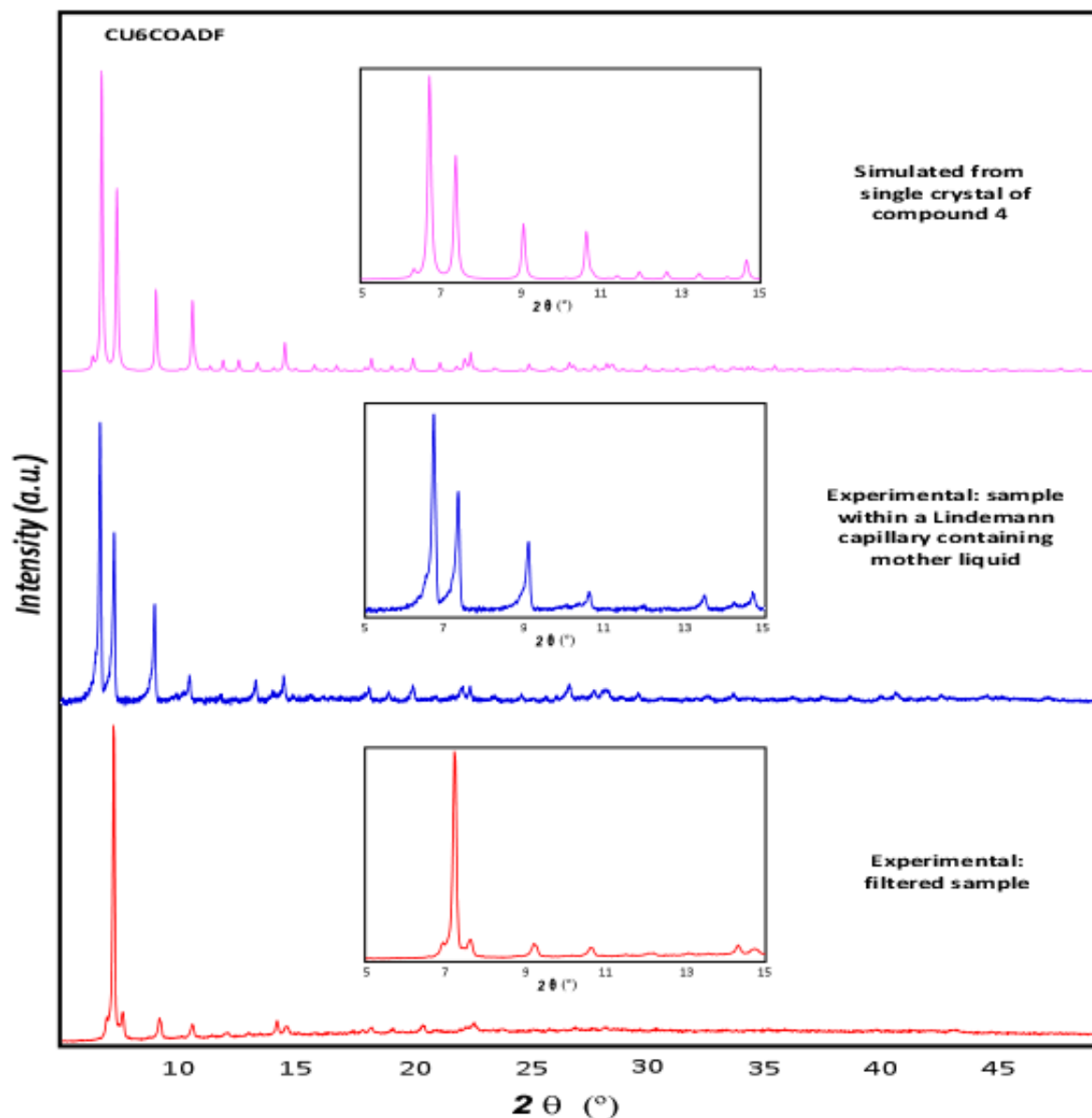


Figure 3.5. Powder X-ray diffraction patterns for compound CU6COADF: simulated one (top), sample in mother liquid (middle) and filtered sample (bottom). Depicted in the insets an amplification of the 5–15° area for a better comparison.

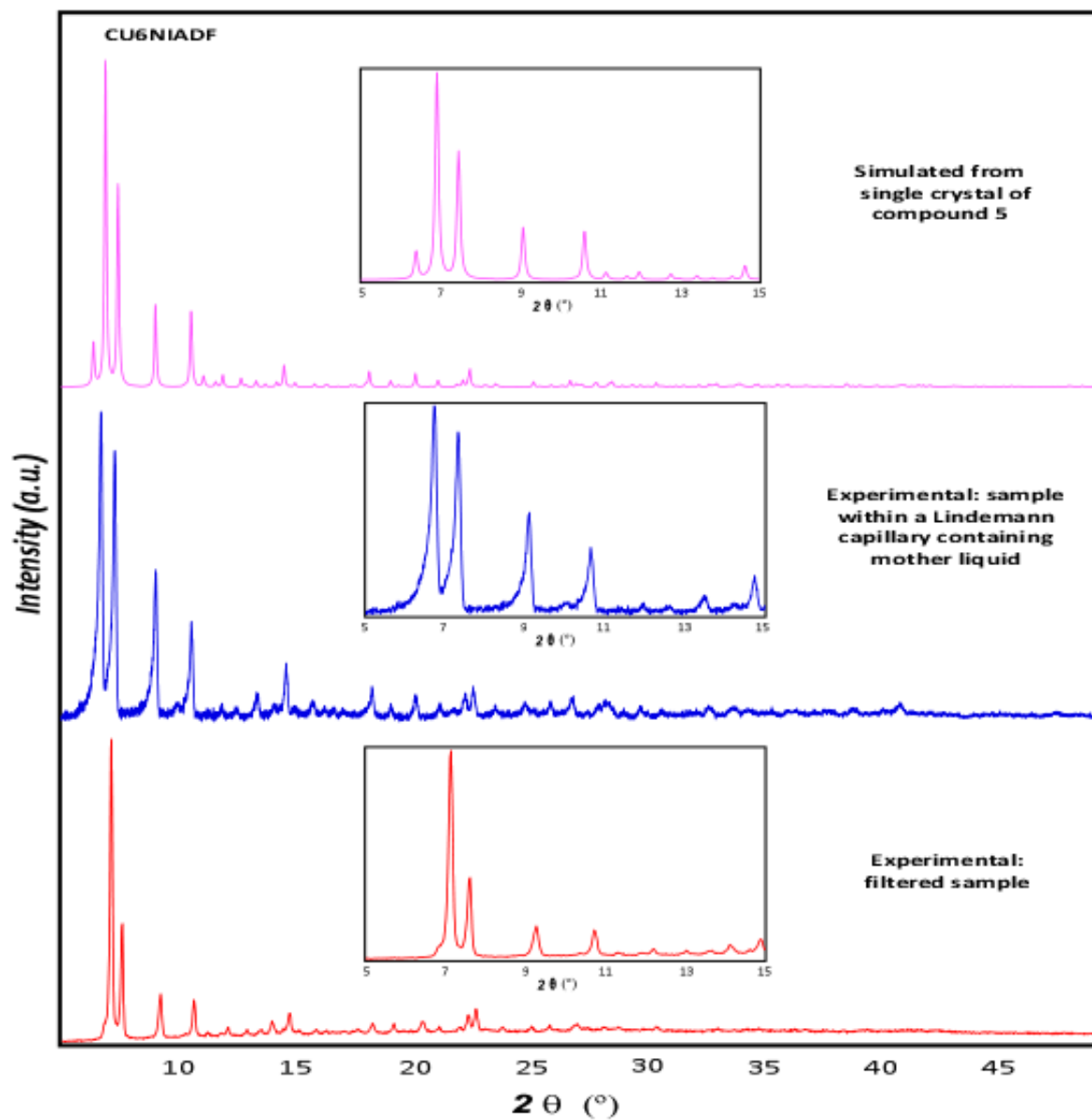


Figure 3.6. Powder X-ray diffraction patterns for compound CU6NIADF: simulated one (top), sample in mother liquid (middle) and filtered sample (bottom). Depicted in the insets an amplification of the 5–15° area for a better comparison.

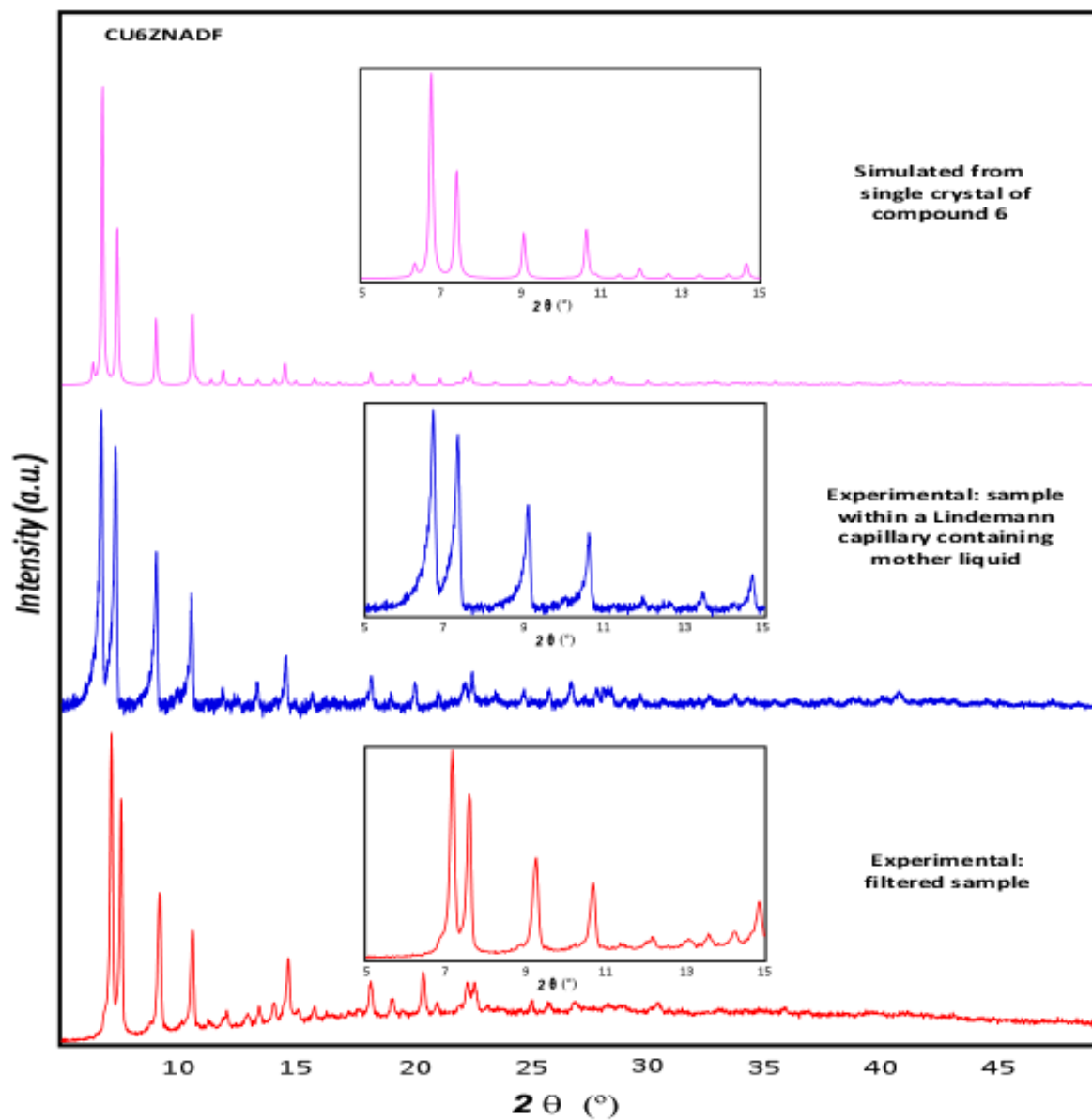


Figure 3.7. Powder X-ray diffraction patterns for compound CU6ZNADF: simulated one (top), sample in mother liquid (middle) and filtered sample (bottom). Depicted in the insets an amplification of the 5–15° area for a better comparison.

3.3. CRYSTALLOGRAPHIC ANALYSIS

The crystallographic data, the refinement conditions and parameters used in the structural resolution of each compound described in this chapter have been gathered in Table 3.4. All non-hydrogen atoms were refined anisotropically, except those corresponding to disordered entities. The hydrogen atoms belonging to organic entities have been geometrically fixed and refined according to a riding model with an isotropic thermal parameter linked to the atom to which they are attached (120 %). For the hydrogen atoms of the coordination water molecules cases the routine CALC-OH¹⁶¹ implemented in WinGX¹⁶² interface has been employed. The refinement of coordination water hydrogen atoms has been performed using an isotropic thermal parameter of 150 % regarding their parent atom. The crystallization water molecules of all the compounds, has not been possible to position the hydrogen atoms geometrically due to the disorder that these structures present.

As in the previous chapter, during the structural resolution of the compounds, the existence of a static disorder in the adenine molecules of two coplanar positions of the nitrogenous base with inverted orientation with respect to the coordination mode (μ - κ N3: κ N9 / μ - κ N9: κ N3). In all the compounds, this effect has been seen in at least two adenine of the asymmetric entity (in the heterometallics compound with nickel and zinc all of them are disordered). The disorder was modelled including the peaks observed as atoms split in two positions (A and B), to which common free occupancy factors were assigned to each of the subgroups with the condition that the two occupancy factors add up to 100 %.

Single-crystal diffraction X-ray Diffraction Data for structure determination were collected on Agilent Technologies Supernova diffractometers. The data reduction was done with the CrysAlisPro program.¹⁶³ Crystal structures were solved by direct methods using the SIR92¹⁶⁴ for CU6COADF, CU6ZNADF SUPERFLIP¹⁶⁵ for CU6NIADF and SHELXS¹⁶⁶ programs and refined by full-matrix least-squares on F^2 including all reflections (WINGX). The crystal structure of some of these compounds shows disorder on the positions of some of the adeninato ligands and/or the aromatic ring of the dicarboxylic ligands. The disorder was modelled distributing the disordered atoms over two positions and fixing the sum of their occupation factors to one. The high disorder that some solvent molecules present precluded their modeling and, as a consequence, the electron density was subtracted from the reflection data by the SQUEEZE method¹⁶⁷ as implemented in PLATON.¹⁶⁸

It is noteworthy that the crystal structure of all compounds display the presence of great channels in which the solvent molecules are placed. The high disorder of some of these entities precluded their modeling and, therefore, the electron density at the voids of the crystal structure was subtracted from the reflection data by the SQUEEZE method as implemented in PLATON. The electron density provided by the SQUEEZE routine matches the expected from the number of the species hosted in the channels. Once the process has been carried out, it is verified that the holes generated by the program are susceptible to the presence of a water molecule, taking as an example the value of ten electrons for each molecule. Although in most compounds, there is not a big difference with respect to the water molecules observed between single-crystal and thermogravimetric analysis. In all cases, the molecular weight used in the magnetic analysis was the obtained by single-crystal data.

Table 3.4. Crystallographic data and refinement details of compounds CU6COADF, CU6NIADF and CU6ZNADF.

	CU6COADF	CU6NIADF	CU6ZNADF
formula	C ₂₈ H ₄₂ CoCu ₆ N ₂₄ O ₁₀	C ₃₄ H ₈₂ Cu ₆ NiN ₃₀ O ₃₅	C ₃₄ H ₉₂ Cu ₆ N ₃₀ O ₄₀ Zn
formula weight	2001.54	1911.24	2007.98
crystal system	Monoclinic	Monoclinic	Monoclinic
space group	C 2/c (15)	C 2/c (15)	C 2/c (15)
a	36.179(3)	36.245(4)	36.207(4)
b	16.4648(4)	16.4286(5)	16.4605(4)
c	18.0085(15)	17.8649(19)	17.9932(19)
α	90	90	90
β	133.431(15)	135.19(2)	133.753(18)
γ	90	90	90
V (Å ³)	7790(2)	7498(2)	7746(2)
Z	4	4	4
T (K)	170.0(1)	170.0(1)	170.0(1)
λ (Å)	0.71073	0.71073	0.71073
Sizes (mm)	0.08, 0.08, 0.02	0.07, 0.07, 0.04	0.06, 0.03, 0.03
Shape	Cubic	Cubic	Square
Colour	Green	Blue	Blue
Max. and medium Δ/σ	0.001 / 0.000	0.000/0.000	0.000 / 0.000
θ interval (°)	2.094 – 24.999	2.094 – 24.998	2.093 – 24.998
hkl interval	-42 ≤ h ≤ 42; -19 ≤ k ≤ 19 -21 ≤ l ≤ 21	-42 ≤ h ≤ 43; -19 ≤ k ≤ 19; -21 ≤ l ≤ 21	-42 ≤ h ≤ 42; -19 ≤ k ≤ 17; -21 ≤ l ≤ 21
ρ _c (g·cm ⁻³)	1.707	1.707	1.722
μ (cm ⁻¹)	1.922	1.922	2.028
F(000)	4108	4108	4120
S ^a	1.076	1.700	1.594
R _{int}	0.0354	0.0311	0.0371
Parameters	412	377	390
Weight scheme ^c	Shelx	Shelx	Shelx
final R indices			
[I > 2σ(I)] R ₁ ^b /wR ₂ ^c	0.0943/0.2834	0.1385/0.4153	0.1151/0.3742
all data R ₁ ^b /wR ₂ ^c	0.1123/0.3022	0.1696/0.4435	0.1385/0.3948
^a S=[∑w(F ₀ ² -F _c ²) ² /(N _{obs} -N _{param})] ^{1/2} . ^b R ₁ =∑ F ₀ - F _c /∑ F ₀ . ^c wR ₂ =[∑w(F ₀ ² -F _c ²) ² /∑wF ₀ ²] ^{1/2} ; w = 1/[σ ² (F ₀ ²) + (aP) ² + b] where P = (max(F ₀ ² ,0) + 2F _c ²)/3; CU6COADF (a =0.1806, b = 48.9128); CU6NIADF (a =0.2000, b =0) and CU6ZNADF (a =0.2000, b =0).			

3.3.1. Structural description of heterometallics compounds

Crystal structures of heterometallics compounds: CU6COADF, CU6NIADF and CU6ZNADF consist of an asymmetric unit of wheel shaped heptanuclear cationic entities with formula $[\text{Cu}_6\text{M}^{\text{II}}(\mu\text{-ade-}\kappa\text{N3}:\kappa\text{N9})_6(\mu_3\text{-OH})_6(\mu\text{-H}_2\text{O})_6]^{2+}$ where (M^{II} : Co, Ni or Zn), half fumarate counterions and crystallization water molecules. The connectivity within the heptanuclear entities is essentially identical to the compound described in chapter 2 with the code CU7ADF-1, with a central $[\text{M}^{\text{II}}(\text{OH})_6]^{4-}$ (M^{II} : Co, Ni or Zn) core connected to the six copper(II) metal centers comprising the external ring, Table 3.5–3.7. The peripheral copper atoms are further connected among them through the double $\mu\text{-H}_2\text{O}$ and $\mu\text{-ade-}\kappa\text{N3}:\kappa\text{N9}$ bridge, Figure 3.8. The elongation at the peripheral copper atoms takes place along the metal-water coordination bonds, in such a way that the coordinated water molecules are less strongly held to the complex entity than the adeninato ligands that establish shorter coordination bonds. All the metal centers of heterometallics compounds present an octahedral geometry without the usual Jahn-Teller tetragonal elongation for the homometallics compounds. This allows the possibility of being able to exchange only the central copper atom for other transition metals. In any case, the heptameric entity can be considered as a rigid building unit as all the components establish at least two coordination bonds.

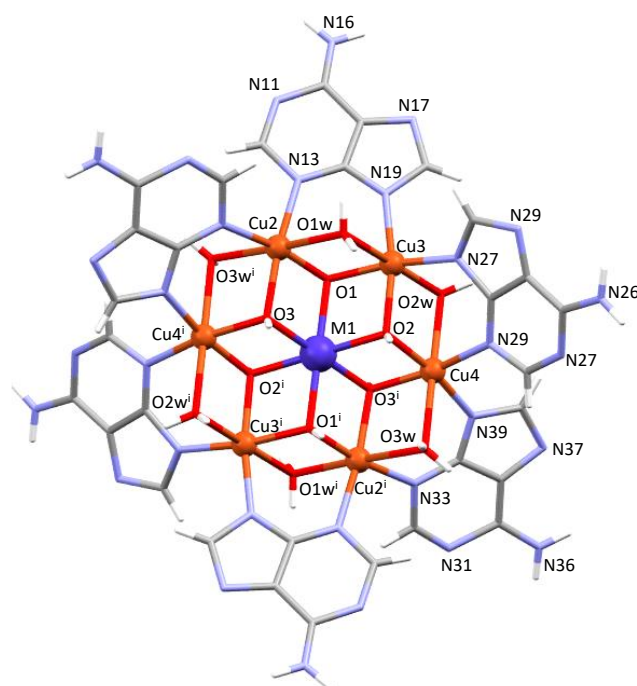


Figure 3.8. Scheme of the heptameric cluster labeled of compounds CU6COADF, CU6NIADF and CU6ZNADF, where the purple atom is Co, Ni and Zn respectively.

Table 3.5. Distances and angles (Å, deg) for compound CU6COADF.^a

Co1–O1	2.008(4)	Co1–O2	2.074(5)	Co1–O3	2.075(6)
Cu2–O1	1.982(5)	Cu2–O3	1.991(4)	Cu2–N13	2.032(8)
Cu2–N33i	2.030(10)	Cu2–O1w	2.369(9)	Cu2–O3wi	2.495(11)
Cu3–O1	1.967(5)	Cu3–O2	1.976(5)	Cu3–N19	1.986(8)
Cu3–N29	1.957(10)	Cu3–O1w	2.485(9)	Cu3–O2w	2.474(7)
Cu4–O2	1.984(5)	Cu4–O3i	1.964(6)	Cu4–N23	1.995(10)
Cu4–N39	2.023(10)	Cu4–O2w	2.464(7)	Cu4–O3w	2.519(9)
Co1…Cu2	3.101(11)	Cu1…Cu3	3.130(11)	Cu1…Cu4	3.109(11)
Cu2…Cu3	3.101(17)	Cu2…Cu4i	3.126(16)	Cu3…Cu4	3.114(16)
Co1–O1–Cu2	99.2(2)	Co1–O1–Cu3	101.1(2)	Cu2–O1–Cu3	103.5(3)
Co1–O2–Cu3	101.2(3)	Co1–O2–Cu4	100.0(3)	Cu3–O2–Cu4	103.7(3)
Co1–O3–Cu2	99.4(3)	Co1–O3–Cu4i	100.6(3)	Cu2–O3–Cu4i	104.4(3)
Cu2–O1w–Cu3	79.4(3)	Cu3–O2w–Cu4	78.2(2)	Cu2i–O3w–Cu4	77.1(3)

^a Symmetry: (i) 3/2 – x, 1/2 – y, 1 – z.**Table 3.6.** Distances and angles (Å, deg) for compound CU6NIADF.^a

Ni1–O1	2.063(9)	Ni1–O2	1.994(10)	Ni1–O3	2.072(7)
Cu2–O1	1.974(8)	Cu2–O3 ⁱ	1.957(9)	Cu2–N13	1.980(2)
Cu2–N33 ⁱ	2.022(14)	Cu2–O1w	2.600(2)	Cu2–O3w ⁱ	2.405(19)
Cu3–O1	1.953(10)	Cu3–O2	2.008(10)	Cu3–N19	2.044(18)
Cu3–N23	2.031(18)	Cu3–O1w	2.490(2)	Cu3–O2w	2.446(12)
Cu4–O2	1.978(9)	Cu4–O3	1.942(10)	Cu4–N29	1.890(3)
Cu4–N39	2.042(18)	Cu4–O2w	2.476(12)	Cu4–O3w	2.485(19)
Ni1…Cu2	3.0873(15)	Ni1…Cu3	3.0901(16)	Ni1…Cu4	3.080(17)
Cu2…Cu3	3.093(2)	Ni2…Cu4 ⁱ	3.072(3)	Cu3…Cu4	3.093(2)
Ni1–O1–Cu2	99.7(4)	Ni1–O1–Cu3	100.6(5)	Cu2–O1–Cu3	103.9(5)
Ni1–O2–Cu3	101.1(5)	Ni1–O2–Cu4	101.7(5)	Cu3–O2–Cu4	101.8(5)
Ni1–O3–Cu2 ⁱ	100.0(4)	Ni1–O3–Cu4 ⁱ	100.2(4)	Cu2i–O3–Cu4	104.0(5)
Cu2–O1w–Cu3	74.8(7)	Cu3–O2w–Cu4	77.9(4)	Cu2i–O3w–Cu4	77.8(6)

^a Symmetry: (i) 3/2 – x, 1/2 – y, 1 – z.

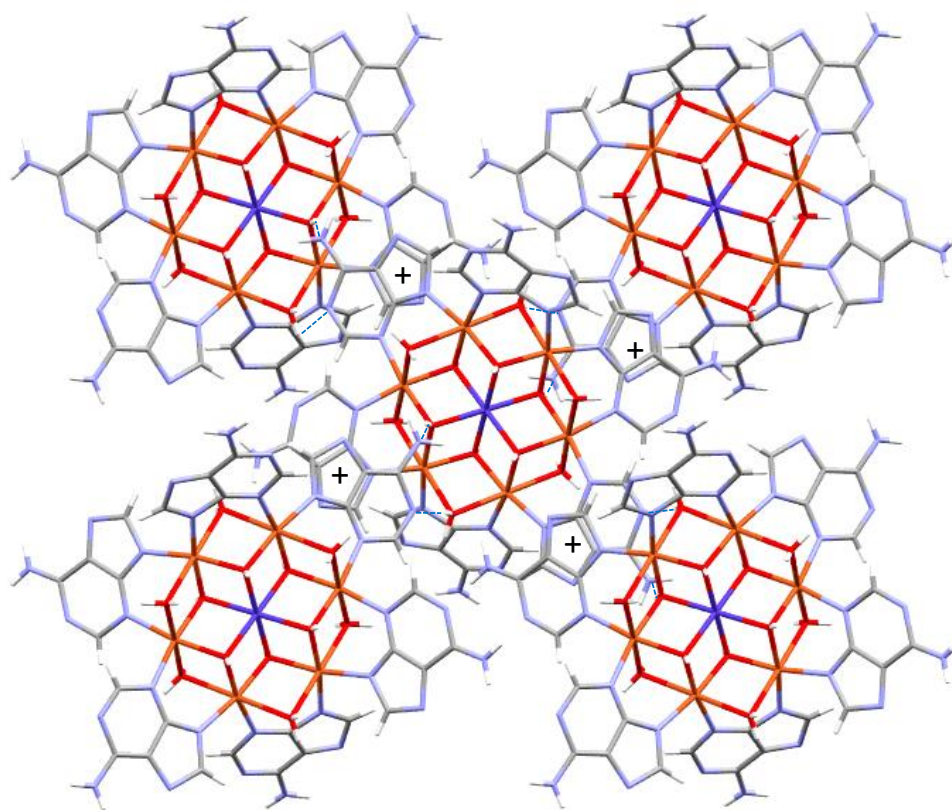
Table 3.7. Distances and angles (Å, deg) for compound CU6ZNADF.^a

Zn1–O1	2.038(8)	Zn1–O2	2.062(6)	Zn1–O3	2.051(7)
Cu2–O1	1.984(8)	Cu2–O3 ⁱ	1.959(8)	Cu2–N13	1.977(13)
Cu2–N39 ⁱ	2.042(14)	Cu2–O1w	2.455(10)	Cu2–O3w ⁱ	2.520(11)
Cu3–O1	1.980(7)	Cu3–O2	1.958(8)	Cu3–N19	1.963(14)
Cu3–N29	1.979(12)	Cu3–O1w	2.467(11)	Cu3–O2w	2.489(12)
Cu4–O2	1.983(7)	Cu4–O3	1.982(6)	Cu4–N23	2.037(12)
Cu4–N33	2.061(17)	Cu4–O2w	2.363(13)	Cu4–O3w	2.482(12)
Zn1···Cu2	3.0834(12)	Zn1···Cu3	3.1028(13)	Zn1···Cu4	3.0831(11)
Cu2···Cu3	3.1002(18)	Cu2···Cu4 ⁱ	3.0927(18)	Cu3···Cu4	3.0774(19)
Zn1–O1–Cu2	100.1(4)	Zn1–O1–Cu3	101.1(4)	Cu2–O1–Cu3	102.9(4)
Zn1–O2–Cu3	101.0(3)	Zn1–O2–Cu4	99.3(3)	Cu3–O2–Cu4	102.7(4)
Zn1–O3–Cu2 ⁱ	100.5(4)	Zn1–O3–Cu4	99.7(3)	Cu2 ⁱ –O3–Cu4	103.4(4)
Cu2–O1w–Cu3	78.1(3)	Cu3–O2w–Cu4	78.7(4)	Cu2 ⁱ –O3w–Cu4	76.4(4)

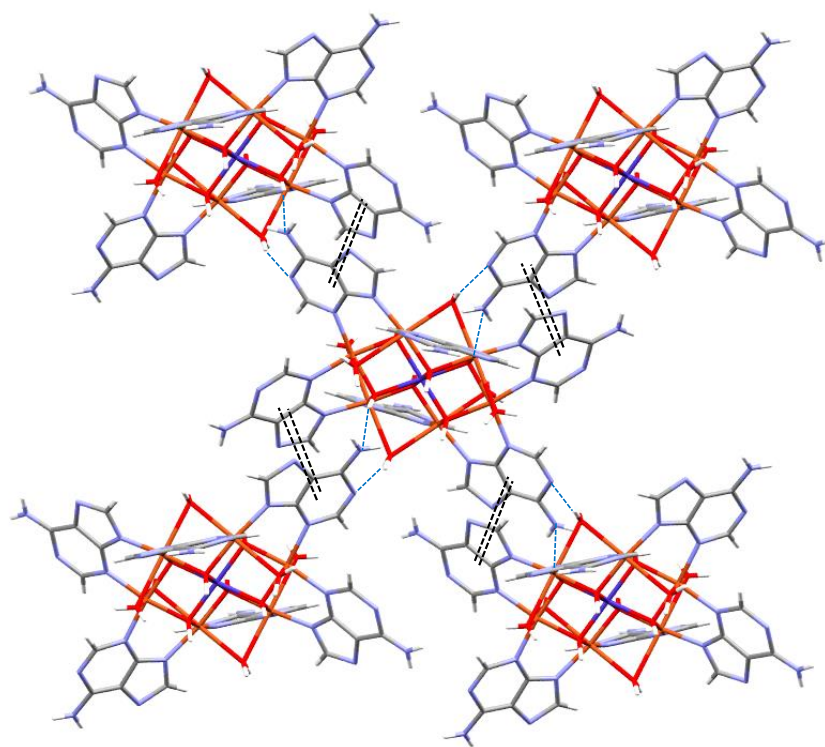
^a Symmetry: (i) $3/2 - x, 1/2 - y, 1 - z$.

In all the heterometallics compounds the supramolecular architecture is sustained by two mayor non-covalent interactions. The first one comes from an adeninato···adeninato π – π stacking interactions taking place between four *trans* adeninato ligand of the central heptamer and each one of four adjacent heptamers, Figure 3.9. These connections between heptameric units are reinforced with the second interaction, a double additional hydrogen bond involving the hexagonal ring (NX1) and the amino group (NX6) of the adeninato ligand of the adjacent heptameric entity and a hydroxide and a water molecule of the central cluster.

The supramolecular architecture of compounds is completed by direct hydrogen bonding interactions (Table 3.8–10) between the carboxylate groups of the fumarate anion located on the two adeninato ligands that not take part in the above interactions and a hydroxide and a coordination water molecule cluster of the original and another heptamer, Figure 3.10. Each carboxylate group of the organic anion is attached to the nearest cationic layer by two $O_{\text{anion}} \cdots H-O_{\text{cation}}$ hydrogen bonds, one with a hydroxide group and the other one with a water molecule coordinated to the same copper atom, to form a supramolecular $R_2^2(8)$ synthon.



(a)



(b)

Figure 3.9. Crystal packing of heterometallics compounds sustained by supramolecular interactions connecting the structural entities (hydrogen bond: dotted lines; π - π interaction: double dashed lines or + symbol).

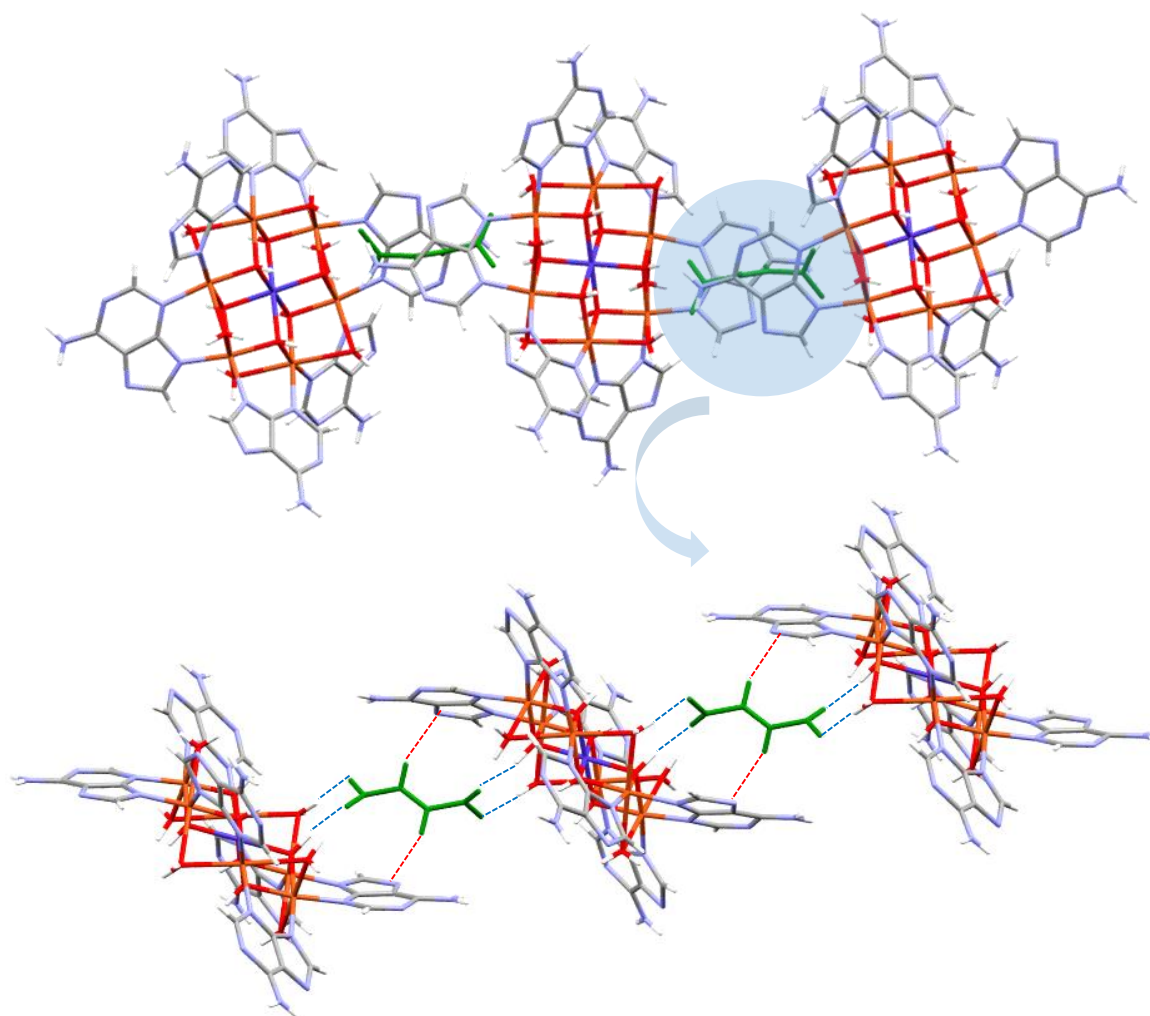


Figure 3.10. Insertion of the fumarate anion between the heptameric entity and (b) hydrogen bond interaction between the two cluster involved.

Unlike the CU7ADFA-1/2 compound, the fumarate anion in the heterometallic compounds, it is arranged between two adeninato ligands (one from the central cluster and one adjacent to it). The fumarate is still sandwiched between them but its vinylic hydrogen atoms are pointing perpendicularly to the aromatic system of the adeninato ligand in a T shaped π -interaction, Figure 3.11a/b. These anions are the ones that interact and expand the layers formed by the heptameric entities. This difference to the M–OH bond distance modification in the core of the heptameric entity because of the different coordination environment taking place for the Jahn-Teller distorted of copper(II) and the regular cobalt, nickel and zinc metal centers. Although this modification changes the resulting supramolecular interactions as previously described, but it does not change the porous nature of the heterometallic compound, as described below.

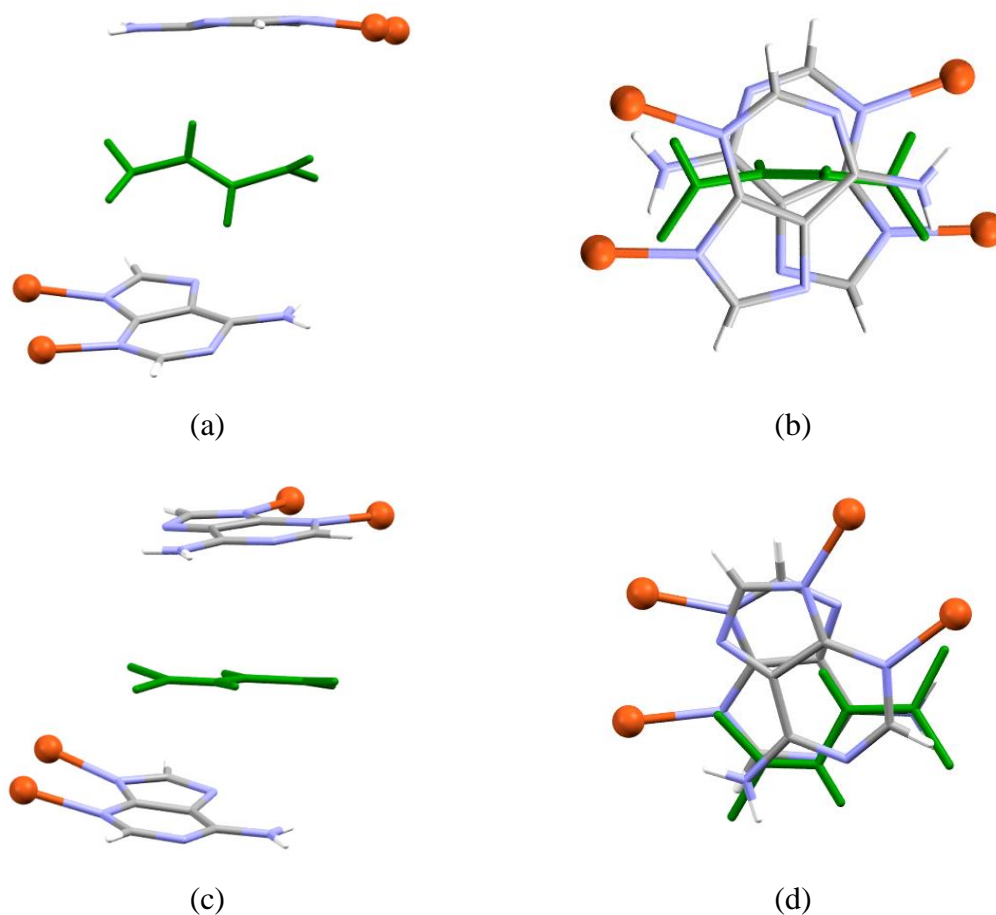


Figure 3.11. Representation of the fumarate anion between two different adeninato ligands in (a) and (b) heterometallic compounds and (c) and (d) in CU7ADFA-1/2.

Table 3.8. Structural parameters (\AA , $^\circ$) of the supramolecular interactions in CU6COADF.^a

Hydrogen-bonding interactions					
D–H \cdots A ^b	H \cdots A	D \cdots A	D–H \cdots A		
O2–H2 \cdots O49	1.83	2.81(2)	170		
O1w–H11w \cdots O48	1.79	2.65(2)	176		
O2w–H21w \cdots N31 ⁱ	1.78	2.61(3)	164		
π – π interactions ^c					
ring – ring	packing	angle	DC	DZ	DXY
1pa \cdots 3pa ⁱ	A \cdots A	4.0	4.06	3.62	1.91
X–H \cdots π interactions ^d					
	packing	H–Perp	H \cdots Cg	X–H \cdots Cg	X–H \cdots ring
C42–H42 \cdots 2pa ⁱⁱⁱ	F \cdots A	2.64	2.81	143	61

^aSymmetry codes: (i) $3/2 - x, -1/2 + y, 3/2 - z$ (ii) $3/2 - x, -1/2 + y, 3/2 - z$; (iii) $2 - x, y, 1/2 - z$. ^bD: donor; A: acceptor. ^cAngle: dihedral angle between the planes (deg), DC: distance between the centroids of the rings (\AA), DZ: interplanar distance (\AA), DXY: lateral displacement (\AA), pa: adenine pentagonal ring, ha: adenine hexagonal ring. ^dH–Perp: Perpendicular distance of H to ring plane; H \cdots Cg: distance of H to the centroid of the ring; X–H \cdots Cg: X–H \cdots Cg angle; X–H \cdots ring: angle of the X–H bond with the aromatic ring.

Table 3.9. Structural parameters (Å, °) of the supramolecular interactions in CU6NIADF.^a

Hydrogen-bonding interactions					
D–H...A ^b		H...A	D...A	D–H...A	
O3–H3...N16A ⁱ		1.93	2.91(3)	177	
O2w–H21w...N11 ⁱⁱ		2.05	2.91(2)	172	
O3w–H32w...O49		1.78	2.61(3)	164	
π – π interactions ^c					
ring – ring	packing	angle	DC	DZ	DXY
1pa...3pa ⁱⁱ	A...A	6.0	4.10	3.67	1.78
X–H... π interactions ^d					
	packing	H–Perp	H...Cg	X–H...Cg	X–H...ring
C42–H42...2pa ⁱⁱⁱ	F...A	2.54	2.76	143	61

^aSymmetry codes: (i) $3/2 - x, 1/2 + y, 1/2 - z$ (ii) $3/2 - x, -1/2 + y, 1/2 - z$; (iii) $2 - x, y, 1/2 - z$. ^bD: donor; A: acceptor. ^cAngle: dihedral angle between the planes (deg), DC: distance between the centroids of the rings (Å), DZ: interplanar distance (Å), DXY: lateral displacement (Å), pa: adenine pentagonal ring, ha: adenine hexagonal ring. ^dH–Perp: Perpendicular distance of H to ring plane; H...Cg: distance of H to the centroid of the ring; X–H...Cg: X–H...Cg angle; X–H...ring: angle of the X–H bond with the aromatic ring.

Table 3.10. Structural parameters (Å, °) of the supramolecular interactions in CU6ZNADF.^a

Hydrogen-bonding interactions					
D–H...A ^b		H...A	D...A	D–H...A	
O1–H1...O48		1.86	2.83(2)	172	
O2–H2...N36A ⁱ		1.90	2.88(2)	176	
O1w–H11w...N31 ⁱ		2.25	2.93(2)	135	
O2w–H21w...O49		1.81	2.68(2)	171	
π – π interactions ^c					
ring – ring	packing	angle	DC	DZ	DXY
2pa...3pa ⁱⁱ	A...A	4.0	4.09	3.65	1.91
X–H... π interactions ^d					
	packing	H–Perp	H...Cg	X–H...Cg	X–H...ring
C42–H42...1pa ⁱⁱⁱ	A...A	2.36	2.66	136	71

^aSymmetry codes: (i) $x, 1 - y, 1/2 + z$ (ii) $-x, -y + 2, -z + 2$; (iii) $3/2 - x, 1/2 - y, 1 - z$. ^bD: donor; A: acceptor. ^cAngle: dihedral angle between the planes (deg), DC: distance between the centroids of the rings (Å), DZ: interplanar distance (Å), DXY: lateral displacement (Å), pa: adenine pentagonal ring, ha: adenine hexagonal ring. ^dH–Perp: Perpendicular distance of H to ring plane; H...Cg: distance of H to the centroid of the ring; X–H...Cg: X–H...Cg angle; X–H...ring: angle of the X–H bond with the aromatic ring.

The resulting supramolecular architecture of compound CU6COADF, CU6NIADF and CU6ZNADF shows a two-dimensional channels with ovoid holes surrounded by the N-site of the adeninato ligands belonging to heptameric cations generating the box described in the isorecticular compounds of chapter 2. The voids are connected with corridors with an approximate radius of 4.9, 4.1 and 3.4 Å, respectively (Figure 3.12). The greater value of the corridor in compound CU6COADF generate a higher value of the pore volume comparing

with the other ones. It can be explained with the different stages of dehydration of the compounds. The volume of these channels, occupied by the crystallization water molecules has a range of 2449–2841 Å³ per unit cell (36%, 33% and 36% respectively of the total volume as calculated by PLATON). A computational analysis shows an accessible surface area value of 1365, 349 and 450 m²·g⁻¹ and a pore volume of 0.273, 0.235 and 0.267 cm³·g⁻¹ respectively, Table 3.11.

Table 3.11. Experimental data of the computational analysis of the voids of compounds.

Compounds	Pore (Å)	Corridor min/max (Å)	Void volume (Å ³)	Void (%)	Surface area (m ² /g)	Pore volume (mL/g)
CU6COADF	6.1 x 7.1	4.4 x 7.4	2841	36	1365	0.273
CU6NIADF	4.8 x 5.8	3.4 x 6.3	2449	33	349	0.235
CU6ZNADF	5.1 x 6.4	3.3 x 6.6	2799	36	450	0.267

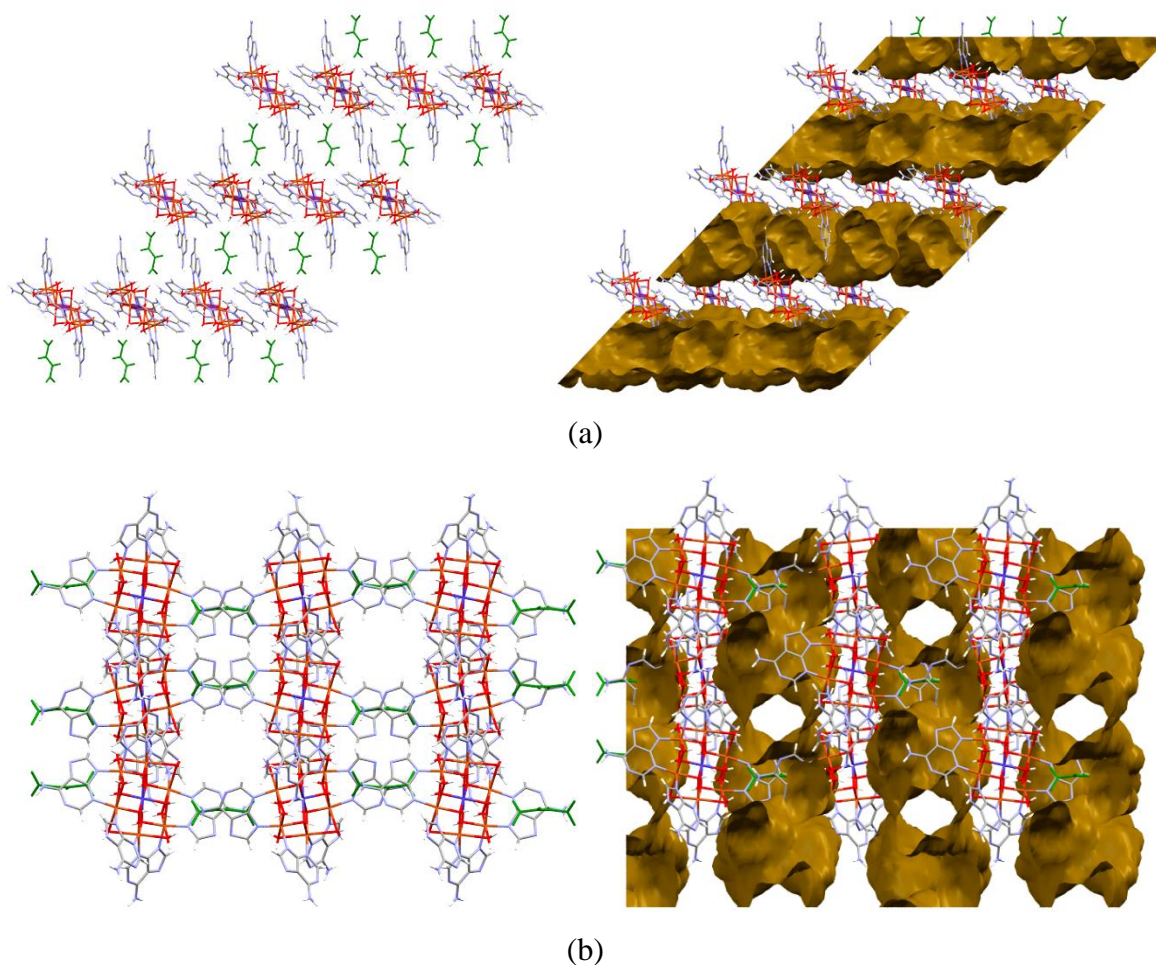


Figure 3.12. Crystal packing and views of contact surface of the 2D network of channels in CU6COADF along (a) the *b*-axis and (b) the *c*-axis.

3.3.2. Temperature variable XRPD experiments.

Variable-temperature X-ray powder diffraction data (Figures 3.13 and 3.14) show that the crystallinity is retained with a modification of the peak pattern after the release of the crystallization water molecules (*ca.* 80 °C) and even after the removal of the coordination ones (*ca.* 140 °C), remaining stable up to 180 °C.

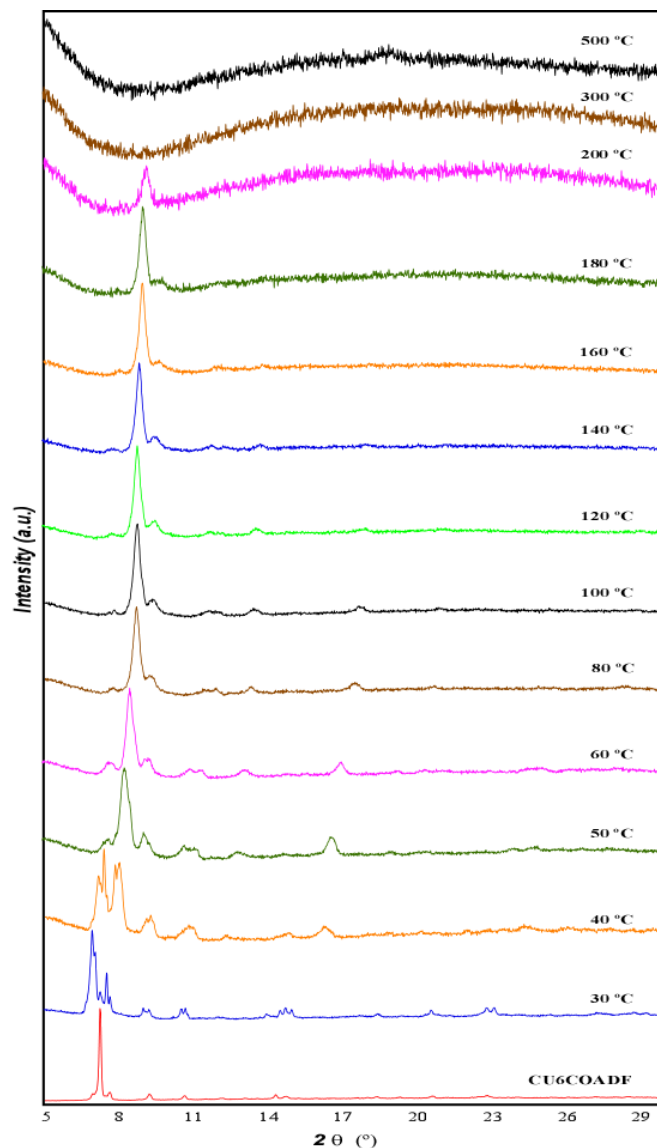


Figure 3.13. Thermodiffractometric data compared with fresh sample (bottom) of CU6COADF.

Heterometallic adenine nucleobase based SMOFs in catalyst

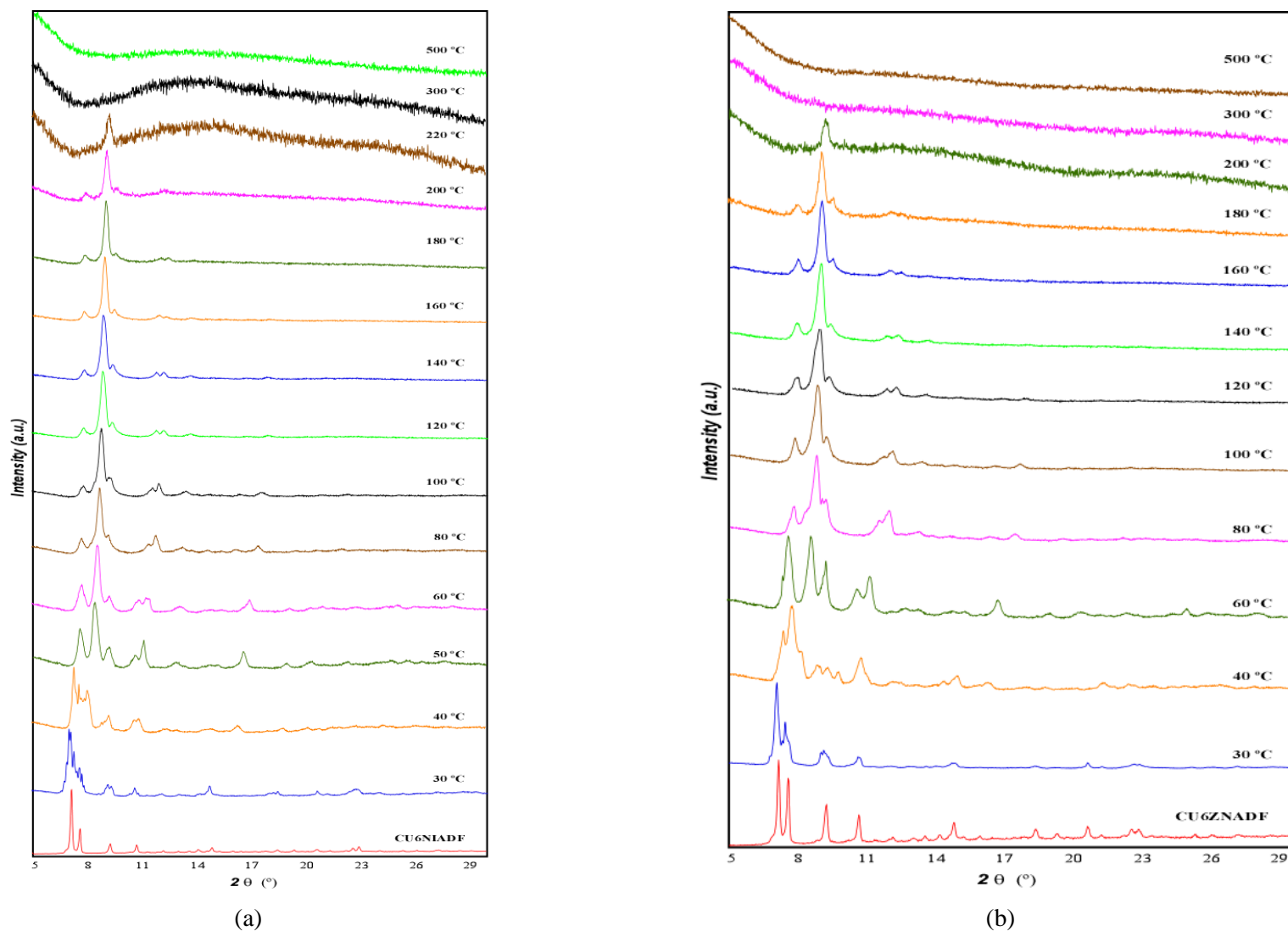


Figure 3.14. Thermogravimetric data compared with fresh sample (bottom) of (a) CU6NIADF and (b) CU6ZNAADF.

3.3.3. Catalysis properties

All the catalytic materials were prepared according to the following method. Around 300 mg of the fresh SMOFs was introduced in a tubular furnace (Nabertherm) to perform its thermolysis in a four stepped procedure. It starts heating the sample from room temperature to 600 °C at 5 °C·min⁻¹ in a N₂ atmosphere. The residue is then kept at 600 °C for eight hours, after which the oven is switched off and left cooling at room temperature to the initial 25 °C, while maintaining the N₂ atmosphere. Finally the sample is kept in an oxygen atmosphere for one hour.

Catalytic tests for CO₂ thermocatalytic reduction experiments were performed using a Flowrence[®] Avantium parallel reactor consisting of 16 tubular fixed-bed quartz reactors (2 mm ID, length 300 mm). Reactors are placed in a furnace and the flow is distributed equally over the 16 channels by means of a microfluidic glass distributor. In each reactor, around 0.05 g of sieved catalyst particles (150–300 µm) were loaded onto a 9.5 cm long coarse SiC (particle grit 40) bed that ensures the catalyst bed lies on the isothermal zone of the reactor. One reactor was always used without catalyst as a blank. Before catalytic run, the catalyst is reduced in situ at 450 °C for 1 h in H₂ atmosphere. Reactions were performed with a mixed feed containing 20 vol % of CO₂ and 80 vol % of H₂ in the temperature range of 350–650 °C. In addition, 0.5 mL·min⁻¹ of He was mixed with the feed and used as an internal standard.

Product analyses were performed in an Agilent 7890B GC equipped with two sample loops with a TCD and 2 FIDs detectors. After flushing the loops for 15 min, the products are injected. One sample loop is directed towards the TCD channel with 2 Haysep pre-columns and a MS5A column, where He, H₂, CH₄ and CO are separated. Gases that have longer retention times than CO₂ on the Haysep column (Column 4 Haysep Q 0.5 m G3591-80023) are backflushed. Further separation of permanent gases is done on another Haysep column (Column 5 Haysep Q 6 Ft G3591-80013) to separate CO₂ before going to a MS5A column. The other sample loop is directed towards an Innowax pre-column (5 m, 0.2 mm OD, 0.4 µm film). In the first 0.5 min of the method, the gases coming from the pre-column are sent to the Gaspro column (Gaspro 30 M, 0.32 mm OD). After 0.5 min, the valve is switched and gases are sent to an Innowax column (45 m, 0.2 mm OD, 0.4 µm). Products from both columns are analyzed through a FID. The Gaspro column separates C₁-C₈ paraffins and olefins, while the Innowax column separates oxygenates and aromatics.

The conversion (X), selectivity (S_i), yield (Y_i), and space–time yield (STY_i) of an individual or lumped species i were respectively defined as

$$X_{\text{CO}_2}(\%) = \left(1 - \frac{C_{\text{He,blk}} \cdot C_{\text{CO}_2,\text{R}}}{C_{\text{He,R}} C_{\text{CO}_2,\text{blk}}}\right) \times 100 \quad (1)$$

$$S_i(\%) = \frac{\left(\frac{C_{i,\text{R}}}{C_{\text{He,R}}}\right)}{\left(\frac{C_{\text{CO}_2,\text{blk}}}{C_{\text{He,blk}}} - \frac{C_{\text{CO}_2,\text{R}}}{C_{\text{He,R}}}\right)} \times 100 \quad (2)$$

$$Y_i(\%) = \frac{X_{\text{CO}_2} \cdot S_i}{100} \quad (3)$$

$$STY_i = \frac{\frac{X_{\text{CO}_2}}{100} \cdot \frac{S_i}{100} \cdot M_i \cdot GHSV}{22.4} \quad (4)$$

where $C_{\text{He,blk}}$, $C_{\text{He,R}}$, $C_{\text{CO}_2,\text{blk}}$, and $C_{\text{CO}_2,\text{R}}$ are the concentrations of He in the blank, He in the reactor effluent, CO_2 in the blank, and CO_2 in the reactor effluent, respectively, $C_{i,\text{R}}$ is the concentration of the product, M_i is the molecular weight of product i , and $GHSV$ is the CO_2 gas hourly space velocity in $\text{L} \cdot \text{g}_{\text{cat}}^{-1} \cdot \text{h}^{-1}$. The concentrations of all species were determined by GC analysis.

3.3.3.1 Homometallic catalysts

Homometallics SMOFs were subjected to the thermolysis procedure above described. X-ray diffraction data of the resulting bulk products (**CU7ADFA_{cat}**, **CU7ADNAPH_{cat}** and **CU7ADBZ_{cat}**) shows a non-planar background from which three peaks emerge at 2θ values of 43.3° , 50.4° , and 74.1° (the first one being the most intense) that agree with those expected for the metallic Cu^0 fcc phase (Figure 3.15). The metal content of all the three thermolysis products, determined by ICP-OES analysis, indicate that there is a progressive decrease, in the following order: **CU7ADFA_{cat}** (Cu content = 45.3%) < **CU7ADNAPH_{cat}** (39.2%) < **CU7ADBZ_{cat}** (2 x benzoate counterion; 32.7%). These results indicate that the increase of the mass of the organic counterion in the precursor renders a greater carbon content in the catalyst. TEM images (Figure 3.16), taken on the samples after the inert atmosphere thermolysis procedure, show a material in which there is a fine and homogeneous distribution of copper in the form of very small aggregates (below-10 nm). These particles are closer to each other in **CU7ADFA_{cat}** than in **CU7ADNAPH_{cat}** and **CU7ADBZ_{cat}**, due to the lower amount of the carbonaceous matrix in the former. Diffractograms were acquired over a 2θ range of $10\text{--}80^\circ$ with step size of 0.1° a scan speed

of 0.5 s per step. ICDD's Powder Diffraction File (PDF-4+, 2019)²¹⁵ database used for phase identification.

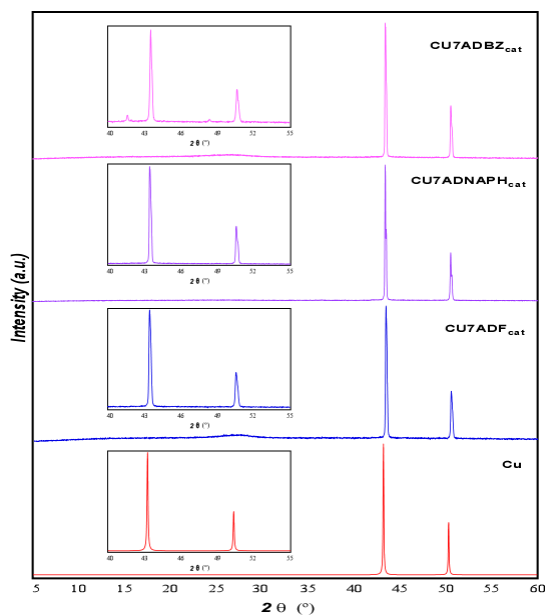


Figure 3.15. Powder X-ray diffraction patterns: (bottom) simulated from single-crystal of Cu^0 and experimental one measured on filtered samples of $\text{CU7ADF}_{\text{cat}}$, $\text{CU7ADNAPH}_{\text{cat}}$ and $\text{CU7ADBZ}_{\text{cat}}$ (top). Depicted in the insets an amplification of the 40–55° area for a better comparison.

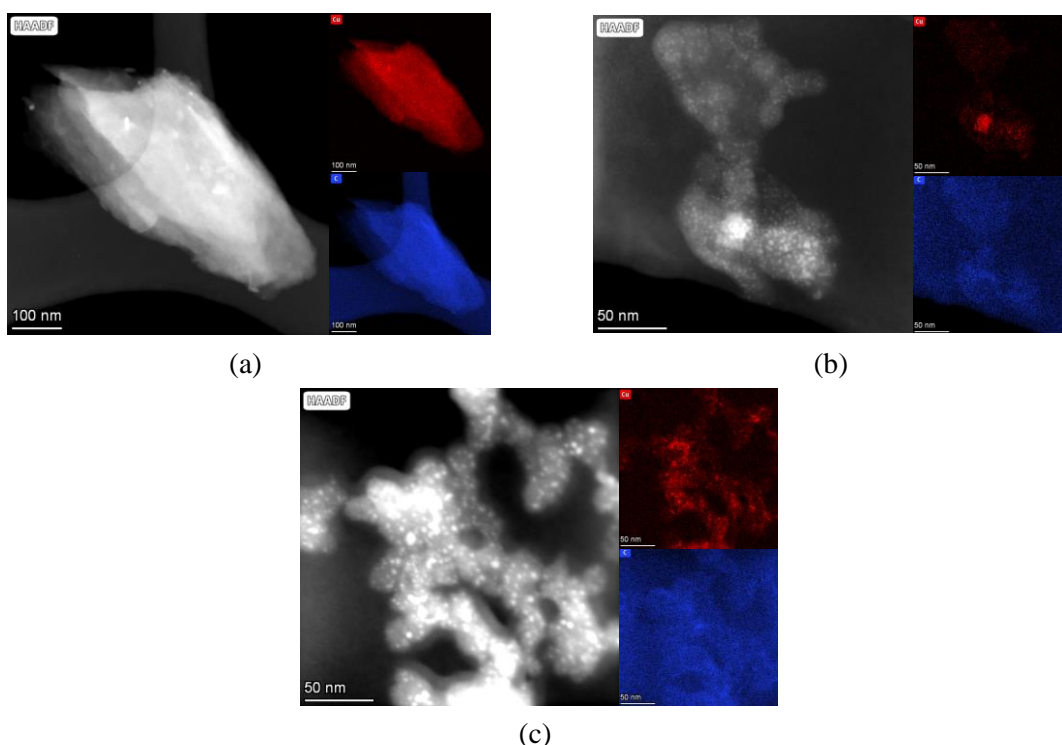


Figure 3.16. High-angle annular dark field TEM images (left) and the corresponding EDX elemental maps (right) for the catalyst derived: (a) $\text{CU7ADF}_{\text{cat}}$, (b) $\text{CU7ADNAPH}_{\text{cat}}$ and (c) $\text{CU7ADBZ}_{\text{cat}}$.

²¹⁵ Gates-Rector, S.; Blanton, T. *Powder Diffr.* **2019**, *34* (4), 352–360.

These products (**CU7ADF_{cat}**, **CU7ADNAPH_{cat}** and **CU7ADBZ_{cat}**) coming from the thermolysis of the fresh compounds were employed for the catalytic hydrogenation of CO₂. The CO₂ conversion and selectivity towards CO over a temperature range of 350–550 °C have been reported in Figure 3.17 for the three catalysts. The conversion increases with the temperature obtaining negligible values at 350 °C, below 5% at 450 °C, and at 550 °C the conversion value starts getting close to the benchmark material (Cu-Zn-Al catalyst, 64%)²¹⁶ but only for the fumarate based catalyst (**CU7ADF_{cat}**, 44%). These results also indicate the carbon content increase lowers the thermocatalytic performance, probably because the main contribution of the carbonous matrix in these catalysts is to isolate the copper nanoparticles from interacting with the CO₂ molecules. In addition, the selectivity towards CO of the best performing homometallic catalyst (at 550 °C) it is still at 85% (with a significant formation of CH₄) which is far below the selectivity provided by the benchmark catalyst (>99%).

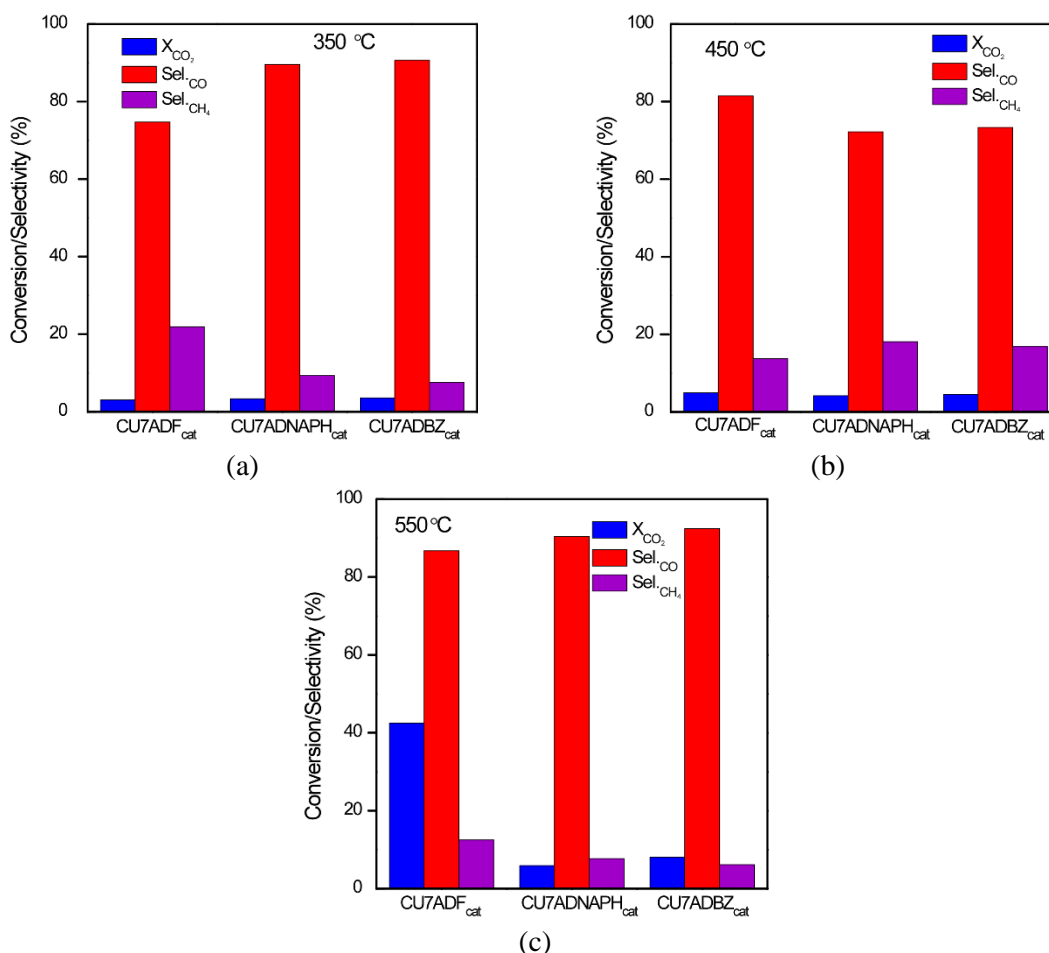


Figure 3.17. Results of the thermocatalytic reduction of CO₂ at 350 °C (a), 450 °C (b) and 550 °C (c) using the homometallic catalysts: conversion (blue) and selectivity towards CO (red) and CH₄ (purple).

²¹⁶ Stone, F. S.; Waller, D. *Top. Catal.* **2003**, 22 (3–4), 305–318.

The TEM analysis of the best performing homometallic catalyst after the catalytic reaction ($\text{CU7ADF}_{\text{cat(POS)}}$) shows that the copper nanoparticles have evolved into bigger ones (ca. 50 nm) well separated by the carbonaceous matrix (Figure 3.18). During the thermocatalytic experiment the oxygen content present in the catalysts also disappears from both the carbonaceous matrix and the surface of the copper particles.

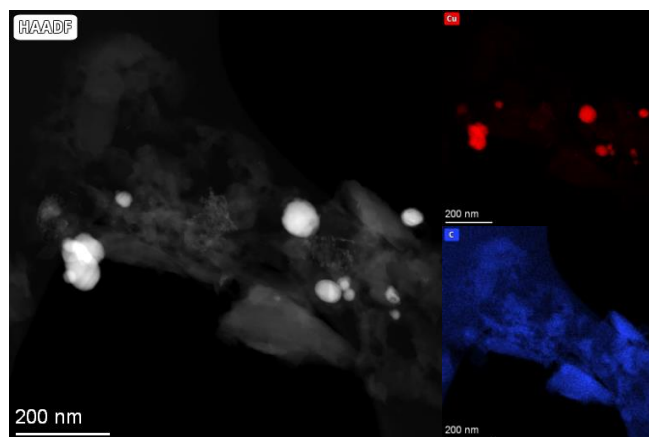


Figure 3.18. High-angle annular dark field TEM images (left) and the corresponding EDX elemental maps (right) for $\text{CU7ADF}_{\text{cat}}$ after the thermocatalytic experiment ($\text{CU7ADF}_{\text{cat(POS)}}$).

3.3.3.2 Heterometallic catalysts

Based on the above described results, the next step consists in improving the catalyst's performance by introducing another metal such as Co, Ni and Zn and it will be focused on SMOFs based on the fumarate anion in order to avoid the encapsulation effect resulting from a greater carbonaceous matrix. The syntheses were accordingly modified as detailed in the synthesis section. Single crystal X-ray diffraction confirmed as previously predicted that this new metal centers did only accommodate at the central position of the cluster fixing a maximum for the copper replacement that can be achieved in these heterometallic precursors (14.3% atomic). The heterometallic precursors was subjected to the same thermolysis process previously described. The metal content of the resulting new heterometallic catalyst (CUCO_{cat} , CUNI_{cat} and CUZN_{cat}) was determined by ICP-OES analysis (Cu: 39.0%; Co: 6.1%, Ni: 5.6% and Zn: 5.3%). The total metal content agrees fairly well with that found for the homometallic analogue ($\text{CU7ADF}_{\text{cat}}$: 45%). Furthermore, the metal loadings of the benchmark Cu-Zn-Al catalyst, that will be employed in the CO_2 thermocatalytic reduction experiment for comparative purposes was also measured (Cu: 43.7%; Zn: 15.6%; Al: 3.6%).

The XRPD pattern shows the same features observed for the homometallic catalysts, with the presence of the same three peaks described for the previous ones that belong to the cubic phase of copper, Figure 3.19. No additional peaks are observed. It means the cobalt, nickel and zinc atoms are incorporated into the Cu^0 phase as a solid solution. It is sound with the solubility limits reported for these copper-metal systems, which is above the employed Co-Ni-Zn/Cu ratio present in the precursors.²¹⁷

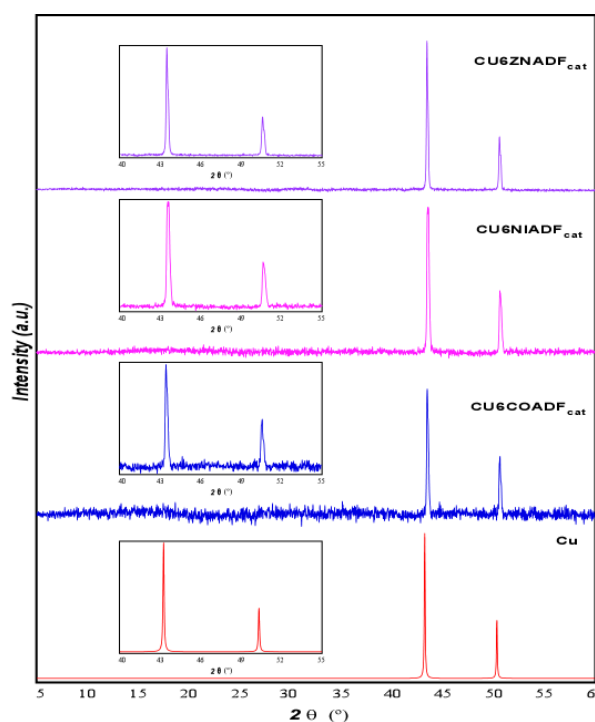


Figure 3.19. Powder X-ray diffraction patterns: (bottom) simulated pattern from single-crystal of Cu and experimental pattern measured on filtered samples of compounds **CU6COADF_{cat}**, **CU6NIADF_{cat}** and **CU6ZNADF_{cat}** (top). Depicted in the insets an amplification of the 40–55° area for a better comparison.

The heterometallic catalyst was also tested in the Avantium reactor (Figure 3.20). The CO_2 conversion and selectivity towards CO show a very significant improvement at 550 °C with values approaching those of benchmark Cu-Zn-Al catalyst in catalyst **CU6ZNADF** (conversion: 44.9 vs 63.69; selectivity: 98.6 vs 99.8), Figure 3.21. Interestingly not such improvement is achieved at temperatures 350 and 450 °C. The results indicated below make us opt for the compound **CU6ZNADF** for which we will carry out the complete characterization.

²¹⁷ Gierlotka, W.; Chen, S. W. *J. Mater. Res.* **2008**, *23* (1), 258–263.

Heterometallic adenine nucleobase based SMOFs in catalyst

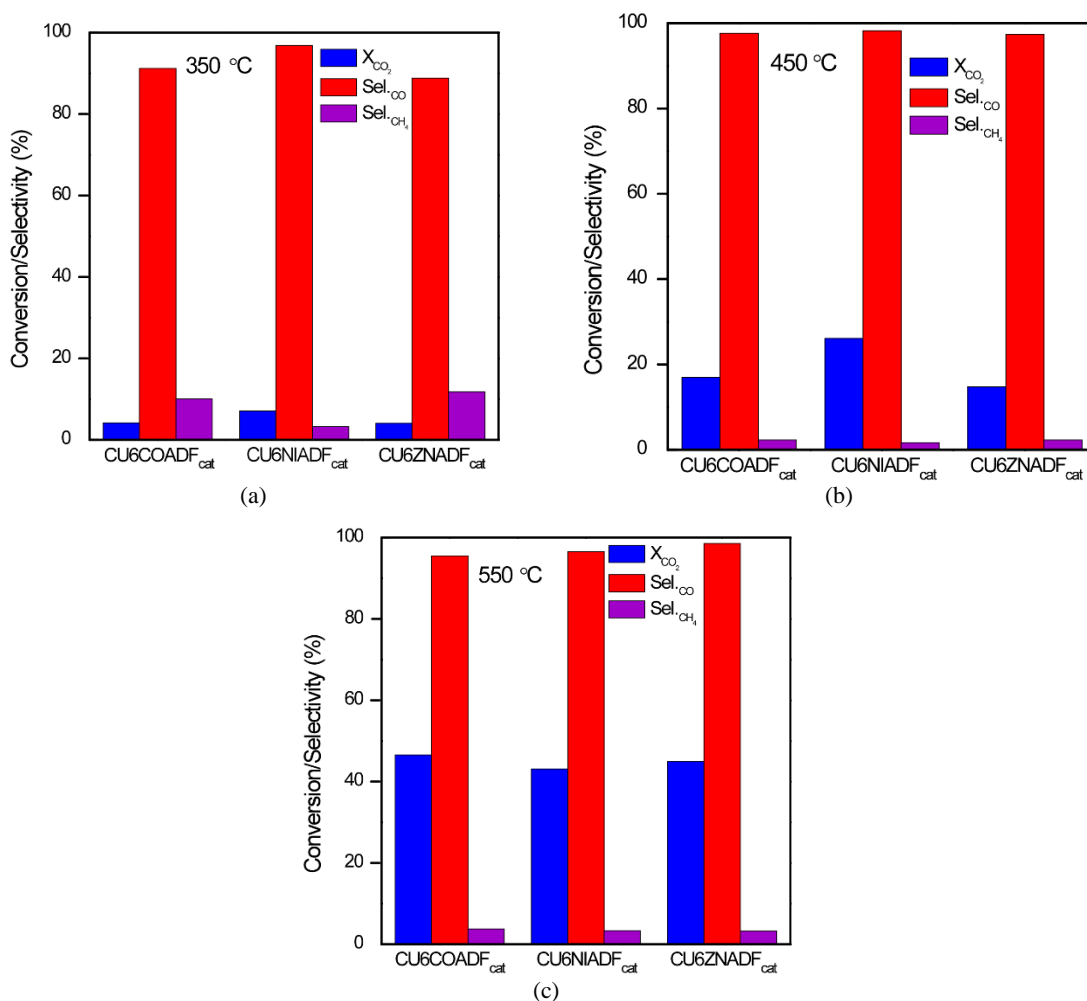


Figure 3.20. Results of the thermocatalytic reduction of CO₂ at 350 °C (a), 450 °C (b) and 550 °C (c) using the heterometallic catalysts: conversion (blue) and selectivity towards CO (red) and CH₄ (purple).

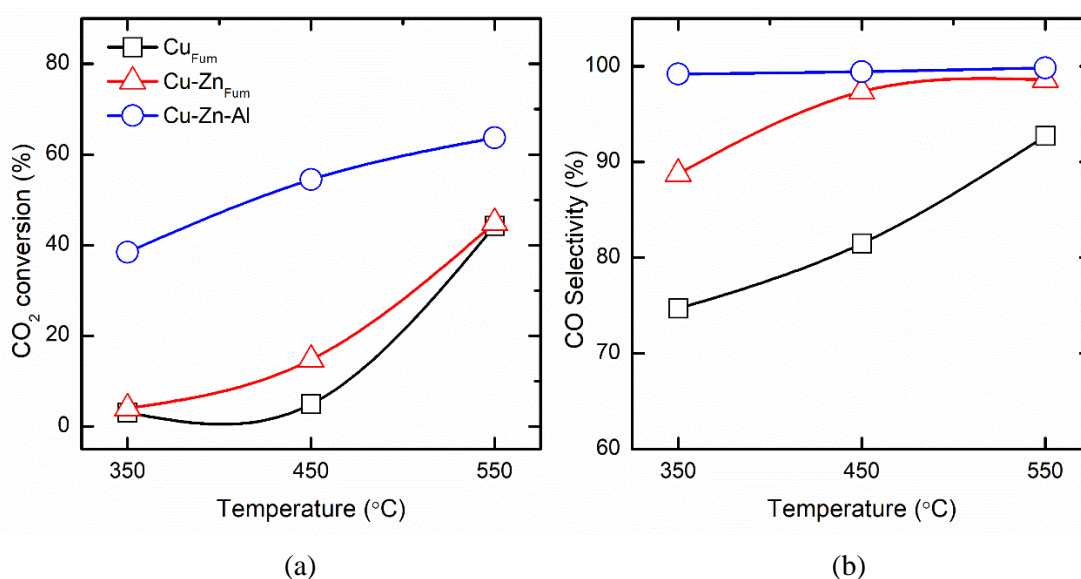


Figure 3.21. (a) CO₂ conversion and (b) selectivity of CO over the catalysts in the temperature range of 350–550 °C. Reaction conditions: 1 bar, 350–550 °C, GHSV= 19,040 mL g_{cat}⁻¹ h⁻¹.

Again TEM images show an evolution from very small nanoparticles (2-5 nm) for the sample obtained directly from the thermolysis process that evolve during the thermocatalytic reaction into *ca.* 50 nm nanoparticles embedded in a carbonaceous matrix observed for the homometallic analogues and the elemental mapping indicates clearly an even distribution of copper and zinc within these particles (Figure 3.22). Another interesting feature is the almost complete disappearance of oxygen from the carbonaceous matrix, as in the analogous homometallic catalyst, but it does not completely disappear from the metal particle surface.

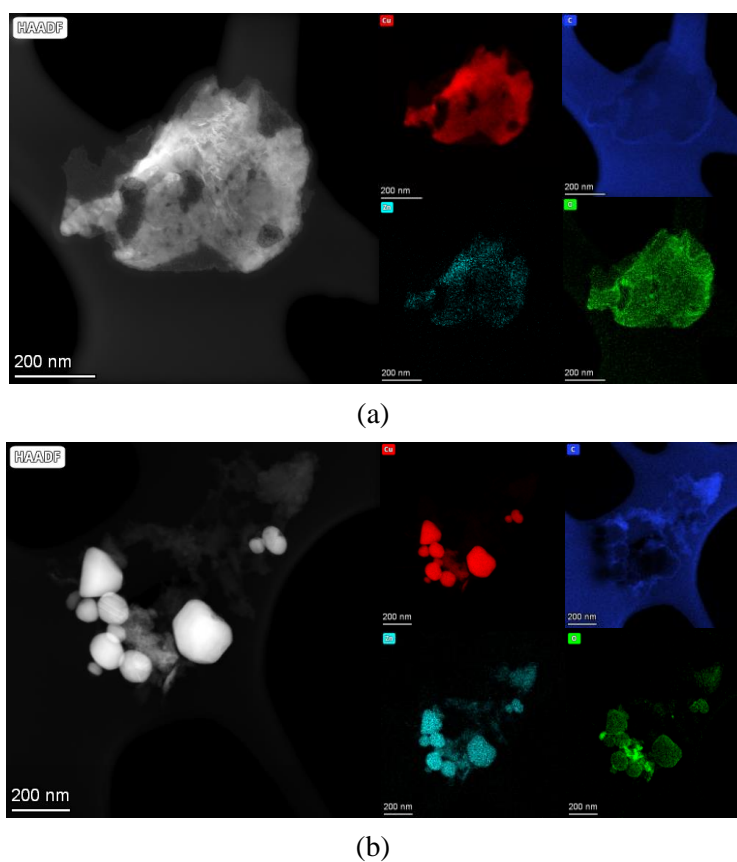


Figure 3.22. High-angle annular dark field TEM images and the corresponding EDX elemental maps for the heterometallic catalyst prior ($\text{CU6ZNADF}_{4\text{cat}}$) and after the thermocatalytic CO_2 reduction experiment ($\text{CU6ZNADF}_{\text{cat}(\text{pos})}$).

The time on stream (TOS) analysis for the studied catalysts, carried out at 550 °C for almost 50 hours, indicate a time improving space time yields (STY) for $\text{CU6ZNADF}_{\text{cat}}$ that approaches that of benchmark Cu-Zn-Al catalyst. They provide a sharp contrast with those of the homometallic analogue ($\text{CU7ADF}_{\text{cat}}$). On the other hand, the selectivity towards CO is also very good and stable. It is worth mentioning that selectivity on the CO_2 reduction products is key for their incorporation in industrial processes, Figure 3.23.

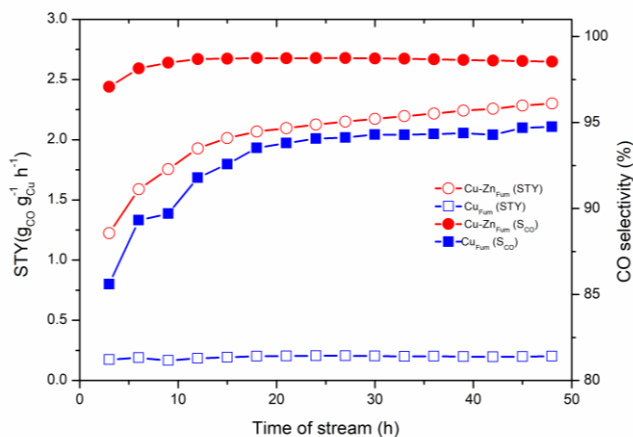


Figure 3.23. Time on stream catalytic performance of CU7ADF_{cat} and CU6ZNADF_{cat}. Reaction conditions: 1 bar, 550 °C, GHSV= 6457 mL g_{cat}⁻¹ h⁻¹.

In order to get a deeper insight into the mechanism of the CO₂ thermocatalytic reduction, it is necessary to employ a surface specific technique such as X-ray photoelectron spectroscopy (XPS). In this sense, the XPS spectra of CU7ADF_{cat} was measured before and after its activation under an atmosphere of 5% H₂ in helium with the same heating ramp (25 °C to 450 °C in one hour) as performed during the catalytic experiments. This activation was performed on a dedicated chamber within the XPS equipment that allows a direct transference of the sample to the measurement chamber without exposure to room atmosphere.

The results (Figure 3.24 and 3.25) indicate that there are clear changes on the spectra prior and after the activation procedure. In the catalyst obtained from the homometallic precursor, the initial mixture of Cu^{II} (probably CuO; 2p_{3/2}; 934.5 eV) and Cu^I (probably Cu₂O; 2p_{3/2}; 932.3 eV) converge in a single signal after the activation procedure assigned to Cu⁰ (2p_{3/2}; 932.1 eV), see Table 3.12). There is also an almost complete disappearance of oxygen signals that go from a 14% atomic ratio at the surface level to an almost indistinguishable from the background (1.8%). In the case of the heterometallic Cu/Zn catalyst (CU6ZNADF_{cat}) the same changes are observed for the copper element. The zinc signal prior to the activation (2p_{3/2}; 1021.6 eV) is difficult to assign either to Zn⁰ or Zn^{II}, but chemically it seems logical to assign to Zn^{II} as we have previously confirmed the appearance of copper(II) which is more difficult to oxidize than zinc. It would be present as a substitutional solid solution in the form of Cu_{1-x}Zn_xO. After the activation, this signal splits in two new ones, a first one with a lower binding energy (2p_{3/2}; 1020.9 eV) and another with a higher binding energy (2p_{3/2}; 1022.2 eV) that we have associated to formation of Zn⁰ and

ZnO, respectively. The latter resulting from the reduction of the copper(II) atoms. All the above can be summarized in the following reactions:

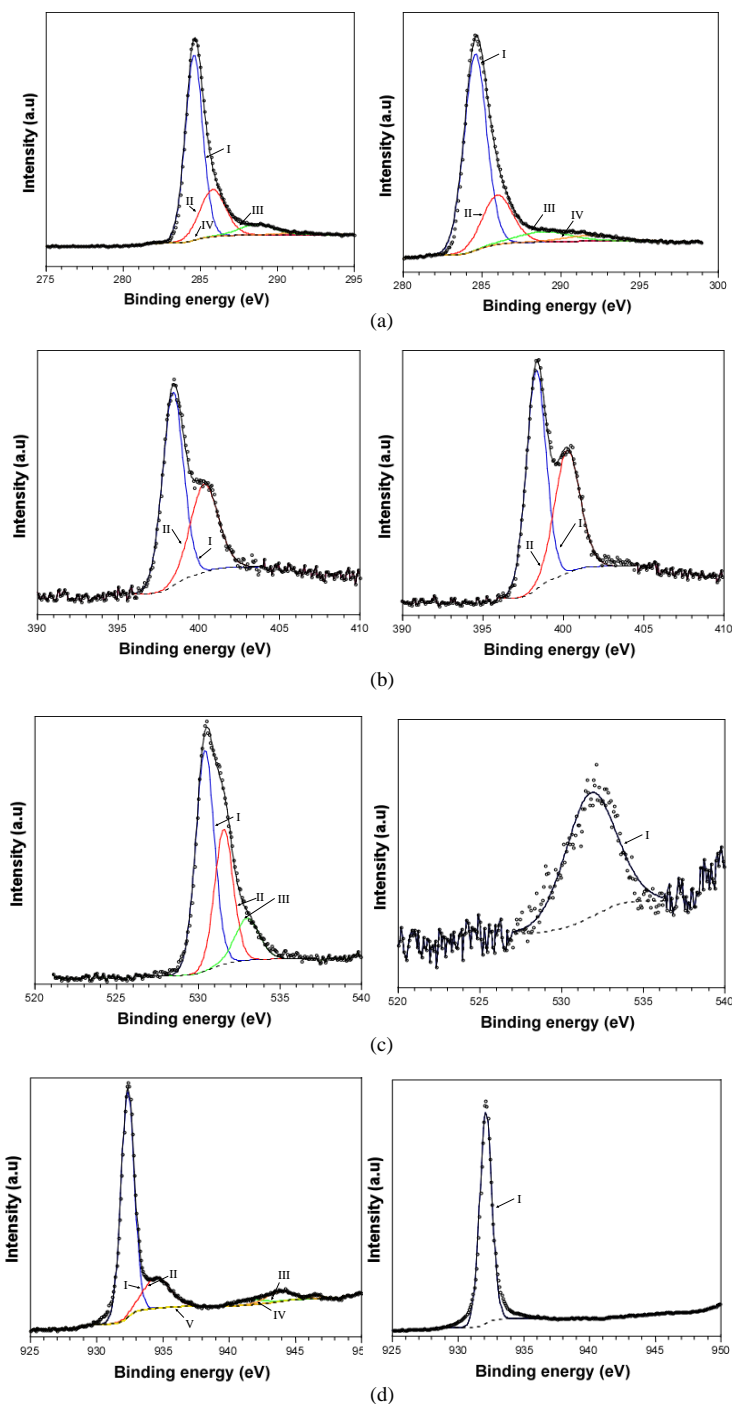
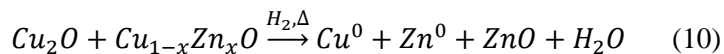
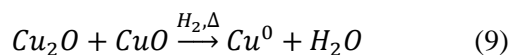


Figure 3.24. Representation of the XPS specters (a) Carbon, (b) Nitrogen, (c) Oxygen and (d) Copper of compound **CU7ADF1_{cat}**.

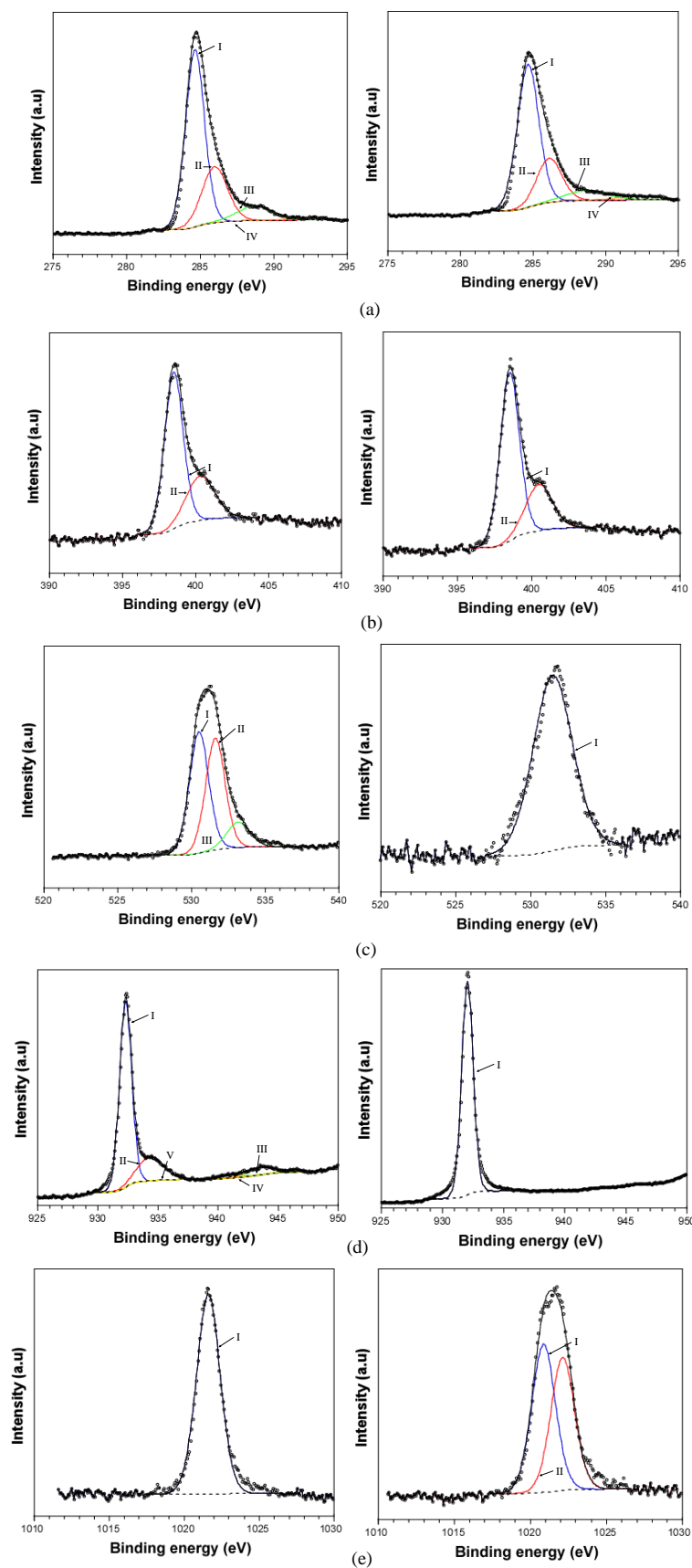


Figure 3.25. Representation of the XPS specters (a) Carbon, (b) Nitrogen, (c) Oxygen, (d) Copper and (e) Zinc of compound **CU₆ZNADF_{cat}**.

X-ray photoelectron spectroscopy (XPS) measurements were performed in a SPECS system (Berlin, Germany) equipped with a Phoibos 150 1D-DLD analyzer and Al K α monochromatic radiation source. (1486.7 eV). An initial analysis was carried out to determine the elements present (wide scan: step energy 1 eV, dwell time 0.1 s, pass energy 80 eV) and detailed analyses of the detected elements were performed (detail scan: step energy 0.08 eV, dwell time 0.1 s, pass energy 30 eV) with an electron exit angle of 90°. The spectrometer was previously calibrated with Ag (Ag 3d5/2, 368.26 eV). Spectra were fitted using CasaXPS 2.3.16 software, which models Gauss-Lorentzian contributions, after background subtraction (Shirley).²¹⁸

Table 3.12. Experimental data of compound **CU7ADF** and **CU6ZNADF** before and after the reaction.

CU7ADF				
Element	Before reaction		After reaction	
	Binding energy (eV)	Atom percentage (%)	Binding energy (eV)	Atom percentage (%)
C 1s	291.4	69.2	291.9	70.2
O 1s	530.5/ 531.6/ 533.1	14.0	531.8	1.8
N 1s	398.4/ 400.4	8.5	398.4/ 400.3	11.3
Cu^I 2p 3/2	932.4	8.3	932.1	16.7
Cu^{II} 2p 3/2	934.5			
CU6ZNADF				
Element	Before reaction		After reaction	
	Binding energy (eV)	Atom percentage (%)	Binding energy (eV)	Atom percentage (%)
C 1s	292.3	62.8	292.3	60.4
O 1s	530.6/ 531.7/ 533.2	18.0	531.5	7.2
N 1s	398.5/ 400.4	9.4	398.5/ 400.5	12.4
Cu^I 2p 3/2	932.3	7.5	932.1	15.9
Cu^{II} 2p 3/2	934.4			
Zn 2p 3/2	1021.6	2.3	1020.9 /1022.2	4.1

This proposal is also supported by the fact that the oxygen calculated at the surface is reduced during the activation but still fall far from disappearing (18.0 vs 7.2%). From

²¹⁸ Fairley, N.; Fernandez, V.; Richard-Plouet, M.; Guillot-Deudon, C.; Walton, J.; Smith, E.; Flahaut, D.; Greiner, M.; Biesinger, M.; Tougaard, S.; Morgan, D.; Baltrusaitis, J. *Appl. Surf. Sci. Adv.* **2021**, 5 (May), 100112.

these experiments we can also conclude that there is a clear enrichment of zinc at the surface level in comparison with amount found in the bulk material by ICP Zn/Cu ratio: 0.126 vs 0.307–0.258).

Translating these results into a plausible hypothesis for the reaction mechanism requires an explanation for both the significant increase of the conversion rate of CO₂ and selectivity towards CO when zinc is incorporated in the copper nanoparticles. In this sense, the presence of ZnO clusters at the surface of the nanoparticles helps the adsorption of CO₂ and increases in this way the conversion. On the other hand, the increase of selectivity towards CO requires another explanation. Accordingly, the formation of CO must be understood as the first step of the reduction of CO₂ and an any increase of the selectivity towards this specie seems to be due to factors that facilitate its desorption prior further reduction takes place. A relatively pristine Cu⁰ surface, as that of **CU7ADF_{cat}** after activation, seems favorable to retain the CO molecules through chemisorption once they are formed. However at the surface of the **CU6ZNADF_{cat}** there are Cu⁰ (properly Cu_{1-x}Zn_x) and ZnO regions. At low temperatures they would remain quite static on the surface and desorption would be quite slow, accounting for its low conversion values at low temperatures, as the temperature is raised the mobility of the chemisorbed CO molecules increases, as well as their capacity to be desorbed, leading to an increase of the conversion but still far from the desired target values. However, at the surface of the **CU6ZNADF_{cat}** there are Cu⁰ and ZnO regions. The first one acts as the reduction region described for the homometallic catalyst but at high temperature when the chemisorbed CO molecules can move over the surface they are prone to find ZnO regions (or, perhaps zinc atoms alloyed with copper) where the interaction with the CO molecules is going to be diminished facilitating their desorption and precluding its conversion to further reduced species, which turns into an increase of selectivity.²¹⁹

²¹⁹ Wang, Y.; Winter, L. R.; Chen, J. G.; Yan, B. *Green Chem.* **2021**, *23*, 249–267.

Chapter 4:

Zr-SMOFs: The chemistry of zirconium/carboxylate clustering

4.1. Introduction

4.2. Synthesis and chemical characterization

4.3. Crystallographic analysis

4.4. Results and discussion

4.1. INTRODUCTION

The interest on the design and preparation of discrete polynuclear metal-organic entities has resurfaced,²²⁰ not only in the areas of classical magnetism²²¹ and drug development,²²² but also in the discovery of new building units to design metal-organic frameworks (MOFs) which show endless applications based on the tailorability of their porosity.²²³ The key point for this fascinating diversity relies on the modular building up of their crystalline structure based on the combination of organic linkers and secondary building units (SBUs) consisting mainly of metal nodes or clusters.²²⁴ Until recently, novel topologies emerged basically from the change of the organic linkers, e.g. moving from ditopic to tritopic linkers. However, this approach has led to a never ending increase of the complexity and cost of the bridging ligands employed to develop new MOFs.²²⁵

The other constituent, the SBU, seems to be less explored as usually the synthetic chemistry relies on the self-assembled metal-oxide-hydroxide polynuclear entities and they apparently show little variability under the conventional synthetic conditions employed for the preparation of these materials.²²⁶ This clustering chemistry is a key point in the design and synthesis of the secondary building units that comprise metal-organic frameworks (MOFs) based on group IV metals.

This fact is evident when analyzing the reported structures for the zirconium/carboxylate MOF family, which are mostly based on the neutral $[\text{Zr}_6(\text{O})_4(\text{OH})_4(\text{OOC})_{12}]$ SBU.²²⁷ Although the resulting systems are both chemically and thermally robust mostly due to the strength of the Zr–O bond,^{56,228} the diversity of the

²²⁰ Vardhan, H.; Yusubov, M.; Verpoort, F. *Coord. Chem. Rev.* **2016**, *306*, 171–194.

²²¹ Mínguez Espallargas, G.; Coronado, E. *Chem. Soc. Rev.* **2018**, *47* (2), 533–557.

²²² (a) Sarker, M.; Jhung, S. H. *J. Mol. Liq.* **2019**, *296*, 112060. (b) Samanta, S. K.; Isaacs, L. *Coord. Chem. Rev.* **2020**, *410*, 213181.

²²³ Ju, Z.; Liu, G.; Chen, Y. S.; Yuan, D.; Chen, B. *Chem. - A Eur. J.* **2017**, *23* (20), 4774–4777.

²²⁴ (a) Zhou, Hong-Cai; Long, Jeffrey R.; Yaghi, O. M. *Rev. Chem.* **2012**, *112*, 673–674. (b) Eddaoudi, M.; Moler, D. B.; Li, H.; Chen, B.; Reineke, T. M.; O’Keeffe, M.; Yaghi, O. M. *Acc. Chem. Res.* **2001**, *34* (4), 319–330.

²²⁵ (a) Chen, T. H.; Popov, I.; Kaveevivitchai, W.; Miljanić, O. Š. *Chem. Mater.* **2014**, *26* (15), 4322–4325. (b) Qin, J. S.; Yuan, S.; Zhang, L.; Li, B.; Du, D. Y.; Huang, N.; Guan, W.; Drake, H. F.; Pang, J.; Lan, Y. Q.; Alsalmeh, A.; Zhou, H. C. *J. Am. Chem. Soc.* **2019**, *141* (5), 2054–2060. (c) Xu, X.; Li, S.; Liu, Q.; Liu, Z.; Yan, W.; Zhao, L.; Zhang, W.; Zhang, L.; Deng, F.; Cong, H.; Deng, H. *ACS Appl. Mater. Interfaces* **2019**, *11* (1), 973–981. (d) Mallick, A.; Liang, H.; Shekhah, O.; Jia, J.; Mouchaham, G.; Shkurenko, A.; Belmabkhout, Y.; Alshareef, H. N.; Eddaoudi, M. *Chem. Commun.* **2020**, *56* (12), 1883–1886.

²²⁶ (a) Cheng, S.; Chen, W.; Zhao, L.; Wang, X.; Qin, C.; Su, Z. *Inorganica Chim. Acta* **2021**, *516* (5268), 120174. (b) Gosselin, A. J.; Rowland, C. A.; Bloch, E. D. *Chem. Rev.* **2020**, *120* (16), 8987–9014.

²²⁷ (a) Chen, Z.; Hanna, S. L.; Redfern, L. R.; Alezi, D.; Islamoglu, T.; Farha, O. K. *Coord. Chem. Rev.* **2019**, *386*, 32–49. (b) Yuan, S.; Qin, J. S.; Lollar, C. T.; Zhou, H. C. *ACS Cent. Sci.* **2018**, *4* (4), 440–450.

²²⁸ (a) Ding, M.; Cai, X.; Jiang, H. L. *Chem. Sci.* **2019**, *10* (44), 10209–10230. (b) Healy, C.; Patil, K. M.; Wilson, B. H.; Hermanspahn, L.; Harvey-Reid, N. C.; Howard, B. I.; Kleinjan, C.; Kolien, J.; Payet, F.;

porous features and topology relies entirely on the organic linker side. Regarding the zirconium/carboxylate entities, there are also some early works on discrete $Zr_6(O)_4(OH)_4$ clusters using small monocarboxylates as capping agents.²²⁹ In this context, more recently, in situ pair distribution function (PDF) analysis confirmed the presence of the hexameric zirconium cluster in the metal salt precursor/DMF/HCl solution prior to the addition of the carboxylic organic ligand. As previously stated, the novel members of zirconium MOF family rely on increasingly more complex and expensive polycarboxylic ligands. Therefore, there is a great interest in developing novel architectures based on low-cost aromatic polycarboxylic ligands by modifying the features of the SBUs.²³⁰ In this sense, a deep research work on the early stages of the formation of these polynuclear entities is required.¹⁹³

Taking into account these premises, we have thoroughly analyzed the formation of discrete zirconium-oxide-hydroxide entities in alcoholic media using simple monocarboxylic benzoate and hydroxybenzoate ligands to avoid the polymerization that would hinder this kind of studies. A crucial stage of the setup of the Zr–O/OH polynuclear entities resides on the oxygen source from which these species emerge. In this sense, a precise control of the amount of water is crucial for the first steps of the formation of these entities.²³¹ On the other hand, the acidity of the reaction media exerts a strong influence on the deprotonation of the coordinated water molecules to afford bridging hydroxide and oxide anions but also on the readiness of the carboxylic ligands to coordinate to the metal centers.¹³¹ In this chapter, the first stages of the zirconium-carboxylate clustering process in alcohol/water mixtures are studied in detail using the monocarboxylic benzoic and hydroxybenzoic acids to avoid the polymerization.

Mass-spectroscopy measurements performed on the reactions revealed the presence of hexa- and pentanuclear species even at low pH values and also evidenced the acid–base nature and pH dependence of the transformation between both species. The control on the chemistry governing the equilibria between these species has allowed us

Telfer, S. G.; Kruger, P. E.; Bennett, T. D. *Coord. Chem. Rev.* **2020**, *419*, 213388.

²²⁹ (a) Kickelbick, G.; Wiede, P.; Schubert, U. *Inorganica Chim. Acta* **1999**, *284* (1), 1–7. (b) Kickelbick, G.; Schubert, U. *Chem. Ber.* **1997**, *130* (4), 473–478. (c) Piszczek, P.; Radtke, A.; Grodzicki, A.; Wojtczak, A.; Chojnacki, J. *Polyhedron* **2007**, *26* (3), 679–685. (d) Guo, L. Y.; Su, H. F.; Kurmoo, M.; Tung, C. H.; Sun, D.; Zheng, L. S. *J. Am. Chem. Soc.* **2017**, *139* (40), 14033–14036.

²³⁰ (a) García-Raso, A.; Terrón, A.; Roselló, Y.; Frontera, A.; Castillo, O.; Beobide, G.; Pérez-Yáñez, S.; Escudero-Adán, E. C.; Fiol, J. J. *CrystEngComm* **2020**, *22* (25), 4201–4205. (b) Marshall, R. J.; Forgan, R. S. *Eur. J. Inorg. Chem.* **2016**, *2016* (27), 4310–4331.

²³¹ Stern, R. D.; Kingsbury, R. S.; Persson, K. A. *Inorg. Chem.* **2021**, *60* (20), 15456–15466.

to isolate seven new compounds in the solid state. Those discrete zirconium entities range from the ubiquitous hexanuclear $[\text{Zr}_6(\mu_3\text{-O})_4(\mu_3\text{-OH})_4]^{12+}$ core with the anionic forms of selected monocarboxylic ligands $[\text{Zr}_6(\text{O})_4(\text{OH})_4(\text{L})_8(\text{H}_2\text{O})_8]^{4-}$ where is L = benzoate, 2-hydroxybenzoate or salicylate, 3-hydroxybenzoate) to a previously unknown pentanuclear $[\text{Zr}_5(\mu_3\text{-O})_2(\mu_3\text{-OH})_2(\mu\text{-OH})_4]^{10+}$ core $[\text{Zr}_5(\text{O})_2(\text{OH})_6(\text{L})_4(\text{H}_2\text{O})_{11}(\text{ROH})]^{6-}$ where L = benzoate; R = Et or Pr), Figure 4.1.

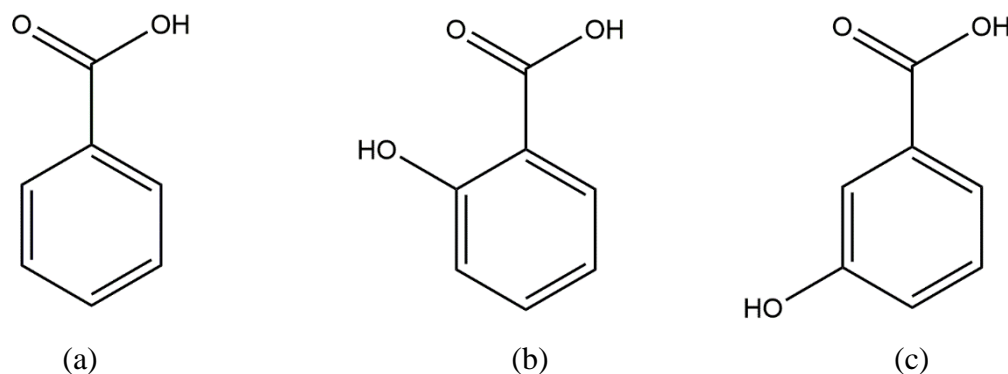


Figure 4.1. Schematic representation of the monocarboxylic ligands used in this chapter (a) benzoic acid, (b) 2-hydroxybenzoic acid and (c) 3-hydroxybenzoic acid.

Interestingly, in the case of the former octahedral shaped hexanuclear entities the coordination of the carboxylic ligands can be frozen in a cationic intermediate state in which only some of the available positions are occupied, leaving what can be called a carboxylate-unsaturated SBU.²³² It is worth mentioning that zirconium based MOFs are frequently carboxylate defective (due to random linker vacancies or to the restraints coming from the topology of the framework) but, in contrast to the compounds reported herein, the charge is balanced by the incorporation at these defective positions of smaller monocarboxylate ligands (formiato and acetato) or by hydroxide anions.²³³ It will be also shown, how the non-covalent interactions coming from the hydroxyl-substituted positions direct the arrangement of the monocarboxylic ligands towards different symmetries regarding the unoccupied carboxylate positions: these have been placed in a square arrangement for benzoate (ZR6BZ-1/2) and 3-hydroxybenzoate (ZR63H) ligands and in a tetrahedral one for the 2-hydroxybenzoate (ZR62H) ligand, Figure 4.2.

²³² Pan, L.; Heddy, R.; Li, J.; Zheng, C.; Huang, X. Y.; Tang, X.; Kilpatrick, L. *Inorg. Chem.* **2008**, *47* (13), 5537–5539.

²³³ (a) Feng, L.; Pang, J.; She, P.; Li, J. L.; Qin, J. S.; Du, D. Y.; Zhou, H. C. *Adv. Mater.* **2020**, *32* (44), 1–31. (b) Hurlock, M. J.; Hao, L.; Kriegsman, K. W.; Guo, X.; O’Keeffe, M.; Zhang, Q. *ACS Appl. Mater. Interfaces* **2021**, *13* (44), 51945–51953.

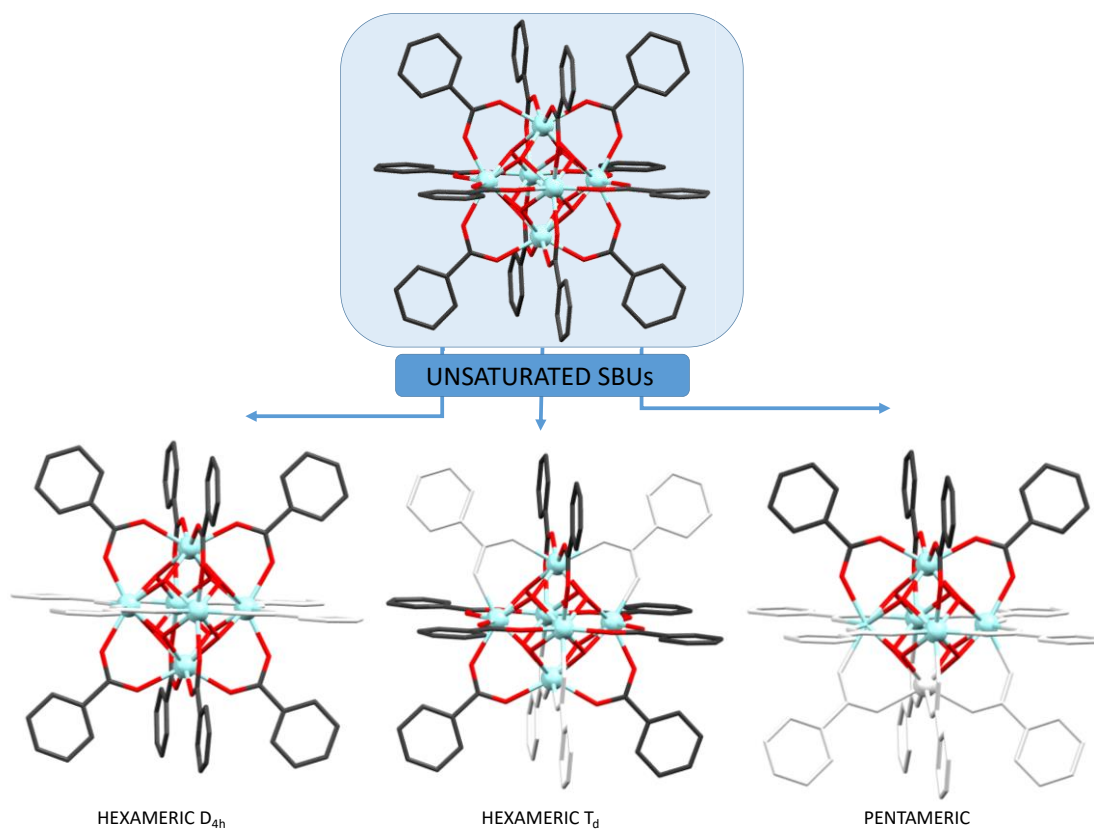


Figure 4.2. Schematic description of the unsaturated species obtained in this work and their relation with the well-known $[\text{Zr}_6(\text{O})_4(\text{OH})_4(\text{OOC})_{12}]$ fragment found in many MOFs (missing ligands are coloured in light grey).

4.2. SYNTHESIS AND CHEMICAL CHARACTERIZATION

4.2.1. Synthesis

We report herein the synthesis and characterization of seven compounds listed in Table 4.1. In all compounds, suitable single-crystals have been obtained to carry out their structural characterization by X-ray diffraction.

It is worth mentioning that the ZR6BZ-1/2 compounds are prepared using different synthesis conditions, verifying that the presence of water in the media is crucial. In contrast, the ZR63H-1/2 compounds were obtained from the same synthesis but at two different crystallization times. The first compound was isolated after two days while the second was obtained after seven days. All characterization measurements were performed on the compound with code 2.

After the removal of the sample from the mother liquid, the crystals are not longer stable and they loss crystallinity. This is due to the mismatch between the size of the cationic zirconium clusters and the size of the chloride counterions. Therefore, the homogeneity and purity of the bulk samples was checked by elemental analysis and by comparison of the experimental X-ray powder diffractogram performed with the compounds still submerged in the reaction media inside a Lindemann capillary with the simulated diffraction pattern obtained from the single-crystal X-ray data, see section 4.2.4. The thermal stability and the magnetic features of these compounds were also analyzed in detail.

Table 4.1. Formula and code of the compounds based on Zr-carboxylate cluster in this chapter.

Compound	Code
$[\text{Zr}_6(\mu_3\text{-O})_4(\mu_3\text{-OH})_4(\mu\text{-OOC}\text{C}_6\text{H}_5)_8(\text{H}_2\text{O})_8]\text{Cl}_4 \cdot \text{EtOH} \cdot 35\text{H}_2\text{O}$	ZR6BZ-1
$[\text{Zr}_6(\mu_3\text{-O})_4(\mu_3\text{-OH})_4(\mu\text{-OOC}\text{C}_6\text{H}_5)_8(\text{H}_2\text{O})_8]\text{Cl}_4 \cdot 15\text{H}_2\text{O}$	ZR6BZ-2
$[\text{Zr}_6(\mu_3\text{-O})_4(\mu_3\text{-OH})_4(\mu\text{-OOC}\text{C}_6\text{H}_5\text{O})_8(\text{H}_2\text{O})_8]\text{Cl}_4 \cdot 28\text{H}_2\text{O}$	ZR62H
$[\text{Zr}_6(\mu_3\text{-O})_4(\mu_3\text{-OH})_4(\mu\text{-OOC}\text{C}_6\text{H}_5\text{O})_8(\text{H}_2\text{O})_8]\text{Cl}_4 \cdot 27\text{H}_2\text{O}$	ZR63H-1
$[\text{Zr}_6(\mu_3\text{-O})_4(\mu_3\text{-OH})_4(\mu\text{-OOC}\text{C}_6\text{H}_5\text{O})_8(\text{H}_2\text{O})_8]\text{Cl}_4 \cdot \text{EtOH} \cdot 24\text{H}_2\text{O}$	ZR63H-2
$[\text{Zr}_5(\mu_3\text{-O})_2(\mu_3\text{-OH})_2(\mu\text{-OH})_4(\mu\text{-OOC}\text{C}_6\text{H}_5)_4(\text{H}_2\text{O})_{11}\text{EtOH}]\text{Cl}_6 \cdot 2\text{EtOH} \cdot 10\text{H}_2\text{O}$	ZR5BZET
$[\text{Zr}_5(\mu_3\text{-O})_2(\mu_3\text{-OH})_2(\mu\text{-OH})_4(\mu\text{-OOC}\text{C}_6\text{H}_5)_4(\text{H}_2\text{O})_{11}\text{PrOH}]\text{Cl}_6 \cdot 2\text{PrOH} \cdot 11\text{H}_2\text{O}$	ZR5BZPR

4.2.1.1. Synthesis of compounds ZR6BZ-1/2 and ZR5BZET

For the synthesis of these three compounds, a solution of 0.3870 g (1.66 mmol) of $ZrCl_4$ dissolved in 4.8/0.2 mL of an ethanol/water solution was added dropwise to an 8 mL ethanol solution containing 0.4054 g (3.32 mmol) of benzoic acid. The resulting colourless solution was basified dropwise with water until pH \sim 0.0 (ZR6BZ-2), pH \sim 0.5 (ZR6BZ-1), or left at pH $<$ -0.2 (ZR5BZET). Reaction mixtures were left to evaporate at room temperature and colourless single-crystals appeared after 3-7 days. Yield: 6, 10 and 16% respectively (based on metal). ZR6BZ-1 1H MAS NMR δ (300 MHz): 7.2 ppm [aromatic H], 3.6 ppm [Zr-OH₂]. ^{13}C MAS NMR δ (300 MHz): 172 ppm [COOH], 132 ppm [C aromatic]. ZR6BZ-2 1H MAS NMR δ (300 MHz): 7.2 ppm [aromatic H], 3.6 ppm [Zr-OH₂]. ^{13}C MAS NMR δ (300 MHz): 172 ppm [COOH], 132 ppm [C aromatic]. ZR5BZET 1H MAS NMR δ (300 MHz): 7.0 ppm [Aromatic H], 4.3 ppm [Zr-OH₂], 3.0 ppm [CH₂], 0.4 ppm [CH₃]. ^{13}C MAS NMR δ (300 MHz): 172 ppm [COOH], 130 [C aromatic], 58 ppm [CH₂], 17 ppm [CH₃].

4.2.1.2. Synthesis of compound ZR62H and ZR63H-1/2

For the synthesis of these compounds, a solution of 0.3870 g (1.66 mmol) of $ZrCl_4$ dissolved in 4.8/0.2 mL of an ethanol/water solution was added dropwise to an 8 mL ethanol solution containing the corresponding ligand, 0.4586 g (3.32 mmol) of 2-hydroxybenzoic acid for compound ZR62H or 3-hydroxybenzoic acid for compound ZR63H. The resulting colourless solution was basified dropwise with water until pH \sim 0.5 (ZR62H) or pH \sim 1.0 (ZR63H-1/2). Reaction mixtures were left to evaporate at room temperature and colourless single-crystals appeared after 2-7 days. Yield: 10 and 13 % respectively (based on metal). ZR62H 1H MAS NMR δ (300 MHz): 9.6 ppm [C-OH], 6.5 ppm [aromatic H], 2.96 ppm [Zr-OH₂]. ^{13}C MAS NMR δ (300 MHz): 173 ppm [COOH], 159 ppm [C-OH], 137 and 113 ppm [C aromatic]. ZR63H-2, 1H MAS NMR δ (300 MHz): 7.1 ppm [aromatic H], 4.3 ppm [Zr-OH₂]. ^{13}C MAS NMR δ (300 MHz): 172 ppm [COOH], 154 ppm [C-OH], 132 and 120 ppm [C aromatic].

4.2.1.3. Synthesis of compound ZR5BZPR

ZR5BZPR compound was prepared mixing a solution of $ZrCl_4$ (0.3870 g, 1.66 mmol) in 2.5/2.5 mL ethanol/propanol mixture and benzoic acid (0.4054 g, 3.32 mmol) in 8 mL propanol. The resulting colourless solution was left at pH $<$ -0.2. Slow evaporation of the reaction mixture at room temperature yielded colourless single-crystals

four days later. Yield: 14 % (based on metal). ^1H MAS NMR δ (300 MHz): 7.3 ppm [aromatic H], 4.5 ppm [Zr-OH₂], 2.5 ppm [CH₂], -0.5 ppm [CH₃]. ^{13}C MAS NMR δ (300 MHz): 172 ppm [COOH], 131 [C aromatic], 63 ppm [CH₂], 22 ppm [CH₂], 9 ppm [CH₃].

Regarding the measured pH values, if the calibration of the electrode is performed in aqueous buffers, but the measurement is performed in a different solvent, the measured pH requires to subtract a correction constant: ${}^s\text{pH} = {}^w\text{pH} - \delta$, where ${}^s\text{pH}$ and ${}^w\text{pH}$ would in this case correspond to the pH for solvent media and measured pH, while δ is a correction constant. This constant depends on the solvent and it can be approached to -2.54 for ethanol. The pH values mentioned in this work have not been corrected and correspond to ${}^w\text{pH}$.²³⁴

All the chemicals were of reagent grade and used as commercially obtained, except ethanol that was dehydrated using anhydrous CaSO₄ in the synthesis of compounds ZR5BZET and ZR5BZPR.

²³⁴ (a) Gibson, G. T. T.; Mohamed, M. F.; Neverov, A. A.; Brown, R. S. *Inorg. Chem.* **2006**, *45* (19), 7891–7902. (b) Robinson, R. G. B. M. P.; R. A. *J. Phys. Chem.* **1963**, *67* (9), 1833–1838.

4.2.2. Infrared spectroscopy

Infrared spectroscopy has turned out to be a useful technique for the initial characterization of the synthesized compounds, as it allows verifying the existence of the bands corresponding to the employed carboxylate anions. Figure 4.3 shows the infrared spectra for the compounds presented in this chapter. Table 4.2 lists the wavenumbers of the most relevant observed bands, their relative intensity and the assignment that has been proposed.

The analysis performed over dry samples shows, in all cases, the presence of the aromatic carboxylic ligands and the signals arising from the cluster. At high frequencies, in the 3600–2800 cm^{-1} spectral region, all the spectra exhibit a broad and intense band centered at $\sim 3380 \text{ cm}^{-1}$ that corresponds to the stretching of O–H bond from water molecules. Intense vibrational bands around 1600 cm^{-1} are attributed to the antisymmetric stretching vibrations of the carboxylate groups whereas the symmetric stretching vibrations of the carboxylate groups appear around 1400 cm^{-1} . The presence of the hydroxyl group in compounds ZR62H and ZR63H-2 is confirmed by the presence of an additional band at 1231–1253 cm^{-1} corresponding to its in-plane vibration mode.²³⁵

The remaining bands at lower frequencies are attributed to the bending modes of the aromatic rings and the stretching of Zr–O_{oxide/hydroxide/carboxylate} bonds.

Due to the loss of crystallinity once the crystals have been removed from the mother liquor and filtered for their subsequent characterization, a test has been carried out to verify the final compound is a modification of the same, once it has lost some of the water and ethanol solvation molecules located in the voids. For it, the ATR-FTIR spectra of the compounds while submerged in their mother liquids was measured (Figure 4.4 and it was observed that most of the signals for the benzoate ligand were maintained while all those for ethanol disappeared with the elimination of the solvent.

²³⁵ (a) Atzori, C.; Shearer, G. C.; Maschio, L.; Civalleri, B.; Bonino, F.; Lamberti, C.; Svelle, S.; Lillerud, K. P.; Bordiga, S. *J. Phys. Chem. C* **2017**, *121* (17), 9312–9324. (b) Hayashi, Soichi; Kimura, N. C. *Bull. Inst. Chem. Res. - Kyoto Univ.* **1966**, *44* (4), 335–340. (c) Jadrijevic-Mladar Takac, M.; Topić, D. V. *Acta Pharm.* **2004**, *54* (3), 177–191. (d) Trivedi, M. K.; Dahryn Trivedi, A. B.; Khemraj Bairwa, H. S. *Nat. Prod. Chem. Res.* **2015**, *03* (05), 1000186.

Zr-SMOFs: The chemistry of zirconium/carboxylate clustering

Table 4.2. Infrared spectra bands (cm^{-1}) of compounds of chapter 4.^a

Benzoic acid	2/3-Hydroxybenzoic	ZR6BZ-1	ZR6BZ-2	ZR62H	ZR63H-2	ZR5BZET	ZR5BZPR	Assignment ^{a,b}
3400s	3400s	3370vs	3410vs	3340s	3380s	3420vss	3410vs	$\nu_s\text{O—H}$, $\nu\text{C—H}$
1700s	1662s	1600s	1600s	1622s	1608s	1600s	1600s	$\nu_{as}\text{COO}^-$
1580s	1558s/1610s	1555s/1525s	1555s/1528vs	1586s/1551s	1564s/1533w	1560m/1531vs	1560s/1520vs	$\nu_s\text{C=C}$
1495s	1501s/1450s	1495s	1490s	1484m/1466s	1493w/1448s	1490m	1490s	$\nu_s\text{C—C}$
1432f	1387s	1420vs	1420vs	1395vs	1413s	1415vs	1410vs	$\nu_s\text{COO}^-$
1298F	1315m	1305m	1300m	1311s	1302s	1310m	1306m	$\nu_s\text{C—O}$
—	1200s	—	—	1244vs	1253s/1231w	—	—	$\delta_{ip}\text{O—H}$
1158m/1178m	1159s	1180s/1155m	1180s/1155m	1160s/1144s	1160m/1120s	1175m/1152w	1180m/1155w	$\delta_{ip}\text{C—H}_{arom}$
1056m	1085m	1065s	1070s	1097m	1075s	1070m	1070m	$\delta_{ip}\text{CCH}$
1014m	1014m	1025s	1020s	1026s	1000s	1018m	1020m	δ_{ring}
948s	948s	935m	930m	951m	942s	942m	940m	$\delta_{oop}\text{O—H}$
830m	808s	840w	840w	808s	795s	840w	840w	$\nu_{as}\text{C—C}$
724s	759s	720s	720s	755vs	764vs	720s	720vs	$\delta_{ip}\text{C—H}$, $\nu_{as}\text{Zr—O—Zr}$
655f	—	660vs	653vs	648m	657vs	674s/650m	671s/650m	Zr—O_{carbo} , $\delta_{ip}\text{C—H}$
—	—	—	—	—	—	524w	519w	$\nu\text{Zr—O}_{carbo}$
—	—	465m	460m	475w/422w	457m	458m	470m	Zr—O

^avs: very strong, s: strong, m: medium, w: weak. ^bs: symmetric, as: antisymmetric, ν : stretching vibration, δ : bending vibration, ip = in plane, oop = out of plane.

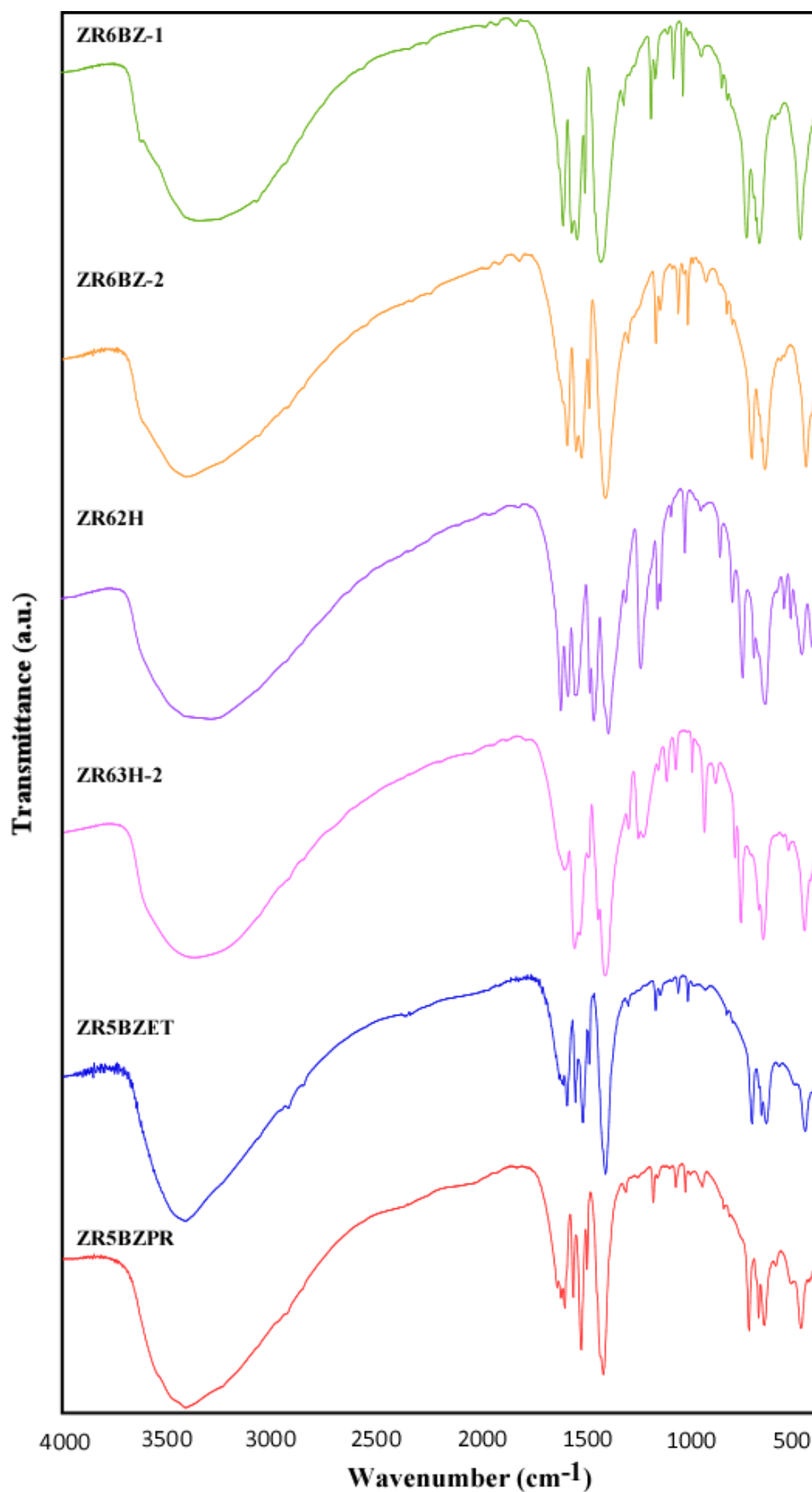


Figure 4.3. Infrared spectra of compound ZR6BZ-1 (red), ZR6BZ-2 (blue), ZR62H (pink), ZR6BZ3H-2 (purple), ZR5BZET (orange) and ZR5BZPR (green).

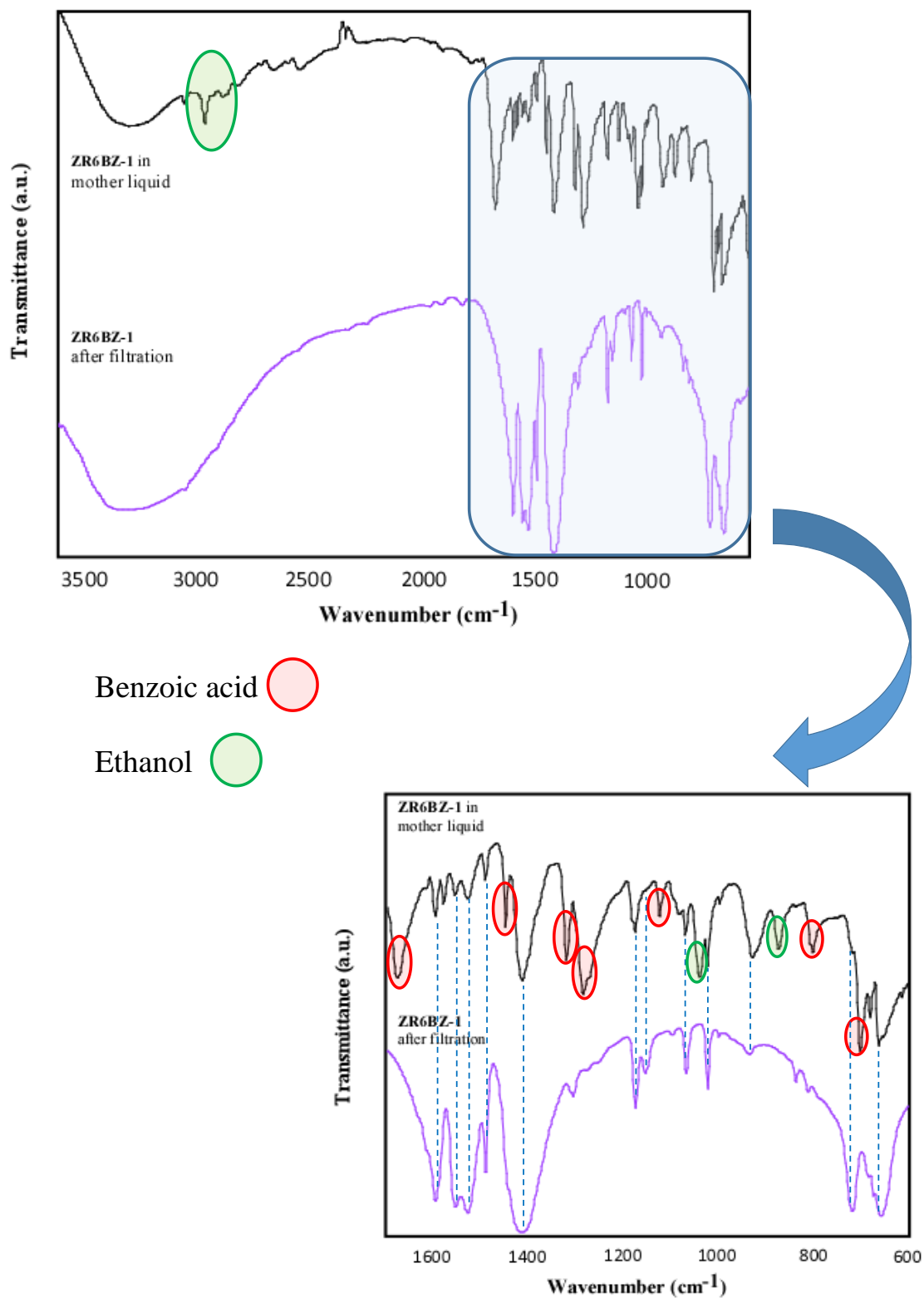


Figure 4.4. FTIR spectra of compounds ZR6BZ-1 in mother liquid (black line) and the comparison with the spectra done after filtration (purple line). Bands assigned to benzoic acid and ethanol present in the mother liquor are coloured in red and green, respectively.

4.2.3. Thermal analysis

The results of the thermal analyses (TG/ATD curves) of the compounds studied in this chapter are plotted in Figure 4.5, while the processes occurring in each degradation stage are gathered in Table 4.3. The thermogravimetric analysis of these compounds were performed in synthetic air (79% N₂, 21% O₂) from 30 °C to 800 °C with a temperature increase rate of 5 °C/min.

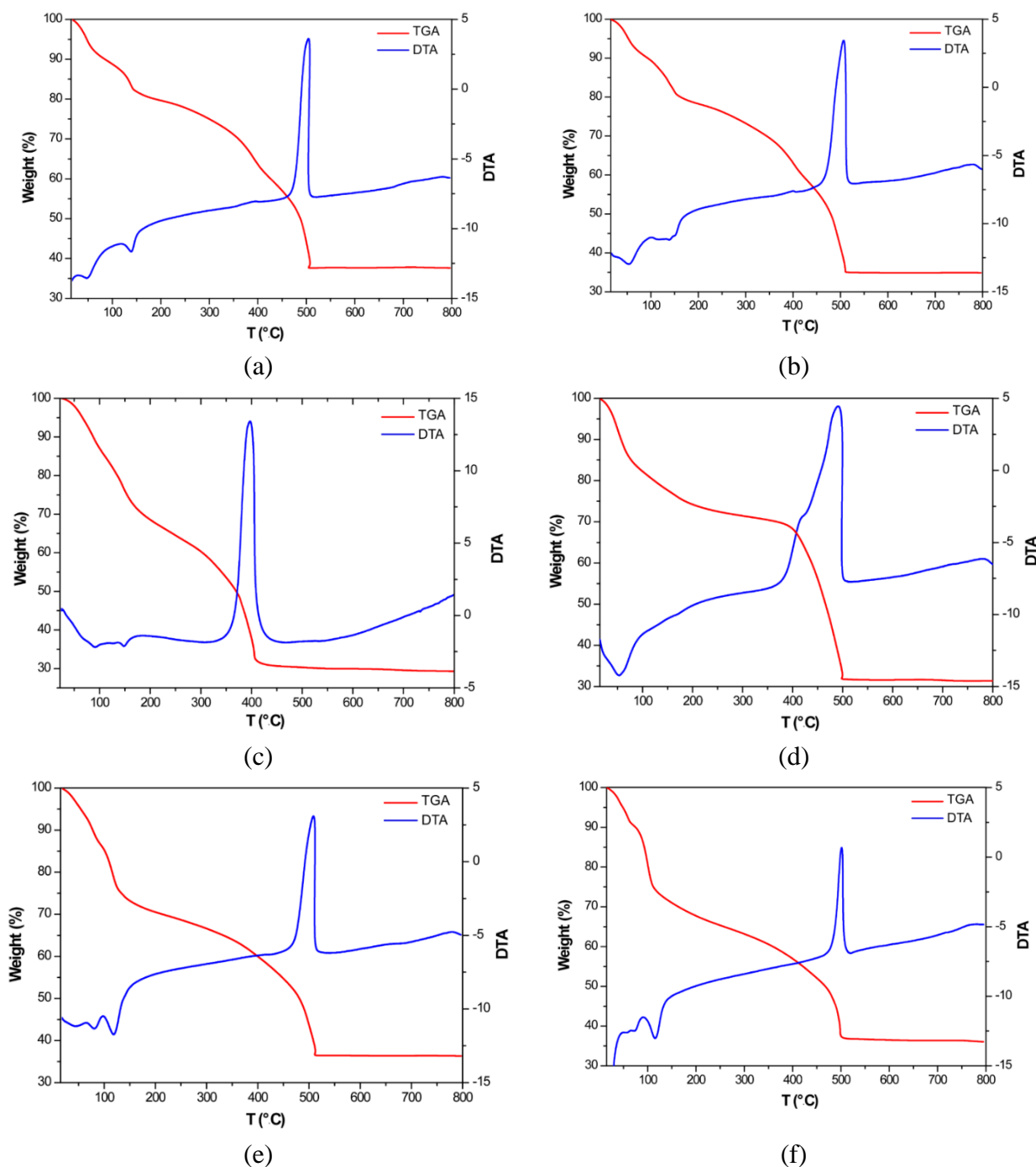


Figure 4.5. Thermogravimetric data (TGA-DTA curves) for compounds (a) ZR6BZ-1, (b) ZR6BZ-2, (c) ZR62H, (d) ZR63H-2, (e) ZR5BZET and (f) ZR5BZPR.

Table 4.3. Thermoanalytic data for compounds ZR6BZ-1/2, ZR6SA, ZR63H, ZR5BZET and ZR6BZPR.^a

Step	T _i	T _{peak}	T _f	ΔH	Δm(%)	ΣΔm(%)	ΣΔm(%) _{theor}
ZR6BZ-1							
1	25	50	70	Endo	9.00	9.00	9.15 (-10 H ₂ O)
2	95		115		3.60	12.60	12.86 (-2 HCl)
3	115	140	145	Endo	4.10	16.70	16.56 (-2 HCl)
4	330	505	800	Exo	45.78	62.48	62.59 (ZrO ₂)
ZR6BZ-2							
1	25	60	85	Endo	9.10	9.10	9.21 (-11 H ₂ O)
2	85	140	160	Endo	10.45	19.55	19.45 (-8 H ₂ O + -2 HCl)
3	160		250		3.18	22.73	22.83 (-2 HCl)
4	250	410	800	Exo	42.57	65.3	65.23 (ZrO ₂)
ZR62H							
1	25	90	125	Endo	17.78	17.78	17.94 (-25 H ₂ O)
2	125	150	180	Endo	11.45	29.23	29.48 (-8 H ₂ O + -4 HCl)
3	180	396	800	Exo	41.35	70.58	70.62 (ZrO ₂)
ZR63H-2							
1	25	55	85	Endo	15.69	15.69	15.46 (-21 H ₂ O)
2	85	165	250	Endo	11.81	27.5	27.88 (-8 H ₂ O + -4 HCl)
3	350	490	800	Exo	42.27	69.77	69.78 (ZrO ₂)
ZR5BZET							
1	25	35	75		8.87	8.87	9.14 (-6 H ₂ O + Ethanol)
2	75	80	95	Endo	4.38	13.25	13.47 (2 HCl)
3	95	120	165	Endo	14.64	27.89	28.02 (11 H ₂ O + Ethanol)
4	165	508	800	Exo	35.56	63.45	63.42 (ZrO ₂)
ZR5BZPR							
1	25	60	65	Endo	9.10	9.10	9.42 (-9 H ₂ O)
2	110	100	115	Endo	16.13	25.23	25.32 (-11 H ₂ O + -2 HCl)
3	150	495	800	Exo	38.63	63.86	63.87 (ZrO ₂)

^a T_i = initial temperature; T_{peak} = DTA peak temperature; T_f = final temperature; ΔH = type of process according to DTA, Δm(%) = mass loss percentage for each process; ΣΔm(%) = total mass loss percentage; ΣΔm(%)_{theor} = theoretical total mass loss percentage.

The thermograms show three main weight loss stages. First, crystallization solvent molecules are released at a temperature range of 25–85 °C. Thereafter, the compounds lose the coordination water molecules at 85–250 °C range where the release of the chloride anions as hydrogen chloride takes place by acquiring a proton from the four hydroxide groups of the corresponding cluster. After that, the framework decomposition takes place to lead ZrO₂ as final residue at 500 °C. It corresponds to a mixture of the monoclinic (PDF reference code 01-072-0597) and tetragonal (PDF reference code 01-071-1282) phases of ZrO₂.

4.2.4. Powder X-ray diffraction

Due to the loss of crystallinity of these compounds upon their removal from the mother liquid, the purity was ensured by means of X-ray powder diffraction performed over samples introduced in a Lindemann capillary and immersed in the synthesis mother liquid, Figures 4.6–4.11. A Rigaku Smartlab automatic diffractometer with a capillary fixation head was used and the diffraction data was collected in continuous rotation in the range $3^\circ < 2\theta < 65^\circ$.

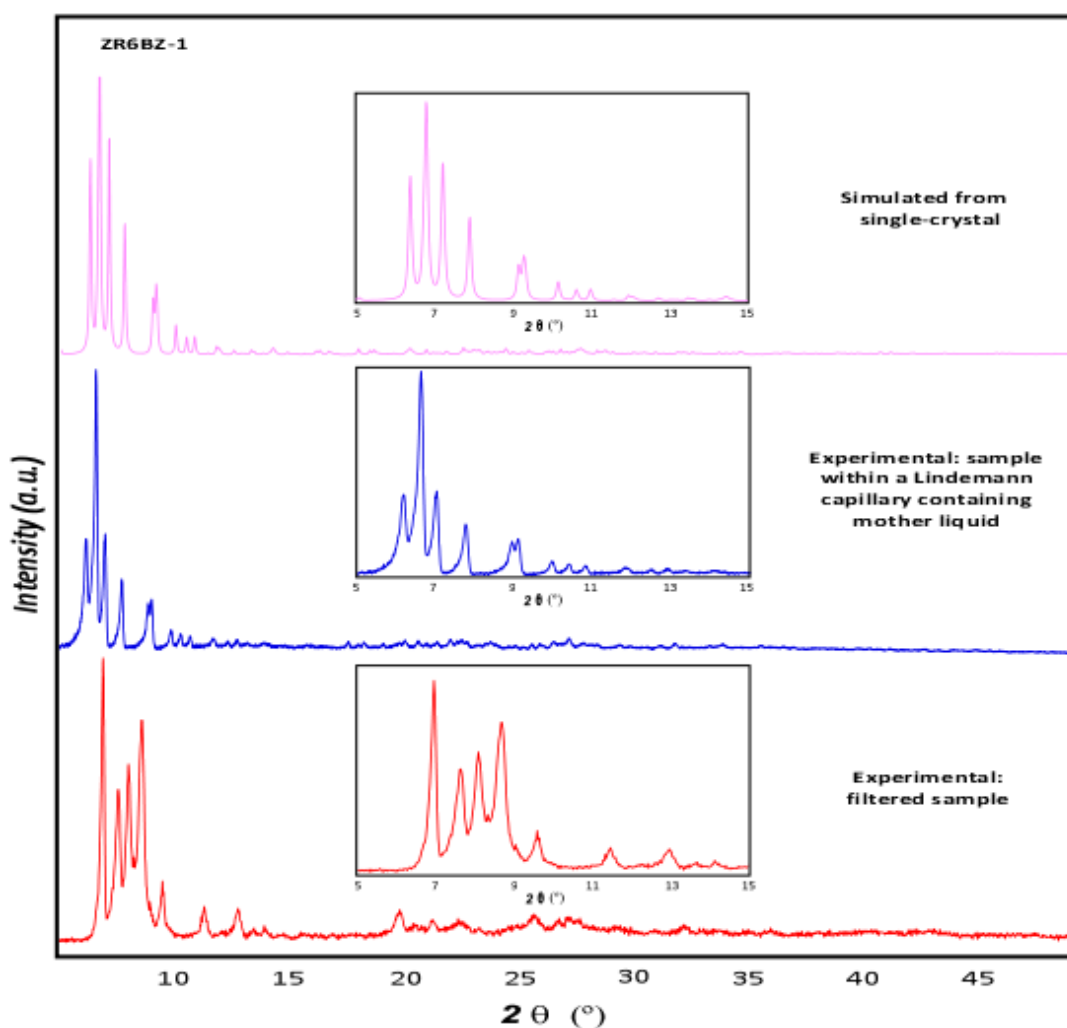


Figure 4.6. Powder X-ray diffraction patterns: simulated pattern of compound ZR6BZ-1 (top), experimental (bottom). Depicted in the insets an amplification of the 5–15° area for a better comparison.

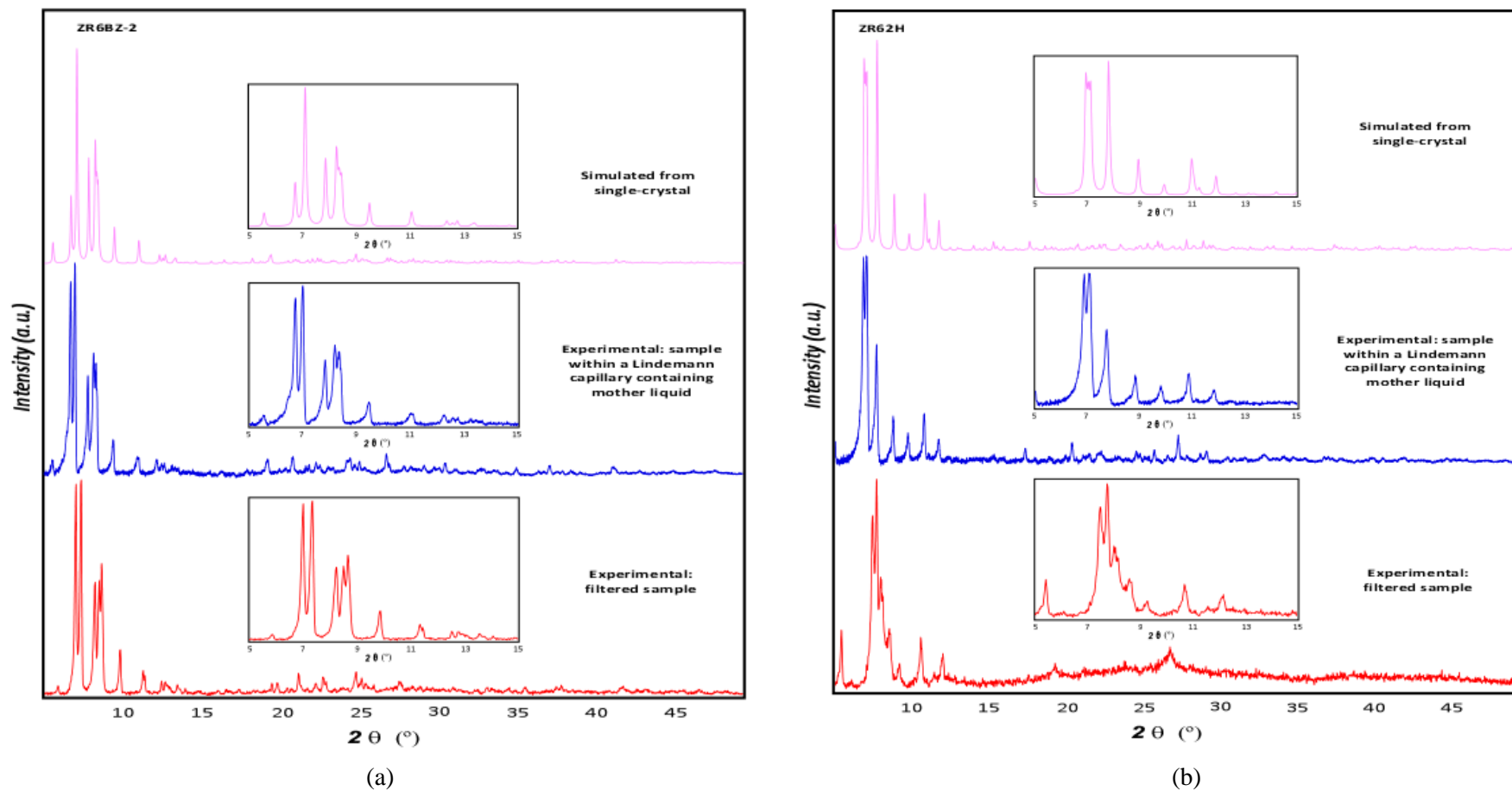


Figure 4.7. Powder X-ray diffraction patterns: simulated pattern of compound (a) ZR6BZ-2 and (b) ZR62H (top), experimental (bottom). Depicted in the insets an amplification of the 5–15° area for a better comparison.

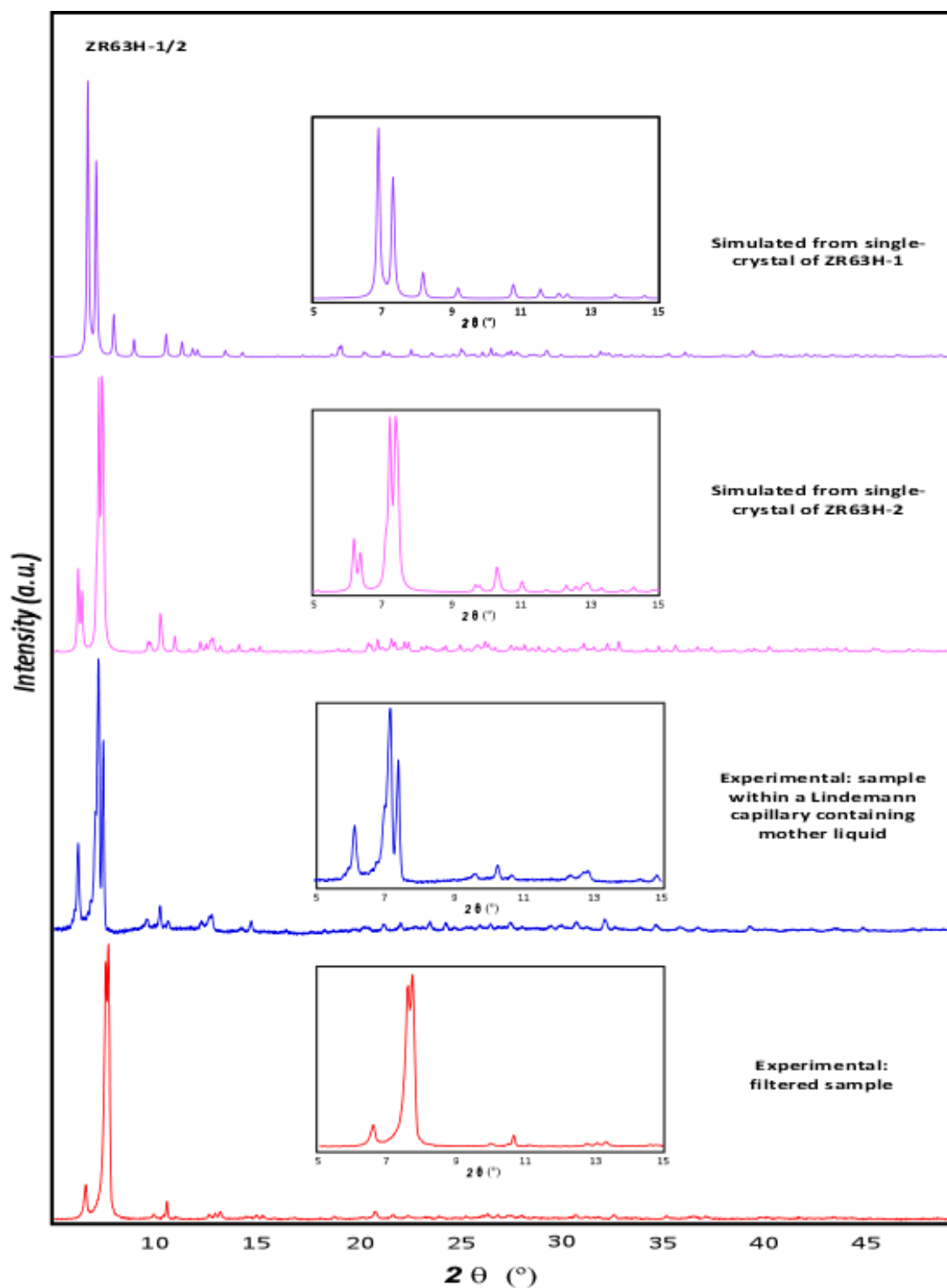


Figure 4.8. Powder X-ray diffraction patterns: simulated pattern of compound ZR63H-1/2, experimental (bottom). Depicted in the insets an amplification of the $5-15^\circ$ area for a better comparison

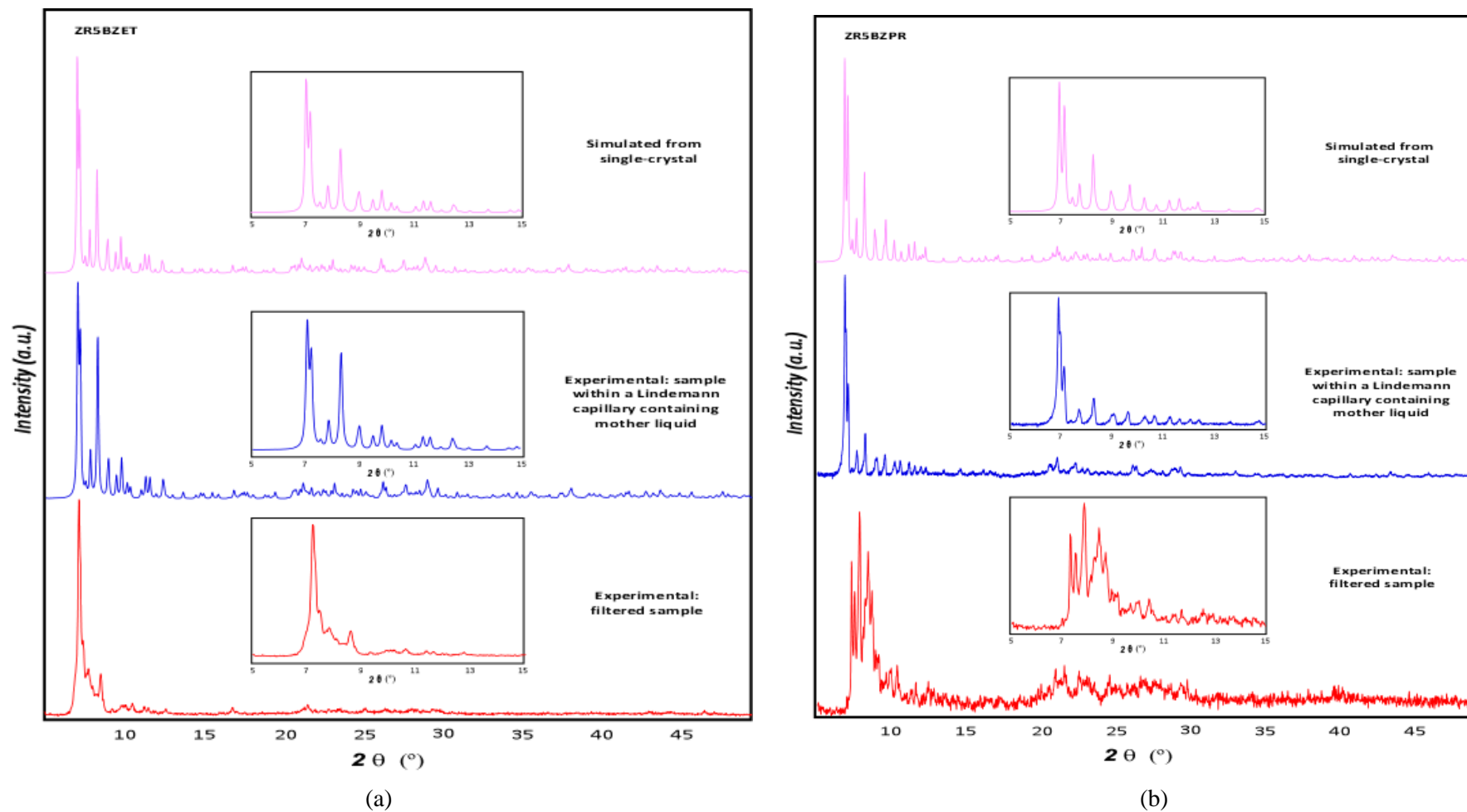


Figure 4.9. Powder X-ray diffraction patterns: simulated pattern of compound (a) ZR5BZET and (b) ZR5BZPR (top), experimental (bottom). Depicted in the insets an amplification of the 5–15° area for a better comparison.

4.2.5 Solid state nuclear magnetic resonance (NMR)

Solid state magic angle spinning (MAS) ^1H - and ^{13}C -NMR measurements have been carried out in order to verify that the cluster of the unsaturated entities remain stable after removing them from their mother liquors. Solid state measurements did not allow us to integrate the NMR signals to see how many atoms they correspond to. However, it allows us to prove the presence of benzenecarboxylato ligand in ZR6BZ-1/2, ZR6BZET and ZR5BZPR and the corresponding hydroxylated benzenecarboxylato in ZR62H and ZR63H-1/2.

In hexameric-benzoate compounds ^{13}C -NMR spectra (Figure 4.10) show two different signals at 172 ppm attributable to the carbon of the carboxylate group and another one, at 130 ppm, with a higher intensity, assigned to the aromatic carbons. In the case of ^1H -NMR two different signals are also observed. The first one at a value around 3.6 ppm is associated to the hydrogen atoms of the water molecules of the cluster (blue). The second one, around 7.2 ppm is related to the hydrogen atoms of aromatic ring.

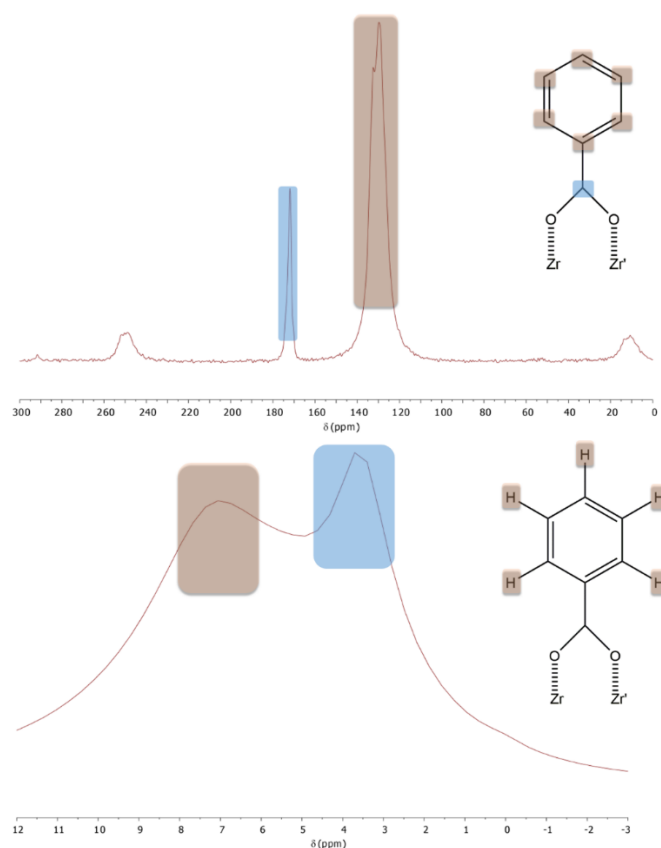


Figure 4.10. ^{13}C -NMR (upper) and ^1H -NMR (bottom) MAS NMR spectra for bulk samples of compounds ZR6BZ-1/2.

Zr-SMOFs: The chemistry of zirconium/carboxylate clustering

^{13}C -NMR spectra shows four different signals for compounds ZR62H and ZR63H-1/2, the first one around 173 and 171 ppm, respectively, attributable to the carbon of the carboxylato group, the second one around 160 ppm attributable to the carbon of the hydroxide group, the last two ones around 137 and 113 or 131–128 and 121–115 ppm respectively, belong to the remaining aromatic carbons. In the case of ^1H -NMR three and two different signals are also observed. The first one at a value around 2.9 and 4.3 ppm is associated to the water molecules of the cluster. The second one, around 6.5 and 7.1 ppm respectively is due the aromatic hydrogen atoms (blue). In addition, a signal located at 9.6 ppm in ZR62H is attributable the hydroxyl group.

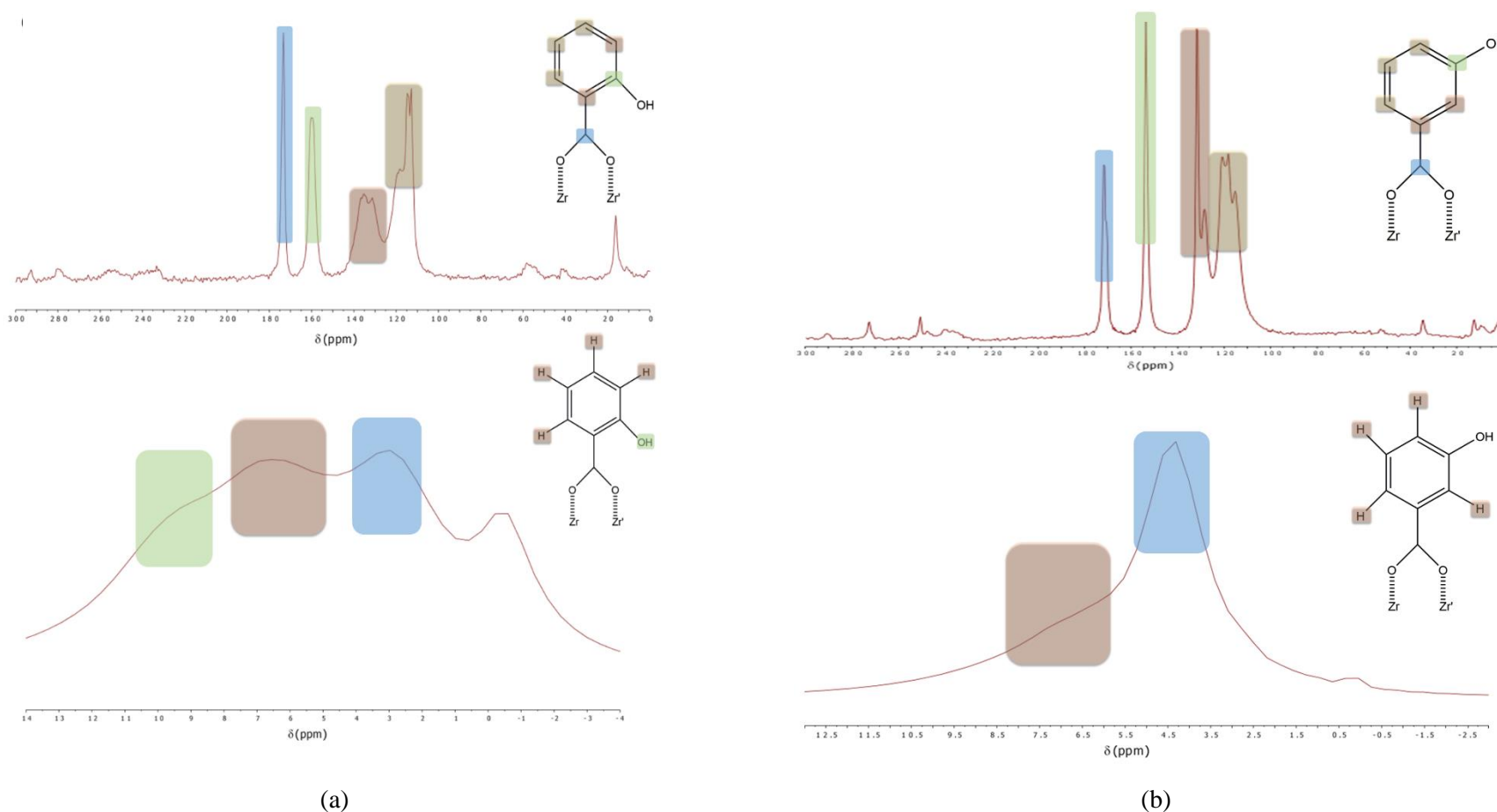


Figure 4.11. ^{13}C -NMR (upper) and ^1H -NMR (bottom) MAS NMR spectra for (a) ZR62H and (b) ZR63H-1/2.

Zr-SMOFs: The chemistry of zirconium/carboxylate clustering

^{13}C -NMR spectra shows four and five different signals for the compounds ZR5BZET and ZR5BZPR, the first one *ca.* 172 ppm attributable to the carbon of the carboxylato group, the second one *ca.* 130 ppm attributable to the aromatic ones, the last two and three signals belong to the ethanol/propanol molecule attached to the cluster appearing around 58 (CH_2) and 17 (CH_3) ppm and 63 and 23 (CH_2) and 12 (CH_3) ppm, respectively. In the case of ^1H -NMR a broad band can be separated into three different contributions: the first one at a value around 7.0 and 7.3 ppm attributable to the aromatic hydrogen atoms, a second one around 4.3 and 4.5 ppm associated to the water molecules of the cluster, the third one around 3.0 and 2.5 ppm attributable to the CH_2 group of the solvent molecule of the pentameric entity respectively. A separated fourth signal around 0.4 and -0.5 ppm is associated to the CH_3 group of the ethanol/propanol molecule is also visible.

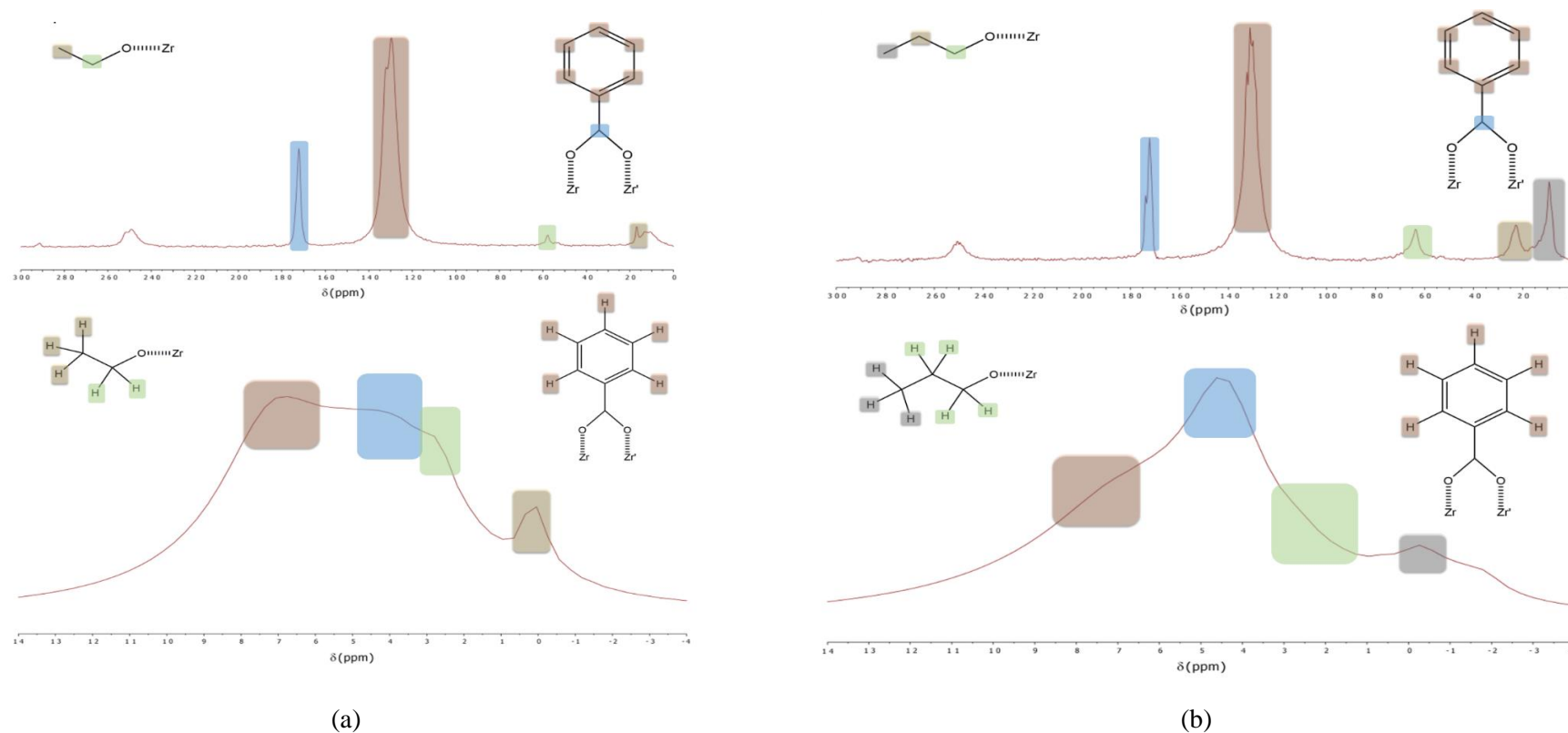


Figure 4.12. ^{13}C -NMR (upper) and ^1H -NMR (bottom) MAS NMR spectra for (a) ZR5BZET and (b) ZR5BZPR.

4.3. CRYSTALLOGRAPHIC ANALYSIS

Single-crystal X-ray diffraction data for structure determination were collected on Agilent Technologies Supernova diffractometers. The data reduction was done with the CrysAlisPro program.¹⁶³ Crystal structures were solved by direct methods using the SIR92¹⁶⁴ for ZR63H-1 and SUPERFLIP¹⁶⁵ for ZR6BZ-1/2, ZR6SA, ZR63H-2, ZR5BZET and ZR5BZPR and SHELX¹⁶⁶ programs and refined by full-matrix least-squares on F^2 including all reflections (WinGX).¹⁶²

The crystallographic data and the refinement conditions and parameters used in the structural solution of each compound have been gathered in Table 4.4. All non-hydrogen atoms were refined anisotropically, except those corresponding to disordered entities. The hydrogen atoms belonging to organic entities have been geometrically fixed and refined according to a riding model with an isotropic thermal parameter linked to the atom to which they are attached (120%). For the hydrogen atoms of the coordination water molecules the routine CALC-OH¹⁶¹ implemented in WinGX interface has been employed. The refinement of coordination water hydrogen atoms has been performed using an isotropic thermal parameter of 150% regarding their parent atom. For the crystallization water molecules and solvent ethanol molecules of all the compounds, it has not been possible to locate the hydrogen atoms geometrically due to the disorder that these structures present.

During the structural solution of the compounds, the existence of a static disorder in some of the benzoate and derivatives carboxylate ligands has been observed, as well as a hydroxide/oxide disorder. In ZR6BZ-2 the benzoate ligands have been disordered in two positions. In the case of ZR62H salicylato ligands are disordered over two coplanar positions. The disorder was modelled placing the hydroxyl groups split in two positions (A and B), with occupancy factors that add up to 100%, Figure 4.13. In compound ZR63H-1 disorder between the hydroxide and the oxide group of the cluster has been observed and modelled in two positions (A and B) following the same process above described. Compounds ZR6BZ-1 and ZR63H-2 are refined as a two component twin with batch scale factor (BASF) parameters of 0.073 and 0.354, respectively. The high disorder that some solvent molecules present precluded their modeling and, as a consequence, the electron density was subtracted from the reflection data by the SQUEEZE method¹⁶⁷ as implemented in PLATON.¹⁶⁸

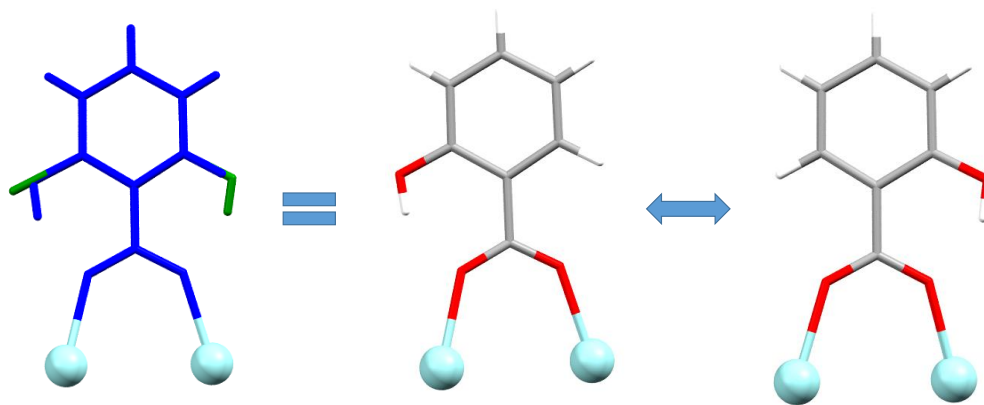


Figure 4.13. Disorder of the 3-hydroxybenzoate ligand with two coplanar orientations coloured in (A) blue and (B) green.

Zr-SMOFs: The chemistry of zirconium/carboxylate clustering

Table 4.4. Crystallographic data and structure refinement details of compounds ZR6BZ-1, ZR6BZ-2, ZR62H, ZR63H-1/2, ZR5BZET and ZR5BZPR.^{a,b}

	ZR6BZ-1	ZR6BZ-2	ZR62H	ZR6BZ3H-1	ZR6BZ3H-2	ZR5BZET	ZR5BZPR
empirical formula	C ₅₈ H ₁₃₆ Cl ₄ O ₆₈ Zr ₆	C ₅₆ H ₉₀ Cl ₄ O ₄₇ Zr ₆	C ₅₆ H ₁₁₆ Cl ₄ O ₆₈ Zr ₆	C ₅₆ H ₁₁₄ Cl ₄ O ₆₇ Zr ₆	C ₅₈ H ₁₁₄ Cl ₄ O ₆₅ Zr ₆	C ₃₄ H ₈₅ O ₄₀ Cl ₆ Zr ₅	C ₃₇ H ₉₃ Cl ₆ O ₄₁ Zr ₅
formula weight	2610.78	2204.39	2566.60	2548.59	2540.64	1802.81	1862.91
crystal system	Monoclinic	Triclinic	Monoclinic	Monoclinic	Monoclinic	Triclinic	Triclinic
space group	<i>Cc</i>	<i>P</i> $\bar{1}$	<i>P</i> 2 ₁ / <i>n</i> (14)	<i>I</i> 2/ <i>m</i>	<i>P</i> 2 ₁ / <i>n</i> (14)	<i>P</i> $\bar{1}$	<i>P</i> $\bar{1}$
<i>a</i>	27.4376(7)	14.5136(11)	15.7858(4)	13.8590(2)	17.0207(5)	12.8221(6)	12.8348(3)
<i>b</i>	27.6947(8)	16.1144(8)	25.2488(7)	24.8654(3)	23.6707(5)	12.8803(5)	12.9736(3)
<i>c</i>	27.7040(9)	19.1548(11)	25.1063(7)	15.1787(2)	24.8316(6)	21.7800(8)	21.9129(4)
α	90	80.923(4)	90	90	90	92.867(3)	93.420(2)
β	108.540(3)	79.585(5)	97.311(3)	98.1800(10)	91.793	100.776(4)	101.463(2)
γ	90	89.049(5)	90	90	90	101.501(4)	98.994(2)
V (Å ³)	19959.1(11)	4350.6(5)	9925.3(5)	5177.51(12)	9999.6(4)	3448.4	3516.50(14)
Z	8	2	4	2	4	2	2
T (K)	100.00(10)	150.00(10)	100.00(10)	150.00(2)	150.00(10)	150.00(10)	150.00(10)
Shape	Plate	Square	Plate	Diamond	Diamond	Diamond	Plate
Colour	Colourless	Colourless	Colourless	Colourless	Colourless	Colourless	Colourless
Max. and medium Δ/σ	0.001 / 0.000	0.000 / 0.000	0.001 / 0.000	0.001 / 0.000	0.001 / 0.000	0.000 / 0.000	0.001 / 0.000
θ interval (°)	2.752 – 24.999	1.972 – 25.796	2.883 – 26.029	3.437 – 74.580	3.622 – 75.429	1.947 – 26.770	4.462 – 74.259
hkl interval	-32 ≤ h ≤ 32; -32 ≤ k ≤ 32; -32 ≤ l ≤ 32	-18 ≤ h ≤ 18; -20 ≤ k ≤ 19; -22 ≤ l ≤ 24	-20 ≤ h ≤ 20; -31 ≤ k ≤ 32 -32 ≤ l ≤ 30	-42 ≤ h ≤ 43; -19 ≤ k ≤ 19; -21 ≤ l ≤ 21	-14 ≤ h ≤ 21; -29 ≤ k ≤ 29; -31 ≤ l ≤ 31	-16 ≤ h ≤ 16; -16 ≤ k ≤ 13; -26 ≤ l ≤ 24;	-16 ≤ h ≤ 15; -16 ≤ k ≤ 16; -18 ≤ l ≤ 27;
λ (Å)	0.71073	0.71073	0.71073	1.54184	1.54184	0.71073	1.54184
ρ_c (g·cm ⁻³)	1.738	1.683	1.718	1.635	1.688	1.736	1.759
μ (cm ⁻¹)	0.821	0.908	0.824	6.653	6.873	1.053	8.804
<i>F</i> (000)	10688	2220	7243	2588	5160	1822	1890
S ^a	0.792	1.008	1.009	1.084	1.042	0.880	1.034
R _{int}	0.0890	0.0700	0.1311	0.0399	0.0809	0.0664	0.0301
Parameters	1252	859	961	254	1053	665	743
Weight scheme ^c	Shelx	Shelx	Shelx	Shelx	Shelx	Shelx	Shelx
final R indices							
[I > 2 σ (I)] R ₁ ^b /wR ₂ ^c	0.0751/0.1948	0.0842/0.1975	0.0673/0.1519	0.0602/0.1828	0.0950/0.2699	0.0608/0.1371	0.0505/0.1426
all data R ₁ ^b /wR ₂ ^c	0.1896/0.2267	0.1762/0.2672	0.1501/0.1976	0.0686/0.1925	0.1308/0.2904	0.1278/0.1527	0.0544/0.1462
^a S = $[\sum w(F_o^2 - F_c^2)^2 / (N_{obs} - N_{param})]^{1/2}$. ^b R ₁ = $\sum F_o - F_c / \sum F_o $. ^c wR ₂ = $[\sum w(F_o^2 - F_c^2)^2 / \sum wF_o^2]^{1/2}$; w = 1/[$\sigma^2(F_o^2) + (aP)^2 + b$] where P = (max(F _o ² , 0) + 2F _c ²)/3; ZR6BZ-1 (a = 0.1171, b = 0); ZR6BZ-2 (a = 0.0973, b = 0); ZR62H (a = 0.0642, b = 0); ZR63H-1 (a = 0.1109, b = 38.7354); ZR63H-2 (a = 0.1549, b = 68.9610); ZR5BZET (a = 0.0575, b = 0); ZR5BZPR (a = 0.0793, b = 21.0678).							

4.4. RESULTS AND DISCUSSION

4.4.1. Structural description of compounds

The single-crystal X-ray diffraction analysis of hexameric compounds revealed a hexameric entity ($[\text{Zr}_6(\text{O})_4(\text{OH})_4(\text{OOC})_8(\text{H}_2\text{O})_8]^{4+}$) closely related to the well-known $[\text{Zr}_6(\text{O})_4(\text{OH})_4(\text{OOC})_{12}]$ SBU found in many MOFs,¹⁴⁹ chloride counterions and crystallization water/ethanol molecules. In compounds ZR5BZET and ZR5BZPR, a pentameric entity is revealed, $[\text{Zr}_5(\text{O})_2(\text{OH})_6(\text{OOC})_4(\text{H}_2\text{O})_{11}(\text{alcohol})]^{6+}$, by additionally removing one of the metal centers. Due to the higher positive charge of the pentameric entity, the crystal structure is completed by a higher content of chloride counterions than the hexameric ones and water and ethanol solvent molecules, Figure 4.14.

The hydroxide or oxide anions are positioned alternately in the center of each triangular face of the metal defining the square pyramid or octahedron. It means the hexameric entity has a $[\text{Zr}_6(\text{O})_4(\text{OH})_4]$ core whereas the pentameric shows a $[\text{Zr}_5(\text{O})_2(\text{OH})_6]$ core, in which the lack of a sixth zirconium atom implies that the four hydroxides pointing toward the vacant are not polarized enough to produce the observed alternation of oxides/hydroxides of the triangular faces (Figure 4.15). The external coordination positions of the metal atoms, all of them showing a cubic antiprism geometry, are occupied by water molecules and carboxylate ligands. The coordination bond distances found follow the same trend for all the entities. Zr–O_{oxide} distances are always the shortest ones (2.00–2.14 Å), those involving the oxygen atoms of the carboxylate groups are between 2.16–2.28 Å, whereas those of hydroxides and water molecules are the longest ones with values between 2.18–2.37 Å. The distance between adjacent zirconium atoms within the polynuclear entities is in the range of 3.47–3.54 Å, Tables 4.6–12.

Zr-SMOFs: The chemistry of zirconium/carboxylate clustering

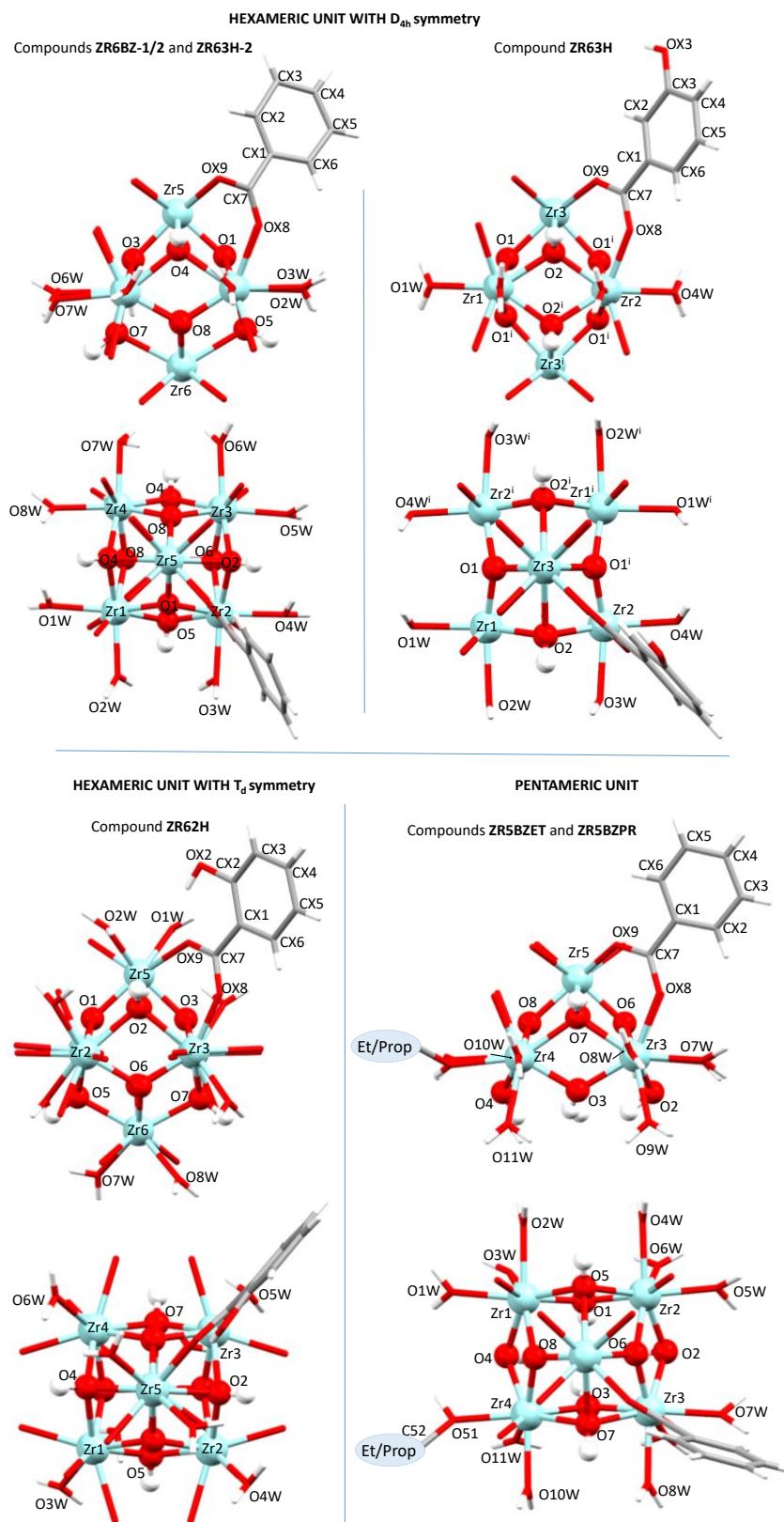


Figure 4.14. Zirconium clusters showing the numbering scheme. For the sake of clarity, only one of the coordinated carboxylato ligands is represented.

Table 4.6. Distances and angles (Å, deg) for compound ZR6BZ-1.

Zr1–O1	2.068(2)	Zr1–O1w	2.203(2)	Zr1–O2w	2.185(2)
Zr1–O4	2.227(2)	Zr1–O5	2.166(2)	Zr1–O8	2.092(2)
Zr1–O18	2.245(2)	Zr1–O58	2.198(2)	Zr2–O1	2.089(2)
Zr2–O2	2.270(2)	Zr2–O3w	2.196(2)	Zr2–O4w	2.209(2)
Zr2–O5	2.256(2)	Zr2–O6	2.040(2)	Zr2–O28	2.300(2)
Zr2–O69	2.258(2)	Zr3–O2	2.269(2)	Zr3–O3	2.068(2)
Zr3–O5w	2.230(2)	Zr3–O6	2.08(2)	Zr3–O6w	2.218(2)
Zr3–O7	2.274(2)	Zr3–O38	2.260(2)	Zr3–O78	2.250(2)
Zr4–O3	2.077(2)	Zr4–O4	2.201(2)	Zr4–O7	2.183(2)
Zr4–O7w	2.251(2)	Zr4–O8	2.020(2)	Zr4–O8w	2.196(1)
Zr4–O48	2.217(2)	Zr4–O88	2.246(2)	Zr5–O1	2.052(2)
Zr5–O2	2.273(2)	Zr5–O3	2.067(2)	Zr5–O4	2.378(1)
Zr5–O19	2.129(2)	Zr5–O29	2.238(2)	Zr5–O39	2.186(2)
Zr5–O49	2.167(2)	Zr6–O5	2.387(2)	Zr6–O6	2.082(2)
Zr6–O7	2.355(2)	Zr6–O8	2.087(2)	Zr6–O59	2.233(2)
Zr6–O68	2.188(2)	Zr6–O79	2.192(2)	Zr6–O89	2.187(2)
Zr7–O9	2.061(2)	Zr7–O9w	2.185(2)	Zr7–O10w	2.192(2)
Zr7–O12	2.242(2)	Zr7–O13	2.189(2)	Zr7–O16	2.082(1)
Zr7–O98	2.197(1)	Zr7–O138	2.276(1)	Zr8–O9	2.008(2)
Zr8–O10	2.251(1)	Zr8–O11w	2.203(2)	Zr8–O12w	2.230(2)
Zr8–O13	2.194(2)	Zr8–O14	2.062(2)	Zr8–O108	2.227(2)
Zr8–O148	2.170(2)	Zr9–O10	2.215(1)	Zr9–O11	2.071(2)
Zr9–O13w	2.216(2)	Zr9–O14	2.092(2)	Zr9–O14w	2.297(2)
Zr9–O15	2.236(1)	Zr9–O118	2.209(2)	Zr9–O158	2.288(2)
Zr10–O11	2.133(2)	Zr10–O12	2.216(2)	Zr10–O15	2.276(1)
Zr10–O15w	2.209(2)	Zr10–O16	2.096(1)	Zr10–O16w	2.206(2)
Zr10–O128	2.300(2)	Zr10–O168	2.276(2)	Zr11–O9	2.143(2)
Zr11–O10	2.325(2)	Zr11–O11	2.011(2)	Zr11–O12	2.341(2)
Zr11–O99	2.203(2)	Zr11–O109	2.276(2)	Zr11–O119	2.225(2)
Zr11–O129	2.210(2)	Zr12–O13	2.345(2)	Zr12–O14	2.041(2)
Zr12–O15	2.323(1)	Zr12–O16	2.044(1)	Zr12–O139	2.133(2)
Zr12–O149	2.178(2)	Zr12–O159	2.192(2)	Zr12–O169	2.132(2)

Table 4.7. Distances and angles (Å, deg) for compound ZR6BZ-2.

Zr1–O1	2.073(6)	Zr1–O1w	2.223(7)	Zr1–O2w	2.206(8)	Zr1–O4	2.235(6)
Zr1–O5	2.245(7)	Zr1–O8	2.082(6)	Zr1–O18	2.237(6)	Zr1–O59	2.221(6)
Zr2–O1	2.070(7)	Zr2–O2	2.241(7)	Zr2–O3w	2.239(7)	Zr2–O4w	2.219(7)
Zr2–O5	2.208(6)	Zr2–O6	2.081(6)	Zr2–O28	2.256(6)	Zr2–O68	2.228(7)
Zr3–O2	2.227(7)	Zr3–O3	2.043(6)	Zr3–O5w	2.224(9)	Zr3–O6	2.055(7)
Zr3–O6w	2.246(9)	Zr3–O7	2.236(7)	Zr3–O38	2.271(8)	Zr3–O78	2.226(8)
Zr4–O3	2.096(6)	Zr4–O4	2.227(6)	Zr4–O7	2.224(6)	Zr4–O7w	2.213(7)
Zr4–O8	2.070(6)	Zr4–O8w	2.202(7)	Zr4–O48	2.244(7)	Zr4–O88	2.287(6)
Zr5–O1	2.058(7)	Zr5–O2	2.377(7)	Zr5–O3	2.066(6)	Zr5–O4	2.367(6)
Zr5–O19	2.207(7)	Zr5–O29	2.208(5)	Zr5–O39	2.184(8)	Zr5–O49	2.169(7)
Zr6–O5	2.381(7)	Zr6–O6	2.068(6)	Zr6–O7	2.367(6)	Zr6–O8	2.070(6)
Zr6–O58	2.185(7)	Zr6–O69	2.177(7)	Zr6–O79	2.202(9)	Zr6–O89	2.169(6)

Table 4.8. Distances and angles (Å, deg) for compound ZR62H.

Zr1–O1	2.066(5)	Zr1–O3w	2.212(5)	Zr1–O4	2.295(5)	Zr1–O5	2.260(5)
Zr1–O8	2.069(5)	Zr1–O18	2.172(5)	Zr1–O38	2.250(5)	Zr1–O69	2.204(5)
Zr2–O1	2.078(5)	Zr2–O2	2.273(5)	Zr2–O4w	2.208(5)	Zr2–O5	2.272(5)
Zr2–O6	2.067(5)	Zr2–O39	2.224(5)	Zr2–O48	2.203(5)	Zr2–O77	2.219(5)
Zr3–O2	2.299(5)	Zr3–O3	2.060(5)	Zr3–O5w	2.203(5)	Zr3–O6	2.057(5)
Zr3–O7	2.276(5)	Zr3–O28	2.174(5)	Zr3–O49	2.224(5)	Zr3–O58	2.234(5)
Zr4–O3	2.070(5)	Zr4–O4	2.237(5)	Zr4–O6w	2.198(5)	Zr4–O7	2.321(5)
Zr4–O8	2.065(5)	Zr4–O59	2.201(5)	Zr4–O67	2.233(5)	Zr4–O88	2.181(5)
Zr5–O1	2.062(5)	Zr5–O1w	2.191(6)	Zr5–O2	2.212(5)	Zr5–O2w	2.201(5)
Zr5–O3	2.071(5)	Zr5–O4	2.231(5)	Zr5–O19	2.267(5)	Zr5–O29	2.277(5)
Zr6–O5	2.227(5)	Zr6–O6	2.074(5)	Zr6–O7	2.221(5)	Zr6–O7w	2.203(5)
Zr6–O8	2.059(5)	Zr6–O8w	2.224(5)	Zr6–O79	2.249(5)	Zr6–O89	2.267(5)

Table 4.9. Distances and angles (Å, deg) for compound ZR63H-1.^a

Zr1–O1A	2.141(7)	Zr1–O2A	2.410(9)	Zr1–O17I	2.180(4)	Zr1–O272	2.182(4)
Zr2–O1A	2.013(7)	Zr2–O1w	2.211(6)	Zr2–O2A	2.151(8)	Zr2–O2w	2.224(7)
Zr2–O172	2.266(4)	Zr3–O2A	2.158(8)	Zr3–O3w	2.221(6)	Zr3–O4w	2.199(6)
Zr3–O1A ⁱ	2.025(7)	Zr3–O271 ⁱ	2.237(5)	Zr3–O1A ⁱⁱ	2.237(5)	Zr3–O2A ⁱⁱⁱ	2.158(8)

^a Symmetry: (i) 2 – x, y, 1 – z, (ii) 2 – x, 1 – y, 1 – z, (iii) x, 1 – y, z.

Table 4.10. Distances and angles (Å, deg) for compound ZR63H-2.

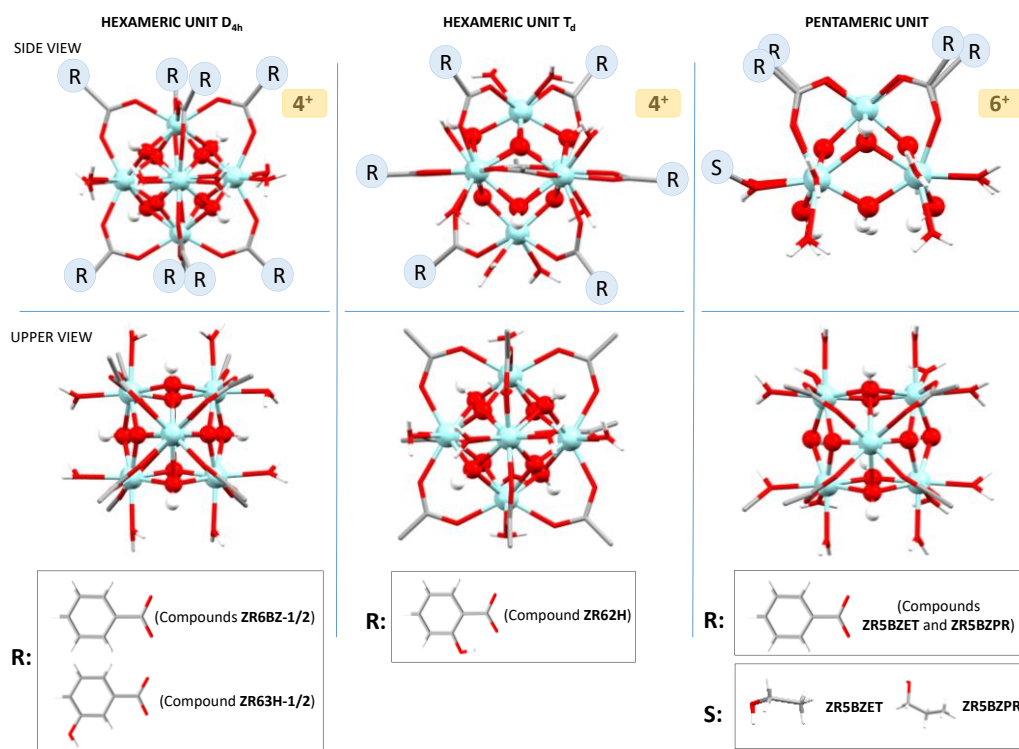
Zr1–O1	2.073(8)	Zr1–O1w	2.244(9)	Zr1–O2w	2.217(1)	Zr1–O4	2.210(9)
Zr1–O5	2.214(9)	Zr1–O8	2.070(9)	Zr1–O18	2.222(1)	Zr1–O59	2.230(8)
Zr2–O1	2.067(9)	Zr2–O2	2.241(8)	Zr2–O3w	2.208(1)	Zr2–O4w	2.211(9)
Zr2–O5	2.236(9)	Zr2–O6	2.065(9)	Zr2–O29	2.240(1)	Zr2–O68	2.235(1)
Zr3–O2	2.209(8)	Zr3–O3	2.075(9)	Zr3–O5w	2.21(1)	Zr3–O6	2.073(9)
Zr3–O6w	2.200(1)	Zr3–O7	2.206(9)	Zr3–O39	2.291(1)	Zr3–O78	2.238(1)
Zr4–O3	2.067(9)	Zr4–O4	2.245(8)	Zr4–O7	2.224(8)	Zr4–O7w	2.223(9)
Zr4–O8	2.051(9)	Zr4–O8w	2.200(9)	Zr4–O49	2.235(1)	Zr4–O88	2.290(8)
Zr5–O1	2.063(8)	Zr5–O2	2.340(8)	Zr5–O3	2.065(1)	Zr5–O4	2.330(9)
Zr5–O19	2.211(8)	Zr5–O28	2.172(9)	Zr5–O38	2.194(8)	Zr5–O48	2.203(1)
Zr6–O5	2.361(9)	Zr6–O6	2.065(9)	Zr6–O7	2.352(9)	Zr6–O8	2.084(8)
Zr6–O58	2.202(8)	Zr6–O69	2.196(1)	Zr6–O79	2.174(8)	Zr6–O89	2.176(9)

Table 4.11. Distances and angles (Å, deg) for compound ZR5BZET.

Zr1–O1	2.110(5)	Zr1–O1w	2.176(5)	Zr1–O2w	2.215(5)	Zr1–O3w	2.296(5)
Zr1–O4	2.159(5)	Zr1–O5	2.252(5)	Zr1–O8	2.074(5)	Zr1–O18	2.242(4)
Zr2–O1	2.126(5)	Zr2–O2	2.162(5)	Zr2–O4w	2.216(5)	Zr2–O5	2.249(5)
Zr2–O5w	2.193(5)	Zr2–O6	2.064(5)	Zr2–O6w	2.284(4)	Zr2–O28	2.219(5)
Zr3–O2	2.144(5)	Zr3–O3	2.135(5)	Zr3–O6	2.055(5)	Zr3–O7	2.244(5)
Zr3–O7w	2.185(5)	Zr3–O8w	2.206(6)	Zr3–O9w	2.273(5)	Zr3–O38	2.249(5)
Zr4–O3	2.120(5)	Zr4–O4	2.155(5)	Zr4–O7	2.249(5)	Zr4–O8	2.067(5)
Zr4–O10w	2.202(6)	Zr4–O11w	2.310(5)	Zr4–O48	2.207(4)	Zr4–O51	2.244(5)
Zr5–O5	2.373(5)	Zr5–O6	2.059(5)	Zr5–O7	2.381(5)	Zr5–O8	2.070(5)
Zr5–O19	2.169(5)	Zr5–O29	2.202(6)	Zr5–O39	2.161(5)	Zr5–O49	2.185(5)

Table 4.12. Distances and angles (Å, deg) for compound ZR5BZPR.

Zr1–O1	2.125(4)	Zr1–O1w	2.198(4)	Zr1–O2w	2.214(4)	Zr1–O3w	2.307(4)
Zr1–O4	2.162(3)	Zr1–O5	2.252(3)	Zr1–O8	2.064(4)	Zr1–O18	2.238(4)
Zr2–O1	2.124(4)	Zr2–O2	2.162(4)	Zr2–O4w	2.215(4)	Zr2–O5	2.254(3)
Zr2–O5w	2.214(4)	Zr2–O6	2.070(3)	Zr2–O6w	2.287(3)	Zr2–O28	2.225(4)
Zr3–O2	2.141(4)	Zr3–O3	2.124(4)	Zr3–O6	2.060(4)	Zr3–O7	2.250(3)
Zr3–O7w	2.201(4)	Zr3–O8w	2.224(4)	Zr3–O9w	2.284(4)	Zr3–O38	2.254(4)
Zr4–O3	2.130(4)	Zr4–O4	2.155(4)	Zr4–O7	2.247(3)	Zr4–O8	2.072(3)
Zr4–O10w	2.207(4)	Zr4–O11w	2.304(4)	Zr4–O48	2.206(3)	Zr4–O51	2.242(4)
Zr5–O5	2.364(4)	Zr5–O6	2.053(3)	Zr5–O7	2.369(4)	Zr5–O8	2.063(3)
Zr5–O19	2.170(4)	Zr5–O29	2.203(4)	Zr5–O39	2.178(4)	Zr5–O49	2.195(4)

**Figure 4.15.** Summary of the polynuclear entities present in compounds.

All the hexameric clusters present a hexameric structure with the previously described octahedral geometry of the cluster in which instead of the expected twelve carboxylato ligands only eight are anchored to the hexanuclear $Zr_6(O)_4(OH)_4$ core (benzoato in ZR6BZ-1/2; 2-hydroxybenzoato in ZR62H; 3-hydroxybenzoato in ZR63H-1/2). The remaining coordination positions lacking carboxylate groups (herein after: carboxylate unsaturated positions) are filled with water molecules. In spite of the apparent

similarity between these compounds, the arrangement of the carboxylato ligands provides a source of isomerism in these octahedrally shaped polynuclear entities. In compounds with benzoate and 3-hydroxybenzoato ligands the eight carboxylate groups bridge the equatorial and apical zirconium atoms. The coordination positions located at the equatorial edges of the octahedron are occupied by water molecules affording a D_{4h} symmetry, Figure 4.15. The metal coordination environment at apical positions consist of two oxides, two hydroxides and four oxygen atoms from carboxylate groups. However, the equatorial zirconium coordination environment consists of two oxides, two hydroxides, two oxygen atoms from carboxylate groups and two water molecules.

In contrast, the compound with 2-hydroxybenzoato ligand shares many of the features of the previously described octahedral clusters but the presence of the hydroxyl residue so close to the $Zr_6O_4(OH)_4$ core disfavours positioning four carboxylate groups around the apical zirconium positions and instead of the previously described D_{4h} arrangement, now a T_d symmetry is achieved. In this new arrangement all the equatorial edges are occupied by the carboxylato ligands but only half of the equatorial-apical linking edges are occupied in an alternated way. Alternatively, it can be described focusing on the carboxylate lacking edges that are arranged in a tetrahedral disposition. Therefore, the coordination environment of the apical zirconium is composed of two oxide molecules, two hydroxides, two water molecules, and two carboxylate groups. On the other hand, the equatorial zirconium coordination environment consists of two oxides, two hydroxides, three carboxylate groups and a single water molecule. As usually happens for 2-hydroxybenzoate anion and 2-hydroxybenzoic acid molecules an intramolecular hydrogen bond between the hydroxyl residue and one of the carboxylato oxygen atoms is observed.

Compounds ZR5BZET and ZR5BZPR consist of square-based pyramidal pentameric entities in which the absence of the sixth zirconium atom is accompanied with the reduction of the number of anchored benzoato ligands, from eight to four. These four carboxylate ligands are located bridging the zirconium atoms in the basal plane with the apical one. The lack of the sixth zirconium atom also exerts its influence in a lower polarization capacity and instead of the four oxide/four hydroxide composition for the polynuclear core a two oxide/six hydroxide ratio is observed. Again, the remaining positions to complete the eight coordination environment of the zirconium atoms are occupied by water molecules. As a result, the coordination environment of the apical

zirconium is composed of two oxides, two hydroxides, and four oxygen atoms from four carboxylate groups, whereas the coordination environment consists of one oxide, three hydroxides, a single carboxylate oxygen atom and three water molecules for three of the four basal plane zirconium atoms. The fourth zirconium in the basal plane shows a different coordination and gets coordinated to an alcohol molecule (ethanol in compound ZR5BZET and propanol in compound ZR5BZPR). Therefore, instead of having three coordinated water molecules, it only presents two and the alcohol molecule replaces the third one.

The cationic nature of the polynuclear entities implies the ionic interactions with the chloride counterions play a key role in directing the crystal packing of these compounds. In ZR6BZ-1/2 and ZR62H, ionic interactions are also reinforced by strong hydrogen bonds established by chloride counterions and the bridging hydroxide anions located in half of the triangular faces of the octahedrally shaped hexameric entities ($d_{\text{OH}\cdots\text{Cl}}$: 2.97–3.26 Å), Tables 4.13–4.15. These chloride counterions are tetrahedrally arranged around the metal-organic clusters but the size difference between the big cationic entities and the comparatively small chloride anions difficult achieving a strong packing of the crystal structure and thus, requires a huge amount of solvent molecules to provide some cohesiveness to the overall 3D architecture (Figure 4.16–4.17). In compound ZR6BZ-1 this anion acts as acceptor of the hydrogen bonding interactions involving the four bridging hydroxides of the two crystallographically independent of one cluster and three in the other one. The remaining chloride counterion is more loosely interacting with the cluster through the coordinated water molecules being disordered over two positions.

Table 4.13. Structural parameters (\AA , deg) of hydrogen bonding interactions in ZR6BZ-1.

Hydrogen-bonding interactions			
D–H...A ^a	H...A	D...A	D–H...A
O2–H2...C110	2.38	3.24(2)	170
O4–H4...C14	2.28	3.14(2)	170
O5–H5...C12	2.14	3.11(2)	166
O7–H7...C15	2.28	3.13(2)	166
O10–H10...C17	2.01	2.97(2)	167
O12–H120...C16A	2.04	3.01(2)	168
O13–H130...C18A	2.11	3.09(3)	170
O15–H150...O1E	1.99	2.86(2)	171
O1w–H12w...C14	2.26	3.09(2)	172
O2w–H21w...C12	2.24	3.15(2)	170
O3w–H31w...C12	2.14	3.14(2)	171
O4w–H42w...C110	2.31	3.17(2)	170
O5w–H52w...C110	2.46	3.32(3)	173
O6w–H62w...C15	2.19	3.14(2)	168
O7w–H71w...C15	2.18	3.03(2)	173
O8w–H82w...C14	2.12	3.08(2)	174
O9w–H91w...C16A	2.31	3.16(3)	169
O10w–H201...C18A	2.23	3.11(2)	170
O10w–H202...O17w	1.89	2.75(4)	173
O11w–H211...C18A	2.67	3.5(3)	161
O11w–H212...O18w	1.68	2.58(3)	172
O12w–H222...C17	2.39	3.33(2)	170
O13w–H232...C17	2.05	3.00(2)	172
O14w–H242...O1E	1.91	2.87(2)	175
O15w–H252...O1E	2.39	3.22(3)	172
O16w–H262...C16A	2.46	3.28(3)	165

^aD: donor; A: acceptor.

Table 4.14. Structural parameters (\AA , deg) of hydrogen bonding interactions in ZR6BZ-2.^a

Hydrogen-bonding interactions			
D–H...A ^b	H...A	D...A	D–H...A
O2–H2...C11A	2.41	3.26(1)	172
O4–H4...C12	2.27	3.13(7)	171
O5–H5...C13	2.34	3.20(8)	175
O7–H7...C14	2.26	3.20(9)	160
O1w–H11w...O10w	1.86	2.71(1)	178
O1w–H12w...C12	2.27	3.11(7)	169
O2w–H22w...C13	2.24	3.08(7)	175
O3w–H31w...C13	2.24	3.10(8)	176
O4w–H41w...C11	1.99	2.86(1)	168
O4w–H42w...C11 ⁱ	2.35	3.24(1)	165
O5w–H51w...O9w	1.86	2.74(2)	173
O5w–H52w...O12w	2.17	3.03(1)	179
O6w–H62w...C14	2.30	3.17(1)	170
O7w–H72w...C14	2.17	3.05(1)	172
O8w–H81w...C12	2.19	3.06(7)	174
O8w–H82w...O11w	1.83	2.69(1)	171

^aSymmetry codes: (i) $2 - x, 1 - y, -z$. ^bD: donor; A: acceptor.**Table 4.15.** Structural parameters (\AA , deg) of hydrogen bonding interactions in ZR62H.^a

Hydrogen-bonding interactions			
D–H...A ^b	H...A	D...A	D–H...A
O2–H2...C11	2.11	3.06(5)	163
O4–H4...C13	2.05	3.00(5)	163
O5–H5...C12	2.06	3.04(5)	171
O7–H7...C14 ⁱ	2.21	3.16(5)	161
O1w–H11w...C13	2.29	3.02(6)	165
O2w–H21w...C11	2.20	3.07(5)	178
O3w–H31w...C12	2.34	3.20(5)	174
O4w–H41w...C11	2.26	3.11(5)	170
O5w–H52w...C14 ⁱ	2.26	3.12(5)	168
O6w–H61w...C13	2.22	3.07(5)	175
O7w–H71w...C12	2.36	3.21(5)	173
O8w–H81w...C14	2.24	3.09(5)	161
C23–H23...O22 ⁱⁱ	2.53	3.45(1)	169

^aSymmetry codes: (i) $2 - x, 1 - y, -z$; (ii) $2 - x, -y, 2 - z$. ^bD: donor; A: acceptor.

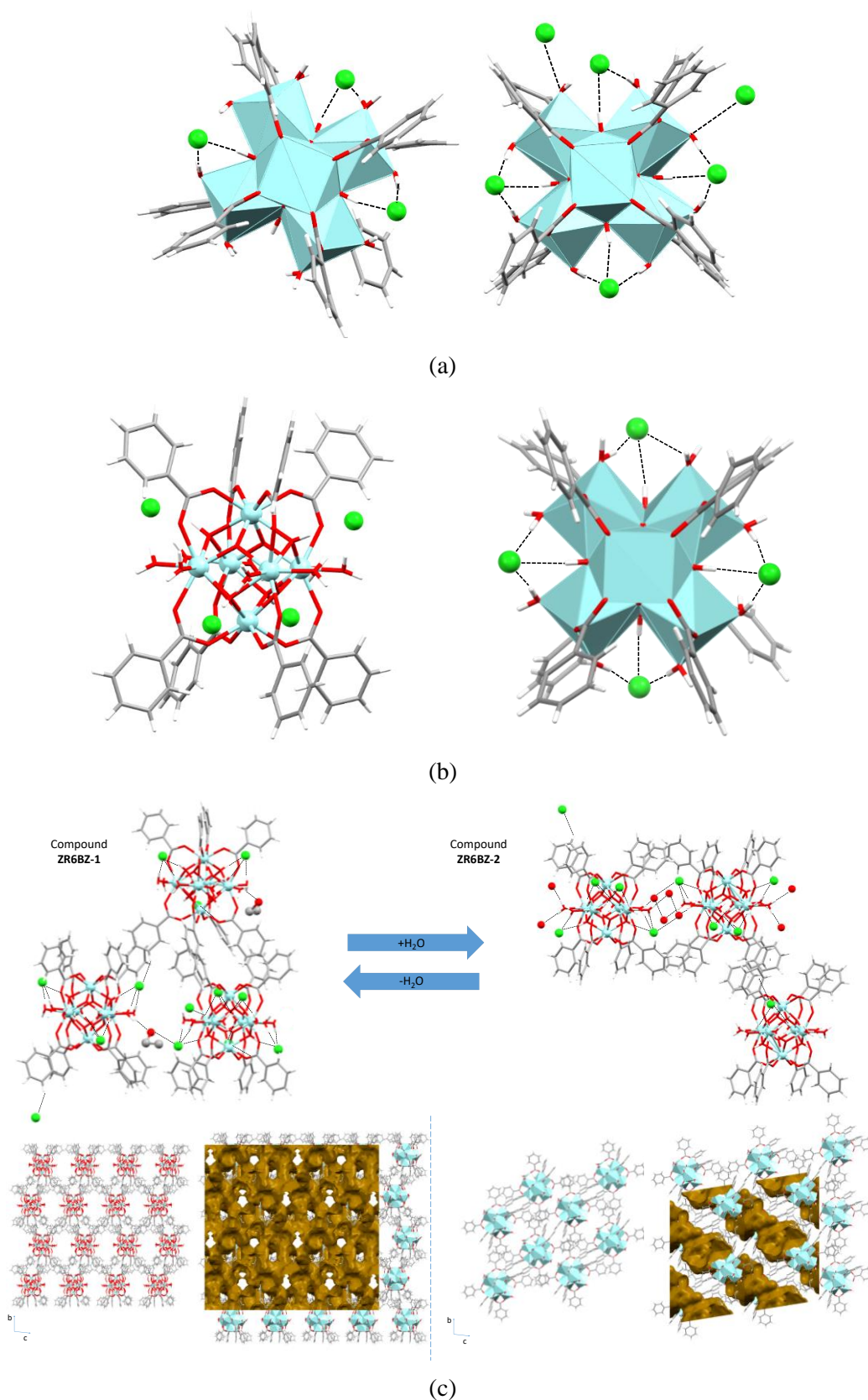


Figure 4.16. Hexameric entity (a) and (b) chloride interactions in hexameric benzoate compounds respectively and (c) crystal packing of compounds ZR6BZ-1/2.

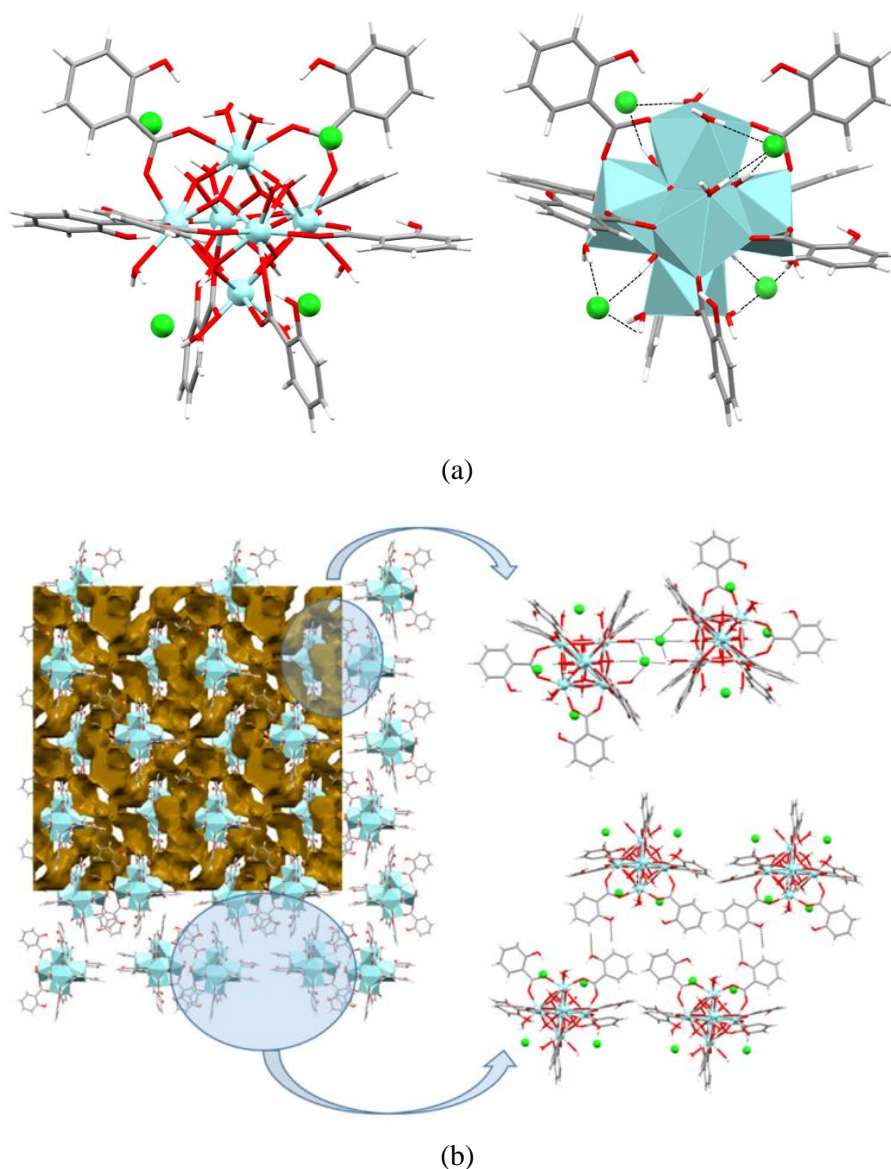


Figure 4.17. (a) Hexameric entity and (b) crystal packing of compound ZR62H.

In the case of compound ZR63H-1/2, the hydroxyl residues protruding from the hexameric entities provide a better placement for the chloride counterions to establish hydrogen bonding interactions. These features also generate an interaction pathway in both compounds between the neighboring hexameric entities, which involves 3-hydroxybenzoate ligands and the coordinated water molecules as hydrogen-bonding donors towards the chloride counterions, Table 4.16 and 4.17. These interactions only spread along the (101) crystallographic plane and the 3D cohesiveness requires again a great amount of solvent molecules.

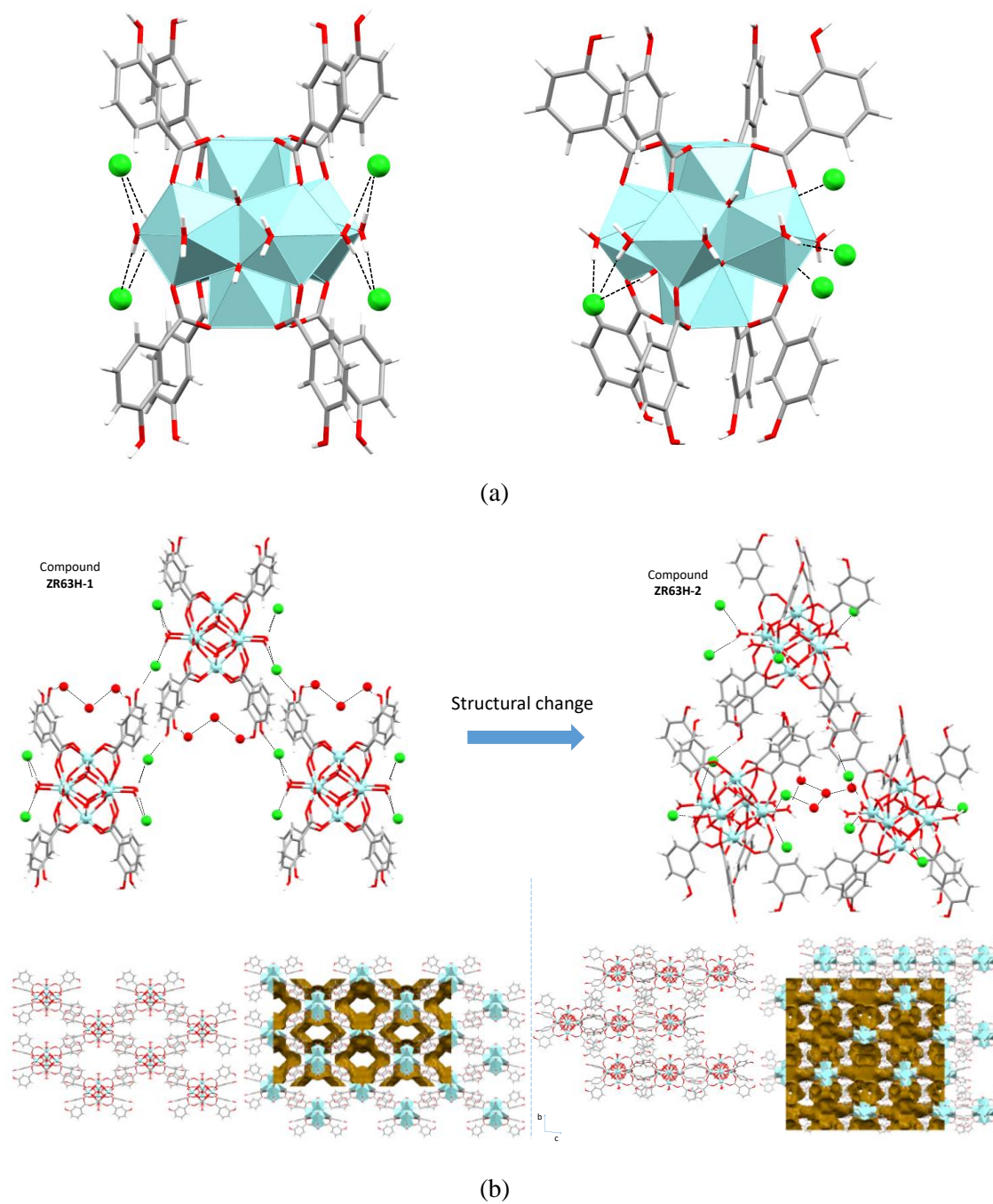


Figure 4.18. (a) Hexameric entity and (b) crystal packing of compound ZR63H-1/2 respectively.

Table 4.16. Structural parameters (Å, deg) of hydrogen bonding interactions in ZR63H-1.^a

Hydrogen-bonding interactions			
D-H...A ^b	H...A	D...A	D-H...A
O1w-H1w...Cl1 ⁱ	2.31	3.16(6)	175
O4w-H4w...Cl1 ⁱⁱ	2.40	3.25(6)	174
O13-H13...Cl1	2.21	3.08(8)	171
O23-H23...O5w	2.01	2.90(2)	161

^aSymmetry codes: (i) $5/2 - x, 1/2 - y, 1/2 - z$, (ii) $-1/2 + x, 1/2 + y, 1/2 + z$. ^bD: donor; A: acceptor.

Table 4.17. Structural parameters (Å, deg) of hydrogen bonding interactions in ZR63H-2.^a

Hydrogen-bonding interactions			
D-H...A ^b	H...A	D...A	D-H...A
O2-H2...O11w	1.92	2.76(1)	167
O4-H4...O21w	1.95	2.79(2)	169
O5-H5...Cl1 ⁱ	2.27	3.13(1)	172
O7-H7...O12w ⁱⁱ	1.90	2.74(1)	170
O1w-H11w...O21w	2.01	2.83(2)	156
O1w-H12w...O13w	1.91	2.76(1)	167
O2w-H21w...Cl1 ⁱ	2.30	3.17(1)	170
O2w-H22w...Cl3	1.85	2.69(2)	166
O3w-H31w...Cl1 ⁱ	2.29	3.16(1)	172
O3w-H32w...O24w	1.78	2.62(2)	164
O4w-H41w...O28w	1.86	2.69(2)	158
O4w-H42w...O17w	1.95	2.80(1)	162
O5w-H51w...Cl2	2.23	3.08(1)	164
O5w-H52w...O11w	1.86	2.70(1)	161
O6w-H61w...O12w ⁱⁱ	1.91	2.76(2)	166
O6w-H62w...O27w	1.78	2.61(2)	163
O7w-H71w...Cl4A ⁱⁱⁱ	2.13	2.96(1)	167
O7w-H72w...Cl3	2.23	3.10(1)	170
O8w-H81w...O15w	1.92	2.74(2)	159
O8w-H88w...O19w	1.86	2.67(2)	155
O13-H13...O20W	1.84	2.69(2)	176
O23-H23...Cl3 ^{iv}	2.19	3.06(1)	167
O33-H33...Cl1	2.19	3.05(1)	170
O4-H43...O14w	1.88	2.73(1)	172
O53-H53...O23w	1.83	2.69(2)	170
O63-H63...O10w	1.94	2.74(3)	165
O73-H73...O10w	1.85	2.65(3)	156
O83-H83...O23w	1.82	2.66(2)	167

^aSymmetry codes: (i) $1/2 + x, 1/2 - y, 1/2 + z$; (ii) $-1/2 + x, 1/2 - y, 1/2 + z$; (iii) $1/2 - x, 1/2 + y, 5/2 - z$; (iv) $1/2 - x, -1/2 + y, 3/2 - z$. ^bD: donor; A: acceptor.

The 6+ charge of the pentameric species implies the presence of six chloride counterions but only three of them are strongly hydrogen bonded to the bridging hydroxide anions. Two of them as previously described for most of the hexameric entities, take part in the interaction with the hydroxides placed in the triangular faces and the third one occupies a position close to what would be the sixth zirconium atom if the cluster would have evolved towards the hexameric entity. In this position, the chloride anion acts as acceptor of the hydrogen bonding interactions involving the four bridging hydroxides located in the basal plane of the cluster. The remaining three chloride counterions are more loosely interacting with the cluster through the coordinated water molecules, Tables 4.18 and 4.19. In fact, one of these chlorides is disordered over two positions indicative of the less specific interactions they establish, Figure 4.19.

In all compounds, solvent molecules account for a great portion of the total volume of the solid (21.9–33.3%) and their loss after the removal of the crystals from the mother liquid implies a transformation of the crystal structure. In fact, this great amount of solvent molecules seems to saturate the capacity of the aromatic monocarboxylic ligands to establish supramolecular interactions and no π -stacking has been observed among them. Only compound with the salicylic acid ligand exhibits some weak double C–H \cdots O hydrogen bonds involving the 2-hydroxybenzoate ligands from adjacent hexanuclear entities. The fluidity of the supramolecular network involving such a huge amount of solvent molecules allows us to isolate compounds ZR6BZ-1/2 and ZR63H-1/2 which can be considered two solvation stages of the same compound, in spite of the fact that they exhibit completely different unit cell parameters and space group. All in all, although the structure collapse difficulties the characterization of bulk samples, the homogeneity of the crystalline phase was assessed by powder X-ray diffraction analyses over samples introduced in Lindemann tubes and the stability of the clusters upon their removal from mother liquors was addressed on the basis of solid state ^1H - and ^{13}C - MAS-NMR spectroscopy previously described in section 4.2.5.

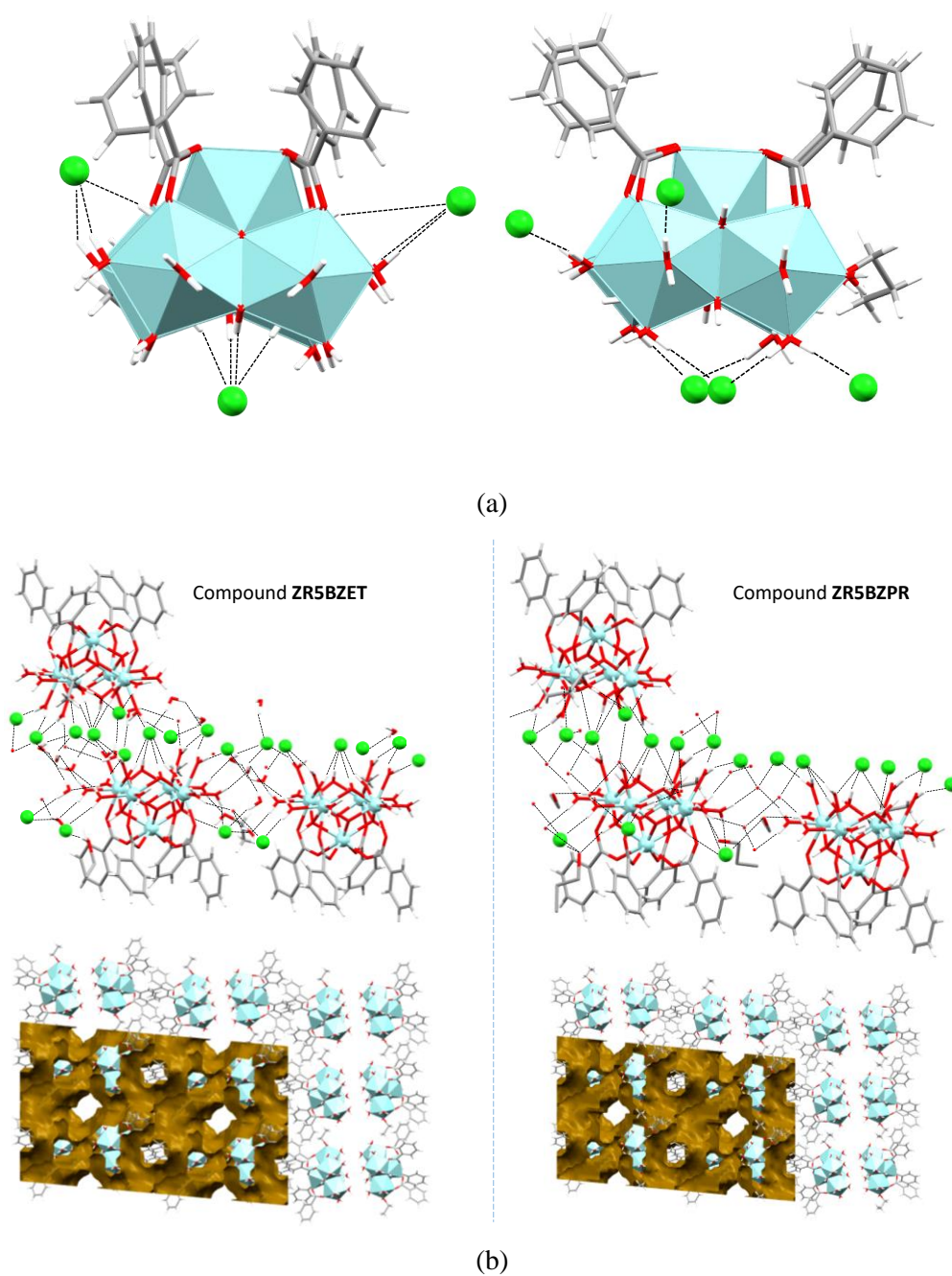


Figure 4.19. (a) Pentameric asymmetric entity and chloride interactions of compounds ZR5BZET and ZR5BZPR respectively and (b) crystal packing of compounds.

Table 4.18. Structural parameters (\AA , deg) of hydrogen bonding interactions in ZR5BZET.^a

Hydrogen-bonding interactions			
D–H...A ^b	H...A	D...A	D–H...A
O1–H1...C11	2.29	3.14(5)	164
O3–H3...C11	2.33	3.19(5)	160
O4–H4...C11	2.45	3.31(4)	170
O5–H5...O2E	1.97	2.93(1)	170
O7–H7...C14	2.31	3.26(5)	164
O1w–H11w...C16	2.15	3.01(5)	172
O1w–H12w...O18w	1.70	2.59(1)	170
O2w–H21w...O14w	1.83	2.69(8)	167
O2w–H22w...O12w ⁱ	1.90	2.76(7)	164
O3w–H31w...C13	2.10	3.03(5)	164
O3w–H32w...C11	2.70	3.50(5)	161
O4w–H41w...C15A	2.38	3.23(5)	174
O4w–H42w...O16w	1.77	2.63(8)	159
O5w–H51w...O15w	1.78	2.69(8)	168
O5w–H52w...C16 ⁱⁱ	2.21	3.07(5)	167
O6w–H61w...O17w	1.81	2.66(9)	165
O6w–H62w...C11 ⁱⁱⁱ	2.34	3.20(5)	167
O7w–H71w...O15w	1.75	2.69(8)	158
O8w–H81w...O12w	1.82	2.70(7)	173
O8w–H88w...C14	2.22	3.05(4)	164
O9w–H81w...C12	2.18	3.09(5)	167
O9w–H92w...C12 ^{iv}	2.24	3.12(5)	163
O10w–H101...O19w	1.78	2.66(1)	169
O10w–H102...O1E	1.84	2.71(2)	175
O11w–H111...C12	2.35	3.20(5)	168
O11w–H112...O20w ^v	1.88	2.73(1)	166
O51–H51...C16	2.29	3.16(5)	167
O2E–HO2E...C15A	2.17	3.05(9)	175

^aSymmetry codes: (i) $1 + x, y, z$, (ii) $x, -1 + y, z$, (iii) $1 - x, 1 - 1 + y, 1 - z$, (iv) $2 - x, 1 - y, 1 - z$, (v) $x, 1 + y, z$. ^bD: donor; A: acceptor.

Table 4.19. Structural parameters (\AA , deg) of hydrogen bonding interactions in ZR5BZPR.^a

Hydrogen-bonding interactions			
D–H...A ^b	H...A	D...A	D–H...A
O1–H1...C11	2.64	3.61(4)	174
O2–H2...O16w	2.11	3.08(6)	172
O3–H3...C12	2.67	3.63(4)	171
O4–H4A...C15 ⁱ	2.49	3.46(3)	176
O4–H4B...C11 ⁱⁱ	2.42	3.36(3)	164
O5–H5...O1PA	1.95	2.94(9)	167
O7–H7...C14B	2.20	3.15(5)	163
O1w–H11w...C15 ⁱ	2.19	3.07(4)	176
O2w–H21w...O13w	1.81	2.67(6)	174
O2w–H22w...O12w ⁱⁱⁱ	1.91	2.78(5)	168
O3w–H31w...C11	2.21	3.09(4)	166
O3w–H32w...C13	2.19	3.05(4)	173
O4w–H41w...C16A	2.23	3.10(5)	171
O4w–H42w...O14w	1.76	2.63(7)	168
O5w–H51w...O16w	1.83	2.69(6)	176
O5w–H52w...C15	2.22	3.09(4)	170
O6w–H61w...O18A	1.87	2.71(1)	165
O6w–H62w...C11	2.31	3.18(4)	172
O7w–H71w...O16w	1.81	2.69(6)	162
O7w–H72w...O21w ^{iv}	2.00	2.81(8)	153
O8w–H81w...O12w	1.85	2.71(5)	171
O8w–H88w...C14B	2.20	3.06(4)	167
O9w–H81w...C12	2.18	3.08(4)	173
O9w–H92w...C12 ^v	2.31	3.10(4)	165
O10w–H101...O17A	1.80	2.66(1)	174
O10w–H102...O2P	1.84	2.69(2)	178
O11w–H111...O15w	1.76	2.75(7)	168
O11w–H112...C12	2.04	3.16(4)	174
O51–H51...C15 ⁱ	2.22	3.09(4)	175

^aSymmetry codes: (i) $x, 1 + y, z$; (ii) $1 - x, 1 - y, 1 - z$, (iii) $-1 + x, y, z$, (iv) $1 + x, y, z$, (v) $2 - x, 1 - y, 1 - z$. ^bD: donor; A: acceptor.

4.4.2. Mass spectrometry

To evaluate the first stages of the clustering process of zirconium-carboxylate systems in alcoholic media, we have carried out Electrospray ionization–Mass spectrometry (ESI-MS) measurements of the species present in solution upon the dissolution of $ZrCl_4$ and the corresponding benzoic ligand in anhydrous ethanol.²³⁶ The pH value of the resulting media was controlled by the addition of water to allow a precise control of the acidity at different pH values (–0.5, 0.0, 0.5 and 1.0). This variation exerts a strong influence on the species that are built up as confirmed by means of mass-spectrometry. In these studies, the appearances of pentameric and hexameric zirconium entities in which the carboxylic ligands are coordinated to the metal centers were detected.

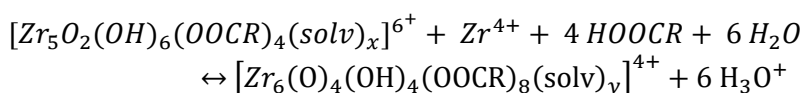
The experiments were run both in positive and negative ionization mode, but positive mode showed to be more informative as in the negative mode only signals belonging to the presence of organic molecules, coming probably from the ionization and subsequent fragmentation of the solvent molecules, were detected. However, the negative ionization modes provide some clues on the zirconium speciation. The small amount of water present in the ethanol solvent is enough to allow the presence of chloride/hydroxide/oxide mixed zirconium species. It is also worth mentioning that the presence of hydroxides and oxides helps providing polynuclear entities.

Figures 4.20 and 4.21 shows the ESI+ mass spectra in the m/z 870–950 range obtained for the $ZrCl_4$ /benzoic acid system at different very acidic pH conditions (0, 0.5 and 0.8). All spectra show two major signals centered at m/z 884 and 927 with a 0.5 spacing of the peaks indicative of 2+ charge states for both species. No species with charge greater than 2+ have been observed. The assigned molecular formula for the heavier signal is chemically sound and agrees well with the $[Zr_6(O)_4(OH)_4]$ core features of the ubiquitous zirconium based hexameric SBU. However, the benzoate anions only partially occupy the peripheral positions around this core in such a way that the number of carboxylate groups attached to the cluster is reduced from the expected 12 (the well-known $[Zr_6(O)_4(OH)_4(OOC)_{12}]$ SBU found in many MOFs) to 8 providing a carboxylate-

²³⁶ (a) Ji, B. Q.; Su, H. F.; Jagodič, M.; Jagličić, Z.; Kurmoo, M.; Wang, X. P.; Tung, C. H.; Cao, Z. Z.; Sun, D. *Inorg. Chem.* **2019**, 58 (6), 3800–3806. (b) Deng, Y. K.; Su, H. F.; Xu, J. H.; Wang, W. G.; Kurmoo, M.; Lin, S. C.; Tan, Y. Z.; Jia, J.; Sun, D.; Zheng, L. S. *J. Am. Chem. Soc.* **2016**, 138 (4), 1328–1334. (c) Hu, Y. Q.; Zeng, M. H.; Zhang, K.; Hu, S.; Zhou, F. F.; Kurmoo, M. *J. Am. Chem. Soc.* **2013**, 135 (21), 7901–7908. (d) Wang, Z.; Zhuo, H. Y.; Hu, A. Y.; Su, H. F.; Zhao, Q. Q.; Wang, X. P.; Tung, C. H.; Sun, D. *Isr. J. Chem.* **2019**, 59 (3), 280–285.

unsaturated entity. This hexameric unsaturated species incorporates two additional hydroxide anions to provide the observed 2+ charge state and solvent molecules complete the coordination sphere of the cluster.

Similarly, the signal centered at 884 has been assigned to a pentameric zirconium entity with 2+ charge in which twelve solvent molecules, four benzoate ligands and four chlorides stabilize a $[\text{Zr}_5(\text{O})_2(\text{OH})_6]$ core. Interestingly, the signals assigned to the hexameric and pentameric species show important modifications in their relative intensities as a function of the pH. The addition of water and subsequent dilution driven mild basification of the media results in a relative decrease of the intensity for the signal belonging to the pentameric species, whereas that related to the hexameric species increases considerably. This fact can be interpreted as an acid-base equilibrium between the two polynuclear species according to the chemical reaction provided in the Scheme 4.1.



Scheme 4.1. Acid-base equilibrium governing the transformation between pentameric and hexameric species.

The formula obtained for the pentameric species seems to be closely related to that of the hexameric cluster by releasing one zirconium atom and losing four benzoate ligands, and at the same time, reducing the amount of oxides and increasing the hydroxide amount to keep invariable the total amount of core bridging oxide/hydroxide ligands at eight. Thus there is a probable connection between the zirconium oxide/hydroxide species that can be rationalized starting with the well-known $[\text{Zr}_4(\text{OH})_8(\text{solv})_{16}]^{8+}$ tetrameric entity,²³⁷ usually employed as commercial reagent in the form of its chloride salt,²³⁸ that in the presence of carboxylic ligands evolves to a pentanuclear $[\text{Zr}_5(\text{O})_2(\text{OH})_6(\text{OOC})_4(\text{solv})]^{6+}$ species. The greater polarization effect of the fifth zirconium(IV) center promotes the deprotonation of two of the hydroxides to provide a two oxide/six hydroxide core. Upon basification, these pentanuclear entities evolve into hexanuclear $[\text{Zr}_6(\text{O})_4(\text{OH})_4(\text{OOC})_8(\text{H}_2\text{O})]^{4+}$ species by the incorporation of a sixth zirconium that again increases the polarization at the hydroxide anions leading to a final four oxide/four hydroxide core. Further pH increases, favoring the deprotonation of the

²³⁷ Rao, N.; Holerca, M. N.; Klein, M. L.; Pophristic, V. *J. Phys. Chem. A* **2007**, *111* (45), 11395–11399.

²³⁸ Clearfield, A.; Vaughan, P. A. *Acta Crystallogr.* **1956**, *9* (7), 555–558.

carboxylic ligands, would probably lead to the neutral $[\text{Zr}_6(\text{O})_4(\text{OH})_4(\text{OOC})_{12}]$ cluster found as SBU in most of the zirconium based MOFs. Figure 4.21 shows the comparison between the experimental and theoretical formulas attributed to the signals found in a basified sample at a pH value of 0.8, Table 4.20.

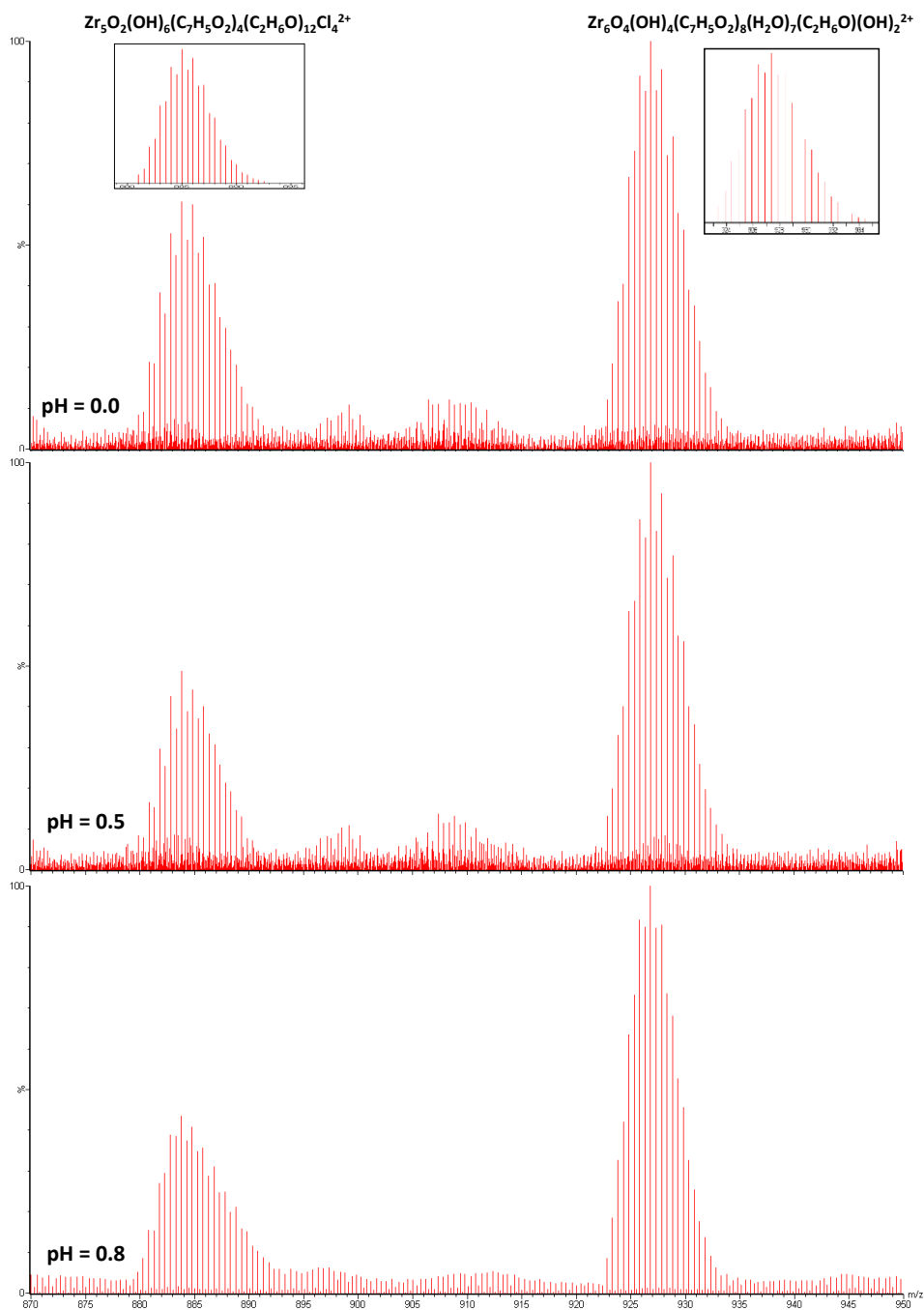


Figure 4.20. Influence of the pH in the ESI+-MS spectra signals of ZrCl₄/benzoic acid system. Signals belonging to pentameric and hexameric zirconium species are identified in the *m/z*: 870–950 range.

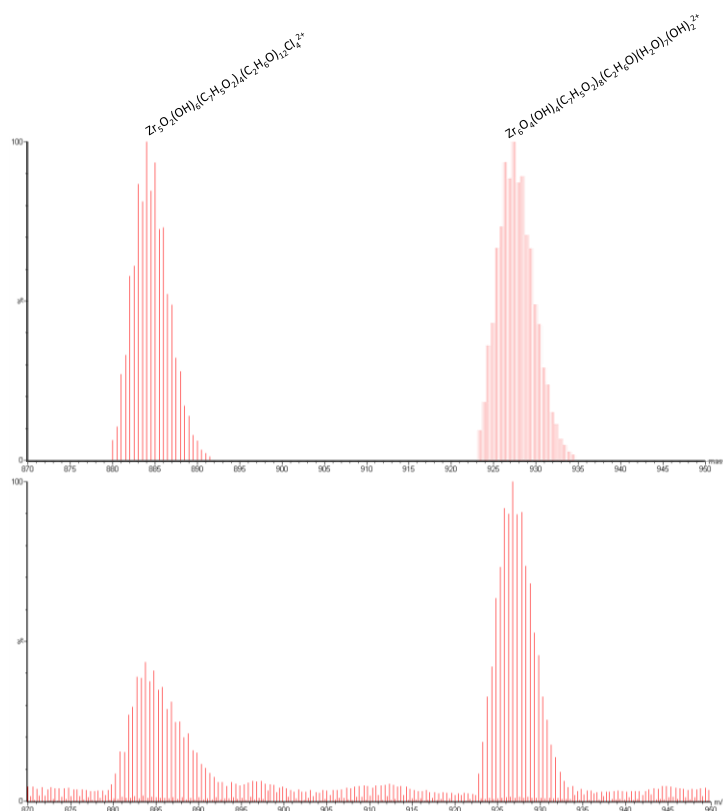


Figure 4.21. Comparison of the experimental and simulated isotopic patterns for the pentameric/hexameric species in the ESI(+)-MS spectrum of the ZrCl₄/benzoato system in water/ethanol mixtures at pH = +0.8.

Table 4.20. Comparison of the experimental and simulated isotopic patterns for the pentameric/hexameric species in the ESI(+)-MS spectrum of the ZrCl₄/benzoato system in water/ethanol mixtures at different pH values.^a

EXPERIMENTAL		SIMULATED		
(m/z) _{max}	Δ _{m/z} [*]	(m/z) _{max}	Δ _{m/z} [*]	Formula
883.84	881.84–887.34	884.01	882.01–887.01	Zr ₅ O ₂ (OH) ₆ (C ₇ H ₅ O ₃) ₄ (C ₂ H ₆ O) ₁₂ Cl ₄ ²⁺
926.86	924.36–929.87	926.89	924.39–929.39	Zr ₆ O ₄ (OH) ₄ (C ₇ H ₅ O ₂) ₈ (H ₂ O) ₇ (C ₂ H ₆ O)(OH) ₂ ²⁺

^aWidth at half height with respect to the maximum peak of the species isotopic distribution pattern (measured as the peak closest to that value).

The same studies performed using 2- and 3-hydroxybenzoic acid provided similar outcomes but with the presence of a greater dispersion of the pentameric and hexameric species due to variations on the solvent molecules (water and ethanol that interchange between them). In the case of the ZrCl₄ and 2-hydroxybenzoic (Figure 4.22 and 4.23; Table 4.21 and 4.22) or 3-hydroxybenzoic acids, at low pH values we find a huge noisy spectral background, with signals associated to pentameric species, together with low intensity signals in the higher m/z region that correspond to hexameric entities. The m/z spacing of the signals indicates a 2+ charge for all the species found in solution. As the

pH value is increased, through the dropwise addition of water, we can observe how the main signals corresponding to pentameric species decrease in intensity, the background noise disappears and the signals belonging to hexameric species begin to acquire a greater intensity, as observed in the images below.

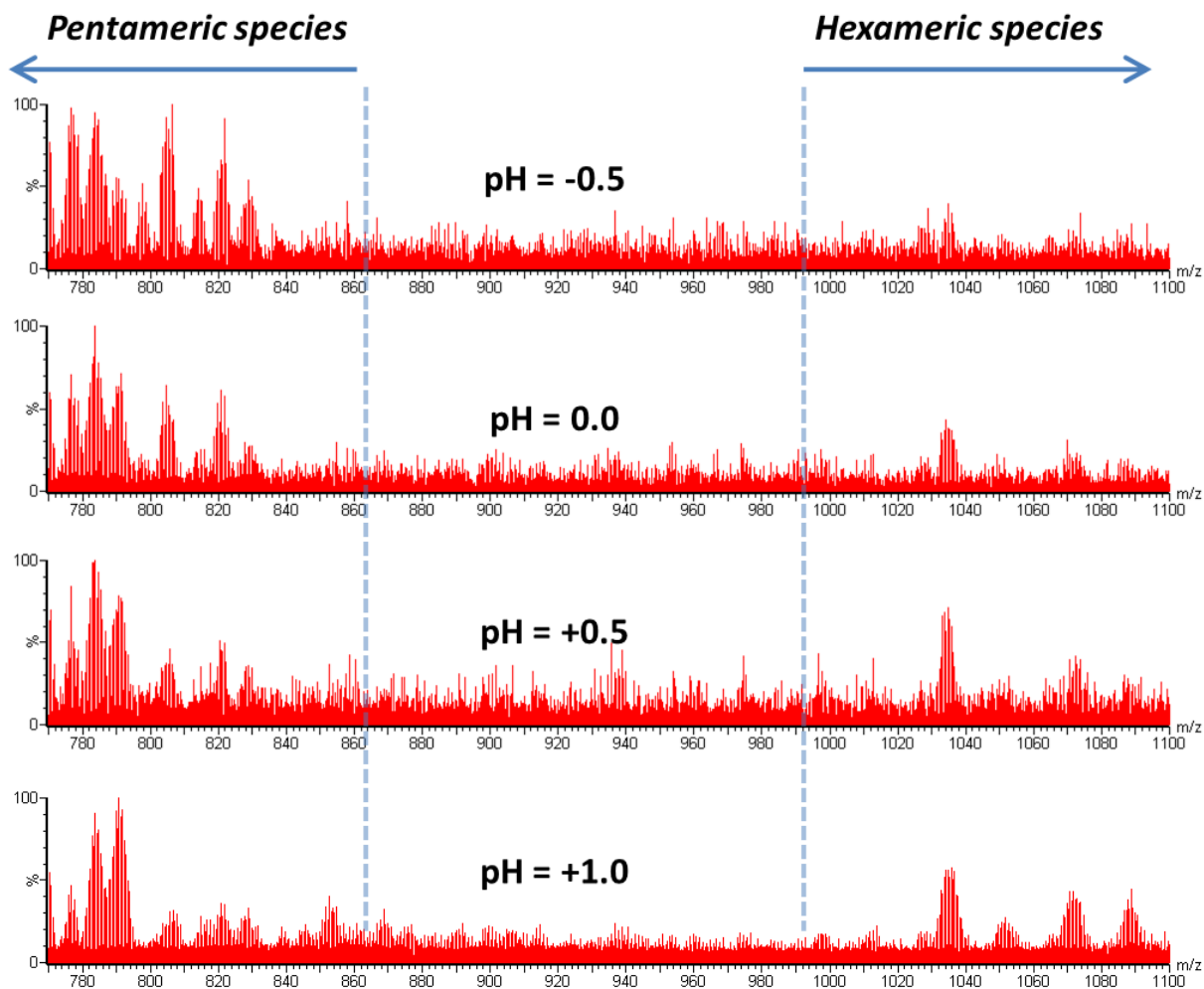
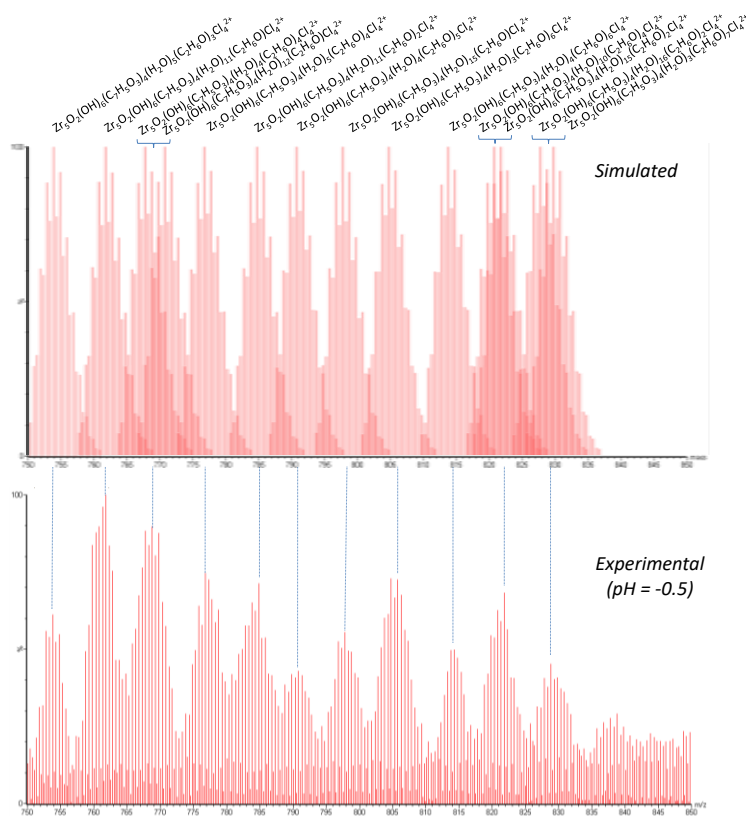
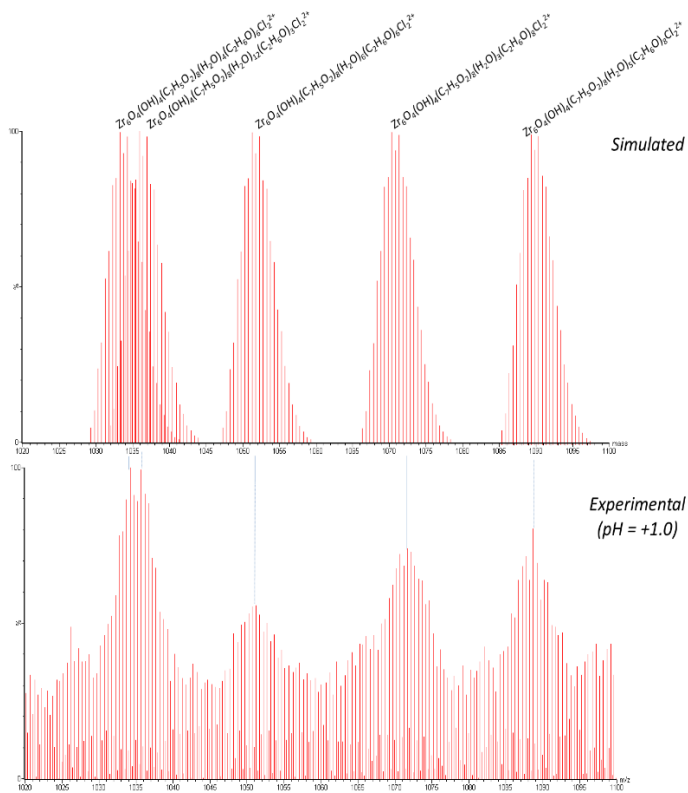


Figure 4.22. Comparison of the different mass spectra obtained for the ZrCl₄/2-hydroxybenzoic acid system in water/ethanol mixtures at different acidic pH values.



(a)



(b)

Figure 4.23. Comparison of the experimental and simulated isotopic patterns for the pentameric and hexameric species of the ZrCl₄/2-hydroxybenzoic acid system at pH (a) -0.5 and (b) 1.0.

Table 4.21. Comparison of the experimental and simulated isotopic patterns for the hexameric species in the ESI(+)-MS spectrum of the ZrCl₄/2-hydroxybenzoic acid system in water/ethanol mixtures at pH = -0.5.^a

EXPERIMENTAL		SIMULATED		
(m/z) _{max}	Δ _{m/z} [*]	(m/z) _{max}	Δ _{m/z} [*]	Formula
753.79	751.80–755.79	753.84	751.84–755.84	Zr ₅ O ₂ (OH) ₆ (C ₇ H ₅ O ₃) ₄ (H ₂ O) ₅ (C ₂ H ₆ O) ₃ Cl ₄ ²⁺
761.79	758.79–763.80	761.83	759.83–763.82	Zr ₅ O ₂ (OH) ₆ (C ₇ H ₅ O ₃) ₄ (H ₂ O) ₁₁ (C ₂ H ₆ O)Cl ₄ ²⁺
768.80	765.81–770.80	767.86	765.86–769.86	Zr ₅ O ₂ (OH) ₆ (C ₇ H ₅ O ₃) ₄ (H ₂ O) ₄ (C ₂ H ₆ O) ₄ Cl ₄ ²⁺
		770.83	768.83–772.83	Zr ₅ O ₂ (OH) ₆ (C ₇ H ₅ O ₃) ₄ (H ₂ O) ₁₂ (C ₂ H ₆ O)Cl ₄ ²⁺
776.81	774.82–779.82	776.86	774.86–779.86	Zr ₅ O ₂ (OH) ₆ (C ₇ H ₅ O ₃) ₄ (H ₂ O) ₅ (C ₂ H ₆ O) ₄ Cl ₄ ²⁺
784.82	780.82–786.82	784.85	780.32–787.82	Zr ₅ O ₂ (OH) ₆ (C ₇ H ₅ O ₃) ₄ (H ₂ O) ₁₁ (C ₂ H ₆ O) ₂ Cl ₄ ²⁺
790.83	overlapping–792.83	790.88	788.88–793.88	Zr ₅ O ₂ (OH) ₆ (C ₇ H ₅ O ₃) ₄ (H ₂ O) ₄ (C ₂ H ₆ O) ₅ Cl ₄ ²⁺
797.78	795.77–800.79	797.85	795.85–800.85	Zr ₅ O ₂ (OH) ₆ (C ₇ H ₅ O ₃) ₄ (H ₂ O) ₁₅ (C ₂ H ₆ O)Cl ₄ ²⁺
804.79	802.79–807.79	804.89	802.89–807.89	Zr ₅ O ₂ (OH) ₆ (C ₇ H ₅ O ₃) ₄ (H ₂ O) ₃ (C ₂ H ₆ O) ₆ Cl ₄ ²⁺
813.79	811.79–816.75	813.90	811.90–816.90	Zr ₅ O ₂ (OH) ₆ (C ₇ H ₅ O ₃) ₄ (H ₂ O) ₄ (C ₂ H ₆ O) ₆ Cl ₄ ²⁺
820.81/821.81	818.80–823.30	820.87	818.87–823.87	Zr ₅ O ₂ (OH) ₆ (C ₇ H ₅ O ₃) ₄ (H ₂ O) ₁₅ (C ₂ H ₆ O) ₂ Cl ₄ ²⁺
		821.89	819.89–824.89	Zr ₅ O ₂ (OH) ₆ (C ₇ H ₅ O ₃) ₄ (H ₂ O) ₁₀ (C ₂ H ₆ O) ₄ Cl ₄ ²⁺
828.82	825.82 – 831.31	827.91	825.91–830.91	Zr ₅ O ₂ (OH) ₆ (C ₇ H ₅ O ₃) ₄ (H ₂ O) ₃ (C ₂ H ₆ O) ₇ Cl ₄ ²⁺
		829.88	827.88–832.88	Zr ₅ O ₂ (OH) ₆ (C ₇ H ₅ O ₃) ₄ (H ₂ O) ₁₆ (C ₂ H ₆ O) ₂ Cl ₄ ²⁺

^aWidth at half height with respect to the maximum peak of the species isotopic distribution pattern.

Table 4.22. Comparison of the experimental and simulated isotopic patterns for the hexameric species in the ESI(+)-MS spectrum of the $\text{ZrCl}_4/2$ -hydroxybenzoic acid system in water/ethanol mixtures at pH = 1.0

EXPERIMENTAL		SIMULATED		
$(m/z)_{\text{max}}$	$\Delta_{m/z}^*$	$(m/z)_{\text{max}}$	$\Delta_{m/z}^*$	Formula
1035.71	1030.72–1037.71	1032.86	1030.86–1035.86	$\text{Zr}_6\text{O}_4(\text{OH})_4(\text{C}_7\text{H}_5\text{O}_3)_8(\text{H}_2\text{O})_2(\text{C}_2\text{H}_6\text{O})_4\text{Cl}_2^{2+}$
		1035.84	1033.84–1038.84	$\text{Zr}_6\text{O}_4(\text{OH})_4(\text{C}_7\text{H}_5\text{O}_3)_8(\text{H}_2\text{O})_9(\text{C}_2\text{H}_6\text{O})_2\text{Cl}_2^{2+}$
1051.22	1048.23–1055.63	1049.86	1047.86–1052.86	$\text{Zr}_6\text{O}_4(\text{OH})_4(\text{C}_7\text{H}_5\text{O}_3)_8(\text{H}_2\text{O})_{10}(\text{C}_2\text{H}_6\text{O})\text{Cl}_2^{2+}$
		1050.88	1048.88–1053.88	$\text{Zr}_6\text{O}_4(\text{OH})_4(\text{C}_7\text{H}_5\text{O}_3)_8(\text{H}_2\text{O})_4(\text{C}_2\text{H}_6\text{O})_4\text{Cl}_2^{2+}$
1071.71	1068.21–1074.66	1071.86	1069.86–1074.87	$\text{Zr}_6\text{O}_4(\text{OH})_4(\text{C}_7\text{H}_5\text{O}_3)_8(\text{H}_2\text{O})_{14}(\text{C}_2\text{H}_6\text{O})\text{Cl}_2^{2+}$
1087.72/1088.71	1085.72–1090.67	1087.91/1088.92	1085.92–1090.91	$\text{Zr}_6\text{O}_4(\text{OH})_4(\text{C}_7\text{H}_5\text{O}_3)_8(\text{H}_2\text{O})_3(\text{C}_2\text{H}_6\text{O})_6\text{Cl}_2^{2+}$

*Width at half height with respect to the maximum peak of the species isotopic distribution pattern (measured as the peak closest to that value).

It is worth mentioning that in the case of 3-hydroxybenzoato ligand signals associated with hexameric species do not begin to have notoriety until pH increase its value from $\text{pH} < 0$ to $\text{pH} \approx 1.5$, (Figure 4.24, 4.25; Table 4.23).

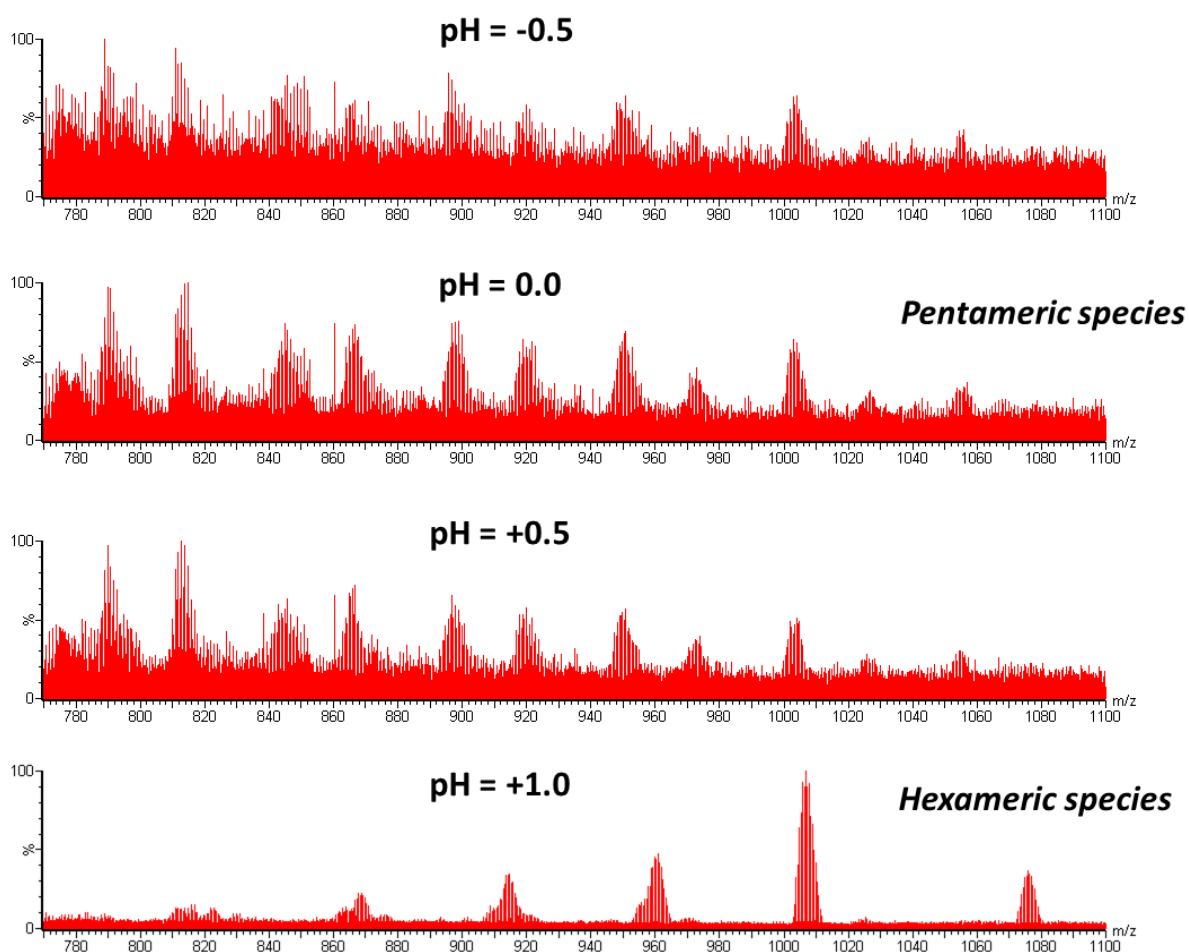
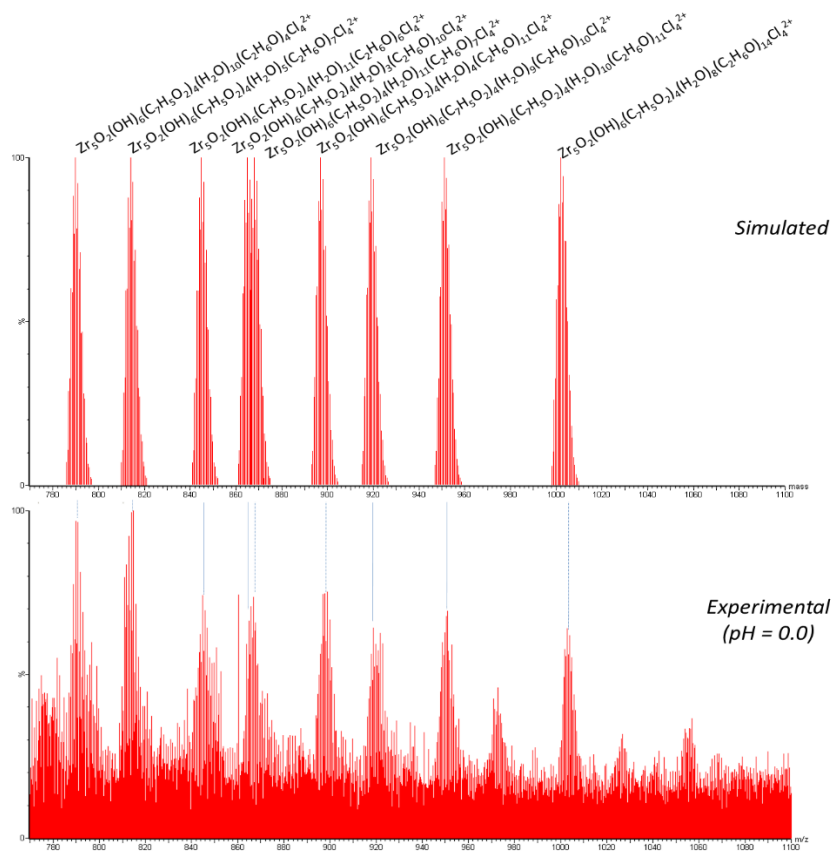
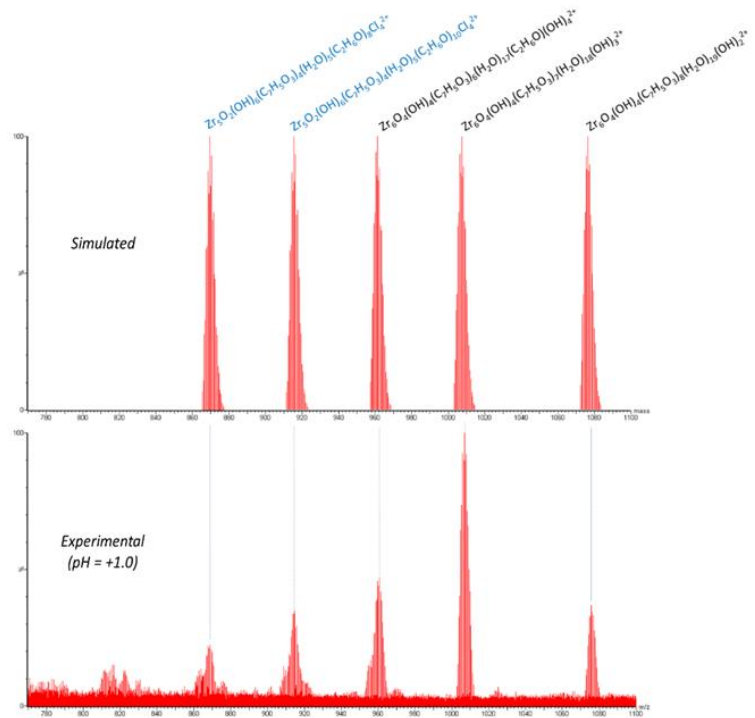


Figure 4.24. Comparison of the different mass spectra obtained for the $\text{ZrCl}_4/3$ -hydroxybenzoic acid system in water/ethanol mixtures at different very acidic pH values.



(a)



(b)

Figure 4.25. Comparison of the experimental and simulated isotopic patterns for the pentameric and hexameric species of the $ZrCl_4/3$ -hydroxybenzoic acid system at pH (a) 0.0 and (b) 1.0

Table 4.23. Comparison of the experimental and simulated isotopic patterns for the hexameric species in the ESI(+)-MS spectrum of the ZrCl₄/3-hydroxybenzoic acid system in water/ethanol mixtures at pH = 0.0 and 1.0

EXPERIMENTAL		SIMULATED		
(m/z) _{max}	$\Delta_{m/z}^*$	(m/z) _{max}	$\Delta_{m/z}^*$	Formula
790.83	787.83–794.82	790.87	788.37–793.37	Zr ₅ O ₂ (OH) ₆ (C ₇ H ₅ O ₃) ₄ (H ₂ O) ₄ (C ₂ H ₆ O) ₅ Cl ₄ ²⁺
813.85	810.87–816.82	813.89	811.39–816.39	Zr ₅ O ₂ (OH) ₆ (C ₇ H ₅ O ₃) ₄ (H ₂ O) ₄ (C ₂ H ₆ O) ₆ Cl ₄ ²⁺
844.82	841.84–847.83	844.91	842.90–847.40	Zr ₅ O ₂ (OH) ₆ (C ₇ H ₅ O ₃) ₄ (H ₂ O) ₁₀ (C ₂ H ₆ O) ₅ Cl ₄ ²⁺
866.86	863.39–869.33	866.91	864.91–869.91	Zr ₅ O ₂ (OH) ₆ (C ₇ H ₅ O ₃) ₄ (H ₂ O) ₁₅ (C ₂ H ₆ O) ₄ Cl ₄ ²⁺
897.83	894.34–899.82	897.92	894.47–899.97	Zr ₅ O ₂ (OH) ₆ (C ₇ H ₅ O ₃) ₄ (H ₂ O) ₂₁ (C ₂ H ₆ O) ₃ Cl ₄ ²⁺
918.85	916.38–924.81	918.98	916.98–921.48	Zr ₅ O ₂ (OH) ₆ (C ₇ H ₅ O ₃) ₄ (H ₂ O) ₈ (C ₂ H ₆ O) ₉ Cl ₄ ²⁺
950.83	946.86–953.81	951.01	949.01–954.01	Zr ₅ O ₂ (OH) ₆ (C ₇ H ₅ O ₃) ₄ (H ₂ O) ₉ (C ₂ H ₆ O) ₁₀ Cl ₄ ²⁺
972.86	969.88–976.81	973.01	970.01–975.51	Zr ₅ O ₂ (OH) ₆ (C ₇ H ₅ O ₃) ₄ (H ₂ O) ₁₄ (C ₂ H ₆ O) ₉ Cl ₄ ²⁺
1002.85	1000.37–1006.83	1003.07	1001.07–1006.07	Zr ₅ O ₂ (OH) ₆ (C ₇ H ₅ O ₃) ₄ (H ₂ O) ₂ (C ₂ H ₆ O) ₁₅ Cl ₄ ²⁺
pH = 1.0				
868.78	866.27–870.78	868.94	866.94–871.44	Zr ₅ O ₂ (OH) ₆ (C ₇ H ₅ O ₃) ₄ (H ₂ O) ₅ (C ₂ H ₆ O) ₈ Cl ₄ ²⁺
914.79	911.79–916.79	914.98	912.98–917.48	Zr ₅ O ₂ (OH) ₆ (C ₇ H ₅ O ₃) ₄ (H ₂ O) ₅ (C ₂ H ₆ O) ₁₀ Cl ₄ ²⁺
960.81	958.30–962.81	960.90	958.40–963.40	Zr ₆ O ₄ (OH) ₄ (C ₇ H ₅ O ₃) ₆ (H ₂ O) ₁₇ (C ₂ H ₆ O)(OH) ₄ ²⁺
1006.83	1004.33–1009.33	1006.89	1004.39–1009.39	Zr ₆ O ₄ (OH) ₄ (C ₇ H ₅ O ₃) ₇ (H ₂ O) ₁₈ (OH) ₃ ²⁺
1075.84	1073.34–1078.34	1075.91	1073.41–1078.41	Zr ₆ O ₄ (OH) ₄ (C ₇ H ₅ O ₃) ₈ (H ₂ O) ₁₉ (OH) ₂ ²⁺

*Width at half height with respect to the maximum peak of the species isotopic distribution pattern.

4.4.3. Conclusions

In summary, in this chapter it is shown that there is plenty of chemistry still to be discovered about the first stages of the zirconium-carboxylate cluster formation. The results rendered herein must be understood as frozen images along this process but also reveal the opportunities that arise from a fine control of the synthetic conditions. In fact, among the intermediate species that can be found in the formation of Zr-carboxylate clusters, a structure in which the 12 carboxylato ligands bridge the 12 Zr–Zr edges is the lowest in energy according to quantum mechanical calculations.²³⁹ However, this report does not take into account the specific synthetic conditions at which these entities grow. This work confirms that small modifications of the pH of the media can considerably affect in the isolation of clusters with different nuclearity and carboxylate-ligand content. In addition, species with unsaturated carboxylate and/or metal positions can be a starting point to develop a richer chemistry by completing those vacancies with different carboxylic ligands or metal centers.²⁴⁰

Once the system was understood, it was tested with other types of carboxylates widely used in MOF/SMOF chemistry, such as amino acids. Amino acids with a carboxylate group (–COOH) and an amino group (–NH₂) in each part of their chain are compounds that can generate very interesting supramolecular chemistry thanks to their structural diversity. The possibility of being able to use their D or L stereoisomer may give rise to the chance of using them for chiral catalysis or separation. In this way, three new compounds have been synthesized with this type of ligand, generating chiral SMOFs.

Bearing all this in mind and once the synthesis and knowledge of the zirconium-carboxylate system was well controlled amino acids were chosen as terminal ligands to provide additional hydrogen bonds that could improve the stability of those compounds. These compounds are organic molecules that we find in our body mostly in the L-enantiomeric form, except in the case of glycine, which only has one of them, since it does not present a quaternary carbon that provides the chiral characteristic as it does in the other cases. The chirality of these compounds is very important in many areas such as in biology catalytic activity, chiral separation, etc. This just started new line has

²³⁹ Whalter, P.; Puchberger, M.; Kogler, F. R.; Schwarz, K.; Schubert, U. *Phys. Chem. Chem. Phys.* **2009**, *11* (19), 3640–3647.

²⁴⁰ Ma Ntep, T. J. M.; Reinsch, H.; Moll, B.; Hastürk, E.; Gökpınar, S.; Breitzke, H.; Schlüsener, C.; Schmolke, L.; Buntkowsky, G.; Janiak, C. *Chem. - A Eur. J.* **2018**, *24* (53), 14048–14053.

allowed obtaining the analogous hexameric entities of the amino acids alanine and tryptophan (L and D), Figure 4.26, Table 4.24.

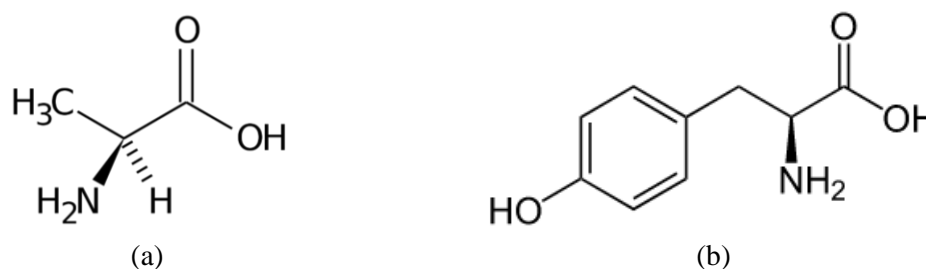


Figure 4.26. Scheme of the aminoacids employed (a) alanine and (b) tryptophan.

Table 4.24. Crystallographic data and refinement details of ZR6LALA, ZR6LTIR and ZR6DTIR.

	ZR6LALA	ZR6LTIR	ZR6DTIR
empirical formula	C ₂₄ H ₁₂₆ Cl ₁₂ N ₈ O ₅₇ Zr ₆	C ₇₂ H ₁₆₂ Cl ₁₂ N ₈ O ₆₇ Zr ₆	C ₇₂ H ₁₅₈ Cl ₁₂ N ₈ O ₆₅ Zr ₆
formula weight	2412.04	3184.81	3148.77
crystal system	Orthorhombic	Orthorhombic	Orthorhombic
space group	<i>I</i> 222 (23)	<i>P</i> 2 ₁ 2 ₁ 2 (18)	<i>P</i> 2 ₁ 2 ₁ 2 (18)
<i>a</i>	18.7285(2)	28.2023(4)	28.1804(2)
<i>b</i>	15.0456(1)	26.0318(5)	26.0321(2)
<i>c</i>	16.9428(2)	17.6891(3)	17.6857(2)
α	90	90	90
β	90	90	90
γ	90	90	90
<i>V</i> (Å ³)	4774.2(8)	12986.6(4)	12974.1(2)
<i>Z</i>	2	4	4
<i>T</i> (K)	150.01(10)	150.00(4)	150.0(10)
λ (Å)	1.54184	1.54184	0.71073
Sizes (mm)	0.10, 0.05, 0.03	0.09, 0.08, 0.03	0.10, 0.02, 0.02
Shape	Plate	Square	Plate
Colour	Colourless	colourless	Colourless
Max. and medium Δ/σ	0.000 / 0.000	0.001 / 0.000	0.001 / 0.000
θ interval (°)	3.518 – 74.342	1.642 – 27.423	1.723 – 27.393
hkl interval	-23 ≤ h ≤ 15; -18 ≤ k ≤ 17 -20 ≤ l ≤ 21	-36 ≤ h ≤ 36; -32 ≤ k ≤ 32 -22 ≤ l ≤ 22	-36 ≤ h ≤ 25; -33 ≤ k ≤ 31; -20 ≤ l ≤ 21;
ρ_c (g·cm ⁻³)	1.678	1.629	1.612
μ (cm ⁻¹)	9.117	0.808	0.806
<i>F</i> (000)	2452	6520	6440
<i>S</i> ^a	1.058	1.041	1.043
<i>R</i> _{int}	0.0579	0.0994	0.0455
Parameters	199	1469	1445
Flack	0.025(1)	-0.11(2)	-0.013(1)
Weight sheme ^c	Shelx	Shelx	Shelx
final <i>R</i> indices			
[<i>I</i> > 2 σ (<i>I</i>)] <i>R</i> ₁ ^b / <i>wR</i> ₂ ^c	0.0517 / 0.1401	0.0651 / 0.1359	0.0500 / 0.1250
all data <i>R</i> ₁ ^b / <i>wR</i> ₂ ^c	0.0526 / 0.1415	0.1000 / 0.1584	0.0633 / 0.1342

^a*S* = $[\sum w(F_o^2 - F_c^2)^2 / (N_{\text{obs}} - N_{\text{param}})]^{1/2}$. ^b*R*₁ = $\sum ||F_o| - |F_c|| / \sum |F_o|$. ^c*wR*₂ = $[\sum w(F_o^2 - F_c^2)^2 / \sum wF_o^2]^{1/2}$; $w = 1/[\sigma^2(F_o^2) + (aP)^2 + b]$ where $P = (\max(F_o^2, 0) + 2F_c^2)/3$; **ZR6LALA** (*a* = 0.0872, *b* = 20.4590); **ZR6LTIR** (*a* = 0.0572, *b* = 0) and **ZR6DTIR** (*a* = 0.0669, *b* = 26.0490).

For the synthesis of these three compounds, a solution of 0.3870 g (1.66 mmol) of ZrCl₄ dissolved in 4.8/0.2 mL of an ethanol/water solution was added dropwise to an 8 and 5 mL ethanol/water solution containing 0.2228 and 0.4513 g (2.50 mmol) of the aminoacid ligand respectively. The resulting colourless solution was basified dropwise

with water until pH= -1. Reaction mixtures were left to evaporate at room temperature in large test tube slowing the evaporation process and colourless single-crystals appeared after 5 days.

The cluster present in the three compounds described below contains the hexameric cluster $[\text{Zr}_6(\text{OH})_4(\text{O})_4(\text{COOR}^+)_8]^{12+}$. The positive charge of the cations is balanced by chloride anions giving rise the formulas $[\text{Zr}_6(\text{OH})_4\text{O}_4(\text{H}_2\text{O})_8(\text{C}_3\text{H}_7\text{NO}_2)_8]\text{Cl}_{12} \cdot 25\text{H}_2\text{O}$, $[\text{Zr}_6(\text{OH})_4\text{O}_4(\text{H}_2\text{O})_8(\text{C}_9\text{H}_{11}\text{NO}_3)_8]\text{Cl}_{12} \cdot 27\text{H}_2\text{O}$ and $[\text{Zr}_6(\text{OH})_4\text{O}_4(\text{H}_2\text{O})_8(\text{C}_9\text{H}_{11}\text{NO}_3)_8]\text{Cl}_{12} \cdot 25\text{H}_2\text{O}$, respectively. In all cases, the amino acids, due to the highly acidic conditions of synthesis, are protonated in the amino position of the ligand, going from the previous amount of 4+ to 12+, as can be seen in Figures 4.27 and 4.28.

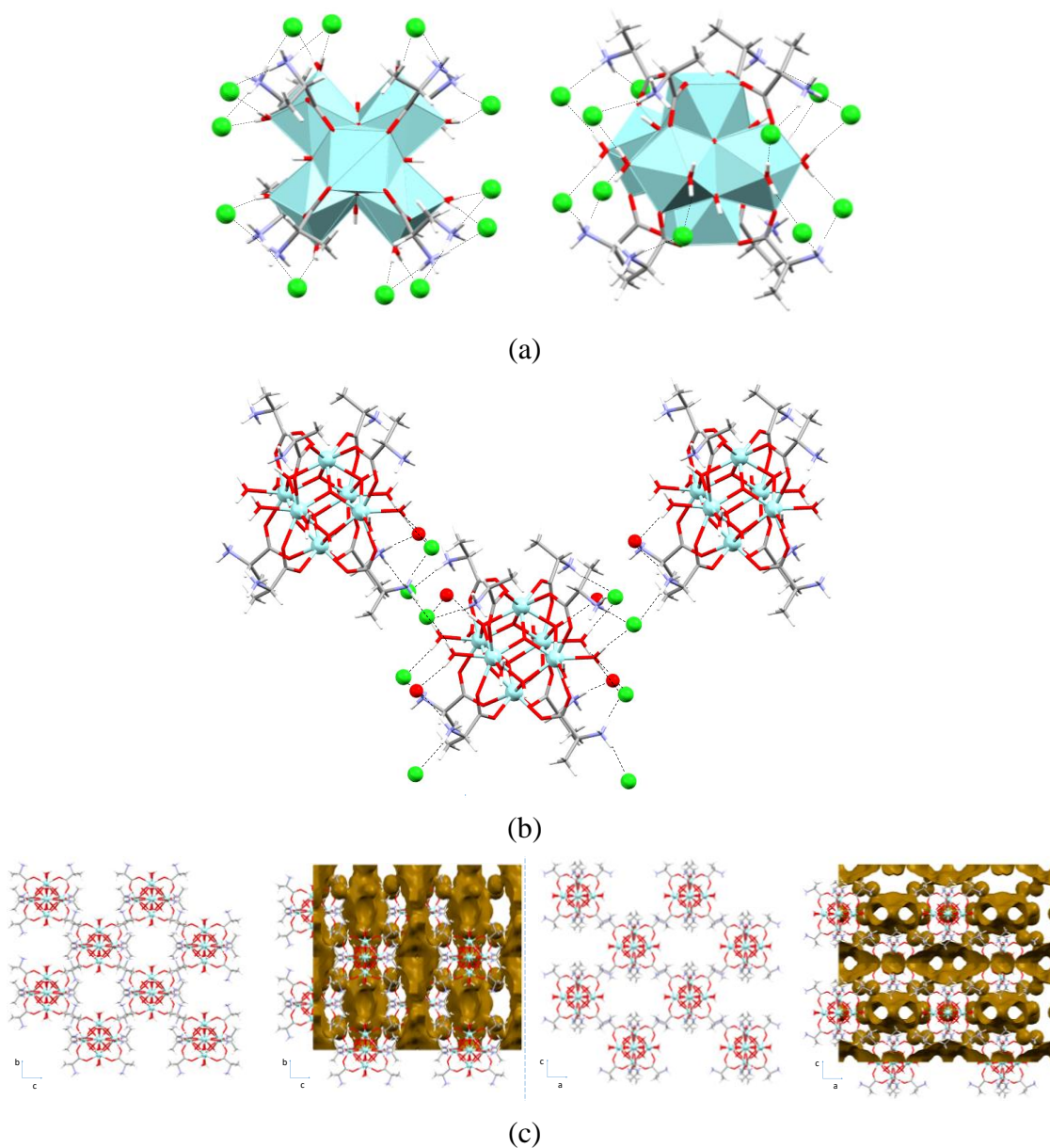


Figure 4.27. Supramolecular interactions and crystal packing of ZR6LALA

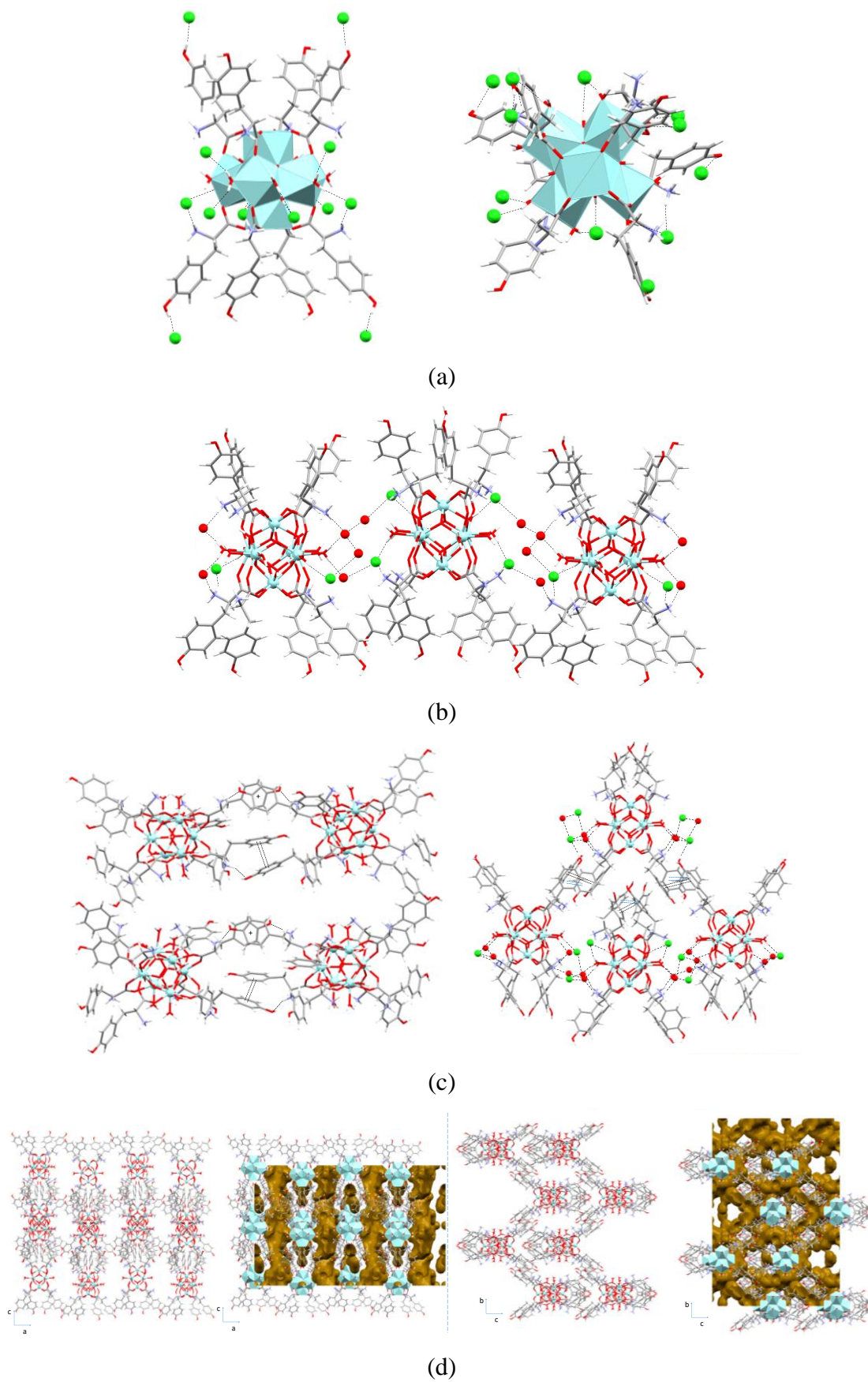


Figure 4.28. (a, b, c) Supramolecular interactions and (d) crystal packing of ZR6DTIR and ZR6LTIR.

4.4.4. Further applications

It is worth mentioning that the results obtained here reveal that in spite of the cationic nature of the zirconium clusters reported herein, their chemistry shows some resemblance with that of the anionic polyoxometalates (POMs), as the acidity of the media is also here a key factor in the final nuclearities of the resulting clusters.²⁴¹ However, differences arise from the fact that the oxidation state of the zirconium cation is not as high as those displayed by the typical metals in POMs (mainly V, Mo and W). This implies that the polarizing capability of zirconium is not that high and it cannot promote the complete deprotonation of all the coordinated water molecules to afford an oxide rich environment able to stabilize these metal ions. Instead of that, the formation of zirconium based entities with higher nuclearities than the classical $[\text{Zr}_4(\text{OH})_8(\text{H}_2\text{O})_{16}]^{8+}$ cation will require the presence of coordinated carboxylate groups bridging and holding together the metal centers.

This study has given rise to a new line of research where these clusters have been used to obtain a new compound, with a very similar synthesis procedure with POM as counterion of the structure. The presence of this large volume anion stabilizes the system, generating a balanced structure by incorporating a 4- charged POM. The combination of the before described ZR6BZ cluster and a Keggin type polyoxotungstate into a compound of formula $[\text{Zr}_6(\mu_3\text{-O})_4(\mu_3\text{-OH})_4(\mu\text{-OOC}\text{C}_6\text{H}_5)_8(\text{H}_2\text{O})_8][\text{SiW}_{12}\text{O}_{40}]$ named Zr₆/W₁₂ led to a chemically and photochemically stable porous material in which a synergistic effect allows to markedly overpass the photochemical activity of the single ionic components toward the photooxidation of a dye. During the last few years, zirconium based metal-organic frameworks (MOFs) have been intensively explored as heterogeneous photocatalysts due to both the ad-hoc setting of the surface chemistry and the proficient chemical stability provided by Zr–O bonds. Nonetheless, the adequate selection of the counterion can amend such drawbacks. In this sense, polyoxometalates (POMs) constitute a fine solution since their size is comparable to that of zirconium clusters and their anionic charge is relatively high, so the combination of both type of entities can yield highly insoluble and stable ionic molecular compounds. Furthermore, POMs have a recognized catalytic and photocatalytic activity²⁴² so they can potentially act as co-catalyst and boost the overall performance. In fact, there are many examples in the literature where the

²⁴¹ Gumerova, N. I.; Rompel, A. *Chem. Soc. Rev.* **2020**, *49* (21), 7568–7601.

²⁴² Streb, C.; Kastner, K.; Tucher, J. *Phys. Sci. Rev.* **2019**, *4* (6), 1–10.

incorporation of POMs inside the pores of MOFs has increased the catalytic performance of the latter.²⁴³ Last but not least, the packing of such macro-ionic entities is expected to render a meaningful amount of void volume or pores in the crystal structure,²⁴⁴ which might increase the surface area of the catalyst.

The crystal structure of Zr_6/W_{12} (Figure 4.29) resembles a NaCl type packing of ions, in which each molecular building unit is surrounded by six counterions. However, the distance between the centroids of the ionic entities is different depending on their relative disposition. Expressly, the approach of the POM along the axial position of the Zr_6 -cluster is hindered by the phenyl rings and it leads to centroid...centroid distances of 13.7–14.8 Å. In contrast, the equatorial edge of the Zr_6 -cluster allows the POM to get closer (10.6–11.2 Å), and thus, it favours the formation of hydrogen bonds involving the coordination water molecules and the oxide anions of the POM surface ($Ow-H\cdots O_{POM}$: 2.68–3.21 Å, 145–170°). This hydrogen bonding scheme gives rise to a binodal 2D square lattice (**sql**) in which each ionic entity is linked to four counterions.

This kind of compounds can exhibit semiconductor-like behaviour, in such a way that when the material is irradiated with a photon of energy equal to or higher than the HOMO/LUMO energy difference, the photogenerated holes and electrons have oxidizing and reducing capabilities.²⁴⁵ Among the different potential applications, their use as photocatalysts for the oxidation of organic substrates is of remarkable interest in the area of advanced oxidation processes, including degradation of pollutants and waste treatment.²⁴⁶ In this regard, the assessment of the degradation of a dye provides a suitable tool to evaluate the photocatalytic performance of a given material. Therefore, it has been explored with good results the capability of the nanoparticulated compound to photodegrade methylene blue and compared it with the performance provided by referential insoluble forms of $[Zr_6O_4(OH)_4(\text{benzene-1,4-dicarboxylato})_6]_n$ and $Cs_{3.5}H_{0.5}[SiW_{12}O_{40}]$ (UiO-66 and Cs/W₁₂, respectively).²⁴⁷

²⁴³ (a) Mialane, P.; Mellot-Draznieks, C.; Gairola, P.; Duguet, M.; Benseghir, Y.; Oms, O.; Dolbecq, A. *Chem. Soc. Rev.* **2021**, *50* (10), 6152–6220. (b) Liu, Y.; Tang, C.; Cheng, M.; Chen, M.; Chen, S.; Lei, L.; Chen, Y.; Yi, H.; Fu, Y.; Li, L. *ACS Catal.* **2021**, *11* (21), 13374–13396.

²⁴⁴ Shimoyama, Y.; Uchida, S. *Chem. Lett.* **2021**, *50* (1), 21–30.

²⁴⁵ (a) Lan, J.; Wang, Y.; Huang, B.; Xiao, Z.; Wu, P. *Nanoscale Adv.* **2021**, *3* (16), 4646–4658. (b) Nasalevich, M. A.; Van Der Veen, M.; Kapteijn, F.; Gascon, J. *CrystEngComm* **2014**, *16* (23), 4919–4926.

²⁴⁶ Wang, J. L.; Xu, L. J. *Crit. Rev. Environ. Sci. Technol.* **2012**, *42* (3), 251–325.

²⁴⁷ Kamiya, Y.; Sano, S.; Miura, Y. K.; Uchida, Y.; Ogawa, Y.; Iwase, Y.; Okuhara, T.; Degnan, T. F. *Chem. Lett.* **2010**, *39* (8), 881–883.

In conclusion, it has been demonstrated how the combination of a zirconium metal-organic cluster and a polyoxotungstate into a single ionic molecular material yields a chemically and photochemically stable porous material. Furthermore, the HOMO/LUMO energy distribution provides a Z-scheme mechanism with spatially separated reduction and oxidation units, which could prolong the lifetime of photogenerated e^-/h^+ and explains the synergetic boosting of the catalytic performance provided by the coexistence of the metal-organic and polyoxometalate clusters. All in all, this line of work opens the opportunity to design novel heterogeneous photocatalysts based on the hybridization of metal-organic clusters and polyoxometalates, given that the stability of the material and the potential to get an enhanced performance can be achieved by the rational selection of the ionic building blocks.

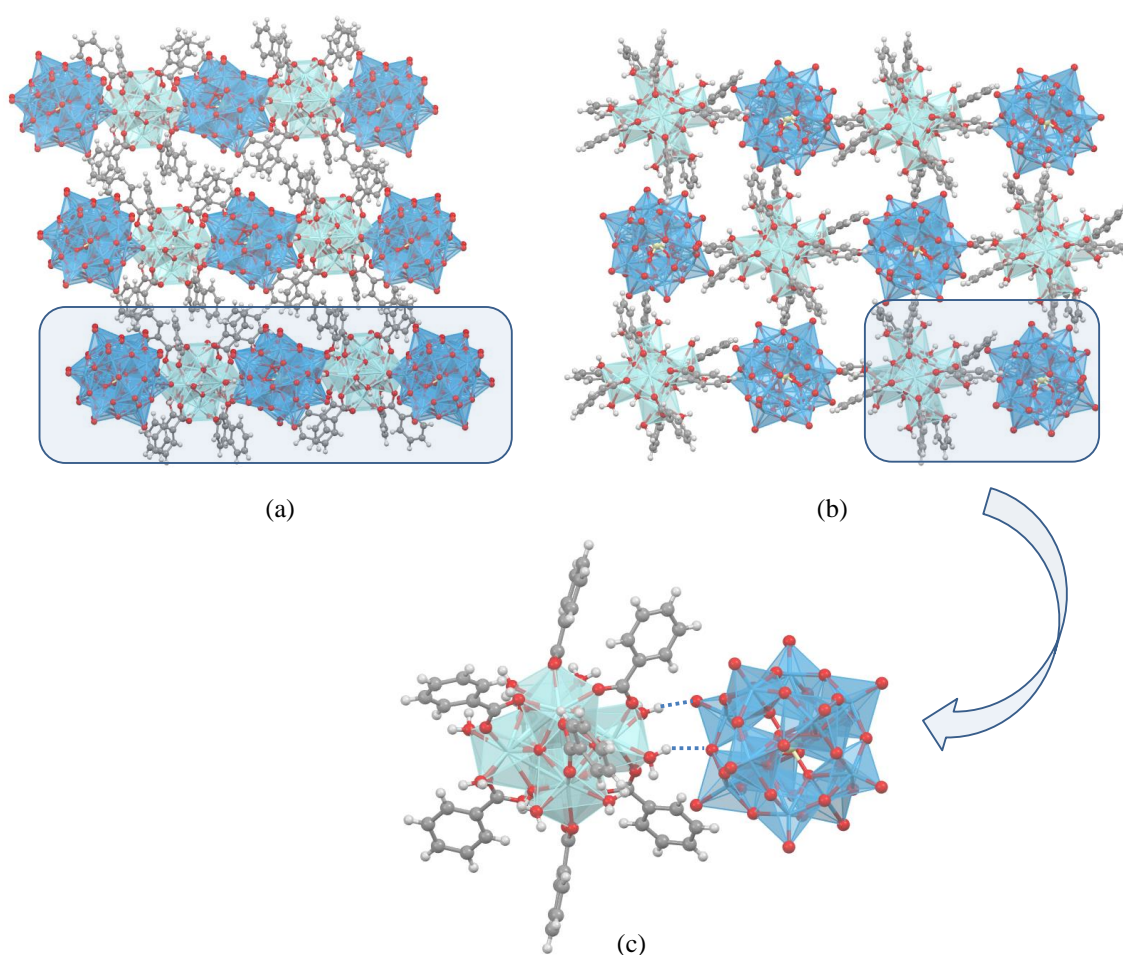


Figure 4.29. (a) View of the crystal packing of Zr_6/W_{12} along b -axis. (b) Hydrogen-bonded two-dimensional square lattice and (c) detail of the hydrogen bonding interactions established between adjacent molecular building blocks.

Chapter 5:

Zirconium-polycarboxylate gel systems as substrate to develop advanced fluorescence sensing devices

5.1. Introduction

5.2. Synthesis and chemical characterization

5.3. Results and discussion

5.1. INTRODUCTION

For several years, metal–organic frameworks (MOF) have been one of the most important research fields in the world of materials science with huge different applications. However, there are situations where their stability is not ideal and the material is not able to withstand the conditions required by the application. An option to increase the stability of the system is the use of zirconium based metal-organic materials.⁵⁸ Among them, several new compounds based on gels (MOGs, Metal-Organic Gels) have been prepared in our research group, where porous Zr-trimesate gels lacking crystalline ordering were obtained. XPS measurements indicated that it is build up by the same $[\text{Zr}_6(\text{O})_4(\text{OH})_4]^{12+}$ clusters described in the previous chapter, connected by polycarboxylato ligands.

As the title of the thesis indicates, this work aims to generate materials where we combine porosity with another easily measurable property to generate chemical sensors. Materials with high porosity are ideal because they enable a strong interaction between molecules in solution and the material itself. However, incorporating high porosity in a solid is not trivial and usually requires a very precise synthetic design. In our case, SMOFs (Supramolecularly assembled Metal-Organic Frameworks) materials, described in chapters 2 and 3, placed within the microporous regime (< 2 nm) and with interesting magnetic properties. However, they are unable to build up materials with luminescence properties due to the presence of incomplete d shell transition metals. Therefore, we decided to employ the chemically robust zirconium(IV) based MOGs (Metal-Organic Gels) with meso/macroporous regime (> 2 nm) and complete shell configuration for the purpose of developing chemical sensors in solution based on luminescence.

The fast, massive and chaotic growth of the latter material, taking place in just few minutes, promotes the presence of many defects such as non-coordinating carboxylic groups of the trimesate ligand and bridging ligand vacants that are not so abundant in the crystalline MOF. However, it also provides some advantages, the great number of nucleation points created in seconds involve very small particulate sizes (which implies a great surface/volume ratio) and a fast and non-reversible coordination reaction, due to the strength of the Zr-O bond, that implies also a very easy route towards the anchorage of carboxylic group containing fluorescent molecules. In other words, the synthesis of the MOG is controlled kinetically instead of thermodynamically, as happens in MOFs, and therefore there is a lower chance for the material to reject the fluorescence carboxylic

molecule from been incorporated. However, it is worth mentioning that prior to get success in the incorporation of the carboxylic fluorophores the research work described in the previous was crucial in order to determine the synthetic key parameter to achieve our goal.

In order to get the more specific luminescent response three fluorophores were simultaneously incorporated emitting in blue, yellow and red, respectively. The interaction of these fluorophores with the adsorbed molecules in solution modifies their luminescent signals giving rise to a color and relative intensities of the three emissions that is characteristic of the adsorbed molecule. The selected fluorophores have been fluorescein (HF), containing a single carboxylic group able to bond the Zr metal atoms, the 2,6- naphthalene dicarboxylic acid (H₂NDC) who presents two carboxylic groups, and the 4,4',4'',4'''-(porphine-5,10,15,20-tetrayl)tetrakisbenzoic acid (H₄TCPP) molecule with four different bridging capable carboxylic groups. Apart from, we need also a measurement procedure that would overcome the mechanical weakness that gels usually present. It required us to move into the engineering of these materials by combining with more mechanically robust others to generate composite materials that fulfill all the requirements to get a fully functional sensoric material.

5.2. SYNTHESIS AND CHEMICAL CHARACTERIZATION

5.2.1. Synthesis

We report herein the synthesis and characterization of gel and SiO₂-gel composites compounds listed in Table 5.1.

All the reagents and solvents were purchased from Sigma-Aldrich and used without any prior purification. For the preparation of zirconium(IV) based gels: zirconium(IV) chloride was used as the metal source and benzene-1,3,5-tricarboxylic acid (trimesic acid, H₃BTC) was used as the 3D structure sustaining main bridging ligand. As fluorophores: Fluorescein (HF), Naphthalene-2,6-dicarboxylic acid (H₂NDC) and 4,4',4'',4'''-(porphine-5,10,15,20-tetrayl)tetrakisbenzoic acid (H₄TCPP) were selected (Figure 5.1). For the formation of zirconium(IV) based gels-quartz composites silicon dioxide was used.

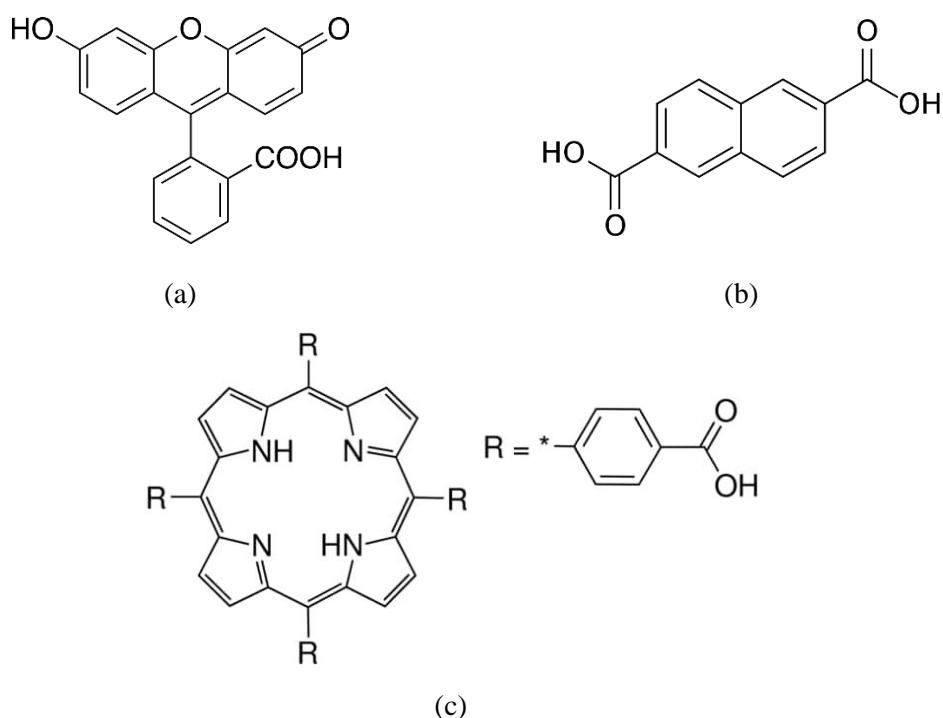


Figure 5.1. Fluorophores compounds employed in this chapter: (a) Fluorescein, (b) naphthalen-2,6-dicarboxylic acid and (c) 4,4',4'',4'''-(porphine-5,10,15,20-tetrayl)tetrakisbenzoic acid.

5.2.1.1. Synthesis of MOGs and MOG-SiO₂composites functionalized with fluorophore molecules

0.389 g (1.66 mmol) of ZrCl₄ was dissolved in a methanolic/aqueous solution (4.8 mL and 0.2 mL, respectively) and an 8 mL methanolic solution containing a mixture of trimesic acid and the corresponding carboxylic group containing fluorescent molecule was added. The Zr:COOH ratio is always maintained at 1:2. The mixtures with the best luminescence performance are reported in Table 5.1. The final solution was sonicated on an ultrasound bath at room temperature until the solution turned from transparent to translucent (*ca.* 2–3 mins). The vial inversion probe corroborated the gelation of the reaction mixture.

The same amount of reagents and synthetic procedure is employed to obtain the MOGs-SiO₂composites but adding 170 mmol of micrometric quartz crystals under 24h of prolonged vigorous stirring.

Table 5.1. Reagent amounts employed (mmols).

Code	ZrCl ₄ (mmol)	H ₃ BTC (mmol)	HF (mmol)	H ₂ NDC (mmol)	H ₄ TCPP (mmol)	SiO ₂ (mmol)
Zr-BTC	1.66	1.107	–	–	–	–
Zr-BTC-F	1.66	1.090	0.050	–	–	–
Zr-BTC-NDC	1.66	0.560	–	0.820	–	–
Zr-BTC-TCPP	1.66	1.105	–	–	0.001	–
Zr-BTC-SiO ₂	1.66	1.107	–	–	–	85
Zr-BTC-F-SiO ₂	1.66	1.090	0.050	–	–	85
Zr-BTC-NDC-SiO ₂	1.66	0.560	–	0.820	–	85
Zr-BTC-TCPP-SiO ₂	1.66	1.105	–	–	0.001	85
Zr-BTC-ALL-SiO ₂	1.66	1.069	0.050	0.030	0.001	85

5.3. RESULTS AND DISCUSSION

5.3.1. Initial MOG optimization

In order to obtain the Zr-BTC gels, a synthesis optimization work was initially carried out by modifying the methanol/water mixture (from 0.1 to 2 mL) to be used (always maintaining the final solvent volume at 5 mL with methanol), the order and form of addition, and the use of methanol or ethanol. In all the cases, we obtained an amorphous material. In the optimization of the amount of water, the best results were obtained with the addition of 0.2 mL of water. When a greater amount is added, the gelling time increases considerably from a few minutes to hours.¹³¹ The order of addition plays an important role, the addition of methanol on the zirconium, before that of water, gave better results for a complete dissolution of the reagents. Finally, this mixture was added to the trimesic solution.

Another aspect that was studied during the synthesis was the pH to be used, since it had to be a compendium between not too acidic, so that the trimesic acid and the other ligands can be deprotonated and anchored to the cluster, and a pH at which the fluorescence capacity is active. In the case of fluorescein, a study of fluorescence as a function of pH was carried out, in which we saw how fluorescence was more intense at very acidic pH from 0.5 to 2.9, where it disappeared until it reappeared at pH values above 7.

5.3.2. Zr-BTC-Fluorescein gel optimization

Different amounts of fluorescein were tested from 0.5 % of the total carboxylate groups to 10% with respect to the stoichiometric amount of carboxylate anions required by the $[\text{Zr}_6\text{O}_4(\text{OH})_4(\text{OOCR})_{12}]$ SBU. All of them provided an intense orange colour (Figure 5.3), from where gel monoliths were obtained using a straw. These monoliths were washed thoroughly with MeOH during several days to remove the uncoordinated fluorescein. The optimum amount that provided the more intense fluorescence after the washing procedure corresponds to 1.5% of the total carboxylate groups belonging to fluorescein (the remaining carboxylate groups are provided by the trimesic acid). Samples obtained using higher fluorescein amount provided a less intense fluorescence, as shown in Figure 5.4, due to a self-quenching effect.

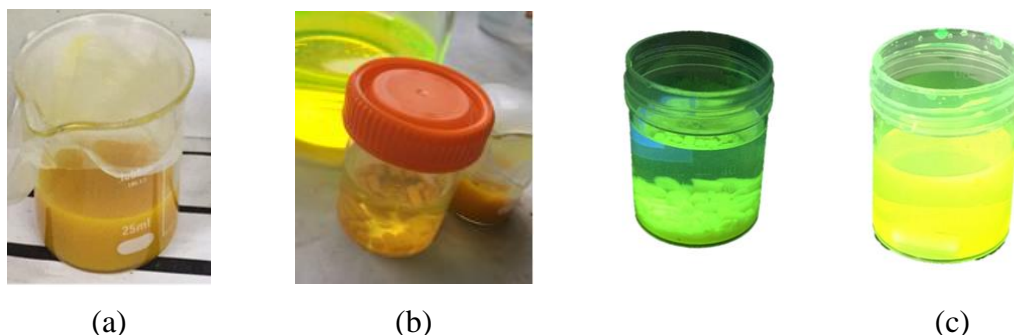


Figure 5.3. (a) Zr-BTC-F gel under the optimum conditions detailed in Table 5.1, (b) Monoliths obtained with the straw, (c and d) Monoliths and initial washing solution showing a large fluorescent intensity under a UV lamp (365 nm), respectively.

As we have checked, initially the fluorescein was not completely anchored to the system, so it was decided to modify the concentration used by testing four different dilution ratios of the fluorescein concentration as a function of the initial 2%; 1%; 0.67%; 0.5%, Figure 5.4a. As seen in Figure 5.4b, the best result was obtained for the sample 2%. In this way, the washing was reduced to a single solvent change on the same day and with the consequent saving of material. In addition, a significant change in the intensity of the material was achieved, increasing it considerably compared to the original due to the elimination of the self-quenching provided by the ligand itself.

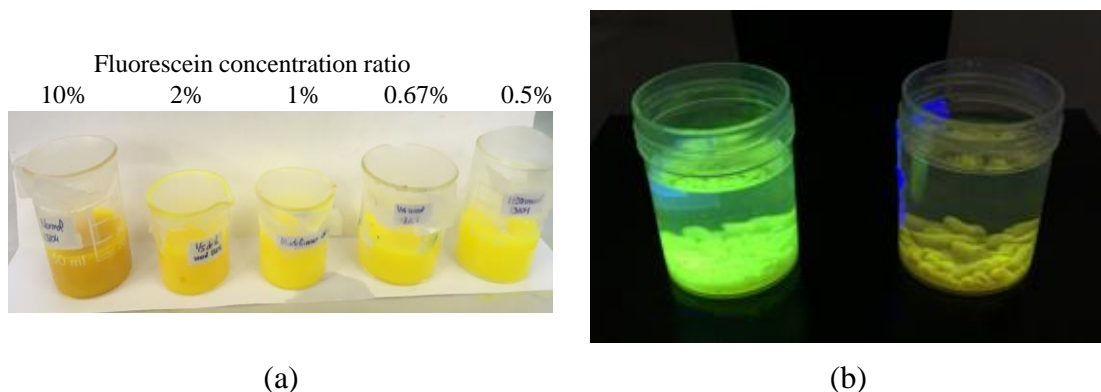


Figure 5.4. (a) Gels obtained at different fluorescein amounts, (b) Fluorescence exhibited by the washed monoliths obtained at 1.5% of fluorescein provided carboxylates (left) and 10% (right) under excitation at 365 nm.

5.3.3 Zr-BTC-Fluorescein gel qualitative sensing applications

The first application that was thought for this type of materials was their use as a fluorescent sensor, where according to the solvent with which it would be in contact or molecules present in the medium, its fluorescent signal would be modified, observing an increase or decrease. Initially, two monoliths of the optimal concentration of fluorescein

were introduced into each vial with 10 mL of different solvents (acetone, water, water/NaCl, acetic acid, methanol, ethanol and hexane). As can be seen in Figure 5.5, in most cases there was no significant change in fluorescent intensity (at least under the naked eye), keeping the solution colourless, but three cases should be noted. In the case of acetic acid, it was observed how, when the monoliths were introduced, they began to dissolve, giving the solution a yellowish colour and fluorescent signal after a few minutes. This may be due to the carboxylate group present in acetic that breaks the coordination bond that fluorescein establishes with the metal cluster $[\text{Zr}_6(\text{O})_4(\text{OH})_4(\text{L})_n]$ releasing it into the medium. In the case of water, the solution remains colourless as in other cases, but the monoliths decrease their fluorescence intensity substantially. Interestingly, when NaCl is dissolved in water (1M), the fluorescence intensity of the monolith in the vial remains quite high, unlike the previous case.

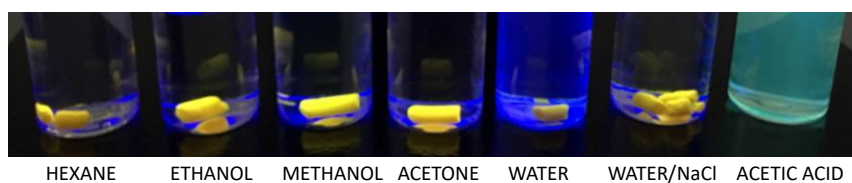


Figure 5.5. Fluorescence of monoliths submerged in different solvents and irradiated at 365 nm.

On the other hand, performing the same qualitative experiments in aqueous solutions of different compounds a clear variation of the luminescence intensity happens, which indicates the porosity of the host is adequate to provide a strong enough interaction between the fluorophores anchored to the Zr-BTC skeleton and the guest molecules within the pores of the metallogel (Figure 5.6). It is worth remarking the uracile and phenylalanine solutions in which the fluorescent intensity of the monolith is increased considering the reference water vial and the solution containing indole that causes the complete elimination of the fluorescence.

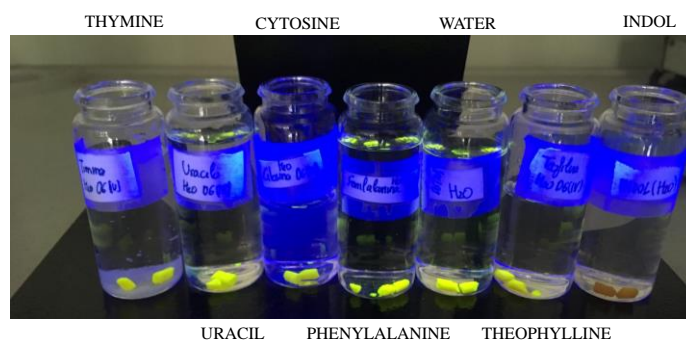


Figure 5.6. Fluorescence of monoliths submerged in aqueous solutions of different compounds and irradiated at 365 nm.

Finally, we carried out a CO₂ supercritical drying procedure to obtain the corresponding metal-organic aerogel (MOA). In this way, all the solvent placed inside the gel it is replaced by air, maintaining the microstructure of the material (in other words, without its shrinkage). After the supercritical drying procedure was completed the integrity of the monoliths was retained although their size was slightly reduced (Figure 5.7).

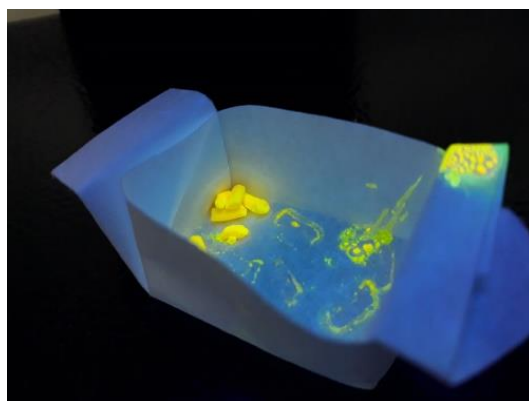


Figure 5.7. Fluorescence of the monoliths of Zr-BTC-F MOA after the supercritical drying procedure.

5.3.4 Zr-BTC-Fluorescein gel fluorescence measurements

Once we have qualitatively observed some fluorescence intensity changes of the monoliths in the presence of different solvents and molecules in water, we performed some quantitative fluorescence measurements. However, these measurements showed no reproducibility (Figure 5.8). The reason for this is that although evident qualitative change of the fluorescence emission took place on the monoliths as described above, the gelatinous nature of the metallogel means that any manipulation on the monoliths causes a deformation that strongly affects the luminescence output. This effect coming from the self-quenching effects of the fluorophore molecules changes upon any alteration of the density of the metallogel. It means these Zr-BTC-F metallogels could behave as low-pressure sensors but hardly as chemical sensors.

Therefore, we developed an alternative strategy in which we reproduced the same conditions employed for the synthesis of the metallogels but in the presence of ten times SiO₂ microcrystals and under vigorous stirring.

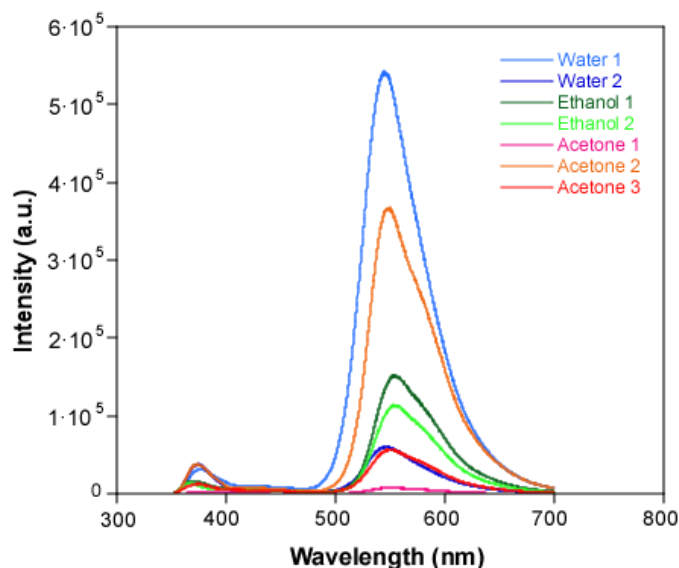


Figure 5.8. Fluorescent intensity signals of the monoliths of the MOG-fluorescein sample in different solvents where the poor reproducibility of the measurements has been checked.

5.3.5. Zr-BTC-Fluorophore and quartz-sand composite

The poor mechanical properties of the above described pure gels made difficult to ensure that the fluorescence changes are only due to the interaction with the molecules and no due to mechanical changes during the physical manipulation. So that, a composite approach was employed in which the metallogel synthesis is performed in the presence of a great amount of micrometric quartz particles (90% quartz and 10% metallogel) and under vigorous and constant stirring. The constant stirring prevents the formation of a gel and instead of that a sand-like product is obtained. This product was thoroughly washed with methanol using a soxhlet equipment. The washing procedure was continued until the solvent remained colourless. Finally, the product was dried under room conditions. SEM microscopy images (Figure 5.9) of the resulting product showed quartz microparticles (with a darker bright) and smaller nanometric particles of the dried metallogel (xerogel, brighter particles). The latter appears magnified in the upper part of Figure 5.9. In situ EDX measurements verified the presence of Zr in the sample and FTIR spectroscopy the presence of trimesato ligand, which corroborates the formation of the Zr-BTC-F and quartz composite.

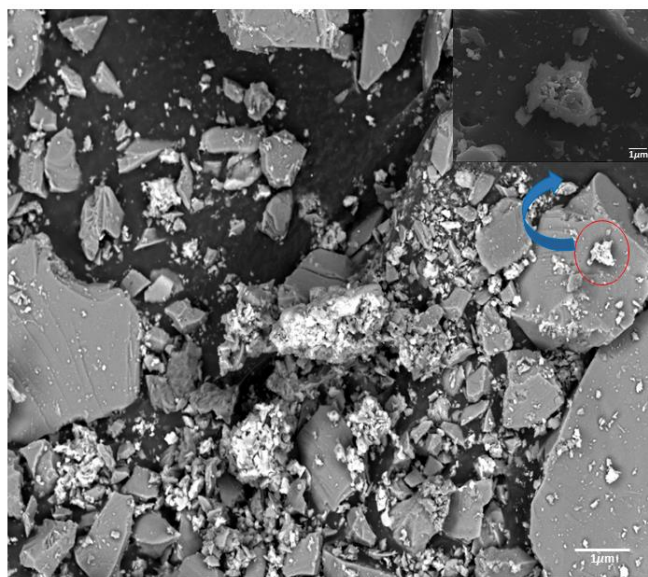


Figure 5.9. SEM micrographs at 1000 magnification of a Zr-BTC-F-SiO₂ sample. In the upper right part it can be seen at 25000 magnification.

The chemical stability of the composite material is similar to that of the metallogel, and shows also a guest selective response. However in this case, the response remained stable upon manipulation allowing quantitative measurements. In fact, the size difference between the quartz microcrystals and the Zr-BTC-F nanoparticles prevents the collapse of its porous nature when pressure is applied. The packing of the quartz microparticles, when pressure is applied, left many voids in which the far smaller Zr-BTC-F particles can accommodate and withstand the pressure without any noticeable change in fluorescence.

The same optimization of the employed fluorophore concentration performed for fluorescein was also applied to naphthalene-2,6-dicarboxylic acid (H₂NDC) and 4,4',4'',4'''-(porphine-5,10,15,20-tetrayl)tetrakis benzoic acid (H₄TCPP). For an optimum fluorescence in Zr-BTC-NDC sample the fluorophore concentration in the form of carboxylate percentage must be raised up to 17%. In the case of Zr-BTC-TCPP sample, the very effective self-quenching effect that the fluorophore molecule exhibits requires its concentration, in carboxylate group percentage, to be lowered to a surprisingly low value of 0.03%. Being able to incorporate simultaneously these three fluorophores in the Zr-BTC gel matrix, we have been able to provide a source of deep blue (421 nm; Zr-BTC-NDC), yellow (530 nm; Zr-BTC-F) and red (680 nm; Zr-BTC-TCPP) emissions that are sensible to presence of adsorbate molecules inside the porous metal-organic material (Figure 5.10). These three fluorophores have been selected because their emission lies

very close to the three basic colours (blue, yellow and red) and their combination can provide the maximum visible colour variation as it will be described later. It is worth mentioning that Zr-BTC compound is also able to provide a fluorescence response at violet (393.0 nm) but it is too weak to be used effectively for sensing purposes.

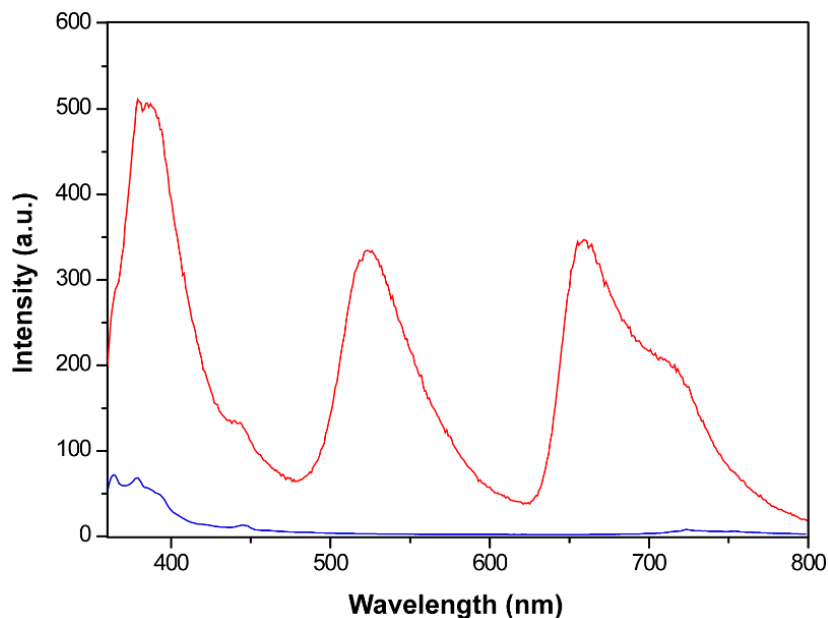


Figure 5.10. Physical measurements of the fluorescence intensity of the modified quartz with H₂NDC, fluorescein and H₂TCPP (red) and quartz-BTC (blue) sample.

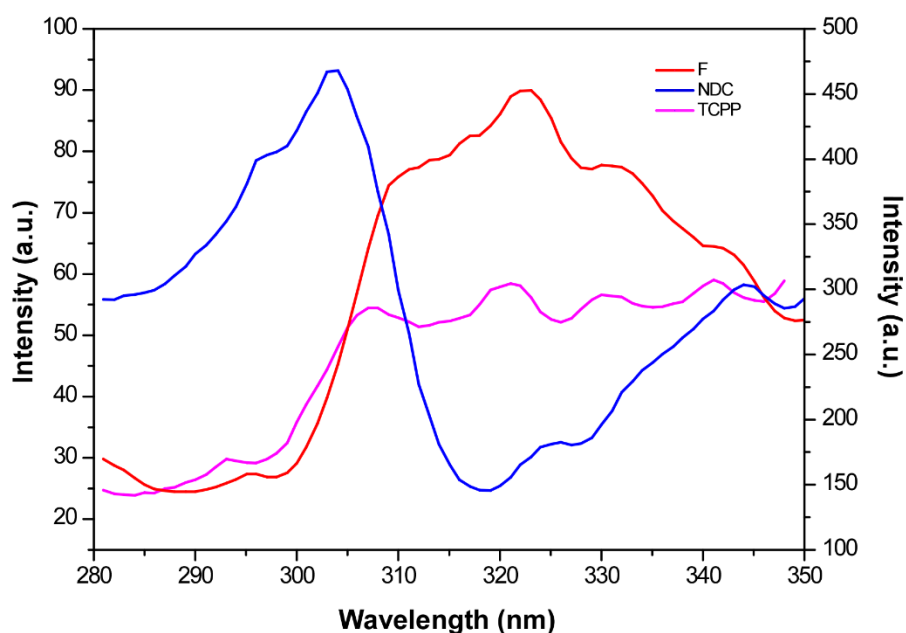
Interestingly the excitation spectra for the emission signals of the three fluorophores provide different maximum values in the 280-350 nm. Zr-BTC-NDC²⁴⁸ provides a clear maximum around 305 nm, Zr-BTC-F at 325 nm and Zr-BTC-TCPP provides a more or less constant value between 310-350 nm. Having in main that the most intense signal corresponds to Zr-BTC-NDC, we decided to employ a wavelength of 325 nm for their simultaneous excitations in order to maximize the other two weaker signals (Figure 5.11). The fluorophore anchored to the cluster system undergoes a slight shift of the fluorescence maximum towards higher wavelength positions with respect to the free molecule dissolved in water, 530 vs 500 nm (fluorescein)²⁴⁹, 421 vs 426 nm (2,6-NDC)²⁵⁰, 680 vs 643 nm (H₂TCPP)²⁵¹, Figure 5.12.

²⁴⁸ Tella, A. C.; Owalude, S. O.; Omotoso, M. F.; Olatunji, S. J.; Ogunlaja, A. S.; Alimi, L. O.; Popoola, O. K.; Bourne, S. A. *J. Mol. Struct.* **2018**, *1157*, 450–456.

²⁴⁹ Seybold, P. G.; Gouterman, M.; Callis, J. *Photochem. Photobiol.* **1969**, *9* (3), 229–242.

²⁵⁰ (a) Gangu, K. K.; Dadhich, A. S.; Mukkamala, S. B. *Inorg. Nano-Metal Chem.* **2017**, *47* (3), 313–319. (b) Ding, Y.; Pan, L.; Li, S.; He, H.; Zhang, D.; Hu, X.; Zhang, R.; Wang, Y.; Zhai, X.; Meng, Q. *J. Nanomater.* **2018**, *2018*, 5426427.

²⁵¹ (a) Quiroz-Segoviano, R. I. Y.; Serratos, I. N.; Rojas-González, F.; Tello-Solís, S. R.; Sosa-Fonseca, R.; Medina-Juárez, O.; Menchaca-Campos, C.; García-Sánchez, M. A. *Molecules* **2014**, *19* (2), 2261–2285. (b) Makarska-Bialokoz, M. *J. Fluoresc.* **2012**, *22* (6), 1521–1530.



5.11. Excitation values of the the fluorophores employed.

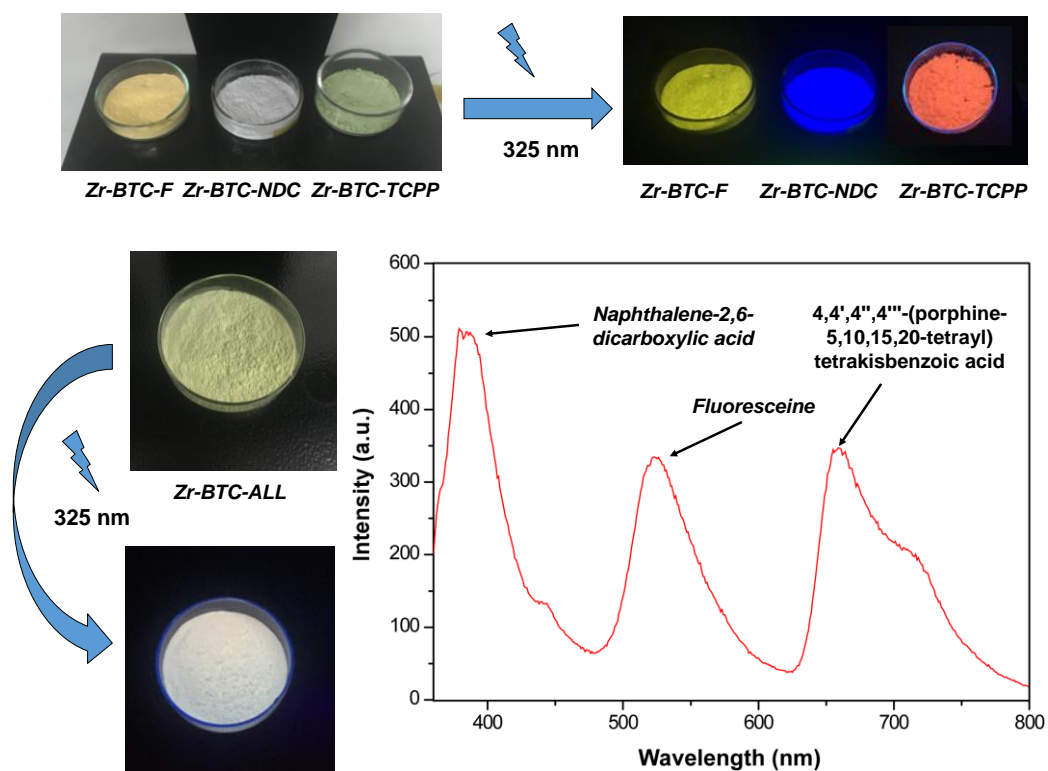
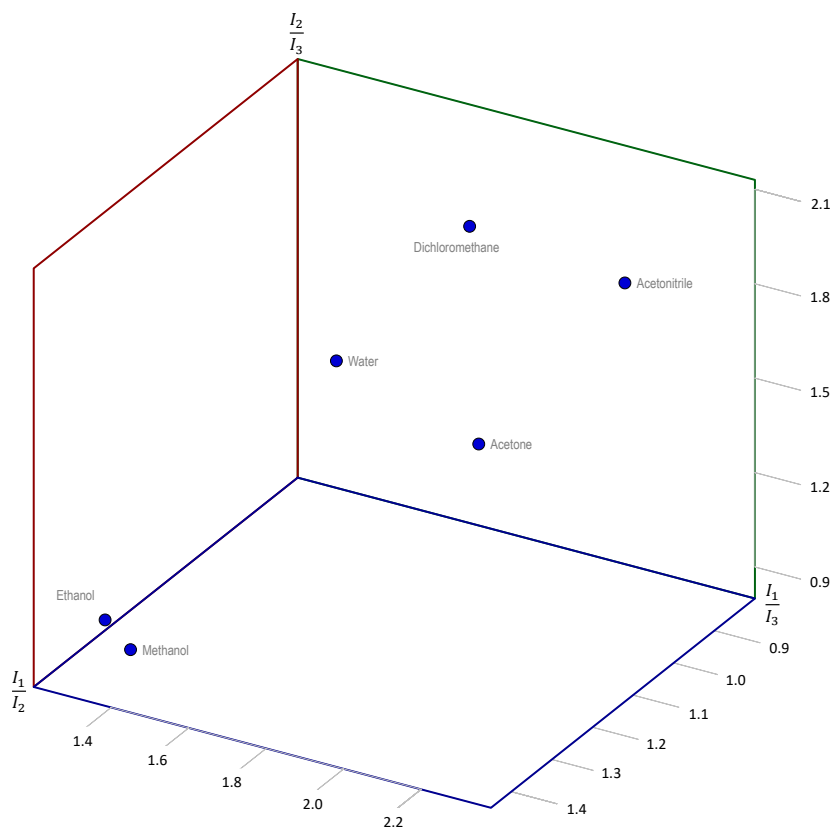
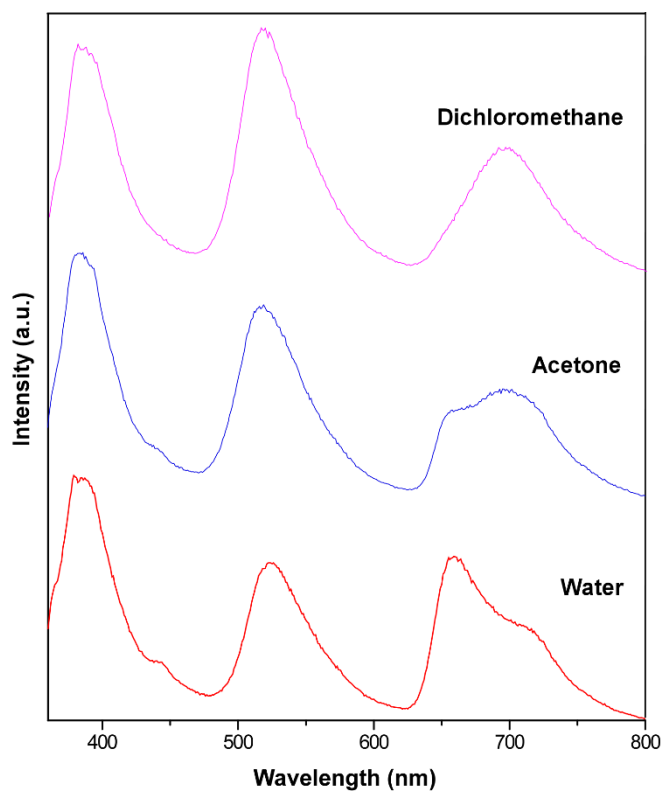


Figure 5.12. Images of the Zr-BTC-Fluorophore-SiO₂ composites. Top left: colour of the composites containing a single fluorophore irradiated by daylight. Top right: fluorescence emission of the composites containing a single fluorophore irradiated at 365 nm. Bottom left: Zr-BTC-F/NDC/TCPP-SiO₂ under daylight and irradiated at 365 nm (notice the white colour emerging from the combination of the three elemental colours). Bottom right: Fluorescence emission spectra of Zr-BTC-F/NDC/TCPP-SiO₂ under excitation at 325 nm.

As for Zr-BTC-F, the chemical stability in different solvents has been checked by monitoring the luminescence of the washing solutions. No leakage of the fluorophore has been observed, even when using acetic acid as solvent. This fact indicates the anchorage of these dicarboxylate (NDC) and tetracarboxylate (TCPP) fluorophore molecules is stronger attached to the zirconium cluster than the monocarboxylic fluorescein molecule, which leached in the presence of acetic acid and other carboxylic molecules. It is worthy noting that although the fluorescence signal of the composite is retained in all the solvents employed (methanol, water, ethanol, dimethylformamide, dimethylsulfoxide, acetone, toluene, dichloromethane, chloroform, acetonitrile) the intensity of the emission peaks changes while the position of the maximum does not change. The intensity of these fluorescence emission peaks can be employed for a sensing purpose but as the intensity of fluorescence signal is greatly dependent on the intensity of the excitation source and the amount of sample among other parameters. To avoid this dependence, relative intensities were employed. In this sense, we can differentiate the solvents in just one measurement of the fluorescence response of these particles submerged in the corresponding solvent. In order to perform this measurement a quartz cuvette originally designed for the measurement of liquids was employed. There, 0.1 g of the Zr-BTC-F composite was placed submerged in the solvent and with the help of a centrifuge the particles are attached to the quartz window. This procedure provides a convenient way to ensure reproducible fluorescence measurement. At <https://youtu.be/yvKpa-jrrR0> you can find a video showing the details of this procedure. All the measurements were repeated thrice in order to verify the reproducibility of the data (Table 5.3). The results are displayed in a three-dimensional graph in Figure 5.12 in which we can observe how the solvents can be easily differentiated among them.



(a)



(b)

Figure 5.12. (a) Three-dimensional representation of the relative fluorescence intensities for the different solvents and (b) spectra of some of the employed solvents.

On the other hand, the selected luminescence colour mixture (blue, yellow and red) coming from the fluorophores allows also a naked eye distinguishable fluorescence colour change depending on the quenching performance of the solvent molecules towards each fluorophore, Figure 5.13.

Table 5.3. Fluorescence intensity values for the differents solvents.

Solvent	I1 (NDC)	I2 (Flourescein)	I3 (TCPP)	Mean _{I1/I2}	Mean _{I1/I3}	Mean _{I2/I3}	$\sigma_{I1/I2}$	$\sigma_{I1/I3}$	$\sigma_{I2/I3}$
Water	513	336	333	1.01	1.52	1.49	0.01	0.04	0.03
	515	341	353						
	511	334	347						
Acetone	562	433	251	1.27	2.16	1.70	0.03	0.08	0.03
	553	440	257						
	545	439	262						
Methanol	622	443	411	1.45	1.45	1.00	0.04	0.06	0.07
	622	420	428						
	629	429	453						
Ethanol	512	381	393	1.36	1.29	0.95	0.05	0.06	0.02
	514	365	384						
	506	384	412						
Acetonitrile	598	520	240	1.12	2.38	2.13	0.03	0.10	0.04
	576	523	251						
	574	521	245						
Dichloromethane	411	451	229	0.93	1.78	1.92	0.01	0.02	0.04
	402	432	226						
	402	429	228						

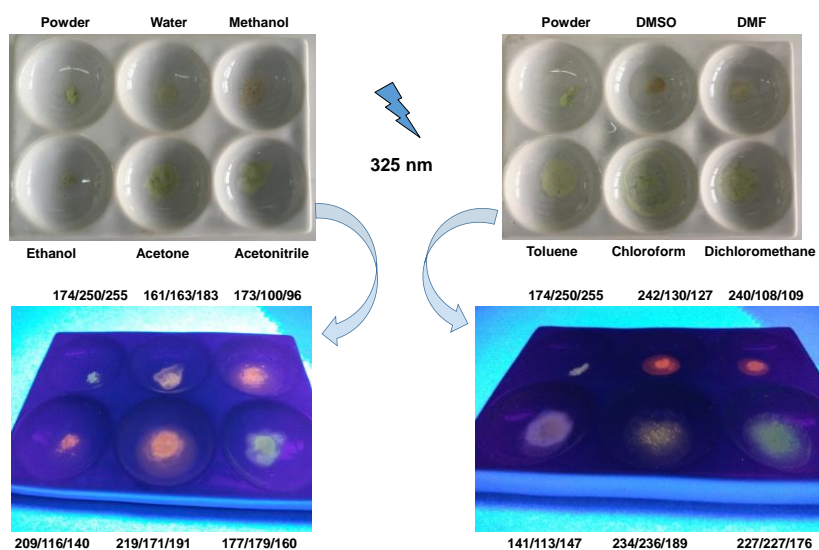
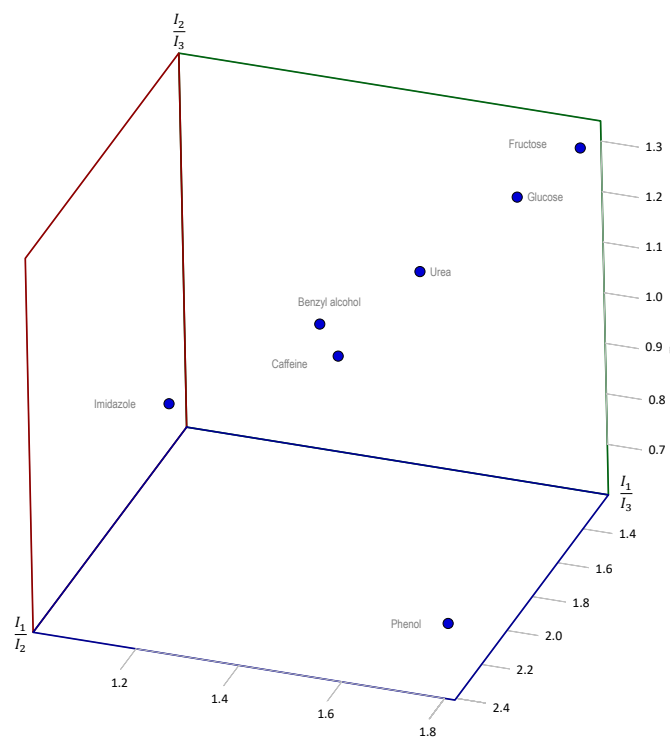


Figure 5.13. Colours emerging from the Zr-BTC-F/NDC/TCPP-SiO₂ composite submerged in different solvents upon irradiation at 365 nm. RGB codes are indicated.

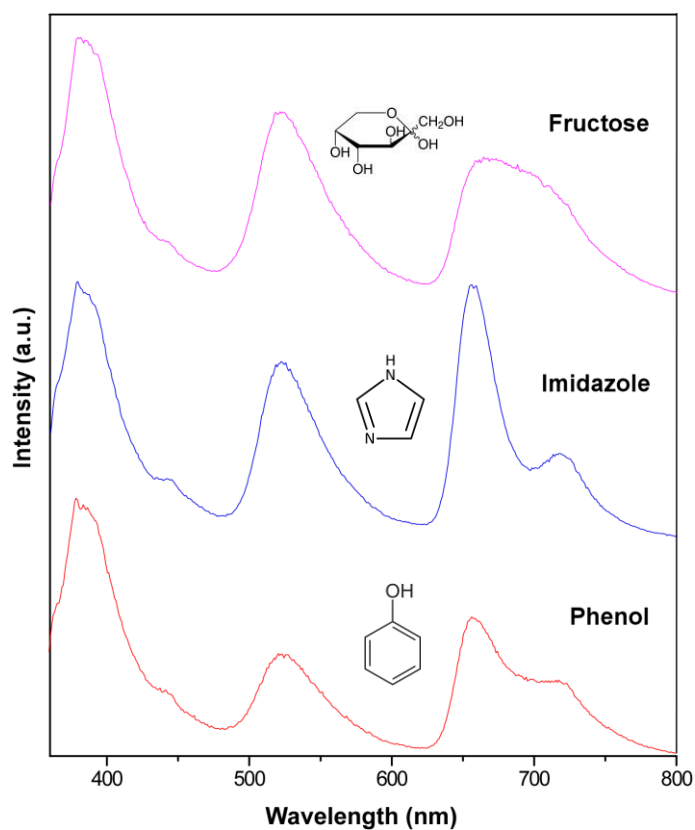
A similar approach can be envisaged to identify different molecules in solution. In this case, the procedure consist in preparing 10 mL of an aqueous solution containing 0.1 g of the corresponding analyte (100 μ L if liquid). From this solution, 2 mL are taken and 0.1 g of the Zr-BTC-F/NDC/TCPP-SiO₂ composite are added. The mixture is left for while under continuous stirring and afterwards placed in the previously described cuvette, centrifuged and its fluorescence measured under excitation at 325 nm. Again the obtained relative intensities of the three fluorophores are represented in a 3D graph that allow an easy and straightforward differentiation between the analytes (Figure 5.14, Table 5.4).

Table 5.3. Fluorescence intensity values for the differents solvents.

Solvent	I1 (NDC)	I2 (Flourescein)	I3 (TCPP)	Mean _{I1/I2}	Mean _{I1/I3}	Mean _{I2/I3}	$\sigma_{I1/I2}$	$\sigma_{I1/I3}$	$\sigma_{I2/I3}$
Glucosa	505	368	314	1.38	1.70	1.23	0.02	0.09	0.05
	516	368	289						
	521	381	304						
Urea	518	356	328	1.43	1.52	1.07	0.02	0.09	0.06
	521	368	332						
	520	369	368						
Fructose	511	380	276	1.36	1.82	1.34	0.02	0.02	0.03
	522	386	289						
	514	371	283						
Imidazole	517	369	510	1.41	1.02	0.72	0.02	0.04	0.04
	529	378	499						
	518	361	526						
Benzyl alcohol	508	349	379	1.42	1.32	0.93	0.03	0.04	0.03
	512	366	381						
	502	359	395						
Caffeine	486	346	383	1.52	1.38	0.91	0.10	0.12	0.05
	468	297	311						
	477	300	316						
Phenol	427	182	241	2.41	1.81	0.75	0.06	0.04	0.01
	438	179	237						
	436	178	239						



(a)



(b)

Figure 5.14. (a) Three-dimensional representation of the relative fluorescence intensities for the different analytes dissolved in water and (b) spectra of the employed molecules.

CONCLUSIONS

This work has been very extensive both in the type of compounds prepared, characterization techniques and approaches towards sensing applications but the main results are summarized below:

- SMOF materials provide a straightforward route to obtain porous materials when the selection of the organic ligands and counterions is performed carefully to provide stable and predictable supramolecular interactions patterns. This has been the case when employing $[\text{Cu}_6\text{M}(\text{OH})_6(\text{adeninato})_6(\text{H}_2\text{O})_6]^{n+}$ (M: Co^{II} , Ni^{II} , Cu^{II} , Zn^{II}) cationic entities in combination with organic anions that are able to establish π -stacking interactions with the adeninato ligands of the heptameric entities. The predictability of the resulting porous crystal structure has allowed the preparation of an isorecticular series of SMOFs in which dicarboxylate organic anions of increasing length are employed to provide an increasing degree of void percentage and pore size.
- The paramagnetic nature of these SMOFs has been employed to determine the adsorption capacity of these compounds in solution by means of the modification of their attraction toward a magnetic field by the mass incorporated in its pores.
- SMOF materials are well suited materials to provide metal nanoparticles supported on a carbonaceous matrix that can be useful in many applications. Herein we have focused on CO_2 thermocatalytic reduction towards CO and we have been able to analyze the effect of the carbonaceous matrix on the performance of the catalyst. In fact, a great amount of this matrix helps limiting the size of the nanoparticles by reducing their chances to coalesce but at the same time it can isolate them from interacting with CO_2 . The porous nature of the precursors helps keeping the metal nanoparticle size small without the necessity of a great amount of carbonaceous matrix. In fact, the organic content in the metal-organic precursor determines the final amount of the carbonaceous matrix in the catalyst and as it has been probed for the homometallic series of precursors the best performing one is that containing the small fumarate counterion.
- On the other hand, these precursors also provide a facile route to work with alloy nanoparticles as many of these metal-organic compounds can be obtained as solid state substitutional solutions of different metal centers. It has allowed us to get $\text{Cu}_{1-x}\text{Zn}_x$ nanoparticles with ZnO aggregates in its surface, as demonstrated here by XPS and EDX mappings, that play a key role in improving the CO_2

thermocatalytic reduction both by providing better CO₂ adsorption and easier CO release sites.

- It has been shown that there is plenty of chemistry still to be discovered about the first stages of the zirconium-carboxylate cluster formation. The results rendered here must be understood as frozen images along this process but also reveal the opportunities that arise from a fine control of the synthetic conditions. In fact, among the intermediate species that can be found in the formation of Zr-carboxylate clusters, a structure in which the 12 carboxylate ligands bridge the 12 Zr–Zr edges is the lowest in energy according to quantum mechanical calculations. However, this report does not take into account the specific synthetic conditions at which these entities grow. Our work confirms that small modifications of the pH of the media can considerably affect in the isolation of clusters with different nuclearities and carboxylate-ligand contents. In addition, species with unsaturated carboxylate and/or metal positions can be a starting point to develop a richer chemistry by completing these vacancies with different carboxylic ligands or metal centers. In this sense, it has been possible to isolate zirconium hexameric entities with only eight carboxylate groups attached to the cluster and the remaining free four carboxylate positions arranged in a square planar or tetrahedral disposition. An unprecedented pentameric entity closely related to the hexameric ones by the release of one of the apical zirconium positions is also achieved, being able to reveal the acid–base nature and pH dependence of the transformation between both species. As a final remark, it is worth to mention that the results obtained here reveal that in spite of the cationic nature of the zirconium clusters reported herein, their chemistry shows some resemblance with that of the anionic polyoxometalates (POMs), as the acidity of the media is also here a key factor in the final nuclearities of the resulting clusters. However, differences arise from the fact that the oxidation state of the zirconium cation is not as high as those displayed by the typical addenda metals in POMs (mainly V, Mo, and W). This implies that the polarizing capability of zirconium is not that high and it cannot promote the complete deprotonation of all the coordinated water molecules to afford an oxide rich environment able to stabilize these metal ions. Instead of this, the formation of zirconium-based entities with higher nuclearities than the classical $[\text{Zr}_4(\text{OH})_8(\text{H}_2\text{O})_{16}]^{8+}$ cation will require the presence of coordinated carboxylate groups bridging and holding together the metal centers.

REFERENCES

In this work, the references are mentioned as footnotes in the different chapters. In this section, the full references can be found, displayed in alphabetical order of the first author and, then, the rest of the authors are considered. When this criterion is not enough, the publication name and the first page will be taken into account. The reference style followed is the recommended by the American Chemical Society.

A. Altomare, G. Cascarano, C. Giacovazzo, A. Guagliardi, M. C. Burla, G. P. & M. C. SIR92 - a Program for Automatic Solution of Crystal Structures by Direct Methods. *J. Appl. Crystallogr.* **1994**, 1978, 8898.

Acharya, P.; Chattopadhyaya, J. Electrostatic Cross-Modulation of the Pseudoaromatic Character in Single-Stranded RNA by Nearest-Neighbor Interactions. *Pure Appl. Chem.* **2005**, 77 (1), 291–311.

Almarsson, Ö.; Zaworotko, M. J. Crystal Engineering of the Composition of Pharmaceutical Phases. Do Pharmaceutical Co-Crystals Represent a New Path to Improved Medicines? *Chem. Commun.* 2004, 17, 1889–1896.

Alothman, Z. A. A Review: Fundamental Aspects of Silicate Mesoporous Materials. *Materials.* **2012**, 5 (12), 2874–2902.

An, J.; Farha, O. K.; Hupp, J. T.; Pohl, E.; Yeh, J. I.; Rosi, N. L. Metal-Adeninate Vertices for the Construction of an Exceptionally Porous Metal-Organic Framework. *Nat. Commun.* **2012**, 3.

An, J.; Fiorella, R. P.; Geib, S. J.; Rosi, N. L. Synthesis, Structure, Assembly, and Modulation of the CO₂ Adsorption Properties of a Zinc-Adeninate Macrocyclic. *J. Am. Chem. Soc.* **2009**, 131 (24), 8401–8403.

An, J.; Geib, S. J.; Rosi, N. L. Cation-Triggered Drug Release from a Porous Zinc-Adeninate Metal-Organic Framework. *J. Am. Chem. Soc.* **2009**, 131 (24), 8376–8377.

Arunan, E.; Desiraju, G. R.; Klein, R. A.; Sadlej, J.; Scheiner, S.; Alkorta, I.; Clary, D. C.; Crabtree, R. H.; Dannenberg, J. J.; Hobza, P.; Kjaergaard, H. G.; Legon, A. C.; Mennucci, B.; Nesbitt, D. J. Definition of the Hydrogen Bond (IUPAC Recommendations 2011). *Pure Appl. Chem.* **2011**, 83 (8), 1637–1641.

Atzori, C.; Shearer, G. C.; Maschio, L.; Civalieri, B.; Bonino, F.; Lamberti, C.; Svelle, S.; Lillerud, K. P.; Bordiga, S. Effect of Benzoic Acid as a Modulator in the Structure of UiO-66: An Experimental and Computational Study. *J. Phys. Chem. C* **2017**, 121 (17), 9312–9324.

Azuah, R. T.; Kneller, L. R.; Qiu, Y.; Tregenna-Piggott, P. L. W.; Brown, C. M.; Copley, J. R. D.; Dimeo, R. M. DAVE: A Comprehensive Software Suite for the Reduction, Visualization, and Analysis of Low Energy Neutron Spectroscopic Data. *J. Res. Natl. Inst. Stand. Technol.* **2009**, 114 (6), 341–358.

Bai, Y.; Dou, Y.; Xie, L. H.; Rutledge, W.; Li, J. R.; Zhou, H. C. Zr-Based Metal-Organic Frameworks: Design, Synthesis, Structure, and Applications. *Chem. Soc. Rev.* **2016**, 45 (8), 2327–2367.

Bao, Z.; Xie, D.; Chang, G.; Wu, H.; Li, L.; Zhou, W.; Wang, H.; Zhang, Z.; Xing, H.; Yang, Q.; Zaworotko, M. J.; Ren, Q.; Chen, B. Fine Tuning and Specific Binding Sites with a Porous Hydrogen-Bonded Metal-Complex Framework for Gas Selective Separations. *J. Am. Chem. Soc.* **2018**, 140 (13), 4596–4603.

Barbour, L. J. Crystal Porosity and the Burden of Proof. *Chem. Commun.* **2006**, 11, 1163–1168.

Batten, S. R.; Champness, N. R.; Chen, X. M.; Garcia-Martinez, J.; Kitagawa, S.; Öhrström, L.; O’Keeffe, M.; Suh, M. P.; Reedijk, J. Coordination Polymers, Metal-Organic Frameworks and the Need for Terminology Guidelines. *CrystEngComm* **2012**, 14 (9), 3001–3004.

Batten, S. R.; Champness, N. R.; Chen, X. M.; Garcia-Martinez, J.; Kitagawa, S.; Öhrström, L.; O’Keeffe, M.; Suh, M. P.; Reedijk, J. Terminology of Metal-Organic Frameworks and Coordination Polymers (IUPAC Recommendations 2013). *Pure Appl. Chem.* **2013**, 85 (8), 1715–1724.

- Batten, S. R.; Hoskins, B. F.; Robson, R. Two Interpenetrating 3D Networks Which Generate Spacious Sealed-off Compartments Enclosing of the Order of 20 Solvent Molecules in the Structures of $\text{Zn}(\text{CN})(\text{NO}_3)(\text{Tpt})_{2/3} \cdot \text{cndot} \cdot \text{solv}$ (tpt= 2,4,6-Tri(4-Pyridyl)-1,3,5-Triazine, solv= .apprx.3/4 $\text{C}_2\text{H}_2\text{Cl}_4$.cndot.3/4 CH_3OH or .apprx.3/2 CHCl_3 .cndot.1/3 CH_3OH).Cndto. *J. Am. Chem. Soc.* **1995**, *117* (19), 5385–5386.
- Batten, S. R.; Robson, R. Interpenetrating Nets: Ordered, Periodic Entanglement. *Angew. Chemie - Int. Ed.* **1998**, *37* (11), 1460–1494.
- Baumann, A. E.; Burns, D. A.; Liu, B.; Thoi, V. S. Metal-Organic Framework Functionalization and Design Strategies for Advanced Electrochemical Energy Storage Devices. *Commun. Chem.* **2019**, *2* (1), 1–14.
- Bazer-Bachi, D.; Assié, L.; Lecocq, V.; Harbuzaru, B.; Falk, V. Towards Industrial Use of Metal-Organic Framework: Impact of Shaping on the MOF Properties. *Powder Technol.* **2014**, *255*, 52–59.
- Beck, W. M.; Calabrese, J. C.; Kottmair, N. D. Palladium(II) and Platinum(II) Complexes with Nucleobases and Nucleosides. Crystal Structure of Trans-Bis(Adeninato)Bis(Tri-n-Butylphosphine)Palladium(II). *Inorg. Chem.* **1979**, *18* (1), 176–182.
- Beobide, G.; Castillo, O.; Cepeda, J.; Luque, A.; Pérez-Yáñez, S.; Román, P.; Thomas-Gipson, J. Metal-Carboxylato-Nucleobase Systems: From Supramolecular Assemblies to 3D Porous Materials. *Coord. Chem. Rev.* **2013**, *257* (19–20), 2716–2736.
- Beobide, G.; Castillo, O.; Luque, A.; Pérez-Yáñez, S. Porous Materials Based on Metal-Nucleobase Systems Sustained by Coordination Bonds and Base Pairing Interactions. *CrystEngComm* **2015**, *17* (16), 3051–3059.
- Bergaoui, M.; Khalfaoui, M.; Awadallah-F, A.; Al-Muhtaseb, S. A Review of the Features and Applications of ZIF-8 and Its Derivatives for Separating CO_2 and Isomers of C3- and C4- Hydrocarbons. *J. Nat. Gas Sci. Eng.* **2021**, *96* (October), 104289.
- Bernstein, J.; Davis, R. E.; Shimoni, L.; Chang, N. Patterns in Hydrogen Bonding: Functionality and Graph Set Analysis in Crystals. *Angew Chem Int Ed* **1995**, *34*, 1555–1573.
- Bheekhun, N.; Abu Talib, A. R.; Hassan, M. R. Aerogels in Aerospace: An Overview. *Adv. Mater. Sci. Eng.* **2013**, *2013*, 1–19.
- Blatov, V. A. Multipurpose Crystallochemical Analysis with the Program Package TOPOS. *IUCr CompComm Newsl.* **2006**, *7*, 4–38.
- Blatov, V. A.; Shevchenko, A. P.; Proserpio, D. M. Applied Topological Analysis of Crystal Structures with the Program Package Topospro. *Cryst. Growth Des.* **2014**, *14* (7), 3576–3586.
- Blazevic, A.; Rompel, A. The Anderson-Evans Polyoxometalate: From Inorganic Building Blocks via Hybrid Organic-Inorganic Structures to Tomorrows “Bio-POM.” *Coord. Chem. Rev.* **2016**, *307*, 42–64.
- Bleaney, B.; Bowers, K. Anomalous Paramagnetism of Copper Acetate. *Proc R Soc Lond. A* **1952**, *214* (1119), 451–465.
- Boca, R. A Handbook of Magnetochemical Formulae; Elsevier: Amsterdam, Netherlands, **2012**.
- Boström, H. L. B.; Burrows, A.; Cass, M.; Chanteux, G.; Laybourn, A.; Li, Y.; Papathanasiou, K.; Patel, K.; Yaghi, O.; Yang, S. RSC Prize and Award Talk: 2020 Sustainable Water Award: General Discussion. *Faraday Discuss.* **2021**, *231*, 150–151.
- Braga, D.; Grepioni, F.; Orpen, G. Crystal Engineering: From Molecules and Crystals to Materials; Ed.; Springer Science Business Media Dordrecht: Erice, Italy, **1999**.
- Brown, D. The Chemical Bond in Inorganic Chemistry. The Bond Valence Model; Oxford science publications: Oxford, England, **2006**.
- Brown, O. L. I. The Clausius-Clapeyron Equation. *J. Chem. Educ.* **1950**, *2* (6), 1950–1951.

- Brunet, P.; Simard, M.; Wuest, J. D. Molecular Tectonics. Porous Hydrogen-Bonded Networks with Unprecedented Structural Integrity. *J. Am. Chem. Soc.* **1997**, *119* (11), 2737–2738.
- Bueken, B.; Van Velthoven, N.; Willhammar, T.; Stassin, T.; Stassen, I.; Keen, D. A.; Baron, G. V.; Denayer, J. F. M.; Ameloot, R.; Bals, S.; De Vos, D.; Bennett, T. D. Gel-Based Morphological Design of Zirconium Metal-Organic Frameworks. *Chem. Sci.* **2017**, *8* (5), 3939–3948.
- Burneo, I.; Stylianou, K. C.; Rodríguez-Hermida, S.; Juanhuix, J.; Fontrodona, X.; Imaz, I.; Maspoch, D. Two New Adenine-Based Co(II) Coordination Polymers: Synthesis, Crystal Structure, Coordination Modes, and Reversible Hydrochromic Behavior. *Cryst. Growth Des.* **2015**, *15* (7), 3182–3189.
- Burch, N. C.; Jasuja, H.; Walton, K. S. Water Stability and Adsorption in Metal-Organic Frameworks. *Chem. Rev.* **2014**, *114* (20), 10575–10612.
- Cai, M.; Qin, L.; You, L.; Yao, Y.; Wu, H.; Zhang, Z.; Zhang, L.; Yin, X.; Ni, J. Functionalization of MOF-5 with Mono-Substituents: Effects on Drug Delivery Behavior. *RSC Adv.* **2020**, *10* (60), 36862–36872.
- Cai, W.; Bocarsly, J. D.; Gomez, A.; Letona Lee, R. J.; Metta-Magaña, A.; Seshadri, R.; Echegoyen, L. High Blocking Temperatures for DyScS Endohedral Fullerene Single-Molecule Magnets. *Chem. Sci.* **2020**, *11* (48), 13129–13136.
- Canivet, J.; Fateeva, A.; Guo, Y.; Coasne, B., Adsorption in MOFs : Fundamentals and Applications. *Chem. Soc. Rev.* **2014**, *43* (16), 5594–5617.
- Carné, A.; Carbonell, C.; Imaz, I.; Maspoch, D. Nanoscale Metal–Organic Materials. *Chem. Soc. Rev.* **2011**, *40* (1), 291–305.
- Cavka, J. H.; Jakobsen, S.; Olsbye, U.; Guillou, N.; Lamberti, C.; Bordiga, S.; Lillerud, K. P. A New Zirconium Inorganic Building Brick Forming Metal Organic Frameworks with Exceptional Stability. *J. Am. Chem. Soc.* **2008**, *130* (42), 13850–13851.
- Cepeda, J.; Castillo, O.; García-Terán, J. P.; Luque, A.; Pérez-Yáñez, S.; Roman, P. Supramolecular Architectures and Magnetic Properties of Self-Assembled Windmill-like Dinuclear Copper(II) Complexes with Purine Ligands. *Eur. J. Inorg. Chem.* **2009**, *16*, 2344–2353.
- Cepeda, J.; Pérez-Yáñez, S. Funtzio Anitzeko Polimero Metal-Organiko Porotsuak (MOF): Etorkizuneko Material Adimendunei Begira. *EKAIA Euskal Herriko Unibertsitateko Zientzi eta Teknol. Aldizkaria* **2017**, *31* (31), 105–116.
- Cheetham, A. K.; Férey, G.; Loiseau, T. Open-Framework Inorganic Materials. *Angew. Chemie - Int. Ed.* **1999**, *38* (22), 3268–3292.
- Chen, T. H.; Popov, I.; Kaveevivitchai, W.; Miljanić, O. Š. Metal-Organic Frameworks: Rise of the Ligands. *Chem. Mater.* **2014**, *26* (15), 4322–4325.
- Chen, Y.; Huang, X.; Zhang, S.; Li, S.; Cao, S.; Pei, X.; Zhou, J.; Feng, X.; Wang, B. Shaping of Metal-Organic Frameworks: From Fluid to Shaped Bodies and Robust Foams. *J. Am. Chem. Soc.* **2016**, *138* (34), 10810–10813.
- Chen, Z.; Hanna, S. L.; Redfern, L. R.; Alezi, D.; Islamoglu, T.; Farha, O. K. Reticular Chemistry in the Rational Synthesis of Functional Zirconium Cluster-Based MOFs. *Coord. Chem. Rev.* **2019**, *386*, 32–49.
- Chen, Z.; Kirlikovali, K. O.; Li, P.; Farha, O. K. Reticular Chemistry for Highly Porous Metal-Organic Frameworks: The Chemistry and Applications. *Acc. Chem. Res.* **2022**, *55* (4), 579–591.
- Cheng, S.; Chen, W.; Zhao, L.; Wang, X.; Qin, C.; Su, Z. Synthesis, Crystal Structure and Iodine Capture of Zr-Based Metal-Organic Polyhedron. *Inorganica Chim. Acta* **2021**, *516* (5268), 120174.
- Chui, S. S. Y.; Lo, S. M. F.; Charmant, J. P. H.; Orpen, A. G.; Williams, I. D. A Chemically Functionalizable Nanoporous Material [Cu₃(TMA)₂(H₂O)₃](N). *Science*, **1999**, *283* (5405), 1148–1150.

- Clearfield, A.; Vaughan, P. A. The Crystal Structure of Zirconyl Chloride Octahydrate and Zirconyl Bromide Octahydrate. *Acta Crystallogr.* **1956**, *9* (7), 555–558.
- Connolly, B. M.; Aragoes-Anglada, M.; Gandara-Loe, J.; Danaf, N. A.; Lamb, D. C.; Mehta, J. P.; Vulpe, D.; Wuttke, S.; Silvestre-Albero, J.; Moghadam, P. Z.; Wheatley, A. E. H.; Fairen-Jimenez, D. Tuning Porosity in Macroscopic Monolithic Metal-Organic Frameworks for Exceptional Natural Gas Storage. *Nat. Commun.* **2019**, *10* (1), 1–11.
- Cook, T. R.; Zheng, Y. R.; Stang, P. J. Metal-Organic Frameworks and Self-Assembled Supramolecular Coordination Complexes: Comparing and Contrasting the Design, Synthesis, and Functionality of Metal-Organic Materials. *Chem. Rev.* **2013**, *113* (1), 734–777.
- Cozak, D.; Mardhy, A.; Olivier, M. J.; Beauchamp, A. L. N7/O6 Chelation in a Complex with an Analogue of Guanine. Preparation, Spectroscopic Study, and Crystal Structure of Bis(H5-Cyclopentadienyl)(Theophyllinato)Titanium(III). *Inorg. Chem.* **1986**, *25* (15), 2600–2606.
- Cram, D. J.; Cram, J. M. Host Guest Chemistry. *Science*, **1974**, *183* (4127), 803–809.
- CrysAlisPro. Oxford Diffraction /Agilent Technologies UK Ltd: Yarnton, England.
- Cysewski, P. A Post-SCF Complete Basis Set Study on the Recognition Patterns of Uracil and Cytosine by Aromatic and p-Stacking Interactions with Amino Acid Residues. *Phys. Chem. Chem. Phys.* **2008**, *10*, 2636–2645.
- Das, S.; Heasman, P.; Ben, T.; Qiu, S. Porous Organic Materials: Strategic Design and Structure-Function Correlation. *Chem. Rev.* **2017**, *117* (3), 1515–1563.
- de Meester, P.; Skapski, A. C. Crystal Atructure of Octachlorobis(Adeninium)Tricopper(II) Tetrahydrate : A Trinuclear Complex with Bridging Adenine. *J. Chem. Soc. Dalt. Trans.* **1972**, *1596*, 2400–2404.
- de Meester, P.; Skapski, A. C. Crystal Structure of Dibromodiadeniumcopper(II) Dibromide: A Complex with Unidentate Adenine. *J. Chem. Soc. Dalt. Trans.* **1972**, *424*, 424–427.
- De Meester, P.; Skapski, A. C. Crystal Structure of Dichlorotetra-Mu-Adenine-Dicopper(II) Chloride Hexahydrate. *Inorg. Phys. Theor.* **1970**, *A13*, 2167–2169.
- Deng, H.; Grunder, S.; Cordova, K. E.; Valente, C.; Furukawa, H.; Hmadeh, M.; Gándara, F.; Whalley, A. C.; Liu, Z.; Asahina, S.; Kazumori, H.; O’Keeffe, M.; Terasaki, O.; Stoddart, J. F.; Yaghi, O. M. Large-Pore Apertures in a Series of Metal-Organic Frameworks. *Science*, **2012**, *336* (6084), 1018–1023.
- Deng, Y. K.; Su, H. F.; Xu, J. H.; Wang, W. G.; Kurmoo, M.; Lin, S. C.; Tan, Y. Z.; Jia, J.; Sun, D.; Zheng, L. S. Hierarchical Assembly of a {Mn^{II}₁₅Mn^{III}₄} Brucite Disc: Step-by-Step Formation and Ferrimagnetism. *J. Am. Chem. Soc.* **2016**, *138* (4), 1328–1334.
- Deria, P.; Bury, W.; Hod, I.; Kung, C. W.; Karagiari, O.; Hupp, J. T.; Farha, O. K. MOF Functionalization via Solvent-Assisted Ligand Incorporation: Phosphonates vs Carboxylates. *Inorg. Chem.* **2015**, *54* (5), 2185–2192.
- Desiraju, G. R. Crystal Engineering. The Design of Organic Solids; Elsevier: Amsterdam, Netherlands, **1989**.
- Desiraju, G. R. Crystal Engineering: From Molecule to Crystal. *J. Am. Chem. Soc.* **2013**, *135* (27), 9952–9967.
- Desiraju, G. R. Designing Organic Crystals. *Prog. Solid State Chem* **1987**, *17*, 295–353.
- Desiraju, G. R. The Supramolecular Synthons in Crystal Engineering. *Angew. Chem. Ed. Engl.* **1995**, *34*, 2311–2327.
- Devic, T.; Serre, C. High Valence 3p and Transition Metal Based MOFs. *Chem. Soc. Rev.* **2014**, *43* (16), 6097–6115.

- Dhotel, A.; Chen, Z.; Delbreilh, L.; Youssef, B.; Saiter, J. M.; Tan, L. Molecular Motions in Functional Self-Assembled Nanostructures. *Int. J. Mol. Sci.* **2013**, *14* (2), 2303–2333.
- Ding, M.; Cai, X.; Jiang, H. L. Improving MOF Stability: Approaches and Applications. *Chem. Sci.* **2019**, *10* (44), 10209–10230.
- Ding, Y.; Pan, L.; Li, S.; He, H.; Zhang, D.; Hu, X.; Zhang, R.; Wang, Y.; Zhai, X.; Meng, Q. Fabrication and Investigation of 26NCA Films Exhibiting Tunable Blue Fluorescence Based on LVPVDM. *J. Nanomater.* **2018**, *2018*, 5426427.
- Düren, T.; Millange, F.; Férey, G.; Walton, K. S.; Snurr, R. Q. Calculating Geometric Surface Areas as a Characterization Tool for Metal–Organic Frameworks. *J. Phys. Chem. C* **2007**, *111* (42), 15350–15356.
- Earnshaw, A. Introduction to Magnetochemistry; Academic Press: London, England, **1968**.
- Eddaoudi, M.; Kim, J.; Rosi, N.; Vodak, D.; Wachter, J.; O’Keeffe, M.; Yaghi, O. M. Systematic Design of Pore Size and Functionality in Isorecticular MOFs and Their Application in Methane Storage. *Science* **2002**, *295* (5554), 469–472.
- Eddaoudi, M.; Moler, D. B.; Li, H.; Chen, B.; Reineke, T. M.; O’Keeffe, M.; Yaghi, O. M. Modular Chemistry: Secondary Building Units as a Basis for the Design of Highly Porous and Robust Metal–Organic Carboxylate Frameworks. *Acc. Chem. Res.* **2001**, *34* (4), 319–330.
- Etter, M. C. Encoding and Decoding Hydrogen-Bond Patterns of Organic Compounds. *Acc. Chem. Res.* **1990**, *23* (3), 120–126.
- Etter, M. C. Hydrogen Bonds as Design Elements in Organic Chemistry. *J. Phys. Chem.* **1991**, *95* (8), 4601–4610.
- Etter, M. C.; Urbakzyk-lipkowska, Z.; Zia-ebrahimi, S. M.; Panunto, T. W. Hydrogen Bond Directed Cococrystallization and Molecular Recognition Properties of Diarylureas. *J. Am. Chem. Soc.* **1990**, *112* (3), 8415–8426.
- Fairley, N.; Fernandez, V.; Richard-Plouet, M.; Guillot-Deudon, C.; Walton, J.; Smith, E.; Flahaut, D.; Greiner, M.; Biesinger, M.; Tougaard, S.; Morgan, D.; Baltrusaitis, J. Systematic and Collaborative Approach to Problem Solving Using X-Ray Photoelectron Spectroscopy. *Appl. Surf. Sci. Adv.* **2021**, *5* (May), 100112.
- Farrugia, L. J. WinGX and ORTEP for Windows: An Update. *J. Appl. Crystallogr.* **2012**, *45* (4), 849–854.
- Feng, D.; Chung, W. C.; Wei, Z.; Gu, Z. Y.; Jiang, H. L.; Chen, Y. P.; Darensbourg, D. J.; Zhou, H. C. Construction of Ultrastable Porphyrin Zr Metal–Organic Frameworks through Linker Elimination. *J. Am. Chem. Soc.* **2013**, *135* (45), 17105–17110.
- Feng, L.; Pang, J.; She, P.; Li, J. L.; Qin, J. S.; Du, D. Y.; Zhou, H. C. Metal–Organic Frameworks Based on Group 3 and 4 Metals. *Adv. Mater.* **2020**, *32* (44), 1–31.
- Férey, G. Hybrid Porous Solids: Past, Present, Future. *Chem. Soc. Rev.* **2008**, *37* (1), 191–214.
- Férey, G. Microporous Solids: From Organically Templated Inorganic Skeletons to Hybrid Frameworks...Ecumenism in Chemistry. *Chem. Mater.* **2001**, *13* (10), 3084–3098.
- Férey, G.; Serre, C. Large Breathing Effects in Three-Dimensional Porous Hybrid Matter: Facts, Analyses, Rules and Consequences. *Chem. Soc. Rev.* **2009**, *38* (5), 1380–1399.
- Férey, G.; Serre, C.; Mellot-Draznieks, C.; Millange, F.; Surblé, S.; Dutour, J.; Margiolaki, I. A Hybrid Solid with Giant Pores Prepared by a Combination of Targeted Chemistry, Simulation, and Powder Diffraction. *Angew. Chemie - Int. Ed.* **2004**, *43* (46), 6296–6301.
- Férey, G.; Serre, C.; Millange, F.; Dutour, J.; Surblé, S.; Férey, G.; Serre, C.; Millange, F.; Dutour, J. A Chromium Terephthalate-Based Solid with Unusually Large Pore Volumes and Surface Area. *Science*, **2005**, *309*, 2040–2042.

- Fidalgo-marijuan, A.; Barandika, G. Fe–TPP Coordination Network with Metalloporphyrinic Neutral Radicals and Face-to-Face and Edge-to-Face π – π Stacking. *Inorg. Chem.* **2013**, *52*, 8074–8081.
- Finn, M. G.; Fokin, V. V. Click Chemistry: Function Follows Form. *Chem. Soc. Rev.* **2010**, *39* (4), 1231–1232.
- Formalik, F.; Neimark, A. V.; Rogacka, J.; Firlej, L.; Kuchta, B. Pore Opening and Breathing Transitions in Metal-Organic Frameworks: Coupling Adsorption and Deformation. *J. Colloid Interface Sci.* **2020**, *578*, 77–88.
- Forrest, K. A.; Pham, T.; Chen, K. J.; Jiang, X.; Madden, D. G.; Franz, D. M.; Hogan, A.; Zaworotko, M. J.; Space, B. Tuning the Selectivity between C₂H₂ and CO₂ in Molecular Porous Materials. *Langmuir* **2021**, *37* (47), 13838–13845.
- Fournier, J. H.; Maris, T.; Wuest, J. D.; Guo, W.; Galoppini, E. Molecular Tectonics. Use of the Hydrogen Bonding of Boronic Acids to Direct Supramolecular Construction. *J. Am. Chem. Soc.* **2003**, *125* (4), 1002–1006.
- Freund, R.; Canossa, S.; Cohen, S. M.; Yan, W.; Deng, H.; Guillerm, V.; Eddaoudi, M.; Madden, D. G.; Fairen-Jimenez, D.; Lyu, H.; Macreadie, L. K.; Ji, Z.; Zhang, Y.; Wang, B.; Haase, F.; Wöll, C.; Zaremba, O.; Andreato, J.; Wuttke, S.; Diercks, C. S. 25 Years of Reticular Chemistry. *Angew. Chemie - Int. Ed.* **2021**, *60* (45), 23946–23974.
- Fujita, M.; Washizu, S.; Ogura, K.; Kwon, Y. J. Preparation, Clathration Ability, and Catalysis of a Two-Dimensional Square Network Material Composed of Cadmium(II) and 4, 4'-Bipyridine. *J. Am. Chem. Soc.* **1994**, *116* (3), 1151–1152.
- Furukawa, H.; Cordova, K. E.; O’Keeffe, M.; Yaghi, O. M. The Chemistry and Applications of Metal-Organic Frameworks. *Science*, **2013**, *341* (6149), 1320444.
- Furukawa, H.; Gándara, F.; Zhang, Y. B.; Jiang, J.; Queen, W. L.; Hudson, M. R.; Yaghi, O. M. Water Adsorption in Porous Metal-Organic Frameworks and Related Materials. *J. Am. Chem. Soc.* **2014**, *136* (11), 4369–4381.
- Furukawa, H.; Go, Y. B.; Ko, N.; Park, Y. K.; Uribe-Romo, F. J.; Kim, J.; O’Keeffe, M.; Yaghi, O. M. Isoreticular Expansion of Metal-Organic Frameworks with Triangular and Square Building Units and the Lowest Calculated Density for Porous Crystals. *Inorg. Chem.* **2011**, *50* (18), 9147–9152.
- Furukawa, H.; Ko, N.; Go, Y. B.; Aratani, N.; Choi, S. B.; Choi, E.; Yazaydin, A. Ö.; Snurr, R. Q.; O’Keeffe, M.; Kim, J.; Yaghi, O. M. Ultrahigh Porosity in Metal-Organic Frameworks. *Science*, **2010**, *329* (5990), 424–428.
- Gagnon, C.; Hubert, J.; Rivest, R.; Beauchamp, A. L. Crystal Structure of Di- μ -Adeninium-Dsilver(I) Perchlorate Monohydrate. *Inorg. Chem.* **1977**, *16* (10), 2469–2473.
- Gándara, F. Metal-Organic Frameworks: Nuevos Materiales Con Espacios Llenos de Posibilidades. *An. R. Soc.* **2012**, *108* (3), 190–196.
- Gándara, F.; Bennett, T. D. Crystallography of Metal-Organic Frameworks. *IUCrJ* **2014**, *1*, 563–570.
- Gangu, K. K.; Dadhich, A. S.; Mukkamala, S. B. Synthesis, Crystal Structure and Fluorescent Properties of Two Metal-Organic Frameworks Constructed from Cd(II) and 2,6-Naphthalene Dicarboxylic Acid. *Inorg. Nano-Metal Chem.* **2017**, *47* (3), 313–319.
- García-Raso, A.; Terrón, A.; Roselló, Y.; Frontera, A.; Castillo, O.; Beobide, G.; Pérez-Yáñez, S.; Escudero-Adán, E. C.; Fiol, J. J. Metal Removal from the Secondary Building Unit of Bio-MOF-1 by Adenine N6-Alkylation While Retaining the Overall 3D Porous Topology. *CrystEngComm* **2020**, *22* (25), 4201–4205.
- García-Terán, J. P.; Castillo, O.; Luque, A.; García-Couceiro, U.; Román, P.; Lezama, L. An Unusual 3D Coordination Polymer Based on Bridging Interactions of the Nucleobase Adenine. *Inorg. Chem.* **2004**, *43* (15), 4549–4551.

- Gates-Rector, S.; Blanton, T. The Powder Diffraction File: A Quality Materials Characterization Database. *Powder Diffr.* **2019**, *34* (4), 352–360.
- Gattuso, G.; Manfredi, G.; Sammartano, S. Quantitative Study on the Non-Covalent Interactions between ATP and Caffeine, Theophylline and Theobromine in Aqueous Solution. *Fluid Phase Equilib.* **2011**, *308* (1–2), 47–54.
- Ghose, R. Complex Formation of Adenine-Uracil Base Pair with Some Transition Metal Ions. *Inorganica Chim. Acta* **1989**, *156* (2), 303–306.
- Gibson, G. T. T.; Mohamed, M. F.; Neverov, A. A.; Brown, R. S. Potentiometric Titration of Metal Ions in Ethanol. *Inorg. Chem.* **2006**, *45* (19), 7891–7902.
- Gierlotka, W.; Chen, S. W. Thermodynamic Descriptions of the Cu-Zn System. *J. Mater. Res.* **2008**, *23* (1), 258–263.
- Gil, A.; Santamaría, L.; Korili, S. A.; Vicente, M. A.; Barbosa, L. V.; de Souza, S. D.; Marçal, L.; de Faria, E. H.; Ciuffi, K. J. A Review of Organic-Inorganic Hybrid Clay Based Adsorbents for Contaminants Removal: Synthesis, Perspectives and Applications. *J. Environ. Chem. Eng.* **2021**, *9* (5), 105808.
- Giles-Mazón, E. A.; Germán-Ramos, I.; Romero-Romero, F.; Reinheimer, E.; Toscano, R. A.; Lopez, N.; Barrera-Díaz, C. E.; Varela-Guerrero, V.; Ballesteros-Rivas, M. F. Synthesis and Characterization of a Bio-MOF Based on Mixed Adeninate/Tricarboxylate Ligands and Zinc Ions. *Inorganica Chim. Acta* **2018**, *469*, 306–311.
- Gładysiak, A.; Nguyen, T. N.; Anderson, S. L.; Boyd, P. G.; Palgrave, R. G.; Bacsá, J.; Smit, B.; Rosseinsky, M. J.; Stylianou, K. C. Shedding Light on the Protonation States and Location of Protonated N Atoms of Adenine in Metal-Organic Frameworks. *Inorg. Chem.* **2018**, *57* (4), 1888–1900.
- Gong, W.; Xie, H.; Idrees, K. B.; Son, F. A.; Chen, Z.; Sha, F.; Liu, Y.; Cui, Y.; Farha, O. K. Water Sorption Evolution Enabled by Reticular Construction of Zirconium Metal-Organic Frameworks Based on a Unique [2.2]Paracyclophane Scaffold. *J. Am. Chem. Soc.* **2022**, *144* (4), 1826–1834.
- Gong, Y. N.; Zhong, D. C.; Lu, T. B. Interpenetrating Metal-Organic Frameworks. *CrystEngComm* **2016**, *18* (15), 2596–2606.
- Gong, Y.; Zhou, Y. C.; Yang, H.; Zhang, H. X.; Proserpio, D. M.; Zhang, J. A New Approach towards Tetrahedral Imidazolate Frameworks for High and Selective CO₂ Uptake. *Chem. Commun.* **2011**, *47* (20), 5828–5830.
- Gonzalez-Pérez, J. M.; Alarcon-Payer, C.; Castiñeiras, A.; Pivetta, T.; Lezama, L.; Choquesillo-Lazarte, D.; Crisponi, G.; Niclós-Gutiérrez, J. A Windmill-Shaped Hexacopper(II) Molecule Built up by Template Dicopper (II) with Aqua (Oxydiacetato)Copper(II). *Inorg. Chem.* **2006**, *139* (2), 877–882.
- Gosselin, A. J.; Rowland, C. A.; Bloch, E. D. Permanently Microporous Metal-Organic Polyhedra. *Chem. Rev.* **2020**, *120* (16), 8987–9014.
- Grimme, S. Do Special Noncovalent π - π Stacking Interactions Really Exist? *Angew Chem Int Ed* **2008**, *47*, 3430–3434.
- Groom, C. R.; Bruno, I. J.; Lightfoot, M. P.; Ward, S. C. The Cambridge Structural Database. *Acta Crystallogr. Sect. B Struct. Sci. Cryst. Eng. Mater.* **2016**, *72* (2), 171–179.
- Gropp, C.; Canossa, S.; Wuttke, S.; Gándara, F.; Li, Q.; Gagliardi, L.; Yaghi, O. M. Standard Practices of Reticular Chemistry. *ACS Cent. Sci.* **2020**, *6* (8), 1255–1273.
- Guillerm, V.; Grancha, T.; Imaz, I.; Juanhuix, J.; MasPOCH, D. Zigzag Ligands for Transversal Design in Reticular Chemistry: Unveiling New Structural Opportunities for Metal-Organic Frameworks. *J. Am. Chem. Soc.* **2018**, *140* (32), 10153–10157.
- Gumerova, N. I.; Rompel, A. Polyoxometalates in Solution: Speciation under Spotlight. *Chem. Soc. Rev.* **2020**, *49* (21), 7568–7601.

- Guo, L. Y.; Su, H. F.; Kurmoo, M.; Tung, C. H.; Sun, D.; Zheng, L. S. Core-Shell {Mn₇C(Mn,Cd)₁₂} Assembled from Core {Mn₇} Disc. *J. Am. Chem. Soc.* **2017**, *139* (40), 14033–14036.
- Gupta, R. K.; Riaz, M.; Ashafaq, M.; Gao, Z.-Y.; Varma, R. S.; Li, D.-C.; Cui, P.; Tung, C.-H.; Sun, D. Adenine-Incorporated Metal–Organic Frameworks. *Coord. Chem. Rev.* **2022**, *464*, 214558.
- Hadjiliadis, N.; Sletten, E. Metal Complex- DNA Interactions; Wiley: Hoboken, New Jersey, (United States), **2009**.
- Hanikel, N.; Prévot, M. S.; Fathieh, F.; Kapustin, E. A.; Lyu, H.; Wang, H.; Diercks, N. J.; Glover, T. G.; Yaghi, O. M. Rapid Cycling and Exceptional Yield in a Metal-Organic Framework Water Harvester. *ACS Cent. Sci.* **2019**, *5* (10), 1699–1706.
- Hayashi, Soichi; Kimura, N. C. Infrared Spectra and Molecular Configuration of Benzoic Acid (Special Issue on Physical Chemistry). *Bull. Inst. Chem. Res. - Kyoto Univ.* **1966**, *44* (4), 335–340.
- He, Y.; Xiang, S.; Chen, B. A Microporous Hydrogen-Bonded Organic Framework for Highly Selective C₂H₂/C₂H₄ Separation at Ambient Temperature. *J. Am. Chem. Soc.* **2011**, *133* (37), 14570–14573.
- Healy, C.; Patil, K. M.; Wilson, B. H.; Hermanspahn, L.; Harvey-Reid, N. C.; Howard, B. I.; Kleinjan, C.; Kolien, J.; Payet, F.; Telfer, S. G.; Kruger, P. E.; Bennett, T. D. The Thermal Stability of Metal-Organic Frameworks. *Coord. Chem. Rev.* **2020**, *419*, 213388.
- Herdes, C.; Sarkisov, L. Computer Simulation of Volatile Organic Compound Adsorption in Atomistic Models of Molecularly Imprinted Polymers. *Lagmuir* **2009**, *25*, 5352–5359.
- Hisaki, I.; Xin, C.; Takahashi, K.; Nakamura, T. Designing Hydrogen-Bonded Organic Frameworks (HOFs) with Permanent Porosity. *Angew. Chemie - Int. Ed.* **2019**, *58* (33), 11160–11170.
- Holst, J. R.; Trewin, A.; Cooper, A. I. Porous Organic Molecules. *Nat. Chem.* **2010**, *2* (11), 915–920.
- Hoskins, B. F.; Robson, R. Infinite Polymeric Frameworks Consisting of Three Dimensionally Linked Rod-like Segments. *Am. Chem. Soc.* **1989**, *111* (15), 5964–5965.
- Hou, J.; Sapnik, A. F.; Bennett, T. D. Metal-Organic Framework Gels and Monoliths. *Chem. Sci.* **2020**, *11* (2), 310–323.
- Howarth, A. J.; Liu, Y.; Li, P.; Li, Z.; Wang, T. C.; Hupp, J. T.; Farha, O. K. Chemical, Thermal and Mechanical Stabilities of Metal-Organic Frameworks. *Nat. Rev. Mater.* **2016**, *1* (15018), 1–16.
- Howarth, A. J.; Peters, A. W.; Vermeulen, N. A.; Wang, T. C.; Hupp, J. T.; Farha, O. K. Best Practices for the Synthesis, Activation, and Characterization of Metal–Organic Frameworks. *Chem. Mater.* **2017**, *29* (1), 26–39.
- Hu, Y. Q.; Zeng, M. H.; Zhang, K.; Hu, S.; Zhou, F. F.; Kurmoo, M. Tracking the Formation of a Polynuclear Co₁₆ Complex and Its Elimination and Substitution Reactions by Mass Spectroscopy and Crystallography. *J. Am. Chem. Soc.* **2013**, *135* (21), 7901–7908.
- Hubert, J.; Beauchamp, A. L. Structure of μ₃-(adeninato-N3, N7, N9)-Tris[Methylmercury(II)] Nitrate. *Acta Crystallogr.* **1980**, *B36*, 2613–2616.
- Hunter, C. A.; Lawson, K. R.; Urch, C. J. Aromatic Interactions. *J. Chem. Soc. Perkin Trans* **2001**, *2*, 651–669.
- Hunter, C. A.; Sanders, J. K. M. The Nature of P-p Interactions. *J. Am. Chem. Soc.* **1990**, *112* (2), 5525–5534.
- Hurlock, M. J.; Hao, L.; Kriegsman, K. W.; Guo, X.; O’Keeffe, M.; Zhang, Q. Evolution of 14-Connected Zr₆ Secondary Building Units through Postsynthetic Linker Incorporation. *ACS Appl. Mater. Interfaces* **2021**, *13* (44), 51945–51953.
- Husain, A.; Parveen, R.; Dastidar, P. New Series of ZnII/CdII Mixed Ligand Coordination Polymers: Toward the Design of Metallogels. *Cryst. Growth Des.* **2015**, *15* (10), 5075–5085.

- Hüsing, N.; Schubert, U. Aerogels-Airy Materials: Chemistry, Structure and Properties. *Angew Chem Int Ed Engl* **1998**, *37*, 22–45.
- Imaz, I.; Rubio-Martínez, M.; An, J.; Solé-Font, I.; Rosi, N. L.; Maspoch, D. Metal-Biomolecule Frameworks (MBioFs). *Chem. Commun.* **2011**, *47* (26), 7287–7302.
- Ishizaki, K.; Komarneni, S.; Nanko, M. Porous Materials. Applications of Porous Materials, Netherland.; Springer Science Business Media Dordrecht, **1998**.
- Izatt, R. M.; Schoedel, A.; Yaghi, O. M. Macrocyclic and Supramolecular Chemistry: How Izatt–Christensen Award Winners Shaped the Field; John Wiley & Sons, **2016**.
- Jadrijevic-Mladar Takac, M.; Topić, D. V. FT-IR and NMR Spectroscopic Studies of Salicylic Acid Derivatives. II. Comparison of 2-Hydroxy- and 2,4- and 2,5-Dihydroxy Derivatives. *Acta Pharm.* **2004**, *54* (3), 177–191.
- James, S. L. Metal–Organic Frameworks. *Chem. Soc. Rev.* **2003**, *32* (5), 276–288.
- Ji, B. Q.; Su, H. F.; Jagodič, M.; Jagličić, Z.; Kurmoo, M.; Wang, X. P.; Tung, C. H.; Cao, Z. Z.; Sun, D. Self-Organization into Preferred Sites by Mg^{II}, Mn^{II}, and Mn^{III} in Brucite-Structured M₁₉ Cluster. *Inorg. Chem.* **2019**, *58* (6), 3800–3806.
- Jiang, H.; Alezi, D.; Eddaoudi, M. A Reticular Chemistry Guide for the Design of Periodic Solids. *Nat. Rev. Mater.* **2021**, *6* (6), 466–487.
- Jiang, J.; Zhao, Y.; Yaghi, O. M. Covalent Chemistry beyond Molecules. *J. Am. Chem. Soc.* **2016**, *138* (10), 3255–3265.
- Johnson, I. M.; Prakash, H.; Prathiba, J.; Raghunathan, R.; Malathi, R. Spectral Analysis of Naturally Occurring Methylxanthines (Theophylline, Theobromine and Caffeine) Binding with DNA. *PLoS One* **2012**, *7* (12).
- Ju, Z.; Liu, G.; Chen, Y. S.; Yuan, D.; Chen, B. From Coordination Cages to a Stable Crystalline Porous Hydrogen-Bonded Framework. *Chem.- A Eur. J.* **2017**, *23* (20), 4774–4777.
- Juneau, M.; Vonglis, M.; Hartvigsen, J.; Frost, L.; Bayerl, D.; Dixit, M.; Mpourmpakis, G.; Morse, J. R.; Baldwin, J. W.; Willauer, H. D.; Porosoff, M. D. Assessing the Viability of K-Mo₂C for Reverse Water-Gas Shift Scale-up: Molecular to Laboratory to Pilot Scale. *Energy Environ. Sci.* **2020**, *13* (8), 2524–2539.
- Jung, J. H.; Lee, J. H.; Silverman, J. R.; John, G. Coordination Polymer Gels with Important Environmental and Biological Applications. *Chem. Soc. Rev.* **2013**, *42* (3), 924–936.
- Junk, A.; Riess, F. From an Idea to a Vision: There’s Plenty of Room at the Bottom. *Am. J. Phys.* **2006**, *74* (9), 825–830.
- Kalmutzki, M. J.; Hanikel, N.; Yaghi, O. M. Secondary Building Units as the Turning Point in the Development of the Reticular Chemistry of MOFs. *Sci. Adv.* **2018**, *4* (10), 1–16.
- Kamiya, Y.; Sano, S.; Miura, Y. K.; Uchida, Y.; Ogawa, Y.; Iwase, Y.; Okuhara, T.; Degnan, T. F. Microporous Acidic Cesium Salt of 12-Tungstosilicic Acid Cs₃H₃Si₁₂O₄₀ as a Size-Selective Solid Acid Catalyst. *Chem. Lett.* **2010**, *39* (8), 881–883.
- Kickelbick, G.; Schubert, U. Oxozirconium Methacrylate Clusters: Zr₆(OH)₄O₄(OMc)₁₂ and Zr₄O₂(OMc)₁₂ (OMc= Methacrylate). *Chem. Ber.* **1997**, *130* (4), 473–478.
- Kickelbick, G.; Wiede, P.; Schubert, U. Variations in Capping the Zr₆O₄(OH)₄ Cluster Core: X-Ray Structure Analyses of [Zr₆(OH)₄O₄(OOC-CH=CH₂)₁₀]₂(μ-OOC-CH=CH₂)₄ and Zr₆(OH)₄O₄(OOCR)₁₂ (PrOH) (R = Ph, CMe = CH₂). *Inorganica Chim. Acta* **1999**, *284* (1), 1–7.
- Kim, H.; Cho, H. J.; Narayanan, S.; Yang, S.; Furukawa, H.; Schiffres, S.; Li, X.; Zhang, Y. B.; Jiang, J.; Yaghi, O. M.; Wang, E. N. Characterization of Adsorption Enthalpy of Novel Water-Stable Zeolites and Metal–Organic Frameworks. *Sci. Rep.* **2016**, *6* (January), 1–8.

- Kim, H.; Kim, Y.; Yoon, M.; Lim, S.; Park, S. M.; Seo, G.; Kim, K. Highly Selective Carbon Dioxide Sorption in an Organic Molecular Porous Material. *J. Am. Chem. Soc.* **2010**, *132* (35), 12200–12202.
- Kim, J.; Chen, B.; Reineke, T. M.; Li, H.; Eddaoudi, M.; Moler, D. B.; O’Keeffe, M.; Yaghi, O. M. Assembly of Metal-Organic Frameworks from Large Organic and Inorganic Secondary Building Units: New Examples and Simplifying Principles for Complex Structures. *J. Am. Chem. Soc.* **2001**, *123* (34), 8239–8247.
- Kirchon, A.; Feng, L.; Drake, H. F.; Joseph, E. A.; Zhou, H. C. From Fundamentals to Applications: A Toolbox for Robust and Multifunctional MOF Materials. *Chem. Soc. Rev.* **2018**, *47* (23), 8611–8638.
- Kistler, S. S. Coherent Expanded Aerogels and Jellies. *Nature* **1931**, *127* (741), 3211.
- Kistler, S. S. Coherent Expanded Aerogels. *J. Phys. Chem.* **1932**, *36* (1), 52–64.
- Kitagawa, S.; Kitaura, R.; Noro, S. I. Functional Porous Coordination Polymers. *Angew. Chemie - Int. Ed.* **2004**, *43* (18), 2334–2375.
- Kitagawa, S.; Matsuda, R. Chemistry of Coordination Space of Porous Coordination Polymers. *Coord. Chem. Rev.* **2007**, *251* (21–24), 2490–2509.
- Kondo, M.; Yoshitomi, T.; Seki, K.; Matsuzaka, H.; Kitagawa, S. Three-Dimensional Framework with Channeling. *Angew Chem Int Ed Engl* **1997**, *36* (16), 1725–1727.
- Kornienko, N.; Zhao, Y.; Kley, C. S.; Zhu, C.; Kim, D.; Lin, S.; Chang, C. J.; Yaghi, O. M.; Yang, P. Metal-Organic Frameworks for Electrocatalytic Reduction of Carbon Dioxide. *J. Am. Chem. Soc.* **2015**, *137* (44), 14129–14135.
- Kurmoo, M. Magnetic Metal–Organic Frameworks. *Chem. Soc. Rev.* **2009**, *38* (5), 1353–1379.
- Lan, J.; Wang, Y.; Huang, B.; Xiao, Z.; Wu, P. Application of Polyoxometalates in Photocatalytic Degradation of Organic Pollutants. *Nanoscale Adv.* **2021**, *3* (16), 4646–4658.
- Lauher, J. W. A Versatile Molecular Trap Built from Hydrogen-Bonded Tiles. *Science*, **2011**, *333* (6041), 415–416.
- Lehn, J. M. Cryptates: Inclusion Complexes of Macropolycyclic Receptor Molecules. *Chem., Pure Appl.* **1978**, *50*, 871–892.
- Leite Ferreira, B.J.M.; Brandão, P.; Dos Santos, A.M.; Gai, Z.; Cruz, C.; Reis, M.S.; Santos, T. M.; Félix, V. Heptacopper(II) and Dicopper(II)-Adenine Complexes: Synthesis, Structural Characterization, and Magnetic Properties. *J. Coord. Chem.* **2015**, *68*, 2770–2787.
- Lett, M. A. C. P.; Gardner, G. B.; Venkataramant, D.; Mooreh, J. S.; Lee, S. Hinged Coordination Network. *Lett. to Nat.* **1995**, *374* (April), 792–795.
- Li, D.; Kassymova, M.; Cai, X.; Zang, S.; Jiang, H. Photocatalytic CO₂ Reduction over Metal-Organic Framework-Based Materials. *Coord. Chem. Rev.*, **2020**, *412*, 213262.
- Li, H.; Eddaoudi, M.; Groy, T. L.; Yaghi, O. M. Establishing Microporosity in Open Metal-Organic Frameworks: Gas Sorption Isotherms for Zn(BDC) (BDC = 1,4-Benzenedicarboxylate) *J. Am. Chem. Soc.* **1998**, *120* (33), 8571–8572.
- Li, H.; Eddaoudi, M.; O’Keeffe, M.; Yaghi, O. M. Design and Synthesis of an Exceptionally Stable and Highly. *Nature* **1999**, *402* (November), 276–279.
- Li, H.; Wang, K.; Sun, Y.; Lollar, C. T.; Li, J.; Zhou, H. C. Recent Advances in Gas Storage and Separation Using Metal–Organic Frameworks. *Mater. Today* **2018**, *21* (2), 108–121.
- Li, P.; Vermeulen, N. A.; Malliakas, C. D.; Gómez-Gualdrón, D. A.; Howarth, A. J.; Mehdi, B. L.; Dohnalkova, A.; Browning, N. D.; O’Keeffe, M.; Farha, O. K. Bottom-up Construction of a Superstructure in a Porous Uranium-Organic Crystal. *Science*, **2017**, *356* (6338), 624–627.

- Li, R.; Zhang, W.; Zhou, K. Metal–Organic-Framework-Based Catalysts for Photoreduction of CO₂. *Adv. Mater.* **2018**, *30* (35), 1–31.
- Li, T.; Chen, D. L.; Sullivan, J. E.; Kozłowski, M. T.; Johnson, J. K.; Rosi, N. L. Systematic Modulation and Enhancement of CO₂:N₂ selectivity and Water Stability in an Isorecticular Series of Bio-MOF-11 Analogue. *Chem. Sci.* **2013**, *4* (4), 1746–1755.
- Li, W. K.; Zhou, G. D.; Mak, T. C. W. *Advanced Structural Inorganic Chemistry*; Oxford University Press: Oxford, England, **2008**.
- Lin, R. B.; He, Y.; Li, P.; Wang, H.; Zhou, W.; Chen, B. Multifunctional Porous Hydrogen-Bonded Organic Framework Materials. *Chem. Soc. Rev.* **2019**, *48* (5), 1362–1389.
- Lin, X.; Telepeni, I.; Blake, A. J.; Dailly, A.; Brown, C. M.; Simmons, J. M.; Zoppi, M.; Walker, G. S.; Thomas, K. M.; Mays, T. J.; Hubberstey, P.; Champness, N. R.; Schröder, M. High Capacity Hydrogen Adsorption in Cu(II) Tetracarboxylate Framework Materials: The Role of Pore Size, Ligand Functionalization, and Exposed Metal Sites. *J. Am. Chem. Soc.* **2009**, *131* (6), 2159–2171.
- Lippert, B. Alterations of Nucleobase PKa Values upon Metal Coordination: Origins and Consequences. *Prog. Inorg. Chem.* **2005**, *54*, 385.
- Little, M. A.; Cooper, A. I. The Chemistry of Porous Organic Molecular Materials. *Adv. Funct. Mater.* **2020**, *30* (41), 1–30.
- Liu, P.S.; Chen, G. F. *Porous Materials Processing and Applications*; Elsevier Inc: Amsterdam, Netherlands, **2014**.
- Liu, W.; Zhai, P.; Li, A.; Wei, B.; Si, K.; Wei, Y.; Wang, X.; Zhu, G.; Chen, Q.; Gu, X.; Zhang, R.; Zhou, W.; Gong, Y. Electrochemical CO₂ Reduction to Ethylene by Ultrathin CuO Nanoplate Arrays. *Nat. Commun.* **2022**, *13* (1), 1–12.
- Liu, X.; Wang, X.; Kapteijn, F. Water and Metal-Organic Frameworks: From Interaction toward Utilization. *Chem. Rev.* **2020**, *120* (16), 8303–8377.
- Liu, Y.; Dai, J.; Zhang, Z.; Yang, Y.; Yang, Q.; Ren, Q.; Bao, Z. Crystal Structure Transformation in Hydrogen-Bonded Organic Frameworks via Ion Exchange. *Chem. - An Asian J.* **2021**, *16* (23), 3978–3984.
- Liu, Y.; Tang, C.; Cheng, M.; Chen, M.; Chen, S.; Lei, L.; Chen, Y.; Yi, H.; Fu, Y.; Li, L. Polyoxometalate@metal-Organic Framework Composites as Effective Photocatalysts. *ACS Catal.* **2021**, *11* (21), 13374–13396.
- Liu, Y.; Wu, H.; Guo, L.; Zhou, W.; Zhang, Z.; Yang, Q.; Yang, Y.; Ren, Q.; Bao, Z. Hydrogen-bonded Metal–Nucleobase Frameworks for Efficient Separation of Xenon and Krypton. *Angew. Chemie* **2022**, *6102*, 1–10.
- Liu, Z.-Y.; Zhang, H.-Y.; Yang, E.-C.; Liu, Z.-Y.; Zhao, X.-J. A (3,6)-Connected Layer with an Unprecedented Adeninate Nucleobase-Derived Heptanuclear Disc. *Dalt. Trans.* **2015**, *44*, 5280–5283.
- Long, J. R.; Yaghi, O. M. The Pervasive Chemistry of Metal-Organic Frameworks. *Chem. Soc. Rev.* **2009**, *38* (5), 1213–1214.
- Lu, W.; Wei, Z.; Gu, Z. Y.; Liu, T. F.; Park, J.; Park, J.; Tian, J.; Zhang, M.; Zhang, Q.; Gentle, T.; Bosch, M.; Zhou, H. C. Tuning the Structure and Function of Metal-Organic Frameworks via Linker Design. *Chem. Soc. Rev.* **2014**, *43* (16), 5561–5593.
- Ma Ntep, T. J. M.; Reinsch, H.; Moll, B.; Hastürk, E.; Gökpınar, S.; Breitzke, H.; Schlüsener, C.; Schmolke, L.; Buntkowsky, G.; Janiak, C. Realizing the Potential of Acetylenedicarboxylate by Functionalization to Halofumarate in ZrIV Metal–Organic Frameworks. *Chem. - A Eur. J.* **2018**, *24* (53), 14048–14053.
- Macrae, C. F.; Edgington, P. R.; McCabe, P.; Pidcock, E.; Shields, G. P.; Taylor, R.; Towler, M.; Van De Streek, J. Mercury: Visualization and Analysis of Crystal Structures. *J. Appl. Crystallogr.* **2006**, *39* (3), 453–457.

- MacRae, C. F.; Sovago, I.; Cottrell, S. J.; Galek, P. T. A.; McCabe, P.; Pidcock, E.; Platings, M.; Shields, G. P.; Stevens, J. S.; Towler, M.; Wood, P. A. Mercury 4.0: From Visualization to Analysis, Design and Prediction. *J. Appl. Crystallogr.* **2020**, *53*, 226–235.
- Makarska-Bialokoz, M. Spectroscopic Study of Porphyrin-Caffeine Interactions. *J. Fluoresc.* **2012**, *22* (6), 1521–1530.
- Maleki, H. Recent Advances in Aerogels for Environmental Remediation Applications: A Review. *Chem. Eng. J.* **2016**, *300*, 98–118.
- Maleki, H.; Durães, L.; Portugal, A. An Overview on Silica Aerogels Synthesis and Different Mechanical Reinforcing Strategies. *J. Non. Cryst. Solids* **2014**, *385*, 55–74.
- Mallick, A.; Liang, H.; Shekhah, O.; Jia, J.; Mouchaham, G.; Shkurenko, A.; Belmabkhout, Y.; Alshareef, H. N.; Eddaoudi, M. Made-to-Order Porous Electrodes for Supercapacitors: MOFs Embedded with Redox-Active Centers as a Case Study. *Chem. Commun.* **2020**, *56* (12), 1883–1886.
- Marshall, R. J.; Forgan, R. S. Postsynthetic Modification of Zirconium Metal-Organic Frameworks. *Eur. J. Inorg. Chem.* **2016**, *2016* (27), 4310–4331.
- Martinez, C. R.; Iverson, B. L. Rethinking the Term “Pi-Stacking.” *Chem. Sci.* **2012**, *3* (7), 2191–2201.
- Martínez-Pinilla, E.; Oñatibia-Astibia, A.; Franco, R. The Relevance of Theobromine for the Beneficial Effects of Cocoa Consumption. *Front. Pharmacol.* **2015**, *6*, 1–5.
- Mastalerz, M.; Oppel, I. M. Rational Construction of an Extrinsic Porous Molecular Crystal with an Extraordinary High Specific Surface Area. *Angew. Chemie - Int. Ed.* **2012**, *51* (21), 5252–5255.
- McKeown, N. B. Nanoporous Molecular Crystals. *J. Mater. Chem.* **2010**, *20* (47), 10588–10597.
- Mialane, P.; Mellot-Draznieks, C.; Gairola, P.; Duguet, M.; Benseghir, Y.; Oms, O.; Dolbecq, A. Heterogenisation of Polyoxometalates and Other Metal-Based Complexes in Metal-Organic Frameworks: From Synthesis to Characterisation and Applications in Catalysis. *Chem. Soc. Rev.* **2021**, *50* (10), 6152–6220.
- Miller, K. P. H. Review of the Chemistry of Alchemy: From Dragon’s Blood to Donkey Dung - How Chemistry Was Forged. *J. Chem. Educ.* **2015**, *92* (6), 969–970.
- Mínguez Espallargas, G.; Coronado, E. Magnetic Functionalities in MOFs: From the Framework to the Pore. *Chem. Soc. Rev.* **2018**, *47* (2), 533–557.
- Moghadam, P. Z.; Li, A.; Wiggin, S. B.; Tao, A.; Maloney, A. G. P.; Peter, A.; Ward, S. C.; Fairen-jimenez, D. The Development of a CSD Subset: A Collection of Metal-Organic Frameworks for Past, Present and Future. *Chem. Mater.* **2017**, *29* (7), 2618–2625.
- Mohamed, T. A.; Shabaan, I. A.; Zoghaib, W. M.; Husband, J.; Farag, R. S.; Alajhaz, A. E. N. M. A. Tautomerism, Normal Coordinate Analysis, Vibrational Assignments, Calculated IR, Raman and NMR Spectra of Adenine. *J. Mol. Struct.* **2009**, *938* (1–3), 263–276.
- Mondal, K. C.; Mereacre, V.; Kostakis, G. E.; Lan, Y.; Anson, C. E.; Prisecaru, I.; Waldmann, O.; Powell, A. K. A Strongly Spin-Frustrated Fe^{III}₇ Complex with a Canted Intermediate Spin Ground State of S=7/2 or 9/2. *Chem. - A Eur. J.* **2015**, *21* (30), 10835–10842.
- Morris, R. E.; Brammer, L. Coordination Change, Lability and Hemilability in Metal-Organic Frameworks. *Chem. Soc. Rev.* **2017**, *46* (17), 5444–5462.
- Morris, W.; Wang, S.; Cho, D.; Auyeung, E.; Li, P.; Farha, O. K.; Mirkin, C. A. Role of Modulators in Controlling the Colloidal Stability and Polydispersity of the UiO-66 Metal-Organic Framework. *ACS Appl. Mater. Interfaces* **2017**, *9* (39), 33413–33418.
- Nakamoto, K. Infrared and Raman Spectra of Inorganic and Coordination Compounds: Part A: Theory and Applications in Inorganic Chemistry; John Wiley & Sons, Inc.: New York, United States of America, **2008**.

- Nardelli, M. Modeling Hydroxyl and Water H Atoms. *J. Appl. Crystallogr.* **1999**, *32* (3), 563–571.
- Nasalevich, M. A.; Van Der Veen, M.; Kapteijn, F.; Gascon, J. Metal-Organic Frameworks as Heterogeneous Photocatalysts: Advantages and Challenges. *CrystEngComm* **2014**, *16* (23), 4919–4926.
- Nguyen, T. T. M.; Le, H. M.; Kawazoe, Y.; Nguyen, H. L. Reticular Control of Interpenetration in a Complex Metal-Organic Framework. *Mater. Chem. Front.* **2018**, *2* (11), 2063–2069.
- Nugent, P. S.; Rhodus, V. Lou; Pham, T.; Forrest, K.; Wojtas, L.; Space, B.; Zaworotko, M. J. A Robust Molecular Porous Material with High CO₂ Uptake and Selectivity. *J. Am. Chem. Soc.* **2013**, *135* (30), 10950–10953.
- Nune, S. K.; Thallapally, P. K.; McGrail, B. P. Metal Organic Gels (MOGs): A New Class of Sorbents for CO₂ Separation Applications. *J. Mater. Chem.* **2010**, *20* (36), 7623–7625.
- O’Keeffe, M.; Yaghi, O. M. Deconstructing the Crystal Structures of Metal-Organic Frameworks and Related Materials into Their Underlying Nets. *Chem. Rev.* **2012**, *112* (2), 675–702.
- Oar-Arteta, L.; Wezendonk, T.; Sun, X.; Kapteijn, F.; Gascon, J. Metal Organic Frameworks as Precursors for the Manufacture of Advanced Catalytic Materials. *Mater. Chem. Front.* **2017**, *1* (9), 1709–1745.
- Olea, D.; Alexandre, S. S.; Amo-Ochoa, P.; Guijarro, A.; De Jesús, F.; Soler, J. M.; De Pablo, P. J.; Zamora, F.; Gómez-Herrero, J. From Coordination Polymer Macrocrystals to Nanometric Individual Chains. *Adv. Mater.* **2005**, *17* (14), 1761–1765.
- Ong, T. T.; Kavuru, P.; Nguyen, T.; Cantwell, R.; Wojtas, L.; Zaworotko, M. J. 2:1 Cocrystals of Homochiral and Achiral Amino Acid Zwitterions with Li⁺ Salts: Water-Stable Zeolitic and Diamondoid Metal-Organic Materials. *J. Am. Chem. Soc.* **2011**, *133* (24), 9224–9227.
- Pajares, A.; Prats, H.; Romero, A.; Viñes, F.; de la Piscina, P. R.; Sayós, R.; Homs, N.; Illas, F. Critical Effect of Carbon Vacancies on the Reverse Water Gas Shift Reaction over Vanadium Carbide Catalysts. *Appl. Catal. B Environ.* **2020**, *267* (January), 118719.
- Palatinus, L.; Chapuis, G. SUPERFLIP - A Computer Program for the Solution of Crystal Structures by Charge Flipping in Arbitrary Dimensions. *J. Appl. Crystallogr.* **2007**, *40* (4), 786–790.
- Pan, L.; Heddy, R.; Li, J.; Zheng, C.; Huang, X. Y.; Tang, X.; Kilpatrick, L. Synthesis and Structural Determination of a Hexanuclear Zirconium Glycine Compound Formed in Aqueous Solution. *Inorg. Chem.* **2008**, *47* (13), 5537–5539.
- Panunto, T. W.; Urbanczyk-lipkowska, Z.; Johnson, R.; Etter, M. C. Hydrogen-Bond Formation in Nitroanilines : The First Step in Designing Acentric Materials. *J. Am. Chem. Soc.* **1987**, *109* (7), 7786–7797.
- Parent, L. R.; Pham, C. H.; Patterson, J. P.; Denny, M. S.; Cohen, S. M.; Gianneschi, N. C.; Paesani, F. Pore Breathing of Metal–Organic Frameworks by Environmental Transmission Electron Microscopy. *J. Am. Chem. Soc.* **2017**, *139* (40), 13973–13976.
- Park, K. S.; Ni, Z.; Côté, A. P.; Choi, J. Y.; Huang, R.; Uribe-Romo, F. J.; Chae, H. K.; O’Keeffe, M.; Yaghi, O. M. Exceptional Chemical and Thermal Stability of Zeolitic Imidazolate Frameworks. *Proc. Natl. Acad. Sci. U. S. A.* **2006**, *103* (27), 10186–10191.
- Park, Y. K.; Sang, B. C.; Kim, H.; Kim, K.; Won, B. H.; Choi, K.; Choi, J. S.; Ahn, W. S.; Won, N.; Kim, S.; Dong, H. J.; Choi, S. H.; Kim, G. H.; Cha, S. S.; Young, H. J.; Jin, K. Y.; Kim, J. Crystal Structure and Guest Uptake of a Mesoporous Metal-Organic Framework Containing Cages of 3.9 and 4.7 nm in Diameter. *Angew. Chemie - Int. Ed.* **2007**, *46* (43), 8230–8233.
- Pasán, J.; Sanchiz, J.; Ruiz-Pérez, C.; Lloret, F.; Julve, M. Polymeric Networks of Copper(II) Phenylmalonate with Heteroaromatic N-Donor Ligands: Synthesis, Crystal Structure, and Magnetic Properties. *Inorg. Chem.* **2005**, *44* (22), 7794–7801.
- Paul, A. K.; Sanyal, U.; Natarajan, S. Use of Polyazaheterocycles in the Assembly of New Cadmium Sulfate Frameworks: Synthesis, Structure, and Properties. *Cryst. Growth Des.* **2010**, *10* (9), 4161–4175.

- Pauling, L. The Nature of Chemical Bond: II The One-Electron Bond and the Three-Electron Bond. *J Am. Chem. Soc.* **1931**, *1367*, 3225–3237.
- Pauling, L. The Nature of the Chemical Bond, 2nd ed.; University Press: New York, United States of America, **1948**.
- Pedersen, C. J. Cyclic Polyethers and Their Complexes with Metal Salts. *J Am. Chem. Soc.* **1967**, *89* (26), 7017–7036.
- Pedersen, C. J. Cyclic Polyethers and Their Complexes with Metal Salts. *J Am. Chem. Soc.* **1967**, *89* (10), 2495–2496.
- Pena, C. Supramolecular Systems: Chemistry, Types and Applications. Chemistry Research and Applications; Nova Science Publishers Inc: New York, United States of America, **2016**.
- Pepinsky, R. Single-Crystal Neutron Analysis of Tetragonal BaTiO₃. *Phys. Rev. A At. Mol. Opt. Phys* **1955**, *100*, 971.
- Pérez-Aguirre, R.; Artetxe, B.; Beobide, G.; Castillo, O.; de Pedro, I.; Luque, A.; Pérez-Yáñez, S.; Wuttke, S. Ferromagnetic Supramolecular Metal-Organic Frameworks for Active Capture and Magnetic Sensing of Emerging Drug Pollutants. *Cell Reports Phys. Sci.* **2021**, *2* (5), 100421.
- Pérez-Aguirre, R.; Beobide, G.; Castillo, O.; De Pedro, I.; Luque, A.; Pérez-Yáñez, S.; Rodríguez Fernández, J.; Román, P. 3D Magnetically Ordered Open Supramolecular Architectures Based on Ferrimagnetic Cu/Adenine/Hydroxide Heptameric Wheels. *Inorg. Chem.* **2016**, *55*, 7755–7763.
- Pérez-Yáñez, S.; Beobide, G.; Bhadbhade, M.; Cepeda, J.; Fröba, M.; Hoffmann, F.; Luque, A.; Román, P. Improving the Performance of a Poorly Adsorbing Porous Material: Template Mediated Addition of Microporosity to a Crystalline Submicroporous MOF. *Chem. Commun.* **2012**, *48* (6), 907–909.
- Perez-Yáñez, S.; Beobide, G.; Castillo, O.; Cepeda, J.; Luque, A. Supramolecular Metal-Organic Frameworks Based on Metal-Nucleobase Entities.; Nova Science Publishers Inc: New York, United States of America, **2017**.
- Pérez-Yáñez, S.; Beobide, G.; Castillo, O.; Cepeda, J.; Luque, A.; Aguayo, A. T.; Román, P. Open-Framework Copper Adeninate Compounds with Three-Dimensional Microchannels Tailored by Aliphatic Monocarboxylic Acids. *Inorg. Chem.* **2011**, *50* (12), 5330–5332.
- Pérez-Yáñez, S.; Beobide, G.; Castillo, O.; Cepeda, J.; Luque, A.; Román, P. Directing the Formation of Adenine Coordination Polymers from Tunable Copper(II)/Dicarboxylato/Adenine Paddle-Wheel Building Units. *Cryst. Growth Des.* **2012**, *12* (6), 3324–3334.
- Pérez-Yáñez, S.; Castillo, O.; Cepeda, J.; García-Terán, J. P.; Luque, A.; Román, P. Supramolecular Architectures of Metal-Oxalato Complexes Containing Purine Nucleobases. *Inorganica Chim. Acta* **2011**, *365* (1), 211–219.
- Pérez-Yáñez, S.; Castillo, O.; Cepeda, J.; García-Terán, J. P.; Luque, A.; Román, P. Analysis of the Interaction between Adenine Nucleobase and Metal-Malonato Complexes. *Eur. J. Inorg. Chem.* **2009**, *2* (26), 3889–3899.
- Perfecto-Irigaray, M.; Beobide, G.; Castillo, O.; Da Silva, I.; García-Lojo, D.; Luque, A.; Mendia, A.; Pérez-Yáñez, S. A Hexagonal Polymorph of UiO-66. *Chem. Commun.* **2019**, *55* (42), 5954–5957.
- Persson, C. G. A. Overview of Effects of Theophylline. *J. Allergy Clin. Immunol.* **1986**, *78*, 780–787.
- Piszczek, P.; Radtke, A.; Grodzicki, A.; Wojtczak, A.; Chojnacki, J. The New Type of [Zr₆(μ₃-O)₄(μ₃-OH)₄] Cluster Core: Crystal Structure and Spectral Characterization of [Zr₆O₄(OH)₄(OOCR)₁₂] (R = But, C(CH₃)₂Et). *Polyhedron* **2007**, *26* (3), 679–685.
- Polarz, S.; Smarsly, B. Nanoporous Materials. *J. Nanosci. Nanotechnol.* **2002**, *2* (6), 581–612.

- Qin, J. S.; Yuan, S.; Zhang, L.; Li, B.; Du, D. Y.; Huang, N.; Guan, W.; Drake, H. F.; Pang, J.; Lan, Y. Q.; Alsalmeh, A.; Zhou, H. C. Creating Well-Defined Hexabenzocoronene in Zirconium Metal-Organic Framework by Postsynthetic Annulation. *J. Am. Chem. Soc.* **2019**, *141* (5), 2054–2060.
- Quiroz-Segoviano, R. I. Y.; Serratos, I. N.; Rojas-González, F.; Tello-Solís, S. R.; Sosa-Fonseca, R.; Medina-Juárez, O.; Menchaca-Campos, C.; García-Sánchez, M. A. On Tuning the Fluorescence Emission of Porphyrin Free Bases Bonded to the Pore Walls of Organo-Modified Silica. *Molecules* **2014**, *19* (2), 2261–2285.
- Rachuri, Y.; Kurisingal, J. F.; Chitumalla, R. K.; Vuppala, S.; Gu, Y.; Jang, J.; Choe, Y.; Suresh, E.; Park, D. W. Adenine-Based Zn(II)/Cd(II) Metal-Organic Frameworks as Efficient Heterogeneous Catalysts for Facile CO₂ Fixation into Cyclic Carbonates: A DFT-Supported Study of the Reaction Mechanism. *Inorg. Chem.* **2019**, *58* (17), 11389–11403.
- Radhakrishnan, K.; Burgula, L. N.; Kundu, L. M. Watson-Crick and Hoogsteen Tri-Base Pairing: A Co-Crystal Structure of 6-Isopropyluracil and Adenine Nucleobases. *RSC Adv.* **2013**, *3* (20), 7282–7284.
- Rangnekar, N.; Mittal, N.; Elyassi, B.; Caro, J.; Tsapatsis, M. Zeolite Membranes- a Review and Comparison with MOFs. *Chem. Soc. Rev.* **2015**, *44* (20), 7128–7154.
- Rao, N.; Holerca, M. N.; Klein, M. L.; Pophristic, V. Computational Study of the Zr 4+ Tetranuclear Polymer, [Zr₄(OH)₈(H₂O)₁₆]⁸⁺. *J. Phys. Chem. A* **2007**, *111* (45), 11395–11399.
- Reger, D. L.; Debreczeni, A.; Smith, M. D. Homochiral, Supramolecular Frameworks Built from a Zinc(II) Tetramer or Cadmium(II) Dimer Containing Enantiopure Carboxylate Ligands Functionalized with a Strong $\Pi \cdots \pi$ Stacking Synthone. *Eur. J. Inorg. Chem.* **2012**, *4*, 712–719.
- Reger, D. L.; Debreczeni, A.; Smith, M. D. Zinc Paddle-Wheel Dimers Containing a Strong $\Pi \cdots \pi$ Stacking Supramolecular Synthone: Designed Single-Crystal to Single-Crystal Phase Changes and Gas/Solid Guest Exchange. *Inorg. Chem.* **2011**, *50* (22), 11754–11764.
- Reger, D. L.; Debreczeni, A.; Smith, M. D.; Jezierska, J.; Ozarowski, A. Copper(II) Carboxylate Dimers Prepared from Ligands Designed to Form a Robust $\Pi \cdots \pi$ Stacking Synthone: Supramolecular Structures and Molecular Properties. *Inorg. Chem.* **2012**, *51* (2), 1068–1083.
- Ren, J.; Huang, Y.; Zhu, H.; Zhang, B.; Zhu, H.; Shen, S.; Tan, G.; Wu, F.; He, H.; Lan, S.; Xia, X.; Liu, Q. Recent Progress on MOF-Derived Carbon Materials for Energy Storage. *Carbon Energy* **2020**, *2* (2), 176–202.
- Richard P. Feynman. There's Plenty of Room at the Bottom. *J. Eng. Sci.* **1960**, *4* (2), 22–36.
- Robinson, R. G. B. M. P.; R. A. Interpretation of pH Measurements in Alcohol-Water Solvents. *J. Phys. Chem.* **1963**, *67* (9), 1833–1838.
- Rojas, S.; Devic, T.; Horcajada, P. Metal Organic Frameworks Based on Bioactive Components. *J. Mater. Chem. B* **2017**, *5* (14), 2560–2573.
- Rojas-González, P. X.; Castiñeiras, A.; González-Pérez, J. M.; Choquesillo-Lazarte, D.; Niclós-Gutiérrez, J. Interligand Interactions Controlling the μ -N7,N9-Metal Bonding of Adenine (AdeH) to the N-Benzyliminodiacetato(2-) Copper(II) Chelete and Promoting the N9 versus N3 Tautomeric Proton Transfer: Molecular and Crystal Structure of [Cu₂(NBzIDA)₂(H₂O)₂ (μ -N7,N9-Ade(N3)H)]·3H₂O. *Inorg. Chem.* **2002**, *41* (24), 6190–6192.
- Rosi, N. L.; Kim, J.; Eddaoudi, M.; Chen, B.; O'Keeffe, M.; Yaghi, O. M. Rod Packings and Metal-Organic Frameworks Constructed from Rod-Shaped Secondary Building Units. *J. Am. Chem. Soc.* **2005**, *127* (5), 1504–1518.
- Rowsell, J. L. C.; Yaghi, O. M. Metal-Organic Frameworks: A New Class of Porous Materials. *Microporous Mesoporous Mater.* **2004**, *73* (1–2), 3–14.
- Rubio-Martinez, M.; Avci-Camur, C.; Thornton, A. W.; Imaz, I.; Maspocho, D.; Hill, M. R. New Synthetic Routes towards MOF Production at Scale. *Chem. Soc. Rev.* **2017**, *46* (11), 3453–3480.

- Samanta, S. K.; Isaacs, L. Biomedical Applications of Metal Organic Polygons and Polyhedra (MOPs). *Coord. Chem. Rev.* **2020**, *410*, 213181.
- Santos-Lorenzo, J.; San José-Velado, R.; Albo, J.; Beobide, G.; Castaño, P.; Castillo, O.; Luque, A.; Pérez-Yáñez, S. A Straightforward Route to Obtain Zirconium Based Metal-Organic Gels. *Microporous Mater.* **2019**, *284*, 128–132.
- Sarker, M.; Jung, S. H. Zr-MOF with Free Carboxylic Acid for Storage and Controlled Release of Caffeine. *J. Mol. Liq.* **2019**, *296*, 112060.
- Schmidt, G. M. J. Photodimerization in the Solid State. *Pure Appl. Chem.* **1971**, *27* (4), 647–678.
- Schukraft, G. E. M.; Ayala, S.; Dick, B. L.; Cohen, S. M. Isoreticular Expansion of PolyMOFs Achieves High Surface Area Materials. *Chem. Commun.* **2017**, *53* (77), 10684–10687.
- Serre, C.; Millange, F.; Thouvenot, C.; Noguès, M.; Marsolier, G.; Louër, D.; Férey, G. Very Large Breathing Effect in the First Nanoporous Chromium(III)-Based Solids: MIL-53 or $\text{Cr}^{\text{III}}(\text{OH})\{\text{O}_2\text{C}-\text{C}_6\text{H}_4-\text{CO}_2\} \cdot \{\text{HO}_2\text{C}-\text{C}_6\text{H}_4-\text{CO}_2\text{H}\}_x \cdot \text{H}_2\text{O}_y$. *J. Am. Chem. Soc.* **2002**, *124* (45), 13519–13526.
- Seybold, P. G.; Gouterman, M.; Callis, J. Calorimetric, Photometric and Lifetime Determinations of Fluorescence Yields of Fluorescein Dyes. *Photochem. Photobiol.* **1969**, *9* (3), 229–242.
- Shah, S. S. A.; Najam, T.; Wen, M.; Zang, S.-Q.; Waseem, A.; Jiang, H.-L. Metal–Organic Framework-Based Electrocatalysts for CO_2 Reduction. *Small Struct.* **2021**, *2100090*, 2100090.
- Shao, D.; Wang, X. Y. Development of Single-Molecule Magnets. *Chinese J. Chem.* **2020**, *38* (9), 1005–1018.
- Sharples, J. W.; Collison, D.; McInnes, E. J. L.; Schnack, J.; Palacios, E.; Evangelisti, M. Quantum Signatures of a Molecular Nanomagnet in Direct Magnetocaloric Measurements. *Nat. Commun.* **2014**, *5*, 3–8.
- Shekhah, O.; Liu, J.; Fischer, R. A.; Wöll, C. MOF Thin Films: Existing and Future Applications. *Chem. Soc. Rev.* **2011**, *40* (2), 1081–1106.
- Sheldrick, G. M. A Short History of SHELX. *Acta Crystallogr. Sect. A Found. Crystallogr.* **2008**, *64* (1), 112–122.
- Sheldrick, G. M. Crystal Structure Refinement with SHELXL. *Acta Crystallogr. Sect. C Struct. Chem.* **2015**, *71*, 3–8.
- Shimoyama, Y.; Uchida, S. Structure-Function Relationships of Porous Ionic Crystals (PICS) Based on Polyoxometalate Anions and Oxo-Centered Trinuclear Metal Carboxylates as Counter Cations. *Chem. Lett.* **2021**, *50* (1), 21–30.
- Simard, Michel; Su, D.; Wuest, J. D. Use of Hydrogen Bonds to Control Molecular Aggregation. Self-Assembly of Three-Dimensional Networks with Large Chambers. *J. Am. Chem. Soc.* **1991**, *113* (9), 4696–4698.
- Sletten, E. Crystallographic Studies of Metal–Nucleotide Base Complexes. II. Bis-(6-Hydroxypurine) Copper(II) Chloride Trihydrate. *Acta Crystallogr. Sect. B Struct. Crystallogr. Cryst. Chem.* **1970**, *26* (10), 1609–1614.
- Sletten, E. Crystallographic Studies of Metal–Nucleotide Base Complexes. I. Triclinic Bis-(6-Aminopurine)Copper(II) Tetrahydrate. *Acta Crystallogr. Sect. B Struct. Crystallogr. Cryst. Chem.* **1969**, *25* (8), 1480–1491.
- Song, Y.; Yin, X.; Tu, B.; Pang, Q.; Li, H.; Ren, X.; Wang, B.; Li, Q. Metal-Organic Frameworks Constructed from Mixed Infinite Inorganic Units and Adenine. *CrystEngComm* **2014**, *16* (15), 3082–3085.

- Sowunmi, A. R.; Folayan, C. O.; Anafi, F. O.; Ajayi, O. A.; Omisanya, N. O.; Obada, D. O.; Dodoo-Arhin, D. Dataset on the Comparison of Synthesized and Commercial Zeolites for Potential Solar Adsorption Refrigerating System. *Data Br.* **2018**, *20*, 90–95.
- Spek, A. L. PLATON SQUEEZE: A Tool for the Calculation of the Disordered Solvent Contribution to the Calculated Structure Factors. *Acta Crystallogr. Sect. C Struct. Chem.* **2015**, *71*, 9–18.
- Spek, A. L. Single-Crystal Structure Validation with the Program PLATON. *J. Appl. Crystallogr.* **2003**, *36* (1), 7–13.
- Spokoiny, A. M.; Kim, D.; Sumrein, A.; Mirkin, C. A. Infinite Coordination Polymer Nano- and Microparticle Structures. *Chem. Soc. Rev.* **2009**, *38* (5), 1218–1227.
- Stang, Peter J.; Olenyuj, B. Self-Assembly, Symmetry and Molecular Architecture: Coordination as the Motif in the Rational Design of Supramolecular Metallacyclic Polygons and Polyhedra. *Acc. Chem. Res.* **1997**, *30*, 502–518.
- Steiner, T. The Hydrogen Bond in the Solid State. *Angew Chem Int Ed* **2002**, *41*, 48–76.
- Stern, R. D.; Kingsbury, R. S.; Persson, K. A. Aqueous Stability of Zirconium Clusters, Including the Zr(IV) Hexanuclear Hydrolysis Complex $[\text{Zr}_6\text{O}_4(\text{OH})_4(\text{H}_2\text{O})_{24}]^{12+}$, from Density Functional Theory. *Inorg. Chem.* **2021**, *60* (20), 15456–15466.
- Stone, F. S.; Waller, D. Cu-ZnO and Cu-ZnO/Al₂O₃ Catalysts for the Reverse Water-Gas Shift Reaction. The Effect of the Cu/Zn Ratio on Precursor Characteristics and on the Activity of the Derived Catalysts. *Top. Catal.* **2003**, *22* (3–4), 305–318.
- Streb, C.; Kastner, K.; Tucher, J. Polyoxometalates in Photocatalysis. *Phys. Sci. Rev.* **2019**, *4* (6), 1–10.
- Stylianou, K. C.; Warren, J. E.; Chong, S. Y.; Rabone, J.; Bacsá, J.; Bradshaw, D.; Rosseinsky, M. J. CO₂ Selectivity of a 1D Microporous Adenine-Based Metal–Organic Framework Synthesised in Water. *Chem. Commun.* **2011**, *47* (12), 3389–3391.
- Su, D.; Wang, X.; Simard, M.; Wuest, J. D. Molecular Tectonics. *Supramol. Chem.* **1995**, *6* (1–2), 171–178.
- Sun, Y.; Zheng, L.; Yang, Y.; Qian, X.; Fu, T.; Li, X.; Yang, Z.; Yan, H.; Cui, C.; Tan, W. Metal–Organic Framework Nanocarriers for Drug Delivery in Biomedical Applications. *Nano-Micro Lett.* **2020**, *12* (1), 1–29.
- Surlblé, S.; Serre, C.; Mellot-Draznieks, C.; Millange, F.; Férey, G. A New Isorecticular Class of Metal–Organic-Frameworks with the MIL-88 Topology. *Chem. Commun.* **2006**, *3*, 284–286.
- Szalda, D. J.; Kistenmacher, T. J.; Marzilli, L. G. Observation of a Direct Interaction between the Carbonyl Oxygen, O(6), of a N(7)-Bonded 6-Oxopurine and a Metal Center. Preparation and Crystal and Molecular Structure of (N-3,4-Benzosalicylidene-N',N'-Dimethylethylenediamine)(Theophyllinato)Copper(II) Mo. *J. Am. Chem. Soc.* **1976**, *98* (26), 8371–8377.
- Tam, A. Y. Y.; Yam, V. W. W. Recent Advances in Metallogels. *Chem. Soc. Rev.* **2013**, *42* (4), 1540–1567.
- Tamames-Tabar, C. .; García-Márquez, A. .; Blanco-Prieto, M. J. .; Serre, C.; Horcajada, P. In *Bio- and Bioinspired Nanomaterials*; Wiley-VCH Verlag GmbH & Co. KGaA: Weinheim, Germany, **2014**.
- Taqi Khan, M. M.; Krishnamoorthy, C. R. Interaction of Metal Inos with Monosubstituted Purines. *J. Inorg. Nucl. Chem.* **1971**, *33*, 1417–1425.
- Tella, A. C.; Owalude, S. O.; Omotoso, M. F.; Olatunji, S. J.; Ogunlaja, A. S.; Alimi, L. O.; Popoola, O. K.; Bourne, S. A. Synthesis, Crystal Structures and Luminescence Properties of New Multi-Component Co-Crystals of Isostructural Co(II) and Zn(II) Complexes. *J. Mol. Struct.* **2018**, *1157*, 450–456.

- Tercero, J.; Ruiz, E.; Alvarez, S.; Rodríguez-Forteza, A.; Alemany, P. Density Functional Study of Magnetostructural Correlations in Cubane Complexes Containing the Cu₄O₄ Core. *J. Mater. Chem.* **2006**, *16* (26), 2729–2735.
- Terzis, A.; Beauchamp, A. L.; Rivest, R. Crystal and Molecular Structure of Tetra-*m*-Adenine-Diaquodocopper(II) Perchlorate Dihydrate, [Cu₂(C₅H₅N₅)₄(H₂O)₂](ClO₄)₄·2H₂O. *Inorg. Chem.* **1973**, *12* (5), 1166–1170.
- Terzopoulou, A.; Nicholas, J. D.; Chen, X. Z.; Nelson, B. J.; Pane, S.; Puigmartí-Luis, J. Metal–organic Frameworks in Motion. *Chem. Rev.* **2020**, *120* (20), 11175–11193.
- Thomas, A. Much Ado about Nothing – a Decade of Porous Materials Research. *Nat. Commun.* **2020**, *11* (1), 11–13.
- Thomas-Gipson, J.; Beobide, G.; Castillo, O.; Cepeda, J.; Luque, A.; Pérez-Yáñez, S.; Aguayo, A. T.; Román, P. Porous Supramolecular Compound Based on Paddle-Wheel Shaped Copper(II)-Adenine Dinuclear Entities. *CrystEngComm* **2011**, *13* (10), 3301–3305.
- Thomas-Gipson, J.; Beobide, G.; Castillo, O.; Fröba, M.; Hoffmann, F.; Luque, A.; Pérez-Yáñez, S.; Román, P. Paddle-Wheel Shaped Copper(II)-Adenine Discrete Entities as Supramolecular Building Blocks to Afford Porous Supramolecular Metal-Organic Frameworks (SMOFs). *Cryst. Growth Des.* **2014**, *14* (8), 4019–4029.
- Thomas-Gipson, J.; Beobide, G.; Castillo, O.; Luque, A.; Pascual-Colino, J.; Pérez-Yáñez, S.; Román, P. Providing Evidence for the Requirements to Achieve Supramolecular Materials Based on Metal-Nucleobase Entities. *CrystEngComm* **2018**, *20* (18), 2528–2539.
- Thomas-Gipson, J.; Pérez-Aguirre, R.; Beobide, G.; Castillo, O.; Luque, A.; Pérez-Yáñez, S.; Román, P. Unravelling the Growth of Supramolecular Metal-Organic Frameworks Based on Metal-Nucleobase Entities. *Cryst. Growth Des.* **2015**, *15*, 975–983.
- Tomic, E. A. Thermal Stability of Coordination Polymers. *J. Appl. Polym. Sci.* **1965**, *9* (11), 3745–3752.
- Tranchemontagne, D. J.; Tranchemontagne, J. L.; O'keeffe, M.; Yaghi, O. M. Secondary Building Units, Nets and Bonding in the Chemistry of Metal–Organic Frameworks. *Chem. Soc. Rev.* **2009**, *38* (5), 1257–1283.
- Trevino, L.; Orndoff, E. Advanced Space Suit Insulation Feasibility Study; American Institute of Physics: Tucson, Arizona, (United States), **2000**.
- Trivedi, M. K.; Dahryn Trivedi, A. B.; Khemraj Bairwa, H. S. Fourier Transform Infrared and Ultraviolet-Visible Spectroscopic Characterization of Biofield Treated Salicylic Acid and Sparfloxacin. *Nat. Prod. Chem. Res.* **2015**, *03* (05), 1000186.
- Tseng, I.; Chang, W.; Wu, J. C. S. Photoreduction of CO₂ Using Sol-Gel Derived Titania and Titania-Supported Copper Catalysts. *Appl. Catal. B Environ.* **2002**, *37*, 37–48.
- Uhlenheuer, D. A.; Petkau, K.; Brunsveld, L. Combining Supramolecular Chemistry with Biology. *Chem. Soc. Rev.* **2010**, *39* (8), 2817–2826.
- Vaidhyanathan, R.; Bradshaw, D.; Rebilly, J. N.; Barrio, J. P.; Gould, J. A.; Berry, N. G.; Rosseinsky, M. J. A Family of Nanoporous Materials Based on an Amino Acid Backbone. *Angew. Chemie - Int. Ed.* **2006**, *45* (39), 6495–6499.
- Vallejo-Sánchez, D.; Amo-Ochoa, P.; Beobide, G.; Castillo, O.; Fröba, M.; Hoffmann, F.; Luque, A.; Ocón, P.; Pérez-Yáñez, S. Chemically Resistant, Shapeable, and Conducting Metal-Organic Gels and Aerogels Built from Dithiooxamidato Ligand. *Adv. Funct. Mater.* **2017**, *27* (15), 1605448.
- Van Crawford, H.; Richardson, H. W.; Wasson, J. R.; Hodgson, D. J.; Hatfield, W. E. Relation between the Singlet-Triplet Splitting and the Cu-O-Cu Bridge Angle in Hydroxo-Bridged Copper Dimers. *Inorg. Chem.* **1976**, *15* (9), 2107–2110.

- Van Den Bogaard, B.; Draijer, R.; Westerhof, B. E.; Van Den Meiracker, A. H.; Van Montfrans, G. A.; Van Den Born, B. J. H. Effects on Peripheral and Central Blood Pressure of Cocoa with Natural or High-Dose Theobromine: A Randomized, Double-Blind Crossover Trial. *Hypertension* **2010**, *56* (5), 839–846.
- Van Vleck, J. H. Nobel Lectures, Physics 1971-1980; World Scientific Publishing Co.: Singapore, Singapore, **1992**.
- Vardhan, H.; Yusubov, M.; Verpoort, F. Self-Assembled Metal-Organic Polyhedra: An Overview of Various Applications. *Coord. Chem. Rev.* **2016**, *306*, 171–194.
- Verma, S.; Mishra, A. K.; Kumar, J. The Many Facets of Adenine: Coordination, Crystal Patterns, and Catalysis. *Acc. Chem. Res.* **2010**, *43* (1), 79–91.
- Villegas-Fernández, M. H.; Carpio-Granillo, M.; Vargas-Hernández, E.; Zuno-Cruz, F. J.; Sánchez-Cabrera, G. Una Revisión General de Las Estructuras Metal-Orgánicas (MOF) Dentro de La Química Inorgánica. *Pädi Boletín Científico Ciencias Básicas e Ing. del ICBI* **2021**, *8* (16), 18–29.
- Wang, H.; Chen, B. H.; Liu, D. J. Metal–Organic Frameworks and Metal–Organic Gels for Oxygen Electrocatalysis: Structural and Compositional Considerations. *Adv. Mater.* **2021**, *33* (25), 1–41.
- Wang, J. L.; Xu, L. J. Advanced Oxidation Processes for Wastewater Treatment: Formation of Hydroxyl Radical and Application. *Crit. Rev. Environ. Sci. Technol.* **2012**, *42* (3), 251–325.
- Wang, X.; Wang, X.; Zhang, X.; Fan, W.; Li, Q.; Jiang, W.; Dai, F.; Sun, D. A Stable Interpenetrated Zn-MOF with Efficient Light Hydrocarbon Adsorption/Separation Performance. *Cryst. Growth Des.* **2020**, *20* (9), 5670–5675.
- Wang, Y.; Winter, L. R.; Chen, J. G.; Yan, B. CO₂hydrogenation over Heterogeneous Catalysts at Atmospheric Pressure: From Electronic Properties to Product Selectivity. *Green Chem.* **2021**, *23* (1), 249–267.
- Wang, Z.; Cohen, S. M. Postsynthetic Modification of Metal–Organic Frameworks. *Chem. Soc. Rev.* **2009**, *38* (5), 1315–1329.
- Wang, Z.; Zhuo, H. Y.; Hu, A. Y.; Su, H. F.; Zhao, Q. Q.; Wang, X. P.; Tung, C. H.; Sun, D. Self-Assembly of A Novel Ag₄₈ Cluster Encapsulating an Unprecedented [Mo₈O₂₈]⁸⁻ Anion Template. *Isr. J. Chem.* **2019**, *59* (3), 280–285.
- Webber, T. E.; Liu, W. G.; Desai, S. P.; Lu, C. C.; Truhlar, D. G.; Penn, R. L. Role of a Modulator in the Synthesis of Phase-Pure NU-1000. *ACS Appl. Mater. Interfaces* **2017**, *9* (45), 39342–39346.
- Walter, P.; Puchberger, M.; Kogler, F. R.; Schwarz, K.; Schubert, U. Chemistry and Physics of Metal Oxide Nanostructures. *Phys. Chem. Chem. Phys.* **2009**, *11* (19), 3640–3647.
- Wheeler, S. E. Understanding Substituent Effects in Noncovalent Interactions Involving Aromatic Rings. *Acc. Chem. Res.* **2013**, *46* (4), 1029–1038.
- Williamson, D. L.; Herdes, C.; Torrente-Murciano, L.; Jones, M. D.; Mattia, D. N-Doped Fe@CNT for Combined RWGS/FT CO₂ Hydrogenation. *ACS Sustain. Chem. Eng.* **2019**, *7* (7), 7395–7402.
- Williamson, P. Scrutinize CO₂ Removal Methods. *Nature* **2016**, *530*, 153–155.
- Wuest, J. D. Engineering Crystals by the Strategy of Molecular Tectonics. *Chem. Commun.* **2005**, *47*, 5830–5837.
- Xu, X.; Li, S.; Liu, Q.; Liu, Z.; Yan, W.; Zhao, L.; Zhang, W.; Zhang, L.; Deng, F.; Cong, H.; Deng, H. Isolated π -Interaction Sites in Mesoporous MOF Backbone for Repetitive and Reversible Dynamics in Water. *ACS Appl. Mater. Interfaces* **2019**, *11* (1), 973–981.
- Yaghi, O. M.; Kalmutzki, M. J.; Diercks, C. S. Introduction to Reticular Chemistry: Metal-Organic Frameworks and Covalent Organic Frameworks; Wiley-VCH Verlag GmbH & Co: Weinheim, Germany, **2019**.

- Yaghi, O. M.; Li, H. Hydrothermal Synthesis of a Metal-Organic Framework Containing Large Rectangular Channels. *J. Am. Chem. Soc.* **1995**, *117* (41), 10401–10402.
- Yaghi, O. M.; O’Keeffe, M.; Ockwig, N. W.; Chae, H. K.; Eddaoudi, M.; Kim, J. Reticular Synthesis and the Design of New Materials. *Nature* **2003**, *423* (6941), 705–714.
- Yakovchuk, P.; Protozanova, E.; Frank-Kamenetskii, M. D. Base-Stacking and Base-Pairing Contributions into Thermal Stability of the DNA Double Helix. *Nucleic Acids Res.* **2006**, *34* (2), 564–574.
- Yang, E. C.; Zhao, H. K.; Feng, Y.; Zhao, X. J. A Tetranuclear Cu^{II}-Based 2D Aggregate with an Unprecedented Tetradentate μ_4 -N1,N3,N7,N9-Adeninate Nucleobase. *Inorg. Chem.* **2009**, *48* (8), 3511–3513.
- Yang, J.; Ni, W.; Ruan, B.; Tsai, L.-C.; Ma, N.; Shi, D.; Jiang, T.; Tsai, F.-C. Review—Design and Synthesis of Fluorescence Sensing Metal-Organic Frameworks. *ECS J. Solid State Sci. Technol.* **2021**, *10* (5), 056003.
- Yang, L.; Pastor-Pérez, L.; Gu, S.; Sepúlveda-Escribano, A.; Reina, T. R. Highly Efficient Ni/CeO₂-Al₂O₃ Catalysts for CO₂ Upgrading via Reverse Water-Gas Shift: Effect of Selected Transition Metal Promoters. *Appl. Catal. B Environ.* **2018**, *232*, 464–471.
- Yang, Y.; Broto-Ribas, A.; Ortín-Rubio, B.; Imaz, I.; Gándara, F.; Carné-Sánchez, A.; Guillerm, V.; Jurado, S.; Busqué, F.; Juanhuix, J.; MasPOCH, D. Clip-off Chemistry: Synthesis by Programmed Disassembly of Reticular Materials. *Angew. Chemie - Int. Ed.* **2022**, *61* (4), 1–9.
- Yuan, D.; Zhao, D.; Sun, D.; Zhou, H. C. An Isorecticular Series of Metal-Organic Frameworks with Dendritic Hexacarboxylate Ligands and Exceptionally High Gas-Uptake Capacity. *Angew. Chemie - Int. Ed.* **2010**, *49* (31), 5357–5361.
- Yuan, S.; Feng, L.; Wang, K.; Pang, J.; Bosch, M.; Lollar, C.; Sun, Y.; Qin, J.; Yang, X.; Zhang, P.; Wang, Q.; Zou, L.; Zhang, Y.; Zhang, L.; Fang, Y.; Li, J.; Zhou, H. C. Stable Metal–Organic Frameworks: Design, Synthesis, and Applications. *Adv. Mater.* **2018**, *30* (37), 1–35.
- Yuan, S.; Qin, J. S.; Lollar, C. T.; Zhou, H. C. Stable Metal-Organic Frameworks with Group 4 Metals: Current Status and Trends. *ACS Cent. Sci.* **2018**, *4* (4), 440–450.
- Zhang, G.; Li, H.; Zhao, F.; Hu, H.; Huang, H.; Li, H.; Han, X.; Liu, R.; Dong, H.; Liu, Y.; Kang, Z. A Cobalt-Based 3D Porous Framework with Excellent Catalytic Ability for the Selective Oxidation of Cis-Cyclooctene. *Dalt. Trans.* **2013**, *42* (26), 9423–9427.
- Zhang, J.; Hu, Y.; Li, Y. Gel Chemistry Interactions, Structures and Properties; Springer Singapore: Singapore, Singapore, **2018**.
- Zhang, J.; Su, C. Y. Metal-Organic Gels: From Discrete Metallogelators to Coordination Polymers. *Coord. Chem. Rev.* **2013**, *257* (7–8), 1373–1408.
- Zhang, M.; Lu, W.; Li, J. R.; Bosch, M.; Chen, Y. P.; Liu, T. F.; Liu, Y.; Zhou, H. C. Design and Synthesis of Nucleobase-Incorporated Metal-Organic Materials. *Inorg. Chem. Front.* **2014**, *1* (2), 159–162.
- Zhao, J.; Teng, Y. L.; Dong, B. X. Thermal Reduction of CO₂ with Activated Alkali Metal Aluminum Hydrides for Selective Methanation. *Energy and Fuels* **2020**, *34* (9), 11210–11218.
- Zhao, S.; Jin, R.; Jin, R. Opportunities and Challenges in CO₂ Reduction by Gold- and Silver-Based Electrocatalysts: From Bulk Metals to Nanoparticles and Atomically Precise Nanoclusters. *ACS Energy Lett.* **2018**, *3* (2), 452–462.
- Zheng, Y.-Z.; Tong, M.-L.; Xue, W.; Zhang, W.-X.; Chen, X.-M.; Grandjean, F.; Long, G. J. A “Star” Antiferromagnet: A Polymeric Iron(III) Acetate That Exhibits Both Spin Frustration and Long-Range Magnetic Ordering. *Angew. Chemie* **2007**, *119* (32), 6188–6192.
- Zhou, H. C. J.; Kitagawa, S. Metal-Organic Frameworks (MOFs). *Chem. Soc. Rev.* **2014**, *43* (16), 5415–5418.

- Zhou, H.; Chen, Z.; Kountoupi, E.; Tsoukalou, A.; Abdala, P. M.; Florian, P.; Fedorov, A.; Müller, C. R. Two-Dimensional Molybdenum Carbide 2D-Mo₂C as a Superior Catalyst for CO₂ Hydrogenation. *Nat. Commun.* **2021**, *12* (1), 1–10.
- Zhou, H.-C.; Long, J. R.; Yaghi, O. Introduction to Metal–Organic Frameworks. *Chem. Rev.* **2012**, *112*, 673–674.
- Zhou, M.; Liu, G.; Liu, G.; Ju, Z.; Su, K.; Du, S.; Du, S.; Tan, Y.; Yuan, D.; Yuan, D. Hydrogen-Bonded Framework Isomers Based on Zr-Metal Organic Cage: Connectivity, Stability and Porosity. *Cryst. Growth Des.* **2020**, *20* (6), 4127–4134.
- Zhu, Z. H.; Wang, H. L.; Zou, H. H.; Liang, F. P. Metal Hydrogen-Bonded Organic Frameworks: Structure and Performance. *Dalt. Trans.* **2020**, *49* (31), 10708–10723.
- Zhuang, Y.; Currie, R.; McAuley, K. B.; Simakov, D. S. A. Highly-Selective CO₂ Conversion via Reverse Water Gas Shift Reaction over the 0.5wt% Ru-Promoted Cu/ZnO/Al₂O₃. *Catalyst. Appl. Catal. A Gen.* **2019**, *575*, 74–86.
- Zou, D.; Liu, D. Understanding the Modifications and Applications of Highly Stable Porous Frameworks via UiO-66. *Mater. Today Chem.* **2019**, *12*, 139–165.

Appendices

A.1. Chemicals

A.2. Instrumental techniques

A.3. Magnetic fitting models

A.4. Publications arising from this work

A.1. CHEMICALS

All chemicals employed for the synthesis of the compounds were of reagent grade and used as commercially obtained. Tables A.1.1 and A.1.2 gather the reactants, formula, commercial supplier (CS), assay (AS), molecular weight (MW), Chemical Abstracts Service number (CAS).

Table A.1.1. Employed reactants.

Name	Formula	CS	AS	M.W. (g/mol)	CAS
Copper(II) nitrate hemipentahydrate	Cu(NO ₃) ₂	Sigma Aldrich	98%	232.59	19004-19-4
Cobalt(II) nitrate hexahydrate	Co(NO ₃) ₂	Sigma Aldrich	≥98%	291.03	10026-22-9
Ni(II) nitrate hexahydrate	Ni(NO ₃) ₂	Sigma Aldrich	98.5%	290.79	13478-00-7
Zinc(II) nitrate hexahydrate	Zn(NO ₃) ₂	Fluka	≥99%	297.48	10196-18-6
Zirconium(IV) chloride	ZrCl ₄	Alfa Aesar	≥99.5%	233.04	10026-11-6
Acetone	C ₃ H ₆ O	Labkem	99.6%	58.08	67-64-1
Acetonitrile	C ₂ H ₃ N	Labkem	≥99%	41.05	75-05-8
Dichloromethane	CH ₂ Cl ₂	Sigma Aldrich	≥99%	84.93	75-09-2
Methanol	CH ₃ OH	Scharlau	≥99%	32.04	67-56-1
Ethanol	C ₂ H ₆ O	Scharlau	≥99.9%	46.07	64-17-5
1-Propanol	C ₃ H ₈ O	Labkem	≥99.5%	60.10	71-23-8
Deuterium oxide	D ₂ O	Sigma Aldrich	99.9%	20.03	7789-20-0
DMF	C ₂₀ H ₁₂ O ₅	Labkem	99.9%	73.09	68-12-2
Sodium hydroxide	NaOH	Labkem	>98%	40.00	1310-73-2
Nitric acid	HNO ₃	Labkem	65%	63.01	7697-37-2

Table A.1.2. Employed ligands.

Name	Formula	CS	AS	M.W.(g/mol)	CAS number
Adenine	C ₅ H ₅ N ₅	Sigma Aldrich	≥99%	135.13	73-24-5
Theobromine	C ₇ H ₈ N ₄ O ₂	Fluka	>98	180.17	83-67-0
Caffeine	C ₈ H ₁₀ N ₄ O ₂	Fluka	>99%	194.20	58-08-2
Theophylline	C ₇ H ₈ N ₄ O ₂	Fluka	>99%	180.17	58-55-9
Benzoic acid	C ₇ H ₆ O ₂	Sigma Aldrich	99.5%	122.12	65-85-0
Terephthalic acid	C ₈ H ₆ O ₄	Sigma Aldrich	98%	166.13	100-21-0
Fumaric acid	C ₄ H ₄ O ₄	Sigma Aldrich	≥99%	116.07	110-17-8
Acetylenedicarboxylic acid	C ₄ H ₂ O ₄	Sigma Aldrich	95%	114.06	142-45-0
Naphthalen-2,6-dicarboxylic acid	C ₁₂ H ₈ O ₄	Sigma Aldrich	95%	216.19	1141-38-4
Biphenyl-4,4'-dicarboxylic acid	C ₁₄ H ₁₀ O ₄	Sigma Aldrich	97%	242.23	787-70-2
Stilbene-4,4'-dicarboxylate	C ₁₆ H ₁₂ O ₄	Sigma Aldrich	98%	268.26	100-31-2
2-Hydroxybenzoic acid	C ₇ H ₆ O ₃	Sigma Aldrich	99%	138.12	99-06-9
3-Hydroxybenzoic acid	C ₇ H ₆ O ₃	Sigma Aldrich	99%	138.12	99-96-7
4,4',4'',4'''-(Porphine-5,10,15,20-tetrayl)tetrakis(benzoic acid)	C ₄₈ H ₃₀ N ₄ O ₈	Sigma Aldrich	75%	790.77	14609-54-2
Fluorescein	C ₂₀ H ₁₂ O ₅	Sigma Aldrich	99%	323.31	2321-07-5
D-(+)-Raffinosa	C ₁₈ H ₃₂ O ₁₆	Sigma Aldrich	≥99%	504.42	17629-30-0
Urea	CH ₄ N ₂ O	Scharlau	99%	60.06	57-13-6
Glucosa	C ₆ H ₁₂ O ₆	Sigma Aldrich	>99.5%	180.16	50-99-7
(D) Fructose	C ₆ H ₁₂ O ₆	Sigma Aldrich	≥99%	180.16	57-48-7
Benzyl alcohol	C ₇ H ₈ O	Sigma Aldrich	99%	108.14	100-51-6
Imidazol					
Sand, white quartz, Silicon dioxide	SiO ₂	Sigma Aldrich		60.08	14808-60-7

A.2. INSTRUMENTAL TECHNIQUES

A.2.1. Infrared spectroscopy

The IR spectra were recorded on a FTIR 8400S Shimadzu spectrometer of the Organic and Inorganic Department of the Science and Technology Faculty of the UPV/EHU in the 4000–400 cm^{-1} spectral region (Figure A.2.1). The measurements were made using the attenuated total reflection (ATR) technique with approximately using 2 mg of each compound and 200 mg of dry KBr. A spectrum correction was made in order to palliate the background noise and be able to appreciate more precisely the IR spectra in this region.

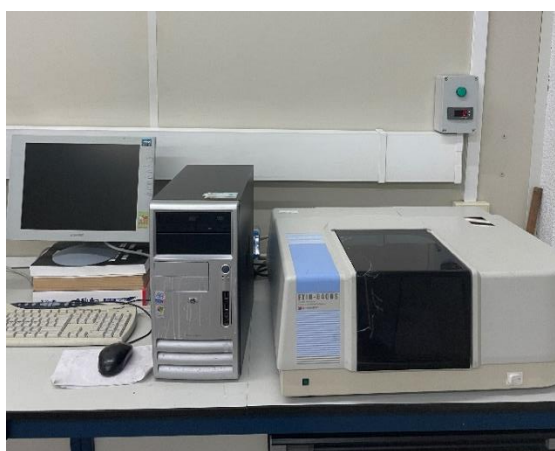


Figure A.2.1. FTIR 8400S Shimadzu spectrophotometer.

A.2.2. Thermal analysis

The thermogravimetric studies (TGA, and DTA) were carried out in a METTLER TOLEDO TGA/SDTA851° thermal analyser of our research group of Inorganic chemistry of the Science and Technology Faculty of the UPV/EHU (Figure A.2.2). The measures were performed in an atmosphere of synthetic air (79% N_2 / 21% O_2) with a flow rate of 50 $\text{cm}^3 \text{min}^{-1}$, between 25 and 600 or 800 $^\circ\text{C}$, with a heating rate of 5 $^\circ\text{C}\cdot\text{min}^{-1}$.



Figure A.2.2. METTLER TOLEDO TGA/SDTA851° thermal analyser.

A.2.3. Elemental analyses and inductively coupled plasma (ICP)

Elemental analyses (C, H, N) were performed on an Organic elemental Thermo Scientific Modelo FLASH 2000 microanalyser (Figure A.2.3A) provided by Burgos University, whereas the metal content was determined by inductively coupled plasma (ICP–AES) performed on a Horiba Yobin Yvon Activa spectrometer (Figure A.2.3B), provided by the SGIker of the University of the Basque Country (UPV/EHU).



(a)



(b)

Figure A.2.3. (a) Organic elemental Thermo Scientific Modelo FLASH 2000 microanalyser and (b) Horiba Yobin Yvon Activa spectrometer.

A.2.4. Single-crystal X-ray diffraction

The single crystal X-ray diffraction data collections were done on an Agilent Technologies Supernova ($\lambda_{\text{Mo-K}\alpha} = 0.71073 \text{ \AA}$ and $\lambda_{\text{Cu-K}\alpha} = 1.5418 \text{ \AA}$) diffractometers of the SGIker of the UPV/EHU (Figure A.2.4).



Figure A.2.4. Agilent Technologies Supernova diffractometer.

A.2.5. X-ray powder diffraction

The X-ray powder diffraction patterns were collected on a Phillips X'PERT powder diffractometer of the SGIKer of the UPV/EHU with Cu-K α radiation ($\lambda = 1.5418 \text{ \AA}$) over the range $5 < 2\theta < 50^\circ$ with a step size of 0.02° and an acquisition time of 2.5 s per step at 25°C (Figure A.2.5). Indexation of the diffraction profiles were made by means of the FULLPROF program (pattern-matching analysis) on the basis of the space group and the cell parameters found for isostructural compounds by single crystal X-ray diffraction.



Figure A.2.5. Phillips X'PERT powder diffractometer.

A Bruker D8 Advance Vario powder diffractometer of the SGIKer of the UPV/EHU with Cu-K $\alpha 1$ ($\lambda = 1.5406 \text{ \AA}$) was used to perform the variable-temperature X-ray powder diffraction measurements, heating the samples from room temperature with a heating rate of $5^\circ\text{C}\cdot\text{min}^{-1}$ and measuring a complete diffractogram every 10°C (Figure A.2.6).



Figure A.2.6. Bruker D8 Advance Vario powder diffractometer.

A.2.6. X powder diffraction in mother liquid

X-ray measurements were obtained by using a Rigaku Smartlab automatic diffractometer operating at 40 kV and 50 mA. The 2theta scans in transmission mode were obtained with parallel beam configuration (CBO), capillary attachment head, automatic attenuator and 1-D DteX250 detector (Figure A.2.7). The diffracción data were collected in continues rotation, from 3 to 65° step size of 0.01° at 0.5°/min scan speed. The capillaries were prepared by taking part of the polycrystalline sample and introducing it into Lindemann capillaries of diameter 0.5 or 0.3 nm. To keep the sample watertight the holes were closed with instant glue.



Figure A.2.7. Rigaku Smartlab diffractometer.

A.2.7. X-Ray Fluorescence (XRF)

X-ray fluorescence measurements were obtained by using a Spectrometer MIDEX SD of X-Ray micro fluorescence by energy dispersion ED-XRF for elemental analysis, commercial house Spectro, Figure A.2.8. It has automatic XYZ tray, automatic collimator changer, X-ray tube with Mo anode, maximum power 40 W; maximum voltage 48 kV and silicon drift detector (SDD) of 30mm² area, and energy resolution FWH less than 150 eV, measured in Mn Kalfa line. Calibration is by FP Plus fundamental parameters.



Figure A.2.8. Rigaku Smartlab diffractometer.

A.2.8. X-Ray Photoelectron Spectroscopy

X-Ray Photoelectron Spectroscopy (XPS) measurements were performed on a SPECS system (Berlin, Germany) equipped with a Phoibos 150 1D-DLD analyzer and monochromatic radiation source Al K α (1486.7 eV). An initial analysis was carried out to determine the elements present (wide scan: step energy 1 eV, dwell time 0.1 s, pass energy 80 eV) and a detailed analysis of the detected elements (detail scan: step energy 0.08 eV, dwell time 0.1 s, pass energy 30 eV) with an electron exit angle of 90°. The spectrometer was previously calibrated with Ag (Ag 3d_{5/2}, 368.26 eV), Figure A.2.9.

The spectra were fitted using CasaXPS 2.3.16 software, which models the Gauss-Lorentzian contributions, after background subtraction (Shirley background subtraction (Shirley)). The concentrations were calculated by correcting the values with relative atomic sensitivity factors (Scofield). The reduction conditions of the samples in the cell were:

- Ramp up to 450 °C, 1 hour, 1 bar, 300 mL·min⁻¹ H₂/Ar (20%), continuous.
- Isotherm 450 °C, 1 hour, 1 bar, 300 mL·min⁻¹ H₂/Ar (20%), continuous.



Figure A.2.9. SPECS system equipped with Phoibos 150 1D-DLD analyser.

A.2.9. Transmission Electron Microscopy

Transmission electron microscopy experiments were performed on a Talos F200i field emission gun instrument equipped with a Bruker X-Flash100 XEDS spectrometer, Figure A.2.10.

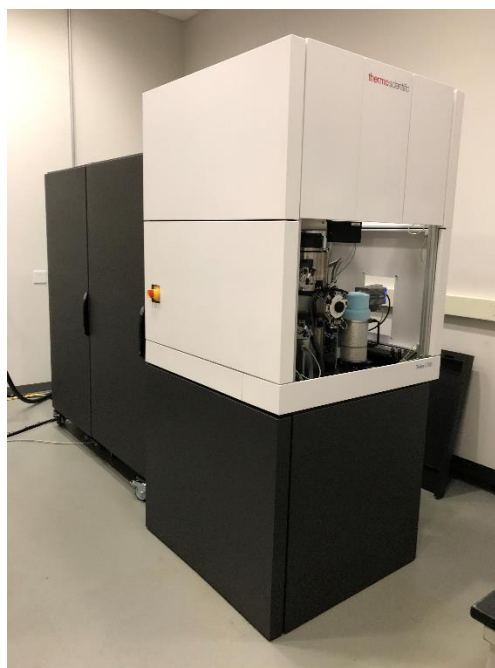


Figure A.2.10. Transmission electron microscopy (TEM).

Elemental maps were performed by XEDS in the STEM mode under high annular dark field (HAADF) detector for Z contrast imaging in STEM conditions (camera length of 160 mm) using a pixel size of 2 nm, a dwell time of 30 min and an image size of 512x512 pixels.

Moreover, EDX microanalyses were carried out using a probe current of 500 pA and a semiconvergence angle of 6 mrad.

The samples for the TEM were prepared by dispersion into ethanol solvent and keeping the suspension in an ultrasonic bath for 15 min, after a drop of suspension was spread onto a TEM copper grid (300 Mesh) covered by a holey carbon film followed by drying under vacuum.

A.2.10. Magnetism measurements

Magnetic susceptibility measurements have been performed using a standard Quantum Design PPMS magnetometer between 2 and 300 K with a field of 1 kOe, Figure A.2.11. Magnetization, as a function of H field, has been measured using the same magnetometer in the range $-50 \text{ H} \cdot \text{kOe}^{-1}$ 50 and at 2 K after cooling the sample to zero field. The susceptibility data were corrected for diamagnetism using Pascal's Tables,¹ temperature-independent paramagnetism and magnetization of the sample support.



Figure A.2.11. Quantum Design PPMS magnetometer system.

¹ Earnshaw, A.; Academic Press: London, England, 1968.

A.2.11. Fluorescence measurements

A Varian Cary-Eclipse Fluorescence spectrofluorometer was used to obtain the fluorescence spectra at room temperature. The spectrofluorometer is equipped with a xenon discharge lamp (peak power equivalent to 75 kW), a Czerny–Turner monochromator, and an R-928 photomultiplier tube which is red sensitive (even 900 nm) with a manual or automatic voltage. The photomultiplier detector voltage was 700 V and the instrument excitation and emission slits were set at 5 nm, Figure A.2.12.



Figure A.2.12. Quantum Design PPMS magnetometer system.

A.3. MAGNETIC FITTING MODELS

Then, the different models and equations used in the analysis of the molar magnetic susceptibility (χ_m) data are exposed. For the dimeric compounds calculations described in Chapter 2, the mathematical model used corresponds to Bleaney-Bowers equation for dimeric model of $S = 1/2$ interacting paramagnetic centres:

$$\chi_m = \frac{Ng^2\beta^2}{kT} f(x) \quad \text{where } f(x) = \frac{2 \exp(x)}{1+3\exp(x)} \quad (X = J / kT)$$

In case of the magnetic models in the following chapters, in contrast, the fitting of the $\chi_m T$ experimental data above 10 K to all the model and the calculation of all the superexchange parameters was performed using the MagProp software tool distributed with DAVE.²⁰² The calculated product $\chi_m T_{\text{calc}}$ was performed using the Van Vleck equation² where:

$$\chi_m = \frac{N\beta^2 J(J+1)g^2}{3kT}$$

It uses the g-factor and the Hund rule that the state of lowest energy is that of maximum spin, and of maximum L compatible with this S.

The DAVE software package is an experimental neutron scattering data reduction, visualization, and analysis system. In order to analyze the magnetic behaviour, the MagProp program module for the workup, visualisation and analysis of magnetic data is used (Figure A.3.1). This program incorporates a Hamiltonian matrix generator that allows generating a matrix representation of a given Hamiltonian from a symbolic expression (Figure A.3.2a). Then the desired magnetic couplings constants are added with the g value expressed as g_x , g_y and g_z , using the common Zeeman terms (Figure A.3.2b). Once the desired Hamiltonian is generated, the value of the $\chi_m T$ product is calculated from the curve imported into the program (Figure A.3.3).

² Van Vleck, J. H. *Nobel Lectures, Physics 1971-1980*; World Scientific Publishing Co.: Singapore, Singapore, **1992**.

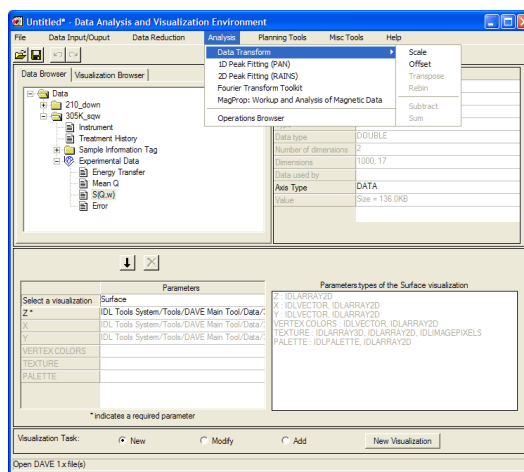
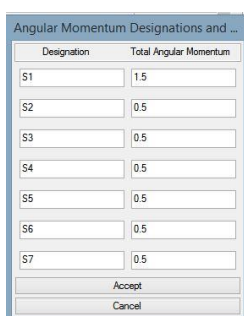
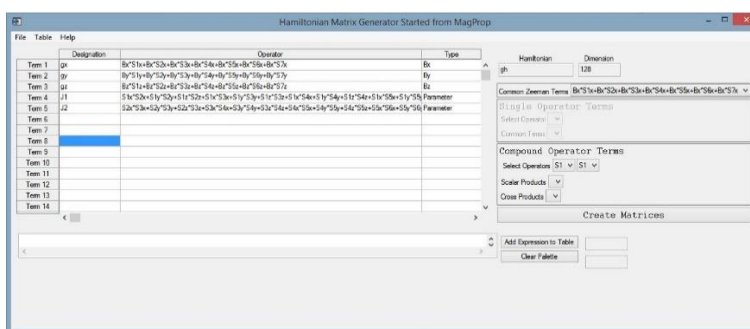


Figure A.5.1. The main application window of DAVE.



(a)



(b)

Figure A.3.2. Hamiltonian generation window corresponding to the Cu₆CrAD compound with a central Cr(III) and a ring of six Cu(II) (a) and Common Zeeman terms window (b).

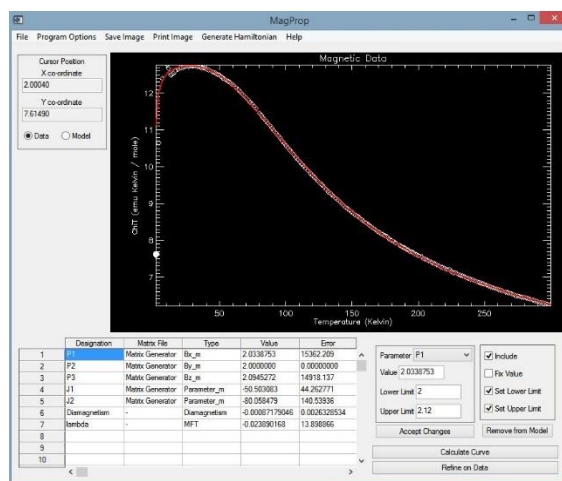


Figure A.3.3. Representation of a magnetic adjustment, using the diamagnetism and molecular field theory factors to adjust the theoretical line. The experimental $\chi_m T$ is indicated as the white line while the theoretical is indicated as a red line.

A.4. PUBLICATIONS ARISING FROM THIS WORK

This work has led to the publication of some articles in international scientific journals that are attached below:

1. Thomas-Gipson, J.; Beobide, G.; Castillo, O.; Luque, A.; Pascual-Colino, J.; Pérez-Yáñez, S.; Román, P. Providing Evidence for the Requirements to Achieve Supramolecular Materials Based on Metal-Nucleobase Entities. *CrystEngComm* **2018**, *20* (18), 2528–2539.
2. Pascual-Colino, J.; Beobide, G.; Castillo, O.; Da Silva, I.; Luque, A.; Pérez-Yáñez, S. Porous Supramolecular Architectures Based on π -Stacking Interactions between Discrete Metal-Adenine Entities and the Non-DNA Theobromine/Caffeine Nucleobases. *Cryst. Growth Des.* **2018**, *18* (6), 3465–3476.
3. Pascual-Colino, J.; Beobide, G.; Castillo, O.; Luque, A.; Pérez-Yáñez, S. Theophylline Alkaloid as Glue of Paddle-Wheel Copper(II)-Adenine Entities to Afford a Rhomboid Chain. *Inorganica Chim. Acta* **2019**, *484*, 437–442.
4. Pascual-Colino, J.; Beobide, G.; Castillo, O.; Lodewyckx, P.; Luque, A.; Pérez-Yáñez, S.; Román, P.; Velasco, L. F. Adenine Nucleobase Directed Supramolecular Architectures Based on Ferrimagnetic Heptanuclear Copper(II) Entities and Benzenecarboxylate Anions. *J. Inorg. Biochem.* **2020**, *202*, 110865.
5. Napal, J.; Artetxe, B.; Beobide, G.; Castillo, O.; Luque, A.; Pascual-Colino, J.; Pérez-Yáñez, S.; Perfecto-Irigaray, M. Merging the Chemistry of Metal-Organic and Polyoxometalate Clusters to Form Enhanced Photocatalytic Materials. *Inorg. Chem. Front.* **2022**, *9* (5), 935–940.
6. Pascual-Colino, J.; Artetxe, B.; Beobide, G.; Castillo, O.; Fidalgo-Mayo, M. L.; Isla-López, A.; Luque, A.; Mena-Gutiérrez, S.; Pérez-Yáñez, S. The Chemistry of Zirconium/Carboxylate Clustering Process: Acidic Conditions to Promote Carboxylate-Unsaturated Octahedral Hexamers and Pentanuclear Species. *Inorg. Chem.* **2022**, *61* (12), 4842–4851.



Cite this: *CrystEngComm*, 2018, 20, 2528

Providing evidence for the requirements to achieve supramolecular materials based on metal–nucleobase entities†

Jintha Thomas-Gipson,^{ab} Garikoitz Beobide,^{ib} Oscar Castillo,^{id *b} Antonio Luque,^{id b} Jon Pascual-Colino,^{id b} Sonia Pérez-Yáñez^{id *bc} and Pascual Román^{id b}

Nucleobases are known as suitable builders of porous materials not only due to their high number of heteroatoms leading to different coordination modes, but also because they establish strong and predictable supramolecular interactions. In this contribution, nucleobases (adenine and guanine), functionalized nucleobases (9-methyladenine) and nucleobase derivatives (6-chloropurine) have been evaluated as ligands for the construction of metal–nucleobase building blocks which can afford supramolecular porous materials, analyzing in detail the requirements that these entities must fulfill and pointing out the relevance of accomplishing the suggested requisites. More concisely, we have evaluated a paddle-wheel shaped dimeric entity, $[\text{Cu}_2(\mu\text{-Hade})_4\text{Cl}_2]\text{Cl}_2\cdot 8\text{H}_2\text{O}$ (1) (where Hade: adenine), a trimeric unit, $[\text{Co}_3(\mu\text{-Hade})_2(\mu\text{-Cl})_4\text{Cl}_2(\text{H}_2\text{O})_4]\cdot 2\text{H}_2\text{O}$ (2), a dimeric entity, $[\text{Cu}_2(\text{Hgua})_2(\text{H}_2\text{gua})_2(\mu\text{-Cl})_2\text{Cl}_2(\text{H}_2\text{O})][\text{CuCl}_4]$ (3) (where Hgua: guanine, H_2gua : guaninium), a monomeric unit with 9-methyladenine as the pendant ligand, $[\text{Co}(\text{9-Meade})_2(\text{H}_2\text{O})_4]\text{Cl}_2\cdot 2\text{H}_2\text{O}$ (4), zigzag chains, $[\text{Cu}_2(\mu\text{-CH}_3\text{COO})_4(\mu\text{-9-Meade})]_n\cdot n\text{CH}_3\text{OH}$ (5), and a monomeric unit with 6-chloropurinato ligands, $[\text{Co}(\text{6-Clpur})_2(\text{H}_2\text{O})_4]\cdot 4\text{H}_2\text{O}$ (6).

Received 29th January 2018,
Accepted 19th March 2018

DOI: 10.1039/c8ce00141c

rsc.li/crystengcomm

Introduction

Metal–organic frameworks (MOFs) are crystalline materials composed of inorganic and organic components.¹ One of the greatest features of MOFs is their porosity, since they exhibit very high surface areas, tunable pore sizes and shapes, and adjustable surface functionalities.² Their unique porous nature makes them suitable to face some of the concerns of our planet since they are being investigated for addressing matters such as the use of hydrogen as a long term fuel, the employment of methane as a transitional fuel, and the capture and sequestration of carbon dioxide as an urgent response to ongoing climate change.³

A rational design of this type of material leads to different properties that can be tuned at will, providing in this way ma-

terials with applications in areas such as luminescence,⁴ magnetism,⁵ electrical conductivity⁶ or catalytic activity,⁷ since they benefit from their hybrid metal–organic nature.

At the beginning, nucleobases were used to afford coordination compounds with the aim of designing biomimetic compounds in order to better understand the interactions between metal ions and constituents of DNA.^{8–10} Nevertheless, with the progress in the field of porous materials, nucleobases have emerged as suitable pillars for the construction of these compounds.^{11–13} The great capacity of nucleobases to provide porous coordination polymers based on their multiple coordinating positions, mainly in purine derivatives, is generally accepted. However, during the last few years, they have also shown potential to afford porous compounds based on their well-known ability to establish complementary hydrogen bond interactions.¹⁴ Taking advantage of this feature, in previously reported works, we proposed some requirements that metal–nucleobase entities should meet to provide porous compounds from the knowledge inferred from our first supramolecular metal–organic frameworks (SMOFs).^{15,16} Metal–nucleobase entities should fulfill the following requisites: (i) a rigid discrete entity, achievable if the nucleobase is anchored to the building unit through multiple positions, usually by two coordination bonds or the combination of a coordination bond and an intramolecular hydrogen bond, (ii) rigid and predictable synthons, such as those provided by complementary hydrogen bonding interactions taking place between

^a Department of Applied Chemistry, Cochin University of Science and Technology, South Kalamassery, 682022 Kochi, Kerala, India

^b Departamento de Química Inorgánica, Facultad de Ciencia y Tecnología, Universidad del País Vasco/Euskal Herriko Unibertsitatea, UPV/EHU, Apartado 644, E-48080 Bilbao, Spain. E-mail: oscar.castillo@ehu.eus, sonia.perez@ehu.eus

^c Departamento de Química Inorgánica, Facultad de Farmacia, Universidad del País Vasco/Euskal Herriko Unibertsitatea, UPV/EHU, E-01006 Vitoria-Gasteiz, Spain

† Electronic supplementary information (ESI) available: Tables of coordination bonds, tables of structural parameters of non-covalent interactions, experimental and theoretical X-ray diffraction patterns, thermogravimetric data and cif files. CCDC 1566047–1566052. For ESI and crystallographic data in CIF or other electronic format see DOI: 10.1039/c8ce00141c

nucleobases, and (iii) a metal coordination geometry that imposes a non-coplanar arrangement of several nucleobases that allows a three-dimensional propagation of the base pairing interactions.

It should be noted that supramolecular assembly processes have been widely studied in the formation of materials with different applications such as fluorescent nucleic acid detection,¹⁷ as a catalyst in the reduction of H₂O₂,¹⁸ and glucose sensing.¹⁹

In this manuscript, we have analyzed the compliance of these requisites upon several metal–nucleobase entities, in order to assess the suitability of the described theory. Different nucleobases have been employed to offer a more extensive analysis.

Experimental

All reagents and solvents were of commercial grade and were used without further purification.

Synthesis procedures

Synthesis of [Cu₂(μ-Hade)₄Cl₂]Cl₂·8H₂O (1). 0.0682 g of adenine (0.5 mmol) dissolved in 60 mL of hot water was added dropwise to a stirring solution of 0.0852 g of CuCl₂·2H₂O (0.5 mmol) dissolved in 5 mL of water. The resulting light blue solution was stirred for 2 hours, leading to a very thin powder. The solution was filtered (bluish powder: amorphous phase) and the filtrate was left for one week until blue single crystals corresponding to compound 1 appeared.

It should be noted that when performing the synthesis in methanol/ethanol or with a stoichiometric ratio of copper: adenine (1:2), the obtained compound corresponds to the previously reported SMOF [Cu₂(μ-Hade)₄Cl₂]Cl₂·*n*CH₃OH,¹⁶ or amorphous phases, respectively.

Yield (based on metal): 40%. Anal. calcd (found) for C₂₀H₃₆Cl₄Cu₂N₂₀O₈: C, 25.19 (25.13); H, 3.81 (3.75); N, 29.38 (29.42); Cu, 13.33 (13.27)%. Main IR features (cm⁻¹): 3440s, 3191s, 2362w, 2338w, 1646vs, 1463m, 1400m, 1343w, 1310w, 1280w, 1203m, 1143m, 1110m, 993w, 906, 791m, 738m, 655m, 619m, 569m, 461m.

Synthesis of [Co₃(μ-Hade)₂(μ-Cl)₄Cl₂(H₂O)₄]·2H₂O (2). Pink coloured single crystals of compound 2 were obtained within one week using diffusion techniques by layering a methanolic solution of 0.0135 g of adenine (0.1 mmol in 10 mL) over an aqueous solution of 0.0119 g of CoCl₂·6H₂O (0.05 mmol in 10 mL).

Direct synthesis results in a blue polycrystalline sample that corresponds to the previously reported SMOF [Co(Hade)₂Cl₂].²⁰

Yield: 10%. Anal. calcd (found) for C₁₀H₂₂Cl₆Co₃N₁₀O₆: C, 15.64 (15.67); H, 2.89 (2.83); N, 18.24 (18.27); Co, 23.02 (22.98)%. Main IR features (cm⁻¹): 3444s, 2360vs, 2340s, 2266w, 1650m, 1633m, 1311w, 1244m, 1186w, 1147w, 983w, 719w, 680w, 668m, 649m, 614w, 536w.

Synthesis of [Cu₂(Hgua)₂(H₂gua)₂(μ-Cl)₂Cl₂(H₂O)] [CuCl₄] (3). A few good quality green crystals of compound 3 together

with some orange crystals corresponding to [Cu₂(Hgua)₂(μ-Cl)₂Cl₄]·2H₂O (ref. 21) were obtained by mixing methanolic solutions of 0.0173 g of CuCl₂·2H₂O (0.1 mmol in 5 mL) and an acidified methanolic solution of 0.0337 g of guanine, dissolved in 40 mL methanol, with 34 μl (0.4 mmol) of concentrated HCl (purity: 37%). Yield: 10%. Anal. calcd (found) for C₂₀H₂₄Cl₈Cu₃N₂₀O₅: C, 21.96 (21.84); H, 2.21 (2.28); N, 25.63 (25.54); Cu, 17.27 (17.36)%. Main IR features (cm⁻¹): 3450s, 1750vs, 1666vs, 1400m, 1383s, 1361m, 1316w, 1196w, 1160w, 1116w, 1073w, 1046w, 993m, 820w, 800w, 763w, 660w, 593w, 543w, 506m, 426w.

Synthesis of [Co(9-Meade)₂(H₂O)₄]Cl₂·2H₂O (4). 0.0298 g (0.2 mmol) of 9-methyladenine dissolved in 20 mL of methanol was added dropwise to a stirring solution of 0.0237 g (0.1 mmol) of CoCl₂·6H₂O dissolved in 5 mL of methanol at room temperature. The pink coloured clear solution formed was stirred at room temperature for two hours and left for evaporation. A few light pink good quality single crystals of compound 4 were formed within one week together with colourless crystals corresponding to 9-methyladenine. Yield: 20%. Anal. calcd (found) for C₁₂H₂₆Cl₂CoN₁₀O₆: C, 26.88 (26.81); H, 4.88 (4.79); N, 26.12 (26.17); Co, 10.99 (11.03)%. Main IR features (cm⁻¹): 3417s, 2740w, 2760w, 2275w, 1947m, 1886w, 1793m, 1663vs, 1600vs, 1576vs, 1500s, 1467s, 1426s, 1416s, 1390w, 1373w, 1346s, 1326m, 1300s, 1266m, 1256s, 1230m, 1196m, 1086w, 1063m, 1047m, 1019m, 978w, 945m, 921m, 898s, 843m, 795m, 760w, 742w, 717m, 684w, 641w, 602w, 585w, 542m.

Synthesis of [Cu₂(μ-CH₃COO)₄(μ-9-Meade)]_{*n*}·*n*CH₃OH (5). 0.0298 g (0.2 mmol) of 9-methyladenine dissolved in 20 mL of methanol was added dropwise to a stirring solution of 0.0199 g (0.05 mmol) of [Cu₂(μ-OOCCH₃)₄(H₂O)₂] dissolved in 5 mL of methanol at room temperature. A green coloured precipitate was obtained immediately. Good quality green single crystals were obtained using diffusion techniques in which a methanolic solution of 9-methyladenine (0.1 mmol, 0.1490 g in 10 mL) was layered over a methanolic solution of copper(II) acetate monohydrate (0.05 mmol, 0.0099 g in 10 mL). Yield: 50%. Anal. calcd (found) for C₁₅H₂₃Cu₂N₅O₉: C, 33.09 (33.01); H, 4.26 (4.39); N, 12.86 (12.77); Cu, 23.34 (23.51)%. Main IR features (cm⁻¹): 3395s, 3288m, 3195s, 1666s, 1626s, 1603vs, 1530w, 1508w, 1475w, 1433s, 1421s, 1385m, 1336m, 1310m, 1258w, 1230s, 1197m, 1083w, 1067w, 1050m, 1020m, 945w, 902w, 880w, 841w, 795m, 760w, 742w, 720m, 685m, 642w, 626w, 603w, 561w, 540w, 530w.

Synthesis of [Co(6-Clpur)₂(H₂O)₄]·4H₂O (6). 0.0309 g (0.2 mmol) of 6-chloropurine dissolved in 20 mL of water was basified with a solution of NaOH (pH = 10.7). Then, 0.0291 g (0.1 mmol) of Co(NO₃)₂·6H₂O dissolved in 5 mL of water was added dropwise to a cold stirring solution of 6-chloropurine. The orange coloured solution formed was stirred for 2 hours and left to evaporate at room temperature. An orange coloured polycrystalline powder corresponding to compound 6 was obtained within three days. Single-crystals were obtained using the following synthesis route: 0.0464 g (0.3 mmol) of 6-chloropurine dissolved in 30 mL of water was

mixed with 0.59 mL (0.4 mmol) of pentylamine and the mixture was stirred in an ice bath for 1 hour. 0.0291 g (0.1 mmol) of $\text{Co}(\text{NO}_3)_2 \cdot 6\text{H}_2\text{O}$ dissolved in 5 mL of water was added dropwise to the cold stirring solution of 6-chloropurine. The orange coloured solution formed was stirred in an ice bath for 2 hours more and left to evaporate. Orange coloured single crystals of compound 6 were formed in three days. Yield: 60%. Anal. calcd (found) for $\text{C}_{10}\text{H}_{20}\text{Cl}_2\text{CoN}_8\text{O}_8$: C, 23.54 (23.63); H, 3.95 (3.87); N, 21.96 (21.99); Co, 11.55 (11.51)%. Main IR features (cm^{-1}): 3442s, 1717w, 1624s, 1593w, 1511w, 1482w, 1451w, 1384vs, 1330w, 1286w, 1250w, 1230w, 1144m, 1100m, 1064w, 990w, 933w, 920w, 855m, 939m, 785w, 750w, 630w, 606w, 595w, 537w, 500w.

Physical measurements

C, H, N elemental analyses were performed on a Euro EA Elemental Analyzer, whereas the metal content was determined by inductively coupled plasma (ICP-AES) performed on a Horiba Jobin Yvon Activa spectrometer. IR spectra were recorded on a FTIR 8400S Shimadzu spectrometer in the 4000–400 cm^{-1} spectral region. KBr pellets were prepared, with an approximate concentration of 2–3%.

Single-crystal X-ray diffraction and structure determination

The crystallographic data and the refinement conditions are given in Table 1. Diffraction data of single crystals were collected using Oxford Diffraction Xcalibur at 100 K (2, 3, 4, 5, and 6) and STOE IPDS II (1) diffractometers. Data reduction was carried out with CrysAlis RED²² and X-Area²³ programs, respectively. Structures were solved by direct methods using

the SIR92 program,²⁴ and refined by full-matrix least-squares on F^2 including all reflections (SHELXL97).²⁵ All calculations were performed using the WINGX crystallographic software package.²⁶ During the data acquisition of these compounds, it became evident that 2 was non-merohedrally twinned. The corresponding twin law is listed here: (0.997 0.007 0.002 0.579 –0.998 0.001 0.942 0.003 –0.999) with a percentage of the minor domain of 47.43%. The chloride counterions and crystallization water molecules located between the complex layers in compound 1 are highly disordered over different positions with a partial occupation factor. In addition, compound 3 shows a disorder related to the orientation of the Jahn–Teller effect on the dimeric unit. This implies that the terminal and bridging chlorido ligands are disordered over two positions with short and significantly longer Cu–Cl distances. This latter disorder also implies that a coordination water molecule is disordered over two positions with a total occupation factor of 0.50. The hydrogen atoms of the disordered water molecules were left unlocated. CCDC 1566047–1566052 contain the supplementary crystallographic data for this paper.

Results and discussion

We have employed adenine, guanine, 9-methyladenine, and 6-chloropurine for designing diverse metal–nucleobase entities that could afford supramolecular metal–organic frameworks, in order to evaluate different possibilities. Therefore, together with the structural characterization of the corresponding compounds, we analyze in more detail whether the metal–nucleobase entities fulfill the requirements that should be met to obtain porous compounds.

Table 1 Crystallographic data and structure refinement details of compounds 1–6

Compound	1	2	3	4	5	6
Formula	$\text{C}_{20}\text{H}_{36}\text{Cl}_4\text{Cu}_2\text{N}_{20}\text{O}_8$	$\text{C}_{10}\text{H}_{22}\text{Cl}_6\text{Co}_3\text{N}_{10}\text{O}_6$	$\text{C}_{20}\text{H}_{24}\text{Cl}_8\text{Cu}_3\text{N}_{20}\text{O}_5$	$\text{C}_{12}\text{H}_{26}\text{Cl}_2\text{CoN}_{10}\text{O}_6$	$\text{C}_{15}\text{H}_{23}\text{Cu}_2\text{N}_5\text{O}_9$	$\text{C}_{10}\text{H}_{20}\text{Cl}_2\text{CoN}_8\text{O}_8$
MW [g mol ⁻¹]	873.49	767.87	1098.81	536.26	544.46	510.17
Crystal system	Orthorhombic	Triclinic	Triclinic	Monoclinic	Triclinic	Monoclinic
Space group	<i>Pbam</i>	<i>P</i> $\bar{1}$	<i>P</i> $\bar{1}$	<i>I</i> 2/ <i>m</i>	<i>P</i> $\bar{1}$	<i>P</i> 2 ₁ / <i>c</i>
<i>a</i> [Å]	13.7405(7)	7.203(2)	7.8461(5)	11.3880(14)	7.3349(8)	10.6365(2)
<i>b</i> [Å]	10.3343(6)	9.520(3)	8.7590(5)	6.7307(7)	8.5513(8)	13.2099(1)
<i>c</i> [Å]	12.1024(7)	9.659(4)	13.1716(8)	14.9009(19)	16.8119(12)	7.3378(1)
α [°]	90	82.49(2)	79.157(5)	90	94.649(7)	90.00
β [°]	90	69.47(2)	77.230(5)	109.960(14)	93.046(7)	110.057(2)
γ [°]	90	77.59(4)	78.526(5)	90	99.041(8)	90.00
<i>V</i> [Å ³]	1718.52(2)	604.7(3)	855.28(9)	1073.5(2)	1035.64(2)	968.48(2)
<i>Z</i>	2	1	1	2	2	2
ρ_{calcd} [g cm ⁻³]	1.843	2.109	2.133	1.659	1.746	1.749
μ [mm ⁻¹]	1.627	2.748	8.550	1.101	2.112	1.221
Reflections collected	7061	4885	5843	4071	6694	6896
Unique data/parameters	2109/132	4885/161	3345/279	1319/93	3849/286	2210/133
<i>R</i> _{int}	0.0722	0.0602	0.0400	0.0217	0.0522	0.0230
Goodness of fit ^a (<i>S</i>)	0.915	0.960	1.049	1.070	1.083	1.075
<i>R</i> ₁ ^b / <i>wR</i> ₂ ^c [<i>I</i> > 2 σ (<i>I</i>)]	0.0521/0.1039	0.0288/0.0666	0.0560/0.1487	0.0260/0.0600	0.0635/0.1080	0.0250/0.0602
<i>R</i> ₁ ^b / <i>wR</i> ₂ ^c [all data]	0.1138/0.1118	0.0388/0.0681	0.0744/0.1629	0.0287/0.0618	0.1019/0.1231	0.0276/0.0617

^a $S = [\sum w(F_o^2 - F_c^2)^2 / (N_{\text{obs}} - N_{\text{param}})]^{1/2}$. ^b $R_1 = \sum |F_o| - |F_c| / \sum |F_o|$. ^c $wR_2 = [\sum w(F_o^2 - F_c^2)^2 / \sum w(F_o^2)^2]^{1/2}$; $w = 1 / [\sigma^2(F_o^2) + (aP)^2 + bP]$, where $P = (\max(F_o^2, 0) + 2F_c^2) / 3$ with $a = 0.0445$ (1), $a = 0.0358$ (2), $a = 0.0974$, $b = 0.5245$ (3), $a = 0.0232$ and $b = 1.4638$ (4), $a = 0.0332$ and $b = 0.0879$ (5), $a = 0.0248$, $b = 0.6272$ (6).

Compound $[\text{Cu}_2(\mu\text{-Hade})_4\text{Cl}_2]\text{Cl}_2\cdot 8\text{H}_2\text{O}$ (1)

The crystal structure of **1** consists of $[\text{Cu}_2(\mu\text{-Hade})_4\text{Cl}_2]^{2+}$ cations, chloride counterions and disordered water molecules. The two copper(II) centers are bridged by four adenine moieties through their N3 and N9 nitrogen atoms resulting in a paddle-wheel like structure (Fig. 1a). This N3,N9 coordination mode is one of the most usual ones for adenine nucleobase as it has been thoroughly analysed in previously reported reviews.^{10,11,27} The copper(II) centers exhibit a distorted square pyramidal geometry with the nitrogen atoms of the adenine ligands placed in the basal plane and the chlorido ligands in the apical position. The dimeric complex is seated on a $2/m$ crystallographic position and shows a UDD conformation, the terms U (up) and D (down) referring to the coordination of each pyrimidinic N3 atoms to the upper and lower metal center, respectively. The dimeric entity resembles the structure of the previously published complex $[\text{Cu}_2(\mu\text{-Hade})_4\text{Cl}_2]\text{Cl}_2\cdot 6\text{H}_2\text{O}$,²⁸ but its crystal structure differs by the number of entrapped water molecules (8 vs. 6). These subtle changes in the number of crystallization water molecules have been attributed in other systems to the synthesis temperature: lowering the temperature helps increase the amount of entrapped water molecules.²⁹

As can be inferred from Fig. 1b, though the $[\text{Cu}_2(\mu\text{-Hade})_4\text{Cl}_2]^{2+}$ units are rigid enough, thus accomplishing the first of the requisites for obtaining porous materials, the presence of crystallization water molecules hinders the nucleobase...nucleobase direct hydrogen bonding interactions (this has been depicted as a red cross). This unfulfillment of the necessary rigid synthons also prevents the compliance of the last requisite (three-dimensional propagation of the base pairing interactions), giving rise to a non-porous material.

The $[\text{Cu}_2(\mu\text{-Hade})_4\text{Cl}_2]^{2+}$ units are held together by hydrogen bonding interactions mediated through the crystallization water molecules, which are in fact disordered altogether with the chloride counterions, giving rise to a complex network of hydrogen bonds. The crystal structure can also be de-

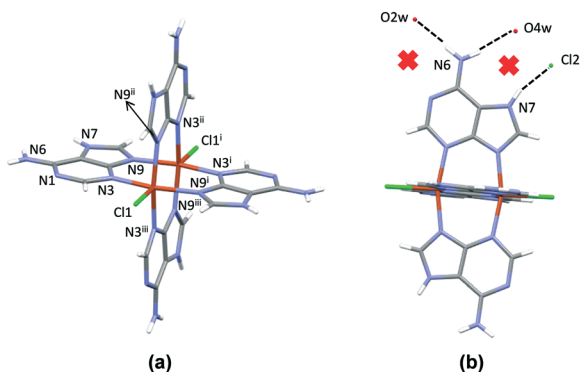


Fig. 1 (a) Dimeric $[\text{Cu}_2(\mu\text{-Hade})_4\text{Cl}_2]^{2+}$ cation present in compound **1**, including the labelling scheme. (b) Unfulfillment of the requisites for obtaining SMOFs in compound **1**. Note that the hydrogen bonding scheme is the same for all nucleobases.

scribed as layers of dimeric entities held together by means of water mediated $\text{Cl1}\cdots\text{Ow}\cdots\text{Ow}\cdots\text{Cl1}$ and weaker $\text{C8-H}\cdots\text{N1}$ hydrogen bonds. Disordered chloride and crystallization water molecules are placed among the sheets and hydrogen bonded to the adenine ligands of two neighbouring ones (Fig. 2).

Compound $[\text{Co}_3(\mu\text{-Hade})_2(\mu\text{-Cl})_4\text{Cl}_2(\text{H}_2\text{O})_4]\cdot 2\text{H}_2\text{O}$ (2)

The metal centers of the linear trinuclear $[\text{Co}_3(\mu\text{-Hade})_2(\mu\text{-Cl})_4\text{Cl}_2(\text{H}_2\text{O})_4]$ units in **2** are held together by four bridging chlorido ligands and two neutral 7*H*-adenine molecules showing a $\mu\text{-}\kappa\text{N3}:\kappa\text{N9}$ coordination mode. Each metal(II) atom presents an octahedral coordination environment, with a Cl_4N_2 donor set for the central cobalt atom and a $\text{CoCl}_3\text{N}_1\text{Ow}_2$ chromophore for the terminal ones (Fig. 3).

The 7*H*-tautomeric form of adenine precludes the Hoogsteen side from establishing complementary nucleobase...nucleobase hydrogen bond interactions, and this face is attached to a solvated O3w water molecule that acts as an acceptor of the two hydrogen bonds. The Watson-Crick side remains available (N1: acceptor, N6: donor).

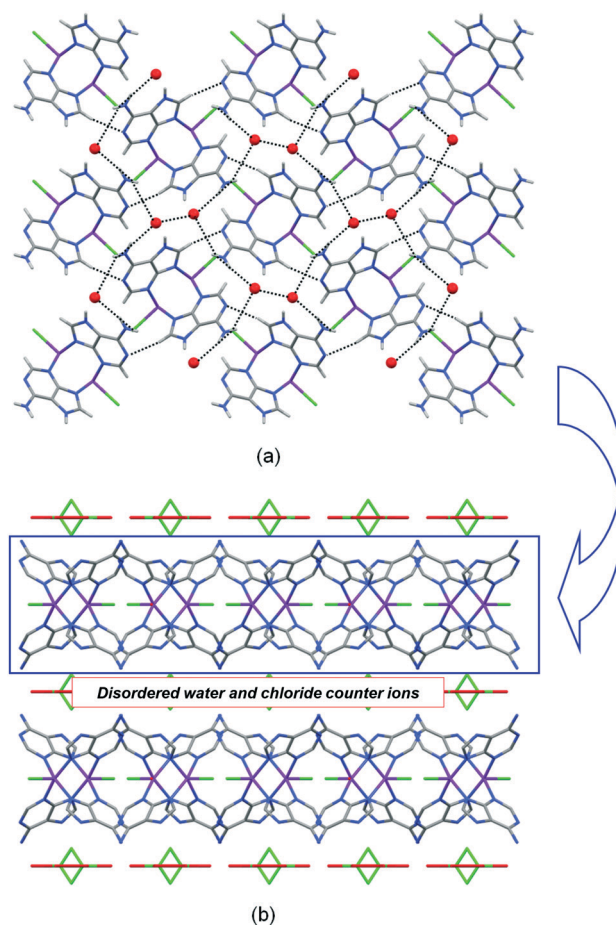


Fig. 2 Graphical insight into the crystal structure of **1**: (a) complex layer of $[\text{Cu}_2(\mu\text{-Hade})_4\text{Cl}_2]^{2+}$ units and water molecules. (b) Projection along the crystallographic *a* axis. Notice that the chloride counterions and interlayer water molecules are disordered.

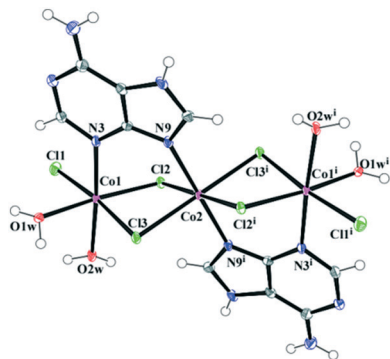


Fig. 3 Trimeric unit in compound 2 together with the labeling scheme.

Moreover, the synthesis was performed in a water/methanol mixture and, as it happens in compound 1, the water molecules disrupt the direct hydrogen bonding interaction between the adenines. In fact, the trimeric units interact through hydrogen bonds between the N1 nitrogen of the adenines and the coordinated water molecules of the neighbouring units in a head-to-tail manner, leading to a 1D chain along the $[0\ 1\ 0]$ direction (Fig. 4). These chains are held together by the abovementioned hydrogen bond, which involves the O3w water molecule, giving rise to a non-porous structure (Fig. 5).

So that, once again, the solvation molecules seem to hinder the achievement of the target porous material (Fig. 6). Despite the rigidity of the trimeric entity in compound 2, the fulfillment of the remaining requisites is hampered by the presence of crystallization water molecules together with the hydrogen bonding interactions involving coordination water molecules, which hinder the adenine...adenine direct hydrogen bonding interactions.

Compound $[\text{Cu}_2(\text{Hgua})_2(\text{H}_2\text{gua})_2(\mu\text{-Cl})_2\text{Cl}_2(\text{H}_2\text{O})][\text{CuCl}_4]$ (3)

There are a few examples of unsubstituted guanines coordinated to a metal center because guanine is highly insoluble in most solvents. Herein, a very acidic medium has been employed in order to promote its solubility and reaction with the copper(II) metal centers. Compound 3 contains two disordered copper(II) cationic $[\text{Cu}_2(\text{Hgua})_2(\text{H}_2\text{gua})_2(\mu\text{-Cl})_2\text{Cl}_2(\text{OH}_2)]^{2+}$ dimeric entities and $[\text{CuCl}_4]^{2-}$ counterions. The dimeric entities, which are disordered over two symmetry center related positions, are based on double chloride bridged

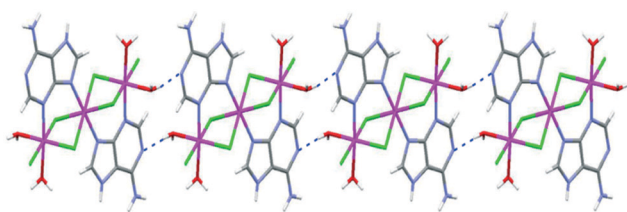


Fig. 4 The head-to-tail hydrogen bonding interactions between the neighbouring trimeric units in compound 2.

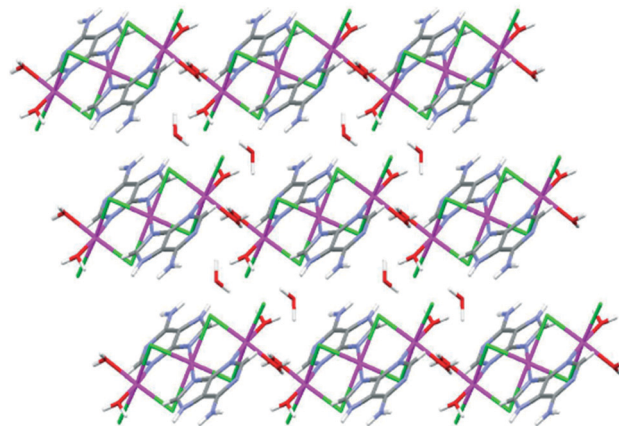


Fig. 5 Crystal packing of compound 2 along the crystallographic b axes, showing crystallization water molecules among the chains of trimers.

copper(II) metal centers (Fig. 7). Each metal center is coordinated to two $1H,3H,7H$ -guaninium/ $1H,7H$ -guanine ligands, in a *trans*-arrangement, *via* N9 positions. This coordination mode is the most frequent in compounds with a guanine nucleobase (Scheme 1).³⁰ The coordination of a cationic molecule to a metal center is not usual but there have been some reported examples.^{21,31–33} There is also a water molecule coordinated to just one of the two metal centers and strongly hydrogen bonded to the adjacent guaninium ligands through the N3 site. It creates an asymmetry in the dimeric entity related to the crystallographic disorder observed for this compound. Therefore, the metal center that is coordinated to a water molecule presents a tetragonally elongated octahedral geometry and the other one a square-pyramidal coordination geometry.

A detailed inspection of the hydrogen-bond donor/acceptor position at the $1H,7H$ -guaninium molecule indicates that both Watson–Crick (OX6/NX1/NX2) and Hoogsteen faces (OX6/NX7) are available for establishing hydrogen bonding interactions. Thus, the copper(II) dimeric entities are linked together through Watson–Crick...Hoogsteen base pairing

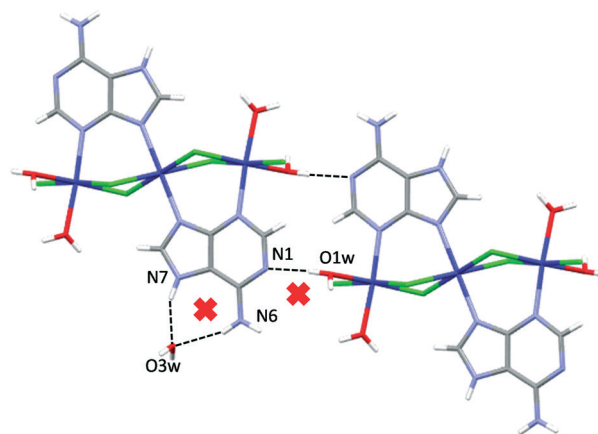


Fig. 6 Noncompliance of the requisites for obtaining SMOFs in compound 2.

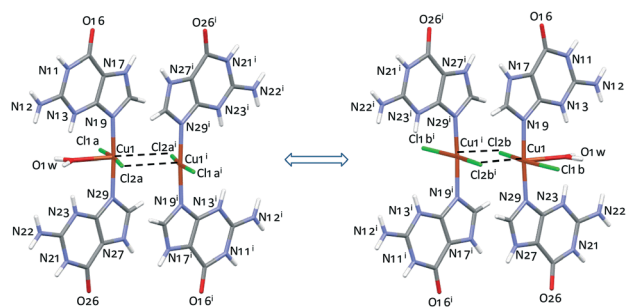
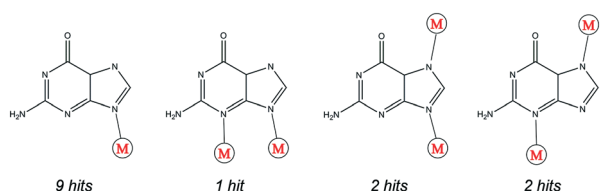


Fig. 7 Disordered dimeric $[\text{Cu}_2(\text{Hgua})_2(\text{H}_2\text{gua})_2(\mu\text{-Cl})_2\text{Cl}_2(\text{H}_2\text{O})]^{2+}$ cations of compound 3.



Scheme 1 Coordination modes of guanine/guaninium and their appearance frequency in the CSD database.

interactions of adjacent entities to provide a double-ladder like supramolecular structure, as shown in Fig. 8. However, the parallel arrangement of the coordinated nucleobases precludes their three-dimensional propagation through supramolecular nucleobase...nucleobase interactions.

The three-dimensional cohesion is achieved by electrostatic forces and hydrogen-bonding interactions involving the nucleobases and the chlorido ligands of the adjacent $[\text{CuCl}_4]^{2-}$ counterions to give a non-porous structure (Fig. 9).

Compound 3 fulfills the requirement of a rigid building block and, unlike the abovementioned compounds, it also obeys the requisite of presenting rigid guanine...guanine synthons. However, the parallel arrangement of the nucleobases hinders the propagation of the supramolecular network into three directions (Fig. 10).

Compound $[\text{Co}(\text{9-Meade})_2(\text{H}_2\text{O})_4]\text{Cl}_2 \cdot 2\text{H}_2\text{O}$ (4)

Taking into account the versatile bonding patterns of puric bases and their biological importance, we have also explored the possibilities of 9-methyladenine that somehow mimics

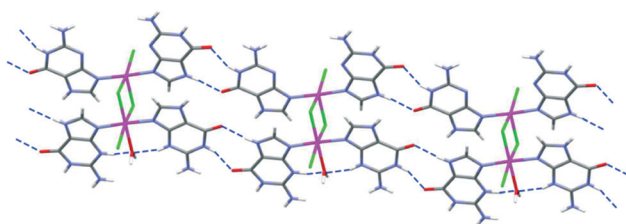


Fig. 8 Base pairing interactions in the crystal structure of compound 3.

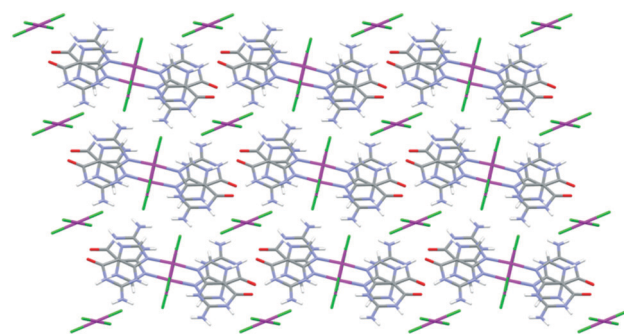


Fig. 9 Crystal packing of compound 3 showing $[\text{CuCl}_4]^{2-}$ counterions among the chains of dimeric entities.

the behaviour of adenosine/deoxyadenosine where the adenine is bonded through N9 to a ribose or deoxyribose, respectively. The alkylation of adenine at the N9 position prevents the N3,N9-bidentate coordination mode, which is essential for it to act as a bridging ligand, from forming paddle-wheel shaped dimeric entities. In fact, a search in the CSD database (version February 2017)³⁰ of transition metal complexes of 9-methyladenine shows the prevalence of the N7 coordination mode, because of the steric hindrance imposed by the methyl group on the neighbouring N3 nitrogen atom which makes its coordination difficult (Scheme 2). It seems obvious that although the N3,N9 coordination mode is precluded, a rigid building unit could be obtained by a double/triple coordination or by having simultaneously a coordination by a position and an intramolecular hydrogen bonding interaction with other positions.

The crystal structure of 4 resulting from the reaction of two equivalents of 9-methyladenine with one equivalent of $\text{CoCl}_2 \cdot 6\text{H}_2\text{O}$ in methanol contains $[\text{Co}(\text{9-Meade})_2(\text{H}_2\text{O})_4]^{2+}$ cations in which the Co^{II} center is octahedrally coordinated to four water molecules in the equatorial plane and to two 9-methyladenine molecules occupying the axial positions through the N7 donor site with the Co–N bonds slightly longer than the Co–O ones. The N7-coordination of

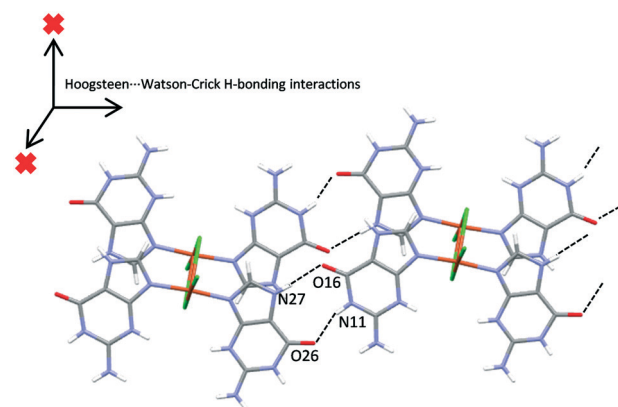
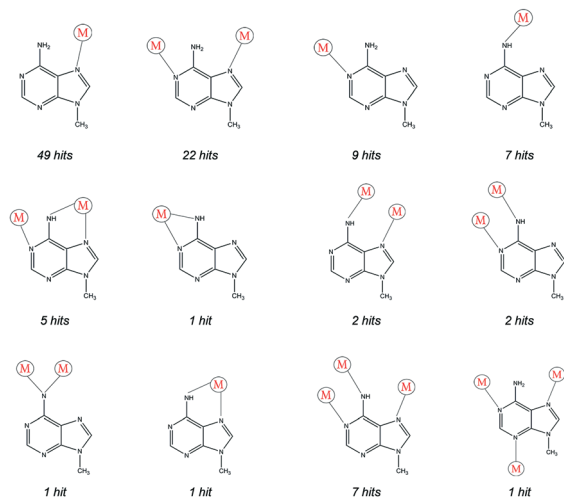


Fig. 10 Compliance of the requisites for obtaining SMOFs in compound 3, where it can be observed that only the last requisite (non-coplanarity of the nucleobase...nucleobase interactions) is unfulfilled.



Scheme 2 Coordination modes of 9-methyladenine and their appearance frequency.

9-methyladenine is reinforced by means of a bifurcated hydrogen bonding interaction involving the amino group of the nucleobase and two coordination water molecules. These interactions provide the desired rigid complex entity (Fig. 11) that exposes outwards the Watson–Crick face of the nucleobase which is available for establishing hydrogen bonding interactions.

The non-methylated adenine molecule could provide three faces able to establish complementary hydrogen bonding interactions: the Watson–Crick face (N1/N6), the Hoogsteen side (N6/N7) and the sugar edge (N3/N9) (Scheme 3). The methylation at N9 precludes the sugar-edge for this purpose and the coordination at N7 does the same for the Hoogsteen side. Therefore, only the Watson–Crick face is available to establish complementary hydrogen bonding interactions in 9-methyladenine.

Indeed, the supramolecular crystal architecture of compound 4 is dominated by the hydrogen-bonding complementary interactions taking place between the Watson–Crick faces that connect the cationic complex entities in supramolecular 1D chains (Fig. 12). However, as it happens for compound 3, the ligands are coplanar, which precludes the existence of supramolecular 3D nucleobase...nucleobase

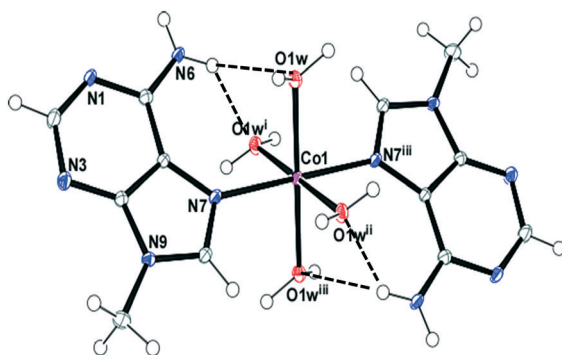
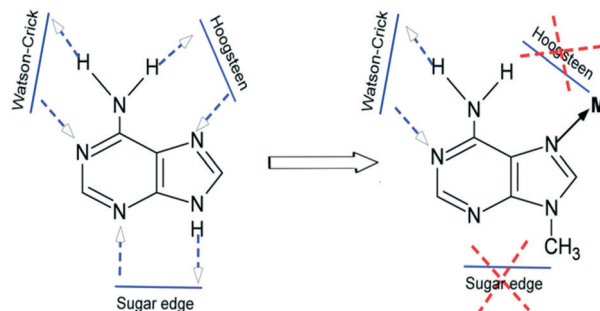


Fig. 11 ORTEP view of the cationic monomeric entity of compound 4.



Scheme 3 Availability of hydrogen bonding faces for free adenine and N7-coordinated 9-methyladenine.

interactions (Fig. 13) and, as a consequence, a non-porous structure is achieved.

The supramolecular chains are held together not only by the electrostatic interactions taking place between the cationic complex and the chloride counterions, but also by a complex network of hydrogen bonding interactions between the water molecules, the N3 position of 9-methyladenine and the chloride counterions.

Compound $[\text{Cu}_2(\mu\text{-CH}_3\text{COO})_4(\mu\text{-9-Meade})]_n \cdot n\text{CH}_3\text{OH}$ (5)

The reaction between 9-methyladenine and $[\text{Cu}_2(\mu\text{-OOCCH}_3)_4(\text{H}_2\text{O})_2]$ in methanol at room temperature afforded a green compound that retains the paddle-wheel shaped $[\text{Cu}_2(\mu\text{-OOCCH}_3)_4]$ core but bridged by $\mu\text{-9-methyladenine-}\kappa\text{N1}:\kappa\text{N7}$ molecules that are anchored to the apical positions of the dimeric entities. Therefore, 9-methyladenine does not coordinate strongly enough to the metal center so as to displace the carboxylato ligands, instead, it is only able to occupy the more labile apical positions. The N1,N7-coordination mode is the second most usual one for 9-methyladenine (see Scheme 2), and herein it is reinforced by the intramolecular hydrogen bonding interactions, implying the exocyclic amino group as the donor and the oxygen atoms from two acetato ligands as acceptors (Fig. 14). The Cu^{II} coordination environment can be described as an elongated square pyramid with the apical Cu–N bond distances longer than the equatorial Cu–O ones. The coordination bond network extends into zig-zag infinite chains that propagate along the $[0\ 1\ 1]$ direction with acetato and 9-methyladenine moieties bridging alternatively the Cu^{II} atoms with metal...metal distances of 2.65 Å and 7.08 Å, respectively.

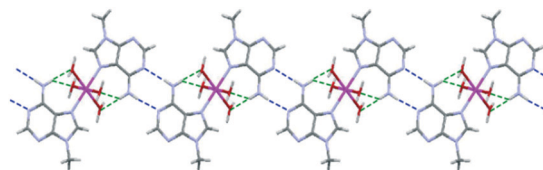


Fig. 12 Supramolecular chain of $[\text{Co}(9\text{-Meade})_2(\text{H}_2\text{O})_4]^{2+}$ complex cations in 4.

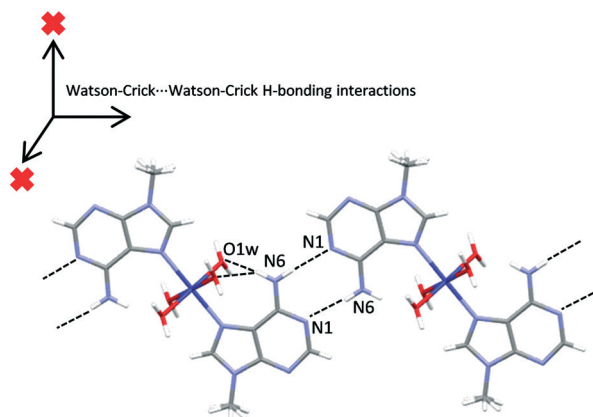


Fig. 13 Compliance of the requisites for obtaining SMOFs in compound 4, where it can be observed that only the last requisite is unfulfilled.

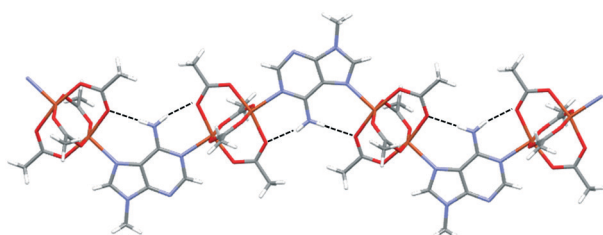


Fig. 14 Fragment of the polymeric chain of compound 5, showing the intramolecular hydrogen bond between the N6–H acceptor sites and the donor oxygen atoms of the carboxylato.

The μ - κ N1: κ N7 coordination mode of 9-methyladenine precludes any possible complementary hydrogen-bonding interaction along either its Watson–Crick or Hoogsteen sides. Therefore, the resulting non-porous supramolecular structure is dominated by weak van der Waals forces, and the hydrogen-bonding interactions between the methanol solvation molecules and the oxygen atoms of the carboxylato ligands (Fig. 15).

In summary, compound 5 is built up from infinite chains in which the coordination and methylation of the adenine hinders any possibility of being involved in hydrogen bonding in-

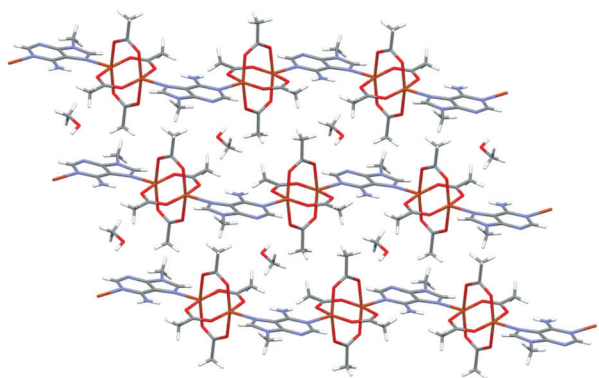


Fig. 15 Crystal packing of compound 5 viewed along the crystallographic *a* axis.

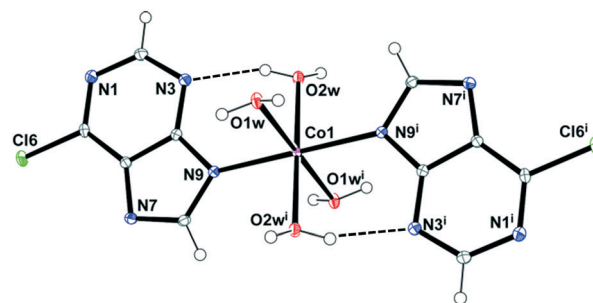
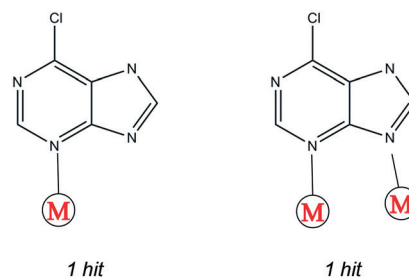


Fig. 16 Monomeric entity of compound 6 together with the labeling scheme.



Scheme 4 Coordination modes of 6-chloropurine and their appearance frequency.

teractions. Therefore, a supramolecular porous material is not obtained, since the interactions among the one-dimensional motifs are dominated by van der Waals interactions.

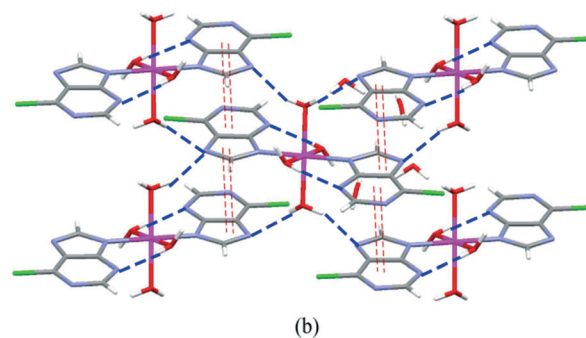
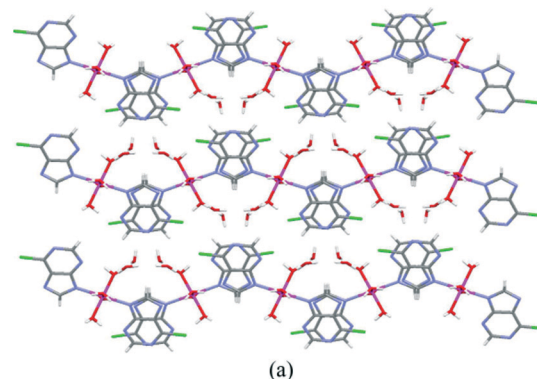


Fig. 17 (a) Crystal packing of compound 6 and (b) hydrogen bonding (blue dashed lines) and π - π stacking interactions (red double dashed lines) between the complex units.

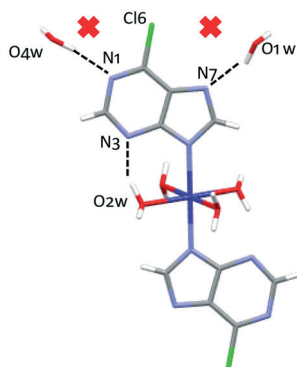


Fig. 18 Compliance of the requisites for obtaining SMOFs in compound 6.

Compound $[\text{Co}(\text{6-Clpur})_2(\text{H}_2\text{O})_4]\cdot 4\text{H}_2\text{O}$ (6)

The crystal structure of 6 contains monomeric $[\text{Co}(\text{6-Clpur})_2(\text{H}_2\text{O})_4]$ entities (Fig. 16) in which the cobalt centers are six-coordinated to two 6-chloropurinate ligands through their N9 atoms in the axial positions and four water molecules in the equatorial ones. As far as we know, this is the first example of a coordination mode for the 6-chloropurine/6-chloropurinate ligand, since only two examples were previously reported in which the 6-chloropurine ligand shows an N3- or N3,N9 coordination mode (see Scheme 4).^{34,35}

The rigidity of the complex entity in this compound is achieved by an intramolecular hydrogen bond between a coordinated water molecule as the donor and the N3 position of the purine as the acceptor. The deprotonation of the chloropurine ligands precludes any complementary nucleobase...nucleobase hydrogen bond interaction, as the nucleobases only contain acceptor sites. In fact, the 3D supramolecular architecture seems to be dominated by the π - π stacking interactions between the purine rings and an extensive network of hydrogen bonding network interactions involving the coordination and crystallization water molecules, and the N1/N7/Cl6 atoms of the 6-chloropurinate ligands giving rise to a non-porous structure (Fig. 17).

Therefore, compound 6 contains a rigid building unit but the porous nature is hampered by the deprotonation of the purine ligands that preclude rigid nucleobase...nucleobase synthons (Fig. 18).

Conclusions

In this manuscript, we have checked the suitability of the principles that we have previously established to design supramolecular metal-organic frameworks (SMOFs) which can be converted to crystal engineering language as follows: (i) the use of rigid building units, (ii) the establishment of predictable and rigid synthons between the building units, and (iii) the non-coplanarity of functional groups involved in the predictable synthons.¹⁶ Appropriate complex entities

that fulfill the above described requirements are those based on purine nucleobases. Therefore, we have checked different metal-nucleobase entities as viable SMOFs builders.

In Table 2, the compliance of the requirements by each of the employed metal-nucleobase entities compared with those presented in compounds $[\text{Co}(\text{thioguaninato})_3]$, $[\text{Co}(\text{Hade})_2\text{Cl}_2]$, $[\text{Cu}_4(\mu_3\text{-ade})_4(\mu\text{-ade})_2(\text{pentylNH}_2)_2(\text{CH}_3\text{OH})_2(\text{CO}_3)_2(\text{H}_2\text{O})_2]$, $[\text{Cu}_8(\mu_3\text{-OH})_4(\mu_4\text{-OH})_4(\text{ade})_4(\mu\text{-ade})_4(\mu\text{-Hade})_2]$ and $[\text{Cu}_2(\mu\text{-Hade})_4\text{Cl}_2]\cdot 2\text{MeOH}$, which follow all the criteria for providing SMOFs, is summarized.

The copper(II) centers in compound 1 are bridged by N3:N9-coordinated neutral adenine ligands to afford a rigid paddle-wheel dimeric entity, but the possible direct base pairing interactions are hindered due to the presence of crystallisation water molecules that control the hydrogen bonding pattern leading to a non-porous structure. Similarly, in the rigid trimeric units of compound 2, the N3:N9-coordination mode of adenine allows the Watson-Crick face to be involved in base pairing, but a non-porous structure is achieved because the N1 atom forms hydrogen bonding with the coordinated water molecules of a neighbouring unit, forming a 1D chain which extends to a 3D network through further hydrogen bonding interactions with crystallization water molecules and coordinated chlorido ligands. In the case of compound 3, rigid nucleobase...nucleobase hydrogen bonding interactions are presented involving the Hoogsteen face of one dimeric entity with the Watson-Crick face of the other one, but the parallel arrangement of the nucleobases precludes the 3D formation of non-coplanar synthons and hence it results in a non-porous material. In compound 4, rigid monomeric units grow into a 1D supramolecular chain by means of base pairing through the Watson-Crick edges of 9-methyladenine with the neighboring monomeric entities. However, like in compound 3, the coplanar arrangement of the nucleobase ligands hinders the three-dimensional propagation of this supramolecular synthon. In compound 5, the coordination bond network extends into zigzag infinite chains by N1:N7 bridging 9-methyladenine ligands precluding the possibility of any direct base pairing. Hence, the supramolecular crystal architecture is dominated by weak van der Waals forces and the hydrogen-bonding interactions between the methanol solvation molecules and the oxygen atoms of the carboxylato ligands. In compound 6, the deprotonation of the N9-coordinated 6-chloropurinate ligands takes out any chance of base pairing and the supramolecular structure is dominated by the π - π stacking interactions between 6-chloropurinate ligands, to provide a non-porous compound.

All these results support our strategy to design supramolecular metal-organic frameworks,^{15,16,20} and confirm that if one or more requirements are not fulfilled, the resulting compound lacks porosity.

As can be noticed, the success of this strategy can be thwarted by the delicate balance of all covalent and noncovalent forces present in the crystal structure, and a slight modification in the molecular components (*i.e.*

Table 2 Compliance of the requirements of each metal–nucleobase entity to obtain SMOFs (part 1)

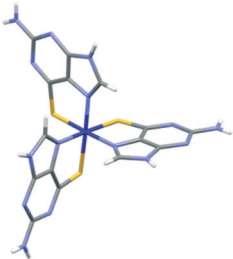
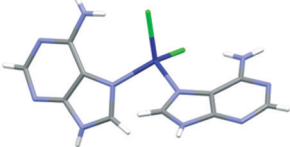
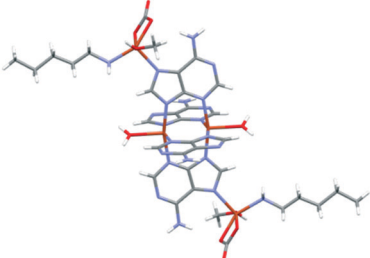
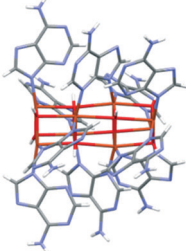
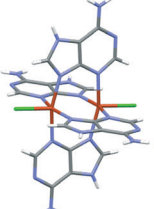
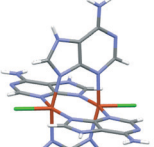
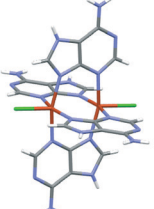
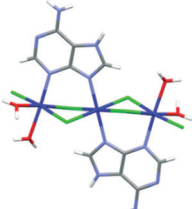
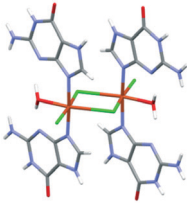
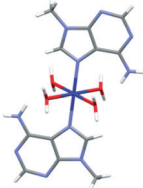
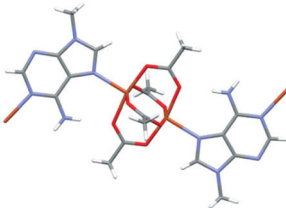
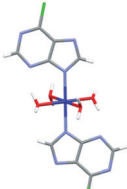
Building unit	Rigidity?	Rigid synthons?	Non-coplanar synthons (≥ 3)?	Porous structure?	Ref.
 [Co(thioguaninato) ₃]	YES	YES	YES	YES	20
 [Co(Hade) ₂ Cl ₂]	YES	YES	YES	YES (but interpenetrated)	20
 [Cu ₄ (μ_3 -ade) ₄ (μ -ade) ₂ (pentylNH ₂) ₂ (CH ₃ OH) ₂ (CO ₃) ₂ (H ₂ O) ₂]	YES	YES	YES	YES	20
 [Cu ₈ (μ_3 -OH) ₄ (μ_4 -OH) ₄ (ade) ₄ (μ -ade) ₄ (μ -Hade) ₂]	YES	YES	YES	YES	20
 [Cu ₂ (μ -Hade) ₄ Cl ₂] ²⁺	YES	YES	YES	YES	16
 + MeOH	YES	NO	NO	NO	1 This work
 + H ₂ O	YES	NO	NO	NO	1 This work
 [Co ₃ (μ -Hade) ₂ (μ -Cl) ₄ Cl ₂ (H ₂ O) ₄]	YES	NO	NO	NO	2 This work

Table 2 (continued)

Building unit	Rigidity?	Rigid synthons?	Non-coplanar synthons (≥ 3)?	Porous structure?	Ref.
 [Cu ₂ (Hgua) ₂ (H ₂ gua) ₂ (μ-Cl) ₂ Cl ₂ (OH ₂)] ²⁺	YES	YES	NO	NO	3 This work
 [Co(9-Meade) ₂ (H ₂ O) ₄] ²⁺	YES	YES	NO	NO	4 This work
 [Cu ₂ (μ-CH ₃ COO) ₄ (μ-9-Meade)]	YES	NO	NO	NO	5 This work
 [Co(6-Clpur) ₂ (H ₂ O) ₄]	YES	NO	NO	NO	6 This work

coordination modes, ligand arrangement, deprotonation or the presence of water molecules) may result in the failure to achieve the desired supramolecular interactions, and therefore, the pursued porous structure.

Conflicts of interest

There are no conflicts to declare.

Acknowledgements

This work has been funded by Ministerio de Economía y Competitividad (MAT2016-75883-C2-1-P) and Universidad del País Vasco/Euskal Herriko Unibertsitatea (PPG17/37, GIU17/50 and PFI17/051). Technical and human support provided by SGIKER (UPV/EHU, MINECO, GV/EJ, ERDF, and ESF) is gratefully acknowledged. Jintha Thomas-Gipson acknowledges the financial support provided by University Grants Commission, Govt. of India through the D. S. Kothari Post-doctoral Fellowship.

Notes and references

- H. C. Zhou, J. R. Long and O. M. Yaghi, *Chem. Rev.*, 2012, **112**, 673–674.
- H. C. Zhou and S. Kitagawa, *Chem. Soc. Rev.*, 2014, **43**, 5415–5418.
- A. Schoedel, Z. Ji and O. M. Yaghi, *Nat. Energy*, 2016, **1**, 16034–16037.
- J. Heine and K. Müller-Buschbaum, *Chem. Soc. Rev.*, 2013, **42**, 9232–9242.
- M. Kurmoo, *Chem. Soc. Rev.*, 2009, **38**, 1353–1379.
- G. Givaja, P. Amo-Ochoa, C. J. Gómez-García and F. Zamora, *Chem. Soc. Rev.*, 2012, **41**, 115–147.
- J.-Y. Lee, O. K. Farha, J. Roberts, K. A. Scheidt, S. T. Nguyen and J. T. Hupp, *Chem. Soc. Rev.*, 2009, **38**, 1450–1459.
- B. Lippert, *Coord. Chem. Rev.*, 2000, **200–202**, 487–516.
- S. Verma, A. K. Mishra and J. Kumar, *Acc. Chem. Res.*, 2010, **43**, 79–91.
- A. Domínguez-Martín, M. P. Brandi-Blanco, A. Matilla-Hernández, H. El Bakkali, V. M. Nurchi, J. M. González-

- Pérez, A. Castiñeiras and J. Niclós-Gutiérrez, *Coord. Chem. Rev.*, 2013, **257**, 2841–2851.
- 11 G. Beobide, O. Castillo, J. Cepeda, A. Luque, S. Pérez-Yáñez, P. Román and J. Thomas-Gipson, *Coord. Chem. Rev.*, 2013, **257**, 2716–2736.
- 12 I. Imaz, M. Rubio-Martínez, J. An, I. Solé-Font, N. L. Rosi and D. Maspoch, *Chem. Commun.*, 2011, **47**, 7287–7302.
- 13 S. L. Anderson and K. C. Stylianou, *Coord. Chem. Rev.*, 2017, **349**, 102–128.
- 14 G. Beobide, O. Castillo, A. Luque and S. Pérez-Yáñez, *CrystEngComm*, 2015, **17**, 3051–3059.
- 15 J. Thomas-Gipson, G. Beobide, O. Castillo, J. Cepeda, A. Luque, S. Pérez-Yáñez, A. T. Aguayo and P. Román, *CrystEngComm*, 2011, **13**, 3301–3305.
- 16 J. Thomas-Gipson, G. Beobide, O. Castillo, M. Fröba, F. Hoffmann, A. Luque, S. Pérez-Yáñez and P. Román, *Cryst. Growth Des.*, 2014, **14**, 4019–4029.
- 17 H. Li, J. Zhai and X. Sun, *PLoS One*, 2011, **6**, e18959.
- 18 J. Tian, S. Liu and X. Sun, *Langmuir*, 2010, **26**, 15112–15116.
- 19 W. Lu, X. Qin, A. M. Asiri, A. O. Al-Youbi and X. Sun, *Analyst*, 2013, **138**, 429–433.
- 20 J. Thomas-Gipson, R. Pérez-Aguirre, G. Beobide, O. Castillo, A. Luque, S. Pérez-Yáñez and P. Román, *Cryst. Growth Des.*, 2015, **15**, 975–983.
- 21 J. P. Declercq, M. Debbaudt and M. Van Meerssche, *Bull. Soc. Chim. Belg.*, 1971, **80**, 527–532.
- 22 *CrysAlis PRO, version 1.171.33.55*, Oxford Diffraction, Wroclaw, Poland, 2010.
- 23 Stoe & Cie, *X-Area, Main Menu Version 1.15*, Stoe & Cie GmbH, Darmstadt, Germany, 2001.
- 24 A. Altomare, M. Cascarano, C. Giacovazzo and A. Guagliardi, *J. Appl. Crystallogr.*, 1993, **26**, 343–350.
- 25 G. M. Sheldrick, *SHELXL-97, Programs for X-ray Crystal Structure Refinement*, University of Göttingen, Göttingen, Germany, 1997.
- 26 L. J. Farrugia, *J. Appl. Crystallogr.*, 2012, **45**, 849–854.
- 27 D. K. Patel, A. Domínguez-Martín, M. P. Brandi-Blanco, D. Choquesillo-Lazarte, V. M. Nurchi and J. Niclós-Gutiérrez, *Coord. Chem. Rev.*, 2012, **256**, 193–211.
- 28 P. de Meester and A. C. Skapski, *J. Chem. Soc. A*, 1971, 2167–2169.
- 29 U. García-Couceiro, O. Castillo, A. Luque, G. Beobide and P. Román, *Inorg. Chim. Acta*, 2004, **357**, 339–344.
- 30 C. R. Groom, I. J. Bruno, M. P. Lightfoot and S. C. Ward, *Acta Crystallogr., Sect. B: Struct. Sci., Cryst. Eng. Mater.*, 2016, **72**, 171–179.
- 31 I. Turel, M. Pecanac, A. Golobic, E. Alessio, B. Serli, A. Bergamo and G. Sava, *J. Inorg. Biochem.*, 2004, **98**, 393–401.
- 32 A. S. Gaballa, H. Schmidt, C. Wagner and D. Steinborn, *Inorg. Chim. Acta*, 2008, **361**, 2070–2080.
- 33 M. Sundaralingam and J. A. Carrabine, *J. Mol. Biol.*, 1971, **61**, 287–309.
- 34 C. Dalby, C. Bleasdale, W. Clegg, M. R. J. Elsegood, B. T. Golding and R. J. Griffin, *Angew. Chem., Int. Ed. Engl.*, 1993, **32**, 1696–1697.
- 35 J. Cepeda, O. Castillo, J. P. García-Terán, A. Luque, S. Pérez-Yáñez and P. Román, *Eur. J. Inorg. Chem.*, 2009, 2344–2353.

Porous Supramolecular Architectures Based on π -Stacking Interactions between Discrete Metal-Adenine Entities and the Non-DNA Theobromine/Caffeine Nucleobases

Jon Pascual-Colino,[†] Garikoitz Beobide,[†] Oscar Castillo,^{*,†} Ivan da Silva,[‡] Antonio Luque,[†] and Sonia Pérez-Yáñez[§]

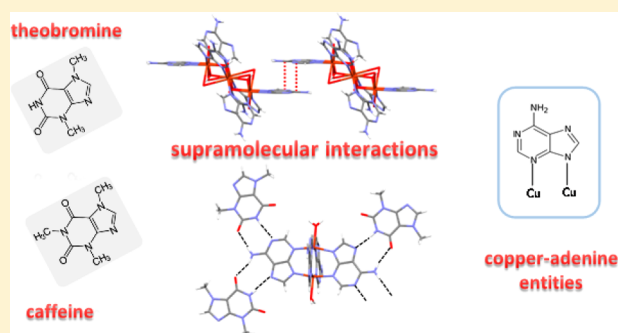
[†]Departamento de Química Inorgánica, Facultad de Ciencia y Tecnología, Universidad del País Vasco, UPV/EHU, Apartado 644, 48080 Bilbao, Spain

[‡]ISIS Facility, STFC Rutherford Appleton Laboratory, Chilton, Oxfordshire OX11 0QX, U.K.

[§]Departamento de Química Inorgánica, Facultad de Farmacia, Universidad del País Vasco, UPV/EHU, 01006 Vitoria-Gasteiz, Spain

S Supporting Information

ABSTRACT: This work is aimed at the analysis of the π - π stacking interactions as the driving force to develop porous supramolecular metal–organic frameworks (SMOFs) as an alternative to more directional hydrogen bonding interactions. Four compounds based on the interaction between rigid copper/adenine entities and theobromine/caffeine molecules have been synthesized: $[\text{Cu}_7(\mu\text{-ade})_6(\mu_3\text{-OH})_6(\mu\text{-H}_2\text{O})_6](\text{theo})_2 \cdot 28\text{H}_2\text{O}$ (1), $[\text{Cu}_2(\mu\text{-ade})_4(\text{H}_2\text{O})_2] \cdot 3\text{Htheo} \cdot 7\text{H}_2\text{O}$ (2), $[\text{Cu}_2(\mu\text{-ade})_4(\text{H}_2\text{O})_2] \cdot 2\text{Htheo} \cdot 18\text{H}_2\text{O}$ (3), and $[\text{Cu}_2(\mu\text{-ade})_4(\text{H}_2\text{O})_2] \cdot (\text{caf}) \cdot 6\text{H}_2\text{O}$ (4). The blue compound 1 is formed by wheel-shaped cationic heptameric units where the copper atoms are bridged by hydroxide anions, water molecules, and adeninato ligands with a $\mu\text{-}\kappa\text{N}3:\kappa\text{N}9$ coordination mode. The assembly of the heptameric entities and the theobrominate anions takes place mainly through π - π stacking interactions involving the adeninato ligands and theobrominate moieties. Although compound 1 exhibits an open-framework with voids representing 37% of the unit cell, the plasticity of the π - π interactions causes a reversible shrinkage of the porous system upon activation that precludes the adsorption of gas molecules. Dark purple compounds 2–4 contain neutral windmill units in which two copper atoms are bridged by four $\mu\text{-}\kappa\text{N}3:\kappa\text{N}9$ adeninato ligands. Their final crystal structure highly depends on the supramolecular interactions of the theobromine and caffeine molecules. In compound 2, two theobromine molecules are hydrogen bonded to the Hoogsteen face of two trans-arranged adeninato ligands, whereas a third theobromine molecule is joined to the Watson–Crick face of one of the previous adeninato ligands. In compound 3, with a lower amount of theobromine, the Watson–Crick interaction is not present. In both compounds, the three-dimensional (3D) crystal structure requires the additional presence of π - π stacks between the theobromine molecules. In compound 4, as the methyl groups of the caffeine molecule do not allow hydrogen bond interactions, the adeninato ligands are hydrogen bonded among them to generate, together with π -stacking interactions, two-dimensional supramolecular sheets containing rectangular windows in which the caffeine molecules are located. Only compound 4 showed permanent porosity, adsorbing a significant amount of CO_2 (0.88 mmol of CO_2/g at 5 bar and 273 K). The magnetic characterization of these compounds indicates a ferrimagnetic behavior for 1 and strong intradimeric antiferromagnetic interactions in compounds 2 and 4.



1. INTRODUCTION

The folding, assembly, and hierarchical structures of biological systems is largely dictated by a combination of noncovalent interactions such as London and/or van der Waals forces, and hydrogen bonds.¹ Thus, the access to manipulate these supramolecular interactions will allow the control of the structure and function of soft materials containing biologically interesting molecules. In this sense, we have previously explored a new type of material, based on discrete metal-nucleobase entities, in which a three-dimensional (3D) crystal building containing potentially accessible voids is sustained by complementary hydrogen bonds, which are also directional and

predictable. These materials have been called supramolecular metal–organic frameworks (SMOFs) due to their analogy to the well-known metal–organic frameworks (MOFs) with which they show close resemblance.^{2,3}

A key factor to afford the porous and robust 3D architectures of SMOFs is the use of rigid and discrete units entangled by predictable supramolecular synthons. The adenine nucleobase (Hade) and its conjugated adeninate anion (ade) are well

Received: February 3, 2018

Revised: April 17, 2018

Published: April 24, 2018

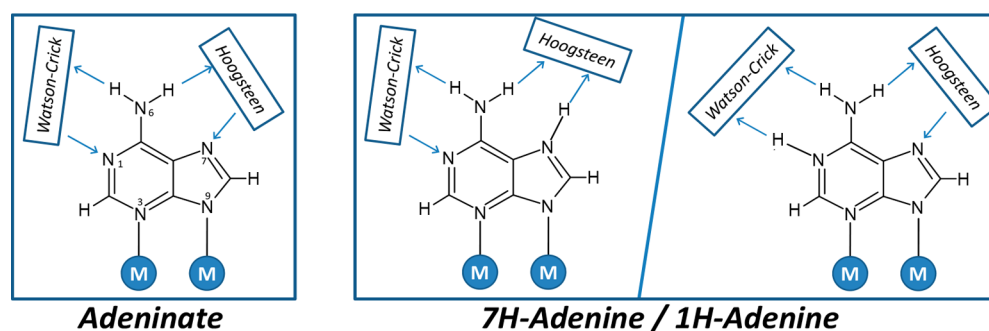


Figure 1. Hydrogen bonding capabilities of μ - κ N3: κ N9 adeninate and μ - κ N3: κ N9 adenine in its two tautomeric forms.

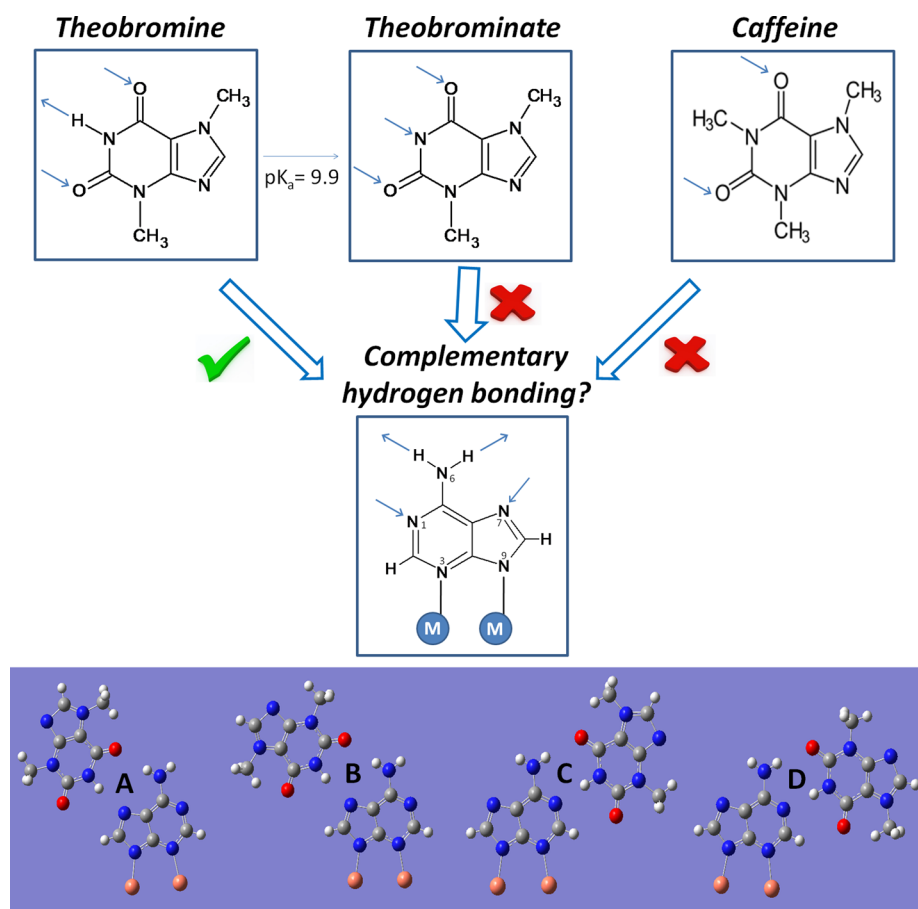


Figure 2. Top: Hydrogen bonding capabilities of the theobromine and caffeine molecules with the μ - κ N3: κ N9 adeninato ligand. Bottom: Detail on the potential complementary hydrogen bonding interactions of the μ - κ N3: κ N9 adeninato with the theobromine molecule.

suit to generate this kind of material owing to its predominant coordination mode (γ - κ N3: κ N9). It favors obtaining rigid polynuclear complex entities such as those present in compounds $[\text{Cu}_7(\mu\text{-ade})_6(\mu_3\text{-OH})_6(\mu\text{-H}_2\text{O})_6](\text{NH}_4)_2(\text{SO}_4)_2 \cdot n\text{H}_2\text{O}$ ($n = 23, 42$)⁴ and $[\text{Cu}_2(\mu\text{-Hade})_4\text{Cl}_2] \cdot 2\text{MeOH}$ (MeOH: methanol).⁵ In these compounds the Watson–Crick (W–C) and Hoogsteen (H) faces of the nucleobases decorate the external surface of the metal-adenine entities, and they are available to establish complementary hydrogen bonding interactions (Figure 1). In principle, it should provide a hydrogen bonded robust porous supramolecular network. However, the results reported to date on compounds containing the wheel-shaped $[\text{Cu}_7(\mu\text{-ade})_6(\mu_3\text{-OH})_6(\mu\text{-H}_2\text{O})_6]^{2+}$ entity did not show the predicted hydrogen bonding interactions between adenines, probably due to the

disrupter effect of the solvent water molecules in which the synthesis is accomplished.⁴ This phenomena has been also reported for compound $[\text{Cu}_2(\mu\text{-Hade})_4\text{Cl}_2]\text{Cl}_2$ in which, depending on the solvent employed, these complementary hydrogen bonding interactions are present (methanol, ethanol, acetonitrile) or not (water).⁶ In fact, the product obtained upon crystallization of the latter dimeric compound in a nonaqueous solvent represented the first example of a robust porous 3D architecture based on adenine-containing complexes in which the self-assembling of the structural units is essentially driven by noncovalent interactions: hydrogen bonds between the W–C faces of adeninato ligands and between the chloride ions and the Hoogsteen faces of the nucleobases.

In any case, as a consequence of the lack of direct nucleobase...nucleobase hydrogen bonding interactions, the

assembling of the heptameric complexes is accomplished by π - π stacking interactions between the adeninato ligands. These π - π stacking interactions are also relevant in the double helix DNA structure, but are clearly less directional than the hydrogen bonding interactions. Hydrogen bonds involving the adeninato ligand are established with the water molecules and the charge balancing counterions that partially occupy the channels present in the structure. Therefore, the resulting 3D porous crystal structures previously reported do not exhibit permanent porosity as they collapse upon activation.⁴

At this point, we aim to increase the robustness of these systems based on the heptameric entities by replacing the counterions occupying the voids by a negatively charged nucleobase derivative: the theobrominate anion (theo). The steric hindrance of the theobrominate methyl groups inhibits its coordination to the copper atoms and, as a consequence, does not alter the rigid metal-adenine entities. Note that it provides both a charge counterbalancing ion and a substantial building block to intercalate in a π - π sustained supramolecular architecture. It is worth noticing that the theobrominate anion cannot establish complementary hydrogen bonds with μ -adeninato- κ N3: κ N9 ligand as it lacks adjacent donor and acceptor positions (Figure 2). Moreover, we also aim to explore the possibilities of self-assembly of neutral $[\text{Cu}_2(\mu\text{-ade})_4(\text{H}_2\text{O})_2]$ complex entities and theobromine (Htheo) or caffeine (caf) neutral molecules as a source of structural diversity for the synthesis of supramolecular porous materials. As in the adenine molecule, the biochemical activity of theobromine and caffeine (derivates of the non DNA xanthine) is dominated by the supramolecular recognition patterns that they can establish.^{7,8}

Keeping all the above in mind, the reaction between copper(II) nitrate, adenine, and theobromine/caffeine gives rise to compounds $[\text{Cu}_7(\mu\text{-ade})_6(\mu_3\text{-OH})_6(\mu\text{-H}_2\text{O})_6](\text{theo})_2 \cdot 28\text{H}_2\text{O}$ (1), $[\text{Cu}_2(\mu\text{-ade})_4(\text{H}_2\text{O})_2] \cdot 3\text{Htheo} \cdot 7\text{H}_2\text{O}$ (2), and $[\text{Cu}_2(\mu\text{-ade})_4(\text{H}_2\text{O})_2] \cdot 2\text{Htheo} \cdot 18\text{H}_2\text{O}$ (3), and $[\text{Cu}_2(\mu\text{-ade})_4(\text{H}_2\text{O})_2] \cdot (\text{caf}) \cdot 6\text{H}_2\text{O}$ (4). Their structures were elucidated by single-crystal X-ray diffraction, allowing studying the supramolecular interactions that direct the crystal building. The involved adsorption and magnetic features of these compounds are also analyzed in detail.

2. EXPERIMENTAL SECTION

2.1. Synthesis of $[\text{Cu}_7(\mu\text{-ade})_6(\mu_3\text{-OH})_6(\mu\text{-H}_2\text{O})_6](\text{theo})_2 \cdot 28\text{H}_2\text{O}$ (1). A total of 0.0489 g (0.2 mmol) of $\text{Cu}(\text{NO}_3)_2 \cdot 3\text{H}_2\text{O}$ dissolved in 10 mL of water was added to 0.0390 g (0.3 mmol) of adenine dissolved in 15 mL of an aqueous methanolic 1:1 hot solution. The blue solution was basified to $\text{pH} \approx 8.8$ with NaOH while the mixture was continuously stirred. The obtained purple solution was added to 0.0540 g of theobromine (0.3 mmol) dissolved in 20 mL of hot water basified with NaOH ($\text{pH} \approx 8.8$). The purple solution was left for evaporation at room temperature, and blue single-crystals were separated after 4 days. Yield: 55% (based on metal). Anal. Calcd (found) for $\text{C}_{44}\text{H}_{112}\text{Cu}_7\text{N}_{38}\text{O}_{44}$: C, 22.76 (23.10); H, 4.86 (4.28); N, 22.92 (22.16); Cu, 19.15 (20.20)%. Main IR features (cm^{-1} ; KBr pellets): 3434vs, 3358w, 3199w, 2944s, 1655vs, 1598w, 1546vs, 1492s, 1454vs, 1402s, 1226m, 1145m, 1032m, 934m, 790m, 730w, 662m, 616w, 549w, 451w.

2.2. Synthesis of $[\text{Cu}_2(\mu\text{-ade})_4(\text{H}_2\text{O})_2] \cdot 3\text{Htheo} \cdot 7\text{H}_2\text{O}$ (2). This compound was obtained by the addition of 0.0676 g (0.5 mmol) of adenine dissolved in 15 mL of an aqueous methanolic 1:1 hot mixture into a stirring solution of 0.0488 g of $\text{Cu}(\text{NO}_3)_2 \cdot 3\text{H}_2\text{O}$ (0.2 mmol). The mixture was basified with NaOH, and the resulting purple solution was added to a 0.0540 g of theobromine (0.3 mmol) dissolved in 20 mL of hot water basified with NaOH to $\text{pH} \approx 8.8$. The purple solution was left evaporating, and purple single-crystals were collected

after 2 days. Yield: 54% (based on metal). Anal. Calcd (found) for $\text{C}_{41}\text{H}_{58}\text{Cu}_2\text{N}_{32}\text{O}_{15}$: C, 36.04 (35.52); H, 4.28 (4.29); N, 32.81 (32.20); Cu, 9.30 (9.72)%. Main IR features (cm^{-1} ; KBr pellets): 3455w, 3351s, 3187s, 2951s, 1700vs, 1645vs, 1594m, 1551s, 1486w, 1459vs, 1401vs, 1229s, 1144s, 1036m, 934m, 786m, 737m, 672s, 614m, 550w, 444s.

2.3. Synthesis of $[\text{Cu}_2(\mu\text{-ade})_4(\text{H}_2\text{O})_2] \cdot 2\text{Htheo} \cdot 18\text{H}_2\text{O}$ (3). This compound was prepared by the above-described procedure but using a lower amount of theobromine (0.0360 g, 0.2 mmol). The final purple solution was left evaporating at room temperature, and after 2 days a mixture of purple crystals was obtained. The X-ray powder diffraction data indicates that it corresponds to a mixture of compounds 2 and 3 (see Supporting Information, Figure S5). As both compounds were indistinguishable by means of color or shape, crystals were randomly selected from the mixture until a specimen of 3 was found and used for single-crystal X-ray study. There are some other examples in the literature for concomitant crystal formation.⁹

2.4. Synthesis of $[\text{Cu}_2(\mu\text{-ade})_4(\text{H}_2\text{O})_2] \cdot (\text{caf}) \cdot 6\text{H}_2\text{O}$ (4). This compound was prepared adding to a 10 mL water solution of 0.0488 g of $\text{Cu}(\text{NO}_3)_2 \cdot 3\text{H}_2\text{O}$ (0.2 mmol) 0.0541 g of adenine (0.4 mmol) dissolved in 15 mL of hot water-methanol (1:1). The resulting solution ($\text{pH} = 4.0$) was basified with NaOH solution to $\text{pH} = 8.8$, and later 0.0785 g of caffeine (0.4 mmol) dissolved in 20 mL of water at 60 °C was added. In few hours a purple solid appeared corresponding to compound $[\text{Cu}_2(\mu\text{-ade})_4(\text{H}_2\text{O})_2] \cdot (\text{caf}) \cdot 6\text{H}_2\text{O}$. Yield 35%. Single crystals of this compound were obtained after 2 weeks using the test tube diffusion technique in which, over the caffeine aqueous solution, the aquo-methanolic solution containing the copper(II) nitrate and adenine mixture was layered carefully. Anal. Calcd (found) for $\text{C}_{28}\text{H}_{42}\text{Cu}_2\text{N}_{24}\text{O}_{10}$: C, 33.57 (33.43); H, 4.23 (4.09); N, 33.55 (32.77); Cu, 12.69 (12.30)%. Main IR features (cm^{-1} ; KBr pellets): 3435f, 3350s, 2949s, 1691vs, 1654m, 1604vs, 1556m, 1487w, 1460w, 1275m, 1188s, 1151s, 1028m, 976m, 931w, 794m, 694w, 655s, 552w.

The homogeneity and purity of bulk samples of compounds 1, 2, and 4 were checked by elemental analysis and X-ray diffraction data.

2.5. Physical Measurements. Elemental analyses (C, H, N) were performed on an Euro EA elemental analyzer, whereas the metal content was determined by atomic absorption spectrometer (AAS) from Perkin Elmer Analyzer 100. The IR spectra were recorded on a FTIR 8400S Shimadzu spectrometer in the 4000–400 cm^{-1} spectral region. Variable-temperature magnetic susceptibility measurements were performed using a standard Quantum Design PPMS magnetometer while heating from 2 to 300 K at 1 kOe range after cooling in the absence (zero-field cooling, ZFC) of the applied field. Magnetization as a function of field (H) was measured using the same magnetometer in the $-80 \leq H/\text{kOe} \leq 80$ at 2 K after cooling the sample in zero field. The susceptibility data were corrected for the diamagnetism estimated from Pascal's Tables,¹⁰ the temperature-independent paramagnetism and the magnetization of the sample holder. Dinitrogen (77 K) and carbon dioxide (273 K) physisorption data were recorded on activated samples (vacuum at 80 °C for 6 h) with a Quantachrome Autosorb-iSorb HP1. The specific surface area was calculated by means of the Brunauer-Emmett-Teller (BET) method using the adsorption branch in 0.01–0.10 relative pressure. Thermogravimetric analyses (TGA) were performed on a METTLER TOLEDO TGA/SDTA851 thermal analyzer in a synthetic air atmosphere (79% N_2 /21% O_2) with a heating rate of 5 °C·min⁻¹. The purity of the samples was assessed by powder X-ray diffraction, TGA, and FTIR analyses (see Supporting Information). Polycrystalline X-ray diffraction data were collected on a PANalytical Xpert PRO diffractometer with Cu- $K\alpha$ radiation ($\lambda = 1.5418 \text{ \AA}$) at 298(2) K. The measurement conditions were 40 kV and 40 mA and a sweep between $5 < 2\theta < 70^\circ$.

2.6. X-ray Diffraction Data Collection and Structure Determination. Single-crystal X-ray diffraction data were collected on an Agilent Technologies Supernova diffractometer with graphite monochromated Mo- $K\alpha$ radiation ($\lambda = 0.71073 \text{ \AA}$) at 100(2) K for compounds 1, 2, and 4, and an Agilent Technologies Supernova diffractometer with Cu- $K\alpha$ radiation ($\lambda = 1.5418 \text{ \AA}$) at 150(1) K for compound 3. Data reduction was done with the CrysAlisPro

Table 1. Crystallographic Data and Structure Refinement Details of Compounds 1–4

	1	2	3	4
empirical formula	C ₄₄ H ₁₁₂ Cu ₇ N ₃₈ O ₄₄	C ₄₁ H ₅₈ Cu ₂ N ₃₂ O ₁₅	C ₃₄ H ₇₂ Cu ₂ N ₂₈ O ₂₄	C ₂₈ H ₄₂ Cu ₂ N ₂₄ O ₁₀
formula weight	2322.49	1366.20	1384.20	1001.88
crystal system	monoclinic	triclinic	triclinic	monoclinic
space group	C2/c (No. 15)	P $\bar{1}$ (No. 2)	P $\bar{1}$ (No. 2)	C2/c (No. 15)
a (Å)	22.6236(14)	10.2142(5)	9.4687(7)	16.0977(8)
b (Å)	15.3261(7)	15.9877(8)	9.8967(6)	19.7853(7)
c (Å)	27.5588(14)	17.5772(11)	15.9452(9)	13.7487(6)
α (deg)	90	94.837(4)	88.697(5)	90
β (deg)	105.705(6)	98.162(5)	76.994(6)	100.785(4)
γ (deg)	90	96.355(4)	86.031(6)	90
V (Å ³)	9198.8(9)	2809.2(3)	1452.34(17)	4301.6(3)
Z	4	2	1	4
ρ_{calcd} (g·cm ⁻³)	1.677	1.615	1.582	1.546
μ (mm ⁻¹)	1.696	0.853	1.803	1.051
goodness of fit (S) ^a	0.980	1.042	1.039	1.066
R _{int}	0.1725	0.0308	0.0415	0.0351
final R indices				
R ₁ ^b /wR ₂ [all data] ^{c,d}	0.1879/0.2715	0.1185/0.2379	0.0811/0.2009	0.1161/0.2435
R ₁ ^b /wR ₂ [I > 2 σ (I)] ^{c,d}	0.0962/0.2231	0.0882/0.2149	0.0706/0.1901	0.0786/0.2142

^aS = $[\sum w(F_0^2 - F_c^2)^2 / (N_{\text{obs}} - N_{\text{param}})]^{1/2}$. ^bR = $\sum \|F_0| - |F_c|| / \sum |F_c|$. ^cRw = $[\sum w(F_0^2 - F_c^2)^2 / \sum w \cdot F_c^2]^{1/2}$. ^dw = $1/[\sigma^2(F_0^2) + (a^*P)^2 + bP]$ where P = $(F_0^2 + 2^*F_c^2)/3$; 1 (a = 0.1180), 2 (a = 0.0930, b = 14.2495), 3 (a = 0.0972, b = 2.7145), 4 (a = 0.1088, b = 18.6618).

program.¹¹ The details of the structure determination and refinement of all compounds are summarized in Table 1.

All the structures were solved by direct methods using the SIR92 program¹² and refined by full-matrix least-squares on F² including all reflections (SHELXL97).¹³ All calculations for these structures were performed using the WINGX crystallographic software package.¹⁴ All the adeninato ligands in 1 and half of them in 2, 3, and 4 are disordered into two coplanar arrangements with inverted orientation regarding the coordination mode (μ - κ N3: κ N9/ μ - κ N3: κ N9).^{15–17} The theobrominate anions of 1 are also disordered over two positions. The disorder has been resolved by including the observed peaks as split atoms in two positions (named A and B) and with occupancy factors common to each of the subgroups with the proviso that they add up to 100%. These atoms have been refined with an isotropic temperature factor, while the rest of the non-hydrogen atoms of the structure have been modeled with anisotropic temperature factors, with the exception of the oxygen atoms of the crystallization water molecules for compound 2. In compounds 1, 3, 4, after the initial structure solution was completed, the difference Fourier map showed the presence of substantial electron density at the voids of the crystal structure that was impossible to model. Therefore, its contribution was subtracted from the reflection data by the SQUEEZE method¹⁸ as implemented in PLATON.¹⁹ This last program has also been employed to corroborate the assigned oxidation states through bond valence sum calculations.

3. RESULTS AND DISCUSSION

3.1. Structural Description of [Cu₇(μ -ade)₆(μ -OH)₆(μ -H₂O)₆](theo)₂·28H₂O (1). The cationic [Cu₇(μ -ade)₆(μ -OH)₆(μ -H₂O)₆]²⁺ entity of 1 consists of a central [Cu(OH)₆]⁴⁻ core, located on an inversion center, that is connected to six additional copper(II) metal centers in a radial and planar arrangement through the hydroxide bridges which adopt a μ ₃-bridging mode, in such a way that they connect the central metal atom to two external ones (Figure 3). It generates a wheel-shaped entity in which water molecules and μ - κ N3: κ N9 adeninato ligands bridge the peripheral copper atoms.

All the metal centers present an octahedral geometry with the usual Jahn–Teller tetragonal elongation (Table S1 of Supporting Information), which is more pronounced for the

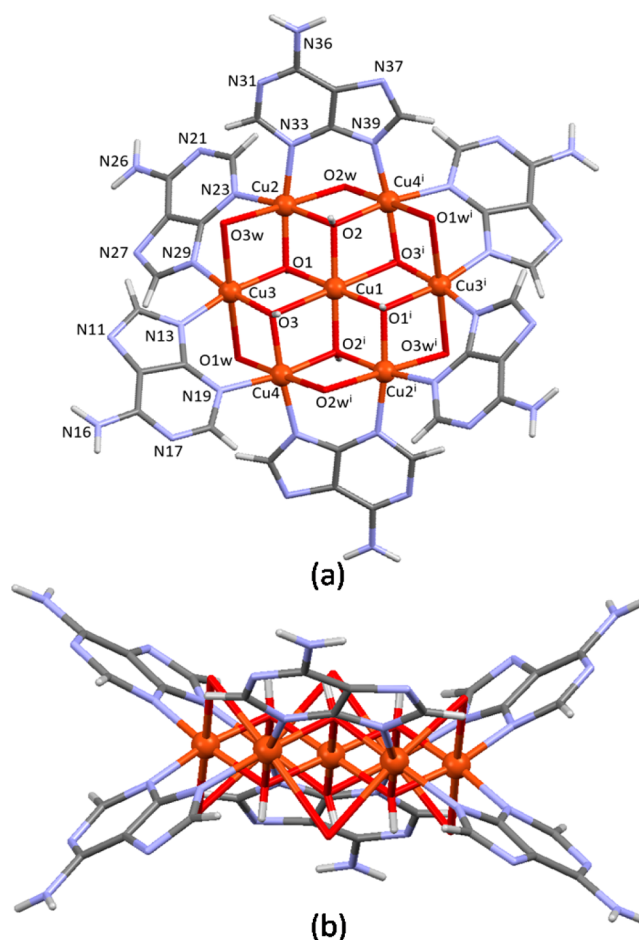


Figure 3. (a, b) [Cu₇(μ ₃-OH)₆(μ -ade)₆(μ -H₂O)₆]²⁺ heptanuclear entity in compound 1.

peripheral copper(II) centers because of the rigidity of the heptanuclear entity. The elongation at the peripheral copper atoms takes place along the metal–water coordination bonds,

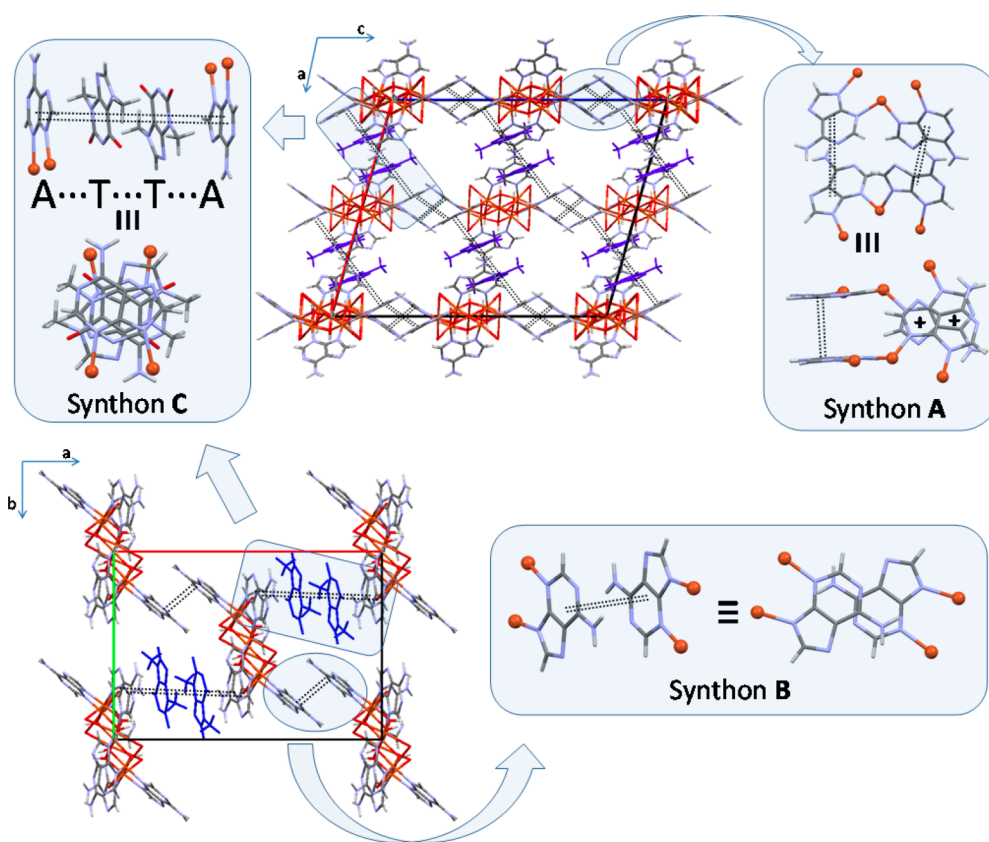


Figure 4. Compound 1: Supramolecular interactions connecting heptanuclear entities in the *ac* (top) and *ab* (bottom) crystallographic planes. Insets show the π - π interactions based rigid synthon along the crystallographic *c* axis (top right) and the more flexible ones in the *ab* plane (top left and bottom right). Double dotted lines and plus signal indicate π - π stacking interactions.

in such a way that the coordinated water molecules are loosely held, with longer coordination bonds than the adeninato ligand.

The heptameric entity is analogous to that found in the crystalline structures of the compounds $[\text{Cu}_7(\mu\text{-ade})_6(\mu_3\text{-OH})_6(\mu\text{-H}_2\text{O})_6](\text{NHEt}_3)_2(\text{SO}_4)_2 \cdot n\text{H}_2\text{O}$ ($n = 23, 42$)⁴ and $[\text{Cu}_7(\mu\text{-ade})_6(\mu_3\text{-OH})_6(\mu\text{-H}_2\text{O})_6](\text{NO}_3)_2 \cdot 6\text{H}_2\text{O}$ ²⁰ and resembles that present in the compound $2\text{D}\text{-}\{[\text{Cu}_7(\mu\text{-ade})_2(\mu_3\text{-OH})(\mu\text{-sip})_2(\mu\text{-H}_2\text{O})_6] \cdot 2.5\text{H}_2\text{O}\}_n$ where four of the adeninato bridges are replaced by two 5-sulphoisophthalate anions.²¹

The use of water as a solvent hinders the presence of direct hydrogen bonding interactions between the adeninato ligands. As a consequence, the crystal structure is dominated by π - π stacking interactions. In the crystal building each cationic complex is surrounded by six others and attached to them through three different rigid synthons (Figure 4). The first one (A) comes from double adeninato \cdots adeninato π - π stacking interactions to provide a synthon that spreads along the crystallographic *c*-axis. The second one (B) involves a single adeninato \cdots adeninato stacking between metal-adenine complexes placed in the same *ab*-plane. The third one consists of pairs of theobrominate anions parallel to each other and to the adeninate ligands to give a $\cdots\text{A}\cdots\text{T}\cdots\text{T}\cdots\text{A}\cdots$ sequence of supramolecular π - π interactions (C) that spreads along the crystallographic *ab*-plane.

Finally the 3D cohesiveness of the crystal structure is reinforced with several hydrogen bonds, for example, those involving the hydroxyl group O3 and the nitrogen N41 of the theobrominate anion and those established between the exocyclic amino group of the adeninato ligand ($X = 3$) and the carbonylic C=O42 of the theobrominate anion. The

structural parameters of the above-described supramolecular interactions are gathered in the Table S4 of Supporting Information.

The voluminous heptameric entity of compound 1 is a rigid construction unit since all its components establish at least two coordination bonds, and, therefore, it meets the first of the structural requirements necessary for the construction of supramolecular porous structures.³ On the other hand, the synthons connecting the heptameric units are relatively rigid, especially synthon A, which accounts for the second requirement. The third requirement is also accomplished as these synthons propagate in three non-coplanar directions. As a consequence, the just described packing of the complex entities and theobrominate anions generates an open structure with channels representing 37% of the unit cell (calculated with PLATON). In these channels a large number of water molecules are placed that establishes hydrogen bonding interactions among them and with the $-\text{NH}_2$ and $-\text{OH}$ groups of the complex entities located in the walls of the channels. The involvement of the theobrominate counterions in the supramolecular packing generates an increase in the void volume percentage in comparison to that reported for the analogous $[\text{Cu}_7(\mu\text{-ade})_6(\mu_3\text{-OH})_6(\mu\text{-H}_2\text{O})_6](\text{NHEt}_3)_2(\text{SO}_4)_2 \cdot 42\text{H}_2\text{O}$ compound (3106 \AA^3 , 33% of the unit cell).

In order to analyze the pore size distribution in compound 1, a procedure implemented in a code developed by Sarkisov²² has been used, in which the Lennard-Jones universal force field parameters are used to describe the adsorbent atoms, while a probe that increases its size gradually analyses the free volume. The results of this analysis show the existence of a network of

interconnected channels with a pore diameter ranging from 4.3 to 5.5 Å (mode: 5.1 Å), upon the subtraction of the crystallization water molecules. This larger channels along the crystallographic axis *b* are interconnected by smaller channels along *a* and *c* directions (Figure 5). On the other hand, a

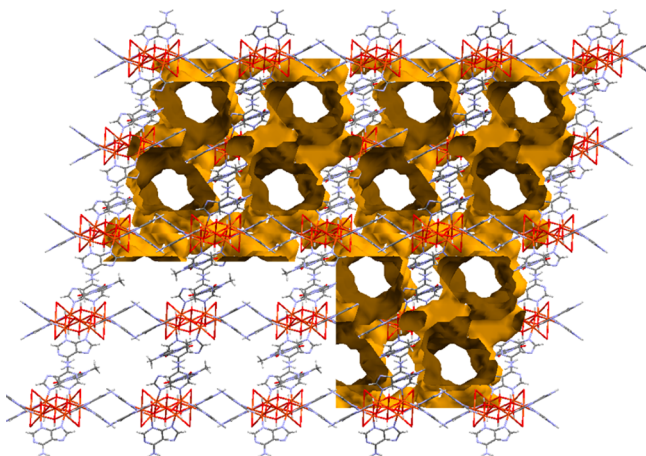


Figure 5. Image showing the channels contact surface along the crystallographic *b* axis for the squeezed form of compound 1.

theoretical accessible surface area value of 256 m²/g and a pore volume of 0.22 cm³/g have also been computed using a Monte Carlo-based integration code,²³ where a molecule with a parameter equal to the Lennard–Jones diameter of N₂ [3.681 Å] probes the structure of the compound.

It is interesting to note that compound 1 and the above-cited [Cu₇(μ-ade)₆(μ₃-OH)₆(μ-H₂O)₆](NH₄Et₃)₂(SO₄)₂·42H₂O compound show the same CdSO₄-like *cds* topology with a (6⁵.8) point symbol (nodes being the heptameric units and connector being the π–π stacking interaction between the adeninato ligands).^{24–26} Nonetheless, the exchange of sulfate anions by the theobrominate anions implies the presence of the above-described additional π–π interactions, which strengthens the crystal structure stability of compound 1. In fact, whereas the thermal removal of the water molecules in the sulfate containing compound produces the collapse of the crystal structure, the thermal degradation study (Figure S1 and Table S5) and the variable-temperature X-ray powder diffraction data of compound 1 (Figure S2) show that the crystallinity is retained after the release of the crystallization water molecules (ca. 100 °C) and even after the removal of the coordination ones (ca. 180 °C), remaining stable up to 300 °C. However, the X-ray diffraction peaks shift toward higher 2θ angles, and the indexation on the variable-temperature X-ray powder diffraction patterns (Figure S8 and Table S9) based on the crystal structure parameters obtained from the single-crystal data show a progressive decreasing of the unit cell volume from 9199 Å³ for the pristine compound to 7142 Å³ at 100 °C (loss of the crystallization water molecules) and to 6417 Å³ at 180 °C (loss of coordination water molecules). This unit cell shrinkage implies an 80% of the void volume present in the pristine sample (3489 Å³). In fact, an activated sample (80 °C, 6 h) of compound 1 (whose X-ray diffraction pattern is equal to those corresponding to the thermally obtained anhydrous compound at 180 °C) is not able to adsorb either N₂ at 77 K or CO₂ at 273 K, so that the dehydration process implies the loss of the porous nature of the compound, but the heptameric entity persists (as it will be discussed below by means of magnetic

measurements) and the crystal structure is flexible enough to allow the complete reversibility of the unit cell shrinkage upon exposure to a water-saturated atmosphere for 24 h (Figure S3).

3.2. Structural Description of [Cu₂(μ-ade)₄(H₂O)₂]·3Htheo·~7H₂O (2). The neutral [Cu₂(μ-ade)₄(H₂O)₂] entity of compound 2 is similar to the paddle-wheel unit found in the SMOF [Cu₂(μ-ade)₄Cl₂]Cl₂·2MeOH,⁵ replacing the apical chlorido ligands by water molecules. The two copper(II) atoms are coordinated to the N3 Pyrimidinic and N9 imidazolic nitrogen atoms of two adeninato ligands (Figure 6), and the

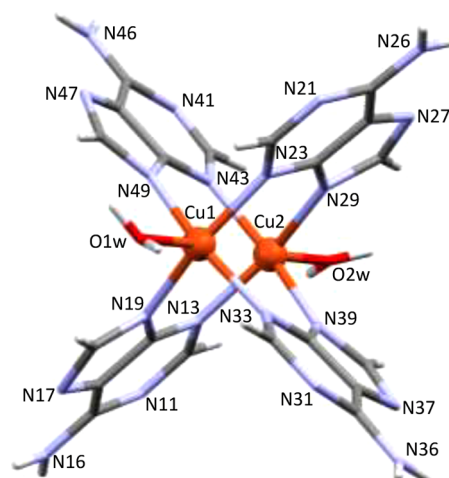


Figure 6. Dimeric entity of compound 2 showing the labeling scheme.

apical position of the square pyramidal environment of the metal is occupied by a water molecule with a Cu–O_w distance longer than those involving the nitrogen atoms (Table S2).

The dihedral angles between adjacent adeninato ligands in the paddle-wheel unit are ca. 90° with a copper...copper distance of 2.956(1) Å. Two of the adeninato ligands transverse to each other (N31 and N41 containing ligands) also show the previously described static disorder with μ-κN3:κN9/μ-κN9:κN3 inverted coordination.

In the crystal structure of compound 2 the presence of solvent water and theobromine molecules disrupt the direct complementary hydrogen bonding interactions between the adeninato ligands from adjacent dimeric entities. However, they are able to self-assemble by means of a combination of π–π stacking and N–H...aromatic interactions involving two trans arranged adeninato ligands (Figure 7). These interactions are geometrically less demanding than the more common complementary hydrogen bonding synthons, and it allows the presence of the above-described static disorder of these two adeninato ligands. The remaining two adeninato ligands, which are not disordered, interact with three theobromine molecules by means of rigid hydrogen bonds interactions (Figure 7d). In this sense, the Watson–Crick side of one of the ordered adeninato ligands establishes a R₂²(8) hydrogen bonds ring with a molecule of theobromine: the exocyclic N16 amino group interacts with the O72 atom of the ketone group, and the pyrimidinic N11 with the theobromine N71 atom (synthon D in Figure 2). This synthon is similar to the pattern of molecular recognition that takes place between adenine and thymine in the DNA double helix. In addition, the Hoogsteen (N16/N17) side of the same adenine ligand forms a R₂²(9) ring with the O66 atom of the ketone group of another theobromine as acceptor and the adjacent N61 nitrogen as donor (synthon A).

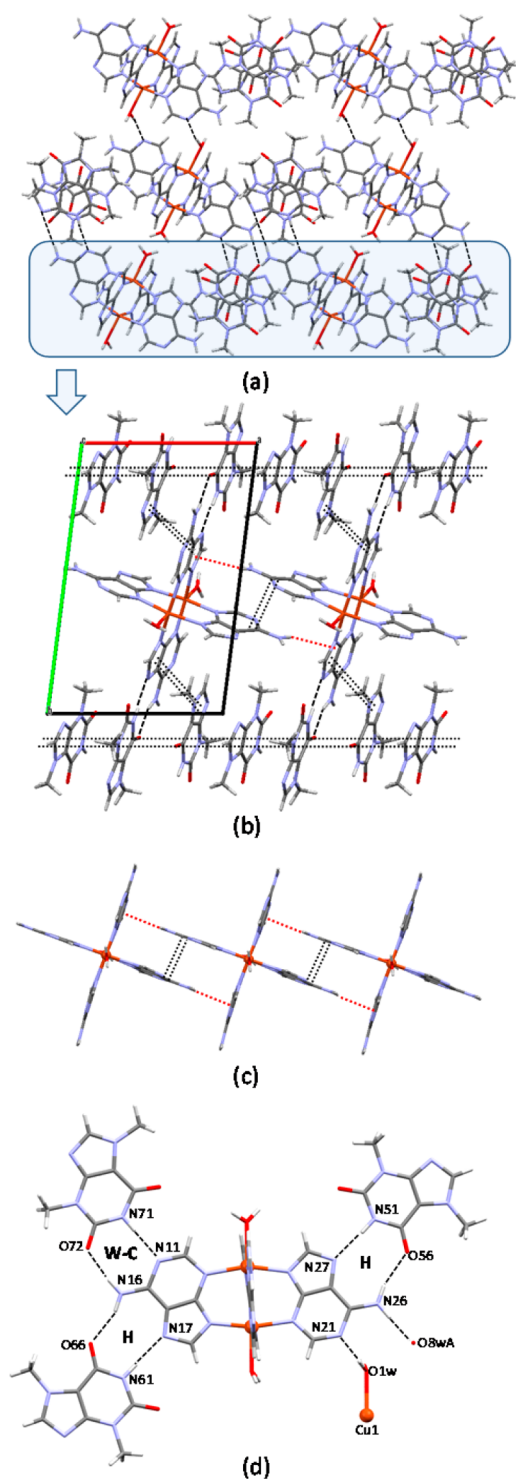


Figure 7. Compound 2: (a, b) crystal packing showing the presence of supramolecular interactions; (c) dimeric entities assembled through π - π stacking (double dashed lines) and N-H \cdots aromatic (red dotted lines) interactions, and (d) theobromine molecules anchored to the dimeric entities by means of complementary hydrogen bonding interactions. “H” and “W-C” stand for Hoogsteen and Watson-Crick faces, respectively.

The CSD²⁷ database does not register any structure in which the adenine (or derivatives) and theobromine bases coexist. However, a simultaneous interaction of adenine with its Watson-Crick and Hoogsteen sides has been found for a 2:1 adenine-isopropyluracil compound (CSD code: BERNAP).²⁸

Recently, several reports have been published on the interaction established by xanthines,^{8,29,30} such as theophylline and theobromine, with biological systems such as DNA, RNA, and ATP inside the cellular structure, and it has been suggested that anchoring with DNA may be produced with the adenine-thymine pair, in a similar molecular recognition pattern observed in the crystal structure of compound 2. The second nondisordered adeninato ligand of the dimeric structure only interacts through its Hoogsteen face with a theobromine molecule through a $R_2^2(9)$ ring of hydrogen bonds, while its W-C side forms hydrogen bonds with a crystallization water molecule and the coordinated O1w water molecule of an adjacent dimeric entity.

Additionally, the theobromine molecules form columns along the crystallographic [100] direction in which they are arranged parallel to each other with interplanar distances of 3.2–3.4 Å, indicative of the presence of offset face-to-face π - π interactions. Complex entities and the theobromine molecules form layers, propagating along the *ab* plane, which are sustained by the above-described supramolecular interaction. Crystallization water molecules are inserted between the layers and joined to them by means of the hydrogen bonds with the coordination water molecules and with the nitrogen atoms of the adeninato ligands. The cohesion between the layers is further sustained by a direct Ow-H \cdots N hydrogen bond that involves the coordination water molecule O1w and the N21 atom of an adeninato ligand from the adjacent layer.

The volume occupied by the water molecules located between the layers is 365 Å³ (13% of the total volume of the unit cell), and it reaches 490 Å³ (18% of the unit cell) if the space occupied by coordinating water molecules is also taken into account. The analysis of the pores present in this compound, carried out following the previously described procedure, indicates the existence of some isolated cavities with a maximum diameter of 3.8 Å (mode: 2.9 Å). According to their isolated nature, these pores are not accessible either for N₂ or for CO₂, as checked by adsorption measurements.

3.3. Structural Description of [Cu₂(μ -ade)₄(H₂O)₂] \cdot 2Htheo \cdot ~18H₂O (3). Crystal structure of this compound contains the same neutral [Cu₂(μ -ade)₄(H₂O)₂] paddle-wheel unit above-described for 2, but it is located on an inversion center. The different complex/theobromine ratio in the formulas (1/3 in 2 versus 1/2 in 3) leads to each centrosymmetric complex to be only surrounded by two theobromine molecules anchored to two trans arranged adeninato ligands by a hydrogen bonding $R_2^2(9)$ ring involving the N1H and ketone O6 sites of the theobromine and the Hoogsteen face of the nucleobase ligands (Figure 8). This hydrogen bonding interaction is similar to that found in compound 2 but lacking the third theobromine ligands that was interacting with the Watson-Crick face belonging to one of the adeninato ligand. It seems to indicate a greater preference of the theobromine molecule for the Hoogsteen face of adenine. On the other hand, the methyl groups of the theobromine molecule preclude further propagation of the hydrogen bonding interactions. As a consequence, the supramolecular architecture is built up by the presence of aromatic interactions that spread in two almost perpendicular directions to generate a 2D arrangement. The first one involves the π - π interactions between the theobromine molecules, and the second one takes place between the adeninato ligands not involved in the hydrogen bonding. These sheets are connected among them by means of additional double Ow-H \cdots N1 hydrogen bonds

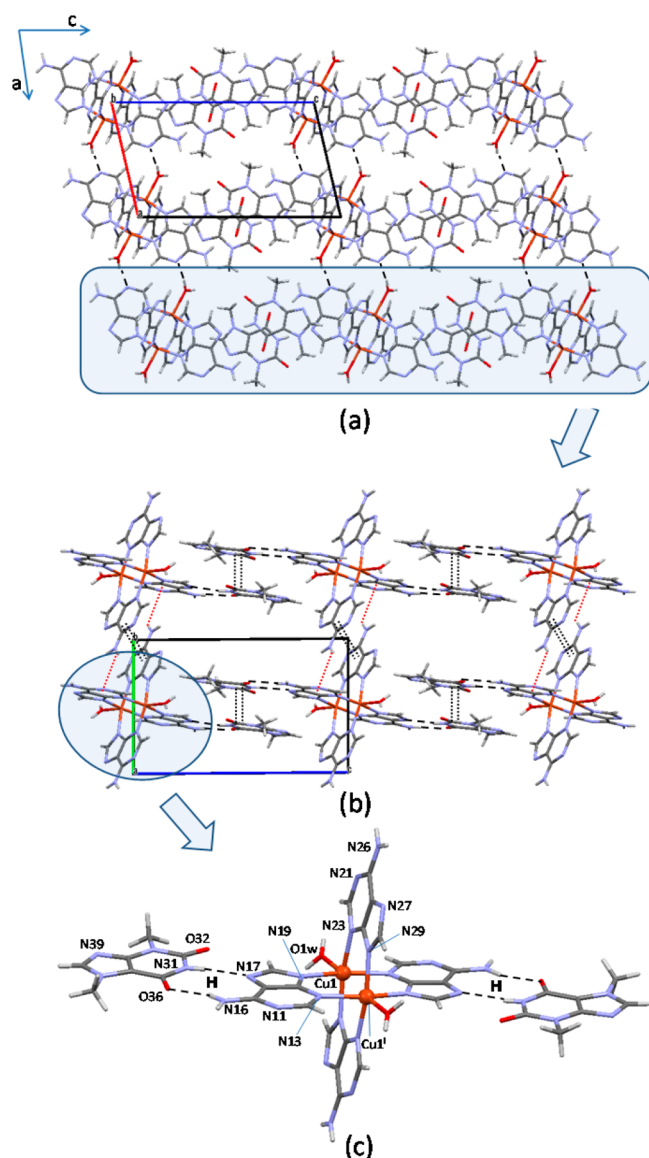


Figure 8. Compound 3: (a, b) Crystal packing showing the presence of supramolecular sheets sustained by complementary hydrogen bonds (dashed lines), π - π stacking (double dashed lines), and N-H...aromatic (red dotted lines) interactions between the dimeric entities and theobromine molecules. (c) Theobromine molecules anchored to the dimeric entities by means of complementary hydrogen bonding interactions.

between the coordinated water molecules and the N1 nitrogen atom of the adeninato ligands. All these supramolecular interactions lead to an interconnected network of one-dimensional channels, which are occupied by crystallization water molecules. These channels represent a 33.0% of the total unit cell volume.

3.4. Structural Description of $[\text{Cu}_2(\mu\text{-ade})_4(\text{H}_2\text{O})_2]\cdot(\text{caf})\cdot\sim 6\text{H}_2\text{O}$ (4). The additional N-methylation of the caffeine precludes its involvement in hydrogen bonding synthons with the adenine ligands, and, as a consequence, the supramolecular architecture of compound 4 is sustained by means of adenine...adenine supramolecular complementary hydrogen bonds and π -stacking interactions with the caffeine molecule. The neutral $[\text{Cu}_2(\mu\text{-ade})_4(\text{H}_2\text{O})_2]$ paddle-wheel units form chains held together by means of hydrogen bonding rings between the

Hoogsteen faces of two neighboring adeninato ligands. These supramolecular ribbons are intertwined to give boxes whose walls are formed by eight adeninate ligands. In the center of each box a caffeine molecule is placed, disordered in two positions related by a 2-fold axis (Figure 9).

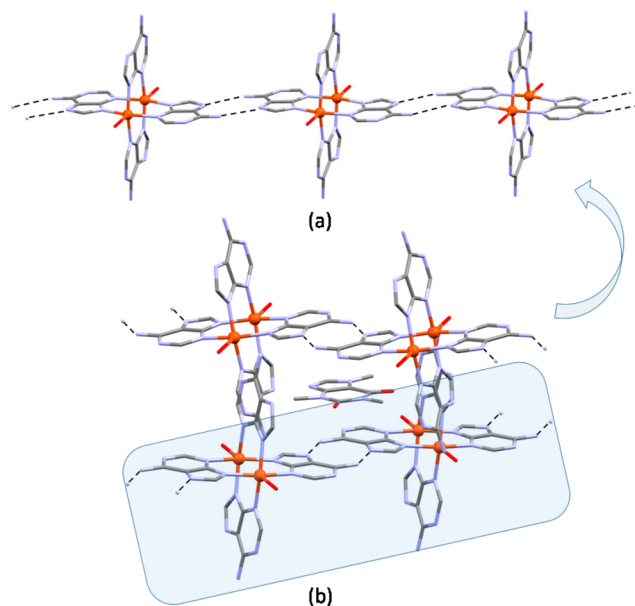


Figure 9. Compound 4: (a) Supramolecular chains sustained by adeninate...adeninate interactions, and (b) insertion of the caffeine molecule in the square-shaped supramolecular box.

Caffeine molecule is disposed parallel to two hydrogen bonded adeninate...adeninate moieties with an interplanar distance of ca. 3.7 Å, and perpendicular to the other four adeninato ligands with the methyl groups of the methylxanthine molecule pointing to the center of the pyrimidinic rings of three adeninato ligands (carbon...centroid average distance of 3.5 Å). It suggests the existence of similar $\text{CH}_3\cdots\pi$ interactions to those described for the compound $[\text{Pt}_2\text{L}_4](\text{NO}_3)_4\cdot 2(\text{caf})$ {L: 1,3-bis(10-(pyridin-3-yl)-9-anthryl)-4,5,6-tris(2-methoxyethoxy)-benzene} in which caffeine molecules are occluded in spherical cavities formed by eight anthracene rings.³¹

The above-described supramolecular assembly generates channels along the [001] direction which imply the 19% of the unit cell volume and host the crystallization water molecules (Figure 10). The pore diameter of these channels ranges from 3.1 to 4.5 Å with a pore volume of 0.13 cm³/g.

Regarding the gas adsorption experiment, although the outgassed sample of compound 4 shows a mass loss of 10.6% (corresponding to all crystallization water molecules), it does not adsorb N₂ at 77 K. The CO₂ adsorption measurements at 273 K between 0 and 5 bar show a significant gas uptake with a saturation value of 0.88 mmol of CO₂/g of compound (Figure 11).

3.5. Magnetic Properties. Figure 12a shows the temperature dependence of the molar magnetic susceptibility (χ_M , blue circles) and $\chi_M T$ (red squares) curves for compound 1. The $\chi_M T$ value per heptameric unit at 300 K is 3.12 cm³ K mol⁻¹, which agrees fairly well with the expected value for seven magnetically noninteracting Cu²⁺ ions.³² This value remains nearly constant upon cooling up to 100 K with a slight increase, but below this temperature a sharp increase is observed to reach

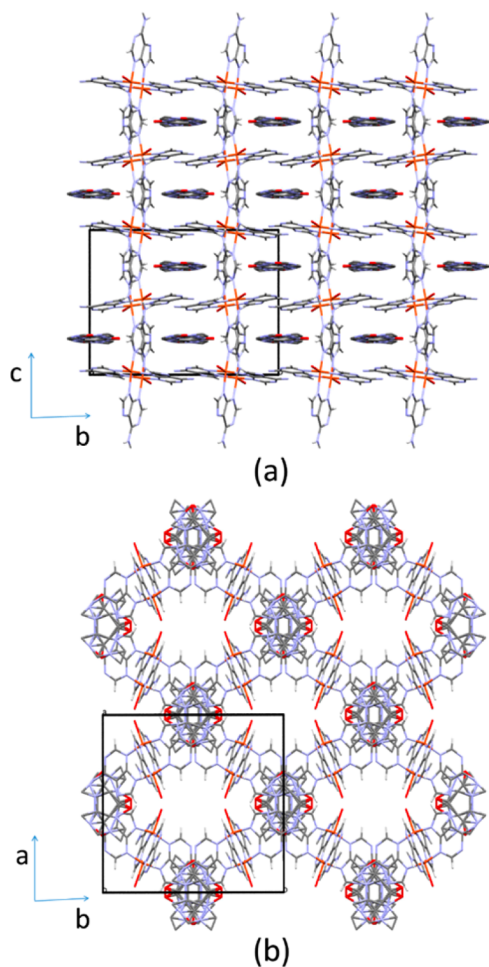


Figure 10. Views of the crystal packing of compound 4 showing (a) the insertion of the caffeine molecules and (b) the channels running along the [001] direction.

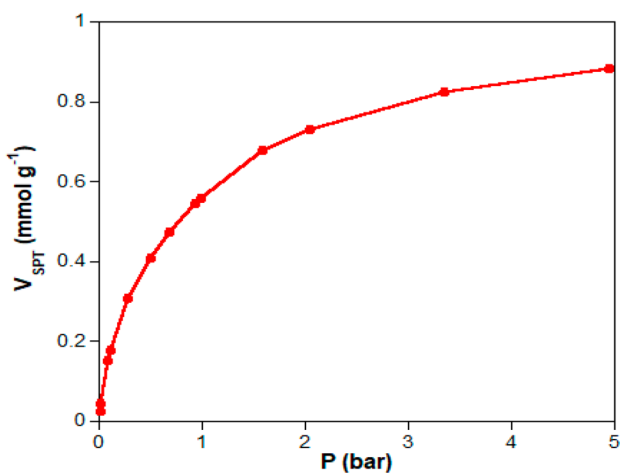


Figure 11. CO₂ adsorption curve at 273 K (0–5 bar) for compound 4.

a maximum of 4.73 cm³ K mol⁻¹ at 6 K. The field dependence of the magnetization at 2 K displays a linear dependence, from 0 to 15 kOe, which slowly tends to saturate at 20 kOe (5.3 μ_B/heptamer). The magnetization at 2 K shows no hysteresis (have neither coercivity nor remanence) at this temperature. This behavior seems to indicate the presence of ferromagnetic heptameric entities in which the central copper(II) atom is

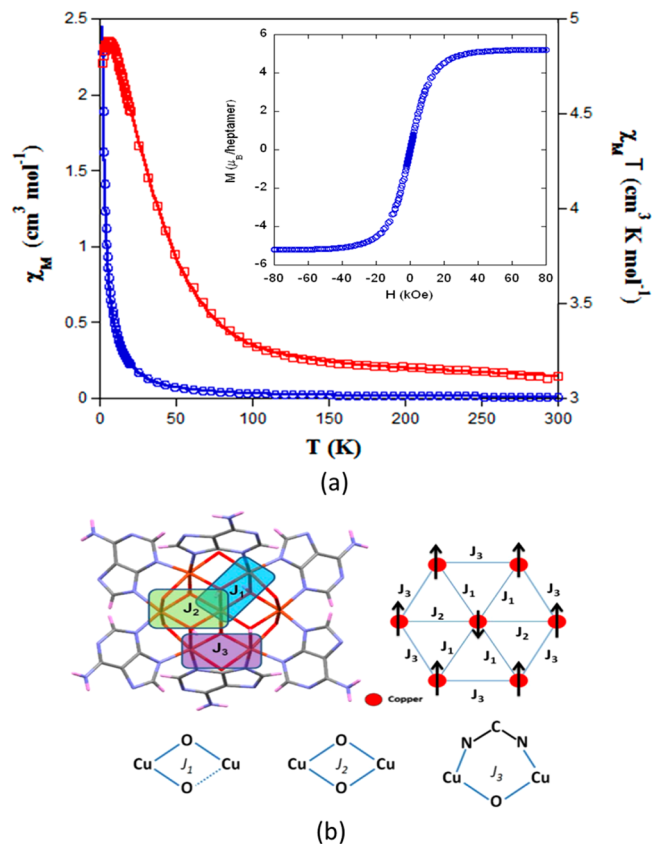


Figure 12. (a) ZFC thermal evolution of the molar magnetic susceptibility (χ_m) and $\chi_m T$ product for compound 1. Magnetization curve at 2 K (inset). The line shows the best fitting of the experimental data. (b) $[\text{Cu}_7(\mu_3\text{-OH})_6(\mu\text{-adeninato-}\kappa\text{N3}:\kappa\text{N9})_6(\mu\text{-H}_2\text{O})_6]^{2+}$ heptanuclear entity emphasizing the relationship of the magnetic topology and 3-J coupling scheme for the local Cu₇ cluster.

antiferromagnetically coupled to the external ferromagnetic hexanuclear ring to provide an $S = 5/2$ ground state.⁴

Taking into account the molecular structure of the $[\text{Cu}_7(\mu_3\text{-OH})_6(\mu\text{-adeninato-}\kappa\text{N3}:\kappa\text{N9})_6(\mu\text{-H}_2\text{O})_6]^{2+}$ heptanuclear entities and the Jahn–Teller elongated octahedron of the central copper(II) atom, the following Hamiltonian (eq 1) was employed to fit the experimental data.

$$\begin{aligned}
 H = & -J_1(\vec{S}_1 \cdot \vec{S}_3 + \vec{S}_1 \cdot \vec{S}_4 + \vec{S}_1 \cdot \vec{S}_5 + \vec{S}_1 \cdot \vec{S}_6) \\
 & - J_2(\vec{S}_1 \cdot \vec{S}_2 + \vec{S}_1 \cdot \vec{S}_7) - J_3(\vec{S}_2 \cdot \vec{S}_3 + \vec{S}_3 \cdot \vec{S}_4 + \vec{S}_4 \cdot \vec{S}_5 + \vec{S}_5 \cdot \vec{S}_6 \\
 & + \vec{S}_6 \cdot \vec{S}_7 + \vec{S}_4 \cdot \vec{S}_7) - g\mu_B \vec{B} \cdot \vec{S}
 \end{aligned} \quad (1)$$

J_1 and J_2 are assigned to the superexchange interactions between the central and the external copper ions taking place through double $\mu\text{-OH}$ bridges. J_1 involves a mixture of equatorial–equatorial, with a Cu–O short distance (<2.0 Å) and equatorial–axial coordinated with short and long distance (Cu4–O3: 1.954(6) Å and Cu1–O3: 2.247(7) Å, respectively), whereas J_2 presents only an equatorial–equatorial arrangement of short distance bridging hydroxides. J_3 represents the superexchange interaction between the external Cu^{II} ions bridged by adeninato, hydroxide, and semicoordinated water molecules. The fitting of the $\chi_m T$ experimental data (Figure 12b) to this model was performed using the MagProp software tool distributed with DAVE.³³ The best fitting parameters (see

the red continuous line in Figure 12) are $J_1 = 25$, $J_2 = -158$, $J_3 = 86 \text{ cm}^{-1}$ and $g = 2.11$.

This behavior and the obtained superexchange values are similar to those published for other similar wheel-shaped copper(II) heptameric entities in which the outer metal atoms are ferromagnetically coupled to each other and antiferromagnetically coupled to the central atom.^{4,20}

As previously stated, the dehydration procedure gives rise to a substantial reorganization of the crystal structure of compound 1. In order to get some insight on the persistence of the heptanuclear entity after this structural rearrangement, the magnetic characterization of an activated sample of compound 1 was accomplished (Figure S7). It shows a similar magnetization curve at 2 K but without reaching to saturation at 65 kOe. In a similar way, the $\chi_M T$ curve is similar to that of the fresh sample, but its maximum at higher temperatures (15 K) with a lower $\chi_M T$ value of $3.41 \text{ cm}^3 \text{ K mol}^{-1}$. Both facts suggest the presence of the heptameric entities in the activated sample, which establish stronger supramolecular antiferromagnetic interactions between them in agreement with the observed shrinkage of the unit cell upon the activation process.

In compounds 2 and 4, the magnetic data (Figure 13) indicate a strong antiferromagnetic interaction between the copper atoms of the dimeric entity mediated by the four μ - $\kappa N3:\kappa N9$ adeninato ligands.

In fact, the values of $\chi_M T$ at room temperature of both compounds (0.64 and $0.75 \text{ cm}^3 \text{ mol}^{-1} \text{ K}$ for compounds 2 and 4, respectively) are slightly below the expected value for two uncoupled paramagnetic copper(II) centers ($0.83 \text{ cm}^3 \text{ mol}^{-1} \text{ K}$, $g = 2.10$) and continuously decrease upon cooling. The χ_M curve shows the typical maximum for these systems around 240 and 200 K, respectively. However, the χ_M curve also shows an increase of its value at low temperatures indicative of the presence of paramagnetic impurities. The susceptibility data have been fitted using the Bleaney–Bowers equation ($H = -JS_1S_2$) for a modified copper(II) dinuclear complex to take into account the paramagnetic impurities (ρ) present in the compound.³⁴ The best fitting values are $g = 2.11$, $J = -271 \text{ cm}^{-1}$, and $\rho = 0.4\%$ for 2 and $g = 2.11$, $J = -256 \text{ cm}^{-1}$, and $\rho = 4.4\%$ for compound 4. The obtained superexchange parameters are within the range observed for compounds with formula $[\text{Cu}_2(\mu\text{-ade-}\kappa N3:\kappa N9)_4(\text{X})_2]^{n+}$ ($n = 0, 2, 4$, $\text{X} = \text{H}_2\text{O}, \text{Cl}, \text{Br}$; $\text{ade} = \text{adenine or adeninate}$) and J ranging from -211 to -316 cm^{-1} .¹⁵

4. CONCLUSIONS

It has been proven that open supramolecular architectures can be achieved using π -stacking intercalators together with metal-adenine discrete rigid entities. Using anionic intercalators to replace the channel occupying inorganic anions that counterbalance the cationic heptameric copper-adenine entities (compound 1), or using neutral intercalators that interact strongly with the neutral copper-adenine dimers (compounds 2, 3, and 4). Additionally, an increase of the stability of compound 1 has been observed with respect to the non-intercalated compounds containing this heptameric metal-adenine discrete entity.⁴

These compounds prove that single π -stacking interactions could be robust and rigid enough to provide open 3D architectures, but apparently not so rigid as to retain their porous structure upon the removal of the solvent molecules. However, the variation of the X-ray powder diffraction pattern with the temperature in compound 1 indicates that double π -

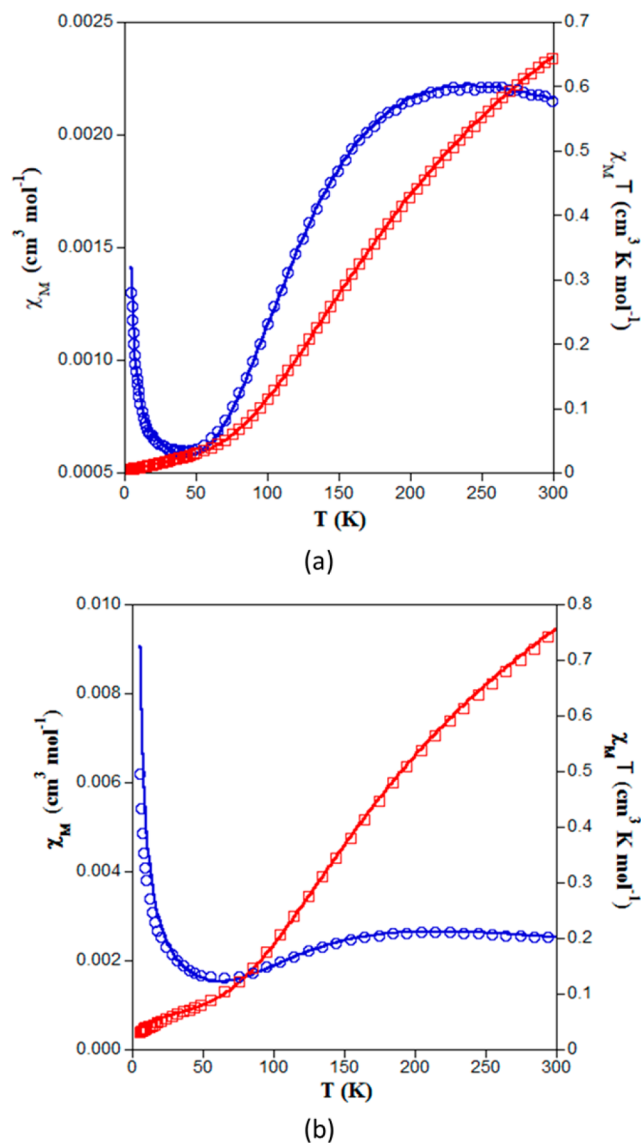


Figure 13. ZFC thermal evolution of the molar magnetic susceptibility (χ_M) (blue points) and $\chi_M T$ (red square) product for 2 (a) and 4 (b). The line shows the fitting of the experimental data.

stacking interactions could be rigid and robust enough for this purpose as the structure shrinks and swells reversibly upon the desolvation and vapor exposure, respectively.

■ ASSOCIATED CONTENT

Supporting Information

The Supporting Information is available free of charge on the ACS Publications website at DOI: 10.1021/acs.cgd.8b00188.

Tables of bond distances and noncovalent interactions, thermogravimetric analysis, X-ray thermogravimetric data, and magnetic behavior (PDF)

Accession Codes

CCDC 1820768–1820771 contain the supplementary crystallographic data for this paper. These data can be obtained free of charge via www.ccdc.cam.ac.uk/data_request/cif, or by emailing data_request@ccdc.cam.ac.uk, or by contacting The Cambridge Crystallographic Data Centre, 12 Union Road, Cambridge CB2 1EZ, UK; fax: +44 1223 336033.

AUTHOR INFORMATION

Corresponding Author

*E-mail: oscar.castillo@ehu.eus.

ORCID

Jon Pascual-Colino: 0000-0001-9751-9332

Garikoitz Beobide: 0000-0002-6262-6506

Oscar Castillo: 0000-0002-5614-9301

Ivan da Silva: 0000-0002-4472-9675

Antonio Luque: 0000-0002-8827-0384

Sonia Pérez-Yáñez: 0000-0003-3342-892X

Notes

The authors declare no competing financial interest.

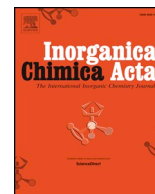
ACKNOWLEDGMENTS

This work has been funded by Universidad del País Vasco/Euskal Herriko Unibertsitatea (PPG17/37, predoctoral PFI17/051 fellowship for J.P.C.) and Ministerio de Economía y Competitividad (MAT2016-75883-C2-1-P). Technical and human support provided by SGIker (UPV/EHU, MICINN, GV/EJ, ESF) is also acknowledged.

REFERENCES

- (1) Uhlenheuer, D. A.; Petkau, K.; Brunsveld, L. Combining supramolecular chemistry with biology. *Chem. Soc. Rev.* **2010**, *39*, 2817–2826.
- (2) Pérez-Yáñez, S.; Beobide, G.; Castillo, O.; Cepeda, J.; Luque, A. In *Supramolecular Systems: Chemistry, Types and Applications*; Pena, C., Ed.; Nova Science Publishers, Inc., 2016; pp 67–92.
- (3) Beobide, G.; Castillo, O.; Luque, A.; Pérez-Yáñez, S. Porous materials based on metal–nucleobase systems sustained by coordination bonds and base pairing interactions. *CrystEngComm* **2015**, *17*, 3051–3059.
- (4) Pérez-Aguirre, R.; Beobide, G.; Castillo, O.; De Pedro, I.; Luque, A.; Pérez-Yáñez, S.; Rodríguez Fernández, J.; Román, P. 3D magnetically ordered open supramolecular architectures based on ferrimagnetic Cu/adenine/hydroxide heptameric wheels. *Inorg. Chem.* **2016**, *55*, 7755–7763.
- (5) Thomas-Gipson, J.; Beobide, G.; Castillo, O.; Cepeda, J.; Luque, A.; Pérez-Yáñez, S.; Aguayo, A. T.; Román, P. Porous supramolecular compound based on paddle-wheel shaped copper(II)–adenine dinuclear entities. *CrystEngComm* **2011**, *13*, 3301–3305.
- (6) Thomas-Gipson, J.; Beobide, G.; Castillo, O.; Fröba, M.; Hoffmann, F.; Luque, A.; Pérez-Yáñez, S.; Román, P. Paddle-wheel shaped copper(II)–adenine discrete entities as supramolecular building blocks to afford porous supramolecular metal-organic frameworks (SMOFs). *Cryst. Growth Des.* **2014**, *14*, 4019–4029.
- (7) Van Den Bogaard, B.; Draijer, R.; Westerhof, B. E.; Van Den Meiracker, A. H.; Van Montfrans, G. A.; Van Den Born, B. J. H. Effects on peripheral and central blood pressure of cocoa with natural or high-dose theobromine: A randomized, double-blind crossover trial. *Hypertension* **2010**, *56*, 839–846.
- (8) Martínez-Pinilla, E.; Oñatibia-Astibia, A.; Franco, R. The relevance of theobromine for the beneficial effects of cocoa consumption. *Front. Pharmacol.* **2015**, *6*, 1–5.
- (9) Husain, A.; Parveen, R.; Dastidar, P. New Series of Zn^{II}/Cd^{II} Mixed Ligand Coordination Polymers: Toward the Design of Metallogels. *Cryst. Growth Des.* **2015**, *15*, 5075–5085.
- (10) Earnshaw, A. *Introduction to Magnetochemistry*; Academic Press: London, 1968.
- (11) *CrysAlisPro*; Agilent Technologies Ltd: Yarnton, Oxfordshire, England, 2014.
- (12) Altomare, A.; Cascarano, G.; Giacovazzo, C.; Guagliardi, A.; Burla, M. C.; Polidori, G.; Camalli, M. SIR92—a program for automatic solution of crystal structures by direct methods. *J. Appl. Crystallogr.* **1994**, *27*, 435.
- (13) Sheldrick, G. M. A short history of SHELX. *Acta Crystallogr., Sect. A: Found. Crystallogr.* **2008**, *64*, 112–122.
- (14) Farrugia, L. J. WinGX and ORTEP for Windows: an update. *J. Appl. Crystallogr.* **2012**, *45*, 849–854.
- (15) Cepeda, J.; Castillo, O.; García-Terán, J. P.; Luque, A.; Pérez-Yáñez, S.; Roman, P. Supramolecular architectures and magnetic properties of self-assembled windmill-like dinuclear copper(II) complexes with purine ligands. *Eur. J. Inorg. Chem.* **2009**, 2344–2353.
- (16) Sletten, E. Crystallographic studies of metal–nucleotide base complexes. I. Triclinic bis-(6-aminopurine)copper(II) tetrahydrate. *Acta Crystallogr., Sect. B: Struct. Crystallogr. Cryst. Chem.* **1969**, *25*, 1480–1491.
- (17) Sletten, E. Crystallographic studies of metal–nucleotide base complexes. II. Bis-(6-hydroxypurine)copper(II) chloride trihydrate. *Acta Crystallogr., Sect. B: Struct. Crystallogr. Cryst. Chem.* **1970**, *26*, 1609–1614.
- (18) Van der Sluis, P.; Spek, A. L. BYPASS: an effective method for the refinement of crystal structures containing disordered solvent regions. *Acta Crystallogr., Sect. A: Found. Crystallogr.* **1990**, *46*, 194–201.
- (19) Spek, A. L. Structure validation in chemical crystallography. *Acta Crystallogr., Sect. D: Biol. Crystallogr.* **2009**, *65*, 148–155.
- (20) Leite Ferreira, B. J. M.; Brandão, P.; Dos Santos, A. M.; Gai, Z.; Cruz, C.; Reis, M. S.; Santos, T. M.; Félix, V. Heptacopper(II) and dicopper(II)–adenine complexes: Synthesis, structural characterization, and magnetic properties. *J. Coord. Chem.* **2015**, *68*, 2770–2787.
- (21) Liu, Z.-Y.; Zhang, H.-Y.; Yang, E.-C.; Liu, Z.-Y.; Zhao, X.-J. A (3,6)-connected layer with an unprecedented adenine nucleobase-derived heptanuclear disc. *Dalt. Trans.* **2015**, *44*, 5280–5283.
- (22) Herdes, C.; Sarkisov, L. Computer Simulation of Volatile Organic Compound Adsorption in Atomistic Models of Molecularly Imprinted Polymers. *Langmuir* **2009**, *25*, 5352–5359.
- (23) Düren, T.; Millange, F.; Férey, G.; Walton, K. S.; Snurr, R. Q. Calculating Geometric Surface Areas as a Characterization Tool for Metal–Organic Frameworks. *J. Phys. Chem. C* **2007**, *111*, 15350–15356.
- (24) Topos Main Page <http://www.topospro.com>, accessed (2018/02/22).
- (25) Blatov, V. A. Multipurpose crystallochemical analysis with the program package TOPOS. *IUCr CompComm Newsl.* **2006**, *7*, 4–38.
- (26) O’Keeffe, M.; Yaghi, O. M. Deconstructing the Crystal Structures of Metal–Organic Frameworks and Related Materials into Their Underlying Nets. *Chem. Rev.* **2012**, *112*, 675–702.
- (27) Groom, C. R.; Bruno, I. J.; Lightfoot, M. P.; Ward, S. C. The Cambridge Structural Database. *Acta Crystallogr., Sect. B: Struct. Sci., Cryst. Eng. Mater.* **2016**, *72*, 171–179.
- (28) Radhakrishnan, K.; Burgula, L. N.; Kundu, L. M. Watson–Crick and Hoogsteen tri-base pairing: a co-crystal structure of a 2:1 complex of 6-isopropyluracil and adenine nucleobases. *RSC Adv.* **2013**, *3*, 7282–7284.
- (29) Gattuso, G.; Manfredi, G.; Sammartano, S. Quantitative study on the non-covalent interactions between ATP and caffeine, theophylline and theobromine in aqueous solution. *Fluid Phase Equilib.* **2011**, *308*, 47–54.
- (30) Johnson, I. M.; Prakash, H.; Prathiba, J.; Raghunathan, R.; Malathi, R. Spectral Analysis of Naturally Occurring Methylxanthines (Theophylline, Theobromine and Caffeine) Binding with DNA. *PLoS One* **2012**, *7*, e50019.
- (31) Yamashina, M.; Matsuno, S.; Sei, Y.; Akita, M.; Yoshizawa, M. Recognition of Multiple Methyl Groups on Aromatic Rings by a Polyaromatic Cavity. *Chem. - Eur. J.* **2016**, *22*, 14147–14150.
- (32) Boca, R. *Handbook of Magnetochemical Formulae*; Elsevier: Amsterdam, 2012.
- (33) Azuah, R. T.; Kneller, L. R.; Qiu, Y.; Tregenna-Piggott, P. L. W.; Brown, C. M.; Copley, J. R. D.; Dimeo, R. M. DAVE: A Comprehensive Software Suite for the Reduction, Visualization, and Analysis of Low Energy Neutron Spectroscopic Data. *J. Res. Natl. Inst. Stand. Technol.* **2009**, *114*, 341–358.

(34) Bleaney, B.; Bowers, K. D. Anomalous paramagnetism of copper acetate. *Proc. R. Soc. London, Ser. A* **1952**, *214*, 451–465.



Research paper

Theophylline alkaloid as glue of paddle-wheel copper(II)-adenine entities to afford a rhomboid chain

Jon Pascual-Colino^a, Garikoitz Beobide^a, Oscar Castillo^{a,*}, Antonio Luque^a, Sonia Pérez-Yáñez^b^a Departamento de Química Inorgánica, Facultad de Ciencia y Tecnología, Universidad del País Vasco, UPV/EHU, Apartado 644, 48080 Bilbao, Spain^b Departamento de Química Inorgánica, Facultad de Farmacia, Universidad del País Vasco, UPV/EHU, 01006 Vitoria-Gasteiz, Spain

ARTICLE INFO

Keywords:

Coordination polymers
Theophylline
Adenine
Paddle-wheel
Metal-nucleobase
Antiferromagnetic

ABSTRACT

This work is aimed at the analysis of the interactions that drive the assembling of coordination metal-organic polymers based on biological molecules. Single-crystal X-ray diffraction data show that the compound 1D- $\{[\text{Cu}_2(\mu\text{-ade})_4(\text{H}_2\text{O})_2] \cdot 2[\text{Cu}(\text{theoph})_2] \cdot n \cdot 10\text{H}_2\text{O}\}_n$ (1) contains neutral rhomboid shaped chains sustained by the tridentate $\mu_3\text{-}\kappa\text{N3}:\kappa\text{N7}:\kappa\text{N9}$ coordination mode of the adenine nucleobase. These chains are formed by dimeric copper/adeninato (ade) cores doubly bridged by monomeric copper/theophyllinato (theoph) entities with the alkaloid acting as peripheral ligand. The lack of direct intermolecular nucleobase–nucleobase interactions, due to their disruption by the crystallization water molecules, does not provide a highly porous material, but the irregular shape of the polymeric chain hinders their packing and allows the presence of a moderate amount of voids (16% of the unit cell volume) in good accordance with its adsorption capacity of 0.38 mmol CO_2/g at 273 K. Thermogravimetric and variable temperature X-ray diffraction analyses show that the compound retains its structure up to 110 °C whereas above this temperature the release of the coordination water molecules produces a significant loss of crystallinity. Magnetic measurements indicate an overall antiferromagnetic behavior with a J value of -267 cm^{-1} within the dimeric entity.

1. Introduction

Crystal engineering of coordination compounds from the self-assembly of transition metal ions with biologically relevant ligands is one of the most challenging issues in current synthetic chemistry [1]. Its relevance is not only because of their intrinsic aesthetic appeal, but also because the analyses of the interaction of biomolecules and their constituents with metal ions in biomimetic artificial systems is a crucial stage in the development of advanced functional materials with tailor-made properties and exploitable applications in therapeutic medicine and material science [2–4].

Biomolecules offer the potential to utilize multiple coordination sites and contain a variety of pre-organized recognition moieties that permit them to take part of well-known supramolecular assembly patterns in a great diversity of macromolecular biological systems [5]. In particular, the nucleobases, key building units of the nucleic acids, have been widely used as bioligands owing to the versatility of their coordination binding modes and their capacities to form robust molecular recognition synthons between them and with other biologically relevant species (via hydrogen bonding and/or $\pi\text{-}\pi$ stacking interactions). For example, the *N*-rich adenine nucleobase (Hade) and its conjugated adeninate anion (ade)

provide high number of donor atoms with different basicity that can act as connectors to metallic ions: two pyrimidinic N1 and N3; two imidazole N7 and N9 and one exocyclic amino group N6 (Fig. 1). Although, the bidentate $\kappa\text{N3}:\kappa\text{N9}$ coordination mode is predominant [6–11], adenine can act as mono-, bi-, tri-, or tetradentate coordination ligand giving rise to compounds with a rich structural diversity. For example, the simultaneous chelating and bridging mode ($\mu_3\text{-}\kappa\text{N3}:\kappa\text{N7}:\kappa\text{N9}$) of the adeninato ligand [12,13] has permitted to obtain compounds ranging from discrete species [7,13–17] to high-dimensional covalent structures [18–21]. We report herein an one-dimensional coordination polymer, $\{[\text{Cu}_2(\mu\text{-ade})_4(\text{H}_2\text{O})_2] \cdot 2[\text{Cu}(\text{theoph})_2] \cdot n \cdot 10\text{H}_2\text{O}\}_n$ (1), in which the adeninato ligand exhibits the above described tridentate coordination mode and the theophylline (1,3-dimethyl-3,7-dihydro-1H-purine-2,6-dione) acts as peripheral ligand. This alkaloid is a methylxanthine, with a moderate solubility in water, found in common food products such as cocoa and tea, and it is commercially available as a bronchodilator in the treatment of asthma due to its diuretic and anti-inflammatory effects [22]. The work is part of our research on metal-biomolecule coordination compounds in which we have recently published the first examples containing simultaneously a purine nucleobase and a xanthine alkaloid (theobromine and caffeine) [23].

* Corresponding author.

E-mail address: oscar.castillo@ehu.es (O. Castillo).<https://doi.org/10.1016/j.ica.2018.09.039>

Received 26 July 2018; Received in revised form 13 September 2018; Accepted 13 September 2018

Available online 14 September 2018

0020-1693/© 2018 Elsevier B.V. All rights reserved.

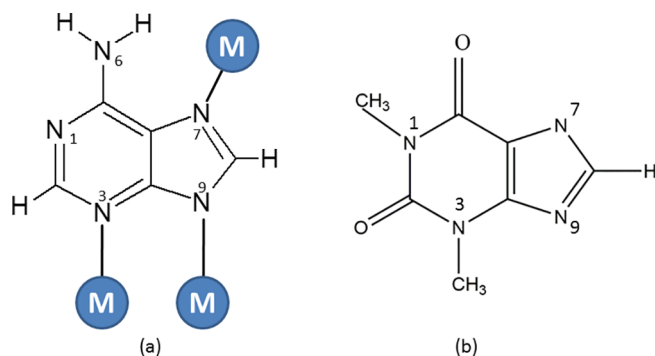


Fig. 1. (a) Adenine nucleobase showing a tricoordinated $\mu_3\text{-}\kappa\text{N}3\text{:}\kappa\text{N}7\text{:}\kappa\text{N}9$ mode. (b) Theophyllinate anion with the atom numbering.

2. Experimental

2.1. Synthesis of $\{[\text{Cu}_2(\mu\text{-ade})_4(\text{H}_2\text{O})_2] \cdot 2[\text{Cu}(\text{theoph})_2] \cdot n \cdot 10\text{H}_2\text{O}\}_n$ (1)

Adenine (0.0390 g, 0.3 mmol) dissolved in 15 mL of water-methanol mixture (1:1) was added to a solution of $\text{Cu}(\text{NO}_3)_2 \cdot 3\text{H}_2\text{O}$ (0.0488 g, 0.2 mmol) in 10 mL of distilled water. The resulting mixture, in continuous stirring, was basified dropwise with a NaOH solution until a pH ~ 9 . Theophylline (0.0721 g, 0.3 mmol), previously dissolved in 20 mL of distilled water at 90 °C and basified to pH ~ 9 , was added to initial purple solution. The final solution was allowed to stand at room temperature. After two months, a mixture of powder and deep purple crystals of compound 1 was obtained. Yield of ca. 20% (based on metal). Anal. Calc. for $\text{C}_{48}\text{H}_{68}\text{Cu}_4\text{N}_{36}\text{O}_{20}$: C, 33.45; H, 3.98; Cu, 14.75; N, 29.26. Found: C, 33.05; H, 3.95; Cu, 14.86; N, 29.43%. Main IR features (cm^{-1} , KBr pellet): 3446vs, 2995w, 1681 s, 1660w, 1622 s, 1572 s, 1496w, 1444w, 1282 m, 1225 m, 1192 m, 1151 m, 985 m, 935w, 792 m, 746 s, 667 m, 648 m, 549 m. Purity of the bulk samples was checked by comparison of the experimental X-ray powder diffractogram with the simulated diffraction pattern obtained from the single-crystal X-ray data [24].

2.2. Physical measurements

Elemental analyses (carbon, hydrogen, and nitrogen) was performed employing a EuroVector, Euro EA Elemental CHNS rapid analyzer, whereas the metal content was determined by inductively coupled plasma atomic emission spectrometer (ICP-AES) from Perkin Elmer Analyst 100. The IR spectra (KBr pellets) was recorded on a FTIR 8400S Shimadzu spectrometer in the 4000–400 cm^{-1} spectral region. Thermal analysis (TG) was performed on a METTLER TOLEDO TGA/SDTA851 thermal analyzer in a synthetic air atmosphere (79% N_2 , 21 % O_2) with heating rate of 5 min^{-1} . The X-ray powder diffraction patterns (XRPD) were collected on a Phillips Xpert PRO powder diffractometer with $\text{Cu-K}\alpha$ radiation tube (1.5418 Å) and a PIXcel rapid detector. The measurement conditions were 40 KV and 40 mA and a sweep between $5 < 2\theta < 50^\circ$. Carbon dioxide (273 K) physisorption data was recorded on an activated sample (vacuum at 50 °C for 4 h) with a Quantachrome Autosorb-iQ. Magnetic measurements were performed on polycrystalline sample taken from the same uniform batch used for the structural determination with a Quantum Design SQUID susceptometer covering the temperature range 2–300 K at a magnetic field of 1 kOe.

2.3. X-ray structure determination

A block like crystal (0.06/0.05/0.04 mm) was mounted on a Agilent Technologies Supernova diffractometer equipped with graphite-monochromated Mo- $\text{K}\alpha$ radiation ($\lambda = 0.71073$ Å) at 100(2) K. Data were processed and corrected for Lorentz and polarization effects. The data

Table 1
Crystal data and structure refinement parameters for 1.

Formula	$\text{C}_{48}\text{H}_{68}\text{Cu}_4\text{N}_{36}\text{O}_{20}$
Formula weight	1723.47
Crystal system	Triclinic
Space group	$P\bar{1}$ (No. 2)
a (Å)	9.1184(5)
b (Å)	11.9896(6)
c (Å)	16.3784(9)
α (°)	90.665(4)
β (°)	105.760(5)
γ (°)	103.134(4)
V (Å ³)	1673.1(2)
ρ_{calc} (g cm^{-3})	1.709
μ (mm^{-1})	1.351
S^a	1.104
R_1, wR_2^b [$I > 2\sigma(I)$]	0.0554, 0.1115
R_1, wR_2^b [all]	0.0676, 0.1167

$$^a S = [\sum w(F_o^2 - F_c^2)^2 / (N_{\text{obs}} - N_{\text{param}})]^{1/2}$$

$$^b R_1 = \sum ||F_o| - |F_c|| / \sum |F_c|, wR_2 = [\sum w(F_o^2 - F_c^2)^2 / \sum wF_c^2]^{1/2}$$

reduction was carried out with the CrysAlisPro program [25]. Crystallographic details for structure 1 are summarized in Table 1. The structure was solved by direct methods using the SIR92 [26]. Full matrix least-squares refinements were performed on F^2 using SHELXL97 [27]. All non-hydrogen atoms were refined anisotropically. All calculations were performed using the WinGX crystallographic software package [28]. During the initial resolution of the structures the presence of highly disordered water molecules was detected in the holes of the crystal structure, therefore the corresponding electronic density was eliminated by the SQUEZEE [29] routine of the PLATON program [30]. Graphical representations, visualization, exploration and the analysis of the structural units and the crystal packing were carried out with the programs PLATON and MERCURY 3.10 [24].

3. Results and discussion

In previous research on systems based on metal, nucleobases and derivatives thereof we have design porous open crystal structures sustained by supramolecular non-covalent interactions (hydrogen bonds and π - π stacking) between discrete copper(II)-adenine entities and non-coordinate anions of xanthine alkaloids such as theobromine and caffeine [23]. In the present case, the higher coordination ability of theophylline produces the coordination polymer 1 with rhombic $[\text{Cu}_6(\text{ad})_4]$ subunits joined together in a chain supported by the tridentate $\mu_3\text{-}\kappa\text{N}3\text{:}\kappa\text{N}7\text{:}\kappa\text{N}9$ coordination mode [5,8,12,13,21] of the adeninato ligands and decorated with theophyllinate anions as peripheral ligands. Fig. 2 represents a fragment of the polymeric structure showing as the dimeric $[\text{Cu}_2(\mu\text{-ade})_4(\text{H}_2\text{O})_2]$ nodes are doubly bridged by bis (theophyllinato)copper(II) entities by means of the bridging adeninato ligand. Table 2 lists the most relevant bond distances in the polymeric chain.

The centrosymmetric dimeric fragment is built up by two copper atoms ($\text{Cu}1$ and $\text{Cu}1^b$) bridged by four adeninato ligands through the pyrimidine $\text{N}x3$ and imidazolic $\text{N}x9$ nitrogen atoms ($x = 1$ or 2) to provide a paddle-wheel shaped core with a $\text{Cu}1\text{-Cu}1^b$ distance of 2.956(7) Å. The square-based pyramidal environment around the $\text{Cu}1$ atom is completed by a water molecule in the apical position with a $\text{Cu}1\text{-O}w$ distance longer than those involving the nitrogen atoms (Table 2). The structural parameters of this building block are similar to those previously reported for analogous dimeric entities [2,14,31–35]. Each dimeric fragment is linked to four neighboring $[\text{Cu}(\text{theoph})_2]$ entities via the $\text{N}x7$ atom from the imidazole ring of adeninato ligand with $\text{Cu}1\text{-Cu}2$ distances of 5.755(7) and 5.924(7) Å. The square-based pyramidal N_4O donor set of the $\text{Cu}2$ atom is filled by the $\text{N}x7$ atoms

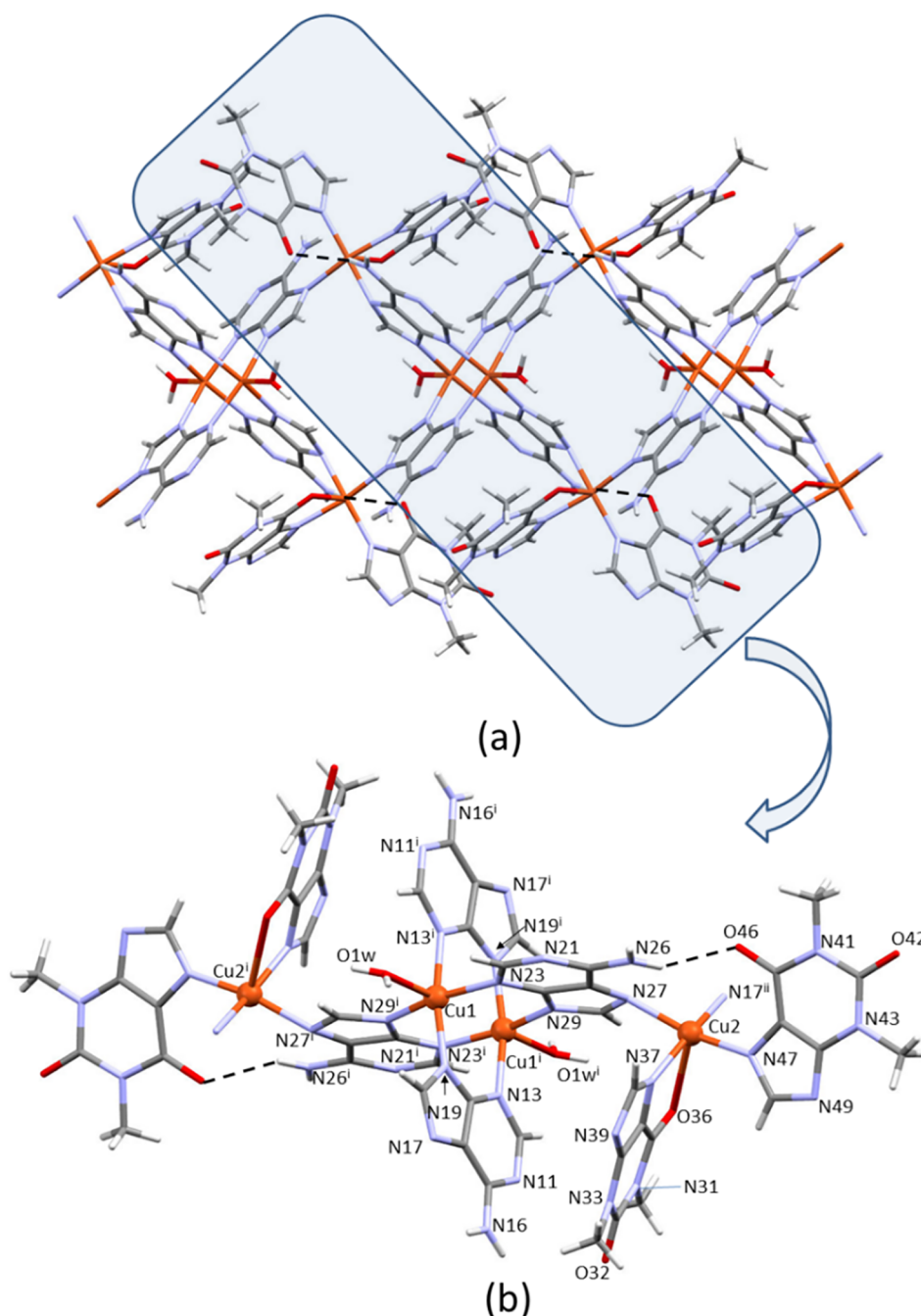


Fig. 2. (a) Polymeric chain in compound 1 showing the intramolecular hydrogen bond N-H...O (dashed line). (b) Detail with the numbering scheme used.

Table 2
Selected bond lengths (Å) for 1.^a

Cu1–N13 ⁱ	2.034(3)	Cu2–N17 ⁱⁱ	2.032(3)	Cu1...Cu1 ⁱ	2.956(7)
Cu1–N19	1.997(3)	Cu2–N27	1.988(3)	Cu1 ⁱ ...Cu2	5.755(7)
Cu1–N23	2.024(4)	Cu2–O36	2.766(3)	Cu1...Cu2 ⁱⁱⁱ	5.924(7)
Cu1–N29 ⁱ	1.998(4)	Cu2–N37	1.991(3)		
Cu1–O1w	2.172(3)	Cu2–N47	1.941(3)		

^a Symmetry codes: (i) $-x + 3, -y + 1, -z + 1$; (ii) $-1 + x, y, z$; (iii) $x + 1, y, z$.

from two adeninato bridges, the imidazolic N47 nitrogen atom of one peripheral monodentate theophyllinate anion and a five-membered chelating ring formed by a second alkaloid molecule attached to the metal by the N37 nitrogen atom and the adjacent ketonic O36 oxygen

atom with a Cu2–O36 distance [2.766(3) Å] substantially greater than the Cu–N but slightly shorter than the sum of the van der Waals radii (1.52 Å for O, 1.43 Å for Cu) [36]. The non-coordination of the carboxyl O46 oxygen atom of the monodentate theophyllinato ligand is stabilized by an interligand N26–H26B...O46 hydrogen bond with the exocyclic amino group of an adjacent adeninato ligand [N...O: 3.099(6) Å and H...O: 2.30 Å, \angle N–H...O: 155°].

A perusal analysis in the crystallographic CSD database [37] of the crystal structures corresponding to theophylline/theophyllinato transition metal complexes (Fig. 3) shows that the κ N7-monodentate coordination mode is predominant and the chelating κ^2 N7,O6 binding is only observed in the compounds [Ti(theoph)(η^5 -C₅H₅)₂] [38] and [Cu(theoph)(L)] (L = N-3,4-benzosallylidine-*N,N*-dimethylethylenediamine) [39]. The titanium(III) complex exhibits a relatively symmetric coordination mode [Ti–N7: 2.211(3) Å, Ti–O6: 2.278(2) Å] whereas

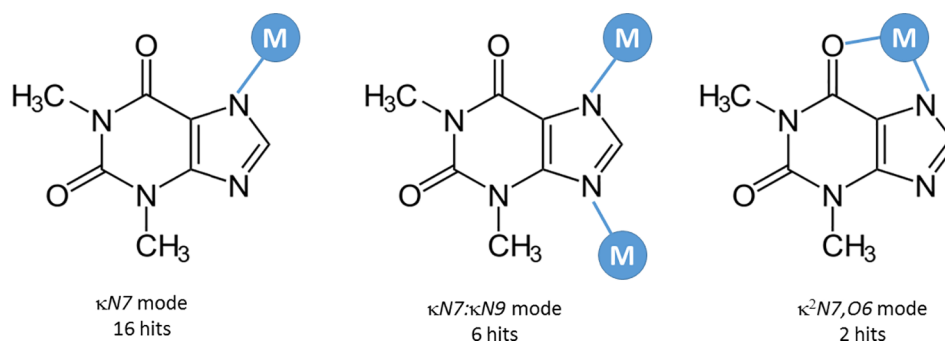


Fig. 3. Coordination modes of the theophylline/theophyllinato ligand.

the copper(II) complex shows a asymmetric binding [Cu–N7: 1.939(3) Å, Cu–O6: 2.919(2) Å] similar than that presented in compound 1.

An analogous alternation of dimeric and monomeric units has been previously described in the three-dimensional compound $\{[\text{Cu}_2(\mu\text{-ade})_4(\text{H}_2\text{O})_2] \cdot 2[\text{Cu}(\text{ox})(\text{H}_2\text{O})] \cdot \sim 14\text{H}_2\text{O}\}_n^{21}$ (ox = oxalate dianion) where the tridentate $\mu_3\text{-}\kappa\text{N3}:\kappa\text{N7}:\kappa\text{N9}$ binding of the adeninato ligands generates a helical network and channels along the direction [001] with a diameter of 13 Å. However, in compound 1, the greater volume of theophyllinato anion with respect to the oxalate, and the coordination of two anions in the monomer unit are probably crucial in preventing the developing of a covalent three-dimensional architecture.

The interconnected rhomboids $[\text{Cu}_6(\text{ade})_4]$ subunits of compound 1 are formed by alternating dimeric (Cu1) and monomeric (Cu2) entities as vertices and a quartet of adenine ligands perpendicularly arranged to the plane of the rhombus as sides. There are no $\pi\text{-}\pi$ interactions between the adeninato ligands since, although they are almost parallel arranged each to other, the nucleobases sited in front are directed towards opposite sides of the chain. In fact, there are not relevant direct supramolecular interactions among the polymeric chains, nor hydrogen bonding nor $\pi\text{-}\pi$ stacking interactions, that could direct the crystal building into an open architecture as observed for compounds where complementary nucleobase–nucleobase interactions are present [14]. In our case, the crystallization water molecules prevail on the competition to establish hydrogen bonds and disrupt the expected direct interactions among the chains. However, the irregular shape and rigidity of the polymeric chain due to the coordination mode of the adeninato ligands, and the presence of intramolecular hydrogen bonds preclude their compact packing. In fact, the resulting inefficient packing generates voids occupied by the crystallization water molecules (Fig. 4).

The thermal degradation of compound 1 under synthetic air atmosphere (Table 3 and Fig. S1 of supplementary information) shows that the crystallization and coordination water molecules are released in an overlapped process between room temperature and 150 °C. Variable-temperature X-ray diffractograms indicate that the sample maintains its crystallinity during this process up to 110 °C. Only above this temperature, at which it probably begins to lose the coordination water molecules, there is a significant decrease in the intensity of the diffraction peaks with the disappearance of several of them (see Fig. S2 of supplementary information). The anhydrous product remains thermally stable up to 195 °C after which it undergoes several decomposition processes to provide CuO as the final residue at temperatures above 500 °C.

In order to assess the adsorption properties of compound 1, a sample was activated in vacuum at 55 °C for 6 h. The outgassed sample undergoes a mass loss of 10.4% (corresponding to all crystallization water molecules), and shows a moderate adsorption of 0.38 mmol CO_2/g (Fig. S5) in agreement with its low pore volume percentage. The calculated volume of the pores is 271 Å³ (16% of the unit cell) with a diameter between 2.1 and 3.7 Å and a pore volume of 0.11 cm³/g [40].

Plot showing the thermal evolution of the magnetic molar susceptibility and the $\chi_{\text{M}}T$ product is depicted in Fig. 5. The room

temperature $\chi_{\text{M}}T$ value (1.38 cm³mol⁻¹K) is lower than that expected for four uncoupled Cu(II) ions (1.50 cm³ mol⁻¹K, considering a $g = 2.00$) and decreases rapidly up to 70 K, reaching a plateau with a value of 0.90 cm³ mol⁻¹K. Below 30 K, the curve decreases again to 0.52 cm³ mol⁻¹K at 2 K. The magnetic behavior of this compound is dominated by the presence of two magnetic exchange pathways, one resulting from the four Cu1–Nx3–Cx4–Nx9–Cu1ⁱ bridges in the dimeric nucleus (J) and the other from the adeninato bridges that join the dimeric entity and four adjacent monomeric entities (Cu1–N29ⁱ–C28ⁱ–N27ⁱ–Cu2ⁱ). We have to take into account that the distances between the monomeric and the dimeric copper entities Cu1–Cu2 is substantially longer in comparison with the intradimeric distance (5.755/5.924 vs 2.956 Å). Additionally, it has been previously reported that the longer imidazolic pathway involves a very weak antiferromagnetic coupling in comparison with the one involving the dimeric core [8,12,21]. As far as we know, there is no magnetic model that could account for the complex magnetic coupling scheme present in this coordination polymer. Therefore, dismissing the weaker magnetic interaction, the susceptibility data have been adjusted using the Bleaney-Bowers equation [41] $H = -JS_1S_2$ modified to take into account the presence of a dimeric entity and two copper monomer entities per formula. The fitting was made with the data above 30 K, obtaining values of $J = -267 \text{ cm}^{-1}$ and $g = 2.13$. These values are in the range found for compounds containing paddle-wheel $[\text{Cu}_2\text{L}_4\text{X}_2]$ entities (L = bridged $\kappa\text{N3}:\kappa\text{N9}$ -coordinated purine derivatives, X = Cl⁻, Br⁻, H₂O) [35] which show J values from -210 to -320 cm^{-1} and the coupling is slightly weaker than that observed for the three-dimensional compound $\{[\text{Cu}_2(\mu\text{-ade})_4(\text{H}_2\text{O})_2] \cdot 2[\text{Cu}(\text{ox})(\text{H}_2\text{O})] \cdot \sim 14\text{H}_2\text{O}\}_n$ ($J = -316 \text{ cm}^{-1}$).²¹ The further decrease of the $\chi_{\text{M}}T$ value upon cooling below 30 K indicates the weaker but also antiferromagnetic nature of the magnetic exchange between the dimeric (Cu1) and monomeric (Cu2) entities through the imidazole ring of the adeninato ligands.

4. Conclusions

In this paper we have prepared and structurally characterized the first coordination polymer where the theophylline alkaloid coexists with a purine nucleobase, the adenine. This biomolecule exhibits a tridentate $\mu_3\text{-}\kappa\text{N3}:\kappa\text{N7}:\kappa\text{N9}$ coordination mode which join together dimeric and monomeric copper(II) entities, to give rise a one-dimensional rhomboid chain. As a consequence of the water strong hydrogen bonding capacity, there are no direct supramolecular interactions between biomolecules belonging to adjacent chains that could direct the crystal structure into a 3D dimensional porous architecture as we have achieved for some other related nucleobase based coordination systems [14,23]. However, the rigidity and irregular shape of the coordination polymer hinders their packing and allows the presence of a significant portion of the total cell volume unit only occupied by solvent molecules. Upon removal of these molecules, the voids are able to adsorb 0.38 mmol CO_2/g of compound at 273 K.

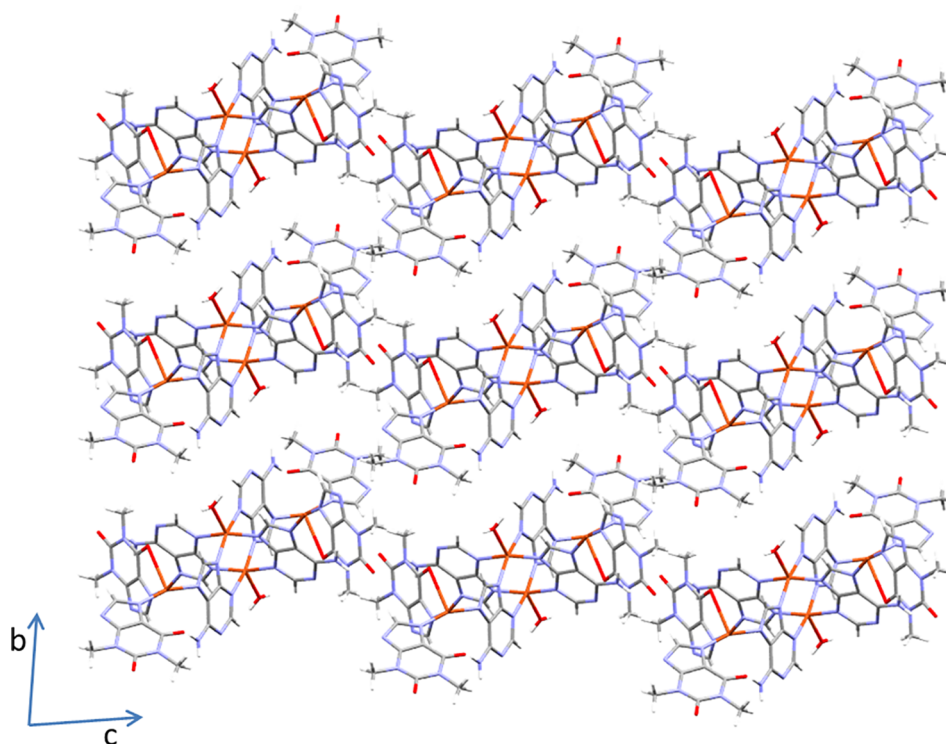


Fig. 4. Projection in the *bc* plane of the crystal packing of compound 1 showing the voids between the polymeric chains.

Table 3
Thermoanalytic data for compound 1.^a

Step	T _i	T _f	Δm(%)	ΣΔm(%)	ΣΔm(%) _{theo}
1	25	150	12.35	12.35	12.53 (– 12 H ₂ O)
2	195	335	9.07	21.42	22.28 (– C ₇ H ₇ N ₄ O ₂)
3	335	400	4.65	26.07	25.88 (– 4 NH ₂)
4	400	500	55.94	82.01	82.02 (CuO as residue)

^a T_i = initial temperature; T_f = final temperature; Δm(%) = mass loss percentage for each process; ΣΔm(%) = total mass loss percentage; ΣΔm(%)_{theo} = theoretical total mass loss percentage.

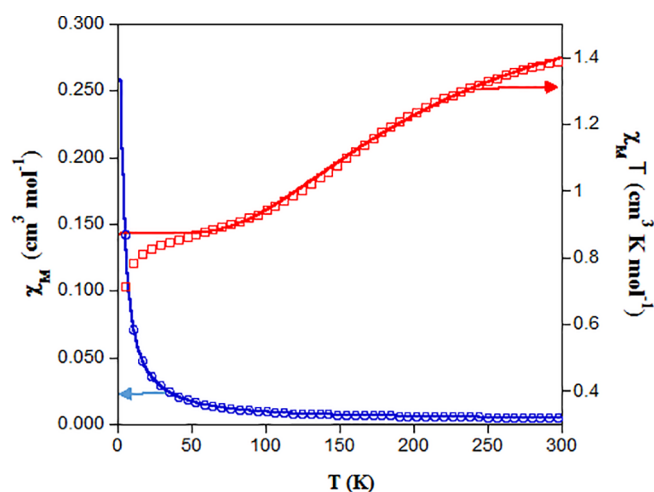


Fig. 5. χ_M (circles) and $\chi_M T$ (squares) curves for compound 1 (continuous lines indicate the fit of the experimental data).

Acknowledgments

This work was funded by the Ministerio de Economía y Competitividad (MAT2016-75883-C2-1-P) and Universidad del País

Vasco/Euskal Herriko Unibertsitatea (PPG17/37, FPI 17/051, predoctoral fellowship for J.P.C.). The authors thank for technical and human support provided by SGIker of UPV/EHU and European Funding (ERDF and ESF).

Appendix A. Supplementary data

Supplementary data to this article can be found online at <https://doi.org/10.1016/j.ica.2018.09.039>.

References

- [1] H.C. Zhou, S. Kitagawa, *Chem. Soc. Rev.* 43 (2014) 5415–5418 and all articles of this special issue.
- [2] J. Thomas-Gipson, G. Beobide, O. Castillo, M. Fröba, F. Hoffmann, A. Luque, S. Pérez-Yáñez, P. Román, *Cryst. Growth Des.* 14 (2014) 4019–4029.
- [3] B. Lippert, J. Müller, *Inorg. Chim. Acta* 452 (2016) 1–2 and all articles of this special issue.
- [4] S. Verma, A. Kumar Mishra, J. Kumar, *Acc. Chem. Res.* 43 (2010) 79–91.
- [5] S.L. Anderson, K.C. Stylianou, *Coord. Chem. Rev.* 349 (2017) 102–128.
- [6] J. Thomas-Gipson, G. Beobide, O. Castillo, A. Luque, J. Pascual-Colino, S. Pérez-Yáñez, P. Román, *CrystEngComm* 20 (2018) 2528–2539.
- [7] G. Beobide, O. Castillo, J. Cepeda, A. Luque, S. Pérez-Yáñez, P. Román, J. Thomas-Gipson, *Coord. Chem. Rev.* 257 (2013) 2716–2736.
- [8] S. Pérez-Yáñez, G. Beobide, O. Castillo, J. Cepeda, A. Luque, A.T. Aguayo, P. Román, *Inorg. Chem.* 50 (2011) 5330–5332.
- [9] R. Gil-García, M. Ugalde, N. Busto, H.J. Lozano, J.M. Leal, B. Perez, G. Madariaga, M. Insausti, L. Lezama, R. Sanz, L.M. Gómez-Sainz, B. García, J. García-Tojal, *Dalton Trans.* 45 (2016) 18704–18718.
- [10] R. Pérez-Aguirre, G. Beobide, O. Castillo, I. de Pedro, S. Pérez-Yáñez, *Inorg. Chim. Acta* 452 (2016) 222–228.
- [11] D.K. Patel, A. Domínguez-Martín, M.P. Brandi-Blanco, D. Choquesillo-Lazarte, V.M. Nurchi, J. Niclós-Gutiérrez, *Coord. Chem. Rev.* 256 (2012) 193–211.
- [12] S. Pérez-Yáñez, G. Beobide, O. Castillo, J. Cepeda, A. Luque, P. Román, *Cryst. Growth Des.* 12 (2012) 3324–3334.
- [13] J.M. González-Pérez, C. Alarcón-Payer, A. Castiñeiras, T. Pivetta, L. Lezama, D. Choquesillo-Lazarte, G. Crisponi, J. Niclós-Gutiérrez, *Inorg. Chem.* 45 (2006) 877–882.
- [14] J. Thomas-Gipson, R. Pérez-Aguirre, G. Beobide, O. Castillo, A. Luque, S. Pérez-Yáñez, P. Román, *Cryst. Growth Des.* 15 (2015) 975–983.
- [15] H.-F. Ma, Q.-Y. Liu, Y.-L. Wang, S.-G. Yin, *Inorg. Chem.* 56 (2017) 2919–2925.
- [16] M. Zhang, W. Lu, J.-R. Li, M. Bosch, Y.-P. Chen, T.-F. Liu, Y. Liua, H.-C. Zhou, *Inorg. Chem. Front.* 1 (2014) 159–162.
- [17] H. Cai, M. Li, X.-R. Lin, W. Chen, G.-H. Chen, X.-C. Huang, D. Li, *Angew. Chem.* 127

- (2015) 10600–10605.
- [18] J. An, S.J. Geib, N.L. Rosi, *J. Am. Chem. Soc.* 132 (2010) 38–39.
- [19] H.-R. Fuand, J. Zhang, *Chem. Eur. J.* 21 (2015) 5700–5703.
- [20] E.A. Giles-Mazón, I. Germán-Ramos, F. Romero-Romero, E. Reinheimer, R.A. Toscano, N. Lopez, C.E. Barrera-Díaz, V. Varela-Guerrero, M.F. Ballesteros-Rivas, *Inorg. Chim. Acta* 469 (2018) 306–311.
- [21] J.P. García-Terán, O. Castillo, A. Luque, U. García-Couceiro, P. Román, L. Lezama, *Inorg. Chem.* 43 (2004) 4549–4551.
- [22] Information, A. P. M. U.S. National Library of Medicine, MedlinePlus <https://medlineplus.gov/spanish/druginfo/meds/a681006-es.html>.
- [23] J. Pascual-Colino, G. Beobide, O. Castillo, I. da Silva, A. Luque, S. Pérez-Yáñez, *Cryst. Growth Des.* 18 (2018) 3465–3476.
- [24] C.F. Macrae, P.R. Edgington, P. McCabe, E. Pidcock, G.P. Shields, R. Taylor, M. Towler, J. van de Streek, *J. Appl. Cryst.* 39 (2006) 453–457.
- [25] Agilent, CrysAlisPro, Agilent Technologies Ltd, Yarnton, Oxfordshire, England, 2014.
- [26] A. Altomare, G. Cascarano, C. Giacovazzo, A. Guagliardi, M.C. Burla, G. Polidori, *M.C. Appl. Cryst.* 27 (1994) 435–436.
- [27] G.M. Sheldrick, *Acta Crystallogr. A* 64 (2008) 112–122.
- [28] L.J. Farrugia, *J. Appl. Cryst.* 45 (2012) 849–854.
- [29] P. Van der Sluis, A.L. Spek, *Acta Crystallogr. A* 46 (1990) 194–201.
- [30] A.L. Spek, *Acta Crystallogr. D* 65 (2009) 148–155.
- [31] P.S. Nugent, V.L. Rhodus, T. Pham, K. Forrest, L. Wojtas, B. Space, M.J. Zaworotko, *J. Am. Chem. Soc.* 135 (2013) 10950–10953.
- [32] G. Beobide, O. Castillo, A. Luque, S. Pérez-Yáñez, *CrystEngComm* 17 (2015) 3051–3059.
- [33] E. Sletten, *Acta Crystallogr. B* 25 (1969) 1480–1491.
- [34] E. Sletten, *Acta Crystallogr. B* 26 (1970) 1609–1614.
- [35] J. Cepeda, O. Castillo, J.P. García-Terán, A. Luque, S. Pérez-Yáñez, P. Román, *Eur. J. Inorg. Chem.* 48 (2009) 2344–2353.
- [36] W.-K. Li, G.-D. Zhou, T.C.W. Mak, In: *Advanced Structural Inorganic Chemistry*, Oxford University Press, Oxford, 2008, p. 139.
- [37] C.R. Groom, I.J. Bruno, M.P. Lightfoot, S.C. Word, *Acta Crystallogr. B* 72 (2016) 171–179.
- [38] D. Cozak, A. Mardhy, M.J. Olivier, A.L. Beauchamp, *Inorg. Chem.* 25 (1986) 2600–2606.
- [39] D.J. Szalda, T.J. Kistenmacher, L. Marzilli, *J. Am. Chem. Soc.* 98 (1976) 8371–8377.
- [40] C. Herdes, L. Sarkisov, *Lagmuir* 25 (2009) 5352–5359.
- [41] B. Bleaney, K.D. Bowers, *Proc. R. Soc. Lond. A. Math. Phys. Sci.* 214 (1952) 451–465.



Adenine nucleobase directed supramolecular architectures based on ferrimagnetic heptanuclear copper(II) entities and benzenecarboxylate anions

Jon Pascual-Colino^a, Garikoitz Beobide^a, Oscar Castillo^{a,*}, Peter Lodewyckx^c, Antonio Luque^a, Sonia Pérez-Yáñez^b, Pascual Román^a, Leticia F. Velasco^c

^a Departamento de Química Inorgánica, Facultad de Ciencia y Tecnología, Universidad del País Vasco, UPV/EHU, Apartado 644, 48080 Bilbao, Spain

^b Departamento de Química Inorgánica, Facultad de Farmacia, Universidad del País Vasco, UPV/EHU, 01006 Vitoria-Gasteiz, Spain

^c Department of Chemistry, Royal Military Academy, Renaissanceaan 30, 1000 Brussels, Belgium

ARTICLE INFO

Keywords:

π -Stacking
Adenine
SMOFs
Heptanuclear
Water uptake
Crystal-structure

ABSTRACT

Two planar organic anions, benzoate and benzene-1,4-dicarboxylate (terephthalate), have been selected as potential π -stacking intercalators among ferrimagnetic $[\text{Cu}_7(\mu\text{-adeninato})_6(\mu_3\text{-OH})_6(\mu\text{-H}_2\text{O})_6]^{2+}$ heptameric discrete entities. The resulting supramolecular architecture is highly dependent on the negative charge density distribution, mainly located in the carboxylate groups of the organic anions. In this sense, the benzoate anion, with just one carboxylate group, does not allow its intercalation between the adeninato ligands as it would imply a high steric hindrance among the heptameric entities. As a consequence, these benzoate anions are located inside the voids of the crystal structure reducing the accessible volume of compound $[\text{Cu}_7(\mu\text{-adeninato})_6(\mu_3\text{-OH})_6(\mu\text{-H}_2\text{O})_6](\text{benzoate})_2 \cdot 17\text{H}_2\text{O}$ (**1**). On the contrary, the terephthalate anion, containing two carboxylate groups at opposite sites, adopts a π -stacking sandwich arrangement between two adeninato ligands that affords the porous open structure of formula $[\text{Cu}_7(\mu\text{-adeninato})_6(\mu_3\text{-OH})_6(\mu\text{-H}_2\text{O})_6](\text{terephthalate}) \cdot n\text{H}_2\text{O}$ (**2a**, **2b**; n : 12 and 24, respectively). In addition to that, the less directional nature of the π -stacking interactions in comparison to the complementary hydrogen bonding based supramolecular metal-organic frameworks (SMOFs), suits them with a flexible architecture able to reversibly adsorb/desorb water (up to a 25–30% at 20 °C) altogether with the expansion/shrinkage of the crystal structure. The bridging adeninato and hydroxido ligands are effective magnetic exchange mediators to provide a $S_T = 5/2$ ferrimagnetic state for the heptanuclear entity.

1. Introduction

Nucleobases are key structure directing agents, as it is well known from the double helix structure of DNA and other biologically relevant systems [1]. Their capacity comes from the rich and diverse combination of hydrogen bond donor and acceptor positions, in many cases close enough to provide complementary hydrogen bonding capability. In this sense, the anchorage of nucleobase to discrete metal-organic entities have been fruitfully employed to build up ordered porous structures known as SMOFs (supramolecular metal-organic frameworks) [2]. SMOFs are compounds that contain potentially accessible voids, in which the 3D crystal building is sustained by supramolecular interactions, mainly hydrogen bonds, as an alternative to the coordination bonds as it happens for the better-known metal-organic frameworks (MOFs) [3].

However, supramolecular recognition capability of the nucleobases does not lie only on these hydrogen-bonding interactions but also on its ability to establish π - π stacking interactions. These latter interactions are less directional than the hydrogen bonds but can play a crucial role on the resulting supramolecular architecture. In fact, calculations on the stability of the DNA indicate that these π - π stacking interactions are crucial to provide stability to the double helix [4].

Therefore, we aimed at getting a deeper insight on the resulting supramolecular assembling coming from the latter interactions. For that purpose, we have selected the rigid and discrete $[\text{Cu}_7(\mu\text{-ade})_6(\mu_3\text{-OH})_6(\mu\text{-H}_2\text{O})_6]^{2+}$ (ade: adeninato) entity in which a central $[\text{Cu}(\text{OH})_6]^{4-}$ core is coordinated to six external copper(II) metal centers which are further bridged by six μ -adeninato- $\kappa\text{N}3:\kappa\text{N}9$ ligands and six semicoordinated bridging water molecules. The cationic nature of these discrete entities provides a rich source for novel compounds just by

* Corresponding author.

E-mail address: oscar.castillo@ehu.eus (O. Castillo).

<https://doi.org/10.1016/j.jinorgbio.2019.110865>

Received 24 July 2019; Received in revised form 27 August 2019; Accepted 15 September 2019

Available online 05 October 2019

0162-0134/ © 2019 Elsevier Inc. All rights reserved.

replacing the counterion, as it has been previously reported when this cationic entity crystallizes with sulphate [5] and nitrate [6] counterions. These inorganic anions lack the capacity to establish π - π stacking interactions. Consequently, the complex entities assembly by means of π - π stacking interactions between the nucleobases and due to their rigidity, the resulting crystal packing exhibits a potentially porous supramolecular structure. However as the counterions are located inside the voids of the structure, the accessible volume is highly reduced. Contrarily, if the counterion can be intercalated within the 3D supramolecular architecture, the pores remain accessible. This approach was achieved employing the planar/aromatic terebrominate anion that gave rise to a flexible porous material, in which the organic anions are sandwiched between the π - π stacking adenines [7]. The structural flexibility taking place in this compound is highly unusual for complementary hydrogen bond sustained porous architectures based on rigid discrete entities [8–11]. The less directional π - π stacking interactions seem to be the source of this behavior as reported for some other π -stacking sustained structures [5].

In this work, we have selected two planar organic anions, benzoate and benzene-1,4-dicarboxylate (terephthalate), in order to analyze the effect of the charge density distribution on the π - π stacking interactions and, as a consequence, on the supramolecular architecture. Indeed, the π - π stacking interaction is usually described as an electrostatic attraction between partial opposite charges located in the interacting molecules [12,13]. In this case, the cationic nature of the discrete heptameric entity imposes a net positive density on the coordinated adeninato ligands (in spite of their formal anionic nature). This fact favours their interactions with the negative charge density of the organic anion, mainly located on the carboxylate groups. Therefore, depending on the presence of two carboxylate groups (terephthalate) or one (benzoate) the organic anion would be able to be sandwiched between π - π stacking adenines or not (Scheme 1). Accordingly, the ligand with just one carboxylate would imply such an approach of the heptameric entities that this option is sterically hindered. As a consequence, the benzoate anions are displaced into the channels reducing the accessible volume. On the contrary, the two carboxylate groups located at opposite sites in the terephthalic anion do not present this steric hindrance and allow a sandwich arrangement of the terephthalic anion between the interacting π - π stacking adenines. This arrangement provides a more open porous supramolecular structure than that

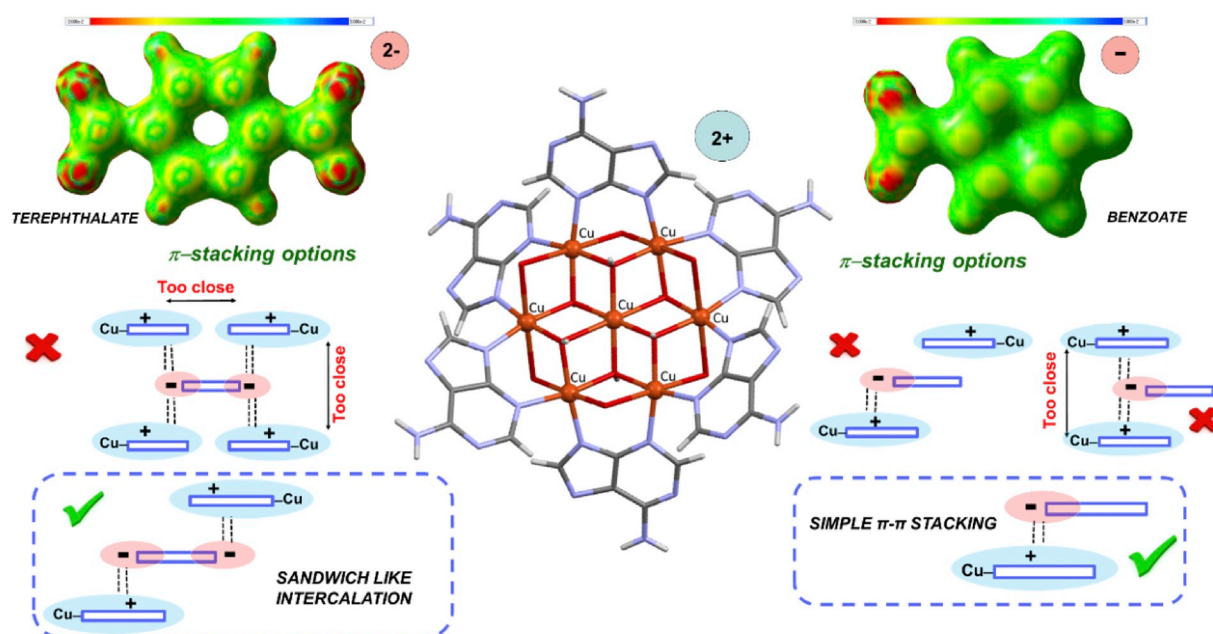
obtained using the benzoate anion, but both of them share the fact that their supramolecular crystal structures are flexible.

Keeping all the above in mind, the reaction between copper(II) nitrate, adenine and benzoic (Hbenz)/terephthalic acid (H₂tereph) gave rise to the compound [Cu₇(μ -ade)₆(μ -OH)₆(μ -H₂O)₆](benz)₂·17H₂O (1) and two phases of formula [Cu₇(μ -ade)₆(μ -OH)₆(μ -H₂O)₆](tereph)_n·nH₂O (2a, 2b; n: 12 and 24, respectively) at different states of hydration. Their crystal structures were elucidated by single-crystal X-ray diffraction, allowing to study the supramolecular interactions that direct the crystal building and the changes taking place during the water adsorption/desorption process. The thermal stability and the magnetic features of these compounds were also analyzed in detail.

2. Experimental

2.1. Physical measurements

Elemental analyses (C, H, N) were performed on a Euro EA elemental analyzer, whereas the metal content was determined by atomic absorption spectrometer (AAS) from Perkin ElmerAnalyzer 100. The IR spectra were recorded on a FTIR 8400S Shimadzu spectrometer in the 4000–400 cm⁻¹ spectral region. Variable-temperature magnetic susceptibility measurements were performed using a standard Quantum Design PPMS magnetometer while cooling from 300 to 2 K at 1 kOe. Magnetization as a function of field (H) was measured using the same magnetometer in the $-50 \leq H/\text{kOe} \leq 50$ at 2 K after cooling the sample in zero field. The susceptibility data were corrected for the diamagnetism estimated from Pascal's Tables [14], the temperature-independent paramagnetism and the magnetization of the sample holder. Dinitrogen (77 K) and carbon dioxide (273 K) physisorption data were recorded on activated samples (vacuum at 30 °C for 6 h) with a Quantachrome Autosorb-iSorb HP1. Water sorption isotherms of the activated samples were carried out at 20 and 35 °C using a gravimetric water sorption analyzer (Aquadyne DVS, Quantachrome Instruments). Thermogravimetric analyses (TG) were performed on a METTLER TOLEDO TGA/SDTA851 thermal analyzer in synthetic air atmosphere (79% N₂/21% O₂) with a heating rate of 5 °C·min⁻¹. Polycrystalline X-ray diffraction data were collected on a PANalytical Xpert PRO diffractometer with Cu – K α radiation ($\lambda = 1.5418 \text{ \AA}$). The measurement conditions have been 40 kV and 40 mA and a sweep between



Scheme 1. Potential supramolecular π - π stacking interactions between the adeninato ligands and the carboxylate anions.

Table 1
Structural parameters (Å, deg) of hydrogen bonding interactions in compound 1.^a

Hydrogen-bonding interactions ^b			
D-H...A	H...A	D...A	D-H...A
N16-H16...N37 ⁱ	2.35	3.05(3)	139
C38-H38...N17 ⁱⁱ	2.57	3.41(2)	149
C28-H28...N21 ⁱⁱⁱ	2.62	3.49(1)	156
O1-H1...O49A	1.66	2.63(2)	175
O1w-H11w...O48A ⁱⁱ	1.75	2.61(2)	167
O3w-H31w...O48A	1.94	2.74(1)	153

^a Symmetry codes: (i) $1/3 + x - y, -2/3 + x, 7/3 - z$; (ii) $2/3 + y, 1/3 - x + y, 7/3 - z$; (iii) $4/3 - x + y, 2/3 - x, -1/3 + z$.

^b D: donor; A: acceptor.

$5 < 2\theta < 70^\circ$.

2.2. X-ray diffraction data collection and structure determination

Single-crystal X-ray diffraction data were collected on an Agilent Technologies Supernova diffractometer with Cu – K α radiation ($\lambda = 1.5418 \text{ \AA}$) at 298(2) K for compound **1** and an Agilent Technologies Supernova diffractometer with graphite monochromated Mo – K α radiation ($\lambda = 0.71073 \text{ \AA}$) at 293(2) K for **2a** and **2b**. Data reduction was done with the CrysAlisPro program [15]. The details of the structure determination and refinement of compounds are summarized in Table S1. Crystal structure coded **2a** was elucidated from a highly twinned specimen.

All the structures were solved by direct methods using the SIR92 program [16] and refined by full-matrix least-squares on F^2 including all reflections (SHELXL97) [17]. All calculations for these structures were performed using the WINGX crystallographic software package [18]. In all cases, some of the adeninato ligands are disordered into two coplanar arrangements with inverted orientation regarding the coordination mode ($\mu\text{-}\kappa\text{N3}:\kappa\text{N9}/\mu\text{-}\kappa\text{N9}:\kappa\text{N3}$) [19–21]. In **1** and **2b** these disordered atoms and crystallization water oxygen atoms have been refined with an isotropic temperature factor while the rest of the non-hydrogen atoms of the structure have been modeled with anisotropic temperature factors. In **2a** due to the low quality of the diffraction data, all the atoms not located in the central $\text{Cu}_7(\text{OH})_6$ inorganic core were kept with isotropic displacement parameters in order to avoid overparametrization. This procedure also allowed a smoother refinement of the crystal structure that otherwise became very unstable. In all compounds after the initial structure solution was completed, the difference Fourier map showed the presence of substantial electron density at the voids of the crystal structure that was impossible to model. Therefore, its contribution was subtracted from the reflection data by the SQUEEZE method [22] as implemented in PLATON [23].

2.3. Syntheses

2.3.1. Synthesis of $[\text{Cu}_7(\mu\text{-ade})_6(\mu_3\text{-OH})_6(\mu\text{-H}_2\text{O})_6](\text{benz})_2 \cdot 17\text{H}_2\text{O}$ (**1**)

0.0489 g (0.2 mmol) of $\text{Cu}(\text{NO}_3)_2 \cdot 3\text{H}_2\text{O}$ dissolved in 10 mL of water were added to 0.0390 g (0.3 mmol) of adenine dissolved in 15 mL of an aqueous methanolic 1:1 hot solution (50 °C). The blue solution was basified to pH ~8.8 with NaOH while the mixture was continuously stirred. The obtained purple solution was added to 0.1221 g of benzoic acid (1.0 mmol) dissolved in 20 mL of warm water basified with NaOH (pH ~8.8). The purple solution was left to evaporate at room temperature and blue single-crystals were obtained after four days. Yield: 60% (based on metal). Anal. Calcd. for $[\text{Cu}_7(\mu\text{-ade})_6(\mu_3\text{-OH})_6(\mu\text{-H}_2\text{O})_6](\text{benz})_2 \cdot 17\text{H}_2\text{O}$, $\text{C}_{44}\text{H}_{86}\text{Cu}_7\text{N}_{30}\text{O}_{33}$ (MW: 2008.15): C 26.32, H 4.31, N 20.92, Cu 22.15; found C 26.10, H 4.35, N 20.97, Cu 22.24%. FTIR (KBr pellets, cm^{-1}): 3465w, 3353vs, 3193w, 2944 s, 1646vs, 1609w, 1468vs, 1384s, 1337 m, 1309s, 1281 m, 1187s, 1150s 1028s, 990 m, 934 m,

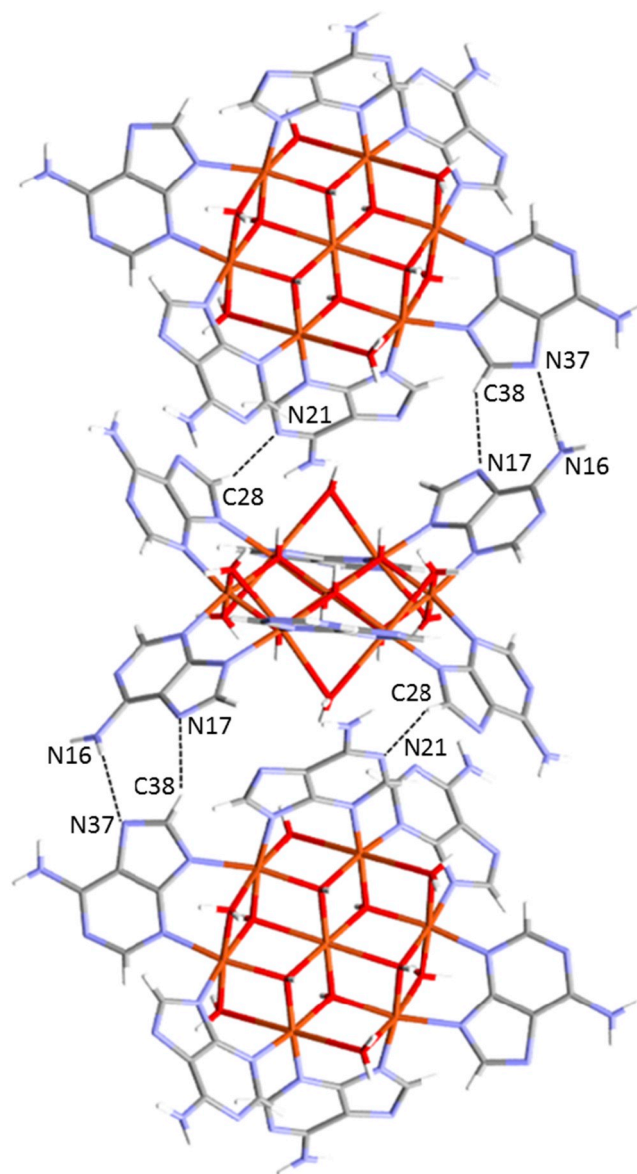


Fig. 1. Hydrogen bonding interactions connecting heptanuclear entities in compound **1**.

803 s, 728 s, 653 s, 568 m, 465 s. The homogeneity and purity of bulk samples of compound **1** were checked by elemental analysis and powder X-ray diffraction data.

2.4. Synthesis of $[\text{Cu}_7(\mu\text{-ade})_6(\mu_3\text{-OH})_6(\mu\text{-H}_2\text{O})_6](\text{tereph}) \cdot 12\text{H}_2\text{O}$ (**2a**) and $[\text{Cu}_7(\mu\text{-ade})_6(\mu_3\text{-OH})_6(\mu\text{-H}_2\text{O})_6](\text{tereph}) \cdot 24\text{H}_2\text{O}$ (**2b**)

Compound **2** was obtained by adding to a 10 mL water solution of 0.0488 g of $\text{Cu}(\text{NO}_3)_2 \cdot 3\text{H}_2\text{O}$ (0.2 mmol), 0.0390 g of adenine (0.3 mmol) dissolved in 15 mL of warm water-methanol mixture (1:1). The resulting solution (pH = 4.0) is basified with NaOH solution to pH ~8.8 and later 0.0997 g of terephthalic acid (0.6 mmol) dissolved in 20 mL of water basified with NaOH at 60 °C is added. In two days a pale blue powder appears corresponding to the formulae $[\text{Cu}_7(\mu\text{-ade})_6(\mu_3\text{-OH})_6(\mu\text{-H}_2\text{O})_6](\text{tereph}) \cdot 12\text{H}_2\text{O}$. Yield 40%. Calcd. for $\text{C}_{38}\text{H}_{70}\text{Cu}_7\text{N}_{30}\text{O}_{28}$ (MW: 1839.97): C 24.80, H 3.83, N 22.84, Cu 24.18; found C 24.72, H 3.78, N 22.76, Cu 24.17%. Main IR features (cm^{-1} ; KBr pellets): 3420 s, 3200 m, 2930 s, 1645vs, 1610s, 1504 m, 1462s, 1400vs, 1308 m, 1192s, 1146s, 933 m, 888w, 742 m, 657 s, 506w.

Blue single-crystals of this compound have been obtained after one

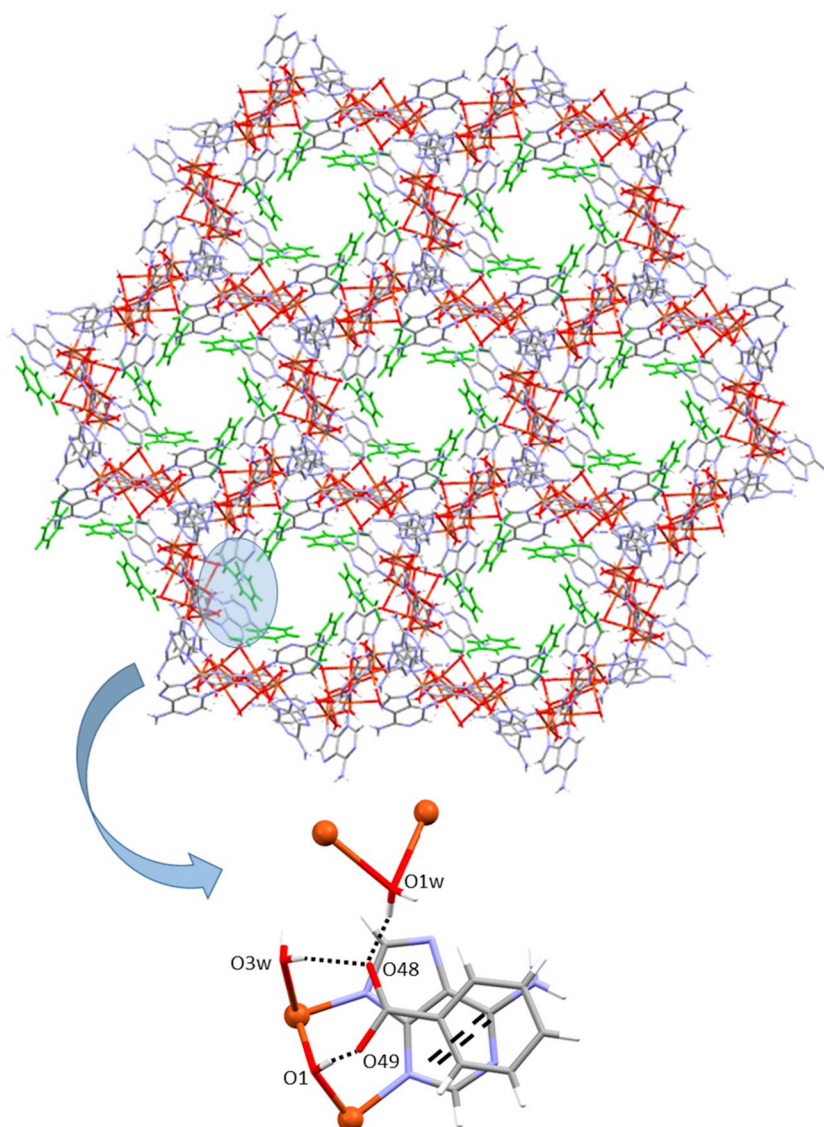


Fig. 2. Arrangement of the organic anions (green colour) and the heptameric complex units in compound 1. Supramolecular benzoate...adeninato interactions are highlighted.

month using test tube diffusion technique in which over the aquo-methanolic solution containing the copper(II) nitrate and adenine mixture, an aqueous solution of the terephthalic acid is layered carefully. Depending on the handling of the crystals: storing them under room conditions (**2a**), or directly picking them from the mother liquid (**2b**) specimens at different hydration stages were achieved.

3. Results and discussion

All the compounds described below contain, in addition to the corresponding organic anion, a cationic wheel-shaped $[\text{Cu}_7(\mu\text{-ade})_6(\mu_3\text{-OH})_6(\mu\text{-H}_2\text{O})_6]^{2+}$ entity in which a central $[\text{Cu}(\text{OH})_6]^{4-}$ core is connected to six outer copper(II) metal centers through μ_3 -hydroxido bridges in a radial and planar arrangement. The external copper atoms are doubly bridged by water molecules and peripheral adeninato ligands which exhibit a bidentate $\mu\text{-}\kappa\text{N}3:\kappa\text{N}9$ coordination mode. All the metal centers present an octahedral geometry with the usual Jahn-Teller tetragonal elongation (Tables S2–S4 of Supplementary information), which is more pronounced for the external copper(II) atoms than for the inner one because of the rigidity of the heptanuclear entity. The elongation of the external copper atoms is located along the water-

metal-hydroxide direction, in such a way the coordinated water molecules, weakly held, have longer coordination bonds than the adeninato ligands. Less pronounced differences are also observed in the central Cu–OH bonds depending whether they are involved in the Jahn-Teller elongation direction or not.

Although the heptameric entity is analogous to that present in the previously reported $[\text{Cu}_7(\mu\text{-ade})_6(\mu_3\text{-OH})_6(\mu\text{-H}_2\text{O})_6](\text{theo})_2 \cdot 28\text{H}_2\text{O}$ [7] (theo: anionic form of the theobromine alkaloid) and $[\text{Cu}_7(\mu\text{-ade})_6(\mu_3\text{-OH})_6(\mu\text{-H}_2\text{O})_6](\text{NH}_4)_2(\text{SO}_4)_2 \cdot n\text{H}_2\text{O}$ compounds [5], the crystal packing and the thermal stability of each compound show substantial differences owing to the molecular features of the selected counterions which lead to different patterns of supramolecular interactions. The crystal building of these previously reported compounds is maintained by a combination of supramolecular $\pi\text{-}\pi$ stacking and hydrogen bonding interactions in addition to the electrostatic forces taking place between the charged entities. In the sulphate containing compounds, the arrangement of the heptameric entities generates voids where sulphate and triethylammonium counterions are sited, together with the crystallization water molecules. The thermal release of these water molecules collapses the crystal building and the compounds lose their crystallinity during the dehydration process. In the theobrominato

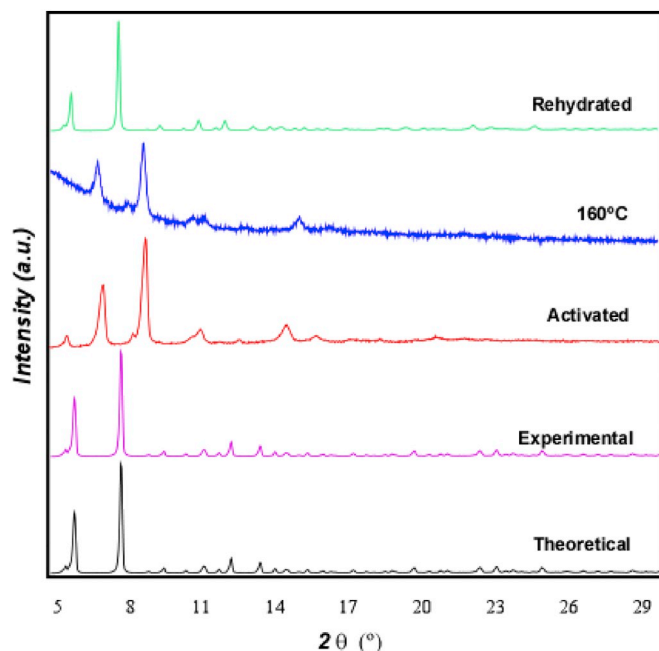


Fig. 3. Powder X-ray diffraction patterns of samples of compound 1.

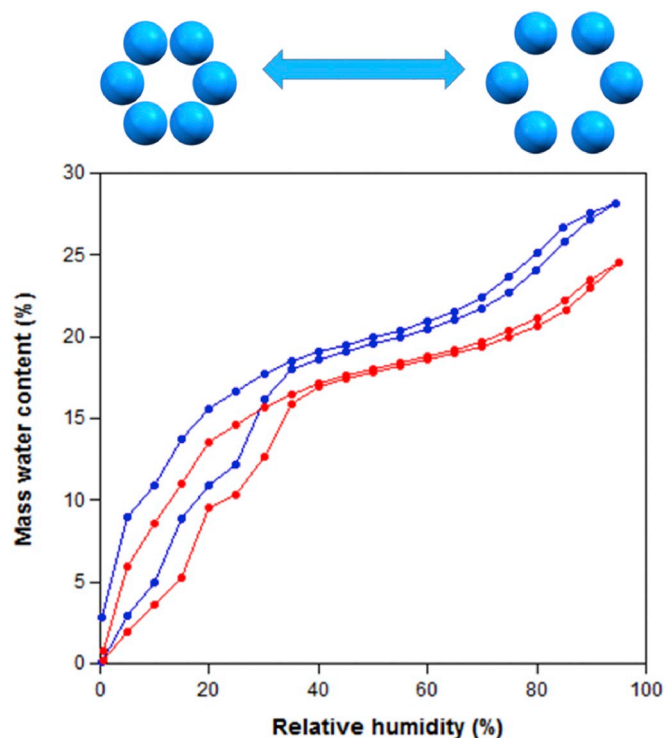


Fig. 4. Water vapour adsorption/desorption isotherms for compound 1 at 20 °C (blue) and 35 °C (red). Schematic representation of the bottle-neck reversible shrinkage in which the spheres depict the six heptameric units that shrink the pore (top).

compound alkaloid...alkaloid pairs are inserted between the adeninato ligands of the heptameric units to give a ...A...T...T...A... (A: adeninato, T: theobrominato) sequence of supramolecular $\pi-\pi$ interactions which leads to an open-framework with voids representing 37% of the unit cell. Those additional $\pi-\pi$ interactions seem to increase the strength of the crystal building as the compound retains its crystallinity up to 300 °C. However, the plasticity of the supramolecular interactions causes a reversible contraction of the porous system after its outgassing,

Table 2

Structural parameters (Å, deg) of hydrogen bonding interactions in compound 2a.^a

D-H...A ^b	H...A	D...A	D-H...A
N16-H16B...N31	2.47	3.25(6)	151
N56-H56B...N21 ⁱ	2.70	3.53(5)	159
C42-H42...N37 ⁱⁱ	2.58	3.32(4)	138
C48-H48...N67 ⁱⁱⁱ	2.60	3.36(5)	139
O5w-H51w...N66 ⁱⁱⁱ	2.09	2.85(5)	149
O1-H1...O771 ^{iv}	1.94	2.90(3)	168
O4-H4...O781	1.92	2.86(3)	161
O1w-H12w...O772 ^v	1.80	2.71(4)	161
O2w-H22w...O771 ^{iv}	2.55	3.43(4)	160
N66-H66B...O782 ⁱ	2.12	2.96(4)	166

^a Symmetry codes: (i) $x, -1 + y, z$; (ii) $-1 + x, -1 + y, z$; (iii) $-x, 1 - y, -z$; (iv) $x, 1 + y, z$; (v) $1 - x, 1 - y, 1 - z$.

^b D: donor; A: acceptor.

which precludes the adsorption of gas molecules, but allows a complete reversal to the initial open structure upon exposure to a water-saturated atmosphere.

3.1. Compound $[\text{Cu}_7(\mu\text{-ade})_6(\mu_3\text{-OH})_6(\mu\text{-H}_2\text{O})_6](\text{benz})_2 \cdot 17\text{H}_2\text{O}$ (1)

According to our expectations the planar benzoate anions establish $\pi-\pi$ stacking interactions with some of the coordinated adeninato ligands. However, as previously described (Scheme 1), the charge distribution does not allow a propagation of this interaction as the approach of a second adeninato ligand from an adjacent heptameric entity is sterically hindered, and sandwich arrangement of the benzoate anion between two adeninato ligands is not observed. As a consequence, the 3D supramolecular architecture of compound 1 differs greatly from the previously reported theobrominato analogous. In fact, there are not additional $\pi-\pi$ stacking interactions among the adeninato ligands and, instead of that, they are assembled together through quite unusual complementary hydrogen bonds (Table 1). Four of the adeninato ligands of each heptameric entity form a hydrogen bonded $\text{R}_2^2(8)$ ring involving the Hooqsteen face of a nucleobase moiety (exocyclic N16 amino group, imidazolic N17 site) and the imidazolic N37 and C38 atoms of an adeninato ligand belonging to an adjacent heptameric entity (Fig. 1). These connections between heptameric units are reinforced with an additional hydrogen bond involving the imidazolic C28-H28 group and the pyrimidinic N21 site of two adjacent heptameric units.

Considering the above described supramolecular interactions, the 3D arrangement of the complex units can be topologically described as a uninodal 4-connected **nbo**-net, in which the nodes are ascribed to the heptameric units and the linkers correspond to the above described hydrogen bonding interactions [24,25]. This topology, based on the niobium oxide structure, can be also found in one of the first reported bioMOFs in which each paddle-wheel dimeric $[\text{Cu}_2(\mu\text{-adeninato})_4]$ unit is linked to four equivalent ones by means of $[\text{Cu}(\text{oxalate})(\text{H}_2\text{O})]$ entities leading to a porous coordination polymer [26].

The three dimensional packing in compound 1 allows the occurrence of channels that are partially occupied by the benzoate anions (Fig. 2) whose phenyl rings are parallel stacked with respect to an adeninato ligand (interplanar distance of 3.60 Å, lateral offset of 1.34 Å). This interaction is reinforced by the presence of hydrogen bonds between the benzoate carboxylate group as acceptor, and one hydroxide group and two coordinated water molecules of neighbouring heptameric units as donors.

However, the benzoate anions do not completely occlude the channels that run along the crystallographic [001] direction. They present a quite irregular shape with ovoid holes of a maximum radius of 6 Å (surrounded by the exocyclic N-site of the adeninato ligands) connected through tube-shaped corridors with an approximate radius of 3 Å on whose walls are located the phenyl rings of the benzoate anions

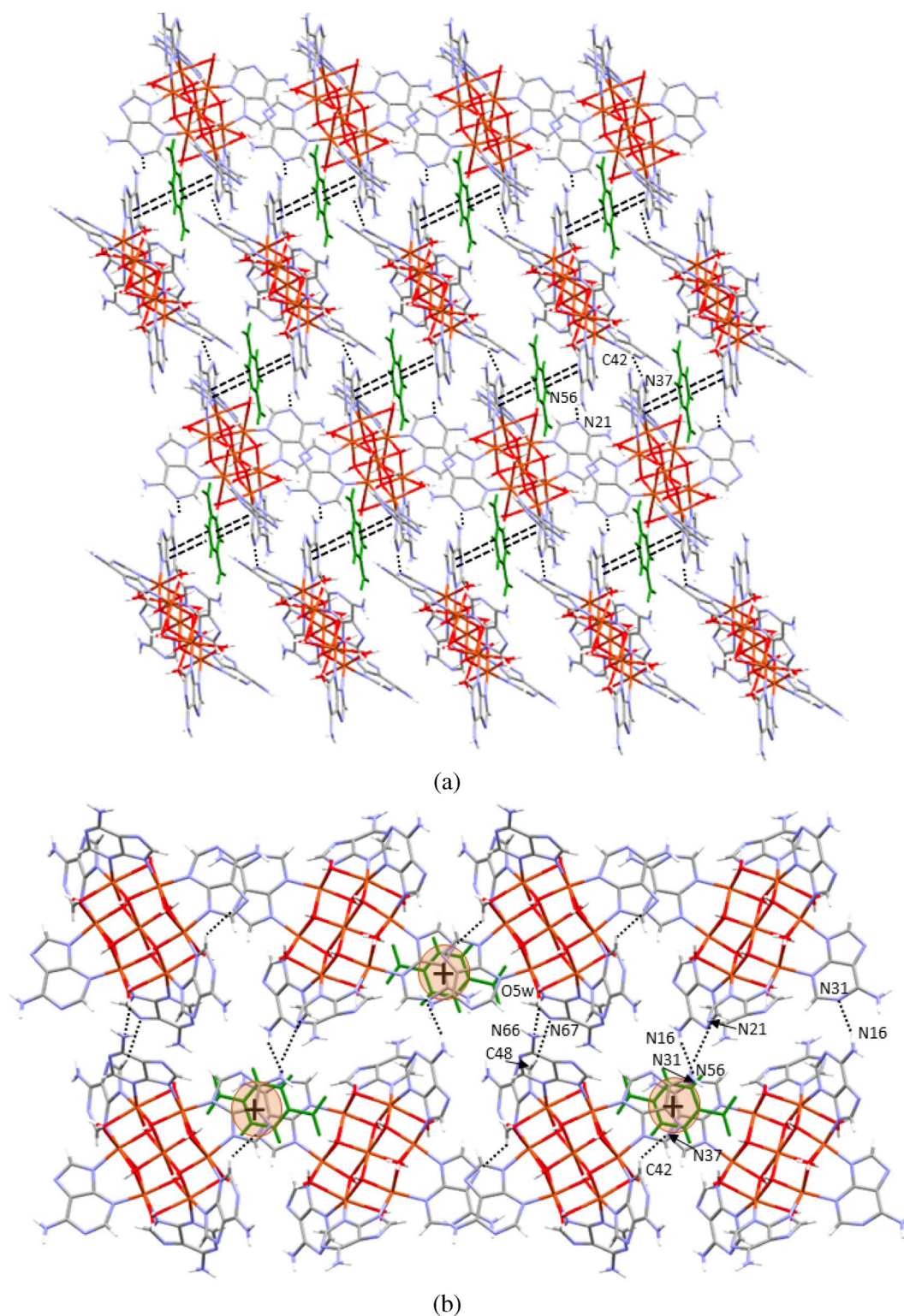
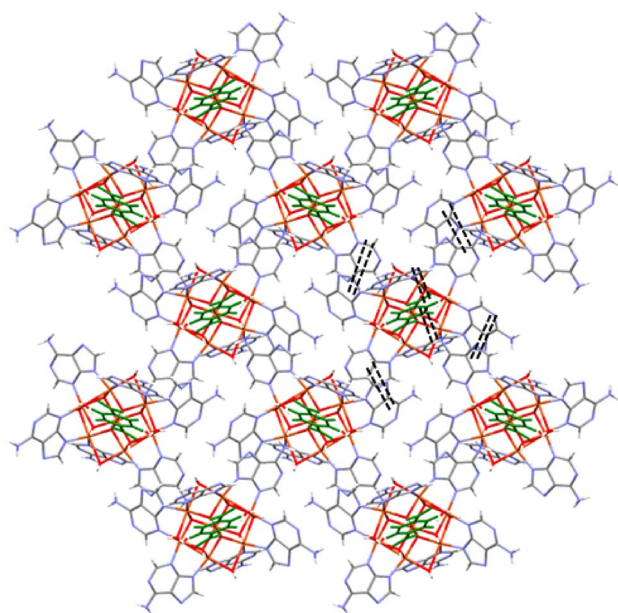


Fig. 5. (a) Crystal packing of compound 2a along the crystallographic *b*-axis (hydrogen bond: dotted lines; π - π interaction: double dashed lines) and (b) supramolecular interactions connecting the structural entities (π - π interaction: + symbol).

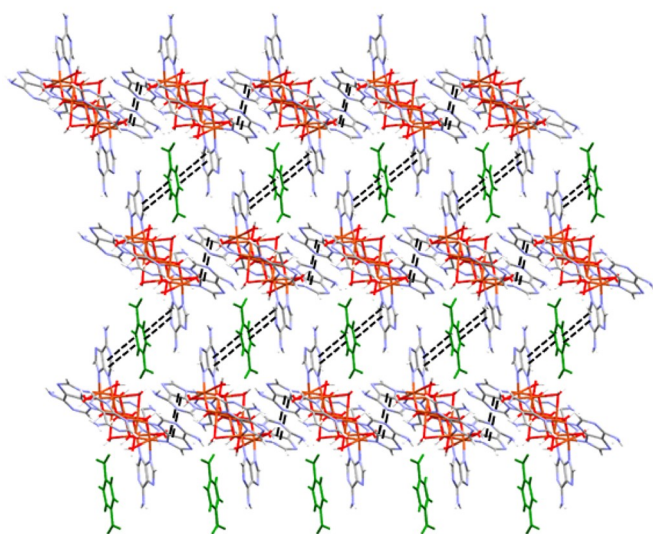
(Fig. 2). The volume of these channels, occupied by the crystallization water molecules, is 5098 \AA^3 (29% of the total volume of the unit cell as calculated by PLATON). A computational analysis reveals an accessible surface area value of $205 \text{ m}^2/\text{g}$ and a pore volume of 0.20 mL/g .

The thermogravimetric (Table S5, Fig. S1) and variable-temperature X-ray powder diffraction data of compound 1 (Fig. S2) indicate that under heating it retains the crystallinity but shows a significant

structural change after the removal of crystallization (*ca.* 85°C) and coordination (*ca.* 160°C) water molecules. The shift of diffraction peaks toward higher 2θ angles and the indexation of the variable-temperature X-ray powder diffraction patterns (Figs. S3–S4, Table S6) show a marked and progressive decrease of the unit cell volume from $17,812 \text{ \AA}^3$ for the pristine compound to $13,064 \text{ \AA}^3$ at 85°C (loss of the crystallization water molecules). This unit cell shrinkage implies a 93%



(a)



(b)

Fig. 6. (a) Layer of heptameric entities in the *bc*-plane of compound **2b**. (b) View along the crystallographic *b*-axis showing the insertion of the organic anion (green colour). Dashed lines represent the π - π interactions connecting the structural entities.

of the void volume present in the pristine sample (5098 \AA^3). The loss of coordination water molecules up to 160°C only implies an additional decrease of 353 \AA^3 . Accordingly to this sharp void volume reduction, compound **1** is not able to adsorb either N_2 at 77 K or CO_2 at 273 K . During the outgassing procedure (by vacuuming at 30°C for 6 h) the colour of compound **1** changes from blue to deep dark green. It undergoes a weight loss mass of 21.0% which fits the expected value for the removal of both crystallization and coordination water molecules (20.6%). The X-ray diffraction pattern of this activated sample (Fig. 3) is equal to that corresponding to the compound heated at 160°C .

As previously stated, the dehydration process implies the shrinkage of the pores but the crystal structure is flexible enough to allow the total rehydration of the sample upon exposure to a water-saturated atmosphere for 24 h to recover the original open crystal structure. This

Table 3

Structural parameters (\AA , deg) of hydrogen bonding interactions in compound **2b**.^a

D-H...A ^b	H...A	D...A	D-H...A
O1-H1...N36 ⁱ	1.87	2.85(2)	175
O2-H2...O471	1.65	2.61(2)	164
O3-H3...O4w	1.85	2.82(2)	174
O1w-H11w...O9w ⁱⁱ	1.90	2.74(2)	165
O1w-H12w...O472 ⁱⁱⁱ	1.93	2.77(2)	162
N16A-H16A...O9w ^{iv}	1.97	2.81(3)	171
O2w-H21w...N31 ⁱ	1.98	2.80(2)	158
O2w-H22w...O6w	1.96	2.84(2)	170
N26B-H26C...O11w ^v	2.05	2.89(4)	165
O3w-H32w...O471	2.20	3.02(2)	162
N36-H36B...O4w ⁱⁱ	2.43	3.19(2)	137
C32-H32...O9w ⁱⁱ	2.50	3.40(2)	163

^a Symmetry codes: (i) $1-x, 1/2+y, 1/2-z$; (ii) $1-x, -1/2+y, 1/2-z$; (iii) $1-x, -y, 1-z$; (iv) $x, -1/2-y, 1/2+z$; (v) $-1+x, 1/2-y, -1/2+z$.

^b D: donor; A: acceptor.

behavior is in good agreement with the water vapour adsorption/desorption curves shown in Fig. 4.

The adsorption/desorption isotherms at 20 and 35°C of compound **1** show some unusual features such as the presence of three different segments on the adsorption curve: a) a relative increase at low humidity values (0 – 40%) which corresponds to the adsorption of a water mass content of 19% ; b) an apparent plateau at intermediate humidity values (40 – 60%) with a small increase on the water intake up to 21% and c) a steeper final segment in which water adsorption rapidly increases again with a maximum water uptake of 28% at a relative humidity value of 95% . In addition to that, the desorption curve shows a thin hysteresis at humidity values above 40% that widens noticeably at lower humidity values. These features have been attributed to the flexible nature of the supramolecular architecture. At low humidity values, the pores are essentially collapsed prone to “bottle-neck” like structure for which wide hysteresis curves are expected. However, as the humidity increases and more water molecules are incorporated into the channels widening them, as a consequence, the “bottle-neck” effect disappears and a thinner hysteresis loop is achieved.

The measurement has been also performed at 35°C showing essentially the same features but with a lower amount of water being adsorbed, as expected for a temperature increase. However, it allows, by comparison with the data obtained at 20°C , to determine the apparent isosteric adsorption heats (Fig. S5). The values, calculated through Clausius-Clapeyron equation [27], at low coverage value (ca. $68 \text{ kJ}\cdot\text{mol}^{-1}$) compare well with other reported values for MOFs [28–30]. It is important to have in mind that due to the flexible nature of the crystal structure the obtained value does not only reflect the adsorption enthalpy value but also the contribution coming from the structural change that water adsorption implies (apparently of endothermic nature). Therefore, the real isosteric adsorption heat would be probably greater. Many works have pointed out that the presence of strongly polar groups on the surface of the voids help improving the adsorbate-substrate interaction. In this sense, the terephthalate carboxylate groups, the amino group of the adeninato and the hydroxido ligand of this compound point out in this way. This phenomenon has been also reported for other flexible porous materials [31].

3.2. Compounds $[\text{Cu}_7(\mu\text{-ade})_6(\mu_3\text{-OH})_6(\mu\text{-H}_2\text{O})_6](\text{tereph})\cdot n\text{H}_2\text{O}$ (**2a**, **2b**)

The asymmetric unit of compound **2a**, at this stage of hydration, consists of two half centrosymmetric heptameric cations, one terephthalate dianion and twelve crystallization water molecules (Table S7, Fig. S6). The ditopic charge distribution of the terephthalate anion allows its insertion between two adeninato ligands with an interplanar

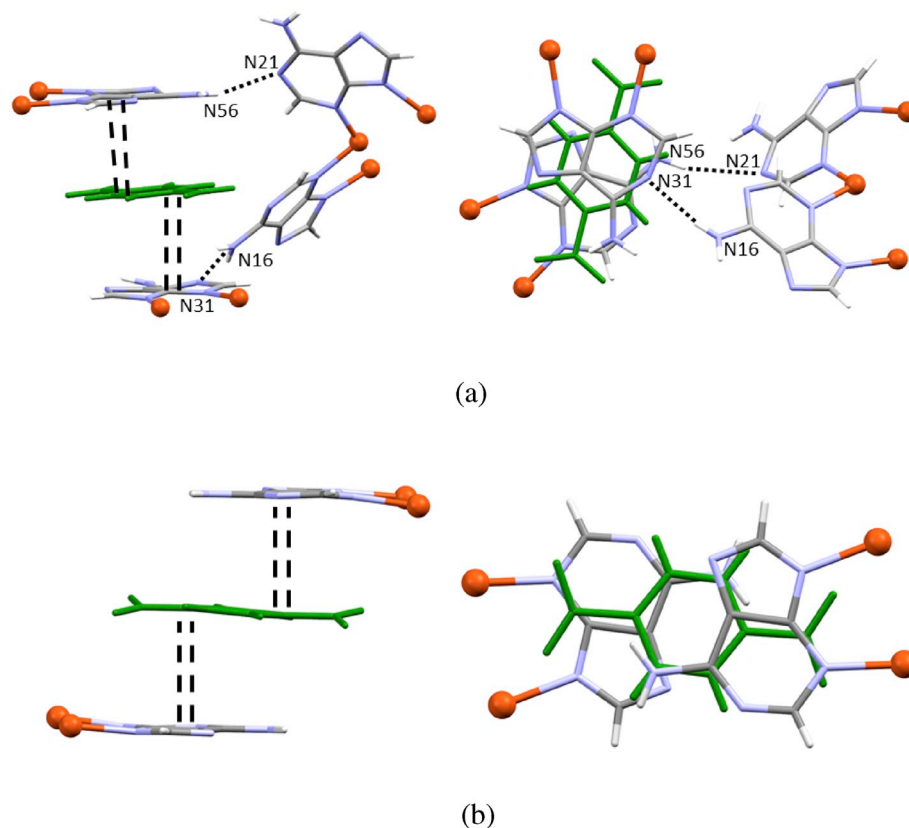


Fig. 7. Arrangement of the terephthalate anion between the adeninato ligands in **2a** (a) and in **2b** (b). Dotted lines indicate hydrogen bonds and double dashed lines represent π - π interactions.

distance of 3.50 Å. Interestingly, the carboxylate groups do not lie just above the adenine aromatic rings but over the adenine chelating ring with the metal centers where the positive charge density is higher. The anchorage of the organic dianion is reinforced by hydrogen bonds involving its carboxylate oxygen atoms as acceptor and one hydroxide, a coordination water molecule and the exocyclic amino group of the adeninato ligands as donors.

The supramolecular architecture of **2a** is completed by direct N-H \cdots N and C-H \cdots N hydrogen bonding interactions (Table 2) between the adeninato ligands of neighbouring heptameric entities and a strong interaction involving a coordination water molecule as donor and an exocyclic amino group as acceptor (Fig. 5).

The supramolecular assembling of the heptameric entities and the terephthalate anions generates some isolated cavities with a maximum diameter of 4 Å (surrounded by the exocyclic N-site of the adeninato ligands) which are occupied by the crystallization water molecules. The total volume of these voids is the 783 Å³ (22% of the total volume of the unit cell).

As reported in the synthesis section, a more hydrated phase of terephthalate containing compound has been also structurally characterized (**2b**) which involves the presence of a total of 24 crystallization water molecules inside the channels. The presence of twelve additional water molecules leads to a significant unit cell volume increase (from 3495 to 4142 Å³) and some relevant changes on the supramolecular interactions take place (Fig. 6, Table 3).

The origin of the supramolecular change comes from the competition on the hydrogen bonds of the adeninato ligands being established with the adjacent nucleobases or with the crystallization water molecules. This is not the first case in which the presence of water has disrupted the direct hydrogen bonding interactions between the nucleobases. For example, compounds of formula [Cu₂(μ -adenine)₄(Cl)₂]Cl₂·2CH₃OH [10] and [Cu₂(μ -adenine)₄(Cl)₂]Cl₂·6H₂O [32] greatly differ in their crystal structure (porous and non-porous,

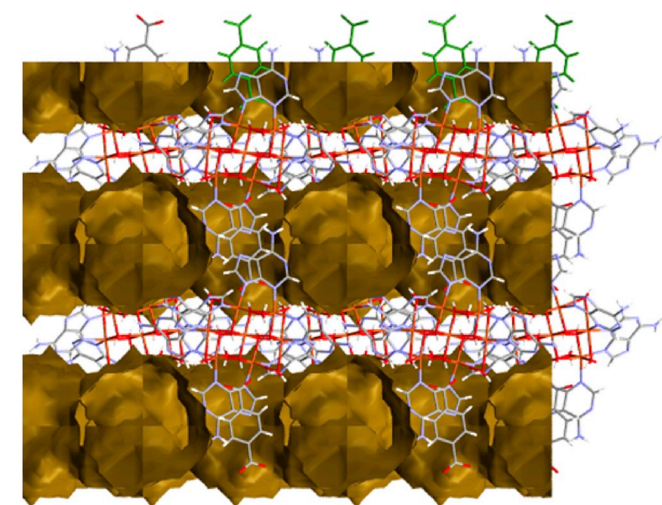
respectively) just due to the presence or not of water solvent molecules.

At low water content, the nucleobases involved in the π - π stacking interaction with the terephthalate anion are tilted in such a way that they are able to establish direct hydrogen bonds, involving Watson-Crick face, with adjacent adenines (Fig. 7). However, at higher content of water, these interactions break up and the adenines align linearly (they become being related by a symmetry center) to expose the Watson-Crick faces to the water molecules located inside the channels. This subtle modification of the dominating hydrogen bonding interactions is also responsible of the observed crystal system change (from monoclinic to triclinic) and a longer distance between the centroids of the two heptameric units related by these π - π interactions (14.6 Å vs 12.8 Å).

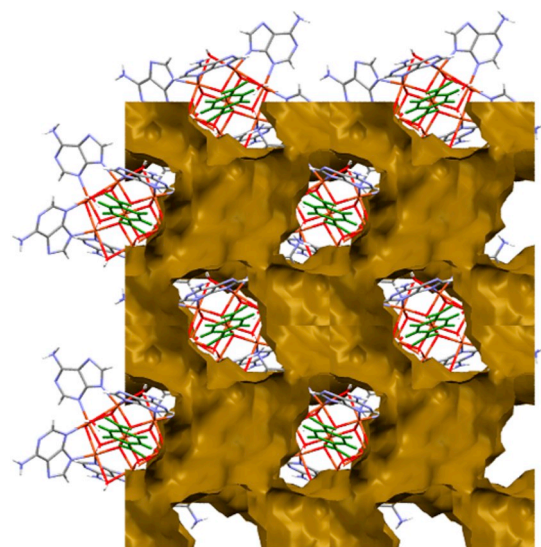
The resulting supramolecular architecture shows the same bidimensional network described for **2a** but the ovoid holes are greater (7 × 6 Å surrounded by the N-site of the adeninato ligands belonging to heptameric cations) as well as the corridors connecting them with an approximate radius of 3 Å (Fig. 8). The volume of these channels, occupied by the crystallization water molecules, is 1541 Å³ per unit cell (37% of the total volume as calculated by PLATON). A computational analysis shows an accessible surface area value of 1048 m²/g and a pore volume of 0.29 mL/g.

The thermoanalytical and variable-temperature X-ray diffraction data of terephthalate containing compounds show that the release of the crystallization water molecules implies a substantial decrease of crystallinity, as revealed by the widening of the diffraction maxima, which is even more notorious with the loss of coordination water molecules (Table S7 and S8, Figs. S6–S9).

As previously stated, compound **2b** suffers a crystal system change from monoclinic to triclinic during the release of the water molecules. It implies a twinning phenomenon of the initial single crystal. In fact, all the crystals selected for the structural characterization were twinned, and all the efforts made for avoiding this twinning were unfruitful. In



(a)



(b)

Fig. 8. Views of contact surface of the 2D network of channels in **2b** along the *c*-axis (a) and the *a*-axis (b).

addition to that, during the water release, the border between the generated domains is getting highly disordered in such a way that they may not be able to come back to the water rich monoclinic phase (**2b**), giving rise to the observed significant amorphization of the sample. In addition, a vacuum activated sample, shows in its X-ray powder diffraction pattern the same loss of crystallinity and a change on the colour from blue to a deep green. This sample was not able to adsorb CO_2 (298 K), neither N_2 (77 K) but it adsorbed water vapour (Fig. 9). It is notorious the presence of pronounced hysteresis curves that do not close at low humidity values. There is still a 6% of water retained, at zero humidity value, a value close to that expected for the coordination water molecules. Despite the adsorption capacity is reduced after the second cycle the starting first points of the adsorption curve are almost the same up to this value, which implies that the amorphization hindered adsorption capability only applies on the crystallization water molecules but not on the coordination ones. The latter conclusion is also reinforced by the fact that desorption curves finish at the same water content. As stated, the partial amorphization of the sample probably contributes to the pronounced hysteresis loops.

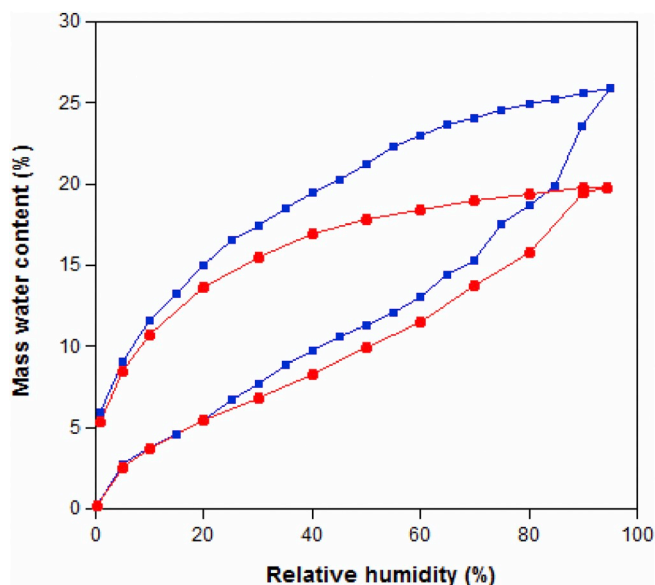
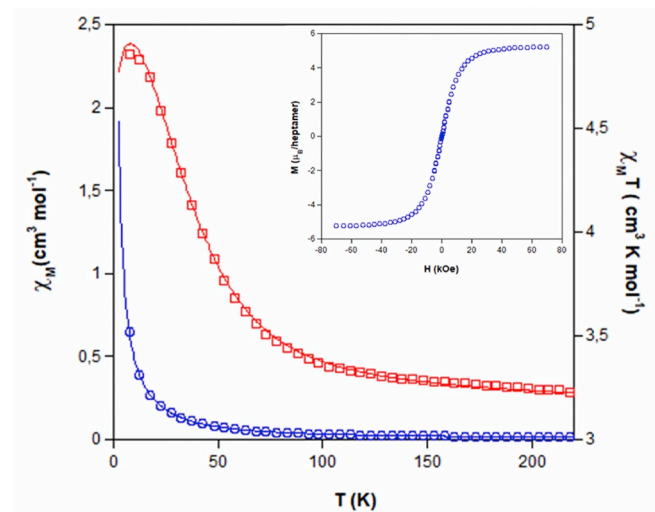
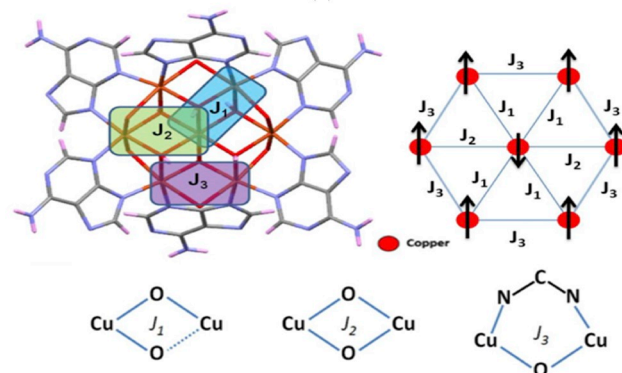


Fig. 9. Water cycling of adsorption/desorption isotherms at 20 °C for an activated sample of compound **2a** (first cycle: blue, second cycle: red).



(a)



(b)

Fig. 10. (a) Thermal evolution of the molar magnetic susceptibility χ_m (o) and $\chi_m T$ (\square) product for compound **1**. Magnetization curve at 2 K (inset). The line shows the best fitting of the experimental data. (b) Magnetic scheme of $[\text{Cu}_7(\mu\text{-ade-}\kappa\text{N3:}\kappa\text{N9})_6(\mu_3\text{-OH})_6(\mu\text{-H}_2\text{O})_6]^{2+}$ heptanuclear entity emphasizing the different relationships of the magnetic topologies and 3-J coupling types for the local Cu^{II} cluster.

3.3. Magnetic properties

The magnetic measurements of compounds **1** and **2** indicate an overall ferrimagnetic behavior within the heptameric copper-adenine entity (Fig. 10). The $\chi_{\text{M}}T$ value at room temperature agrees with the expect value for seven paramagnetic copper(II) metal centers. This value remains basically constant upon cooling and only at temperatures below 100 K starts deviating toward higher values to achieve a maximum of $4.85 \text{ cm}^3 \text{ K mol}^{-1}$ and $5.09 \text{ cm}^3 \text{ K mol}^{-1}$, respectively. The magnetization curve at 2 K shows a linear dependence, from 0 to 12–15 kOe, which slowly tends to saturate to a value of 5.22 and 5.53 μ_{B} /heptamer at 20 kOe. These values which agree with the presence of a central copper(II) metal center antiferromagnetically coupled to the six external ones [5] to provide a $S_{\text{T}} = 5/2$. The magnetization curve shows no hysteresis, indicating that the magnetic contributions are limited to the molecular scale of the heptameric entity without providing a 3D ordering. Only at very low temperature in the $\chi_{\text{M}}T$ curve, it can be observed a slight decrease probably due to the presence of very antiferromagnetic interheptameric coupling mediated through the supramolecular interactions.

Taking into account the molecular structure of the $[\text{Cu}_7(\mu\text{-ade-}\kappa\text{N3}:\kappa\text{N9})_6(\mu_3\text{-OH})_6(\mu\text{-H}_2\text{O})_6]^{2+}$ heptanuclear entity present in both compounds and the Jahn-Teller elongated octahedron of the central copper(II) atom, the following Hamiltonian (Eq. (1)) was employed to fit the experimental data.

$$H = -J_1(\vec{S}_1 \cdot \vec{S}_3 + \vec{S}_1 \cdot \vec{S}_4 + \vec{S}_1 \cdot \vec{S}_3' + \vec{S}_1 \cdot \vec{S}_4') - J_2(\vec{S}_1 \cdot \vec{S}_2 + \vec{S}_1 \cdot \vec{S}_2') - J_3(\vec{S}_2 \cdot \vec{S}_3 + \vec{S}_3 \cdot \vec{S}_4 + \vec{S}_4 \cdot \vec{S}_2' + \vec{S}_2' \cdot \vec{S}_3' + \vec{S}_3' \cdot \vec{S}_4' + \vec{S}_4' \cdot \vec{S}_2) - g\mu_{\text{B}} \vec{B} \cdot \vec{S} \quad (1)$$

J_1 and J_2 couplings are assigned to the superexchange interactions between the central and the external copper ions taking place through double $\mu\text{-OH}$ and $\mu\text{-O}$ bridges. J_1 involves a mixture of short-short and short-long distances. J_2 presents only a short-short Cu–O based arrangement. J_3 represents the superexchange interaction between the external Cu^{II} ions.

The fitting of the $\chi_{\text{m}}T$ experimental data to this model was performed using the MagProp software tool distributed with DAVE [33]. The best fitting parameters (see the red continuous line in Figs. 10a and S11) are $J_1 = -2$, $J_2 = -100$, $J_3 = 67 \text{ cm}^{-1}$ and $g = 2.13$ for compound **1** and $J_1 = 35$, $J_2 = -180$, $J_3 = 100 \text{ cm}^{-1}$ and $g = 2.11$ for compound **2a**. This behavior and the obtained superexchange values are similar to those published for other similar wheel-shaped copper(II) heptameric entities in which the outer metal atoms are ferromagnetically coupled to each other and antiferromagnetically coupled to the central atom [5,6].

4. Conclusions

These compounds have proved that the features of the nucleobases that make them so well suited to deliver a stable complex structure such as those of DNA/RNA, upon which life has evolved, prompt them also as useful tools to develop ordered supramolecular materials. The present work implies the generation of porous materials in which subtle changes such as the negative charge density distribution on simple organic carboxylate anions provides rather different supramolecular architectures. Additionally, the π -stacking interaction mode of the adenines provides flexible structures that response under external stimuli such as the atmosphere humidity. The strong hydrogen bonding capacity of the water guest molecule seems to be the key for the structural reversibility as their interaction with the host inner-surface must compensate the rupture of some direct hydrogen bonding interactions between the nucleobases that are only present in the collapsed crystal structures. The coordination mode of the adeninato ligands also facilitates magnetic interactions that lead to a ferrimagnetic material in this case. It all envisages a fruitful future for the development of metal-organic materials based on so ubiquitous biological molecules.

Declaration of competing interest

The authors declare that there is no conflict of interest.

Acknowledgements

This work has been funded by Universidad del País Vasco/Euskal Herriko Unibertsitatea (PPG17/37, GIU17/050, predoctoral PIF17/051 fellowship for J.P.C.), Gobierno Vasco/Eusko Jaurlaritz (PIBA18-59 and IT1291-19) and Ministerio de Economía y Competitividad (MAT2016-75883-C2-1-P). Technical and human support provided by SGiker (UPV/EHU, MICINN, GV/EJ, ESF) is also acknowledged. *In memoriam* of Professor Juan Manuel Salas Peregrín and his contribution to the research on bioinorganic chemistry in Spain.

Appendix A. Supplementary data

CCDC 1942694–1942696 contain the supplementary crystallographic data for **1**, **2a** and **2b**, respectively. These data can be obtained free of charge via www.ccdc.cam.ac.uk/data_request/cif, or by emailing data_request@ccdc.cam.ac.uk, or by contacting The Cambridge Crystallographic Data Centre, 12 Union Road, Cambridge CB2 1EZ, UK; fax: +44 1223 336033. Supplementary data to this article can be found free of charge online at <https://doi.org/10.1016/j.jinorgbio.2019.110865>.

References

- [1] E. Chargaff, E. Chargaff, J.N. Davidson (Eds.), *In the Nucleic Acids*, 1 Academic Press, New York, 1955, p. 308.
- [2] S. Pérez-Yáñez, G. Beobide, O. Castillo, J. Cepeda, A. Luque, Nova Science Publishers, Inc. pp 67–92, 2016.
- [3] H.C. Zhou, J.R. Long, O.M. Yaghi, *Chem. Rev.* 112 (2012) 673–674.
- [4] P. Yakovchuk, E. Protozanova, M.D. Frank-Kamenetskii, *Nucleic Acids Res.* 34 (2006) 564–574.
- [5] R. Pérez-Aguirre, G. Beobide, O. Castillo, I. De Pedro, A. Luque, S. Pérez-Yáñez, J. Rodríguez Fernández, P. Román, *Inorg. Chem.* 55 (2016) 7755–7763.
- [6] B.J.M. Leite Ferreira, P. Brandão, A.M. Dos Santos, Z. Gai, C. Cruz, M.S. Reis, T.M. Santos, V. Félix, *J. Coord. Chem.* 68 (2015) 2770–2787.
- [7] J. Pascual-Colino, G. Beobide, O. Castillo, I. da Silva, A. Luque, S. Pérez-Yáñez, *Cryst. Growth Des.* 18 (2018) 3465–3476.
- [8] P.S. Nugent, V.L. Rhodus, T. Pham, K.A. Forrest, L. Wojtas, B. Space, M.J. Zaworotko, *J. Am. Chem. Soc.* 135 (2013) 10950–10953.
- [9] W. Gong, D. Chu, H. Jiang, X. Chen, Y. Cui, Y. Liu, *Nat. Commun.* 10 (2019) 600.
- [10] J. Thomas-Gipson, G. Beobide, O. Castillo, J. Cepeda, A. Luque, S. Pérez-Yáñez, A.T. Aguayo, P. Román, *CrystEngComm* 13 (2011) 3301–3305.
- [11] J. Thomas-Gipson, G. Beobide, O. Castillo, M. Fröba, F. Hoffmann, A. Luque, S. Pérez-Yáñez, P. Román, *Cryst. Growth Des.* 14 (2014) 4019–4029.
- [12] C.R. Martínez, B.L. Iverson, *Chem. Sci.* 3 (2012) 2191–2201.
- [13] P. Cysewsky, *Phys. Chem. Chem. Phys.* 10 (2008) 2636–2645.
- [14] A. Earnshaw, *Introduction to Magnetochemistry*, Academic Press, London, 1968.
- [15] *CrysAlisPRO*, Oxford Diffraction/Agilent Technologies UK Ltd, Yarnton, England.
- [16] A. Altomare, G. Cascarano, C. Giacovazzo, A. Guagliardi, M.C. Burla, G. Polidori, M. Camalli, *J. Appl. Crystallogr.* 27 (1994) 435.
- [17] G.M. Sheldrick, *Acta Cryst C* 71 (2015) 3–8.
- [18] L.J. Farrugia, *J. Appl. Crystallogr.* 45 (2012) 849–854.
- [19] J. Cepeda, O. Castillo, J.P. García-Terán, A. Luque, S. Pérez-Yáñez, P. Roman, *Eur. J. Inorg. Chem.* (16) (2009) 2344–2353.
- [20] E. Sletten, *Acta Crystallogr.* B25 (1969) 1480–1491.
- [21] E. Sletten, *Acta Crystallogr.* B26 (1970) 1609–1614.
- [22] P. Van der Sluis, A.L. Spek, *Acta Crystallogr. A* 46 (1990) 194–201.
- [23] A.L. Spek, *Acta Cryst D* 65 (2009) 148–155.
- [24] Topos main page, <http://www.topospro.com>, Accessed date: 10 May 2019.
- [25] V.A. Blatov, A.P. Shevchenko, D.M. Proserpio, *Cryst. Growth Des.* 14 (2014) 3576–3586.
- [26] J.P. García-Terán, O. Castillo, A. Luque, U. García-Couceiro, P. Román, L. Lezama, *Inorg. Chem.* 43 (2004) 4549–4551.
- [27] O.L.I. Brown, *J. Chem. Educ.* 28 (1951) 428.
- [28] H. Furukawa, F. Gándara, Y.-B. Zhang, J. Jiang, W.L. Queen, M.R. Hudson, O.M. Yaghi, *J. Am. Chem. Soc.* 136 (2014) 4369–4381.
- [29] H. Kim, H.J. Cho, S. Narayanan, S. Yang, H. Furukawa, S. Schiffrs, X. Li, Y.-B. Zhang, J. Jiang, O.M. Yaghi, E.N. Wang, *Sci. Rep.* 6 (2016) 19097.
- [30] J. Canivet, A. Fateeva, Y. Guo, B. Coasne, D. Farrusseng, *Chem. Soc. Rev.* 43 (2014) 5594.
- [31] N.C. Burtch, H. Jasuja, K.S. Walton, *Chem. Rev.* 114 (2014) 10575–10612.
- [32] P. De Meester, A.C. Skapski, *J. Chem. Soc. A* 13 (1971) 2167–2169.
- [33] R.T. Azuah, L.R. Kneller, Y. Qiu, P.L.W. Tregenna-Piggott, C.M. Brown, J.R.D. Copley, R.M. Dimeo, *J. Res. Natl. Inst. Stand. Technol.* 114 (2009) 341–358.

RESEARCH ARTICLE

[View Article Online](#)
[View Journal](#) | [View Issue](#)

 Cite this: *Inorg. Chem. Front.*, 2022,
 9, 935

Merging the chemistry of metal–organic and polyoxometalate clusters to form enhanced photocatalytic materials†

 Jon Napal, ^a Beñat Artetxe, ^a Garikoitz Beobide, ^{*a,b} Oscar Castillo, ^{*a,b}
 Antonio Luque, ^{a,b} Jon Pascual-Colino, ^a Sonia Pérez-Yáñez ^{c,b} and
 Maite Perfecto-Irigaray ^a

 Received 8th November 2021,
 Accepted 11th January 2022

DOI: 10.1039/d1qi01411k

rsc.li/frontiers-inorganic

The combination of a zirconium metal–organic cluster and a Keggin type polyoxotungstate into a compound of the formula $[\text{Zr}_6(\mu_3\text{-O})_4(\mu_3\text{-OH})_4(\mu\text{-OOC}_6\text{H}_5)_8(\text{H}_2\text{O})_8][\text{SiW}_{12}\text{O}_{40}]$ led to a chemically and photochemically stable material in which a synergistic effect between the metal–organic cluster and the polyoxometalate allows marked enhancement of the photochemical activity of the single ionic components toward the photooxidation of dyes.

Global energy consumption and concerns with environmental contamination have led to an increased interest in the harvesting of solar energy to conduct chemical reactions that can provide cleaner sources of energy and raw materials or even neutralize hazardous chemicals.¹ In this regard, over the last few years, zirconium-based metal–organic frameworks (MOFs) have been intensively explored as heterogeneous photocatalysts due to both the *ad-hoc* setting of the surface chemistry and the proficient chemical stability provided by Zr–O bonds.^{2,3} Some successful examples include the photocatalytic removal of pollutants,⁴ production of hydrogen,⁵ photoreduction of CO₂,⁶ and selective transformation of organics into valuable chemicals.⁷ The metal clusters and organic ligands building up this type of MOF can be regarded as isolated quantum dots and light-harvesting antennas, respectively.⁸ Accordingly, discrete zirconium clusters can also behave as efficient heterogeneous photocatalysts if they are embedded into an insoluble matrix. Under controlled reaction conditions, Zr(IV) tends to yield hexanuclear clusters of the formula $[\text{Zr}_6\text{O}_4(\text{OH})_4]^{12+}$ in which the charge can be modulated by the anchoring of a variable number (*n*) of carboxylic ligands: $[\text{Zr}_6\text{O}_4(\text{OH})_4(\text{OOCR})_n]^{12-n}$.

When this class of discrete complexes are crystallized using simple counterions (such as chloride, sulphate, *etc.*), compounds of frail stability, soluble in common solvents and therefore, unsuitable as heterogeneous catalysts are obtained. Nonetheless, the adequate selection of the counterion can help overcome such drawbacks. In this sense, polyoxometalates (POMs) constitute a fine solution since their size is comparable to that of zirconium clusters and their anionic charge is relatively high, so the combination of both types of entities can yield highly insoluble and stable ionic molecular compounds. Furthermore, POMs show recognized catalytic and photocatalytic activities¹⁰, so they can potentially act as co-catalysts and boost the overall performance. In fact, there are many examples in the literature where the incorporation of POMs into the pores of MOFs has increased the catalytic performance of the latter.^{11,12} Last but not least, the packing of such macro-ionic entities is expected to render a meaningful amount of void volume or pores in the crystal structure,¹³ which might increase the surface area of the catalyst. Keeping all this in mind, we have selected a Keggin type polyoxometalate of the formula $[\text{SiW}_{12}\text{O}_{40}]^{4-}$ (**W₁₂**) due to its high negative charge, size and intrinsic photocatalytic properties.¹⁴ The net charge of the zirconium cluster has been set by controlling the stoichiometry of the carboxylic ligand (benzoate) to obtain a cationic complex of the formula $[\text{Zr}_6\text{O}_4(\text{OH})_4(\text{OOC}_6\text{H}_5)_8(\text{H}_2\text{O})_8]^{4+}$ (**Zr₆**). The reaction of these entities yielded a compound of the formula $[\text{Zr}_6\text{O}_4(\text{OH})_4(\text{OOC}_6\text{H}_5)_8(\text{H}_2\text{O})_8][\text{SiW}_{12}\text{O}_{40}] \cdot n(\text{EtOH})$, termed **Zr₆/W₁₂**. The modulation of the pH during the synthesis was a critical factor to ensure that both molecular building blocks retain their structural integrity and to exert control on the crystallization process (see details in the ESI†). Precisely, the reac-

^aDepartment of Organic and Inorganic Chemistry, University of the Basque Country, UPV/EHU, P.O. 644, E-48080 Bilbao, Spain. E-mail: oscar.castillo@ehu.eus, garikoitz.beobide@ehu.eus

^bBCMaterials, Basque Center for Materials, Applications and Nanostructures, UPV/EHU Science Park, E-48940 Leioa, Spain

^cDepartment of Organic and Inorganic Chemistry, University of the Basque Country, UPV/EHU, E-01006 Vitoria-Gasteiz, Spain

† Electronic supplementary information (ESI) available: Syntheses, experimental details, crystallographic and chemical characterization, and the CIF file. CCDC 2120444. For ESI and crystallographic data in CIF or other electronic format see DOI: 10.1039/d1qi01411k

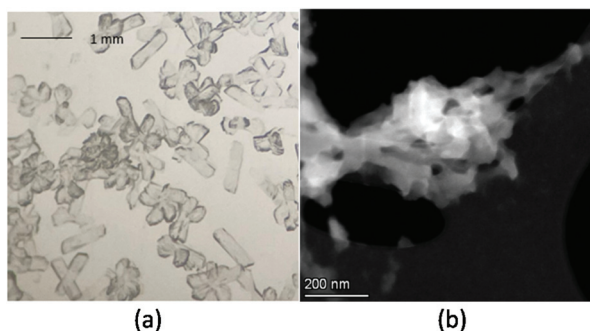


Fig. 1 (a) Optical micrograph of Zr_6/W_{12} -MC and (b) a TEM image of Zr_6/W_{12} -NP.

tion at pH = 0.2 allowed the growth of micrometric crystals (Zr_6/W_{12} -MC) suitable for single crystal X-ray diffraction; however, on setting the pH to 0.8, the ionic ensemble crystallized as aggregates of nanometric particles (Zr_6/W_{12} -NP) (Fig. 1). Chemically, Zr_6/W_{12} -MC and Zr_6/W_{12} -NP only differ in the number of co-crystallized solvent molecules (13 and 11 ethanol molecules per formula), as demonstrated by chemical analyses, thermogravimetry and infrared spectroscopy (ESI).

Single crystal X-ray diffraction data allowed us to elucidate the crystal structure of Zr_6/W_{12} -MC.[†] As expected, the Zr atoms of the $[Zr_6(\mu_3-O)_4(\mu_3-OH)_4(\mu-OCC_6H_5)_8(H_2O)_8]^{4+}$ entity exhibit an octahedral disposition, in such a way that oxide and hydroxide anions are alternately placed in triangular faces. All the oxide and hydroxide anions can be crystallographically distinguished on the basis of the coordination bond distances and the deviations from the plane defined by the three Zr atoms they bind. Hydroxide anions establish longer coordination bonds (2.21–2.26 Å) than oxides (2.06–2.08 Å), due to the weaker bond strength of the former. This fact also implies a greater deviation from the mean plane hydroxide (1.090–1.101 Å) compared to that for the oxide (0.410–0.415 Å). Each benzoate ligand links two Zr atoms in $\mu-\kappa O:\kappa O'$ coordination mode, filling four upper and four lower axial edges of the octahedron. The remaining 4 equatorial edges of the octahedron are completed by eight coordination water molecules (two per Zr-atoms). As a result, all the metal atoms of the cationic cluster exhibit a ZrO_8 type coordination sphere with a square antiprismatic geometry (see further details in Fig. S1 of the ESI[†]).

The $[SiW_{12}O_{40}]^{4-}$ anion (W_{12}) shows the well-known α -Keggin type structure, which is constituted by four $\{W_3O_{13}\}$ trimers formed each by three edge-sharing WO_6 octahedra. These trimers are linked to each other and to the central $\{SiO_4\}$ tetrahedron through corner-sharing in an ideal T_d symmetry. However, as it usually happens, they are disordered over two positions related by a centre of inversion located on the

[†] Crystallographic data. Crystal system: triclinic; space group: $P\bar{1}$; cell parameters: $a = 14.6248(4)$ Å, $b = 15.4043(4)$ Å, $c = 30.7774(8)$ Å, $\alpha = 89.831(2)^\circ$, $\beta = 79.266(2)^\circ$, $\gamma = 66.903(2)^\circ$ and $V = 6247.4(3)$ Å³. See ESI[†] for further details.

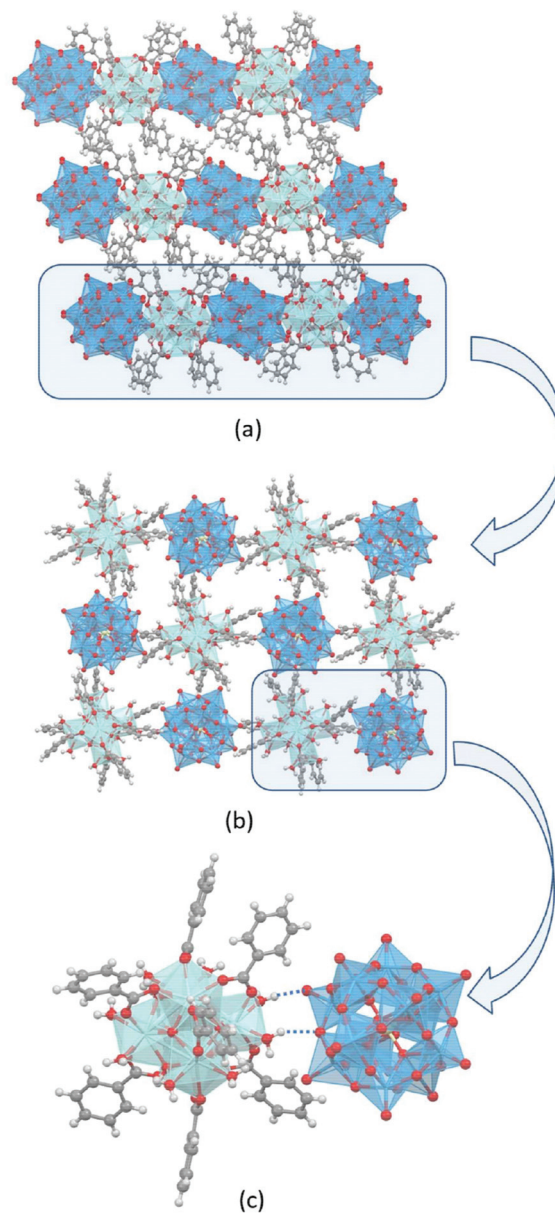


Fig. 2 (a) View of the crystal packing of Zr_6/W_{12} -MC along the b -axis. (b) Hydrogen bonded two-dimensional square lattice and (c) details of the hydrogen bonding interactions established between adjacent molecular building blocks.

central Si atom for one of the crystallographically independent heteropolyoxometalate clusters (Si2) and close to it in the second one (Si1) (Fig. S2[†]).

The crystal structure of Zr_6/W_{12} (Fig. 2) resembles a NaCl type packing of ions, in which each molecular building unit is surrounded by six counterions. However, the distances between the centroids of the ionic entities are different depending on their relative positions. In particular, the approach of the POM along the axial position of the Zr_6 -cluster is hindered by the phenyl rings and it leads to centroid...centroid distances of 13.7–14.8 Å. In contrast, the equatorial edge of the Zr_6 -cluster allows the POM to get closer (10.6–11.2 Å),

and thus, it favours the formation of hydrogen bonds involving the coordination water molecules and the oxide anions of the POM surface ($\text{Ow-H}\cdots\text{O}_{\text{POM}}$: 2.68–3.21 Å, 145–170°). This hydrogen bonding scheme gives rise to a binodal 2D square lattice (**sql**) in which each ionic entity is linked to four counterions. The phenyl groups lie at the upper and lower sides of the supramolecular layer. Apart from the electrostatic and dispersive forces, no other meaningful interactions contribute to the assembly of layers.

According to pore size distribution analysis, the overall packing leaves a 2D network (orthogonal to $[0\bar{2}1]$) in which cavities of 4–5 Å are connected through narrower necks (3.3 Å) (Fig. S3†). The porosity of the structure is 28%, a value close to that found in the close packing of rigid spheres. Despite the geometric surface area ($80 \text{ m}^2 \text{ g}^{-1}$) and pore volume ($0.115 \text{ cm}^3 \text{ g}^{-1}$) being meaningful for such a POM-based material, the N_2 adsorption experiment did not probe any porosity (ESI) as the size of the pore necks is too close to the kinetic diameter of the gas probe inhibiting its diffusion. However, the compound is able to adsorb modest quantities of smaller CO_2 and H_2O molecules at 273 and 293 K, respectively (Fig. S9 and S10†).

According to variable-temperature PXRD experiments (Fig. S6†), the crystal structure remained stable up to 350 °C, which is a relatively high value for such a hybrid material and it is close to thermally most stable MOFs.¹⁵ Similarly, both $\text{Zr}_6/\text{W}_{12}\text{-MC}$ and $\text{Zr}_6/\text{W}_{12}\text{-NP}$ exhibited high chemical stability as they withstand common solvents (water, methanol, and ethanol) and acidic media.

As previously mentioned, this class of compounds when irradiated with photons of energy equal to or higher than the HOMO/LUMO energy difference generate holes and high energy electrons that present oxidizing and reducing capabilities, respectively.^{8,16} Among the different potential applications, their use as photocatalysts for the oxidation of organic substrates is of remarkable interest in the area of advanced oxidation processes, including the degradation of pollutants and waste treatment.¹⁷ In this regard, the assessment of the degradation of a dye provides a suitable tool to evaluate the photocatalytic performance of a given material. Therefore, herein we explored the capability of the nanoparticle compound to photodegrade methylene blue and compared it with the performance provided by referential insoluble forms of each individual macroionic component synthesized for comparative purposes: $[\text{Zr}_6\text{O}_4(\text{OH})_4(\text{benzene-1,4-dicarboxylato})_6]_n$ and $\text{Cs}_{3.5}\text{H}_{0.5}[\text{SiW}_{12}\text{O}_{40}]$ (named **UiO-66** and **Cs/W₁₂**, respectively).^{18,19}

Fig. 3a compares the adsorption and photooxidation capacity of methylene blue for each selected solid. Despite the permanent porosity of the referential compounds (Fig. S7†), the hybrid material surpasses their methylene blue adsorption capacity ($\text{Zr}_6/\text{W}_{12}\text{-NP}$: $73 \mu\text{g mg}^{-1}$; **Cs/W₁₂**: $63 \mu\text{g mg}^{-1}$; and **UiO-66**: $16 \mu\text{g mg}^{-1}$), which can probably be ascribed to both its ionic nature and small particle size. Interestingly, the illumination with a neodymium daylight lamp (100 W) promoted the quantitative photodegradation of the dye in 4 h ($k = 7.7 \times 10^{-3} \text{ min}^{-1}$), while the referential compounds did not exhibit

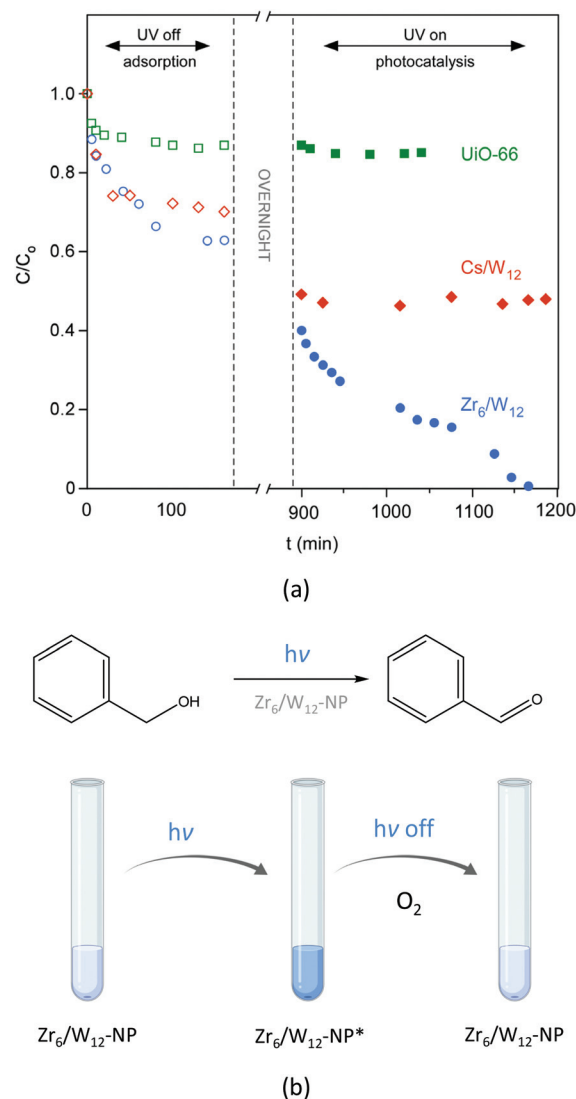


Fig. 3 (a) Capture and photooxidation of methylene blue by $\text{Zr}_6/\text{W}_{12}\text{-NP}$ compared to those shown by **UiO-66** and **Cs/W₁₂**. (b) Scheme of the photooxidation of benzyl alcohol, depicting the colour changes taking place in the $\text{Zr}_6/\text{W}_{12}\text{-NP}$ catalyst.

any substantial activity. Such a result is clear evidence of a synergistic effect between both types of ionic building blocks that comprise our hybrid material. It is worth noting that $\text{Zr}_6/\text{W}_{12}\text{-NP}$ remained stable after the experiment.

Furthermore, $\text{Zr}_6/\text{W}_{12}\text{-NP}$ showed also the capability to selectively photooxidize benzyl alcohol into benzaldehyde as depicted in Fig. 3b. During the reaction, the solid $\text{Zr}_6/\text{W}_{12}\text{-NP}$ catalyst turned from white to blue, while it slowly turned back into a white solid when the irradiation was stopped. Such behaviour allows us to infer that the photooxidation reaction takes place quicker than the photoreduction, so that the electron pumping leads to the reduction of a remnant of $\text{W}(\text{vi})$ into $\text{W}(\text{v})$ in which the population of the formerly empty d -orbitals forms the origin of the blue chromophore. Once the light is turned off, the exposure to air prompts the oxidation of the

Research Article

reduced tungsten and Zr_6/W_{12} -NP becomes white coloured again. This behaviour has been previously observed in some other polyoxotungstates²⁰ and Ti-MOFs, which implies a photoinduced partial and reversible reduction of Ti(IV) to Ti(III).²¹

Again, the photoactivity shown by Zr_6/W_{12} -NP was put in context with the referential UiO-66 and Cs/ W_{12} compounds by collating the absorption under dark conditions and photooxidation under UV illumination (Table 1 and Fig. S21–S23†). The three compounds present a significant adsorption capability, but only Zr_6/W_{12} -NP is able to provide photooxidation activity. This experiment was also conducted using a previously reported material in which H_4W_{12} POM was incorporated into the pores of UiO-66 ($W_{12}@UiO-66$),²² which also shows a synergistic effect between the POM and Zr_6 SBUs. In this case, the obtained conversion percentage is somewhat lower in comparison with Zr_6/W_{12} -NP (Fig. S24†). On the other hand, the results obtained using OH^\cdot and O_2^- scavengers (isopropanol and hydroquinone, respectively)^{23–26} in the photocatalytic oxidation of the benzyl alcohol by Zr_6/W_{12} -NP revealed that hydroxyl radicals must be involved in the oxidation process, whereas superoxide anions do not play any important role under the reaction conditions (see the ESI†).

In order to support the aforementioned statements and to understand the origin of the synergistic effect, density functional theory (DFT) calculations were performed on each separated cluster (Fig. 4). To account for the electrostatic potential experienced by each ion within the crystal, the charges were balanced by siting four monoions (F^- or Li^+) at distances (8 Å) comparable to the intercluster distances found in Zr_6/W_{12} (see further details in the ESI†). It is worth mentioning that the smallest HOMO/LUMO energy difference approaches fairly well to the optical bandgap (3.54 eV) estimated from the absorption edge of the measured UV/Vis spectra.

The highest occupied molecular orbitals (HOMOs) are composed of the contribution of phenyl- π orbitals and μ -O-2p orbitals from the Zr_6 and W_{12} clusters, respectively. Conversely, the lowest unoccupied molecular orbitals (LUMOs), in both cases, have mainly the contribution of empty d -orbitals of the metals. Such orbital disposition suggests that the irradiation of the catalysts induces a ligand-to-metal charge transfer, as it takes place in many metal-based molecular materials.⁸ Besides, the energy distribution allows us to postulate that upon irradiation of the sample, the photogenerated electrons (e^-) in the Zr_6 -cluster can combine with the holes (h^+) located in the HOMO of the W_{12} anion. Such a situation would lead to efficient

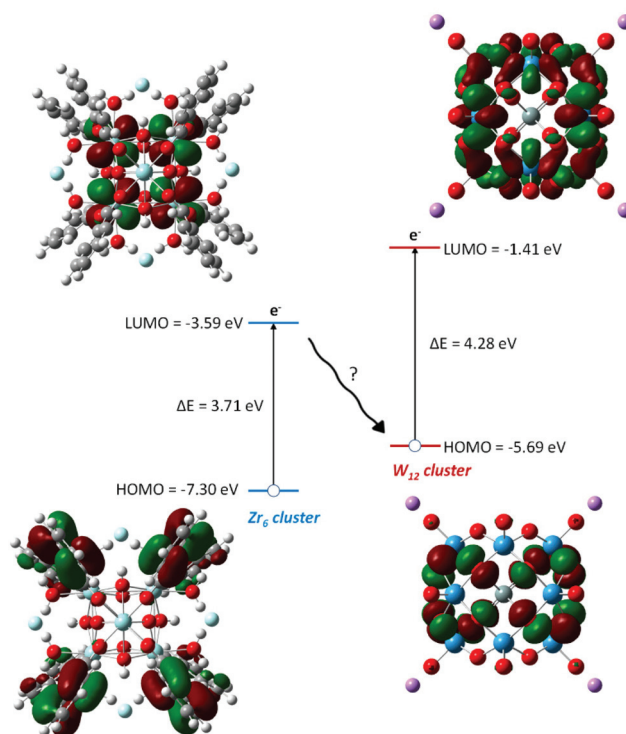


Fig. 4 Molecular orbital plots (isovalue = 0.05) and energies of the HOMO and LUMO for $[Zr_6O_4(OH)_4(OOCC_6H_5)_8(H_2O)_8]^{4+}/F^-$ and $[SiW_{12}O_{40}]^{4-}/Li^+$ ensembles.

spatial separation of the charges by leaving the photogenerated e^-/h^+ in different molecular entities and inhibiting the undesired e^-/h^+ recombination. Thus, it can be inferred that the holes (h^+) located in the Zr_6 -cluster lead to the oxidation reaction, while the reduction is conducted by the photoelectrons pumped into the LUMO of the W_{12} anion. This HOMO/LUMO distribution of the catalyst ensemble fits to a Z-scheme, which mimics the natural photosystems²⁷ and explains well the synergy taking place upon the combination of both metal-clusters.

It can be concluded that this work demonstrates how the combination of a zirconium metal-organic cluster and a polyoxotungstate into a single ionic molecular material yields a chemically and photochemically stable porous material. Furthermore, the HOMO/LUMO energy distribution provides a Z-scheme mechanism with spatially separated reduction and oxidation units, which could prolong the lifetime of photogenerated e^-/h^+ and explain the synergistic boosting of the catalytic performance provided by the coexistence of the metal-organic and polyoxometalate clusters. All in all, this work opens an opportunity to design novel heterogeneous photocatalysts based on the hybridization of metal-organic clusters and polyoxometalates, given that the stability of the material and the potential to afford enhanced performance can be achieved by the rational selection of the ionic building blocks. Furthermore, our approach to the search for synergy in the cationic metal-organic cluster-anionic POM ensembles is

Table 1 Benzyl alcohol removal upon 4 h of continuous stirring under UV light (and without it)

Cs/ W_{12}	Zr_6/W_{12} -NP ^a	UiO-66	$W_{12}@UiO-66$
10% (11%)	52% (31%)	21% (19%)	46% (26%)

^a Addition of the hydroxyl scavenger (isopropanol): 33%; and the addition of the superoxide scavenger (hydroquinone): 55%.

geometrically less constrained in comparison with systems in which polyoxometalates are placed inside the voids of a given MOF, because POMs must meet specific requirements in terms of properties e.g. the size, charge and shape.

Conflicts of interest

There are no conflicts to declare.

Acknowledgements

The authors gratefully acknowledge the financial support from the Basque Government (IT1291-19), from the University of the Basque Country (predoctoral fellowships for J. P. C. and M. P. I.: PIF17/51 and PIF18/175) and from the Spanish Ministry of Science and Innovation (PID2019-108028GB-C21). Technical and human support provided by SGIker (UPV/EHU, MICINN, GV/EJ, and ESF) is also acknowledged.

Notes and references

- M. Melchionna and P. Fornasiero, Updates on the roadmap for photocatalysis, *ACS Catal.*, 2020, **10**, 5493–5501.
- Y. Bai, Y. Dou, L.-H. Xie, W. Rutledge, J.-R. Li and H.-C. Zhou, Zr-based metal-organic frameworks: design, synthesis, structure, and applications, *Chem. Soc. Rev.*, 2016, **45**, 2327–2367.
- Q. Wang, Q. Gao, A. M. Al-Enizi, A. Nafady and S. Ma, Recent advances in MOF-based photocatalysis: environmental remediation under visible light, *Inorg. Chem. Front.*, 2020, **7**, 300–339.
- C.-C. Wang, X.-D. Du, J. Li, X.-X. Guo, P. Wang and J. Zhang, Photocatalytic Cr(VI) reduction in metal-organic frameworks: A mini-review, *Appl. Catal., B*, 2016, **193**, 198–216.
- X. Ma, L. Wang, Q. Zhang and H. Jiang, Switching on the photocatalysis of metal-organic frameworks by engineering structural defects, *Angew. Chem., Int. Ed.*, 2019, **58**, 12175–12179.
- Y. Chen, D. Wang, X. Deng and Z. Li, Metal-organic frameworks (MOFs) for photocatalytic CO₂ reduction, *Catal. Sci. Technol.*, 2017, **7**, 4893–4904.
- H. Liu, C. Xu, D. Li and H.-L. Jiang, Photocatalytic hydrogen production coupled with selective benzylamine oxidation over MOF composites, *Angew. Chem., Int. Ed.*, 2018, **57**, 5379–5383.
- M. A. Nasalevich, M. van der Veen, F. Kapteijn and J. Gascon, Metal-organic frameworks as heterogeneous photocatalysts: advantages and challenges, *CrystEngComm*, 2014, **16**, 4919–4926.
- Y. Wang, L. Feng, K. Zhang, K. Wang, W. Fan, X. Wang, B. Guo, F. Dai, L. Zhang, D. Sun and H. Zhou, Uncovering structural opportunities for zirconium metal-organic frameworks via linker desymmetrization, *Adv. Sci.*, 2019, **6**, 1901855.
- C. Streb, K. Kastner and J. Tucher, Polyoxometalates in photocatalysis, *Phys. Sci. Rev.*, 2019, **4**, 20170177.
- Y. Liu, C. Tang, M. Cheng, M. Chen, S. Chen, L. Lei, Y. Chen, H. Yi, Y. Fu and L. Li, Polyoxometalate@Metal-Organic framework composites as effective photocatalysts, *ACS Catal.*, 2021, **11**, 13374–13396.
- P. Mialane, C. Mellot-Draznieks, P. Gairola, M. Duguet, Y. Benseghir, O. Oms and A. Dolbecq, Heterogenisation of polyoxometalates and other metal-based complexes in metal-organic frameworks: from synthesis to characterisation and applications in catalysis, *Chem. Soc. Rev.*, 2021, **50**, 6152–6220.
- Y. Shimoyama and S. Uchida, Structure-function relationships of porous ionic crystals (PICs) based on polyoxometalate anions and oxo-centered trinuclear metal carboxylates as counter cations, *Chem. Lett.*, 2021, **50**, 21–30.
- E. Papaconstantinou, Photochemistry of polyoxometallates of molybdenum and tungsten and/or vanadium, *Chem. Soc. Rev.*, 1989, **18**, 1–31.
- C. Healy, K. M. Patil, B. H. Wilson, L. Hermanspahn, N. C. Harvey-Reid, B. I. Howard, C. Kleinjan, J. Kolien, F. Payet, S. G. Telfer, P. E. Kruger and T. D. Bennett, The thermal stability of metal-organic frameworks, *Coord. Chem. Rev.*, 2020, **419**, 213388.
- J. Lan, Y. Wang, B. Huang, Z. Xiao and P. Wu, Application of polyoxometalates in photocatalytic degradation of organic pollutants, *Nanoscale Adv.*, 2021, **3**, 4646–4658.
- J. L. Wang and L. J. Xu, Advanced oxidation processes for wastewater treatment: formation of hydroxyl radical and application, *Crit. Rev. Environ. Sci. Technol.*, 2012, **42**, 251–325.
- J. H. Cavka, S. Jakobsen, U. Olsbye, N. Guillou, C. Lamberti, S. Bordiga and K. P. Lillerud, A new zirconium inorganic building brick forming metal organic frameworks with exceptional stability, *J. Am. Chem. Soc.*, 2008, **130**, 13850–13851.
- Y. Kamiya, S. Sano, Y. Miura, Y. Uchida, Y. Ogawa, Y. Iwase and T. Okuhara, Microporous acidic cesium salt of 12-tungstosilicic acid Cs₃HSiW₁₂O₄₀ as a size-selective solid acid catalyst, *Chem. Lett.*, 2010, **39**, 881–883.
- J. M. Cameron, S. Fujimoto, R.-J. Wei, G. N. Newton and H. Oshio, Post-functionalization of a photoactive hybrid polyoxotungstate, *Dalton Trans.*, 2018, **47**, 10590–10594.
- H. L. Nguyen, The chemistry of titanium-based metal-organic frameworks, *New J. Chem.*, 2017, **41**, 14030–14043.
- Q. Zhang, T. Yang, X. Liu, C. Yue, L. Ao, T. Denga and Y. Zhang, Heteropoly acid-encapsulated metal-organic framework as a stable and highly efficient nanocatalyst for esterification reaction, *RSC Adv.*, 2019, **9**, 16357–16365.
- X. Zhao, Y. Zhang, P. Wen, G. Xu, D. Ma and P. Qiu, NH₂-MIL-125(Ti)/TiO₂ composites as superior visible-light photocatalysts for selective oxidation of cyclohexane, *Mol. Catal.*, 2018, **452**, 175–183.

- 24 O. Fónagy, E. Szabó-Bárdos and O. Horváth, 1,4-Benzoquinone and 1,4-hydroquinone based determination of electron and superoxide radical formed in heterogeneous photocatalytic systems, *J. Photochem. Photobiol., A*, 2021, **407**, 113057.
- 25 Y. Zhang, N. Zhang, Z. R. Tang and Y. J. Xu, Graphene transforms wide band gap ZnS to a visible light photocatalyst. the new role of graphene as a macromolecular photosensitizer, *ACS Nano*, 2012, **6**, 9777–9789.
- 26 Y. Zhang, N. Zhang, Z. R. Tang and Y. J. Xu, Transforming CdS into an efficient visible light photocatalyst for selective oxidation of saturated primary C-H bonds under ambient conditions, *Chem. Sci.*, 2012, **3**, 2812–2822.
- 27 Y. Wang, H. Suzuki, J. Xie, O. Tomita, D. J. Martin, M. Higashi, D. Kong, R. Abe and J. Tang, Mimicking natural photosynthesis: solar to renewable H_2 fuel synthesis by z-scheme water splitting systems, *Chem. Rev.*, 2018, **118**, 5201–5241.

The Chemistry of Zirconium/Carboxylate Clustering Process: Acidic Conditions to Promote Carboxylate-Unsaturated Octahedral Hexamers and Pentanuclear Species

Jon Pascual-Colino, Beñat Artetxe, Garikoitz Beobide, Oscar Castillo,* Maria Luz Fidalgo-Mayo, Ainhoa Isla-López, Antonio Luque, Sandra Mena-Gutiérrez, and Sonia Pérez-Yáñez



Cite This: *Inorg. Chem.* 2022, 61, 4842–4851



Read Online

ACCESS |



Metrics & More

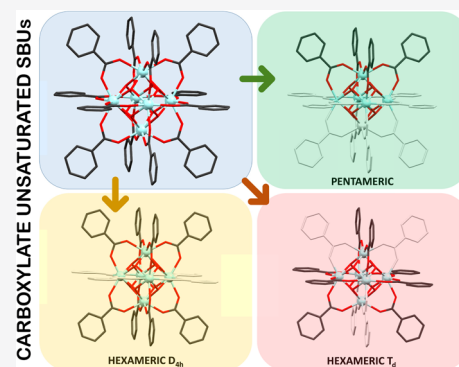


Article Recommendations



Supporting Information

ABSTRACT: Clustering chemistry is a key point in the design and synthesis of the secondary building units that comprise metal–organic frameworks (MOFs) based on group IV metals. In this work, the first stages of the zirconium-carboxylate clustering process in alcohol/water mixtures are studied in detail using the monocarboxylic benzoic and hydroxybenzoic acids to avoid the polymerization. Mass spectroscopy measurements performed on the reactions revealed the presence of hexa- and pentanuclear species even at low pH values and also evidenced the acid–base nature and pH dependence of the transformation between both species. The control on the chemistry governing the equilibria between these species has allowed us to isolate six new compounds in the solid state. The single-crystal X-ray diffraction analysis revealed that they are closely related to the well-known $[\text{Zr}_6(\text{O})_4(\text{OH})_4(\text{OOC})_{12}]$ secondary building unit found in many MOFs by removing carboxylic ligands in the case of the hexameric species ($[\text{Zr}_6(\text{O})_4(\text{OH})_4(\text{OOC})_8(\text{H}_2\text{O})_8]^{4+}$) or by additionally removing one of the metal centers in the case of the pentameric entities ($[\text{Zr}_5(\text{O})_2(\text{OH})_6(\text{OOC})_4(\text{H}_2\text{O})_{11}(\text{alcohol})]^{6+}$). Going in detail, the unsaturated hexameric clusters exhibit different dispositions of their eight carboxylate ligands in such a way that the remaining four carboxylate-free positions are arranged according to a square planar or tetrahedral symmetry. It should be highlighted that the pentameric complexes imply an unprecedented core nuclearity in zirconium clusters and thus their isolation provides a novel building block for the design of metal–organic materials.



1. INTRODUCTION

The interest in the design and preparation of discrete polynuclear metal–organic entities has resurfaced¹ not only in the areas of classical magnetism² and drug development^{3,4} but also in the discovery of new building units to design metal–organic frameworks (MOFs), which show endless applications based on the tailorability of their porosity.⁵ The key point for this fascinating diversity relies on the modular building up of their crystalline structure based on the combination of organic linkers and secondary building units (SBUs) consisting mainly of metal nodes or clusters.^{6–8} Until recently, novel topologies emerged basically from the change of the organic linkers, e.g., moving from ditopic to tritopic linkers. However, this approach has led to a never-ending increase of the complexity and cost of the bridging ligands employed to develop new MOFs.^{9–12}

The other constituent, the SBUs, seems to be less explored, as usually the synthetic chemistry relies on the self-assembled metal-oxide-hydroxide polynuclear entities and they apparently show little variability under the conventional synthetic conditions employed for the preparation of these materials.^{13,14} This fact is evident when analyzing the reported structures for the zirconium/carboxylate MOF family, which are mostly

based on the neutral $[\text{Zr}_6(\text{O})_4(\text{OH})_4(\text{OOC})_{12}]$ SBU. Although the resulting systems are both chemically and thermally robust mostly due to the strength of the Zr–O bond,^{15,16} the diversity of the porous features and topology relies entirely on the organic linker side. Regarding the zirconium/carboxylate entities, there are also some early works on discrete $\text{Zr}_6(\text{O})_4(\text{OH})_4$ clusters using small monocarboxylates as capping agents.^{17–20} In this context, more recently, in situ pair distribution function (PDF) analysis confirmed the presence of the hexameric zirconium cluster in the metal salt precursor/DMF/HCl solution prior to the addition of the carboxylic organic ligand.²¹ As previously stated, the novel members of the zirconium MOF family rely on increasingly more complex and expensive polycarboxylic ligands. Therefore, there is a great interest in developing novel architectures based

Received: November 5, 2021

Published: March 14, 2022



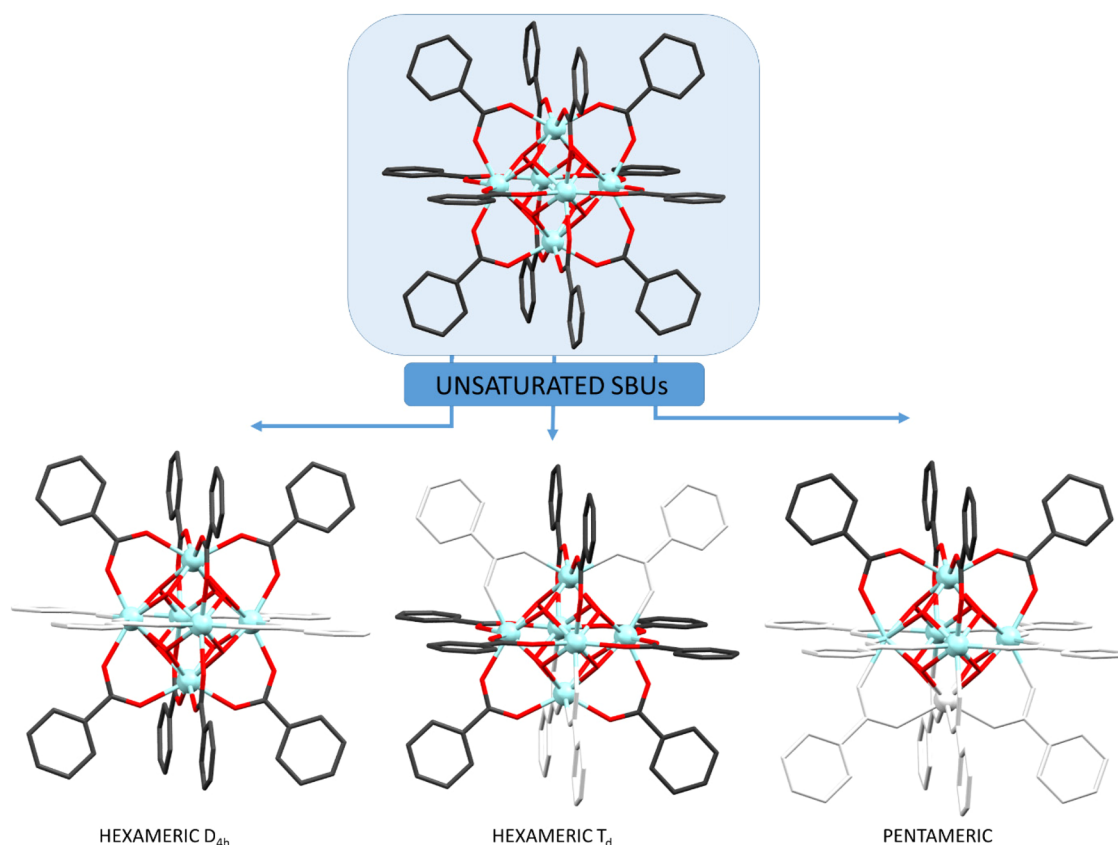


Figure 1. Schematic description of the unsaturated species obtained in this work and their relation with the well-known $[\text{Zr}_6(\text{O})_4(\text{OH})_4(\text{OOC})_{12}]$ fragment found in many MOFs (missing ligands are colored in light gray).

on low-cost aromatic polycarboxylic ligands by modifying the features of the SBUs.^{22,23} In this sense, a deep research work on the early stages of the formation of these polynuclear entities is required.²⁴ Taking into account these premises, we have thoroughly analyzed the formation of discrete zirconium-oxide-hydroxide entities in alcoholic media using simple monocarboxylic benzoato and hydroxybenzoato ligands to avoid the polymerization that would hinder this kind of studies. A crucial stage of the setup of the $\text{Zr}-\text{O}/\text{OH}$ polynuclear entities resides on the oxygen source from which these species emerge. In this sense, a precise control of the amount of water is crucial for the first steps of the formation of these entities.²⁵ On the other hand, the acidity of the reaction media exerts a strong influence on the deprotonation of the coordinated water molecules to afford bridging hydroxide and oxide anions but also on the readiness of the carboxylic ligands to coordinate to the metal centers.²⁶

Herein, we report on several discrete zirconium entities ranging from the ubiquitous hexanuclear $[\text{Zr}_6(\mu_3\text{-O})_4(\mu_3\text{-OH})_4]^{12+}$ core obtained by capping some of the linking positions of the SBUs with the anionic forms of the selected monocarboxylic ligands ($[\text{Zr}_6(\text{O})_4(\text{OH})_4(\text{L})_8(\text{H}_2\text{O})_8]^{4+}$ where $\text{L} = \text{benzoato}$ in **1** and **2**, 2-hydroxybenzoato or salicylato in **3**, and 3-hydroxybenzoato in **4**) to a previously unknown pentanuclear $[\text{Zr}_5(\mu_3\text{-O})_2(\mu_3\text{-OH})_2(\mu\text{-OH})_4]^{10+}$ core ($[\text{Zr}_5(\text{O})_2(\text{OH})_6(\text{L})_4(\text{H}_2\text{O})_{11}(\text{ROH})]^{6+}$ where $\text{L} = \text{benzoato}$; $\text{R} = \text{Et}$ in **5**, Pr in **6**). Interestingly, in the case of the former octahedral-shaped hexanuclear entities, the coordination of the carboxylic ligands can be frozen in a cationic intermediate state in which only some of the available positions are occupied, leaving what can be called a carboxylate-unsaturated SBU

(Figure 1).²⁷ It is worth mentioning that zirconium-based MOFs are frequently carboxylate-defective (due to random linker vacancies or due to the restraints coming from the topology of the framework) but, in contrast to the compounds reported herein, the charge is balanced by the incorporation at these defective positions of smaller monocarboxylato ligands (formato and acetato) or by hydroxide anions.^{28,29} It will be also shown, how the noncovalent interactions coming from the hydroxyl-substituted positions direct the arrangement of the monocarboxylic ligands toward different symmetries regarding the unoccupied carboxylato positions: these have been placed in a square arrangement for benzoato (**1** and **2**) and 3-hydroxybenzoato (**4**) ligands and in a tetrahedral one for the 2-hydroxybenzoato (**3**) ligand.

2. EXPERIMENTAL PROCEDURES

2.1. Chemicals. Zirconium(IV) chloride (ZrCl_4 , Sigma-Aldrich, anhydrous, for synthesis), benzoic acid ($\text{C}_6\text{H}_6\text{O}_2$, Sigma-Aldrich, 99.5%), salicylic acid ($\text{C}_7\text{H}_6\text{O}_3$, Sigma-Aldrich, 99%), 3-hydroxybenzoic acid ($\text{C}_7\text{H}_6\text{O}_3$, Sigma-Aldrich, 99%), absolute ethanol ($\text{C}_2\text{H}_6\text{O}$, Scharlau), propanol ($\text{C}_3\text{H}_8\text{O}$, PanReac, HPLC grade). All the chemicals were of reagent grade and used as commercially obtained, except ethanol that was dehydrated using anhydrous CaSO_4 in the synthesis of compounds **5** and **6**.

2.1.1. Synthesis of Compounds 1, 2, and 5. For the synthesis of these three compounds, a solution of 0.3870 g (1.66 mmol) of ZrCl_4 dissolved in 4.8/0.2 mL of ethanol/water solution was added dropwise to 8 mL of ethanol solution containing 0.4054 g (3.32 mmol) of benzoic acid. The resulting colorless solution was basified dropwise with water until $\text{pH} \approx 0.0$ (**2**), $\text{pH} \approx 0.5$ (**1**), or left at $\text{pH} < -0.2$ (**5**). Reaction mixtures were left to evaporate at room temperature and colorless single crystals appeared after 3–7 days.

2.1.1.1. $[Zr_6(\mu_3-O)_4(\mu_3-OH)_4(\mu-OOCC_6H_5)_8(H_2O)_8]Cl_4 \cdot EtOH \cdot 35H_2O$ (1). Main IR features (cm^{-1} ; KBr pellets): 3370vs, 1600s, 1555s, 1525s, 1495s, 14290vs, 1305m, 1180s, 1155m, 1065s, 1025s, 935m, 840w, 720s, 660vs, 465m. 1H MA NMR δ (300 MHz): 7.2 ppm [aromatic H], 3.6 ppm [Zr-OH₂]. ^{13}C MAS NMR δ (300 MHz): 172 ppm [COOH], 132 ppm [C aromatic].

2.1.1.2. $[Zr_6(\mu_3-O)_4(\mu_3-OH)_4(\mu-OOCC_6H_5)_8(H_2O)_8]Cl_4 \cdot 15H_2O$ (2). Main IR features (cm^{-1} ; KBr pellets): 3410vs, 1600s, 1555s, 1528vs, 1490s, 1420vs, 1300m, 1180s, 1155m, 1070s, 1020s, 930m, 840w, 720s, 653vs, 460m. 1H MAS NMR δ (300 MHz): 7.2 ppm [aromatic H], 3.6 ppm [Zr-OH₂]. ^{13}C MAS NMR δ (300 MHz): 172 ppm [COOH], 132 ppm [C aromatic].

2.1.1.3. $[Zr_5(\mu_3-O)_2(\mu_3-OH)_2(\mu-OH)_4(\mu-OOCC_6H_5)_4(H_2O)_{11}(EtOH)]Cl_5 \cdot 2EtOH \cdot 10H_2O$ (5). Main IR features (cm^{-1} ; KBr pellets): 3420vs, 1622w, 1640w, 1600s, 1560m, 1531vs, 1490m, 1415vs, 1310m, 1175m, 1152w, 1070m, 1018m, 942m, 840w, 720s, 674s, 650m, 524w, 458m. 1H MAS NMR δ (300 MHz): 7.0 ppm [aromatic H], 4.3 ppm [Zr-OH₂], 3.0 ppm [CH₂], 0.4 ppm [CH₃]. ^{13}C MAS NMR δ (300 MHz): 172 ppm [COOH], 130 [C aromatic], 58 ppm [CH₂], 17 ppm [CH₃].

2.1.2. **Synthesis of Compound 6.** Compound 6 was prepared by mixing a solution of ZrCl₄ (0.3870 g, 1.66 mmol) in 2.5/2.5 mL of ethanol/propanol mixture and benzoic acid (0.4054 g, 3.32 mmol) in 8 mL of propanol. The resulting colorless solution was left at pH < -0.2. Slow evaporation of the reaction mixture at room temperature yielded colorless single crystals 4 days later.

2.1.2.1. $[Zr_5(\mu_3-O)_2(\mu_3-OH)_2(\mu-OH)_4(\mu-OOCC_6H_5)_4(H_2O)_{11}(PrOH)]Cl_5 \cdot 2PrOH \cdot 11H_2O$ (6). Main IR features (cm^{-1} ; KBr pellets): 3410vs, 1622w, 1640w, 1600s, 1560s, 1520vs, 1490s, 1410vs, 1306m, 1180m, 1155w, 1070m, 1020m, 940m, 840w, 720vs, 671s, 650m, 519w, 470m. 1H MAS NMR δ (300 MHz): 7.3 ppm [aromatic H], 4.5 ppm [Zr-OH₂], 2.5 ppm [CH₂], -0.5 ppm [CH₃]. ^{13}C MAS NMR δ (300 MHz): 172 ppm [COOH], 131 [C aromatic], 63 ppm [CH₂], 22 ppm [CH₂], 9 ppm [CH₃].

2.1.3. **Synthesis of Compounds 3 and 4.** For the synthesis of these compounds, a solution of 0.3870 g (1.66 mmol) of ZrCl₄ dissolved in 4.8/0.2 mL of ethanol/water solution was added dropwise to 8 mL of ethanol solution containing the corresponding ligand, 0.4586 g (3.32 mmol) of 2-hydroxybenzoic acid for compound 3 or 3-hydroxybenzoic acid for compound 4. The resulting colorless solution was basified dropwise with water until pH \approx 0.5 (3) or pH \approx 1.0 (4). Reaction mixtures were left to evaporate at room temperature and colorless single crystals appeared after 3–7 days.

2.1.3.1. $[Zr_6(\mu_3-O)_4(\mu_3-OH)_4(\mu-OOCC_6H_5)_8(H_2O)_8]Cl_4 \cdot 28H_2O$ (3). Main IR features (cm^{-1} ; KBr pellets): 3340s, 1622s, 1586s, 1551s, 1484m, 1466s, 1395vs, 1311s, 1244vs, 1160s, 1144s, 1097m, 1026s, 951m, 808s, 755vs, 648m, 475w, 422w. 1H MAS NMR δ (300 MHz): 9.6 ppm [C-OH], 6.5 ppm [aromatic H], 2.96 ppm [Zr-OH₂]. ^{13}C MAS NMR δ (300 MHz): 173 ppm [COOH], 159 ppm [C-OH], 137 and 113 ppm [C aromatic].

2.1.3.2. $[Zr_6(\mu_3-O)_4(\mu_3-OH)_4(\mu-OOCC_6H_5)_8(H_2O)_8]Cl_4 \cdot 27H_2O$ (4). Main IR features (cm^{-1} ; KBr pellets): 3380s, 1608s, 1564s, 1533w, 1493w, 1448s, 1413s, 1302s, 1253s, 1231w, 1160m, 1120s, 1075s, 1000w, 942w, 795s, 764vs, 657vs, 457m. 1H MAS NMR δ (300 MHz): 7.1 ppm [aromatic H], 4.3 ppm [Zr-OH₂]. ^{13}C MAS NMR δ (300 MHz): 172 ppm [COOH], 154 ppm [C-OH], 132 and 120 ppm [C aromatic].

Regarding the measured pH values, if the calibration of the electrode is performed in aqueous buffers, but the measurement is performed in a different solvent, the measured pH requires to be subtracted with a correction constant: ${}^s\text{pH} = {}^w\text{pH} - \delta$, where ${}^s\text{pH}$ and ${}^w\text{pH}$ would in this case correspond to the pH for solvent media and the measured pH, while δ is a correction constant. This constant depends of the solvent and it can be approached to -2.54 for ethanol. The pH values mentioned in this work have not been corrected and correspond to ${}^s\text{pH}$.^{30,31}

2.2. Characterization. As the crystals of these compounds lose crystallinity upon their removal from the mother liquor, the purity of the samples was proved by FTIR (Fourier transform infrared spectroscopy, Table S2), TGA (thermogravimetric analysis, Table

S3) and solid state NMR (nuclear magnetic resonance) spectroscopies, together with powder X-ray diffraction (PXRD) experiments performed over samples introduced in Lindemann tubes altogether with their mother liquors and using a Debye Scherrer instrument geometry. Lindemann capillary PXRD data were collected using a Rigaku SmartLab automatic diffractometer operating at 40 kV and 50 mA. The 2θ scans in transmission mode were obtained with parallel beam configuration (CBO), a capillary attachment head, an automatic attenuator, and a 1-D DteX250 detector. The diffraction data were collected in continuous rotation, from 3 to 65° step size of 0.01° at 0.5°/min scan speed. Routine PXRD measurements on filtered off samples were performed on a Philips X'PERT diffractometer (equipped with Cu-K α radiation, $\lambda = 1.5418$ Å) over the range 5° < 2θ < 70° with a step size of 0.02°, a variable automatic divergence slit, and an acquisition time of 2.5 s per step at 293 K.

FTIR spectra of the samples (KBr pellet) were recorded at a resolution of 4 cm^{-1} in the 4000–500 cm^{-1} region using an FTIR 8400S Shimadzu spectrometer. ATR-FTIR spectra of the compounds while submerged in their mother liquids were obtained using an attenuated total reflectance (ATR) device equipped with a special concave head attached to an FTIR 8400S Shimadzu spectrometer.

Thermal analysis was performed on a METTLER TOLEDO TGA/SDTA851 thermal analyzer in a synthetic air (80% N₂, 20% O₂) flux of 50 cm^3 min⁻¹, from room temperature to 800 °C with a heating rate of 5 °C min⁻¹ and about 10–20 mg of sample per run.

Solid state NMR measurements were performed on powder samples. High-resolution solid-state NMR spectra were recorded at 298 K on a Bruker Avance 400 WB spectrometer at 9.4 T, using 100.66 and 400.17 MHz resonance frequencies. The ^{13}C experiments were performed with cross-polarization, high power decoupling, and magic angle spinning (MAS) configurations using a Bruker double-bearing probe head and 4 mm zirconia rotors driven by dry air. The MAS rates were 10 kHz. The Hartmann–Hahn conditions for ^{13}C were matched using adamantane. The recycle delay was 5 s and the contact time was 2 ms. Chemical shifts were established using glycine (Gly) as an external standard (δ_{CO} of Gly = 176.5 ppm).

Electrospray ionization mass spectrometry (MS) analysis was conducted in an infusion of the reaction mixtures to a high-resolution mass spectrometer (Synapt G2 from Waters Cromatografia S.A., time of flight analyzer) at a flow rate of 20 $\mu\text{L}/\text{min}$ by an electrospray ionization source in positive and negative modes. High resolution data were acquired in scan mode, using a mass range of 30–1200 u in resolution mode (FWHM \approx 20,000) and a scan time of 0.1 s. The source temperature was set to 120 °C and the desolvation temperature to 350 °C. The capillary voltage was 2.5 kV (negative) and the cone voltage was 15 V. Nitrogen was used as the desolvation and cone gas at flow rates of 600 and 10 L/h, respectively. Before analysis, the mass spectrometer was calibrated with a sodium formate solution and a leucine enkephalin solution was used for the lock mass correction, monitoring the ions at a mass-to-charge ratio (m/z) of 556.2771. All of the acquired spectra were automatically corrected during acquisition based on the lock mass. Further details are available in the [Supporting Information](#).

Single-crystal XRD data for structure determination were collected on Agilent Technologies Supernova diffractometers ($\lambda\text{MoK}\alpha = 0.71073$ Å for 1, 2, 3, 5 and $\text{CuK}\alpha = 1.54184$ Å for 4 and 6). The data reduction was done with the CrysAlisPro program.³² Crystal structures were solved by direct methods using the SIR92³³ and SHELXS³⁴ programs and refined by full-matrix least-squares on F^2 including all reflections (WINGX).^{35,36} Some crystal structures of some of the reported compounds show crystallographic disorder in the positions of some of the chloride anions and/or the aromatic ring of the carboxylic ligands. The disorder was modeled distributing the disordered atoms over two positions and fixing the sum of their occupation factors to one. The crystal structure of all the compounds revealed the presence of large channels in which the solvent molecules (water, ethanol, and propanol) are placed. The high disorder that solvent molecules present precluded their modeling and, as a consequence, the electron density at the voids of the crystal structure was subtracted from the reflection data by the SQUEEZE method³⁷ as

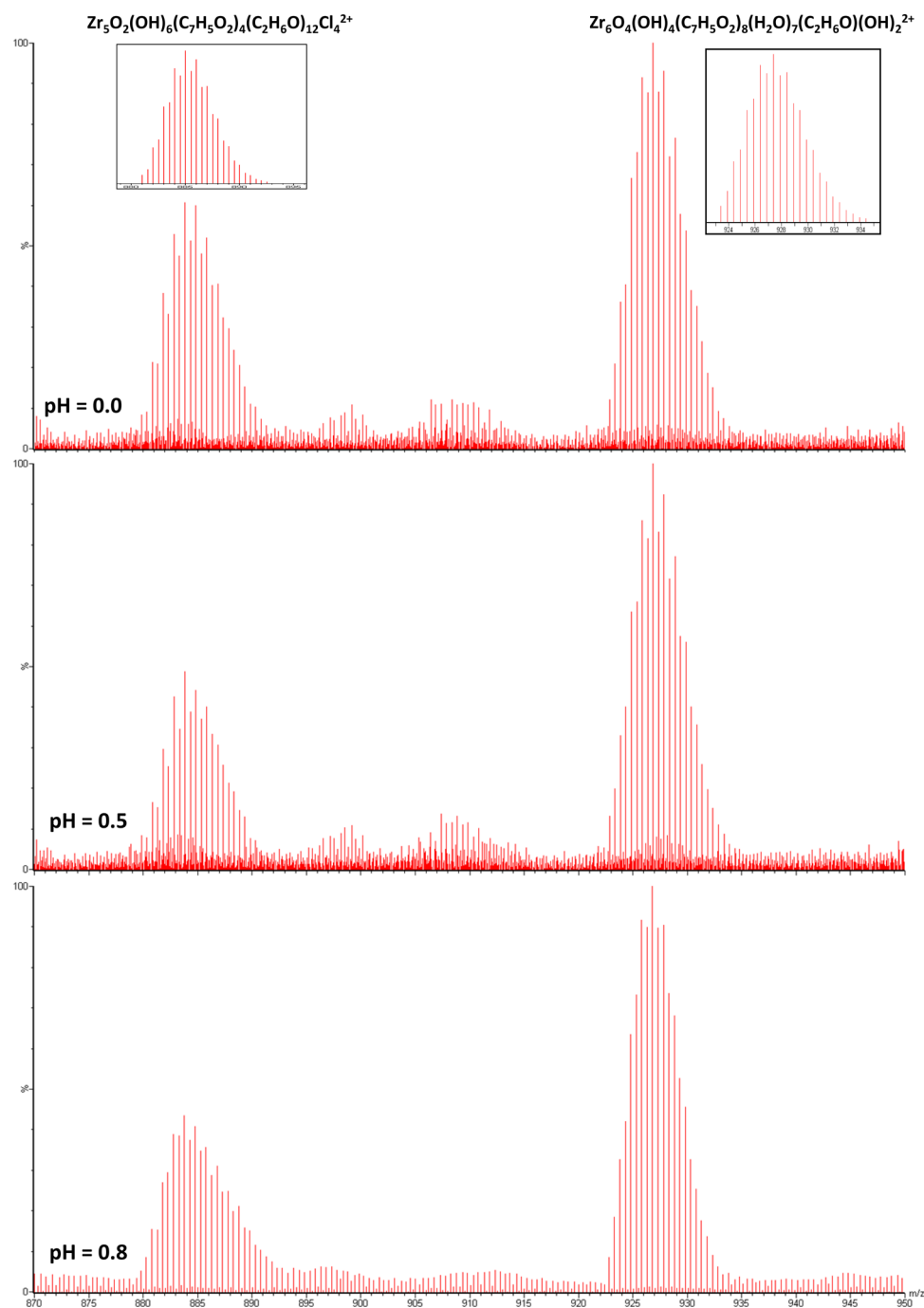


Figure 2. Influence of pH on the ESI⁺ MS spectra signals of the ZrCl₄/benzoic acid system. Signals belonging to pentameric and hexameric zirconium species are identified in the *m/z*: 870–950 range.

implemented in PLATON.³⁸ Details of the structure determination and refinement of all compounds are summarized in Table S1 in the Supporting Information.

3. RESULTS AND DISCUSSION

3.1. Mass Spectrometry. To evaluate the first stages of the clustering process, this work started with the analysis of the species present in solution upon the dissolution of ZrCl₄ and the corresponding benzoic ligand (benzoic, 2-hydroxybenzoic, or 3-hydroxybenzoic acids) in anhydrous ethanol.^{39–43} The pH value of the resulting media was controlled by the addition of water to allow a precise control of the acidity. This variation exerts a strong influence on the species that are built up as

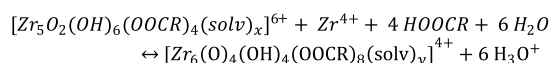
confirmed by means of MS. In these studies, the appearances of pentameric and hexameric zirconium entities in which the carboxylic ligands are coordinated to the metal centers were detected. These species were later on isolated in the solid state and their crystal structures are also reported in this work.

Figure 2 shows the ESI⁺ mass spectra in the *m/z* 870–950 range obtained for the ZrCl₄/benzoic acid system at different very acidic pH conditions (0, 0.5, and 0.8). All spectra show two major signals centered at *m/z* 884 and 927 with a 0.5 spacing of the peaks, indicative of 2+ charge states for both species. No species with charge greater than 2+ have been observed. The assigned molecular formula for the heavier signal is chemically sound and agrees well with the

$[\text{Zr}_6(\text{O})_4(\text{OH})_4]$ core features of the ubiquitous zirconium-based hexameric SBU. However, the benzoate anions only partially occupy the peripheral positions around this core in such a way that the number of carboxylate groups attached to the cluster is reduced from the expected 12 (the well-known $[\text{Zr}_6(\text{O})_4(\text{OH})_4(\text{OOC})_{12}]$ SBU found in many MOFs) to 8 providing a carboxylate-unsaturated entity. This hexameric unsaturated species incorporates two additional hydroxide anions to provide the observed 2+ charge state, and solvent molecules complete the coordination sphere of the cluster.

Similarly, the signal centered at 884 has been assigned to a pentameric zirconium entity with 2+ charge in which 12 solvent molecules, 4 benzoato ligands, and 4 chlorides stabilize a $[\text{Zr}_5(\text{O})_2(\text{OH})_6]$ core. Interestingly, the signals assigned to the hexameric and pentameric species show important modifications in their relative intensities as a function of pH. The addition of water and subsequent dilution-driven mild basification of the media results in a relative decrease of the intensity for the signal belonging to the pentameric species, whereas that related to the hexameric species increases considerably. This fact can be interpreted as an acid–base equilibrium between the two polynuclear species according to the chemical reaction provided in Scheme 1.

Scheme 1. Acid–Base Equilibrium Governing the Transformation between Pentameric and Hexameric Species



The formula obtained for the pentameric species seems to be closely related to that of the hexameric cluster by releasing one zirconium atom and losing four benzoato ligands, and at the same time, reducing the amount of oxides and increasing the hydroxide amount to keep invariable the total amount of core bridging oxide/hydroxide ligands at eight. Thus, there is a probable connection between the zirconium oxide/hydroxide species that can be rationalized starting with the well-known $[\text{Zr}_4(\text{OH})_8(\text{solv})_{16}]^{8+}$ tetrameric entity,⁴⁴ usually employed as a commercial reagent in the form of its chloride salt,⁴⁵ which in the presence of carboxylic ligands evolves to a pentanuclear $[\text{Zr}_5(\text{O})_2(\text{OH})_6(\text{OOC})_4(\text{solv})]^{6+}$ species. The greater polarization effect of the fifth zirconium(IV) center promotes the deprotonation of two of the hydroxides to provide a two oxide/six hydroxide core. Upon basification, these pentanuclear entities evolve into hexanuclear $[\text{Zr}_6(\text{O})_4(\text{OH})_4(\text{OOC})_8(\text{H}_2\text{O})]^{4+}$ species by the incorporation of a sixth zirconium that again increases the polarization at the hydroxide anions leading to a final four oxide/four hydroxide core. Further pH increases, favoring the deprotonation of the carboxylic ligands, would probably lead to the neutral $[\text{Zr}_6(\text{O})_4(\text{OH})_4(\text{OOC})_{12}]$ cluster found as an SBU in most of the zirconium-based MOFs.

The same studies performed using 2- and 3-hydroxybenzoic acid provided similar outcomes but with the presence of a greater dispersion of the pentameric and hexameric species due to variations on the solvent molecules (water and ethanol that interchange between them). They show the same 2+ *m/z* spacing in their signals and the described increase in the relative intensity of the hexameric species upon basification (see Section S5 of the Supporting Information). It is worth

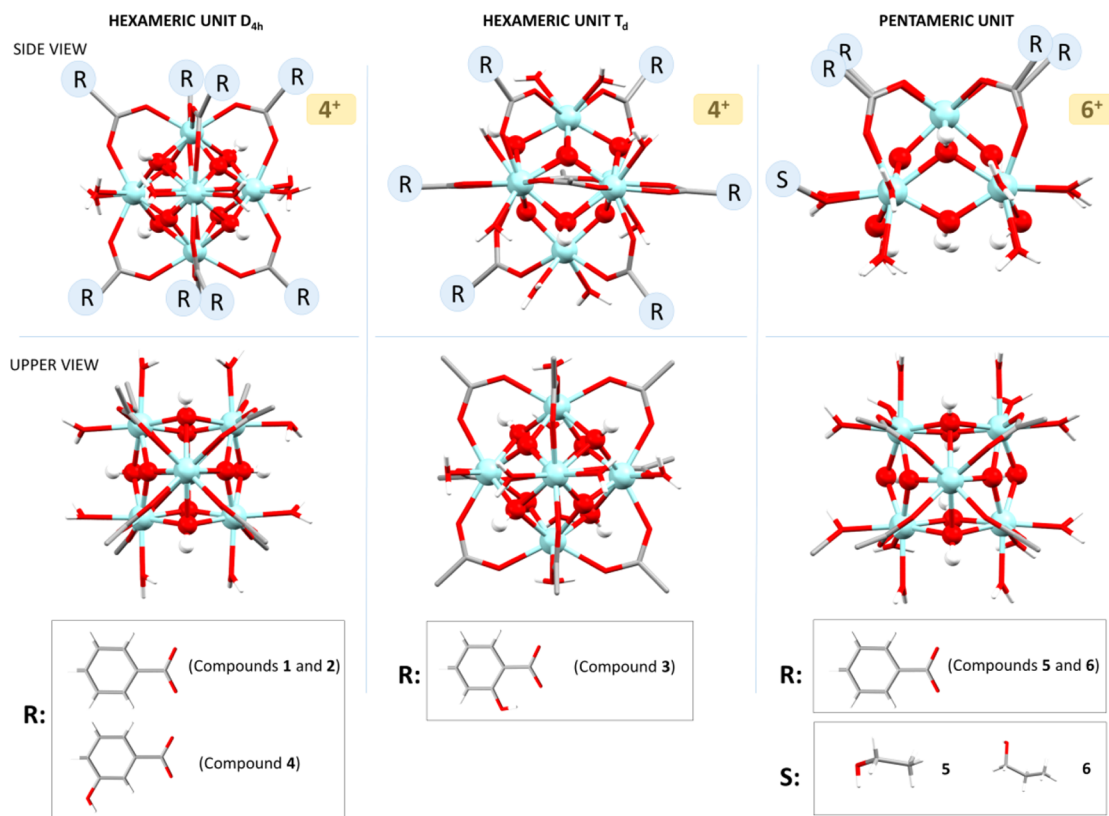


Figure 3. Summary of the polynuclear entities present in compounds 1–6.

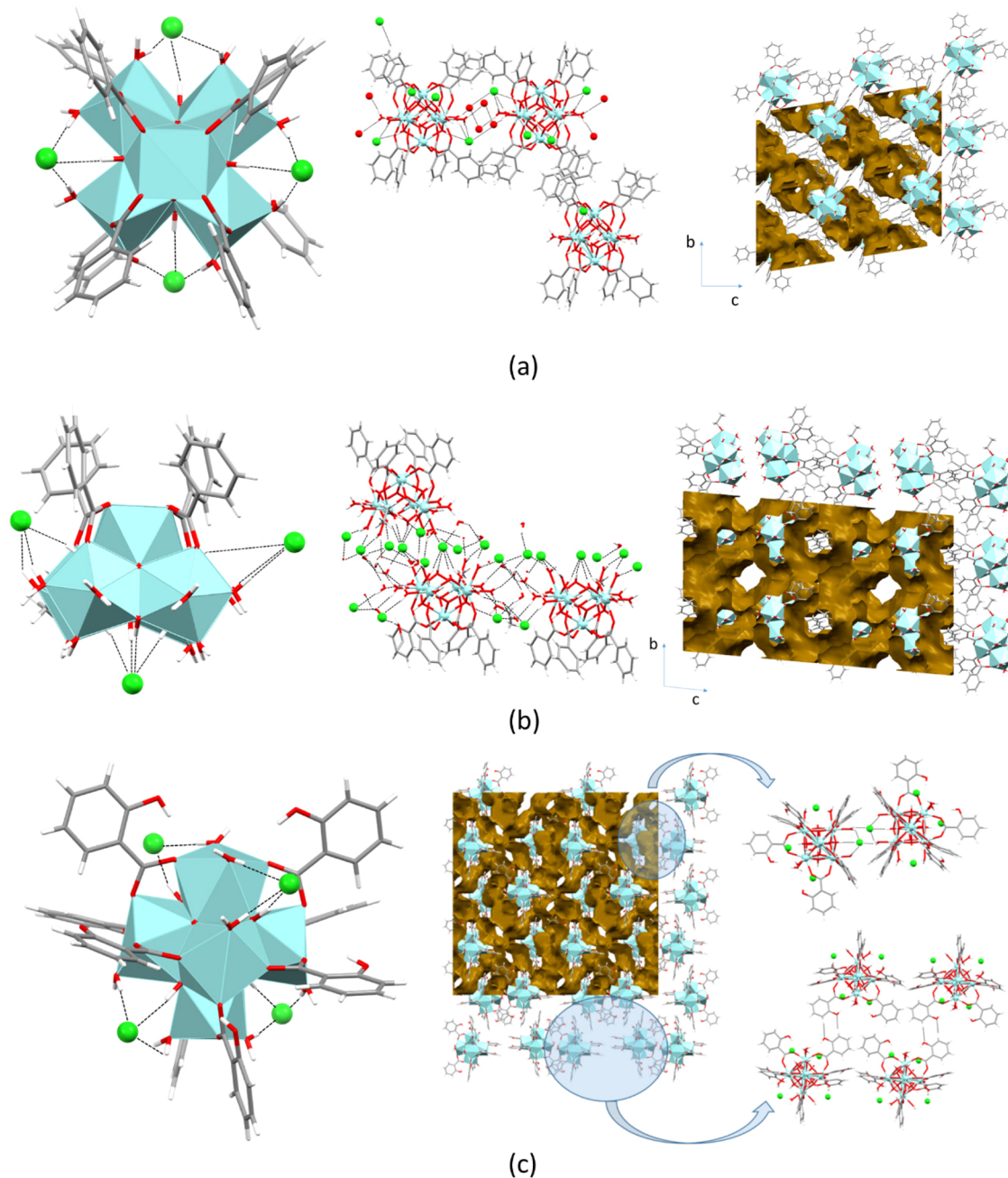


Figure 4. Structural features of compounds **1** (a), **5** (b), and **3** (c). The brownish surfaces depicted in the packing images represent the volume occupied by the noncoordinated solvent molecules.

mentioning that the basification only implies a change from pH < 0 to pH \approx 1.5.

Fortunately, these species were isolated in the solid state and a complete single-crystal XRD structural characterization was performed. As it will be shown below, the results fully corroborate the above described conclusion in such a way that we were able to isolate both pentameric $[\text{Zr}_5(\text{O})_2(\text{OH})_6(\text{OOCR})_4(\text{H}_2\text{O})_{11}(\text{HOR}')]\text{Cl}_6$ (R: C_6H_5 ; R': C_2H_5 , C_3H_7) and carboxylate-unsaturated hexameric $[\text{Zr}_6(\text{O})_4(\text{OH})_4(\text{OOCR})_8(\text{H}_2\text{O})_8]\text{Cl}_4$ (R: C_6H_5 and $\text{C}_6\text{H}_5\text{O}$) compounds as a function of pH.

3.2. Crystal Structure of the Polynuclear Entities. The crystal structure of compounds **1–6** contains the previously identified discrete polynuclear entities (hexameric for compounds **1–4**; pentameric for compounds **5** and **6**) in which the

hydroxide or oxide anions are positioned alternately in the center of each triangular face of the metal defining the square pyramid or octahedron. It means the hexameric entity has a $[\text{Zr}_6(\text{O})_4(\text{OH})_4]$ core whereas the pentamer shows a $[\text{Zr}_5(\text{O})_2(\text{OH})_6]$ core in which the lack of a sixth zirconium atom implies that the four hydroxides pointing toward the vacant are not further polarized to produce the observed alternation of oxides/hydroxides of the triangular faces (Figure 3). The external coordination positions of the metal atoms, all of them showing a cubic antiprism geometry, are occupied by water molecules and carboxylate ligands. The hexameric and pentameric polynuclear entities have a 4+ and 6+ charge, respectively, balanced by chloride counterions. The coordination bond distances found follow the same trend for all the entities. Zr–O_{oxide} distances are always the shortest ones

(2.00–2.14 Å), those involving the oxygen atoms of the carboxylate groups are between 2.16 and 2.28 Å, whereas those of hydroxides and water molecules are the longest ones with values between 2.18 and 2.37 Å. The distance between adjacent zirconium atoms within the polynuclear entities is in the range of 3.47–3.54 Å.

All compounds, except **5** and **6**, present a hexameric structure with the previously described octahedral geometry of the cluster in which instead of the expected 12 carboxylic ligands, only 8 are anchored to the hexanuclear $Zr_6(O)_4(OH)_4$ core (benzoato in **1**, **2**; 2-hydroxybenzoato in **3**; and 3-hydroxybenzoato in **4**). The remaining coordination positions lacking carboxylate groups (herein after: carboxylate-unsaturated positions) are filled with water molecules. In spite of the apparent similarity between compounds **1**–**4**, the arrangement of the carboxylato ligands provides a source of isomerism in these octahedrally shaped polynuclear entities. In compounds **1**, **2** (benzoato), and **4** (3-hydroxybenzoato), the eight carboxylate groups bridge the equatorial and apical zirconium atoms. The coordination positions located at the equatorial edges of the octahedron located are occupied by water molecules affording a D_{4h} symmetry. The metal coordination environment at the apical position consists of two oxides, two hydroxides, and four oxygen atoms from carboxylate groups. However, the equatorial zirconium coordination environment consists of two oxides, two hydroxides, and two oxygen atoms from carboxylate groups and two water molecules.

In contrast, compound **3** (2-hydroxybenzoato ligand) shares many of the features of the previously described octahedral clusters, but the presence of the hydroxyl residue so close to the $Zr_6O_4(OH)_4$ core implies that positioning four carboxylate groups around the apical zirconium positions is now disfavored and instead of the previously described D_{4h} arrangement, now a T_d symmetry is achieved. In this new arrangement, all the equatorial edges are occupied by the carboxylato ligands but only half of the equatorial–apical linking edges are occupied in an alternated way. Alternatively, it can be described focusing on the carboxylate lacking edges that are arranged in a tetrahedral disposition. Therefore, the coordination environment of the apical zirconium is composed of two oxide molecules, two hydroxides, two water molecules, and two carboxylate groups. On the other hand, the equatorial zirconium coordination environment consists of two oxides, two hydroxides, three carboxylate groups, and a single water molecule. As usually happens for 2-hydroxybenzoate anions and 2-hydroxybenzoic acid molecules, an intramolecular hydrogen bond between the hydroxyl residue and one of the carboxylate/carboxylic oxygen atoms is observed.

Compounds **5** and **6** (with benzoato ligands) consist of square-based pyramidal pentameric entities in which the absence of the sixth zirconium atom is accompanied with the reduction of the number of anchored carboxylato ligands from eight to four. These four carboxylato ligands are located bridging the zirconium atoms in the basal plane with the apical one. The lack of the sixth zirconium atom also exerts its influence in a lower polarization capacity and instead of the four oxide/four hydroxide composition for the polynuclear core, a two oxide/six hydroxide ratio is observed. Again, the remaining positions to complete the eight coordination environment of the zirconium atoms are occupied by water molecules. As a result, the coordination environment of the apical zirconium is composed of two oxides, two hydroxides, and four oxygen atoms from four carboxylate groups, whereas

the coordination environment consists of one oxide, three hydroxides, a single carboxylate oxygen atom, and three water molecules for three of the four basal plane zirconium atoms. The fourth zirconium in the basal plane shows a different coordination and gets coordinated to an alcohol molecule (ethanol in compound **5** and propanol in compound **6**). Therefore, instead of having three coordinated water molecules, it only presents two and the third one is replaced by the alcohol molecule.

The cationic nature of the polynuclear entities implies that the ionic interactions with the chloride counterions play a key role in directing the crystal packing of these compounds. In compounds **1**–**3**, ionic interactions are also reinforced by strong hydrogen bonds established by chloride counterions and the bridging hydroxide anions located in half of the triangular faces of the octahedrally shaped hexameric entities ($d_{OH...Cl}$: 2.97–3.26 Å). These chloride counterions are tetrahedrally arranged around the metal–organic clusters but the size difference between the big cationic entities and the comparatively small chloride anions make it difficult to achieve a strong packing of the crystal structure and thus requires a huge amount of solvent molecules to provide some cohesiveness to the overall 3D architecture (Figure 4). In the case of compound **4** (3-hydroxybenzoato), the hydroxyl residues protruding from the hexameric entities provide a better placement for the chloride counterions to establish hydrogen bonding interactions. These features also provide an interaction pathway between the neighboring hexameric entities, which involves 3-hydroxybenzoato ligands and the coordinated water molecules as hydrogen-bond donors toward the chloride counterions. Unfortunately, these interactions only spread along the (101) crystallographic plane and the 3D cohesiveness requires again a great amount of solvent molecules.

The 6+ charge of the pentameric species implies the presence of six chloride counterions but only three of them are strongly hydrogen bonded to the bridging hydroxide anions. Two of them, as previously described for most of the hexameric entities, imply the interaction with the hydroxides placed in the triangular faces and the third one occupies a position close to what would be the sixth zirconium atom if the cluster would have evolved toward the hexameric entity. In this position, the chloride anion acts as an acceptor of the hydrogen bonding interactions involving the four bridging hydroxides located in the basal plane of the cluster. The remaining three chloride counterions are more loosely interacting with the cluster through the coordinated water molecules. In fact, one of these chlorides is disordered over two positions indicative of the less specific interactions they establish.

In all compounds, solvent molecules account for a great portion of the total volume of the solid (21.9–33.3%) and their loss after the removal of the crystals from the mother liquid implies a transformation of the crystal structure. In fact, these great amounts of solvent molecules seem to saturate the capacity of the aromatic monocarboxylic ligands to establish supramolecular interactions, and no π -stacking has been observed among them. Only compound **3** exhibits some weak double C–H...O hydrogen bonds involving the 2-hydroxybenzoato ligands from adjacent hexanuclear entities. The fluidity of the supramolecular network involving such a huge amount of solvent molecules allows us to isolate compounds **1** and **2**, which can be considered two solvation stages of the same compound, in spite of the fact that they

exhibit completely different unit cell parameters and space group. All in all, although the structure collapse makes the characterization of bulk samples difficult, the homogeneity of the crystalline phase was assessed by PXRD analyses over samples introduced in Lindemann tubes, and the stability of the clusters upon their removal from mother liquors was addressed on the basis of solid state ^1H - and ^{13}C -MAS-NMR spectroscopy (see the details in the [Supporting Information](#)).

4. CONCLUSIONS

In summary, we have shown that there is plenty of chemistry still to be discovered about the first stages of the zirconium-carboxylate cluster formation. The results rendered here must be understood as frozen images along this process but also reveal the opportunities that arise from a fine control of the synthetic conditions. In fact, among the intermediate species that can be found in the formation of Zr-carboxylate clusters, a structure in which the 12 carboxylate ligands bridge the 12 Zr–Zr edges is the lowest in energy according to quantum mechanical calculations.⁴⁶ However, this report does not take into account the specific synthetic conditions at which these entities grow. Our work confirms that small modifications of the pH of the media can considerably affect in the isolation of clusters with different nuclearities and carboxylate-ligand contents. In addition, species with unsaturated carboxylate and/or metal positions can be a starting point to develop a richer chemistry by completing these vacancies with different carboxylic ligands or metal centers.⁴⁷ In this sense, it has been possible to isolate zirconium hexameric entities with only eight carboxylate groups attached to the cluster and the remaining free four carboxylate positions arranged in a square planar or tetrahedral disposition. An unprecedented pentameric entity closely related to the hexameric ones by the release of one of the apical zirconium positions is also achieved, being able to reveal the acid–base nature and pH dependence of the transformation between both species.

As a final remark, it is worth to mention that the results obtained here reveal that in spite of the cationic nature of the zirconium clusters reported herein, their chemistry shows some resemblance with that of the anionic polyoxometalates (POMs), as the acidity of the media is also here a key factor in the final nuclearities of the resulting clusters.⁴⁸ However, differences arise from the fact that the oxidation state of the zirconium cation is not as high as those displayed by the typical addenda metals in POMs (mainly V, Mo, and W). This implies that the polarizing capability of zirconium is not that high and it cannot promote the complete deprotonation of all the coordinated water molecules to afford an oxide rich environment able to stabilize these metal ions. Instead of this, the formation of zirconium-based entities with higher nuclearities than the classical $[\text{Zr}_4(\text{OH})_8(\text{H}_2\text{O})_{16}]^{8+}$ cation will require the presence of coordinated carboxylate groups bridging and holding together the metal centers.

■ ASSOCIATED CONTENT

SI Supporting Information

The Supporting Information is available free of charge at <https://pubs.acs.org/doi/10.1021/acs.inorgchem.1c03466>.

Details of spectroscopic data (FTIR, solid state ^1H -NMR and ^{13}C -NMR, and mass spectroscopy), thermogravimetric measurements, PXRD data collection, and crystallographic and structural data ([PDF](#))

Accession Codes

CCDC 2120125–2120130 contain the supplementary crystallographic data for this paper. These data can be obtained free of charge via www.ccdc.cam.ac.uk/data_request/cif, or by emailing data_request@ccdc.cam.ac.uk, or by contacting The Cambridge Crystallographic Data Centre, 12 Union Road, Cambridge CB2 1EZ, UK; fax: +44 1223 336033.

■ AUTHOR INFORMATION

Corresponding Author

Oscar Castillo – *Departamento de Química Orgánica e Inorgánica, Facultad de Ciencia y Tecnología, Universidad del País Vasco/Euskal Herriko Unibertsitatea, UPV/EHU, Bilbao E-48080, Spain; BCMaterials, Basque Center for Materials, Applications and Nanostructures, UPV/EHU Science Park, Leioa E-48940, Spain; orcid.org/0000-0002-5614-9301; Email: oscar.castillo@ehu.eus*

Authors

Jon Pascual-Colino – *Departamento de Química Orgánica e Inorgánica, Facultad de Ciencia y Tecnología, Universidad del País Vasco/Euskal Herriko Unibertsitatea, UPV/EHU, Bilbao E-48080, Spain*

Beñat Artetxe – *Departamento de Química Orgánica e Inorgánica, Facultad de Ciencia y Tecnología, Universidad del País Vasco/Euskal Herriko Unibertsitatea, UPV/EHU, Bilbao E-48080, Spain; orcid.org/0000-0002-7373-4596*

Garikoitz Beobide – *Departamento de Química Orgánica e Inorgánica, Facultad de Ciencia y Tecnología, Universidad del País Vasco/Euskal Herriko Unibertsitatea, UPV/EHU, Bilbao E-48080, Spain; BCMaterials, Basque Center for Materials, Applications and Nanostructures, UPV/EHU Science Park, Leioa E-48940, Spain; orcid.org/0000-0002-6262-6506*

Maria Luz Fidalgo-Mayo – *Departamento de Química Orgánica e Inorgánica, Facultad de Farmacia, Universidad del País Vasco/Euskal Herriko Unibertsitatea, UPV/EHU, Vitoria-Gasteiz E-01006, Spain*

Ainhoa Isla-López – *Departamento de Química Orgánica e Inorgánica, Facultad de Ciencia y Tecnología, Universidad del País Vasco/Euskal Herriko Unibertsitatea, UPV/EHU, Bilbao E-48080, Spain*

Antonio Luque – *Departamento de Química Orgánica e Inorgánica, Facultad de Ciencia y Tecnología, Universidad del País Vasco/Euskal Herriko Unibertsitatea, UPV/EHU, Bilbao E-48080, Spain; BCMaterials, Basque Center for Materials, Applications and Nanostructures, UPV/EHU Science Park, Leioa E-48940, Spain*

Sandra Mena-Gutiérrez – *Departamento de Química Orgánica e Inorgánica, Facultad de Ciencia y Tecnología, Universidad del País Vasco/Euskal Herriko Unibertsitatea, UPV/EHU, Bilbao E-48080, Spain*

Sonia Pérez-Yáñez – *BCMaterials, Basque Center for Materials, Applications and Nanostructures, UPV/EHU Science Park, Leioa E-48940, Spain; Departamento de Química Orgánica e Inorgánica, Facultad de Farmacia, Universidad del País Vasco/Euskal Herriko Unibertsitatea, UPV/EHU, Vitoria-Gasteiz E-01006, Spain*

Complete contact information is available at: <https://pubs.acs.org/10.1021/acs.inorgchem.1c03466>

Author Contributions

The manuscript was written through contributions of all authors. All authors have given approval to the final version of the manuscript.

Notes

The authors declare no competing financial interest.

ACKNOWLEDGMENTS

This work has been funded by Eusko Jaurlaritza/Gobierno Vasco (IT1291-19), Universidad del País Vasco/Euskal Herriko Unibertsitatea (predoctoral fellowship for J.P.C.), and Ministerio de Ciencia e Innovación (PID2019-108028GB-C21). Technical and human support provided by SGIker (UPV/EHU, MICINN, GV/EJ, ESF) is also acknowledged.

REFERENCES

- (1) Vardhan, H.; Yusubov, M.; Verpoort, F. Self-Assembled Metal-Organic Polyhedra: An Overview of Various Applications. *Coord. Chem. Rev.* **2016**, *306*, 171–194.
- (2) Mínguez Espallargas, G.; Coronado, E. Magnetic Functionalities in MOFs: From the Framework to the Pore. *Chem. Soc. Rev.* **2018**, *47*, 533–557.
- (3) Sarker, M.; Jhung, S. H. Zr-MOF with Free Carboxylic Acid for Storage and Controlled Release of Caffeine. *J. Mol. Liq.* **2019**, *296*, No. 112060.
- (4) Samanta, S. K.; Isaacs, L. Biomedical Applications of Metal Organic Polygons and Polyhedra (MOPs). *Coord. Chem. Rev.* **2020**, *410*, No. 213181.
- (5) Ju, Z.; Liu, G.; Chen, Y. S.; Yuan, D.; Chen, B. From Coordination Cages to a Stable Crystalline Porous Hydrogen-Bonded Framework. *Chem. – Eur. J.* **2017**, *23*, 4774–4777.
- (6) Zhou, H.-C. L.; Jeffrey, R.; Yaghi, O. M. Introduction to Metal – Organic Frameworks. *Chem. Rev.* **2012**, *112*, 673–674.
- (7) Eddaoudi, M.; Moler, D. B.; Li, H.; Chen, B.; Reineke, T. M.; O’Keeffe, M.; Yaghi, O. M. Modular Chemistry: Secondary Building Units as a Basis for the Design of Highly Porous and Robust Metal-Organic Carboxylate Frameworks. *Acc. Chem. Res.* **2001**, *34*, 319–330.
- (8) Yaghi, O. M.; O’Keeffe, M.; Ockwig, N. W.; Chae, H. K.; Eddaoudi, M.; Kim, J. Reticular Synthesis and the Design of New Materials. *Nature* **2003**, *423*, 705–714.
- (9) Chen, T. H.; Popov, I.; Kaveevitvachai, W.; Miljanić, O. Š. Metal-Organic Frameworks: Rise of the Ligands. *Chem. Mater.* **2014**, *26*, 4322–4325.
- (10) Qin, J. S.; Yuan, S.; Zhang, L.; Li, B.; Du, D. Y.; Huang, N.; Guan, W.; Drake, H. F.; Pang, J.; Lan, Y. Q.; Alsalmeh, A.; Zhou, H. C. Creating Well-Defined Hexabenzocoronene in Zirconium Metal-Organic Framework by Postsynthetic Annulation. *J. Am. Chem. Soc.* **2019**, *141*, 2054–2060.
- (11) Xu, X.; Li, S.; Liu, Q.; Liu, Z.; Yan, W.; Zhao, L.; Zhang, W.; Zhang, L.; Deng, F.; Cong, H.; Deng, H. Isolated π -Interaction Sites in Mesoporous MOF Backbone for Repetitive and Reversible Dynamics in Water. *ACS Appl. Mater. Interfaces* **2019**, *11*, 973–981.
- (12) Mallick, A.; Liang, H.; Shekhah, O.; Jia, J.; Mouchaham, G.; Shkurenko, A.; Belmabkhout, Y.; Alshareef, H. N.; Eddaoudi, M. Made-to-Order Porous Electrodes for Supercapacitors: MOFs Embedded with Redox-Active Centers as a Case Study. *Chem. Commun.* **2020**, *56*, 1883–1886.
- (13) Cheng, S.; Chen, W.; Zhao, L.; Wang, X.; Qin, C.; Su, Z. Synthesis, Crystal Structure and Iodine Capture of Zr-Based Metal-Organic Polyhedron. *Inorg. Chim. Acta* **2021**, *516*, No. 120174.
- (14) Gosselin, A. J.; Rowland, C. A.; Bloch, E. D. Permanently Microporous Metal-Organic Polyhedra. *Chem. Rev.* **2020**, *120*, 8987–9014.
- (15) Bai, Y.; Dou, Y.; Xie, L. H.; Rutledge, W.; Li, J. R.; Zhou, H. C. Zr-Based Metal-Organic Frameworks: Design, Synthesis, Structure, and Applications. *Chem. Soc. Rev.* **2016**, *45*, 2327–2367.
- (16) Burch, N. C.; Jasuja, H.; Walton, K. S. Water Stability and Adsorption in Metal-Organic Frameworks. *Chem. Rev.* **2014**, *114*, 10575–10612.
- (17) Kickelbick, G.; Schubert, U. Oxozirconium Methacrylate Clusters: $Zr_6(OH)_4O_4(OMc)_{12}$ and $Zr_4O_2(OMc)_{12}$ (OMc = Methacrylate). *Chem. Ber./Recl.* **1997**, *130*, 473–478.
- (18) Kickelbick, G.; Wiede, P.; Schubert, U. Variations in capping the $Zr_6O_4(OH)_4$ cluster core: X-ray structure analyses of $[Zr_6(OH)_4O_4(OOC-CH=CH_2)_{10}]_2(\mu-OOC-CH=CH_2)_4$ and $Zr_6(OH)_4O_4(OOCR)_{12}(PrOH)$ (R = Ph, CMe=CH₂). *Inorg. Chim. Acta* **1999**, *284*, 1–7.
- (19) Piszczek, P.; Radtke, A.; Grodzicki, A.; Wojtczak, A.; Chojnacki, J. The new type of $[Zr_6(\mu_3-O)_4(\mu_3-OH)_4]$ cluster core: Crystal structure and spectral characterization of $[Zr_6O_4(OH)_4(OOCR)_{12}]$ (R = But, C(CH₃)₂Et). *Polyhedron* **2007**, *26*, 679–685.
- (20) Gao, Y.; Kogler, F. R.; Peterlik, H.; Schubert, U. Ring-opening metathesis polymerizations with norbornene carboxylate-substituted metal oxo clusters. *J. Mater. Chem.* **2006**, *16*, 3268–3276.
- (21) Xu, H.; Sommer, S.; Broge, N. L. N.; Gao, J.; Iversen, B. B. The Chemistry of Nucleation: In Situ Pair Distribution Function Analysis of Secondary Building Units During UiO-66 MOF Formation. *Chem. – Eur. J.* **2019**, *25*, 2051–2058.
- (22) Marshall, R. J.; Forgan, R. S. Postsynthetic Modification of Zirconium Metal-Organic Frameworks. *Eur. J. Inorg. Chem.* **2016**, *2016*, 4310–4331.
- (23) García-Raso, A.; Terrón, A.; Roselló, Y.; Frontera, A.; Castillo, O.; Beobide, G.; Pérez-Yáñez, S.; Escudero-Adán, E. C.; Fiol, J. J. Metal Removal from the Secondary Building Unit of Bio-MOF-1 by Adenine N6-Alkylation While Retaining the Overall 3D Porous Topology. *CrystEngComm* **2020**, *22*, 4201–4205.
- (24) Chen, Z.; Hanna, S. L.; Redfern, L. R.; Alezi, D.; Islamoglu, T.; Farha, O. K. Reticular Chemistry in the Rational Synthesis of Functional Zirconium Cluster-Based MOFs. *Coord. Chem. Rev.* **2019**, *386*, 32–49.
- (25) Stern, R. D.; Kingsbury, R. S.; Persson, K. A. Aqueous Stability of Zirconium Clusters, Including the Zr(IV) Hexanuclear Hydrolysis Complex $[Zr_6O_4(OH)_4(H_2O)_{24}]^{12+}$, from Density Functional Theory. *Inorg. Chem.* **2021**, *60*, 15456–15466.
- (26) Santos-Lorenzo, J.; San José-Velado, R.; Albo, J.; Beobide, G.; Castaño, P.; Castillo, O.; Luque, A.; Pérez-Yáñez, S. A Straightforward Route to Obtain Zirconium Based Metal-Organic Gels. *Microporous Mesoporous Mater.* **2019**, *284*, 128–132.
- (27) Pan, L.; Heddy, R.; Li, J.; Zheng, C.; Huang, X. Y.; Tang, X.; Kilpatrick, L. Synthesis and Structural Determination of a Hexanuclear Zirconium Glycine Compound Formed in Aqueous Solution. *Inorg. Chem.* **2008**, *47*, 5537–5539.
- (28) Feng, L.; Pang, J.; She, P.; Li, J.-L.; Qin, J.-S.; Du, D.-Y.; Zhou, H.-C. Metal-Organic Frameworks Based on Group 3 and 4 Metals. *Adv. Mater.* **2020**, *32*, No. 2004414.
- (29) Hurlock, M. J.; Hao, L.; Kriegsman, K. W.; Guo, X.; O’Keeffe, M.; Zhang, Q. Evolution of 14-Connected Zr_6 Secondary Building Units through Postsynthetic Linker Incorporation. *ACS Appl. Mater. Interfaces* **2021**, *13*, 51945–51953.
- (30) Bates, R. G.; Paabo, M.; Robinson, R. A. Interpretation of PH Measurements in Alcohol-Water Solvents. *J. Phys. Chem.* **1963**, *67*, 1833–1838.
- (31) Gibson, G. T. T.; Mohamed, M. F.; Neverov, A. A.; Brown, R. S. Potentiometric Titration of Metal Ions in Ethanol. *Inorg. Chem.* **2006**, *45*, 7891–7902.
- (32) Agilent Technologies UK Ltd. *CrysAlisPRO*, Oxford Diffraction; Agilent Technologies UK Ltd: Yarnton, England.
- (33) Altomare, A.; Cascarano, G.; Giacovazzo, C.; Guagliardi, A.; Burla, M. C.; Polidori, G.; Camalli, M. SIRPOW.92 – a Program for Automatic Solution of Crystal Structures by Direct Methods Optimized for Powder Data. *J. Appl. Crystallogr.* **1994**, *27*, 435–436.
- (34) Sheldrick, G. M. A Short History of SHELX. *Acta Crystallogr., Sect. A: Found. Crystallogr.* **2008**, *64*, 112–122.
- (35) Sheldrick, G. M. Crystal Structure Refinement with SHELXL. *Acta Crystallogr., Sect. C: Struct. Chem.* **2015**, *71*, 3–8.

- (36) Farrugia, L. J. WinGX and ORTEP for Windows: An Update. *J. Appl. Crystallogr.* **2012**, *45*, 849–854.
- (37) Spek, A. L. PLATON SQUEEZE: A Tool for the Calculation of the Disordered Solvent Contribution to the Calculated Structure Factors. *Acta Crystallogr., Sect. C: Struct. Chem.* **2015**, *71*, 9–18.
- (38) Spek, A. L. Single-Crystal Structure Validation with the Program PLATON. *J. Appl. Crystallogr.* **2003**, *36*, 7–13.
- (39) Ji, B.-Q.; Su, H.-F.; Jagodič, M.; Jagličić, Z.; Kurmoo, M.; Wang, X.-P.; Tung, C.-H.; Cao, Z.-Z.; Sun, D. Self-Organization into Preferred Sites by Mg^{II}, Mn^{II}, and Mn^{III} in Brucite-Structured M₁₉ Cluster. *Inorg. Chem.* **2019**, *58*, 3800–3806.
- (40) Guo, L.-Y.; Su, H.-F.; Kurmoo, M.; Tung, C.-H.; Sun, D.; Zheng, L.-S. Core–Shell {Mn₇C(Mn,Cd)₁₂} Assembled from Core {Mn₇} Disc. *J. Am. Chem. Soc.* **2017**, *139*, 14033–14036.
- (41) Deng, Y.-K.; Su, H.-F.; Xu, J.-H.; Wang, W.-G.; Kurmoo, M.; Lin, S.-C.; Tan, Y.-Z.; Jia, J.; Sun, D.; Zheng, L. S. Hierarchical Assembly of a {Mn^{II}₁₅Mn^{III}₄} Brucite Disc: Step-by-Step Formation and Ferrimagnetism. *J. Am. Chem. Soc.* **2016**, *138*, 1328–1334.
- (42) Hu, Y.-Q.; Zeng, M.-H.; Zhang, K.; Hu, S.; Zhou, F.-F.; Kurmoo, M. Tracking the Formation of a Polynuclear Co₁₆ Complex and Its Elimination and Substitution Reactions by Mass Spectroscopy and Crystallography. *J. Am. Chem. Soc.* **2013**, *135*, 7901–7908.
- (43) Wang, Z.; Zhuo, H.-Y.; Hu, A.-Y.; Su, H.-F.; Zhao, Q.-Q.; Wang, X.-P.; Tung, C.-H.; Sun, D. Self-Assembly of A Novel Ag₄₈ Cluster Encapsulating an Unprecedented [Mo₈O₂₈]⁸⁻ Anion Template. *Isr. J. Chem.* **2019**, *59*, 280–285.
- (44) Rao, N.; Holerca, M. N.; Klein, M. L.; Pophristic, V. Computational Study of the Zr⁴⁺ Tetranuclear Polymer, [Zr₄(OH)₈(H₂O)₁₆]⁸⁺. *J. Phys. Chem. A* **2007**, *111*, 11395–11399.
- (45) Clearfield, A.; Vaughan, P. A. The Crystal Structure of Zirconyl Chloride Octahydrate and Zirconyl Bromide Octahydrate. *Acta Crystallogr.* **1956**, *9*, 555–558.
- (46) Walther, P.; Puchberger, M.; Kogler, F. R.; Schwarz, K. Ligand dynamics on the surface of zirconium oxo clusters. *Phys. Chem. Chem. Phys.* **2009**, *11*, 3640–3647.
- (47) Ma Ntep, T. J. M.; Reinsch, H.; Moll, B.; Hastürk, E.; Gökpinar, S.; Breitzke, H.; Schlüsener, C.; Schmolke, L.; Buntkowsky, G.; Janiak, C. Realizing the Potential of Acetylenedicarboxylate by Functionalization to Halofumarate in Zr^{IV} Metal–Organic Frameworks. *Chem. – Eur. J.* **2018**, *24*, 14048–14053.
- (48) Gumerova, N. I.; Rompel, A. Polyoxometalates in Solution: Speciation under Spotlight. *Chem. Soc. Rev.* **2020**, *49*, 7568–7601.

Recommended by ACS

Highly Active Homoleptic Zinc and Magnesium Complexes Supported by Constrained Reduced Schiff Base Ligands for the Ring-Opening Polymerization o...

Tanyawan Pongpanit, Khamphree Phomphrai, *et al.*

OCTOBER 04, 2021
INORGANIC CHEMISTRY

READ 

Time-Dependent Self-Assembly of Copper(II) Coordination Polymers and Tetranuclear Rings: Catalysts for Oxidative Functionalization of Saturate...

Ines F. M. Costa, Alexander M. Kirillov, *et al.*

JUNE 15, 2021
INORGANIC CHEMISTRY

READ 

In Situ Versus Isolated Zinc Catalysts in the Selective Synthesis of Homo and Multi-block Polyesters

Weronika Gruszka, Jennifer A. Garden, *et al.*

MAY 19, 2020
MACROMOLECULES

READ 

Cooperative Heterometallic Catalysts for Lactide Ring-Opening Polymerization: Combining Aluminum with Divalent Metals

Anand J. Gaston, Jennifer A. Garden, *et al.*

JANUARY 29, 2021
INORGANIC CHEMISTRY

READ 

Get More Suggestions >

Este trabajo de tesis tiene por objetivo generar materiales donde se combinen porosidad con otra propiedad fácilmente medible para generar sensores químicos. En este sentido los materiales con porosidad elevada son ideales porque habilitan una fuerte interacción con las moléculas en disolución. En este trabajo se centra en dos tipos de materiales, los SMOFs (con microporosidad $< 2\text{nm}$) y los MOGs (con meso/macroporosidad $> 2\text{nm}$). Por otro lado, la incorporación de una segunda propiedad como el magnetismo o la luminiscencia, requiere de constituyentes muy diferentes. Para disponer de propiedades magnéticas se necesita de la incorporación de materiales con centros paramagnéticos, pero en el caso de las propiedades luminiscentes necesitamos de centros metálicos de capa completa para evitar el quencheo de la señal. Estos mismos materiales se han empleado como precursores de nanopartículas metálicas soportadas sobre una matriz carbonosa que funcionan como eficientes catalizadores de la termorreducción del CO_2 con una alta selectividad hacia CO .

Por lo tanto, se han generado dos familias de materiales, una primera basada en entidades $[\text{Cu}_6\text{M}(\text{OH})_6(\text{adeninato})_6(\text{H}_2\text{O})_6]^{n+}$ (M: Co^{II} , Ni^{II} , Cu^{II} , Zn^{II}) que se ensamblan junto con aniones orgánicos (derivados de nucleobases y moléculas carboxílicas aromáticas, principalmente) para dar lugar a un material poroso (SMOF) con interesantes propiedades magnéticas que permite cuantificar la cantidad de adsorbato incorporado por el material en disolución. La segunda familia basada en materiales metal-orgánicos de $\text{Zr}(\text{IV})$ que se caracterizan por su elevada estabilidad química y por no quenchar la señal luminiscente. Sin embargo, para ser capaces de incorporar diferentes fluoróforos carboxílicos a este material, se ha realizado un estudio previo sobre la formación de los clústeres $[\text{Zr}_6\text{O}_4(\text{OH})_4(\text{OOCR})_x]$ en los estadios iniciales de formación de estos materiales. Así se pudo determinar las condiciones sintéticas requeridas para incorporar de forma simultánea hasta tres fluoróforos que emiten en el azul, amarillo y rojo, respectivamente. La interacción de estos fluoróforos con las moléculas adsorbidas en disolución modifica las señales luminiscentes dando lugar a un color y unas intensidades relativas de las tres emisiones que es característica de la molécula adsorbida.



eman ta zabal zazu

